SYNCHRONIZATION, SWARMING AND EMERGENT BEHAVIORS IN COMPLEX NETWORKS AND NEUROSCIENCE

EDITED BY: Andrea Duggento, Spase Petkoski, Tomislav Stankovski and Nicola Toschi

PUBLISHED IN: Frontiers in Systems Neuroscience, Frontiers in Computational Neuroscience and Frontiers in Physics



frontiers Research Topics



frontiers

Frontiers eBook Copyright Statement

The copyright in the text of individual articles in this eBook is the property of their respective authors or their respective institutions or funders. The copyright in graphics and images within each article may be subject to copyright of other parties. In both cases this is subject to a license granted to Frontiers.

The compilation of articles constituting this eBook is the property of Frontiers.

Each article within this eBook, and the eBook itself, are published under the most recent version of the Creative Commons CC-BY licence. The version current at the date of publication of this eBook is CC-BY 4.0. If the CC-BY licence is updated, the licence granted by Frontiers is automatically updated to the new version.

When exercising any right under the CC-BY licence, Frontiers must be attributed as the original publisher of the article or eBook, as applicable.

Authors have the responsibility of ensuring that any graphics or other materials which are the property of others may be included in the CC-BY licence, but this should be checked before relying on the CC-BY licence to reproduce those materials. Any copyright notices relating to those materials must be complied with.

Copyright and source acknowledgement notices may not be removed and must be displayed in any copy, derivative work or partial copy which includes the elements in question.

All copyright, and all rights therein, are protected by national and international copyright laws. The above represents a summary only. For further information please read Frontiers' Conditions for Website Use and Copyright Statement, and the applicable CC-BY licence.

ISSN 1664-8714
ISBN 978-2-88974-503-6
DOI 10.3389/978-2-88974-503-6

About Frontiers

Frontiers is more than just an open-access publisher of scholarly articles: it is a pioneering approach to the world of academia, radically improving the way scholarly research is managed. The grand vision of Frontiers is a world where all people have an equal opportunity to seek, share and generate knowledge. Frontiers provides immediate and permanent online open access to all its publications, but this alone is not enough to realize our grand goals.

Frontiers Journal Series

The Frontiers Journal Series is a multi-tier and interdisciplinary set of open-access, online journals, promising a paradigm shift from the current review, selection and dissemination processes in academic publishing. All Frontiers journals are driven by researchers for researchers; therefore, they constitute a service to the scholarly community. At the same time, the Frontiers Journal Series operates on a revolutionary invention, the tiered publishing system, initially addressing specific communities of scholars, and gradually climbing up to broader public understanding, thus serving the interests of the lay society, too.

Dedication to Quality

Each Frontiers article is a landmark of the highest quality, thanks to genuinely collaborative interactions between authors and review editors, who include some of the world's best academicians. Research must be certified by peers before entering a stream of knowledge that may eventually reach the public - and shape society; therefore, Frontiers only applies the most rigorous and unbiased reviews.
Frontiers revolutionizes research publishing by freely delivering the most outstanding research, evaluated with no bias from both the academic and social point of view. By applying the most advanced information technologies, Frontiers is catapulting scholarly publishing into a new generation.

What are Frontiers Research Topics?

Frontiers Research Topics are very popular trademarks of the Frontiers Journals Series: they are collections of at least ten articles, all centered on a particular subject. With their unique mix of varied contributions from Original Research to Review Articles, Frontiers Research Topics unify the most influential researchers, the latest key findings and historical advances in a hot research area! Find out more on how to host your own Frontiers Research Topic or contribute to one as an author by contacting the Frontiers Editorial Office: frontiersin.org/about/contact

SYNCHRONIZATION, SWARMING AND EMERGENT BEHAVIORS IN COMPLEX NETWORKS AND NEUROSCIENCE

Topic Editors:
Andrea Duggento, University of Rome Tor Vergata, Italy
Spase Petkoski, INSERM U1106 Institut de Neurosciences des Systèmes, France
Tomislav Stankovski, Saints Cyril and Methodius University of Skopje, North Macedonia
Nicola Toschi, University of Rome Tor Vergata, Italy

Citation: Duggento, A., Petkoski, S., Stankovski, T., Toschi, N., eds. (2022). Synchronization, Swarming and Emergent Behaviors in Complex Networks and Neuroscience. Lausanne: Frontiers Media SA. doi: 10.3389/978-2-88974-503-6

Table of Contents

05 ***Editorial: Synchronization, Swarming and Emergent Behaviors in Complex Networks and Neuroscience***
Andrea Duggento, Spase Petkoski, Tomislav Stankovski and Nicola Toschi

08 ***Global vs. Network-Specific Regulations as the Source of Intrinsic Coactivations in Resting-State Networks***
Shiori Amemiya, Hidemasa Takao and Osamu Abe

20 ***Cooperative Phase Adaptation and Amplitude Amplification of Neuronal Activity in the Vagal Complex: An Interplay Between Microcircuits and Macrocircuits***
Yoshinori Kawai

31 ***Cross-Frequency Coupling in Descending Motor Pathways: Theory and Simulation***
Nirvik Sinha, Julius P. A. Dewald, Charles J. Heckman and Yuan Yang

44 ***Neuronal Degeneration Impairs Rhythms Between Connected Microcircuits***
Samantha N. Schumm, David Gabrieli and David F. Meaney

62 ***Normal Aging: Alterations in Scalp EEG Using Broadband and Band-Resolved Topographic Maps***
Ehtasham Javed, Pierpaolo Croce, Filippo Zappasodi and Cosimo Del Gratta

75 ***Ghost Attractors in Spontaneous Brain Activity: Recurrent Excursions Into Functionally-Relevant BOLD Phase-Locking States***
Jakub Vohryzek, Gustavo Deco, Bruno Cessac, Morten L. Kringelbach and Joana Cabral

90 ***Synaptic Diversity Suppresses Complex Collective Behavior in Networks of Theta Neurons***
Lucas Lin, Ernest Barreto and Paul So

107 ***Theta-Nested Gamma Oscillations in Next Generation Neural Mass Models***
Marco Segneri, Hongjie Bi, Simona Olmi and Alessandro Torcini

125 ***Emergence of Mixed Mode Oscillations in Random Networks of Diverse Excitable Neurons: The Role of Neighbors and Electrical Coupling***
Subrata Ghosh, Argha Mondal, Peng Ji, Arindam Mishra, Syamal K. Dana, Chris G. Antonopoulos and Chittaranjan Hens

136 ***Multifractal and Entropy-Based Analysis of Delta Band Neural Activity Reveals Altered Functional Connectivity Dynamics in Schizophrenia***
Frigyes Samuel Racz, Orestis Stylianou, Peter Mukli and Andras Eke

158 ***Spiking Correlation Analysis of Synchronous Spikes Evoked by Acupuncture Mechanical Stimulus***
Qing Qin, Ya-Jiao Liu, Bo-Nan Shan, Yan-Qiu Che, Chun-Xiao Han, Ying-Mei Qin and Jiang Wang

171 ***Topographic Organization of Correlation Along the Longitudinal and Transverse Axes in Rat Hippocampal CA3 Due to Excitatory Afferents***
Gene J. Yu, Jean-Marie C. Bouteiller and Theodore W. Berger

190 ***On the Validity of Neural Mass Models***
Nicolás Deschle, Juan Ignacio Gossn, Prejaas Tewarie, Björn Schelter and Andreas Daffertshofer

202 ***Scale-Free Dynamics in Animal Groups and Brain Networks***
Tiago L. Ribeiro, Dante R. Chialvo and Dietmar Plenz

212 ***Beta2 Oscillations in Hippocampal-Cortical Circuits During Novelty Detection***
Arthur S. C. França, Nils Z. Borgesius, Bryan C. Souza and Michael X. Cohen

228 ***A Comprehensive Analysis of Multilayer Community Detection Algorithms for Application to EEG-Based Brain Networks***
Maria Grazia Puxeddu, Manuela Petti and Laura Astolfi

245 ***Machine Learning Assisted Chimera and Solitary States in Networks***
Niraj Kushwaha, Naveen Kumar Mendola, Saptarshi Ghosh, Ajay Deep Kachhvah and Sarika Jalan

259 ***Pelvic Pain Alters Functional Connectivity Between Anterior Cingulate Cortex and Hippocampus in Both Humans and a Rat Model***
Wenjun Yu, Xiaoyan Wu, Yunan Chen, Zhiying Liang, Jinxiang Jiang, Afzal Misrani, Yun Su, Yigang Peng, Jian Chen, Binliang Tang, Mengyao Sun, Cheng Long, Jun Shen and Li Yang

frontiers in Computational Neuroscience

EDITORIAL
published: 07 March 2022
doi: 10.3389/fncom.2022.846189

Editorial: Synchronization, Swarming and Emergent Behaviors in Complex Networks and Neuroscience

Andrea Duggento[1]*, *Spase Petkoski*[2], *Tomislav Stankovski*[3,4] and *Nicola Toschi*[1,5]

[1] Department of Biomedicine and Prevention, University of Rome Tor Vergata, Rome, Italy, [2] Institut de Neurosciences des Systèmes, INS, INSERM, Aix Marseille Université, Marseille, France, [3] Faculty of Medicine, Ss Cyril and Methodius University, Skopje, North Macedonia, [4] Department of Physics, Lancaster University, Lancaster, United Kingdom, [5] Department of Radiology, Athinoula A. Martinos Center for Biomedical Imaging, Boston, MA, United States

Keywords: synchronization, time-delayed coupling, swarmalators, brain dynamics, complex networks, effective connectivity, dynamical systems, emergent

Editorial on the Research Topic

Synchronization, Swarming and Emergent Behaviors in Complex Networks and Neuroscience

A vast number of systems in nature display the peculiar ability to spontaneously enter synchrony across multiple spatial and temporal scales, and the study of natural synchronization has inspired numerous transdisciplinary applications in fields ranging from sensor networks and signal transmission to systems biology and physiological systems dynamics. While synchronization between sub-units has been vastly investigated as a function of local as well as coupling dynamics, the recent advent and exponential growth of complex network science has provided novel, fertile ground for deepening our insight into synchronization phenomena as a function of intrinsic, possibly dynamical network properties.

For example, the study of synchronization in hierarchical networks and, in particular, of how global dynamics can emerge from different network motifs and how mesoscale topology and time-delays due to propagation, as well as microscopic properties can influence whole-network synchronization, is beginning to provide solid stepping-stones for a better understanding of complex neuronal networks. In this context, recent neuroscience research has suggested that the synchronization of low-level elements in neural populations are instrumental to the dynamical emergence of higher-lever neural functional units, which in turn interact to generate and regulate complex behavioral patterns in health and disease. Recent simultaneous macro- (gross neural activities) and the micro- (single/multi-neuron activities) scale assessments are also providing evidence for complex, cross-scale brain interactions which are not yet well understood.

The study of synchronization in time-varying networks has very recently posited the existence of so-called "chimera-states", whose appearance and disappearance in neuronal networks has been explained as an interplay of integration and segregation which gives rise to metastability. Similarly, the study of swarming in natural systems has very recently prompted ideas that exploit similarities with synchronization phenomena to define so-called "swarmalators", i.e., units that are able to both swarm and synch, and are possibly governed by unifying physical principles such as energy conservation. Such systems exhibit rich spatiotemporal dynamics and may offer additional insight into mechanistic as well as statistical modeling for natural systems, as well as potential technological applications such as bio-computing and swarm robotics. In this context, two emergent phenomena in the hippocampus, i.e., self-stabilizing maps as well as temporal reorganization through sharing oscillatory dynamics, have provided explanations for decentralized self-organization and distributed communication in the brain.

Often the type of phenomena and the features that arise from the dynamics of the synchronized system are intrinsically pan-scale, and cover both ends of the spectrum of "biological networks," from neuronal functioning to the collective behavior of individuals. For example, in their

OPEN ACCESS

Approved by:
Si Wu,
Peking University, China

***Correspondence:**
Andrea Duggento
duggento@med.uniroma2.it

Received: *30 December 2021*
Accepted: *17 January 2022*
Published: *07 March 2022*

Citation:
Duggento A, Petkoski S, Stankovski T and Toschi N (2022) Editorial: Synchronization, Swarming and Emergent Behaviors in Complex Networks and Neuroscience. Front. Comput. Neurosci. 16:846189. doi: 10.3389/fncom.2022.846189

perspective paper Ribeiro et al. introduced and summarized the striking similarities between flocking in animal group dynamics and neuronal populations in the brain. The parallelism includes the key feature of scale-free correlation functions which (both in animal flocks and mammal brains) arise from the absence of a central control, and inherently lead to better response to external perturbation (e.g., intrusions by predators or external stimuli). The parallelism extends from interaction-length vs. correlation-length considerations, to effects due to structure heterogeneities. Another key feature is the nature of the phase transitions underlying the collective properties of animal groups and neuronal populations, which are at the basis of our understanding of phase-change mechanisms. Ribeiro et al. show that these two key features (near-critical dynamics and scale-free organization) provide maximal information transmission and key dynamic range advantages for both flocks and brains. Cross-frequency coupling is an important aspect of neural interactions, however, its origin is not yet fully understood. One paper Sinha et al. performed a theoretical study about the effect of the number of synaptic layers in descending pathways on the expression of cross-frequency coupling between supraspinal input and the cumulative output of the motoneuron pool using computer simulations of Hodgkin–Huxley like neuron models. They showed that the cross-frequency coupling is dominant in multi-synaptic indirect motor pathways, paving the way for a future human subject study.

This Research Topic also includes an *in-vitro* and *in-vivo* validation of how cross-frequency coupling and oscillatory synchrony give rise to complex communication strategies between clusters of neurons. Kawai explores the emergence of noise-causing stochastic resonance (reverberation) and coherence, resonance-like phenomena in neurons of the vagal complex by using brainstem preparations. Through these phenomena, which are rarely observed in *in-vitro* and *in-vivo*, this study demonstrates the role of neuronal noise with respect to the robustness and resilience of life-sustaining vagal functions.

Another *in-vivo* study França et al. provides evidence that beta2 frequency (20–30 Hz) oscillations in hippocampal activity are linked with novelty detection and processing. In particular, in behavioral task experiments in mice, animals are exposed to different degrees of novelty content. Simultaneous extracellular recordings of the CA1 hippocampal region and mid-prefrontal and posterior parietal cortex are analyzed to demonstrate that beta2 power increases with both spatial and object novelty content, and that novelty modulates oscillatory coherence in hippocampal-cortical circuitry.

Even though the topographic organization of biological networks is often known, their role in influencing the spatiotemporal dynamics of population activity is not understood, creating a theoretical gap between micro- and macro-scale observations. One paper Yu, Bouteiller et al., aims to fill this gap by studying the CA3 subfield of the hippocampus in rats (which has been investigated extensively from a topographical point of view) by providing detailed information about its connectivity.

Hippocampal structures (in humans and rats) are also investigated in Yu, Wu et al., with a two-fold approach that encompasses both human functional magnetic resonance and animal electrophysiology, in combination with molecular and biochemical evaluations. The authors demonstrate that chronic pelvic pain alters functional connectivity between the anterior cingulate cortex and hippocampal pathway.

Two contributions to this Research Topic analyzed neuronal masses that describe the mean-field activity of populations of theta neurons and quadratic integrate and fire (QIF) neurons. These are often referred to as next generation neural mass models (Coombes and Byrne, 2018), and they all stem from the exact mean-field formalism based on the Lorentzian ansatz, introduced in a seminal paper by Montbrió et al. (2015). Theta-nested gamma oscillations were investigated in two variants of neuronal mass of QIF neurons by Segneri et al.: the pyramidal interneuronal network gamma and the interneuronal network gamma. In both set-ups the system is driven with a sinusoidal theta-forcing in the proximity of a Hopf bifurcation, giving rise to the mixed theta-gamma rhythms that always display phase amplitude coupling. These types of mixed oscillations have been reported in many areas of the brain and they have been replicated through optogenetic theta frequency stimulation. In Lin et al. synaptic diversity was shown to suppress the complex collective behavior in networks of theta neurons. Aiming to account for more realistic heterogeneous inter-neuronal coupling strengths, the authors show (analytically) that the collective macroscopic behavior of a network of theta neurons gives rise to complex dynamics, but the increase of synaptic diversity leads to suppression of most of the dynamical structures, selecting simple collective equilibrium states in physiologically relevant regions.

Models of neuronal populations were also analyzed in Schumm et al. in the context of impairment of rhythms between microcircuits caused by neuronal degeneration after traumatic brain injury. The authors studied changes in the synchronization in networks of Izhikevich integrate-and-fire neurons, which also adapt according to spike-timing-dependent plasticity. The results indicate that inherent resilience strongly depends on the connectivity with highly synchronized circuits, which are largely protected against the effects of neuronal deletion.

Often the transition from synchronized to desynchronized states involves a so-called chimera or solitary state (a sort of coexistence of coherent and incoherent dynamical evolution). Kushwaha et al. employ large numerical simulations to investigate whether the creations of chimera and solitary states can be predicted from network topology and distributions of delays between oscillators of the network.

Qin et al. concentrate on ensemble spike events to extract the network evoked by acupuncture manipulations. In their theoretical analysis and numerical simulations they describe network response activities employing Bayesian theory, and estimates of network spike correlations along with *in-silico* experiments, which are used to define the relationship between spike correlations and synchronous spike events.

In Puxeddu et al. the authors conducted a comprehensive, extensive, and systematic comparative analysis among multilayer community detection methods. They looked at three different clustering approaches and four algorithms based on single-layer modularity, multilayer modularity, and evolutionary clustering. First, they analyzed the performance of the methods in ground truth networks. Their results suggested that the performance of

the algorithms depends on the network features, such as the number of clusters, number of layers, and level of noise in the network. Their application to real EEG networks confirms the feasibility and usefulness of these methods.

Javed et al. studied the process of human aging. They used EEG-based scalp level analysis to identify aging-related alterations in synchronized brain regions. Starting from EEG data, the method decomposes the oscillations, calculates instantaneous features (amplitude and frequency), after which it extracts band-wise topographic maps. These topographic maps have shown the capability of capturing age-related changes in both spatial distribution and temporal characterization.

Racz et al. analyzed delta band (0.5–4 Hz) neural activity in schizophrenia. They used multifractal and entropy-based analysis to compare patients to controls, placing special attention on detecting the time-varying properties of neural interactions. Their results imply that the dynamic features of brain connectivity (e.g. multifractal properties and entropy) are potent markers of altered neural dynamics in schizophrenia.

Deschle et al. performed a theoretical study of how well the mass models resemble the real mean dynamics of a neural population. They tested the validity of neural mass models and whether the population under study comprised a mixture of excitatory and inhibitory neurons that are densely (inter-)connected. They found that these methods represent the mean dynamics for specific conditions, but not for all, and conclude that mass models should be used with great care.

In another theoretical contribution, Ghosh et al. employed Izhikevich neuron models to study the emergence of mixed mode oscillations. These are complex firing patterns that are neither spiking nor bursting activity alone. Instead, oscillations are distributed over different amplitudes, and the firings alternate between large and small amplitude oscillations. Ghosh et al. analyze mixed mode oscillations in a random and a small-world network of various neurons for different coupling strengths.

Spontaneous BOLD fMRI activity of the brain in the context of Resting State Networks (RSN) was analyzed by two studies. Amemiya et al. analyzed global vs. network-specific regulations as the source of intrinsic coactivations in the RSN. By using temporal independent component analysis, the authors investigated mechanisms that can give rise to network-specific coactivations. The time lag of global oscillations was shown to contribute to the RSN synchronization as much as the locally confined activities. The results thus confirm an equally important role of network-specific regulation for its coactivation, regardless of whether vascular artifacts contaminate the global component in fMRI measures.

Vohryzek et al. looked for recurrent excursions into functionally-relevant BOLD phase-locking states to adequately assess the biophysical mechanisms governing intrinsic brain activity. Clustering BOLD phase-locking patterns from 100 healthy participants from the Human Connectome Project into a set of k states. The authors demonstrate that the cluster centroids closely overlap with reference functional subsystems. In addition, the results reinforce the mechanistic scenario that RSN is the expression of erratic excursions from a baseline synchronous steady state into weakly-stable partially-synchronized states – i.e., ghost attractors.

In summary, with the advent of mass-scale exploitation of biologically inspired mechanisms as inspiration for artificial intelligence, there has been a surge in renewed interest in complex phenomena in biological networks. The need to understand the global functioning of complex neuronal networks has fueled theoretical and applied research of the classical topics of dynamical systems—such as studies of synchronization—to the now mature but ever-growing field of complex network science. While more and more observations and experiments in neuroscience investigate the functional macro-scale of network organization through a top-down approach, and system biology paradigms are creating an understanding of micro-scale complex phenomena, the physiological mechanisms of biological networks at the "meso-scale" are not yet well understood. This Research Topic collects contributions across theory, methods, and applications of complex networks to provide a reference point for the interested reader in this renewed and ever-increasing field.

AUTHOR CONTRIBUTIONS

All authors listed have made a substantial, direct, and intellectual contribution to the work and approved it for publication.

FUNDING

SP received support from the European Unions Horizon 2020 research and innovation program under grant agreement No. 945539 (SGA3) Human Brain Project.

REFERENCES

Coombes, S., and Byrne, Á. (2018). *Next Generation Neural Mass Models*. New York, NY: Springer International Publishing.

Montbrió, E., Pazó, D., and Roxin, A. (2015). Macroscopic description for networks of spiking neurons. *Phys. Rev. X* 5:021028. doi: 10.1103/PhysRevX.5.021028

Conflict of Interest: The authors declare that the research was conducted in the absence of any commercial or financial relationships that could be construed as a potential conflict of interest.

Publisher's Note: All claims expressed in this article are solely those of the authors and do not necessarily represent those of their affiliated organizations, or those of the publisher, the editors and the reviewers. Any product that may be evaluated in this article, or claim that may be made by its manufacturer, is not guaranteed or endorsed by the publisher.

Copyright © 2022 Duggento, Petkoski, Stankovski and Toschi. This is an open-access article distributed under the terms of the Creative Commons Attribution License (CC BY). The use, distribution or reproduction in other forums is permitted, provided the original author(s) and the copyright owner(s) are credited and that the original publication in this journal is cited, in accordance with accepted academic practice. No use, distribution or reproduction is permitted which does not comply with these terms.

frontiers in Systems Neuroscience

ORIGINAL RESEARCH
published: 29 October 2019
doi: 10.3389/fnsys.2019.00065

Global vs. Network-Specific Regulations as the Source of Intrinsic Coactivations in Resting-State Networks

Shiori Amemiya, Hidemasa Takao and Osamu Abe*

Department of Radiology, Graduate School of Medicine, The University of Tokyo, Tokyo, Japan

Spontaneous neural activities are endowed with specific patterning characterized by synchronizations within functionally relevant distant regions that are termed as resting-state networks (RSNs). Although the mechanisms that organize the large-scale neural systems are still largely unknown, recent studies have proposed a hypothesis that network-specific coactivations indeed emerge as the result of globally propagating neural activities with specific paths of transmission. However, the extent to which such a centralized global regulation, rather than network-specific control, contributes to the RSN synchronization remains unknown. In the present study, we investigated the contribution from each mechanism by directly identifying the global as well as local component of resting-state functional MRI (fMRI) data provided by human connectome project, using temporal independent component analysis (ICA). Based on the spatial distribution pattern, each ICA component was classified as global or local. Time lag mapping of each IC revealed several paths of global or semi-global propagations that are partially overlapping yet spatially distinct to each other. Consistent with previous studies, the time lag of global oscillation, although being less spatially homogenous than what was assumed to be, contributed to the RSN synchronization. However, an equivalent contribution was also shown on the part of the more locally confined activities that are independent to each other. While allowing the view that network-specific coactivation occurs as part of the sequences of global neural activities, these results further confirm an equally important role of the network-specific regulation for its coactivation, regardless of whether vascular artifacts contaminate the global component in fMRI measures.

Keywords: fMRI, resting-state network, spatiotemporal dynamics, spontaneous neural activity, neuronal pathway tracing

OPEN ACCESS

Edited by:
Nicola Toschi,
University of Rome Tor Vergata, Italy

Reviewed by:
Ines R. Violante,
University of Surrey, United Kingdom
Janine Dale Mendola,
McGill University, Canada

****Correspondence:***
Shiori Amemiya
amemiya-tky@umin.ac.jp

Received: *15 August 2019*
Accepted: *14 October 2019*
Published: *29 October 2019*

Citation:
Amemiya S, Takao H and Abe O (2019) Global vs. Network-Specific Regulations as the Source of Intrinsic Coactivations in Resting-State Networks. Front. Syst. Neurosci. 13:65. doi: 10.3389/fnsys.2019.00065

INTRODUCTION

Once considered to be a noisy, stochastic process, spontaneous activity of the cortical neuron is now understood to be by no means random but is endowed with specific patterning that reflects the functional architecture of the underlying network at the level of micro- or meso-circuits (Tsodyks et al., 1999; Kenet et al., 2003). Over the last two decades, it has become apparent that this

is analogously true at the level of large-scale networks that are defined using resting-state functional magnetic resonance imaging (rs-fMRI) (Biswal et al., 1995; Fox and Raichle, 2007). The spatial patterns identified as areas with synchronous oscillation of the blood oxygenation-level dependent (BOLD) signal are termed as resting-state networks (RSNs) (Fox et al., 2005). These networks are closely related to anatomical connectivity among the neural subsystems that have been revealed by a wide variety of visual, sensorimotor, and cognitive task paradigms (Vincent et al., 2007; Zhang et al., 2010). However, the neurophysiology of the phenomenon, or the mechanism that controls and coordinates the intrinsic synchronization across distributed neural systems, largely remains to be established.

While conventional rs-fMRI analyses based on seed-based correlation or independent component analysis (ICA) implicitly assume that the spatial distribution of the synchronous neural activity is temporally constant, animal studies have revealed that spontaneous neural activity is spatiotemporally structured, and propagating waves of activity have been recorded in a variety of species (for review, see Muller and Destexhe, 2012). Neuronal membrane potential in the cortex undergoes a spontaneous transition between up and down states in the absence of sensory inputs (Steriade et al., 1993; Lampl et al., 1999; Petersen et al., 2003; Shu et al., 2003). Population activity of the neurons during the up state manifests as propagating waves not only within a part of the cortex (Petersen et al., 2003; Ferezou et al., 2007; Xu et al., 2007; Civillico and Contreras, 2012), but also throughout the entire brain (Stroh et al., 2013). The spatiotemporal dynamics of the low-frequency oscillation have also been identified by examining the repetitive spatiotemporal patterns (Majeed et al., 2009, 2011; Takeda et al., 2016; Belloy et al., 2018; Abbas et al., 2019) or by analyzing the time lag structures of the rs-fMRI data (Mitra et al., 2014, 2015a; Amemiya et al., 2016; Matsui et al., 2016). An intriguing hypothesis proposed by one of those studies is that the RSN synchronization indeed emerges as the result of several independent global propagations of spontaneous neural activity (Mitra et al., 2015a). Using synthetic time series embedded with the measured time lag structures of the rs-fMRI data, Mitra et al. (2015a) showed that the functional connectivity (FC) matrix representing the RSN synchronization could be reconstructed to a fair approximation. In support of this idea, a recent animal study also showed that a global wave of spontaneous neuronal activity propagating across the networks contributes to within-network coactivations of the neurons that correspond to RSN synchronization (Matsui et al., 2016). Based on these findings it follows that seemingly independent RSN activity can be viewed as being controlled by a single centralized mechanism, through global wave(s) of activity that regulate and constrain the relative relationships of the network activity by determining the order and timing of the activation of each network. However, it remains unclear if this is the sole mechanism that gives rise to the RSN synchronization, as suggested by those studies (Mitra et al., 2015b; Matsui et al., 2016). An alternative, thought non-exclusive, origin of the synchronization would be network-specific coactivations among the neural populations confined within each network (Mohajerani et al., 2013; Ponce-Alvarez et al., 2015). In the neural system, it is generally supposed that diverse physiological mechanisms coexist for rhythm generation and population synchronization for which different levels of integration interact closely with each other (Ivanchenko et al., 2008; Harris-Warrick, 2010; Wang, 2010). For example, in the respiratory central pattern generator of the mammals, rhythm generation is dependent on the endogenously oscillatory neurons that serve as pacemaker, as well as the pattern of synaptic connections within the network that forms a network pacemaker (hybrid pacemaker-network mechanism) (Calabrese, 1998; Rybak et al., 2004, 2007; Sohal et al., 2006; Johnson et al., 2007).

It seems possible, therefore, that multiple mechanisms – namely, global propagation and local synchronization – contribute to the emergence of the coherent RSN activity that characterizes the functional architecture of the brain. In order to address this question, it is imperative to evaluate not only the paths but also the whole picture of the traveling waves. We thus started by identifying the signal time course of the global waves by applying the temporal ICA to rs-fMRI data. In fMRI, virtually all applications of ICA use spatial rather than temporal ICA. Although spatial ICA is suitable for the separation of the spatially distinct activations from each other, temporal ICA would be more appropriate if the aim is to find functionally independent and spatially overlapping activities (Smith et al., 2012), such as what we assume to be multiple global waves.

In contrast to previous studies focusing on estimating the paths of traveling waves by analyzing the signal time lag (Mitra et al., 2014, 2015a; Amemiya et al., 2016; Matsui et al., 2016), direct detection of the traveling waves enables us to infer the likelihood that each mechanism contributes to the emergence of network synchronization, as well as to map the magnitude of each type of activity in each region. Moreover, identification of individual traveling waves allows accurate estimation of the time lag structures, in contrast to previous studies employing a decomposition approach, regardless of the validity of the assumptions that the time lags of multiple waves can be linearly superposed, or that the paths of traveling waves are spatially independent. By comparing the correlation matrix of both the global and the local component to that of the FC matrix, contribution of each type of activity to the RSN synchronization that characterizes the resting state FC was evaluated.

MATERIALS AND METHODS

Overview

A summary of the analysis is presented as a schematic in **Figure 1** to provide an overview of the study. We used data from the WU-Minn Human Connectome Project (HCP) young healthy adults (ages 22–35) S1200 release that provides paired dataset of the same group of subjects (day 1 and day 2). All preprocessing and data analyses were performed for each dataset, respectively, in the same way.

HCP Data

Data of 50 subjects who underwent 3 T resting-state fMRI sessions without quality control issues, and whose mean

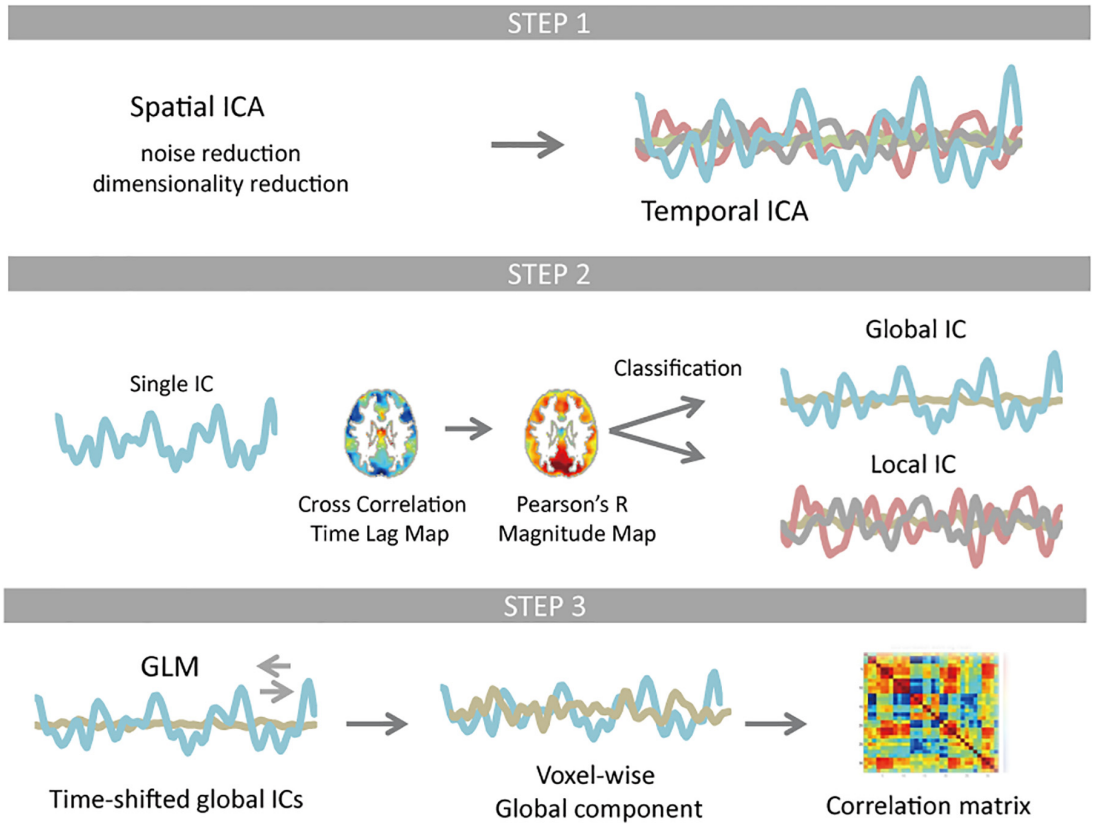


FIGURE 1 | Schematic of the resting-state fMRI data processing. Temporal independent component analysis (ICA) was applied to pre-processed test and re-test dataset, whose dimensionality were reduced to 61 × 120,000 and 62 × 120,000 using spatial ICA, respectively. Each temporal ICA gave 28 and 30 reproducible components (Step 1). For each component (IC time series), a time lag map was obtained by computing the time lag of each voxel relative to the IC time series using cross-correlation, which was further interpolated with parabolic polynomials. Pearson's correlation coefficients were computed between each voxel's time series and the IC time series that was shifted as much as the measured time lag. Classification of ICs was based on spatial distribution pattern of each component. Any component that is more similar to the whole-brain signal than any RSN template in distribution pattern was classified as global (Step 2). Using the time-shifted global ICs as regressors, linear regression analysis was performed for each voxel. All global ICs detected for any single temporal ICA were then integrated. The rest of the signal change was classified as local contribution. The correlation matrix of the global as well as local component was computed and compared with the correlation matrix of the original signal FC matrix (Step 3).

framewise displacement was less than 0.2 mm were included for the analysis. The number of subject was determined by the maximum size of the data that could be processed by a core program for ICA, Multivariate Exploratory Linear Decomposition into Independent Components (MELODIC) (Beckmann and Smith, 2004). HCP imaging and pre-processing protocol have been previously described in detail (Glasser et al., 2013; Smith et al., 2013; Van Essen et al., 2013; Griffanti et al., 2014; Salimi-Khorshidi et al., 2014). In brief, resting-state fMRI data were acquired using a single customized Siemens 3 T scanner housed at Washington University in St. Louis, using a standard 32-channel receive head coil, with 2.0 mm isotropic spatial resolution, 0.72 s repetition time (TR), and 1200 frames, i.e., 14.4 min per run. For each subject, and for each session, two runs with reversed phase encoding directions, RL or LR, with the order counterbalanced across each of two sessions, were acquired (WU-Minn HCP 1200 Subjects Data Release Reference Manual), and the geometric distortions were corrected using spin echo field map EPI scans (Glasser et al., 2013). The data were then subjected to spatial ICA using MELODIC with automatic dimensionality estimation. Using FMRIB's ICA-based X-noisifier (FIX) (Griffanti et al., 2014; Salimi-Khorshidi et al., 2014) that is a machine learning classifier trained on HCP data, spatially specific noise components were identified and removed for each run. Then 24 movement regressors were further regressed out of the data (Smith et al., 2013; Griffanti et al., 2014; Salimi-Khorshidi et al., 2014).

Data Analysis

Further Pre-processing

Further pre-processing and analysis of the data were performed using tools from SPM12 software[1], AFNI libraries[2] and in-house scripts written and implemented in Matlab 9.3 (MathWorks, Natick, MA, United States). Linear trends were removed from the HCP data that had been processed with subject-level ICA

[1]http://www.fil.ion.ucl.ac.uk/

[2]https://afni.nimh.nih.gov/

noise reduction (sICA + FIX), and the data were band-pass filtered at 0.01–0.1 Hz. The pre-processed data were temporally concatenated across runs to create a single 4D dataset of 120,000 timepoints for test and re-test dataset, respectively.

Temporal-ICA

For temporal ICA decomposition of the data, we employed a strategy adapted from Smith et al. (2012) to perform group-wise spatial ICA in advance of the final temporal ICA. The spatial ICA allows further identification of artifact components at the group level, as well as to achieve a high-dimensional functional parcelation of the group data, which reduces the dimensionality of the data to feed into temporal ICA. The overall ICA analysis is described as follows:

$$X_{(V\times T)} = S_{S(V\times K)} \times A_{t(K\times L)} \times S_{t(L\times T)} + E$$

where X is the data matrix of size Voxels × Time points, S_s are the spatial maps estimated by spatial ICA, K is the number of spatial ICA components that were subsequently fed into temporal ICA, after removing noise components. L is the number of temporal ICA components. S_t is the decomposed time series (ICA sources), and A_t is the central mixing matrix of temporal ICA. E combines noise and artifact aspects of the data (Smith et al., 2012).

Group-wise spatial ICA was performed using MELODIC with automatic dimensionality estimation. Of the 61 and 62 ICs generated from dataset 1 and 2, three ICs were classified as artifacts on the basis of their spatial features, respectively. Specifically, activation patterns clearly outlining the intensity edges of the gray matter were classified as noise (Smith et al., 2012; Salimi-Khorshidi et al., 2014; Pruim et al., 2015). For the remaining components, functional nodes' time series were computed using dual regression technique (Filippini et al., 2009), and fed into temporal ICA.

For temporal ICA, we used Icasso algorithm (Himberg et al., 2004) to estimate the most appropriate decomposition yielding a set of reproducible IC clusters. For all possible dimensions or number of components, Icasso was ran with *both* resampling mode that uses random initial condition as well as bootstrapping of the data for 100 times, which pooled all temporal ICA estimates using FastICA (Hyvärinen, 1999) with tanh non-linearity and a symmetric decorrelation approach. We chose the decomposition yielding the maximum number of clusters of reproducible components that gives a stability index Iq larger than 0.5. Iq is computed as the difference between the average intracluster similarities and average intercluster similarities, which reflects the compactness and isolation of a cluster (Himberg et al., 2004). For each dataset, 28 and 30 reproducible clusters were found, respectively.

Identification of the Global Waves

For all temporal ICs, time series of each run, once concatenated to be subjected to a temporal ICA was deconcatenated so that following analyses can be performed for each run separately unless otherwise noted. Firstly, spatiotemporal patterns or paths of traveling waves were estimated for each IC by computing the relative time lag t that gives the best positive fit between each voxel's time series and the time-shifted (±6.3 s or ±9 TR) IC (time series) using cross-correlation analysis. As in our previous study, 12 s limit of propagation delay was set to include whole-brain vascular time lag that can range up to nine seconds (Amemiya et al., 2016). Parabolic interpolation (Meijering, 2002) was further applied to locate the peak time lag t' using the extremum t, as well as the two nearest points given by the cross-correlation analysis.

The magnitude map of each IC was then computed as the Pearson's correlation coefficients between each voxel's time series and the IC time series that was shifted as much as t' using sinc interpolation to give the maximum correlation. Classification of ICs was based on the spatial distribution pattern of each component. We performed template matching using 21 RSN templates (Smith et al., 2012), as well as a whole-brain signal template that is the correlation map of the whole-brain mean signal, averaged over 100 runs (**Supplementary Figure S1**). The whole-brain signal was computed as the average signal within a gray matter mask was created by thresholding MNI template at 10% or larger probability of being gray matter. Pearson's correlation coefficients were computed between each IC and each of the 22 templates within the mask. Any component that is more similar to the whole-brain signal template than any of the RSN templates (i.e., giving a greater correlation coefficient with a whole-brain signal template) was classified as global. Note that our study focuses particularly on examining the existence of coactivations restricted within each RSN, in addition to the globally propagating activities that were assumed to exist throughout the brain and treated as such in the analysis of previous studies. In this context, it would certainly make sense to identify any component whose distribution is restricted within any functionally distinct areas as being *local* as opposed to a functionally and spatially less specific *global* (or more precisely semi-global) pattern.

Using the time-shifted global ICs as regressors, linear regression analysis was performed for each voxel's time series. The global component was then computed as the integral of all global ICs by summing up the shifted time series multiplied by the corresponding regression coefficients. The rest of the signal was classified as local contribution (**Figure 1**).

Estimation of the Likelihood That Each Mechanism Gives Rise to the RSN Synchronization

In order to evaluate the contribution of each mechanism to the emergence of RSN synchronization, we compared regions of interest (ROI)-wise correlation matrices given by each component using a set of 132 ROIs provided as part of the CONN toolbox (Whitfield-Gabrieli and Nieto-Castanon, 2012) that were originally defined from FSL Harvard-Oxford Atlas maximum likelihood cortical or subcortical atlas and cerebellar parcelation from AAL atlas.

For each subject's each run, FC matrix was obtained by computing the Pearson's correlation coefficient between each possible couple of ROI's mean time series (i.e., global + local component). Similarly, three types of correlation matrices were computed by correlating the time series of (1) global component,

(2) local component, (3) global component reconstructed to reflect only time lag of each global IC, respectively. We correlated each matrix against the FC matrix run-wisely, using the correlations above the diagonal of each matrix, transformed to Fisher's Z and tested by using a two-tailed *t*-test over runs against the null hypothesis of no correlation. Next, we examined whether the time lag itself contributes to the RSN synchronization by computing the correlation between the FC matrix and the correlation matrix of the global component that was reconstructed without implementing the magnitude difference. In the presence of time lag, even when the global component is composed of a single IC, the spatial difference of its magnitude can contribute to the characterization of the correlation matrix, let alone the global component composed of multiple ICs. It is therefore important to eliminate the effect to determine if time lag is the source of synchronization. The magnitude of each IC was adjusted to reflect the contribution of each IC that is computed as the root mean square of the mixing matrix of the temporal ICA.

In order to further confirm the relationship between the signal synchronization and the time lag of the global component, for each global component, Pearson's correlation coefficient was computed between the FC matrix and the matrix of relative time lag that is the difference of the time lags between given ROIs.

Contribution of the local component was also assessed by computing the correlation between the FC matrix and the correlation matrix of the local component in the same way. Correlation between the correlation matrices were computed using the upper triangle of each correlation matrix. The threshold of the statistical significance was set at $p = 0.05$, and the Bonferroni correction was used to control for the multiple comparisons.

Origin of the Time Lag

To estimate the origin of the time lag that characterizes the global component, all magnitude (correlation coefficient) and time lag maps of the global ICs that were averaged across subjects were compared with those of the whole-brain signal, respectively. Partial correlation analysis was also performed to control the effect of vascular time lag that was measured using dynamic susceptibility contrast enhanced perfusion imaging (Amemiya et al., 2016). We also compared the time lag structure of the local component and that of the whole-brain signal by computing the Pearson's correlation between the time lag maps with each local IC. A correction for the spatial degrees of freedom was given via Gaussian random field theory and empirical smoothness estimation, which estimated the number of independent resels or resolution elements to be 103.

RESULTS

Identification of the Global Waves

Of the 28 and 30 reproducible ICs for dataset 1 and 2, 7, and 10 were classified as global IC based on the pattern of spatial distribution for each dataset, respectively (**Figure 2** and **Supplementary Figure S2**). The magnitude of the global IC is shown as Pearson's correlation coefficient between the time-shifted global IC and the time series of each voxel, with the corresponding time lag structures showing the paths of each global component (**Figure 2** and **Supplementary Figure S2**). All magnitude and time lag maps shown were obtained by averaging the resulting maps across all subjects' all runs. Time lag maps of the global components showed structural paths of each signal, which is consistent with previous studies suggesting the existence of multiple global waves of activity in the resting state; c25, c07 and c05 show early regions in the rostral and lateral part of the frontal lobes and delayed regions in the medial part of the frontal lobes, insular and inferior frontal gyrus and occipital lobes, while the pattern is almost opposite for c10. C12's path is characterized by early regions in the sensorimotor, auditory, and visual cortex, as well as delayed regions in the association cortex and posterior cingulate cortex, while c07 shows the opposite pattern. C15 resembles c05, c07, c25 pattern, but the delay in the dorsal attention network is more conspicuous (**Figure 2**).

However, there were significant correlations among the paths of global signals (**Supplementary Figures S6A,B**). Some global ICs also showed apparent similarity to the whole-brain signal not only in its spatial distribution characterized by symmetrical involvement of the dorsal cerebral cortex with predominantly high magnitude in the occipital lobes, but also in its propagation pattern: time lag: $|r| = 0.42 \pm 0.21$ (re-test, 0.37 ± 0.23); magnitude: $r = 0.58 \pm 0.15$ (re-test, 0.55 ± 0.12) (**Figure 2** and **Supplementary Figure S2**). Partial correlation analysis controlled for the perfusion time lag also showed sometimes reduced but still significant correlation between the time lag maps of the global ICs and the whole-brain signal: $|r| = 0.40 \pm 0.23$ (re-test, 0.39 ± 0.22). These results suggest that even if multiple global waves of activity coexist in the resting state, the paths of the traveling waves can be substantially overlapped, as can the spatial distribution, which is not simply explained as the result of common background vascular perfusion.

Time lag maps of the global ICs detected from the test dataset were well replicated by the analysis of the re-test dataset. **Supplementary Figure S6C** demonstrates that all global ICs of the test data were significantly positively correlated with at least one global IC of the re-test data.

Consistent with previous studies (Mitra et al., 2014; Amemiya et al., 2016), magnitude and latency of the whole-brain signal were not significantly correlated: $r = -0.10$, $p = 0.32$ (re-test, $r = -0.051$, $p = 0.62$). The majority of the global components showed significant correlation between magnitude and time lag ($p < 0.05$): c07, $r = 0.41$; c10, $r = -0.30$; c12, $r = -0.48$; c12, $r = -0.48$; c25, $r = -0.27$ (re-test, c05, $r = -0.29$; c07, -0.44; c12, $r = -0.31$; c18, $r = -0.36$; c22, $r = -0.24$; c24, $r = -0.25$; c26, $r = -0.42$), which might be caused by the attenuation of the waves of activity during the process of transmission.

Some of the global ICs showed anteroposterior propagation that might correspond to the pattern detected using electroencephalogram in sleeping humans: c22 of the test

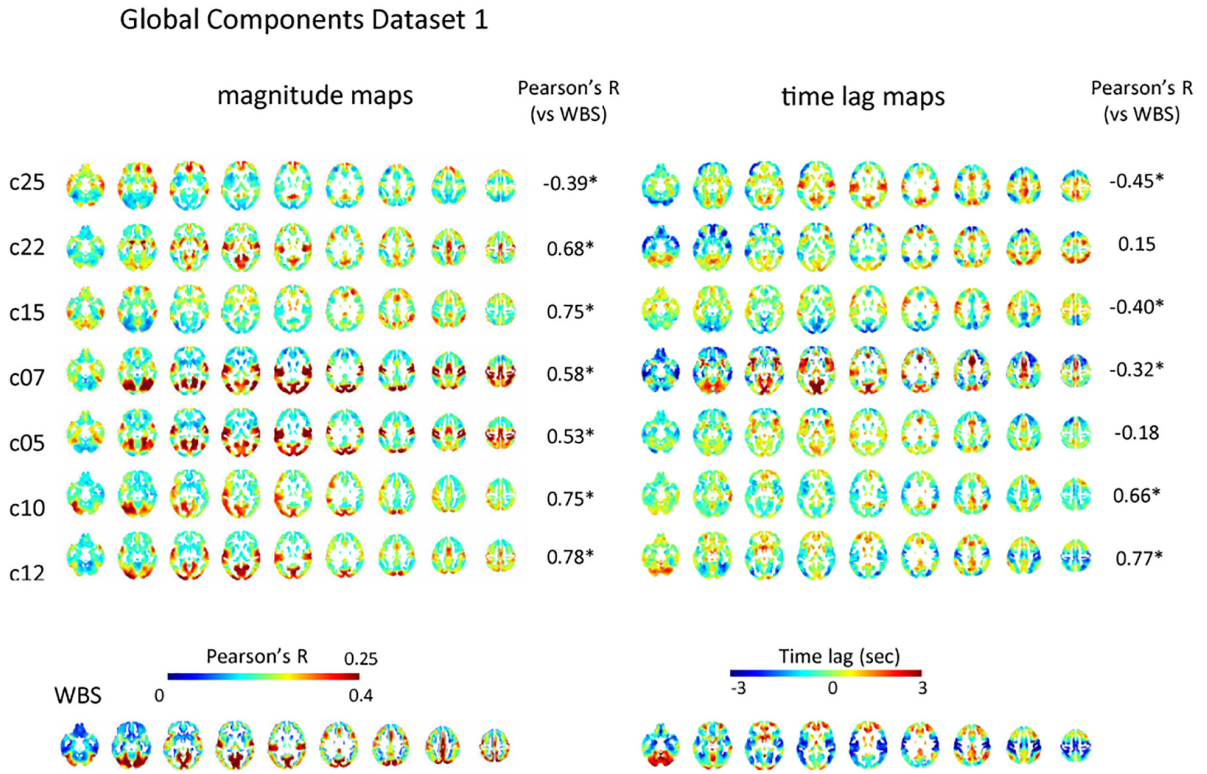


FIGURE 2 | Global component. The spatial distribution of the magnitude of the temporal ICA components for test dataset demonstrates a set of global ICs. The magnitude of the seven global ICs is shown as Pearson's correlation coefficient with the corresponding time lag structures showing its path. All magnitude maps were significantly correlated with the map obtained using the whole-brain signal (WBS), that is characterized by symmetrical high magnitude areas distributed predominantly in the occipital lobes, as well as in the path of propagation that is characterized by early signal in the primary sensorimotor and visual cortex compared with association areas, frontotemporal basal regions or the cerebellum (bottom row). Five of the seven time lag maps were significantly correlated with that of the whole-brain signal. C25, c07, and c05 show early regions in the rostral and lateral part of the frontal lobes and delayed regions in the medial part of the frontal lobes, insular and inferior frontal gyrus and occipital lobes, while the pattern is almost opposite for c10. C12's path is characterized by early regions in the sensorimotor, auditory, and visual cortex, as well as delayed regions in the association cortex and posterior cingulate cortex, while c07 shows the opposite pattern. C15 resembles c05, c07, c25 pattern, but the delay in dorsal attention network is more conspicuous. Pearson's correlation coefficients between time lag and magnitude maps of each global IC and those of the whole-brain signal are also shown.

dataset as well as c22 and c26 of the re-test dataset show early regions in the rostral compared with caudal part of the cerebral cortex.

Contribution of the Global Waves to the RSN Synchronization

The correlation matrix of the global component reconstructed with the detected global ICs showed significant correlation with the FC matrix: $r = 0.31 \pm 0.13$ (re-test, 0.32 ± 0.11), $p < 0.001$ (**Figures 3A,B** and **Supplementary Figures S3A,B**). Significant correlation was found even when the global component was reconstructed without considering the spatial difference of its magnitude: $r = 0.22 \pm 0.13$ (re-test, 0.27 ± 0.11), $p < 0.001$ (**Figure 3C** and **Supplementary Figure S3C**). Furthermore, significant negative correlation between the strength of synchronization (FC) and the relative time lag was also shown for all global waves: $r = -0.19$ to -0.39, $p < 0.001$ (re-test, $r = -0.14$ to -0.40, $p < 0.001$) (**Figures 3E**, **4** and **Supplementary Figures S3E**, **S4**), which suggests that the time lag of the global component can contribute to the RSN synchronization.

Characteristics of the Local Component

The spatial distribution of the magnitude of the 28 and 30 reproducible local ICs is shown in **Figure 5** and **Supplementary Figure S5**, respectively. Each magnitude map of the local ICs showed significant synchronization within functionally relevant structures, which would correspond to spatial maps for the temporally independent functional modes (Smith et al., 2012). In other words, as previously well-explored in Smith et al. (2012), the local ICs could be considered as functional "modes" that in some cases could subdivide and/or reorganize the currently standard spatial RSNs.; e.g., c01-03 contain visual cortex (predominantly extrastriate areas) and ventral sensorimotor cortex; c04 contains right orbitofrontal cortex in addition to sensorimotor and visual cortex; c06 contains extrastriate cortex and basal ganglia; c08 contains sensorimotor cortex, c09, c17, c18 involve frontotemporal network nodes; c11 mainly

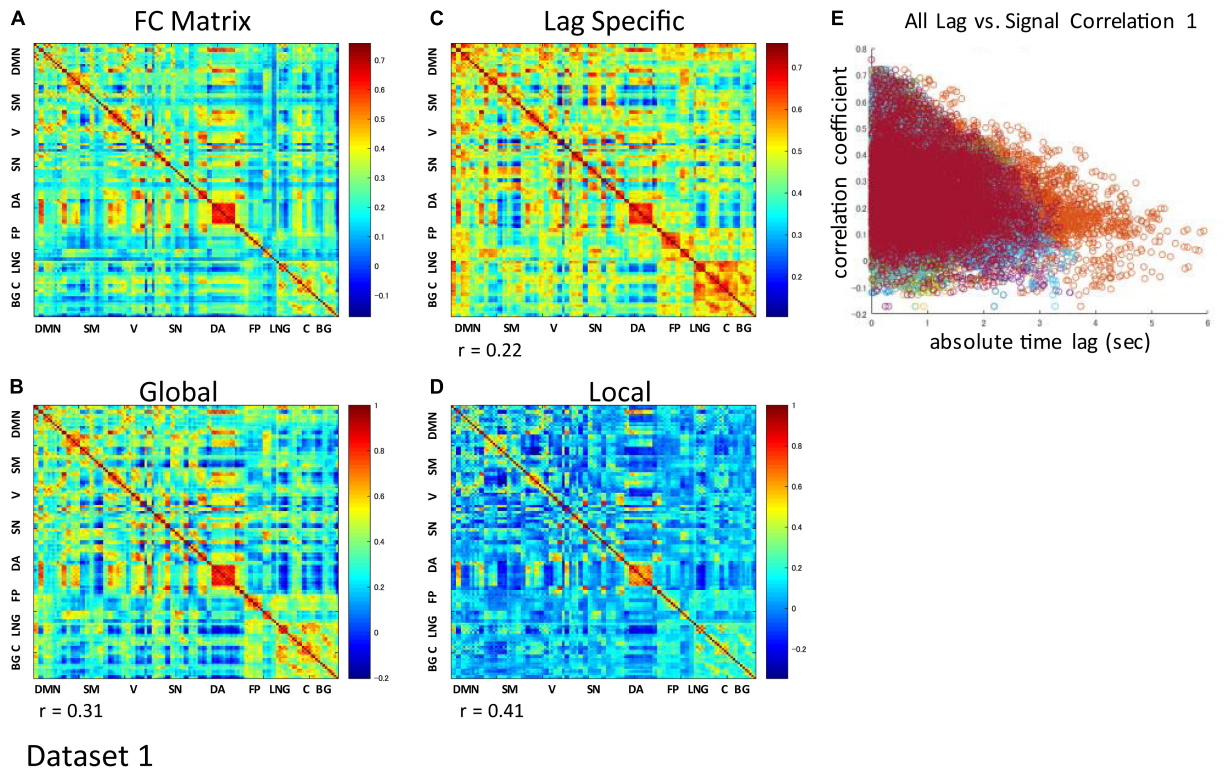


FIGURE 3 | Contribution of each component to RSN synchronization. Whole signal Functional Connectivity (FC) matrix had significant positive correlation with the global component correlation matrix (**A** vs. **B**), suggesting the contribution of the global component to the RSN synchronization. Significant correlation is also shown even when the global component was reconstructed without considering the spatial difference of its magnitude (**A** vs. **C**). Correlation matrix of the local component is also fairly similar to the FC matrix, suggesting an equivalent contribution of locally limited activity to RSN synchronization (**A** vs. **D**). For each global component, there was significant negative correlation between the strength of synchronization (FC) and the relative time lag between each ROI, which confirmed the contribution of the time lag of the global component to RSN synchronization **(E)**.

involves association cortex; c13 and contains primary visual cortex and default mode network nodes in the angular gyrus and posterior cingulate cortex; c14 contains visual cortex and dorsolateral prefrontal cortex; c16 involves relatively widespread areas mainly involving the sensorimotor and primary visual cortex in addition to basal ganglia; c19 contains; c20 and c21 contain dorsal attention network and frontal lobes; c23 involves primary visual cortex and frontal lobes; c24 and c28 contains salience network and frontoparietal network nodes; c26 contains auditory and sensorimotor networks; c27 involves sensorimotor and visual cortex. **Figure 3D** and **Supplementary Figure S3D** show correlation matrices of the local component that are fairly similar to the FC matrix ($r = 0.41$, $p < 0.05$; re-test, $r = 0.42$, $p < 0.05$), suggesting an equivalent or even larger contribution of the local activity to the RSN synchronization that characterizes the FC matrix. The magnitude of the activity of the local component relative to the whole signal was 0.70 for both test and re-test dataset.

DISCUSSION

By applying temporal ICA to the rs-fMRI data, we have identified several global or semi-global waves of slow oscillation that are temporally independent yet spatially overlapping with each other. Although the correlation matrix of the global component showed substantial correlation with the FC matrix, an equivalent or even greater contribution of the local component was also shown. The results indicate that while global waves of activity, although being less spatially homogenous than what was assumed to be, could contribute to the emergence of the RSN, which is partly consistent with previous studies suggesting that within-network synchronization can arise from the time lag of the global waves (Mitra et al., 2015a; Matsui et al., 2016), this does not exclude the contribution of local activity that are more confined within functionally relevant structures.

Multiple Waves of Activity

Although the number of the global IC was slightly varied depending on the dataset, there was substantial overlap among the global ICs detected within or across the temporal ICAs for test and re-test datasets. Moreover, the majority of the global waves detected across the temporal ICAs were significantly correlated with the path of the whole-brain (global mean) signal, which would be the most robust representation of the global signal. Partial correlation analysis that controlled for the effect of vascular time lag also confirmed that significant

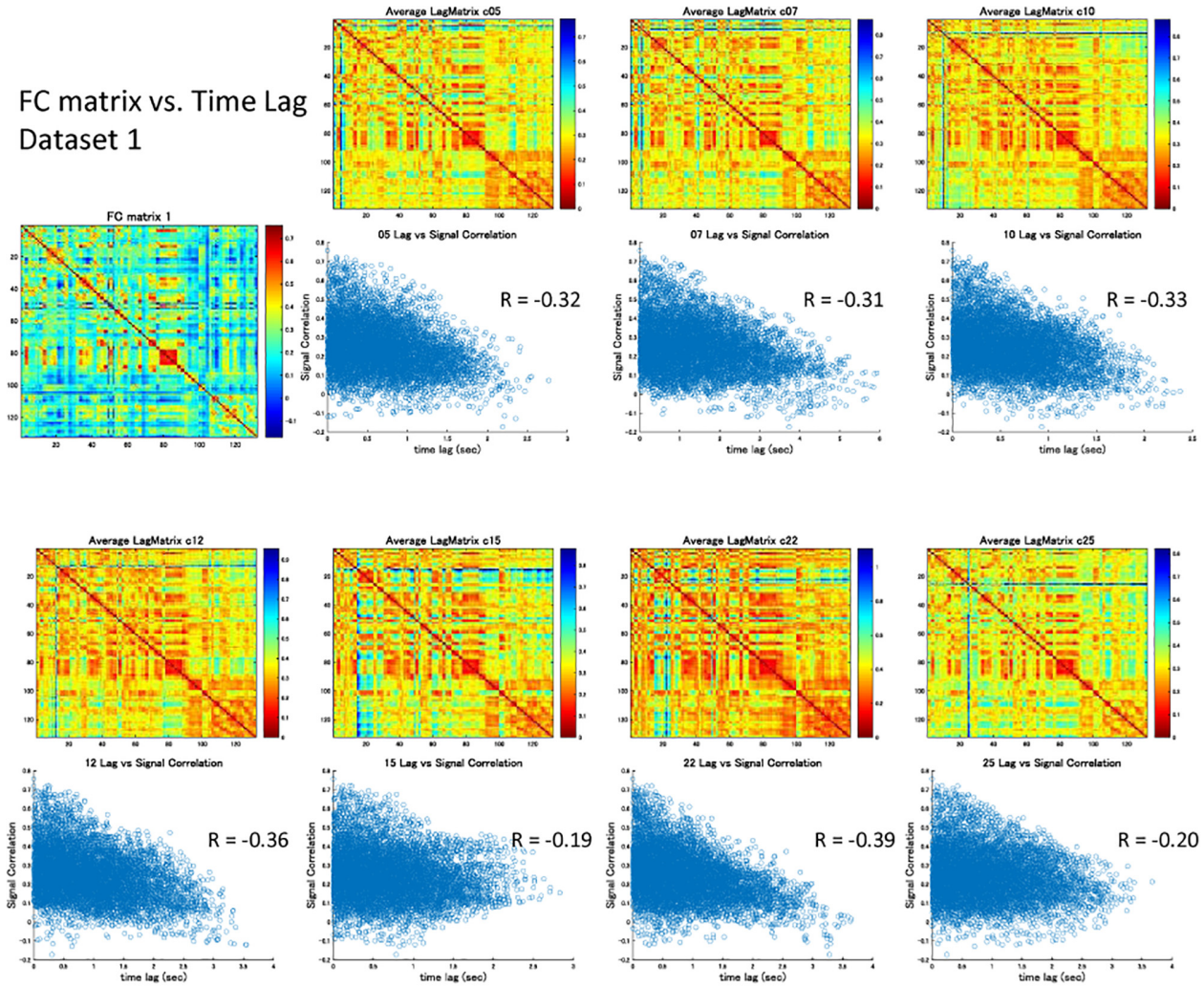


FIGURE 4 | Signal correlation matrix vs. Time lag matrix. For each global component, there was significant negative correlation between the strength of synchronization (FC) and the relative time lag between each ROI, which confirmed the contribution of the time lag of the global component to RSN synchronization.

correlation was still found with the global waves. While these results might support the finding that the global neural activity has a predominant path of propagation (Matsui et al., 2016), they also suggest the existence of multiple overlapping paths of neural oscillations. Some paths of global ICs that share common features with those obtained in the previous studies: c25, c05, c07, c10, and c12 would correspond to the thread 2 reported in Mitra et al. (2015a) that shows a contrast between the rostral and lateral part of the frontal lobes vs. medial part of the frontal lobes, insular and inferior frontal gyrus and occipital lobes, while c15 to thread 8 (note that the polarity of the threads can be inverted). However, there were some other time lag structures representing the paths of propagating neural activity that were not obtained by merely decomposing the measured total time lag as multiple orthogonal components (i.e., threads in Mitra et al., 2015a) or as independent components (Amemiya et al., 2016). Specifically, some global ICs showed anteroposterior propagation that might correspond to the pattern detected using electroencephalogram in sleeping humans (Massimini et al., 2004) or with calcium imaging as well as BOLD imaging in anesthetized mice (Stroh et al., 2013; Matsui et al., 2016). While physiological basis or significance of such global activity remains to be known, all these data further support the view that spatiotemporal pattern of BOLD signal could reflect large-scale dynamics of underlying neuronal activity.

Origin of the Time Lag and Synchronization

Given that cerebral vascular time lag is quite uniform across subjects (Amemiya et al., 2016), existence of multiple paths of traveling BOLD signal suggest the existence of multiple waves of neural signal (Mitra et al., 2015a; Amemiya et al., 2016). Although BOLD represents hemodynamic response to neural activity that is necessarily influenced by the

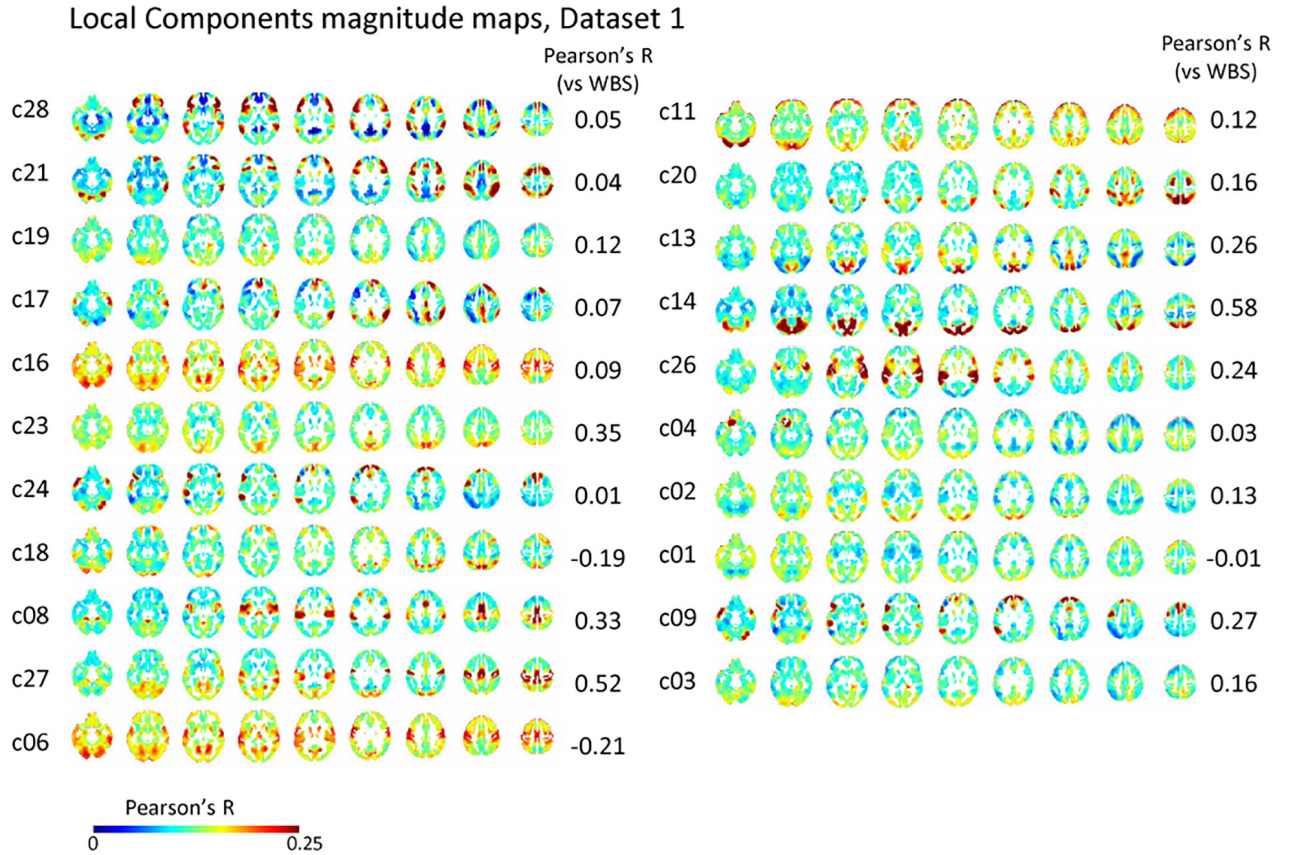


FIGURE 5 | Local component. The spatial distribution of the magnitude of the temporal ICA components for test dataset demonstrates a set of local ICs. Each IC shows significant synchronization within functionally relevant structures that would correspond to spatial maps for the temporally independent functional modes (Smith et al., 2012).

characteristics of the underlying vasculature (Amemiya et al., 2012; Bandettini, 2014), the path of globally propagating activity has been shown to coincide with that of the neuronal calcium signal in mice (Matsui et al., 2016). Assuming that the same holds true for non-anesthetized awake human data, the propagating pattern of global oscillations that are characterized by structured and smooth gradation can be seen as corresponding to a gradual propagation via short-range corticocortical connections. In addition, small time lag observed between distant regions across RSNs may reflect the presence of a mechanism controlling the initiation of spreading activity, mediated via long-range connections in a rapid manner. Such activities might help integrate the spontaneous oscillation of the cortex across RSNs in the whole brain, which is analogous to the concept of synfire chains in synchronous mode (Abeles, 1982, 1991), in which groups of neurons are organized into chains, and the architecture enables precisely timed sequences of spikes to form a propagating wave of activity (Abeles, 1982, 1991; Diesmann et al., 1999).

Alternatively, it would also be possible to assume that the time lag of the global oscillations mainly reflects vascular dynamics for some ICs. Indeed, whole-brain signal and vascular perfusion are known to share similar spatiotemporal characteristics (Amemiya et al., 2014, 2016; Tong et al., 2017). It might be important to note, however, that the source of the time lag is not necessarily identical to the source of the signal, so even if the time lag were totally non-neural in origin, that does not mean that the origin of the global signal is non-neural. This is because perfusion time lag can also be reflected in the time lag of BOLD signal of neural origin (Roc et al., 2006; Amemiya et al., 2012). Therefore, for the ICs whose time lag maps are similar to that of perfusion, e.g., like whole-brain signal, a measurement that is independent of neurovascular coupling would be preferable and perhaps essential for a more precise prediction of the spatiotemporal profile of the underlying neural activity.

Nevertheless, even if the contribution of some global oscillations to the apparent network synchronization were an artifact (Tong et al., 2015), the results of the present study suggest that network-specific synchronization does exist besides such component, which is consistent with the growing evidence supporting the link between BOLD and electroencephalographic or magnetoencephalographic measures of resting state activity (Goldman et al., 2002; Yan et al., 2009; Brookes et al., 2011; Tagliazucchi et al., 2012). Moreover, the present study indicates

that within-network synchronization is dependent on local neural activities that are temporally independent to each other, which necessitates the presence of a mechanism that would be conceived as network-specific pacemaker irrespective of the contribution of the global oscillations.

Technical Issues

In the present study, two large HCP datasets acquired from the same 50 subjects were used to test the reproducibility of the analysis. In temporal ICA, each component's independence is optimized for the axis of *time*. Therefore, the temporal dimensionality or timepoints of the data should be large enough. Although there is no good reason to assume that the number of timepoints should be as large as the number of voxels in original data, when the dimension was reduced during the process of group spatial ICA in advance to temporal ICA. Rather the problem lies in that it is generally difficult and practically impossible to know in advance how many timepoints are needed for an ICA, which is particularly dependent on the non-gaussianity of the data. This is why *post hoc* analysis is generally considered important to validate an ICA.

It is also theoretically apparent that higher spatiotemporal resolution is preferable for a better mapping of the spatiotemporal characteristic of the data. However, identification of the global component is not likely dependent on the spatiotemporal resolution of the BOLD fMRI. This is because ICs are classified according to the pattern of spatial distribution, which is not dependent on the temporal or spatial resolution itself let alone the speed of the traveling waves. Therefore, granting that the time lag maps would become more accurate if the sampling rate or spatial resolution of the data were increased, given that the maps obtained in the present study represent structured and highly similar patterns even across studies for the whole-brain signal (Amemiya et al., 2014; Mitra et al., 2014; Tong et al., 2017), such contribution would be negligible compared with other factors, at least for the range of the neural band of 0.01–0.1 Hz. The same holds true for the slice-time correction. HCP do not recommend us doing slice timing correction for the dataset, because while the effect of the slice timing correction is limited for the short TR (0.72s), slice timing correction interacts with movement correction in ways that have not ever been appropriately addressed in available tools. However, given the fact that it is impossible to align the subjects' head in exactly the same position for every scan for all the subjects, and that the acquisition was performed by using simultaneous multislice imaging with a slice thickness of 2 mm, we consider that the small slice timing differences were expected to be canceled out during the course of spatial normalization and group averaging of the time lag maps, which was confirmed by high correlation among the whole-brain signal time lag maps.

For the preprocessing, we did not apply global signal regression (GSR). Although GSR is a useful process to remove physiological noise like motion artifact, it eliminates any global signal regardless of the origin and can distort the resulting connectivity or activation measures in a complex way (Saad et al., 2012; Gotts et al., 2013; Glasser et al., 2016, 2018; Tang et al., 2019). Therefore, GSR and related approaches still remain controversial. Given that the study aim is to understand the possible contribution of the global signal, we consider it important not to apply GSR for our analysis.

In the present study, detection of the global IC was based on the spatial distribution pattern of each component that was judged by template matching using RSNs as well as the magnitude map of the whole-brain signal, which enabled us to classify an IC into global or local component without setting a threshold for the spatial coverage of that component. Although intuitively, an IC showing a larger spatial coverage would be considered as a global component, such classification is practically very difficult, because there is no objective definition regarding the coverage of a global component, as was the case in the original definition of the RSNs.

Rather, it is important to note that the present study, like previous studies, focuses on identifying slow waves with fixed patterns of propagation. While such an approach is advantageous in exploring the most robust representation of the phenomenon, an analysis allowing more spatiotemporally complex and dynamically changing patterns of propagation will probably reveal a more precise picture of the inter-network activities that may contribute to the integration of the network-specific activities constituting the functional architecture of the brain.

DATA AVAILABILITY STATEMENT

The datasets for this study are openly available at https://www.humanconnectome.org/.

AUTHOR CONTRIBUTIONS

SA contributed to the conception and design of the study, performed the statistical analysis, and wrote the first draft of the manuscript. SA and HT contributed to the interpretation of the data. All authors contributed to the manuscript revision, and read and approved the submitted version.

FUNDING

This work was supported by JSPS Grant-in-Aid for Scientific Research (C 18K07707), and grants from the Takeda Science Foundation, the Tokyo Society of Medical Sciences, and the Japanese Society of Neuroradiology to SA.

SUPPLEMENTARY MATERIAL

The Supplementary Material for this article can be found online at: https://www.frontiersin.org/articles/10.3389/fnsys.2019.00065/full#supplementary-material

REFERENCES

Abbas, A., Belloy, M., Kashyap, A., Billings, J., Nezafati, M., Schumacher, E. H., et al. (2019). Quasi-periodic patterns contribute to functional connectivity in the brain. *Neuroimage* 191, 193–204. doi: 10.1016/j.neuroimage.2019.01.076

Abeles, M. (1982). *Local Cortical Circuits: an Electrophysiological Study*. Berlin: Springer.

Abeles, M. (1991). *Corticonics: Neural Circuits of the Cerebral Cortex*. New York, NY: Cambridge University Press.

Amemiya, S., Kunimatsu, A., Saito, N., and Ohtomo, K. (2012). Impaired hemodynamic response in the ischemic brain assessed with BOLD fMRI. *Neuroimage* 61, 579–590. doi: 10.1016/j.neuroimage.2012.04.001

Amemiya, S., Kunimatsu, A., Saito, N., and Ohtomo, K. (2014). Cerebral hemodynamic impairment: assessment with resting-state functional MR imaging. *Radiology* 270, 548–555. doi: 10.1148/radiol.13130982

Amemiya, S., Takao, H., Hanaoka, S., and Ohtomo, K. (2016). Global and structured waves of rs-fMRI signal identified as putative propagation of spontaneous neural activity. *Neuroimage* 133, 331–340. doi: 10.1016/j.neuroimage.2016.03.033

Bandettini, P. A. (2014). Neuronal or hemodynamic? Grappling with the functional MRI signal. *Brain Connect.* 4, 487–498. doi: 10.1089/brain.2014.0288

Beckmann, C. F., and Smith, S. M. (2004). Probabilistic independent component analysis for functional magnetic resonance imaging. *IEEE Trans. Med. Imaging* 23, 137–152. doi: 10.1109/tmi.2003.822821

Belloy, M. E., Naeyaert, M., Abbas, A., Shah, D., Vanreusel, V., van Audekerke, J., et al. (2018). Dynamic resting state fMRI analysis in mice reveals a set of Quasi-periodic patterns and illustrates their relationship with the global signal. *Neuroimage* 180(Pt B), 463–484. doi: 10.1016/j.neuroimage.2018.01.075

Biswal, B., Yetkin, F. Z., Haughton, V. M., and Hyde, J. S. (1995). Functional connectivity in the motor cortex of resting human brain using echo-planar MRI. *Magn. Reson. Med.* 34, 537–541. doi: 10.1002/mrm.1910340409

Brookes, M. J., Woolrich, M., Luckhoo, H., Price, D., Hale, J. R., Stephenson, M. C., et al. (2011). Investigating the electrophysiological basis of resting state networks using magnetoencephalography. *Proc. Natl. Acad. Sci. U.S.A.* 108, 16783–16788. doi: 10.1073/pnas.1112685108

Calabrese, R. L. (1998). Cellular, synaptic, network, and modulatory mechanisms involved in rhythm generation. *Curr. Opin. Neurobiol.* 8, 710–717. doi: 10.1016/s0959-4388(98)80112-8

Civillico, E. F., and Contreras, D. (2012). Spatiotemporal properties of sensory responses in vivo are strongly dependent on network context. *Front. Syst. Neurosci.* 6:25. doi: 10.3389/fnsys.2012.00025

Diesmann, M., Gewaltig, M. O., and Aertsen, A. (1999). Stable propagation of synchronous spiking in cortical neural networks. *Nature* 402, 529–533. doi: 10.1038/990101

Ferezou, I., Haiss, F., Gentet, L. J., Aronoff, R., Weber, B., and Petersen, C. C. (2007). Spatiotemporal dynamics of cortical sensorimotor integration in behaving mice. *Neuron* 56, 907–923. doi: 10.1016/j.neuron.2007.10.007

Filippini, N., MacIntosh, B. J., Hough, M. G., Goodwin, G. M., Frisoni, G. B., Smith, S. M., et al. (2009). Distinct patterns of brain activity in young carriers of the APOE-epsilon4 allele. *Proc. Natl. Acad. Sci. U.S.A.* 106, 7209–7214. doi: 10.1073/pnas.0811879106

Fox, M. D., and Raichle, M. E. (2007). Spontaneous fluctuations in brain activity observed with functional magnetic resonance imaging. *Nat. Rev. Neurosci.* 8, 700–711. doi: 10.1038/nrn2201

Fox, M. D., Snyder, A. Z., Vincent, J. L., Corbetta, M., Van Essen, D. C., and Raichle, M. E. (2005). The human brain is intrinsically organized into dynamic, anticorrelated functional networks. *Proc. Natl. Acad. Sci. U.S.A.* 102, 9673–9678. doi: 10.1073/pnas.0504136102

Glasser, M. F., Coalson, T. S., Bijsterbosch, J. D., Harrison, S. J., Harms, M. P., Anticevic, A., et al. (2018). Using temporal ICA to selectively remove global noise while preserving global signal in functional MRI data. *Neuroimage* 181, 692–717. doi: 10.1016/j.neuroimage.2018.04.076

Glasser, M. F., Smith, S. M., Marcus, D. S., Andersson, J. L., Auerbach, E. J., Behrens, T. E., et al. (2016). The human connectome project's neuroimaging approach. *Nat. Neurosci.* 19, 1175–1187. doi: 10.1038/nn.4361

Glasser, M. F., Sotiropoulos, S. N., Wilson, J. A., Coalson, T. S., Fischl, B., Andersson, J. L., et al. (2013). The minimal preprocessing pipelines for the human connectome project. *Neuroimage* 80, 105–124. doi: 10.1016/j.neuroimage.2013.04.127

Goldman, R. I., Stern, J. M., Engel, J. Jr., and Cohen, M. S. (2002). Simultaneous EEG and fMRI of the alpha rhythm. *Neuroreport* 13, 2487–2492. doi: 10.1097/01.wnr.0000047685.08940.d0

Gotts, S. J., Saad, Z. S., Jo, H. J., Wallace, G. L., Cox, R. W., and Martin, A. (2013). The perils of global signal regression for group comparisons: a case study of autism spectrum disorders. *Front. Hum. Neurosci.* 7:356. doi: 10.3389/fnhum.2013.00356

Griffanti, L., Salimi-Khorshidi, G., Beckmann, C. F., Auerbach, E. J., Douaud, G., Sexton, C. E., et al. (2014). ICA-based artefact removal and accelerated fMRI acquisition for improved resting state network imaging. *Neuroimage* 95, 232–247. doi: 10.1016/j.neuroimage.2014.03.034

Harris-Warrick, R. M. (2010). General principles of rhythmogenesis in central pattern generator networks. *Prog. Brain Res.* 187, 213–222. doi: 10.1016/B978-0-444-53613-6.00014-9

Himberg, J., Hyvarinen, A., and Esposito, F. (2004). Validating the independent components of neuroimaging time series via clustering and visualization. *Neuroimage* 22, 1214–1222. doi: 10.1016/j.neuroimage.2004.03.027

Hyvärinen, A. (1999). Fast and robust fixed-point algorithms for independent component analysis. *IEEE Trans. Neural Netw.* 10, 626–634. doi: 10.1109/72.761722

Ivanchenko, M. V., Thomas, N., Selverston, A. I., and Rabinovich, M. I. (2008). Pacemaker and network mechanisms of rhythm generation: cooperation and competition. *J. Theor. Biol.* 253, 452–461. doi: 10.1016/j.jtbi.2008.04.016

Johnson, S. M., Wiegel, L. M., and Majewski, D. J. (2007). Are pacemaker properties required for respiratory rhythm generation in adult turtle brain stems in vitro? *Am. J. Physiol. Regul. Integr. Comp. Physiol.* 293, R901–R910. doi: 10.1152/ajpregu.00912.2006

Kenet, T., Bibitchkov, D., Tsodyks, M., Grinvald, A., and Arieli, A. (2003). Spontaneously emerging cortical representations of visual attributes. *Nature* 425, 954–956. doi: 10.1038/nature02078

Lampl, I., Reichova, I., and Ferster, D. (1999). Synchronous membrane potential fluctuations in neurons of the cat visual cortex. *Neuron* 22, 361–374. doi: 10.1016/s0896-6273(00)81096-x

Majeed, W., Magnuson, M., Hasenkamp, W., Schwarb, H., Schumacher, E. H., Barsalou, L., et al. (2011). Spatiotemporal dynamics of low frequency BOLD fluctuations in rats and humans. *Neuroimage* 54, 1140–1150. doi: 10.1016/j.neuroimage.2010.08.030

Majeed, W., Magnuson, M., and Keilholz, S. D. (2009). Spatiotemporal dynamics of low frequency fluctuations in BOLD fMRI of the rat. *J. Magn. Reson. Imaging* 30, 384–393. doi: 10.1002/jmri.21848

Massimini, M., Huber, R., Ferrarelli, F., Hill, S., and Tononi, G. (2004). The sleep slow oscillation as a traveling wave. *J. Neurosci.* 24, 6862–6870. doi: 10.1523/jneurosci.1318-04.2004

Matsui, T., Murakami, T., and Ohki, K. (2016). Transient neuronal coactivations embedded in globally propagating waves underlie resting-state functional connectivity. *Proc. Natl. Acad. Sci. U.S.A.* 113, 6556–6561. doi: 10.1073/pnas.1521299113

Meijering, E. (2002). A chronology of interpolation: from ancient astronomy to modern signal and image processing. *Proc. IEEE* 90, 319–342. doi: 10.1109/5.993400

Mitra, A., Snyder, A. Z., Blazey, T., and Raichle, M. E. (2015a). Lag threads organize the brain's intrinsic activity. *Proc. Natl. Acad. Sci. U.S.A.* 112, E2235–E2244. doi: 10.1073/pnas.1503960112

Mitra, A., Snyder, A. Z., Tagliazucchi, E., Laufs, H., and Raichle, M. E. (2015b). Propagated infra-slow intrinsic brain activity reorganizes across wake and slow wave sleep. *eLife* 4:e10781. doi: 10.7554/eLife.10781

Mitra, A., Snyder, A. Z., Hacker, C. D., and Raichle, M. E. (2014). Lag structure in resting-state fMRI. *J. Neurophysiol.* 111, 2374–2391. doi: 10.1152/jn.00804.2013

Mohajerani, M. H., Chan, A. W., Mohsenvand, M., LeDue, J., Liu, R., McVea, D. A., et al. (2013). Spontaneous cortical activity alternates between motifs defined by regional axonal projections. *Nat. Neurosci.* 16, 1426–1435. doi: 10.1038/nn.3499

Muller, L., and Destexhe, A. (2012). Propagating waves in thalamus, cortex and the thalamocortical system: experiments and models. *J. Physiol. Paris* 106, 222–238. doi: 10.1016/j.jphysparis.2012.06.005

Petersen, C. C., Hahn, T. T., Mehta, M., Grinvald, A., and Sakmann, B. (2003). Interaction of sensory responses with spontaneous depolarization in layer 2/3 barrel cortex. *Proc. Natl. Acad. Sci. U.S.A.* 100, 13638–13643. doi: 10.1073/pnas.2235811100

Ponce-Alvarez, A., Deco, G., Hagmann, P., Romani, G. L., Mantini, D., and Corbetta, M. (2015). Resting-state temporal synchronization networks emerge from connectivity topology and heterogeneity. *PLoS Comput. Biol.* 11:e1004100. doi: 10.1371/journal.pcbi.1004100

Pruim, R. H., Mennes, M., van Rooij, D., Llera, A., Buitelaar, J. K., and Beckmann, C. F. (2015). ICA-AROMA: a robust ICA-based strategy for removing motion artifacts from fMRI data. *Neuroimage* 112, 267–277. doi: 10.1016/j.neuroimage.2015.02.064

Roc, A. C., Wang, J., Ances, B. M., Liebeskind, D. S., Kasner, S. E., and Detre, J. A. (2006). Altered hemodynamics and regional cerebral blood flow in patients with hemodynamically significant stenoses. *Stroke* 37, 382–387. doi: 10.1161/01.str.0000198807.31299.43

Rybak, I. A., Abdala, A. P., Markin, S. N., Paton, J. F., and Smith, J. C. (2007). Spatial organization and state-dependent mechanisms for respiratory rhythm and pattern generation. *Prog. Brain Res.* 165, 201–220. doi: 10.1016/s0079-6123(06)65013-9

Rybak, I. A., Shevtsova, N. A., Paton, J. F., Pierrefiche, O., St-John, W. M., and Haji, A. (2004). Modelling respiratory rhythmogenesis: focus on phase switching mechanisms. *Adv. Exp. Med. Biol.* 551, 189–194. doi: 10.1007/0-387-27023-x_29

Saad, Z. S., Gotts, S. J., Murphy, K., Chen, G., Jo, H. J., Martin, A., et al. (2012). Trouble at rest: how correlation patterns and group differences become distorted after global signal regression. *Brain Connect.* 2, 25–32. doi: 10.1089/brain.2012.0080

Salimi-Khorshidi, G., Douaud, G., Beckmann, C. F., Glasser, M. F., Griffanti, L., Smith, S. M., et al. (2014). Automatic denoising of functional MRI data: combining independent component analysis and hierarchical fusion of classifiers. *Neuroimage* 90, 449–468. doi: 10.1016/j.neuroimage.2013.11.046

Shu, Y., Hasenstaub, A., and McCormick, D. A. (2003). Turning on and off recurrent balanced cortical activity. *Nature* 423, 288–293. doi: 10.1038/nature01616

Smith, S. M., Beckmann, C. F., Andersson, J., Auerbach, E. J., Bijsterbosch, J., Douaud, G., et al. (2013). Resting-state fMRI in the human connectome project. *Neuroimage* 80, 144–168. doi: 10.1016/j.neuroimage.2013.05.039

Smith, S. M., Miller, K. L., Moeller, S., Xu, J., Auerbach, E. J., Woolrich, M. W., et al. (2012). Temporally-independent functional modes of spontaneous brain activity. *Proc. Natl. Acad. Sci. U.S.A.* 109, 3131–3136. doi: 10.1073/pnas.1121329109

Sohal, V. S., Pangratz-Fuehrer, S., Rudolph, U., and Huguenard, J. R. (2006). Intrinsic and synaptic dynamics interact to generate emergent patterns of rhythmic bursting in thalamocortical neurons. *J. Neurosci.* 26, 4247–4255. doi: 10.1523/jneurosci.3812-05.2006

Steriade, M., McCormick, D. A., and Sejnowski, T. J. (1993). Thalamocortical oscillations in the sleeping and aroused brain. *Science* 262, 679–685. doi: 10.1126/science.8235588

Stroh, A., Adelsberger, H., Groh, A., Rühlmann, C., Fischer, S., Schierloh, A., et al. (2013). Making waves: initiation and propagation of corticothalamic Ca2+ waves in vivo. *Neuron* 77, 1136–1150. doi: 10.1016/j.neuron.2013.01.031

Tagliazucchi, E., von Wegner, F., Morzelewski, A., Brodbeck, V., and Laufs, H. (2012). Dynamic BOLD functional connectivity in humans and its electrophysiological correlates. *Front. Hum. Neurosci.* 6:339. doi: 10.3389/fnhum.2012.00339

Takeda, Y., Hiroe, N., Yamashita, O., and Sato, M. A. (2016). Estimating repetitive spatiotemporal patterns from resting-state brain activity data. *Neuroimage* 133, 251–265. doi: 10.1016/j.neuroimage.2016.03.014

Tang, Y., Zhou, Q., Chang, M., Chekroud, A., Gueorguieva, R., Jiang, X., et al. (2019). Altered functional connectivity and low-frequency signal fluctuations in early psychosis and genetic high risk. *Schizophr Res.* 210, 172–179. doi: 10.1016/j.schres.2018.12.041

Tong, Y., Hocke, L. M., Fan, X., Janes, A. C., and Frederick, B. (2015). Can apparent resting state connectivity arise from systemic fluctuations? *Front. Hum. Neurosci.* 9:285. doi: 10.3389/fnhum.2015.00285

Tong, Y., Lindsey, K. P., Hocke, L. M., Vitaliano, G., Mintzopoulos, D., and Frederick, B. D. (2017). Perfusion information extracted from resting state functional magnetic resonance imaging. *J. Cereb. Blood Flow Metab.* 37, 564–576. doi: 10.1177/0271678x16631755

Tsodyks, M., Kenet, T., Grinvald, A., and Arieli, A. (1999). Linking spontaneous activity of single cortical neurons and the underlying functional architecture. *Science* 286, 1943–1946. doi: 10.1126/science.286.5446.1943

Van Essen, D. C., Smith, S. M., Barch, D. M., Behrens, T. E., Yacoub, E., Ugurbil, K., et al. (2013). The WU-minn human connectome project: an overview. *Neuroimage* 80, 62–79. doi: 10.1016/j.neuroimage.2013.05.041

Vincent, J. L., Patel, G. H., Fox, M. D., Snyder, A. Z., Baker, J. T., Van Essen, D. C., et al. (2007). Intrinsic functional architecture in the anaesthetized monkey brain. *Nature* 447, 83–86. doi: 10.1038/nature05758

Wang, X. J. (2010). Neurophysiological and computational principles of cortical rhythms in cognition. *Physiol. Rev.* 90, 1195–1268. doi: 10.1152/physrev.00035.2008

Whitfield-Gabrieli, S., and Nieto-Castanon, A. (2012). Conn: a functional connectivity toolbox for correlated and anticorrelated brain networks. *Brain Connect.* 2, 125–141. doi: 10.1089/brain.2012.0073

Xu, W., Huang, X., Takagaki, K., and Wu, J.-Y. (2007). Compression and reflection of visually evoked cortical waves. *Neuron* 55, 119–129. doi: 10.1016/j.neuron.2007.06.016

Yan, L., Zhuo, Y., Ye, Y., Xie, S. X., An, J., Aguirre, G. K., et al. (2009). Physiological origin of low-frequency drift in blood oxygen level dependent (BOLD) functional magnetic resonance imaging (fMRI). *Magn. Reson. Med.* 61, 819–827. doi: 10.1002/mrm.21902

Zhang, D., Snyder, A. Z., Shimony, J. S., Fox, M. D., and Raichle, M. E. (2010). Noninvasive functional and structural connectivity mapping of the human thalamocortical system. *Cereb. Cortex* 20, 1187–1194. doi: 10.1093/cercor/bhp182

Conflict of Interest: The authors declare that the research was conducted in the absence of any commercial or financial relationships that could be construed as a potential conflict of interest.

Copyright © 2019 Amemiya, Takao and Abe. This is an open-access article distributed under the terms of the Creative Commons Attribution License (CC BY). The use, distribution or reproduction in other forums is permitted, provided the original author(s) and the copyright owner(s) are credited and that the original publication in this journal is cited, in accordance with accepted academic practice. No use, distribution or reproduction is permitted which does not comply with these terms.

frontiers in Systems Neuroscience

ORIGINAL RESEARCH
published: 03 December 2019
doi: 10.3389/fnsys.2019.00072

Cooperative Phase Adaptation and Amplitude Amplification of Neuronal Activity in the Vagal Complex: An Interplay Between Microcircuits and Macrocircuits

*Yoshinori Kawai**

Department of Anatomy, The Jikei University School of Medicine, Nishi-Shimbashi Minato-ku, Tokyo, Japan

Clusters of neurons can communicate with others through the cross-frequency coupling mechanism of oscillatory synchrony. We addressed the hypothesis that neuronal networks at various levels from micro- to macrocircuits implement this communication strategy. An abundance of local recurrent axons of vagal complex (VC) cells establish dense local microcircuits and seem to generate high-frequency noise-causing stochastic resonance (reverberation) and coherence resonance, even in *in vitro* slice preparations. These phenomena were observed *in vitro* as the generation of episodes of higher-frequency noise after an external stimulation and as stimulus-induced or spontaneous high-amplitude signals (postsynaptic activities). The *in vitro* microcircuit networks rarely sustained the stochastic resonance and coherence resonance cooperatively; however, *in vivo* networks involving additional intrabulbar mesocircuits and large-scale macrocircuits were able to sustain them cooperatively. This gave rise to large-scale oscillatory synchrony leading to robust power and coherence of signals with high amplitudes, reaching several millivolts in amplitude from a noise level of ∼100 microV through cardiorespiratory frequency coupling. A regenerative mechanism of neuronal circuits might work for the generation of large-scale oscillatory synchrony. The amplitude and phase of neuronal activity *in vivo* may interact cooperatively to give rise to varying degrees of power and coherence of robust rhythmic activity for distinct physiological roles. The cooperative interaction between phase adaptation and amplitude amplification of neuronal activity may provide diverse nervous systems with both robustness and resilience.

Keywords: resonance, synchrony, noise, fluctuation, brain wave, electrophysiology, emergence, complex adaptive system

OPEN ACCESS

Edited by:
Andrea Duggento,
University of Rome Tor Vergata, Italy

Reviewed by:
Kyriaki Sidiropoulou,
University of Crete, Greece
Srikanth Ramaswamy,
École Polytechnique Fédérale de Lausanne, Switzerland
Sungwoo Ahn,
East Carolina University, United States

***Correspondence:**
Yoshinori Kawai
ykawai@jikei.ac.jp

Received: *16 July 2019*
Accepted: *18 November 2019*
Published: *03 December 2019*

Citation:
Kawai Y (2019) Cooperative Phase Adaptation and Amplitude Amplification of Neuronal Activity in the Vagal Complex: An Interplay Between Microcircuits and Macrocircuits. Front. Syst. Neurosci. 13:72. doi: 10.3389/fnsys.2019.00072

INTRODUCTION

The most salient feature of brain electrical activity is the oscillatory synchrony generated and/or sustained by ensembles of coupled neuronal oscillators (Destexhe et al., 1999; Buzsaki, 2006; Canolty and Knight, 2010; Kawai, 2018b). Clusters of neurons with varying spatial dimensions and connectivity form regenerative neuronal circuits that can elicit

synchronized oscillations. These neuronal circuits also incessantly generate brain activity at the level of noise in the form of local sub- and suprathreshold waves, in addition to spatially distributed large-scale oscillatory synchrony. Previous publications have addressed and emphasized a possible interdependent relationship between wave synchrony and noise, although rarely in real nervous tissues (but see Galán et al., 2006), and mainly in theoretical or simulation-based studies (Ermentrout et al., 2008; Faisal et al., 2008). For example, it has been reported that noise can play a stabilizing role in synchronized oscillations. When adequate random noise is added, stable and synchronized oscillations may appear. Uncorrelated noise may thus sufficiently change the characteristics of a non-oscillating feedback system to produce stable oscillations (Springer and Paulsson, 2006). Theoretical and simulation-based studies predict that stochastic noise or fluctuation in an excitable-system can produce large-scale oscillatory synchrony *via* stochastic or coherence resonance mechanisms (Wiesenfeld and Moss, 1995; Pikovsky and Kurths, 1997; McDonnell and Abbott, 2009; Dodla and Wilson, 2010).

However, noise-based stochastic or coherence resonance-like phenomena have rarely been described with respect to the nervous system, particularly not in real *in vitro* and *in vivo* brain preparations that retain neuronal circuits with varying levels of intactness (Galán et al., 2006). Using brainstem preparations, the present study sought to investigate the structure and dynamics of neuronal activity [subthreshold, spike, local field potential (LFP) activity] at the noise level that may develop into emergent large-scale oscillatory synchrony. In addition, the possible functional significance of such developmental dynamics was evaluated (Kawai, 2018b). Although the significance of noise in neural functions has been both endorsed and refuted in previously published literature (Stein et al., 2005; Ermentrout et al., 2008), the present study would like to stress the quintessential role of neuronal noise in neural functions. Analogous to complex adaptive systems, a cooperative interaction of wave amplitude amplification and phase adaptation is proposed in the present study with respect to the robustness and resilience of these systems (Holland, 1995).

MATERIALS AND METHODS

Animal Preparations and Electrophysiological Recordings

All surgical and experimental procedures were approved by the Institutional Committee for the Care and Use of Experimental Animals at the Jikei University School of Medicine in Japan and were performed in accordance with the Guidelines for Proper Conduct of the Animal Experiments by the Science Council of Japan.

For *in vitro* preparations, Sprague–Dawley rats (postnatal days 18–24; Saitama Experimental Animals Supply, Japan) were deeply anesthetized with ether. After decapitation at the cervical spinal level followed by rapid craniotomy, the brainstem mass including the cerebellum was quickly removed, and a 2–3-mm-thick block containing the area postrema (caudal medulla oblongata) was prepared for coronal slicing. Two slices containing the area postrema for patch-clamp whole-cell recordings were usually available from each animal.

Coronal slices (250–300 μm thickness) were made using a micro slicer (DTK-1000; Dosaka, Japan). Slices containing the area postrema were collected and incubated in standard Ringer's solution for at least 1 h at 37°C. The standard Ringer's solution had the following composition (in mM): 125 NaCl, 2.5 KCl, 2 $CaCl_2$, 1 $MgCl_2$, 1.25 NaH_2PO_4, 26 $NaHCO_3$, and 10 glucose. This solution was continuously bubbled with a mixture of 95% O_2 and 5% CO_2 (pH 7.4, ∼320 mOsm). After the incubation, a single brain slice was transferred to a recording chamber placed on the stage of an upright microscope (BX51WI; Olympus, Japan) and submerged in the continuously superfusing medium (1–2 ml/min). Whole-cell recordings with a high seal resistance (>1 GΩ before break-in) were obtained from cells of the nucleus of the tractus solitarius (NTS) using borosilicate glass pipettes [1.5 mm outer diameter (O.D.); World Precision Instruments, Sarasota, FL, USA]. The electrodes contained (in mM): 140 cesium-acetate, 0.1 $CaCl_2$, 2 $MgCl_2$, 5 TEA, 1 EGTA, 10 HEPES, 5 ATP, and 0.1% biocytin (pH 7.3). Unless specified otherwise, drugs were purchased from Sigma-Aldrich (St. Louis, MO, USA). The resistance of the electrodes filled with this solution ranged from 5 to 12 MΩ. Neuronal signals were recorded in either the voltage-clamp or the current-clamp mode (Multiclamp 700A; Molecular Devices, Foster City, CA, USA). Signals were filtered at 1–2 kHz and digitized at 2–4 kHz.

For detecting inward excitatory postsynaptic currents (EPSCs) and outward inhibitory PSCs (IPSCs) in the same neurons, the membrane potential was clamped first between −60 and −70 mV and then between 0 and 10 mV, respectively. Upward and downward currents of peak amplitudes more than twice the device noise level (∼20 pA) were sampled.

Evoked EPSCs and IPSCs were also recorded and analyzed. Isolated stimuli of 100–200 μs duration were applied at ∼0.1 Hz through tungsten bipolar electrodes with a tip diameter of 20 μm and separation of 150 μm. The electrodes were positioned at the dorsomedial part of the tractus solitarius in coronal slices.

On occasion, the A-type γ-aminobutyric acid ($GABA_A$) receptor antagonist bicuculline methiodide (10 μM) and the non- N-methyl-D-aspartate (NMDA) glutamate receptor antagonist 6-cyano-7-nitroquinoxaline-2,3-dione disodium (10 μM) were bath-applied to isolate excitatory glutamate- and inhibitory GABA-mediated activities, respectively.

For *in vivo* preparations, electrophysiological recordings were carried out using five male Sprague–Dawley rats (weight range, 280–310 g). Animals were anesthetized with an intraperitoneal injection of ketamine (30 mg/kg) and xylazine (24 mg/kg) and placed in a stereotaxic instrument for recording. In most cases, 0.5% isoflurane was additionally administered through a nose mask to obtain sufficient depth of anesthesia during recordings.

Glass electrodes (1.5 mm O.D.; World Precision Instruments) containing 2 M NaCl were used in *in vivo* extracellular recordings. The resistance of the electrodes filled with this solution ranged from 1 to 5 MΩ. After making an incision in the

atlanto-occipital dural membrane, an electrode tip was advanced under a stereoscopic microscope vertically with a motorized micromanipulator (IVM Single; Scientifica, East Sussex, UK) into the exposed left dorsal medulla at the level of the area postrema; the depth was 50–500 μm from the brain surface. Neuronal signals were recorded in alternating current mode with a Multiclamp700A. The amplified signals were analyzed offline using Spike2 (Cambridge Electronic Design Limited, Cambridge, UK) and OriginPro2017 (Lightstone Company, Tokyo, Japan) software.

Simultaneous 16-channel *in vivo* recordings were performed from the vagal complex (VC) using a silicon probe (A1x16-Poly2s-5mm-50s-177-A16; NeuroNexus Technologies Inc., Ann Arbor, MI, USA). The resistance of each electrode specified by the manufacturer was between 0.96 and 1.17 MΩ. Each electrode "site" consisted of a circular platinum metal 15 μm in diameter, arranged by two 8-site-columns, and separated by 50 μm (Blanche et al., 2005). Electrical activities were amplified (A-M Systems Model 3600 Amplifier; Carlsborg, WA, USA), sampled at 1–4 kHz, and stored for offline analysis.

Cardiorespiratory activities were recorded non-invasively with a piezoelectric pulse transducer (PZT; MP100; AD Instruments, New South Wales, NSW, Australia). The PZT transformed the mechanical movement or vibration of the thorax (through touch on the sensor probe patch) into electrical signals that could be divided into heartbeat and respiration components (Sato et al., 2006).

Data Analysis

Event data displays (**Figure 1**) were made using Spike2 menu commands. "Instantaneous frequency (Inst)" takes the inverse of the time difference between the current event and the one preceding it. The event is plotted as a dot. The x-axis dot position is the time event. The y-axis dot position is the instantaneous frequency of that event in Hz with respect to the previous event. "Mean frequency (Mean)" is calculated over the preceding data at each event. "Rate" counts how many events fall within a time period (1 s) and displays the result in the form of a histogram.

Neuronal signals recorded *in vivo* exhibited, to a highly variable degree, a mixture of single- or multi-unit spikes and LFPs, especially when using standard glass electrodes, whereas signals recorded with a silicon probe mostly consisted of LFPs. For 0–10 Hz phase (frequency range of cardiorespiratory rhythms) enhancement, neuronal signals were, in some cases, offline filtered with a low-pass type II Chebyshev filter (Spike2, low-filtered between D.C. and 100 Hz with an order of 2 and a ripple of 60).

Amplitude amplification of *in vitro* spontaneous EPSCs, *in vivo* multiple unit activities (MUAs), and *in vivo* LFPs was evaluated in terms of their height change and signal interval. Records of spontaneous signals (each ∼40-s duration) were sampled from each recording mode. The height of the signal amplification was expressed as a mean signal/noise ratio obtained from several experimental sessions (number: 4–8). Intervals between successive pairs of the amplified signals were measured and expressed as frequency (Hz). Values were expressed as mean ± standard errors.

Cross- and auto-correlograms, as well as fast Fourier transform power spectra, were generated with OriginPro2017. Continuous wavelet transform (CWT) and wavelet coherence using Morse wavelets (default wavelet function) were calculated with MATLAB (The MathWorks, Natick, MA, USA). CWT and wavelet coherence were expressed as time-resolved power and coherence spectra, respectively. A detailed explanation of each formula for numerical analysis was previously provided (Kawai, 2018b).

RESULTS

The caudal parts of the NTS consist of small, densely packed cells which are densely innervated by recurrent local axons that establish both excitatory and inhibitory synaptic transmission (**Figures 1A1,A2**, Negishi and Kawai, 2011). This microcircuit configuration of the caudal NTS seems to constitute an extremely noisy environment. The noise consisted mostly of subthreshold high-frequency postsynaptic activity even in *in vitro* slice preparations (**Figure 1B1**). The frequency of excitatory inward currents recorded from a small cell in the whole-cell mode of the patch-clamp technique was between 1.1 and 18.0 Hz (6.2 ± 1.2 Hz, $n = 12$). The postsynaptic activity was considered to be noise because paired activity recorded simultaneously from two neighboring cells (less than 50 μm in distance) showed no correlation or any specific corresponding spectra (**Figures 1B2,B3**). However, this noisy environment of the NTS rarely developed into a persistent firing even in *in vivo* experiments.

Phase adaptation described in this study represents an increase in the frequency of signal or noise associated with spontaneous or evoked signals of an amplified amplitude. In *in vitro* preparations, subthreshold EPSCs were analyzed because the spontaneous occurrence of spikes was extremely rare in the VC, while spikes were easily evoked after a slight external stimulation of afferent synapses. In contrast, neuronal signal or noise recorded *in vivo* as MUAs and LPFs would consist mostly of spike activity. A possible cooperative relationship between amplitude amplification and phase adaptation was addressed using both *in vitro* and *in vivo* preparations.

Evoked Phase Adaptation of Postsynaptic Activities *in vitro*

Evoked EPSCs were recorded from small NTS cells by minimally stimulating the tractus solitarius (**Figure 1C1**). Each tractus solitarius stimulation elicited usually a monosynaptic EPSC that possibly derived from primary afferents or nearby cells or polysynaptic EPSCs that could last for up to several seconds (solid triangles in **Figures 1C1**, **2**). In a few cases, the tractus solitarius stimulation failed to generate apparent polysynaptic EPSCs (open triangle and arrow in **Figure 1C1**). An evoked elevation of secondary polysynaptic activities was inconsistently observed (**Figure 1C2**). This statistically significant increase in noise frequency after an external stimulation was indicative of "reverberation of recurrent activity" (Tegnér et al., 2002). The reverberation reached 20–30 Hz in the instantaneous frequency (Inst in **Figure 1C2**), more than 10 Hz in the mean frequency

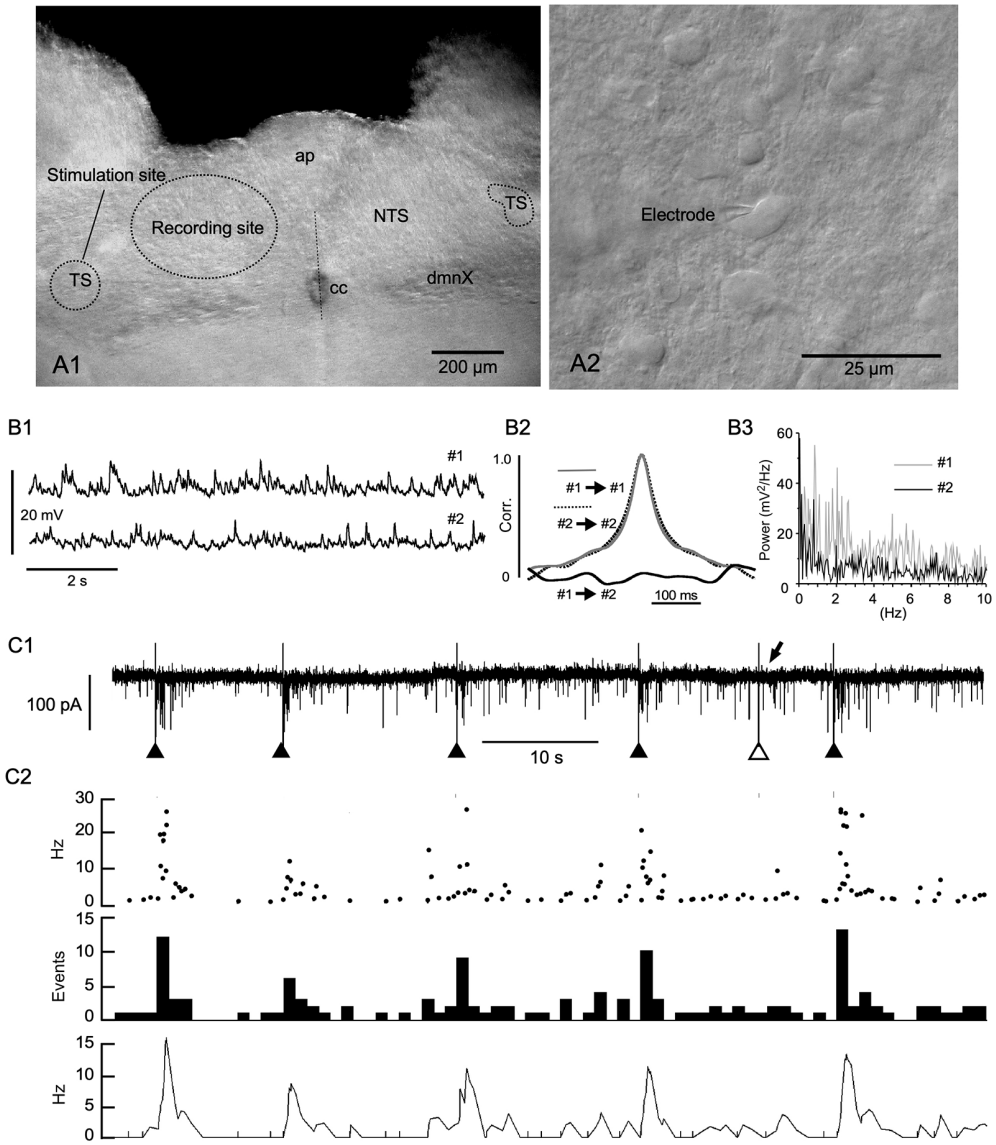


FIGURE 1 | Evoked phase adaptation of postsynaptic activities *in vitro*. **(A1)** A differential interference contrast (DIC) photomicrograph showing the recording and stimulation sites for *in vitro* slice preparations. **(A2)** A DIC photo of higher magnification. An electrode tip is shown. Note the size and density of NTS cells. **(B1)** Postsynaptic potentials (PSPs) recorded from two nearby neurons (#1 and #2) in a slice preparation using the patch-clamp whole-cell technique in the current-clamp mode. **(B2)** Cross- and auto-correlations (Corr.) of the PSPs. The lack of correlation between the PSP activities of the two cells shows that most of these spontaneous PSP activities were noise or fluctuation. **(B3)** Power spectra (0–10 Hz range) of the PSPs (#1 and #2) of 20 s duration. No specific frequency peaks or spectra coincidences between the PSPs are noted, characterizing the PSP activity features as noise. **(C1,2)** The frequency (phase) of noise activities recorded as postsynaptic currents (PSCs) is increased transiently over several seconds after an external stimulation of input fibers (triangles in **C1**). Of six successive stimulations, one (the open triangle in **C1**) fails to elicit a sufficient increase in frequency (arrow in **C1**). The phase adaptation elicited by external inputs are characterized by instantaneous (Inst in **C2**) frequencies of more than 10 Hz, increased mean (Mean in **C2**) events, and rate (Rate in **C2**) frequencies following subthreshold stimulations (gray vertical lines). ap, area postrema; cc, central canal; dmnX, the dorsal motor nucleus of the vagus; NTS, nucleus of the tractus solitarius; TS, tractus solitarius.

(Mean in **Figure 1C2**), 10–15 Hz in the rate count (Rate in **Figure 1C2**) and lasted for 1–5 s (**Figure 1C2**).

Evoked Amplitude Amplification of Postsynaptic Activities *in vitro*

The superimposition of a preceding evoked monosynaptic EPSC and the following multiple polysynaptic EPSCs by adjusting the stimulus artifacts (triangles in **Figure 1C1**; $n = 6$) was utilized to better assess the relationship between them (**Figure 2A**). A reverberation is most evident within ∼1 s following the stimulation (top wave trace, **Figure 2A**). More expanded wave traces (middle and lower traces, **Figure 2A**) indicate that multiple polysynaptic EPSCs appear more frequently near the preceding evoked EPSCs (double arrowheads in the lower

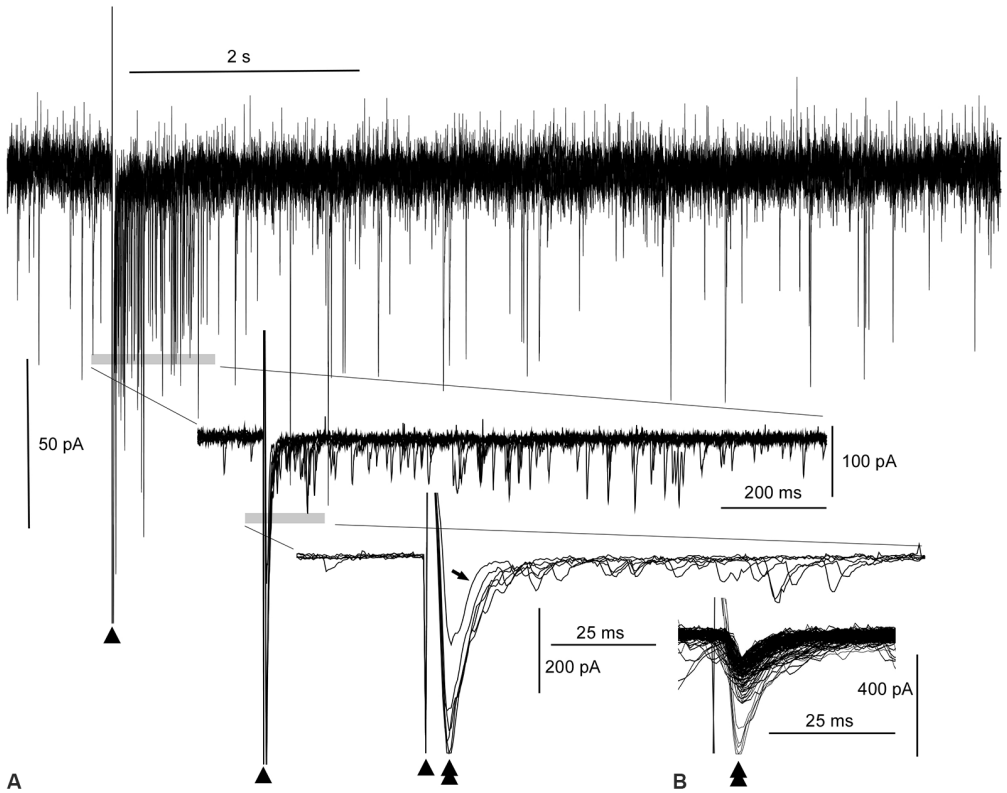


FIGURE 2 | Evoked amplitude amplification of postsynaptic activities *in vitro*. **(A)** Superimposition of six episodes of PSCs following external stimulations (arrowheads), as indicated in **Figure 1**. During the 1-s period after a stimulation, an apparent increase in the frequency of inward PSCs is noted (gray bar in the top wave trace). Both upward and downward stimulus artifacts are truncated in the top wave trace. Traces (middle and bottom) further expanded near the stimulus artifacts reveal high amplitude inward (downward) PSCs (double arrowhead in the bottom trace) following the stimulus artifacts (arrowheads). Out of six PSCs following the stimuli, one PSC of low amplitude fails to give rise to an increase in frequency (arrow in the bottom trace, see also the open arrowhead in **Figure 1C**). In the middle and bottom wave traces, upward traces near the stimulus artifacts are truncated. Note the co-occurrence of preceding high-amplitude PSCs and episodes of high-frequency PSCs for an increase in frequency. **(B)** Inward trough (double arrowheads)-triggered superimposition of both spontaneous and evoked PSCs. The inward evoked PSC with an aborted increase in frequency (tilted arrow, bottom wave trace in **A**) is embedded in many other spontaneous PSCs whose amplitudes are all within the noise level.

expanded wave traces, **Figure 2A**). However, a monosynaptic EPSC of lower amplitude (206 pA) fails to generate a barrage of subsequent multiple polysynaptic EPSCs (arrow in the lower group of traces, **Figure 2A**; see also **Figure 1C1**). It seems that the preceding evoked monosynaptic EPSCs with an amplitude (423 ± 42.1 pA; n = 5) large enough to elicit a reverberation cause the following multiple polysynaptic EPSCs, and thus amplitude amplification and phase adaptation co-occur by external stimulation. Superimposition of spontaneous and evoked EPSCs according to their inward current troughs (**Figure 2B**) indicates that the amplitude of an evoked EPSC failing to elicit a reverberation was within the range (40–260 pA) of that of spontaneous EPSCs, i.e., of a fluctuation (noise) level.

Spontaneous Amplitude Amplification of Electrical Activities *in vitro* and *in vivo*

The mean amplitude of spontaneous EPSCs in patch-clamp whole-cell recordings of the voltage-clamp mode was 40–50 pA in slice preparations (**Figures 3A,B**). The distribution of current amplitudes revealed a logarithmic normal distribution with a long tail. A spontaneous amplitude amplification rarely occurred in less than 2% of EPSCs. The spontaneous EPSCs superimposed with their inward current troughs indicate that several preceding EPSCs are followed by late EPSCs (5–10 ms latency) with a hint of spontaneous phase adaptation, however, on a few rare occasions, if any at all.

In contrast to *in vitro* preparations, a wave amplitude amplification was seen more frequently and conspicuously *in vivo* in terms of occurrence frequency (5–10%) and amplitude amplification (**Figures 3C,D**). Neuronal activities in the NTS recorded with a standard glass electrode comprised mostly a mixture of single- and multi-unit spikes, as well as highly polyphasic and LFP-like longer duration waves of up to several 100 μV in amplitude (i.e., the noise level). In a few cases, neuronal activities with an amplified amplitude (>1 mV) emerged abruptly, ensued sporadically for several seconds, and waned (**Figure 3C**). Similar phenomena of amplitude amplification were confirmed with LFPs recorded using a silicon electrode (**Figure 3D**). Spontaneous amplitude amplification of

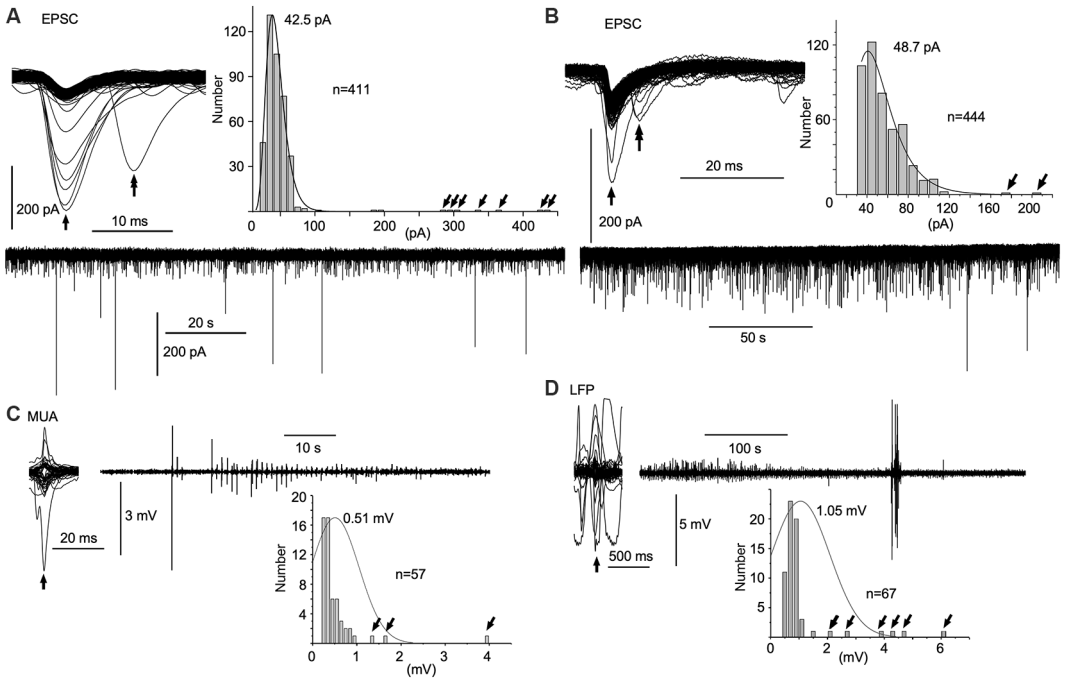


FIGURE 3 | Spontaneous amplitude amplification of electrical activities *in vitro* and *in vivo*. **(A,B)** Two examples of PSCs recorded in slice preparations using the patch-clamp whole-cell technique in the voltage-clamp mode. Inward trough (arrows)-triggered PSCs are superimposed. Several inward PSCs (arrows) are followed by late PSCs (double arrows). Note that high-amplitude PSCs occur randomly with an extremely low frequency in the PSC amplitude histograms (tilted arrows) and the original continuous PSC recordings. Note, the average of PSC amplitudes is 40–50 pA sampled from more than 400 PSCs. **(C)** Inward trough (arrow)-triggered multiple unit activities (MUAs) recorded *in vivo* with a standard glass electrode are superimposed on an original continuous MUA recording. **(D)** Inward trough (arrow)-triggered local field potentials (LFPs) recorded *in vivo* with a silicon electrode are superimposed on an original continuous LFP recording. Note that high-amplitude signals occur sporadically with higher frequency in the amplitude histograms (tilted arrows). In *in vivo* recordings, episodes of repetitive high-amplitude activities over several tens of seconds are spontaneously generated and subdued. EPSC, excitatory postsynaptic current.

neuronal activities was observed in the NTS of both *in vitro* and *in vivo* preparations.

Cooperative Phase Adaptation and Amplitude Amplification of Spontaneous Neuronal Activities *in vivo*

In *in vivo* preparations, it seemed that amplitude amplification occurred in concert with the respiratory rhythm (Kawai, 2018b). In order to verify this in more detail, cardiorespiratory and neuronal NTS activities were simultaneously recorded using a non-invasive PZT placed under the thorax (**Figures 4A1,B**). The power spectra of neuronal (NTS in **Figure 4A2**) and cardiorespiratory (PZT in **Figure 4A2**) rhythms show clear coherence. The respiratory and cardiac fundamental frequencies were ∼1.3 Hz and ∼6.8 Hz, respectively. Superimposition of simultaneous neuronal and PZT activities triggered by each large peak of PZT activity (that roughly corresponds to a transition from the inspiratory to the expiratory phase) indicates that amplitude amplification and higher frequency of noise co-occur during each inspiratory phase (**Figures 4A1,B**). However, strikingly large amplitudes of neuronal activity are concentrated either in the initial (**Figure 4A1**) or the final (**Figure 4B**) segment of an inspiratory phase.

Emergence of Large-Scale Cooperative Phase Adaptation and Amplitude Amplification of Neuronal Activities *in vivo*

Given that each NTS cell fires synchronously during an inspiratory phase, large-scale oscillatory synchrony was expected to be recorded in the VC with silicon multielectrode. Since the silicon electrode had a large vertical dimension of ∼400 μm, the part of the medulla oblongata termed the VC, consisting of the caudal NTS and the dorsal motor nucleus of the vagus nerve, was used instead of the NTS, to improve precision (**Figure 5A**).

As shown in **Figure 3D**, the amplitudes of LFPs changed sporadically. To quantify the three different phases of wave activities, 20-s (**Figure 5B**) and time-resolved (**Figure 5C**; CWT) power spectra were applied to three successive episodes (in magenta, green, and blue; 20 s durations, **Figure 5D**) of LFPs at a certain fixed recording site of the electrode. The power spectra show that the larger the signal amplitude the larger the power and that stronger power signals converge to a 1–3 Hz frequency (delta) band (**Figure 5C**). Time-resolved coherence spectra (wavelet coherence, Wcoh) between trace pairs with different distances (50, 200, and 350 μm) indicated that the shorter the distance of two paired recording sites or the larger the amplitude of the paired waves is, larger is the coherence between

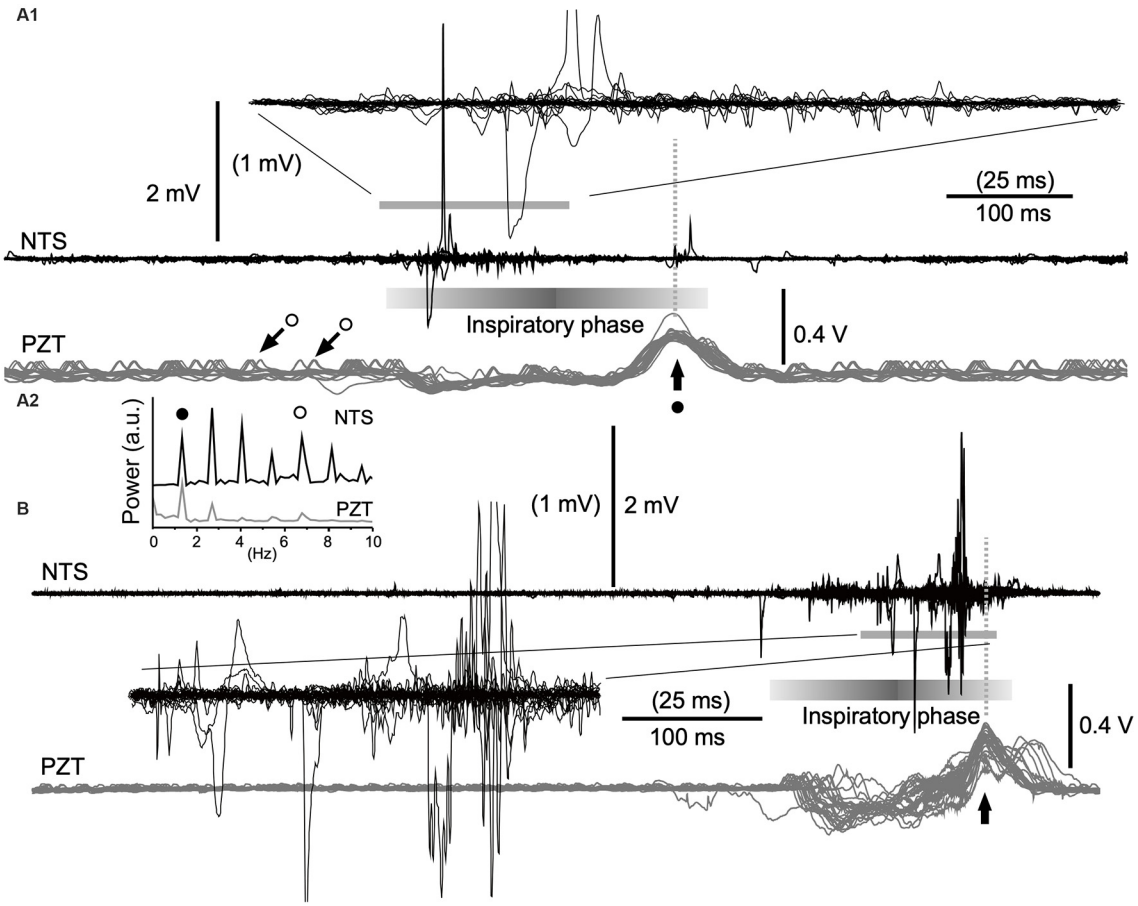


FIGURE 4 | Cooperative phase adaptation and amplitude amplification of neuronal activities *in vivo*. **(A1,B)** Two examples showing high-amplitude neuronal electrical activities recorded with a standard glass electrode. The majority of high-amplitude signals are synchronized with the inspiratory phase according to simultaneously recorded signals (gray traces) of a piezoelectric transducer (PZT) attached to the thorax. The superimposition according to PZT upward peaks (vertical arrows) of simultaneous neuronal (NTS) and PZT recordings shows several tens of consecutive episodes of one respiratory cycle (**A1**, 30 cycles; **B**, 26 cycles). Expanded wave traces are truncated and scaled to values in parentheses **(A1,B)**. **(A2)** Power spectra of neuronal (NTS) and cardiorespiratory (PZT) rhythms. Note synchrony of these two waves. Solid and open circles indicate respiratory and cardiac fundamental frequencies (∼1.3 Hz and ∼6.8 Hz, respectively). They are represented respectively as large (solid circle with arrow) and small (open circles with arrows) upward waves in the PZT trace (**A1**). NTS, nucleus of the tractus solitarius; a.u., arbitrary unit.

those wave pairs (**Figure 5E**). A large amplitude with a large-scale phase adaptation of LFPs generated larger power and coherence over a larger brain area.

Quantitation of Amplitude Amplification and Frequency of Spontaneous Signals

Amplitude amplification of *in vitro* spontaneous EPSCs, *in vivo* MUAs, and *in vivo* LFPs was evaluated according to the height changes and signal intervals (**Figure 6**). Values for amplitude amplification of spontaneous EPSCs, MUAs, and LFPs were 4.3 ± 0.9 ($n = 4$, each session contained 15 samples), 18.6 ± 4.6 ($n = 5$, 17 samples), and 49.6 ± 11.3 ($n = 8$, 18 samples), respectively. Values for the frequency of the amplified signals were 0.28 ± 0.12 ($n = 15$), 1.34 ± 0.16 ($n = 21$), and 0.97 ± 0.07 ($n = 21$), respectively. The frequency of amplified signals in *in vivo* recordings was adapted to a range of respiratory rhythmic cycles (∼1 Hz).

DISCUSSION

Large-scale oscillatory synchrony emerges spontaneously in the VC of anesthetized animals (Kawai, 2018b). Neuronal activity changes incessantly in frequency and amplitude depending on the spatial dimension of the oscillatory synchrony (Destexhe et al., 1999; Buzsaki, 2006). This phenomenon implies that the important properties of neuronal activity, i.e., phase and amplitude, may interact interdependently. The cooperative dynamics of wave amplitude and phase were addressed in the present study with respect to neuronal circuit configuration or dimension.

Microcircuits and Macrocircuits Involving the Vagal Complex

The VC consists of the caudal NTS and the dorsal motor nucleus of the vagus nerve (Ramon y Cajal, 1995;

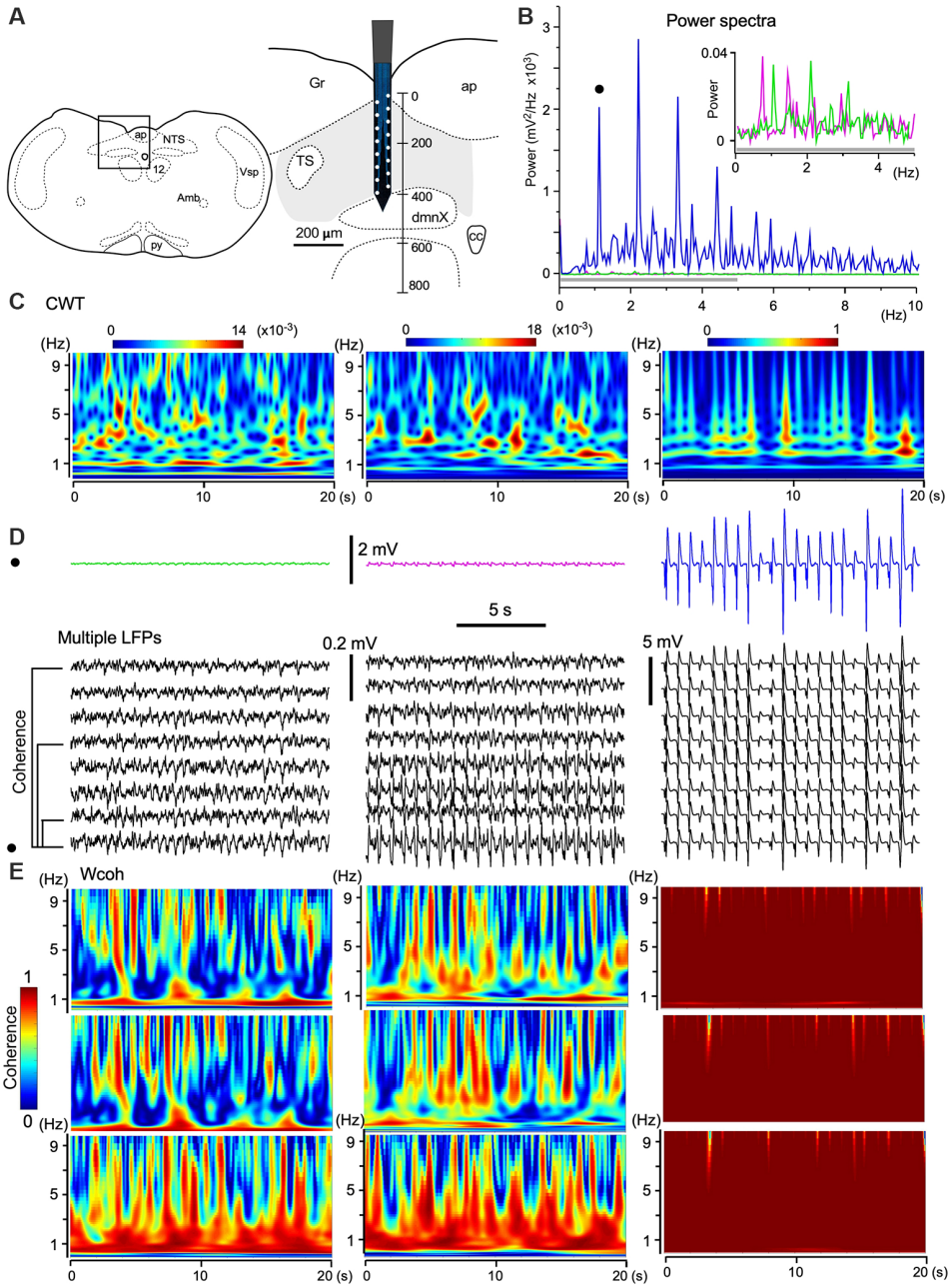


FIGURE 5 | The emergence of large-scale cooperative phase adaptation and amplitude amplification of neuronal activities *in vivo*. **(A)** A silicon electrode records LFPs at multiple sites over a 100 μm along the depth of the vagal complex (VC). Right, Magnification of the picture from an anatomical atlas (left). **(B,C)** Twenty-second **(B)** and time-resolved (**C**; continuous wavelet transform, CWT) power spectra of three successive episodes (20 s) of LFPs at a certain fixed recording site (three traces in **D**, top). **(B)** The power of high-amplitude LFPs (in blue) is increased compared to those of low-amplitude LFPs (in magenta and green, inset for a gray bar region). This representative set of episodes (solid circle in **D**) is one of eight sets of traces (**D**, multiple LFPs). **(E)** Time-resolved coherence spectra (wavelet coherence, Wcoh) between pairs of traces of the representative episode (solid circle in **D**) and of those at different distances (50, 200, and 350 μm apart, **D**, bottom). Note that the shorter the distance of paired sites or the larger the amplitude of paired waves is, the larger the coherence is. Amb, ambiguous nucleus; ap, area postrema; cc, central canal; dmnX, the dorsal motor nucleus of the vagus; Gr, gracilis nucleus; NTS, nucleus of the tractus solitarius; nXII (12), hypoglossal nucleus; py, pyramidal tract; TS, tractus solitarius; Vsp, spinal nucleus of the trigeminal nerves.

Kawai, 2018a,b). The caudal NTS provides multiple connections with diverse brain areas encompassing the telencephalon to the spinal cord, thus establishing large-scale macrocircuits (Kawai, 2018a). Most brain areas innervated by the NTS establish reciprocal connections with the NTS and form regenerative macrocircuits including intrabulbar brainstem mesocircuits that govern a robust rhythmic cardiorespiratory activity. This multiple-nested circuit configuration may implement noise-

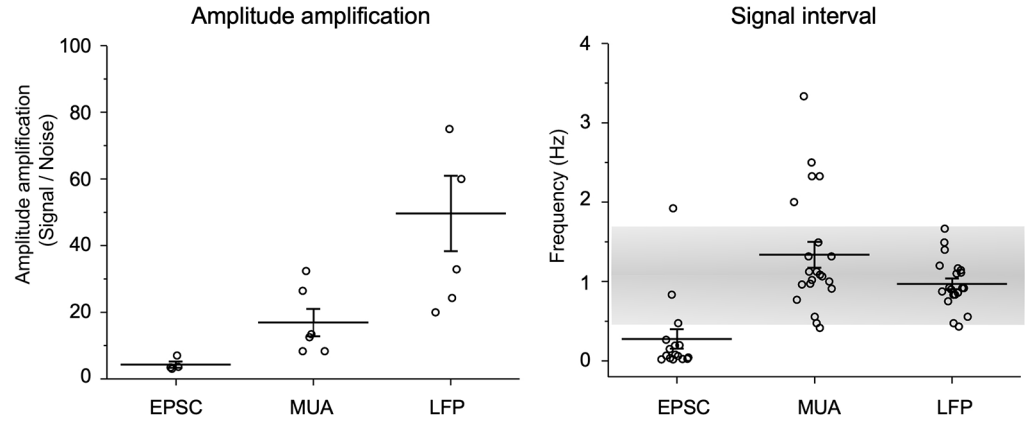


FIGURE 6 | Quantification of amplitude amplification and frequency. Amplitude amplification of *in vitro* spontaneous EPSCs, *in vivo* MUAs, and *in vivo* LFPs are quantified according to height changes and signal intervals. Note that the frequency of amplified signals in *in vivo* recordings adapts to a range of respiratory rhythmic cycles (∼1 Hz: gray shaded range). Values are represented as mean ± standard errors.

based stochastic synchrony that could confer a benefit to such a system in which robust cardiorespiratory rhythmicity and resilience to external perturbation coexist cooperatively. In addition to macrocircuits, the NTS contains microcircuits in which dense recurrent axons generate a highly noisy neuronal activity (Negishi and Kawai, 2011). The noise-based synchrony of cooperative wave phase adaptation and amplitude amplification in NTS microcircuits is specifically attributed to their cytoarchitectural features. The NTS consists of an extremely concentrated assembly of synaptically interconnected small cells (∼11 μm in diameter; Yoshioka et al., 2006). This structural compactness enables a clearer recording of emergent noise-based synchrony in *in vivo* preparations with a typical glass electrode, since the detection of a wave amplitude amplification is relatively easy with a stochastic correlation of noise activity. This may be due to the fact that a given receptive electrical field at an electrode tip would contain much greater numbers of smaller cell soma. This seems to provide a functional significance for sensory processing in reference to intrinsic stochastic synchrony since the NTS is strategically the sole recipient of peripheral viscerosensory information while connecting central macrocircuits governing rhythmic cardiorespiratory activity. This cooperative interplay between microcircuits and macrocircuits would be of functional significance.

Different behaviors of phase adaptation and amplitude amplification in *in vitro* and *in vivo* preparations could result from a developmental change in circuits rather than the different dimensions (micro vs. macro) of matured circuit organization. However, it has been demonstrated anatomically and physiologically that the VC circuit matures until late in the third week of postnatal development, supporting the latter possibility (Yoshioka et al., 2006; Tashiro and Kawai, 2007).

Neuronal Activity as Noise and Signal

The hierarchical architecture of nested neuronal circuits involving the VC could provide the anatomical basis for its unique task for VC for viscerosensory information processing (the caudal NTS) and autonomic output production (the dorsal motor nucleus of the vagus nerve) in addition to centrally generated neuronal activity. The centrally generated neuronal activity consists mostly of spontaneous stochastic noise that can change into signals of varied spatiotemporal dimensions and dynamics based on the cross-frequency coupling of the cardiorespiratory frequency range (Kawai, 2018b).

Wave synchrony and oscillation are, in most cases, phenomena that co-occur during neuronal activity, but the relative proportion of power in a certain macroscopic phenomenon varies according to the required task of the neuronal activity (Destexhe et al., 1999; Buzsaki, 2006). In the large-scale neuronal activity, wave synchrony with large amplitudes would be more appropriate for a signal transfer over longer distances to multiple destinations. For local activities, wave oscillations with a fine-tuned phase (particularly those of the higher gamma frequency range) would be appropriate for holding more precise information. The fundamental feature of ongoing neuronal activity is stochastic fluctuation (noise) to enable a potential development into a signal in either direction according to the changing environment to which individuals must adapt.

Gap junctions between neurons may play an important role in synchronized rhythms (Konopacki et al., 2014). However, this is unlikely to be the case in the VC because intracellular injections of biocytin or lucifer yellow, which can penetrate the junction complex, were not reported to stain any neighboring cells (Yoshioka et al., 2006; Negishi and Kawai, 2011).

Emergence and Development of Stochastic Synchrony

The phenomenon described in the present study seems to be similar to stochastic synchrony investigated in the olfactory bulb (Galán et al., 2006) in that both are likely to be noise-induced synchronization. Correlated noisy inputs are able to generate synchronous oscillation of the gamma frequency range (∼40 Hz) in mitral cells of the olfactory bulb *in vitro*. Of note is the

clear difference in frequency ranges between low (delta–theta for the VC, present study) and high (gamma for olfactory mitral cells; Galán et al., 2006). The stochastic synchrony emerges due to the influence of partially correlated but aperiodic transient inputs; neither synaptic coupling nor oscillatory input is required. In this respect, this phenomenon should be designated as coherence resonance (Pikovsky and Kurths, 1997) but not stochastic resonance (McDonnell and Abbott, 2009). Stochastic resonance has been used to explain noise-dependent entrainment of neuronal firing to a subthreshold oscillatory input in a variety of systems (Wiesenfeld and Moss, 1995; McDonnell and Abbott, 2009), including crayfish mechanoreceptors (Douglass et al., 1993; Moss and Pei, 1995). Although the adaptive feature of spiking synchrony and periodic network bursts was also investigated in neuronal networks (Mainen et al., 1995; Fardet et al., 2018), a relevance to stochastic noise was not addressed. The spontaneous synchrony, in this case, seems to be generated by phase-adaptive ion channel properties rather than stochastic noise.

Complex Adaptive System

The term complex adaptive system states that complex, emergent, and macroscopic properties of the system as a whole (an ensemble) could be self-organized as a result of non-linear dynamics of interacting microscopic elements, where they have no *a priori* plan or meaning (Holland, 1995; Kelso, 2016). The system is also characterized by a high degree of adaptive capacity (adaptation or homeostasis), giving it resilience in the face of perturbation. The microscopic interactions are non-linear, such that small changes in inputs, physical interactions, or stimuli can cause large effects or significant changes in outputs. Any interaction can feedback onto itself directly or after a number of intervening stages. Such feedback can vary in quality. This interaction may be designated as regenerative recurrence or iteration. The overall behavior of the system of elements would not be predicted by the behavior of the individual elements.

The above-mentioned description concerning a complex adaptive system may be applicable to many aspects of stochastic synchrony of the VC neuronal activity revealed in this study. The results show that a stable frequency of robust neuronal activity ranging to respiration rhythms emerges *in vivo* networks and would adapt to a changing environment.

CONCLUSION

The maintenance of rhythmic cardiorespiratory brain activity, which is the most fundamental and robust activity, may be a prerequisite for sustaining life. This robust task is attributed essentially to neuronal networks of the brainstem responsible for rhythmic cardiorespiratory activity (Feldman and Ellenberger, 1988). This task also requires resilience in the face of immediate changes in the environment, which individuals must constantly adapt to (Dick et al., 2014). The activity of the brainstem network involving the VC must obey a system rule in which robustness and resilience cooperatively and dynamically coexist. The most promising candidate for a system model may be that of a complex adaptive system (Holland, 1995; Kelso, 2016). This system contains concepts with several important keywords, including but not limited to robustness and resilience, self-organization, synchrony, non-linear dynamics, and emergence. Studies of system dynamics addressing such perspectives warrant multidisciplinary investigations using both experimental and theoretical approaches.

DATA AVAILABILITY STATEMENT

All datasets generated for this study are included in the article.

ETHICS STATEMENT

The animal study was reviewed and approved by the Care and Use of Experimental Animals at the Jikei University School of Medicine in Japan.

AUTHOR CONTRIBUTIONS

YK planned and performed the experiments, analyzed the results and wrote the manuscript.

ACKNOWLEDGMENTS

We would like to thank an anonymous native editor (Editage; www.editage.jp) for English language editing and valuable suggestions for the manuscript.

REFERENCES

Blanche, T. J., Spacek, M. A., Hetke, J. F., and Swindale, N. V. (2005). Polytrodes: high-density silicon electrode arrays for large-scale multiunit recording. *J. Neurophysiol.* 93, 2987–3000. doi: 10.1152/jn.01023.2004

Buzsaki, G. (2006). *Rhythms of the Brain.* New York, NY: Oxford University Press, Inc.

Canolty, R. T., and Knight, R. T. (2010). The functional role of cross-frequency coupling. *Trends Cogn. Sci.* 14, 506–515. doi: 10.1016/j.tics.2010.09.001

Destexhe, A., Contreras, D., and Steriade, M. (1999). Spatiotemporal analysis of local field potentials and unit discharges in cat cerebral cortex during natural wake and sleep states. *J. Neurosci.* 19, 4595–4608. doi: 10.1523/jneurosci.19-11-04595.1999

Dick, T. E., Hsieh, Y. H., Dhingra, R. R., Baekey, D. M., Galán, R. F., Wehrwein, E., et al. (2014). Cardiorespiratory coupling: common rhythms in cardiac, sympathetic and respiratory activities. *Prog. Brain Res.* 209, 191–205. doi: 10.1016/B978-0-444-63274-6.00010-2

Dodla, R., and Wilson, C. J. (2010). Coherence resonance due to transient thresholds in excitable systems. *Phys. Rev. E Stat. Nonlin. Soft Matter Phys.* 82:021105. doi: 10.1103/physreve.82.021105

Douglass, J. K., Wilkens, L., Pantazelou, E., and Moss, F. (1993). Noise enhancement of information transfer in crayfish mechanoreceptors by stochastic resonance. *Nature* 365, 337–340. doi: 10.1038/365337a0

Ermentrout, G. B., Galán, R. F., and Urban, N. N. (2008). Reliability, synchrony and noise. *Trends Neurosci.* 31, 428–434. doi: 10.1016/j.tins.2008.06.002

Faisal, A. A., Selen, L. P., and Wolpert, D. M. (2008). Noise in the nervous system. *Nat. Rev. Neurosci.* 9, 292–303. doi: 10.1038/nrn2258

Fardet, T., Ballandras, M., Bottani, S., Métens, S., and Monceau, P. (2018). Understanding the generation of network bursts by adaptive oscillatory neurons. *Front. Neurosci.* 12:41. doi: 10.3389/fnins.2018.00041

Feldman, J. L., and Ellenberger, H. H. (1988). Central coordination of respiratory and cardiovascular control in mammals. *Annu. Rev. Physiol.* 50, 593–606. doi: 10.1146/annurev.ph.50.030188.003113

Galán, R. F., Fourcaud-Trocmé, N., Ermentrout, G. B., and Urban, N. N. (2006). Correlation-induced synchronization of oscillations in olfactory bulb neurons. *J. Neurosci.* 26, 3646–3655. doi: 10.1523/jneurosci.4605-05.2006

Holland, J. H. (1995). *Hidden Order: How Adaptation Builds Complexity.* Reading, MA: Helix Books.

Kawai, Y. (2018a). Differential ascending projections from the male rat caudal nucleus of the tractus solitarius: an interface between local microcircuits and global macrocircuits. *Front. Neuroanat.* 12:63. doi: 10.3389/fnana.2018.00063

Kawai, Y. (2018b). Spatiotemporal structure and dynamics of spontaneous oscillatory synchrony in the vagal complex. *Front. Neurosci.* 12:978. doi: 10.3389/fnins.2018.00978

Kelso, J. A. S. (2016). On the self-organizing origins of agency. *Trends Cogn. Sci.* 20, 490–499. doi: 10.1016/j.tics.2016.04.004

Konopacki, J., Bocian, R., Kowalczyk, T., and Klos-Wojtczak, P. (2014). The electrical coupling and the hippocampal formation theta rhythm in rats. *Brain Res. Bull.* 107, 1–17. doi: 10.1016/j.brainresbull.2014.04.007

Mainen, Z. F., Joerges, J., Huguenard, J. R., and Sejnowski, T. J. (1995). A model of spike initiation in neocortical pyramidal neurons. *Neuron* 15, 1427–1439. doi: 10.1016/0896-6273(95)90020-9

McDonnell, M. D., and Abbott, D. (2009). What is stochastic resonance? Definitions, misconceptions, debates, and its relevance to biology. *PLoS Comput. Biol.* 5:e1000348. doi: 10.1371/journal.pcbi.1000348

Moss, F., and Pei, X. (1995). Stochastic resonance. Neurons in parallel. *Nature* 376, 211–212. doi: 10.1038/376211a0

Negishi, Y., and Kawai, Y. (2011). Geometric and functional architecture of visceral sensory microcircuitry. *Brain Struct. Funct.* 216, 17–30. doi: 10.1007/s00429-010-0294-5

Pikovsky, A. S., and Kurths, J. (1997). Coherence resonance in a noise-drived excitable system. *Phys. Rev. Lett.* 78, 775–778. doi: 10.1103/physrevlett.78.775

Ramon y Cajal, S. (1995). *Histology of the Nervous System of Man and Vertebrates.* New York, NY: Oxford University Press.

Sato, S., Yamada, K., and Inagaki, N. (2006). System for simultaneously monitoring heart and breathing rate in mice using a piezoelectric transducer. *Med. Biol. Eng. Comput.* 44, 353–362. doi: 10.1007/s11517-006-0047-z

Springer, M., and Paulsson, J. (2006). Biological physics: harmonies from noise. *Nature* 439, 27–28. doi: 10.1038/439027a

Stein, R. B., Gossen, E. R., and Jones, K. E. (2005). Neuronal variability: noise or part of the signal? *Nat. Rev. Neurosci.* 6, 389–397. doi: 10.1038/nrn1668

Tashiro, Y., and Kawai, Y. (2007). Glial coverage of the small cell somata in the rat nucleus of tractus solitarius during postnatal development. *Glia* 55, 1619–1629. doi: 10.1002/glia.20577

Tegnér, J., Compte, A., and Wang, X. J. (2002). The dynamical stability of reverberatory neural circuits. *Biol. Cybern.* 87, 471–481. doi: 10.1007/s00422-002-0363-9

Wiesenfeld, K., and Moss, F. (1995). Stochastic resonance and the benefits of noise: from ice ages to crayfish and SQUIDs. *Nature* 373, 33–36. doi: 10.1038/373033a0

Yoshioka, M., Okada, T., Inoue, K., and Kawai, Y. (2006). Pattern differentiation of excitatory and inhibitory synaptic inputs on distinct neuronal types in the rat caudal nucleus of the tractus solitarius. *Neurosci. Res.* 55, 300–315. doi: 10.1016/j.neures.2006.04.001

Conflict of Interest: The author declares that the research was conducted in the absence of any commercial or financial relationships that could be construed as a potential conflict of interest.

Copyright © 2019 Kawai. This is an open-access article distributed under the terms of the Creative Commons Attribution License (CC BY). The use, distribution or reproduction in other forums is permitted, provided the original author(s) and the copyright owner(s) are credited and that the original publication in this journal is cited, in accordance with accepted academic practice. No use, distribution or reproduction is permitted which does not comply with these terms.

frontiers in Systems Neuroscience

ORIGINAL RESEARCH
published: 14 January 2020
doi: 10.3389/fnsys.2019.00086

Cross-Frequency Coupling in Descending Motor Pathways: Theory and Simulation

Nirvik Sinha[1,2], *Julius P. A. Dewald*[1,3], *Charles J. Heckman*[1,4] *and Yuan Yang*[1]*

[1] *Department of Physical Therapy and Human Movement Sciences, Feinberg School of Medicine, Northwestern University, Chicago, IL, United States,* [2] *School of Medical Science and Technology, Indian Institute of Technology, Kharagpur, India,* [3] *Department of Biomedical Engineering, Robert R. McCormick School of Engineering and Applied Science, Northwestern University, Evanston, IL, United States,* [4] *Department of Physiology, Feinberg School of Medicine, Northwestern University, Chicago, IL, United States*

Coupling of neural oscillations is essential for the transmission of cortical motor commands to motoneuron pools through direct and indirect descending motor pathways. Most studies focus on iso-frequency coupling between brain and muscle activities, i.e., cortico-muscular coherence, which is thought to reflect motor command transmission in the mono-synaptic corticospinal pathway. Compared to this direct pathway, indirect corticobulbospinal motor pathways involve multiple intermediate synaptic connections via spinal interneurons. Neuronal processing of synaptic inputs can lead to modulation of inter-spike intervals which produces cross-frequency coupling. This theoretical study aims to evaluate the effect of the number of synaptic layers in descending pathways on the expression of cross-frequency coupling between supraspinal input and the cumulative output of the motoneuron pool using a computer simulation. We simulated descending pathways as various layers of interneurons with a terminal motoneuron pool using Hogdkin–Huxley styled neuron models. Both cross- and iso-frequency coupling between the supraspinal input and the motorneuron pool output were computed using a novel generalized coherence measure, i.e., n:m coherence. We found that the iso-frequency coupling is only dominant in the mono-synaptic corticospinal tract, while the cross-frequency coupling is dominant in multi-synaptic indirect motor pathways. Furthermore, simulations incorporating both mono-synaptic direct and multi-synaptic indirect descending pathways showed that increased reliance on a multi-synaptic indirect pathway over a mono-synaptic direct pathway enhances the dominance of cross-frequency coupling between the supraspinal input and the motorneuron pool output. These results provide the theoretical basis for future human subject study quantitatively assessing motor command transmission in indirect vs. direct pathways and its changes after neurological disorders such as unilateral brain injury.

Keywords: cross-frequency coupling, descending motor pathways, computer simulation, Hogdkin–Huxley styled neuron model, n:m coherence

OPEN ACCESS

Edited by:
Spase Petkoski,
INSERM U1106 Institut de Neurosciences des Systèmes, France

Reviewed by:
Tanmoy Banerjee,
University of Burdwan, India
Chie Nakatani,
KU Leuven, Belgium

***Correspondence:**
Yuan Yang
yuan.yang@northwestern.edu

Received: *17 August 2019*
Accepted: *18 December 2019*
Published: *14 January 2020*

Citation:
Sinha N, Dewald JPA, Heckman CJ and Yang Y (2020) Cross-Frequency Coupling in Descending Motor Pathways: Theory and Simulation. Front. Syst. Neurosci. 13:86. doi: 10.3389/fnsys.2019.00086

INTRODUCTION

The human motor system is a highly cooperative network comprised of different groups of neurons. Neural coupling, i.e., the synchronization of neural activity across these groups, is key to signal transmission among functionally related, though anatomically distant, neuronal groups (e.g., the motor cortices and spinal motoneuron pool) through direct and indirect descending pathways (van Wijk et al., 2012). Over decades, most researchers investigating neural coupling in the motor descending pathways have focused on the synchronization between cortical oscillations and muscle activities at the same frequency (i.e., iso-frequency coupling), known as the cortico-muscular coherence (Mima and Hallett, 1999). It is thought to reflect motor command transmission in the mono-synaptic corticospinal tract (Schoffelen et al., 2005). Previous simulation and *in vivo* studies demonstrated that, in this direct descending pathway, despite the non-linearity of individual neurons, neural oscillation of the supraspinal input could be linearly transmitted to the cumulative output of the motoneuron pool at the same frequency (Negro and Farina, 2011a,b). These previous studies explained the origin of iso-frequency coupling between the supraspinal input and the motoneuron pool output with respect to the use of the monosynaptic corticospinal tract as the fastest, direct descending pathways in healthy individuals.

However, the corticospinal tract is not the only motor pathway in humans. There are other indirect pathways (e.g., cortico-reticulospinal tract, rubrospinal tract) in parallel with the direct corticospinal tract (Dum and Strick, 1991; Jang and Seo, 2014). Although contributions from these indirect motor pathways are relatively small compared to the corticospinal tract in healthy individuals, they do still play important roles in various motor control tasks such as postural control during movement (Drew et al., 2004). Furthermore, in some neurological disorders, such as unilateral brain injury, the reliance on these indirect motor pathways may increase due to losses of corticospinal projections (Fries et al., 1993; Jang et al., 2013; Owen et al., 2017). The injury-induced increased reliance on these indirect motor pathways is likely associated with motor impairments (e.g., abnormal limb synergies and spasticity) post unilateral brain injury (Ellis et al., 2012, 2017; McPherson et al., 2018a,c; Li et al., 2019). Thus, investigating the neural coupling in these indirect motor pathways will allow for a more complete understanding of the transmission of motor commands from the brain to muscles, and may pave the way for quantitative assessments of the usage of indirect motor pathways in both normal and pathological motor control.

Compared to the direct corticospinal tract, these indirect motor pathways involve multiple synaptic connections via interneurons. Neuronal processing of synaptic inputs can lead to the modulation of inter-spike intervals which produces cross-frequency coupling, i.e., synchronization across different frequencies between input and output (Koch and Segev, 2000; Markram, 2003; Yang et al., 2018). Our previous work on multi-synaptic ascending sensory pathways (Yang et al., 2016b; Tian et al., 2018), as well as a recent opinion article (Yang et al., 2018), argued that multi-synaptic interaction in a neural pathway can lead to a substantial expression of cross-frequency coupling. However, insights into possible mechanisms underlying neural coupling in the multi-synaptic descending motor pathways are currently lacking. Focusing on the iso-frequency coupling (e.g., cortico-muscular coherence) only one previous study indicated that the input from the indirect motor pathways can reduce the iso-frequency coupling between the cortical input and motoneuron pool output (Negro and Farina, 2011a) while no insight has been provided into the neural mechanisms of cross-frequency coupling. This study aims to systematically evaluate the effect of the number of synaptic connections or interneuron layers on the expression of cross-frequency coupling between supraspinal input and output of the motoneuron pool using computer simulations. We hypothesize that multi-synaptic interaction in an indirect descending motor pathway increases the non-linear distortion of efferent motor signal transmission, resulting in enhanced cross-frequency coupling over iso-frequency coupling.

To test our hypothesis, we simulated descending pathways as various layers of interneurons in cascade with a terminal motoneuron pool, using Hodgkin-Huxley styled neuron models (Booth et al., 1997; Rybak et al., 2006). Both cross- and iso-frequency coupling between the input (which comprised of a supraspinal drive with an independent membrane noise) and the output of the motoneuron pool were computed using a recently developed generalized coherence method (Yang et al., 2016b). The ratio of cross- to iso-frequency coupling was calculated to determine which type (cross- or iso-frequency) of neural coupling is dominant and how it changes with an increasing number of synaptic connections or interneuron layers.

METHODS

Motoneuron and Interneuron Models

We simulated descending pathways as various layers of interneurons in a cascade with a terminal motoneuron pool. All neurons were modeled in the Hodgkin–Huxley style. A two-compartment model comprising of a soma and a dendrite was used for simulating motoneurons (Booth et al., 1997). Because of the lack of adequate experimental data, a single compartment simplification of this model was used to simulate the interneurons (Rybak et al., 2006).

The *motoneuron* model incorporated the following ionic currents (with the corresponding channel conductances): fast sodium (I_{Na} with maximal conductance g_{Na}), persistent (slowly inactivating) sodium (I_{NaP} with maximal conductance g_{NaP}), delayed-rectifier potassium (I_{K} with maximal conductance g_K), calcium-N (I_{CaN} with maximal conductance g_{CaN}), calcium-L (I_{CaL} with maximal conductance g_{CaL}), calcium-dependent potassium ($I_{\mathrm{K,Ca}}$ with maximal conductance $g_{K,Ca}$), and leakage (I_{L} with constant conductance g_L) currents (Lee and Heckman, 2001; Darbon et al., 2004; Rybak et al., 2006; Streit et al., 2006):

$$I_{\mathrm{Na}} = g_{Na} \times m_{Na}^3 \times h_{Na} \times (V - E_{Na});$$
$$I_{\mathrm{NaP}} = g_{NaP} \times m_{NaP} \times h_{NaP} \times (V - E_{Na});$$
$$I_{\mathrm{K}} = g_K \times m_K^4 \times (V - E_K);$$

$$I_{\mathrm{CaN}} = g_{CaN} \times m_{CaN}^2 \times h_{CaN} \times (V - E_{Ca});$$
$$I_{\mathrm{CaL}} = g_{CaL} \times m_{CaL} \times (V - E_{Ca});$$
$$I_{\mathrm{K,Ca}} = g_{K,Ca} \times m_{K,Ca} \times (V - E_K);$$
$$I_{\mathrm{L}} = g_L \times (V - E_L);$$

where V is the membrane potential of the corresponding neuron compartment [i.e., soma ($V_{(S)}$) or dendrite ($V_{(D)}$)] in two-compartment models, or the neuron membrane potential V in the one-compartment interneuron model which is explained later). E_{Na}, E_K, E_{Ca}, and E_L are the reversal potentials for sodium, potassium, calcium and leakage currents, respectively. The variables m and h (with subscripts indicating ionic channels) represent the activation and inactivation variables of the corresponding ionic channels, as described by the following differential equations:

$$\tau_{mi}(V)\frac{d}{dt}m_i = m_{\infty i}(V) - m_i$$
$$\tau_{hi}(V)\frac{d}{dt}h_i = h_{\infty i}(V) - h_i$$

where i indicates the name of the channel, $\mathrm{m}_{\infty\mathrm{i}}(\mathrm{V})$ and $\mathrm{h}_{\infty\mathrm{i}}(\mathrm{V})$ represent the voltage-dependent steady-state activation and inactivation, and $\tau_{\mathrm{mi}}(\mathrm{V})$ and $\tau_{\mathrm{hi}}(\mathrm{V})$ are the corresponding time constants (see Booth et al., 1997; Rybak et al., 2006 for details of these parameters). The instantaneous value of $m_{K,Ca}$ was calculated from the intracellular Ca^{2+} concentration of the corresponding compartment as (Booth et al., 1997):

$$m_{K,Ca} = \frac{Ca}{Ca + K_d}$$

where Ca is the Ca^{2+} concentration of the corresponding compartment of the neuron and K_d is the half-saturation level of this conductance. The kinetics of intracellular Ca^{2+} concentration ($|\mathrm{Ca}|$) were computed separately for each compartment according to the following equation:

$$\frac{d}{dt}|Ca| = -f \times (\alpha I_{Ca} + k_{Ca}|Ca|)$$

where f defines the percentage of free to total Ca^{2+}, α converts the total Ca^{2+} current, I_{Ca}, to Ca^{2+} concentration and k_{Ca} represents the Ca^{2+} removal rate.

The maximal channel conductances, equilibrium potentials and membrane capacitance of the neuron models were set with the same values as in Rybak et al. (2006). The details are specified in the **Appendix**. The equilibrium leakage potentials of the motoneurons and interneurons were set as described in section Simulations.

The dendrite–soma coupling currents (with conductance g_C) for soma ($I_{C(S)}$) and dendrite ($I_{C(D)}$) were calculated as (Booth et al., 1997):

$$I_{\mathrm{C(S)}} = \frac{g_C}{p}\left(V_{(D)} - V_{(S)}\right)$$
$$I_{\mathrm{C(D)}} = \frac{g_C}{1-p}(V_{(S)} - V_{(D)})$$

where p is the parameter defining the ratio of somatic surface area to the total neuronal surface area.

We used conductance-based excitatory post-synaptic potentials (EPSPs) for simulating the synaptic inputs to each motoneuron. The synapses were modeled as exponentially decaying injected currents (I_{SynE} with peak conductance g_{SynE} and reversal potential E_{SynE}): $I_{SynE} = g_{SynE} \times (V - E_{SynE})$ into the soma compartment (Negro and Farina, 2011a). The time constant τ_{synE} for the decay was 5 ms (Rybak et al., 2006). The peak conductance value for synapses on motoneurons was adjusted to produce an EPSP peak of 100 μV (Finkel and Redman, 1983).

With the inclusion of I_{NaP} to the motoneuron dendrite (Rybak et al., 2006), the membrane potentials of the motoneuron soma ($V_{(S)}$) and dendrite ($V_{(D)}$) were computed from the following equations:

$$C\frac{dV_{(S)}}{dt} = -I_{Na(S)} - I_{K(S)} - I_{CaN(S)} - I_{K,Ca(S)} - I_{L(S)} - I_{C(S)} - I_{SynE}$$
$$C\frac{dV_{(D)}}{dt} = -I_{NaP(D)} - I_{CaN(D)} - I_{CaL(D)} - I_{K,Ca(D)} - I_{L(D)} - I_{C(D)}$$

where C is the membrane capacitance and t is time.

The *interneurons* (single-compartment models) contain only a minimal set of ionic currents (Rybak et al., 2006):

$$C\frac{dV}{dt} = -I_{Na} - I_K - I_L - I_{SynE}$$

There is no existing literature reporting experimentally observed values of interneuron EPSPs of the descending pathways. Since interneurons are usually much smaller than motoneurons, they have higher input resistances and smaller somatic surface areas (Bui et al., 2003). Thus, we adjusted peak conductance of synapses on interneurons to produce an EPSP peak of 500 μV.

Input Signal and Connection Configuration

We used a probabilistic connection model (Ferrario et al., 2018) to simulate descending pathways with various layers and 100 neurons per layer (Lüscher et al., 1983) (see **Figure 1**). Each neuron in the first layer was fed by a time-varying injected current into the somatic compartment. The supraspinal input was designed as a Gaussian signal in beta band (15–35 Hz) [mimicking the cortical oscillations observed experimentally during motor tasks (Pfurtscheller and Da Silva, 1999)] with an added membrane noise (see **Figure 2**). The membrane noise was modeled as a bandlimited (1–100 Hz) Gaussian noise, which was independent for each neuron (Maltenfort et al., 1998). The total variance of this stochastic input was a percentage of the constant current injection to produce a mean ISI-CoV of (i) 0.55 for the 1st interneuron layer in case of multi-synaptic pathways (Prut and Perlmutter, 2003), and (ii) 0.2–0.3 for the motoneuron pool in case of the mono-synaptic pathway (Tanji and Kato, 1972; Sturm et al., 1997; Mattei and Schmied, 2002).

For the successive layers, the input to each neuron was the sum of output spike trains (convolved with the EPSP) of neurons

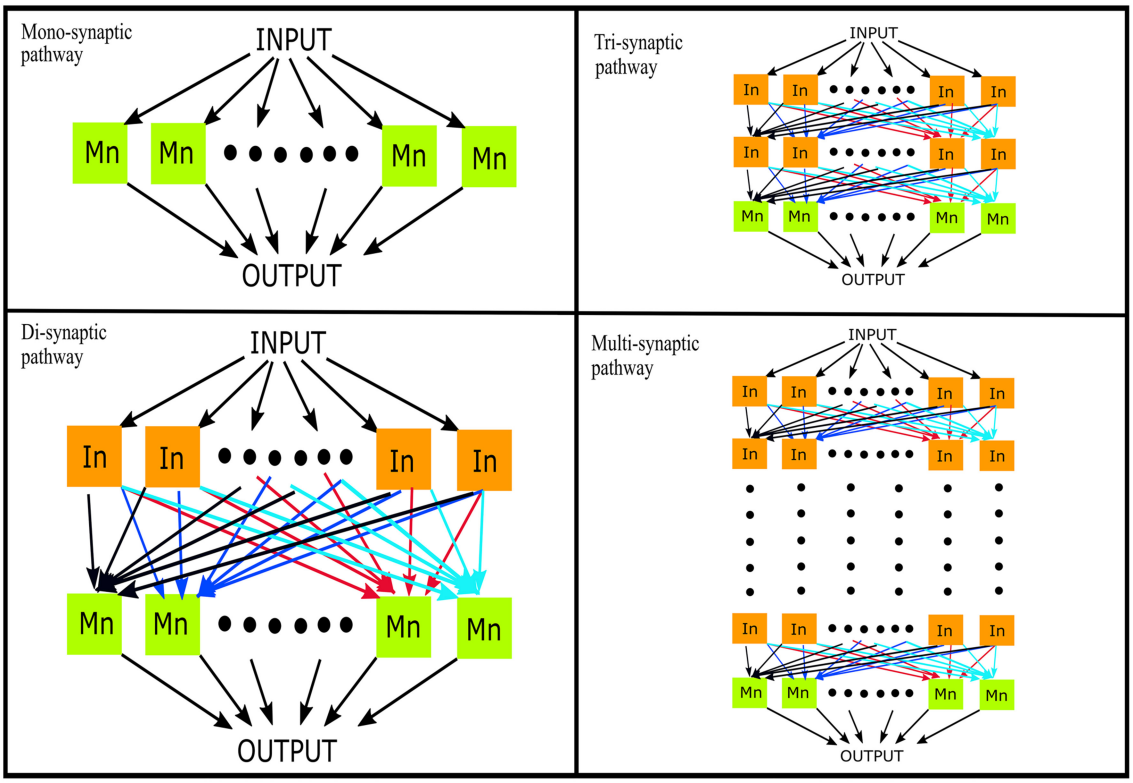


FIGURE 1 | Simulation of descending pathways with various layers ($N = 0, 1, 2, \ldots$) of interneurons in cascade with a terminal motoneuron pool. In, interneuron; Mn, motoneuron.

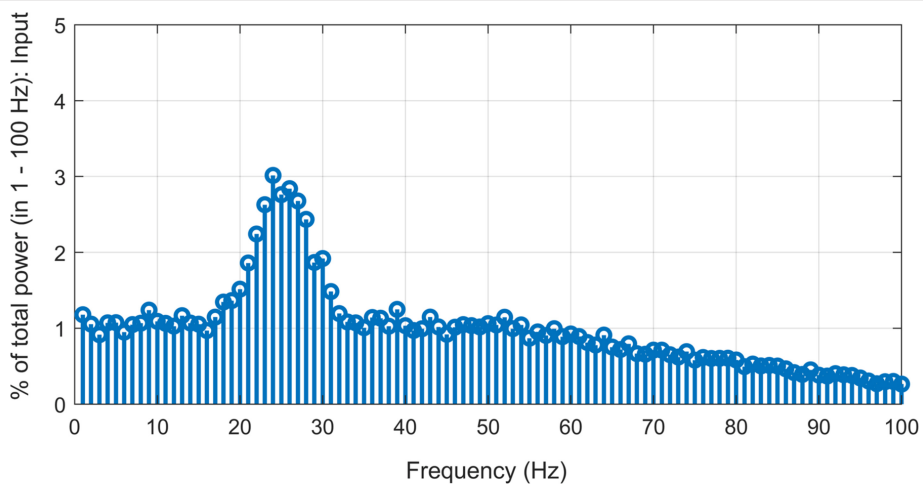


FIGURE 2 | Simulated supraspinal input comprising of a Gaussian signal (15–35 Hz) with added Gaussian noise (1–100 Hz band-limited) with signal-to-noise ratio of ∼−7.5 dB.

randomly sampled from the previous layer. The number of neurons which contributed to the input of each interneuron was set to obtain a mean firing rate in the range of 19–24 spikes/s for the whole interneuron layer. This is in line with previous experimental observations in primate models during flexion/extension tasks (Prut and Perlmutter, 2003). The number of inputs to each motoneuron was set to 100 i.e., the sum of inputs from all interneurons of the terminal interneuron layer. The range of the firing rates was adjusted as explained in section Simulations. The mean firing rate of the active motoneurons (>8 spikes/s; Negro and Farina, 2011a) was thus obtained to be in the range of 16–19 spikes/s. Such a connection model resembles the

anatomical course of various descending motor pathways which, via a varying number of interneuron layers, terminate on spinal motoneuron pools (Matsuyama et al., 2004).

Simulations

Simulations were run at a sampling rate of 1 kHz using 200 epochs with a 1-s duration per epoch. The resulting data were sufficient for a robust neural coupling analysis (Hagihira et al., 2001). Our simulated multi-synaptic pathways represented the part of descending pathway involving only spinal interneurons and motoneurons, since no reticular neurons were simulated due to the complete lack necessary parameters in the existing literature (McDougal et al., 2017). A previous study reported heterogeneity of excitatory spinal interneuron populations based on their firing rates. It found a non-monotonous decline in the mean firing rate histogram with a local peak at ∼50 spikes/s (Prut and Perlmutter, 2003). In the simulations, we mimicked this histogram (see **Figure 3A**) by combining two random exponential distributions of leakage potential (E_L) values for each interneuron layer. The range of E_L was adjusted so that its mean was around −64 mV (Rybak et al., 2006). Motoneuron firing rates have been experimentally reported to be predominantly in the range of 5–30 spikes/s during isometric contractions of limb muscles (for contraction levels ≤60% of maximum voluntary torque) (De Luca and Hostage, 2010). We adjusted the leakage potentials of the motoneurons in the pool to generate a distribution (Rybak et al., 2006) of firing rates in a similar range (see **Figure 3B**).

Neural Coupling Analysis

We used our recently developed generalized coherence measure, i.e., n:m coherence (NMC) (Yang et al., 2016b), to assess cross- and iso-frequency coupling between the simulated input and output signals. The n:m coherence is a straightforward extension of the linear coherence used in corticomuscular coherence (Mima and Hallett, 1999) based on high-order statistics (Nikias and Mendel, 1993) for distinguishably determining cross- and iso-frequency coupling between signals. Thus, the iso-frequency coupling of our results obtained by this method would be comparable to previous corticomuscular coherence studies (Mima and Hallett, 1999; Mima et al., 2001; Yang et al., 2016a, 2018).

Let $X(f)$, $Y(f)$ be the Fourier Transform of two time series (e.g., the input and output signals). The NMC between them is defined as:

$$NMC\left(f_X, f_Y\right) = \frac{\left|S_{XY}\left(f_X, f_Y\right)\right|}{\sqrt{S_X^n\left(f_X\right) S_Y^m\left(f_Y\right)}}$$

for assessing cross-frequency ($f_X \neq f_Y$) and iso-frequency ($f_X = f_Y$) coupling between signals, where m/n is the simple whole number ratio of f_X/f_Y (e.g., if $f_X = 8$, $f_Y = 16$ then $m = 1$, $n = 2$) and

$$S_{XY}\left(f_X, f_Y\right) = < X^n\left(f_X\right)\left(Y^m\left(f_Y\right)\right)^* >,$$
$$S_X^n\left(f_X\right) = < X^n\left(f_X\right)\left(X^n\left(f_X\right)\right)^* >$$

where $< \cdot >$ represents the averaging over epochs and $\mathrm{X^n} = \underbrace{X(f_x) \cdot X(f_x) \cdot \ldots \cdot X(f_x)}_{n}$.

The NMC reflects the strength of iso- or cross-frequency coupling between signals. When $f_X = f_Y$, we have $m = n = 1$, then the NMC is equivalent to the classical (linear) coherence for iso-frequency coupling (Yang et al., 2016a). When $f_X \neq f_Y$, then the NMC indicates the non-linear coupling between signals across different frequency components (i.e., cross-frequency coupling) (Yang et al., 2015). Thus, the n:m mapping can generate harmonic ($m = 1$) and subharmonic coupling ($m > 1$) between the input and the output in the frequency domain (Yang et al., 2016b). As a generalized coherence method, the NMC is a metric indicating cross-frequency coherence between signals, which is different from other cross-frequency coupling methods such as the phase-amplitude coupling (De Hemptinne et al., 2013) reflecting how a low-frequency phase modulates a high-frequency amplitude.

According to Cauchy-Schwarz-inequality, we have:

$$\left|\langle X^n\left(f_X\right)\left(Y^m\left(f_Y\right)\right)^*\rangle\right| \leq \left(\langle\left|X^n\left(f_X\right)\right|^2\rangle\right)^{1/2}\left(\langle\left|Y^m\left(f_Y\right)\right|^2\rangle\right)^{1/2}$$

Thus, the NMC is bounded by 0 and 1, where 1 indicates that two signals are perfectly coupled at the tested frequency pair (f_X, f_Y). As the NMC values are computed by comparing different frequency pairs between signals, the significant threshold was adapted with a Bonferroni correction to control the type I error (family-wise error rate: 0.05) (Yang et al., 2016b). There are 2,100 frequency pairs that were included for Bonferroni corrections, i.e., 21 frequencies in the input (from 15 to 35 Hz at 1 Hz resolution) × 100 frequencies in the output (from 1 to 100 Hz at 1 Hz resolution). More details of the NMC method is available in Yang et al. (2016b).

Since the supraspinal input had added independent noise for each 1st layer neuron, each coupling analysis was repeated 100 times, each time with a different realization of the independent noise (as described in section Input Signal and Connection Configuration) added to the supraspinal input in the same signal-to-noise ratio as the original input (i.e., ∼-7.5 dB). To compare the dominance of cross- vs. iso-frequency coupling, we defined the cross-frequency coupling over iso-frequency coupling index as COI = (CFC–IFC)/(CFC+IFC), where CFC is the sum of all significant cross-frequency coupling values and IFC the sum of all significant iso-frequency coupling. We included only "significant" CFC and IFC values to exclude false positives in the coherence analysis. The range of COI is [−1, 1], where a larger COI indicates a more dominant cross-frequency coupling.

To examine the effect of the number of synaptic/interneuron layers on neural coupling of descending pathways, we computed NMC, IFC, CFC, and COI between the given supraspinal input and the cumulative spike train (CST) output of the simulated motoneuron pool (derived as the sum of individual motoneuron spike trains following Negro and Farina, 2011a). In addition, the IFC, CFC, and COI between the supraspinal input and the

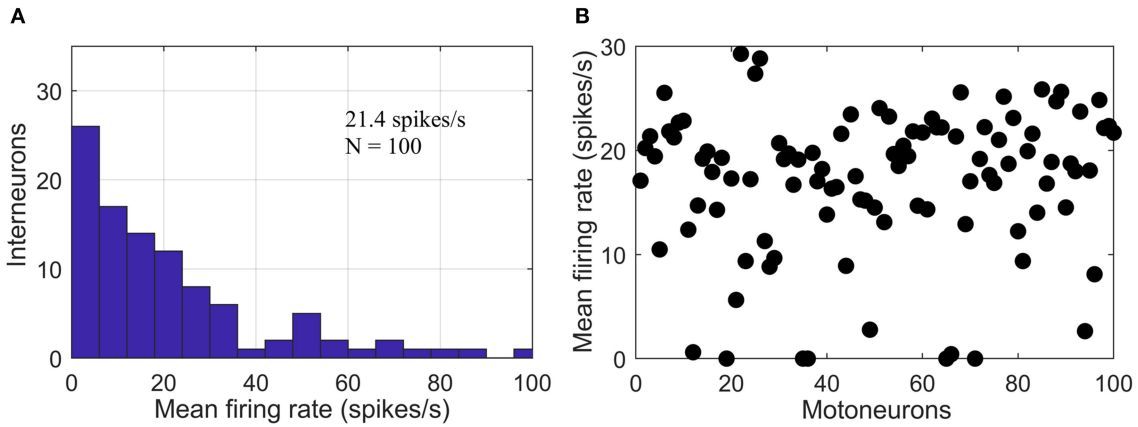


FIGURE 3 | Firing rate of simulated neurons. **(A)** Histogram of mean firing rates of the simulated interneuron layer with a secondary peak at ∼ 50 spikes/s. **(B)** Scatter plot showing the distribution of mean firing rates of the simulated pool of motoneuron.

CST of each successive interneuron layer was also computed to evaluate how they change across layers. Furthermore, we also examined the combined effect of both mono- and multi-synaptic pathways on neural coupling by varying the weight of the input from either pathway (with the same supraspinal input) to the terminal motoneuron pool.

RESULTS

Neural Coupling Between the Supraspinal Input and the Cumulative Output From Motoneuron Pool

Both iso-frequency coupling and cross-frequency coupling were detected in the simulated motor pathways (see **Figure 4**). The detected cross-frequency coupling includes harmonic coupling (i.e., output frequency over input frequency ratio n/m is an integer) and non-integer n:m coupling. This result is in line with previous experimental studies reporting both harmonic and non-integer coupling in the human sensorimotor system (Daffertshofer et al., 2000; Yang et al., 2016a). A higher amount of cross-frequency coupling was observed in the multi-synaptic pathways where there are one or more interneuron layers.

To examine how iso-frequency coupling and cross-frequency coupling evolved with increasing interneuron layers, we computed the IFC, CFC, and COI between the given supraspinal input and the motoneuron pool output for simulated pathways with various layers ($N = 0, 1, 2, 3, \ldots$) of interneurons in cascade with a terminal motoneuron pool (see **Figure 5**). Using one-way ANOVA we found that the number of interneuron layers had significant effect on IFC [$F_{(10,\ 1089)} = 3613.36$, $p < 0.001$], CFC [$F_{(10,\ 1089)} = 2934.50$, $p < 0.001$] and COI [$F_{(10,\ 1089)} = 7108.90$, $p < 0.001$]. We used Tukey's honest significant difference (HSD) criterion for *post-hoc* comparisons, with Bonferroni correction to control the type I error. Hence, we adjusted the threshold p-value as 0.05/k to control the family-wise error rate to be <0.05, where k is the number of *post hoc* comparisons ($k = 10$). We found that the IFC decreased with increasing number of interneuron layers in the pathways ($p < 0.05/10$), while the CFC increased in the pathway with up to three interneuron layers ($p < 0.05/10$). Their combined effect resulted in an initial increase in COI with interneuron layers ($p < 0.05/10$) and a saturation for the pathways with more than three interneuron layers. It was also observed from the COI values that the iso-frequency coupling is only dominant (COI < 0) in the mono-synaptic descending pathway where the supraspinal input directly drives the motoneuron pool without passing through any interneuron layer. Consequently, the cross-frequency coupling became dominant (COI > 0) when there were interneuron layers in the descending pathway.

Neural Coupling Between the Supraspinal Input and the Output From Successive Neuron Layers

Using one-way ANOVA, we also found that the number of interneuron layers had a significant effect at $p < 0.05$ level on the IFC [$F_{(9,\ 990)} = 3235.46$, $p < 0.001$], CFC [$F_{(9,\ 990)} = 2113.54$, $p < 0.001$] and COI [$F_{(9,\ 990)} = 5597.45$, $p < 0.001$] between the supraspinal input and the output from successive interneuron layers. Using Tukey's HSD criterion with Bonferroni correction ($k = 9$), the IFC was observed to decrease across successive interneuron layers ($p < 0.05/9$) while the CFC and COI increased ($p < 0.05/9$) up to the fifth and sixth layer, respectively (see **Figure 6**). Additionally, in multi-synaptic pathways, IFC dropped more at the terminal motoneuron layer of the n-layer pathway in comparison to that of the terminal interneuron layer of the $n + 1$ layer pathway (for $n = 1$–11, unpaired t-test, $p < 0.001$ in all cases).

Combined Effect of Mono-Synaptic and Multi-Synaptic Pathways

In reality, the motor system contains both the mono-synaptic corticospinal tract and multi-synaptic indirect motor pathways. Hence, to examine the combined effect of both types of descending pathways in a motor system, we performed simulations in a system having dual input to the terminal

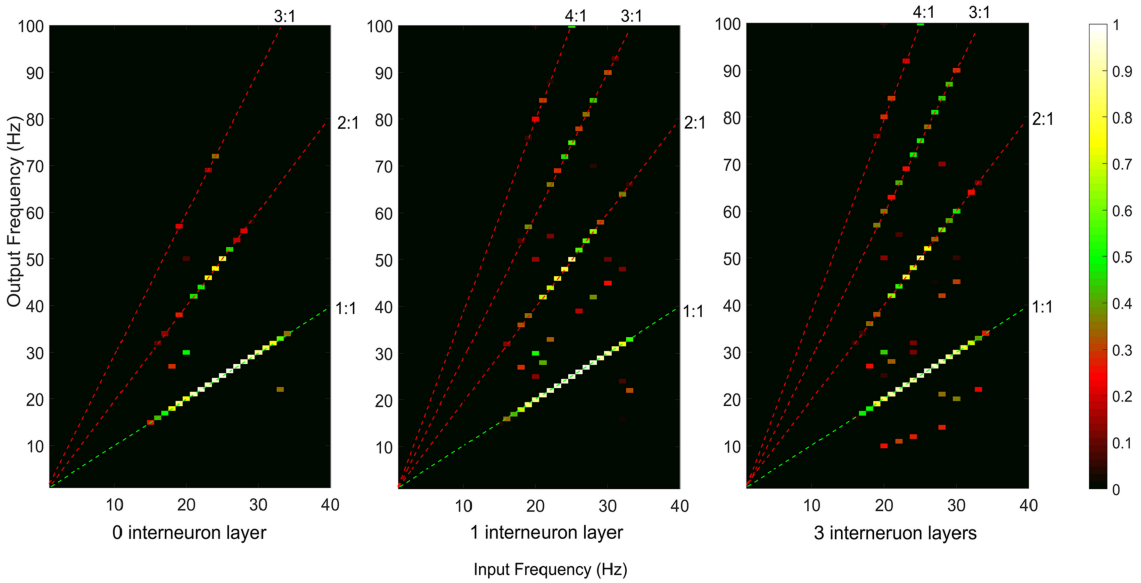


FIGURE 4 | Neural coupling between the supraspinal input and cumulative spike train output of the terminal motoneuron pool for the descending motor pathways with 0, 1, and 3 interneuron layers. The iso-frequency (1:1) coupling is indicated by the green dashed line. The detected cross-frequency coupling including harmonic coupling (i.e., output frequency over input frequency ratio n/m is an integer, e.g., 2:1, 3:1, 4:1, indicated by the red dashed lines) and non-integer n:m coupling (other points in the map).

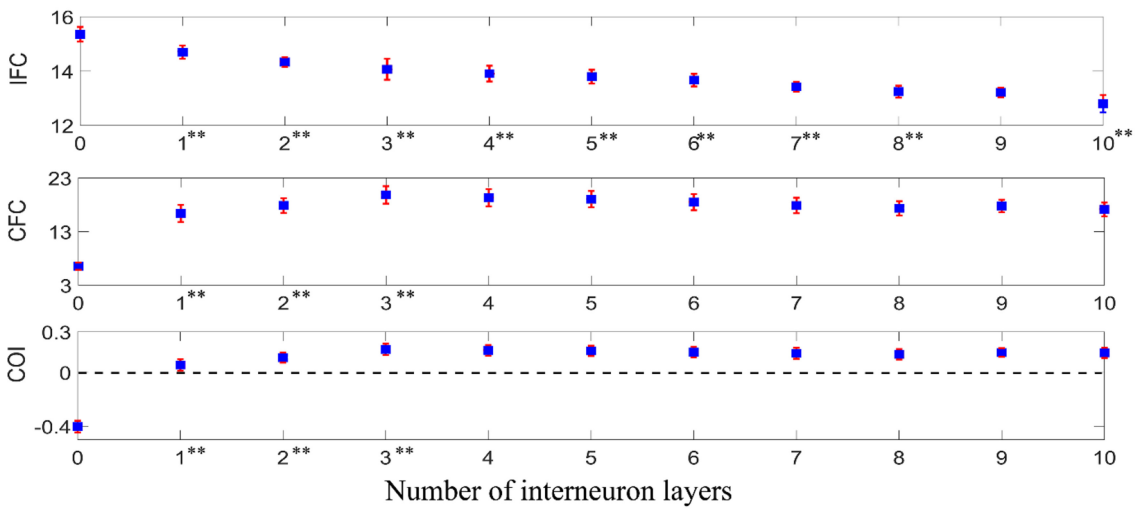


FIGURE 5 | IFC, CFC, and COI between the supraspinal input and the motoneuron pool output in simulated pathways with various layers of interneurons in cascade with a terminal motoneuron pool. The depicted values represent the mean (with ±2 standard deviation as indicated by error bars) calculated from 100 repetitions of the coupling analysis, each being run with a different realization of additive noise to the supraspinal input (as described in section Neural Coupling Analysis). Tukey's test was performed to test for significant decrease in IFC and increase in CFC and COI between the pathways containing $n-1$ and n ($n = 1, 2, 3\ldots$) interneuron layers. To control the family-wise error rate, we set the threshold $p = 0.05/k$ ($k = 10$, i.e., number of comparisons). Asterisks in superscript of the n-th layer number indicate a significant change of the results in the n-interneuron layer motor pathway in comparison to ($n-1$)-interneuron layer motor pathway (**$p < 0.05/10$).

motoneuron pool. The dual input is comprised of (i) a direct supraspinal drive (resembling the monosynaptic corticospinal tract) and (ii) an indirect drive from the same supraspinal input after being passed through two layers of interneurons (resembling a multi-synaptic descending pathway). The relative weights of these two drives were systematically varied to examine their effects on the neural coupling between the supraspinal input and the motoneuron pool output. Using one-way ANOVA, we found that the proportion of direct vs. indirect drive has a significant effect on the IFC [$F_{(5,\ 594)} = 640.63$, $p < 0.001$], CFC

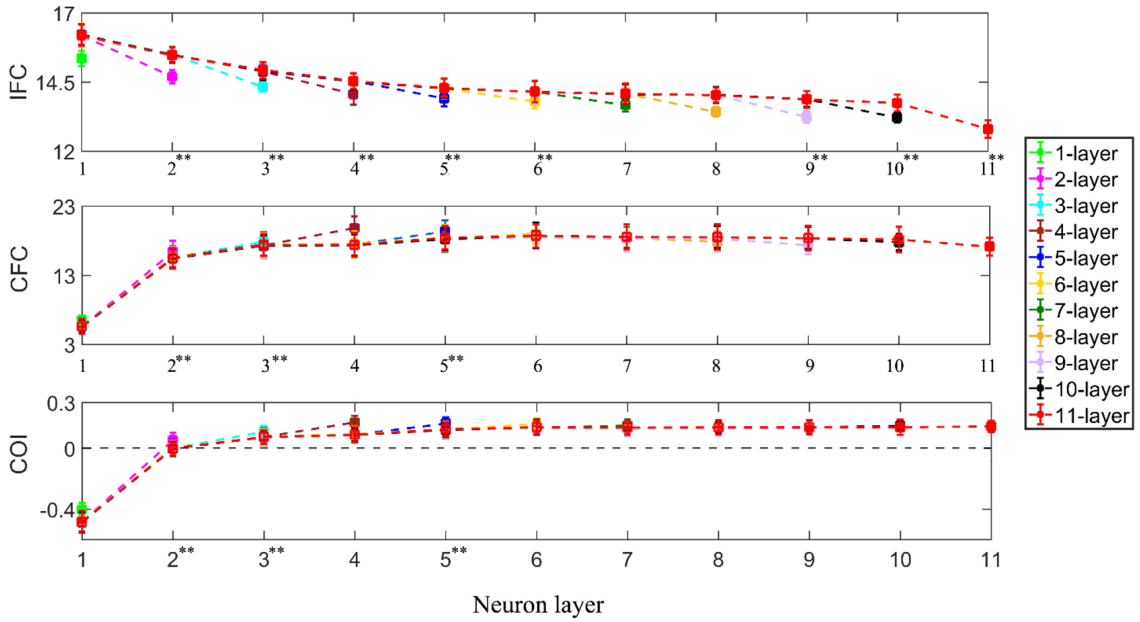


FIGURE 6 | IFC, CFC, and COI between the supraspinal input and cumulative spike train output of successive neuron layers in simulated pathways with various layers of interneurons in cascade with a terminal motoneuron pool. The 1-layer pathway represents the monosynaptic tract. The depicted values represent the mean (with ±2 standard deviation as indicated by error bars) calculated from 100 repetitions of the coupling analysis, each being run with a different realization of additive noise to the supraspinal input (as described in section Neural Coupling Analysis). Tukey's test was performed to test for significant decrease in IFC and increase in CFC and COI between the $n-1$th and nth ($n = 2, 3, 4\ldots$) interneuron layer. To control the family-wise error rate, we set the threshold $p = 0.05/k$ ($k = 9$, i.e., number of comparisons) Asterisks in superscript of the n-th layer number indicate a significant change of the result in that layer in comparison to that of the previous layer (**$p < 0.05/9$).

[$F_{(5,\ 594)} = 5552.81$, $p < 0.001$] and COI [$F_{(5,\ 594)} = 7748.80$, $p < 0.001$]. Using Tukey's HSD criterion with Bonferroni correction ($k = 5$), IFC was found to reduce with increased indirect drive ($p < 0.05/5$), while the CFC increased ($p < 0.05/5$). Their combined effect resulted in the progressive increase of COI ($p < 0.05/5$) (see **Figure 7**).

DISCUSSION

This study investigated neural coupling in descending motor pathways using computer simulations. We simulated the pathways as various layers of interneurons in a cascade with a terminal motoneuron pool, using Hodgkin–Huxley neuron models, to examine the effect of the number of synapses or interneuron layers on the expression of cross-frequency coupling, as well as its ratio over iso-frequency coupling.

Most studies investigating neural coupling in the descending pathways mainly focus on the mono-synaptic corticospinal tract using iso-frequency coupling measures such as cortico-muscular coherence (Mima and Hallett, 1999; Salenius and Hari, 2003; Negro and Farina, 2011b; van Wijk et al., 2012). In this simulation study, we examined both iso- and cross-frequency coupling in the mono-synaptic descending pathway. Our results confirmed the dominance of iso-frequency coupling (as indicated by COI < 0) in the mono-synaptic pathway, though cross-frequency coupling is also present (see **Figure 4**). This result is in line with our previous experimental work using the NMC to assess cross- and iso-frequency coupling between brain and muscle signals during a low-effort (1 Nm) isotonic wrist flexion in healthy young participants, showing that the motor task using the mono-synaptic corticospinal tract mainly generates iso-frequency coupling (Yang et al., 2016a).

Using linear coherence measure alone, a previous modeling study indicated that the recruitment of multi-synaptic indirect motor pathways can reduce the iso-frequency coupling between the supraspinal input and motoneuron pool output (Negro and Farina, 2011a). Consistent with the previous study, we found that the IFC decreases in the multi-synaptic pathways: the more interneuron layers in the pathway, the smaller IFC between the supraspinal input and the motoneuron pool output. However, we also found that the CFC initially increases in the multi-synaptic pathways and is then followed by a saturation after passing a few neuron layers. The combined effect of changes in IFC and CFC leads to the dominance of cross-frequency coupling (as shown by COI > 0) in the multi-synaptic pathways.

The mechanism underlying the changes in IFC and CFC could be associated with the information distortion that occurs across neuron layers leading to decorrelation of the supraspinal input and the motoneuron pool output (Negro and Farina, 2011a). Such distortion is likely caused by the modulation of inter-spike intervals when the motor command is passing through multiple synaptic layers (Koch and Segev, 2000; Markram, 2003; Yang et al., 2018). This modulation could be attributed to (1) heterogeneous recruitment thresholds and spike after-hyperpolarizations of the individual neurons which results in different firing rates for the same steady-state drive (Powers

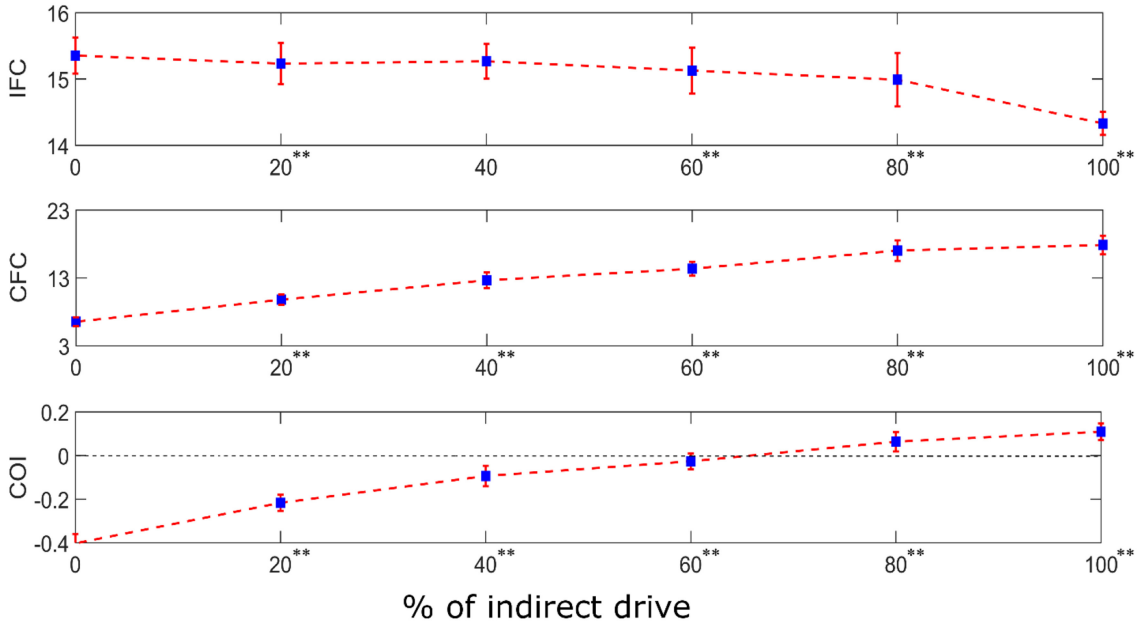


FIGURE 7 | IFC, CFC, and COI between the supraspinal input and cumulative spike train output of the terminal motoneuron pool for the simulated dual input system. The dual input is comprised of (i) a direct supraspinal drive (resembling the monosynaptic corticospinal tract) and (ii) an indirect drive from the same supraspinal input after being passed through two layers of interneurons (resembling a multi-synaptic descending pathway). The relative proportion (in terms of signal power) of the indirect drive in the composite input was systematically varied from 0 to 100% in steps of 20% increments. The depicted values represent the mean (with ±2 standard deviation as indicated by error bars) calculated from 100 repetitions of the coupling analysis, each being run with a different realization of additive noise to the supraspinal input (as described in section Neural Coupling Analysis). Tukey's test was performed to test for significant decrease in IFC and increase in CFC and COI between the successive steps of increase in indirect drive. To control the family-wise error rate, we set the threshold $p = 0.05/k$ ($k = 5$, i.e., number of comparisons). Asterisks in superscript of the percentage values denote significant change ($^{**}p < 0.05/5$).

and Binder, 2001; Heckman and Enoka, 2012; Yang et al., 2018), and (2) the consequent interplay between the time-varying input (as shown **Figure 2**, which is added over the steady-state drive) and different firing rates (as shown in **Figure 3**) of the neurons over the entire pool (Thompson et al., 2018). Thus, besides the input frequecies, the neurons also generate responses at other frequencies, which contain the components that are cross-frequency coupled with the input signal, as well as a certain amount of noise that is not phase-locked to the suprapinal input. Not only the cross-frequency coupled components but also the noise can be cumulatively enhanced when the signal is passing from one layer to the next. After passing a few neuron layers, the reduced signal-to-noise ratio then leads to the saturation of CFC.

In the multi-synaptic pathways, a sharp decrease of IFC was found at the terminal motoneuron pool in comparison to the last interneuron layer. This is likely caused by different neuronal processing properties of the simulated interneurons and motoneurons. The motoneurons modeled in this study had an active dendrite with a persistent inward current as well as calcium dependent potassium currents in both the soma and the dendrite compartments (Heckman et al., 2008). In contrast, the interneurons were modeled without such conductances and had a single compartment only. These differences may have given rise to lower IFC (and higher COI) in motoneuron outputs due to their effects on the neurocomputational properties. Indeed, this study opens a broad new area for exploring the origin of different types of neural coupling at the single neuron level and a detailed analysis of the role of individual ionic conductances on IFC and CFC can be the scope of future studies.

The proposed COI measure reflects the dominance of iso-frequency coupling vs. cross-frequency coupling. Interestingly, the iso-frequency coupling is only dominant in the mono-synaptic pathway, while the cross-frequency coupling is dominant in multi-synaptic pathways. After a unilateral brain injury, damage to the mono-synaptic corticospinal tract can increase the reliance on multi-synaptic indirect motor descending pathways (e.g., cortico-reticulospinal tracts for upper limbs) (Owen et al., 2017; McPherson et al., 2018a; Karbasforoushan et al., 2019). The simulated "dual-drive" model mimicks this pathological condition by varing the ratio of multi-synaptic drive vs. mono-synpatic drive. Our results show that the increased input from the indirect drive leads to a more dominant cross-frequency coupling as reflected by an increased value of COI over the increased percentage of the indirect motor drive. This result is in line with our pilot work on eight participants with hemiparetic stroke. The COI between the brain and muscle signal increases when participants with a unilateral stroke progressively lift the weight of their paretic arm (Yang et al., 2019), thereby enhancing the recruitment of indirect motor pathways to compensate for the loss of corticofugal (i.e., corticospinal and corticobulbar) projections from the lesioned hemisphere (McPherson et al., 2018a).

Thus, the COI can be used as a quantitative measure to indicate the relative usage of multi-synaptic indirect motor pathways vs. mono-synaptic direct corticospinal tract. This measure could have a significant impact on future neuro-pathophysiological studies on individuals with an unilateral brain injury, since recent studies have indicated that motor impairments after a unilateral brain injury could be associated with an increased reliance on multi-synaptic indirect motor pathways following a lesion-induced loss of direct corticospinal projections (Owen et al., 2017; McPherson et al., 2018a; Karbasforoushan et al., 2019). Therefore, a measure that quantitatively determines the usage of indirect motor pathways over direct corticospinal drive could be crucial (1) for evaluating motor recovery following unilateral brain injuries, and (2) for determining the effect of targeted therapeutic interventions (Ellis et al., 2018; McPherson et al., 2018b) that aim to reduce the maladaptive reliance on indirect motor pathways after a hemiparetic stroke. In the future, we will examine both cross-frequency and iso-frequency coupling, as well as the COI, between the brain and muscle signals to characterize the relative ratio of the recruitment of indirect vs. direct motor pathways following unilateral brain injuries, such as hemiparetic stroke and unilateral celebral palsy.

LIMITATIONS

We acknowledged that there are a few limitations of the current study. First, the interneuron model has only a basic set of ionic conductance since the details of the ionic conductances of spinal and reticular interneurons are yet to be explored. However, such reductionist interneuron models have been used in other simulation studies as well, and this simplification is not expected to change the overall results of this study (Maltenfort et al., 1998; Cisi and Kohn, 2008; Williams and Baker, 2009; Negro and Farina, 2011a). Second, there is no existing literature detailing the connection pattern of individual interneuron layers in multi-synaptic descending pathways. However, the probabilistic model used in this simulation has been previously demonstrated to capture global connectivity properties in motor descending pathways well (Humplik and Tkačik, 2017). Thirdly, the number of neurons in each layer of multi-synaptic descending tracts have not yet been experimentally determined. However, compound EPSP recording on motoneurons from spinal interneurons has shown the number of inputs to be $\sim$ 100 (Lüscher et al., 1983). Hence, it is reasonable to assume that the number of descending inputs on the motoneurons from each tract should be in this order. The motoneuron pool size can vary from muscle to muscle (Karpati et al., 2001), in a range from around 100 (e.g., first dorsal interosseous in humans) (Buchthal and Schmalbruch, 1980) to around 800 (e.g., biceps brachii in humans) (Feinstein et al., 1955). Thus, a size of 100 units for a motoneuron pool falls in the lowest part of the range. In this study, the size of 100 units per neuron layer was adopted also for uniformity and computational convenience. Finally, we did not consider synaptic and transmission delays in this work. The overall delay in a motor pathway may be determined based on the onset latency of Transcranial Magnetic Stimulation (TMS) induced Motor Evoked Potential (MEP) in the targeted muscle (Schwerin et al., 2011). However, the latency of MEP can be affected by coil orientation: difference may exist between direct vs. trans-synaptic activation of the pyramidal cells and the measurement of MEP responses in proximal vs. distal muscles. In short, it is still hard to get a "precise" assessment of the delay in a motor pathway. Meanwhile, there is no available experimental data for the delays in each neuron layer that we can included in this simulation work. Moreover, the time delay only has the effect on the relative phase between signals. This will not result in additional resonance components with new frequencies. Thus, the time delay issue will not affect our current results and overall conclusion of this paper.

DATA AVAILABILITY STATEMENT

The datasets generated for this study are available on request to the corresponding author.

AUTHOR CONTRIBUTIONS

NS conducted the simulation and data analysis under the supervision of YY, JD, and CH. NS and YY drafted and wrote the manuscript. JD and CH commented and revised the manuscript.

FUNDING

The research leading to these results has received funding support from the support of the Dixon Translational Research Grants Initiative (PI: YY) at Northwestern Medicine and Northwestern University Clinical and Translational Sciences Institute (UL1TR001422), NIH 1R21HD099710 (PIs: JD, YY), R01HD039343 and R01NS105759 (PI: JD).

REFERENCES

Booth, V., Rinzel, J., and Kiehn, O. (1997). Compartmental model of vertebrate motoneurons for Ca2+-dependent spiking and plateau potentials under pharmacological treatment. *J. Neurophysiol.* 78, 3371–3385. doi: 10.1152/jn.1997.78.6.3371

Buchthal, F., and Schmalbruch, H. (1980). Motor unit of mammalian muscle. *Physiol. Rev.* 60, 90–142. doi: 10.1152/physrev.1980.60.1.90

Bui, T. V., Cushing, S., Dewey, D. E., Fyffe, R. E., and Rose, P. (2003). A comparison of the electrotonic and morphological properties of Renshaw cells, Ia inhibitory interneurons and motoneurons in the cat. *J. Neurophysiol.* 90, 2900–2918. doi: 10.1152/jn.00533.2003

Cisi, R. R., and Kohn, A. F. (2008). Simulation system of spinal cord motor nuclei and associated nerves and muscles, in a web-based architecture. *J. Comput. Neurosci.* 25, 520–542. doi: 10.1007/s10827-008-0092-8

Daffertshofer, A., Peper, C., Frank, T., and Beek, P. (2000). Spatio-temporal patterns of encephalographic signals during polyrhythmic tapping. *Hum. Mov. Sci.* 19, 475–498. doi: 10.1016/S0167-9457(00)00032-4

Darbon, P., Yvon, C., Legrand, J. C., and Streit, J. (2004). INaP underlies intrinsic spiking and rhythm generation in networks of cultured rat spinal cord neurons. *Euro. J. Neurosci.* 20, 976–988. doi: 10.1111/j.1460-9568.2004.03565.x

De Hemptinne, C., Ryapolova-Webb, E. S., Air, E. L., Garcia, P. A., Miller, K. J., Ojemann, J. G., et al. (2013). Exaggerated phase–amplitude coupling in the primary motor cortex in Parkinson disease. *Proc. Natl. Acad. Sci. U.S.A.* 110, 4780–4785. doi: 10.1073/pnas.1214546110

De Luca, C. J., and Hostage, E. C. (2010). Relationship between firing rate and recruitment threshold of motoneurons in voluntary isometric contractions. *J. Neurophysiol.* 104, 1034–1046. doi: 10.1152/jn.01018.2009

Drew, T., Prentice, S., and Schepens, B. (2004). Cortical and brainstem control of locomotion. *Prog. Brain Res.* 143, 251–261. doi: 10.1016/S0079-6123(03)43025-2

Dum, R. P., and Strick, P. L. (1991). The origin of corticospinal projections from the premotor areas in the frontal lobe. *J. Neurosci.* 11, 667–689. doi: 10.1523/JNEUROSCI.11-03-00667.1991

Ellis, M. D., Carmona, C., Drogos, J., and Dewald, J. (2018). Progressive abduction loading therapy with horizontal-plane viscous resistance targeting weakness and flexion synergy to treat upper limb function in chronic hemiparetic stroke: a randomized clinical trial. *Front. Neurol.* 9:71. doi: 10.3389/fneur.2018.00071

Ellis, M. D., Drogos, J., Carmona, C., Keller, T., and Dewald, J. P. (2012). Neck rotation modulates flexion synergy torques, indicating an ipsilateral reticulospinal source for impairment in stroke. *J. Neurophysiol.* 108, 3096–3104. doi: 10.1152/jn.01030.2011

Ellis, M. D., Schut, I., and Dewald, J. P. (2017). Flexion synergy overshadows flexor spasticity during reaching in chronic moderate to severe hemiparetic stroke. *Clin. Neurophysiol.* 128, 1308–1314. doi: 10.1016/j.clinph.2017.04.028

Feinstein, B., Lindegård, B., Nyman, E., and Wohlfart, G. (1955). Morphologic studies of motor units in normal human muscles. *Cells Tissues Organs* 23, 127–142. doi: 10.1159/000140989

Ferrario, A., Merrison-Hort, R., Soffe, S. R., and Borisyuk, R. (2018). Structural and functional properties of a probabilistic model of neuronal connectivity in a simple locomotor network. *Elife* 7:e33281. doi: 10.7554/eLife.33281.019

Finkel, A. S., and Redman, S. J. (1983). The synaptic current evoked in cat spinal motoneurones by impulses in single group 1a axons. *J. Physiol.* 342, 615–632. doi: 10.1113/jphysiol.1983.sp014872

Fries, W., Danek, A., Scheidtmann, K., and Hamburger, C. (1993). Motor recovery following capsular stroke: role of descending pathways from multiple motor areas. *Brain* 116, 369–382. doi: 10.1093/brain/116.2.369

Hagihira, S., Takashina, M., Mori, T., Mashimo, T., and Yoshiya, I. (2001). Practical issues in bispectral analysis of electroencephalographic signals. *Anesth. Analg.* 93, 966–970. doi: 10.1097/00000539-200110000-00032

Heckman, C., Johnson, M., Mottram, C., and Schuster, J. (2008). Persistent inward currents in spinal motoneurons and their influence on human motoneuron firing patterns. *Neuroscientist* 14, 264–275. doi: 10.1177/1073858408314986

Heckman, C. J., and Enoka, R. M. (2012). Motor unit. *Compr. Physiol.* 2, 2629–2682. doi: 10.1002/cphy.c100087

Humplik, J., and Tkačik, G. (2017). Probabilistic models for neural populations that naturally capture global coupling and criticality. *PLoS Comput. Biol.* 13:e1005763. doi: 10.1371/journal.pcbi.1005763

Jang, S. H., Chang, C. H., Lee, J., Kim, C. S., Seo, J. P., and Yeo, S. S. (2013). Functional role of the corticoreticular pathway in chronic stroke patients. *Stroke* 44, 1099–1104. doi: 10.1161/STROKEAHA.111.000269

Jang, S. H., and Seo, J. P. (2014). The distribution of the cortical origin of the corticoreticular pathway in the human brain: a diffusion tensor imaging study. *Somatosens. Mot. Res.* 31, 204–208. doi: 10.3109/08990220.2014.917292

Karbasforoushan, H., Cohen-Adad, J., and Dewald, J. (2019). Brainstem and spinal cord MRI identifies altered sensorimotor pathways post-stroke. *Nat. Commun.* 10:3524. doi: 10.1038/s41467-019-11244-3

Karpati, G., Hilton-Jones, D., and Griggs, R. C. (eds). (2001). *Disorders of Voluntary Muscle., 7th edition* Cambridge: Cambridge University Press.

Koch, C., and Segev, I. (2000). The role of single neurons in information processing. *Nat. Neurosci.* 3:1171. doi: 10.1038/81444

Lee, R., and Heckman, C. (2001). Essential role of a fast persistent inward current in action potential initiation and control of rhythmic firing. *J. Neurophysiol.* 85, 472–475. doi: 10.1152/jn.2001.85.1.472

Li, S., Chen, Y.-T., Francisco, G., Zhou, P., and Rymer, W. Z. (2019). A unifying pathophysiological account for post-stroke spasticity and disordered motor control. *Front. Neurol.* 10:468. doi: 10.3389/fneur.2019.00468

Lüscher, H., Ruenzel, P., and Henneman, E. (1983). Composite EPSPs in motoneurons of different sizes before and during PTP: implications for transmission failure and its relief in Ia projections. *J. Neurophysiol.* 49, 269–289. doi: 10.1152/jn.1983.49.1.269

Maltenfort, M. G., Heckman, C., and Rymer, W. Z. (1998). Decorrelating actions of renshaw interneurons on the firing of spinal motoneurons within a motor nucleus: a simulation study. *J. Neurophysiol.* 80, 309–323. doi: 10.1152/jn.1998.80.1.309

Markram, H. (2003). Elementary principles of nonlinear synaptic transmission. *Computational Models for Neuroscience* (Springer), 125–169. doi: 10.1007/978-1-4471-0085-0_5

Matsuyama, K., Mori, F., Nakajima, K., Drew, T., Aoki, M., and Mori, S. (2004). Locomotor role of the corticoreticular–reticulospinal–spinal interneuronal system. *Prog. Brain Res.* 143, 239–249. doi: 10.1016/S0079-6123(03)43024-0

Mattei, B., and Schmied, A. (2002). Delayed and prolonged effects of a near threshold EPSP on the firing time of human α-motoneurones. *J. Physiol.* 538, 849–865. doi: 10.1113/jphysiol.2001.012701

McDougal, R. A., Morse, T. M., Carnevale, T., Marenco, L., Wang, R., Migliore, M., et al. (2017). Twenty years of ModelDB and beyond: building essential modeling tools for the future of neuroscience. *J. Comput. Neurosci.* 42, 1–10. doi: 10.1007/s10827-016-0623-7

McPherson, J. G., Chen, A., Ellis, M. D., Yao, J., Heckman, C., and Dewald, J. P. (2018a). Progressive recruitment of contralesional cortico-reticulospinal pathways drives motor impairment post stroke. *J. Physiol.* 596, 1211–1225. doi: 10.1113/JP274968

McPherson, J. G., Ellis, M. D., Harden, R. N., Carmona, C., Drogos, J. M., Heckman, C. J., et al. (2018b). Neuromodulatory inputs to motoneurons contribute to the loss of independent joint control in chronic moderate to severe hemiparetic stroke. *Front. Neurol.* 9:470. doi: 10.3389/fneur.2018.00470

McPherson, J. G., Stienen, A. H., Drogos, J. M., and Dewald, J. P. (2018c). Modification of spastic stretch reflexes at the elbow by flexion synergy expression in individuals with chronic hemiparetic stroke. *Arch. Phys. Med. Rehabil.* 99, 491–500. doi: 10.1016/j.apmr.2017.06.019

Mima, T., and Hallett, M. (1999). Corticomuscular coherence: a review. *J. Clin. Neurophysiol.* 16:501. doi: 10.1097/00004691-199911000-00002

Mima, T., Toma, K., Koshy, B., and Hallett, M. (2001). Coherence between cortical and muscular activities after subcortical stroke. *Stroke* 32, 2597–2601. doi: 10.1161/hs1101.098764

Negro, F., and Farina, D. (2011a). Decorrelation of cortical inputs and motoneuron output. *J. Neurophysiol.* 106, 2688–2697. doi: 10.1152/jn.00336.2011

Negro, F., and Farina, D. (2011b). Linear transmission of cortical oscillations to the neural drive to muscles is mediated by common projections to populations of motoneurons in humans. *J. Physiol.* 589, 629–637. doi: 10.1113/jphysiol.2010.202473

Nikias, C. L., and Mendel, J. M. (1993). Signal processing with higher-order spectra. *IEEE Signal Process. Mag.* 10, 10–37. doi: 10.1109/79.221324

Owen, M., Ingo, C., and Dewald, J. (2017). Upper extremity motor impairments and microstructural changes in bulbospinal pathways in chronic hemiparetic stroke. *Front. Neurol.* 8:257. doi: 10.3389/fneur.2017.00257

Pfurtscheller, G., and Da Silva, F. L. (1999). Event-related EEG/MEG synchronization and desynchronization: basic principles. *Clin. Neurophysiol.* 110, 1842–1857. doi: 10.1016/S1388-2457(99)00141-8

Powers, R. K., and Binder, M. D. (2001). Input-output functions of mammalian motoneurons. *Rev. Physiol. Biochem. Pharmacol.* 143, 137–263. doi: 10.1007/BFb0115594

Prut, Y., and Perlmutter, S. I. (2003). Firing properties of spinal interneurons during voluntary movement. I. state-dependent regularity of firing. *J. Neurosci.* 23, 9600–9610. doi: 10.1523/JNEUROSCI.23-29-09600.2003

Rybak, I. A., Shevtsova, N. A., Lafreniere-Roula, M., and Mccrea, D. A. (2006). Modelling spinal circuitry involved in locomotor pattern generation: insights from deletions during fictive locomotion. *J. Physiol.* 577, 617–639. doi: 10.1113/jphysiol.2006.118703

Salenius, S., and Hari, R. (2003). Synchronous cortical oscillatory activity during motor action. *Curr. Opin. Neurobiol.* 13, 678–684. doi: 10.1016/j.conb.2003.10.008

Schoffelen, J.-M., Oostenveld, R., and Fries, P. (2005). Neuronal coherence as a mechanism of effective corticospinal interaction. *Science* 308, 111–113. doi: 10.1126/science.1107027

Schwerin, S. C., Yao, J., and Dewald, J. P. (2011). Using paired pulse TMS to facilitate contralateral and ipsilateral MEPs in upper extremity muscles

of chronic hemiparetic stroke patients. *J. Neurosci. Methods* 195, 151–160. doi: 10.1016/j.jneumeth.2010.11.021

Streit, J., Tscherter, A., and Darbon, P. (2006). Rhythm generation in spinal cultures: Is it the neuron or the network? *Adv. Network Electrophysiol.* 377–408. doi: 10.1007/0-387-25858-2_16

Sturm, H., Schmied, A., Vedel, J. P., and Pagni, S. (1997). Firing pattern of type-identified wrist extensor motor units during wrist extension and hand clenching in humans. *J. Physiol.* 504, 735–745. doi: 10.1111/j.1469-7793.1997.735bd.x

Tanji, J., and Kato, M. (1972). Discharges of single motor units at voluntary contraction of abductor digiti minimi muscle in man. *Brain Res.* 45, 590–593. doi: 10.1016/0006-8993(72)90488-X

Thompson, C. K., Negro, F., Johnson, M. D., Holmes, M. R., McPherson, L. M., Powers, R. K., et al. (2018). Robust and accurate decoding of motoneuron behaviour and prediction of the resulting force output. *J. Physiol.* 596, 2643–2659. doi: 10.1113/JP276153

Tian, R., Yang, Y., Van Der Helm, F. C., and Dewald, J. P. A. (2018). A novel approach for modeling neural responses to joint perturbations using the NARMAX method and a hierarchical neural network. *Front. Comput. Neurosci.* 12:96. doi: 10.3389/fncom.2018.00096

van Wijk, B. C., Beek, P. J., and Daffertshofer, A. (2012). Neural synchrony within the motor system: what have we learned so far? *Front. Hum. Neurosci.* 6:252. doi: 10.3389/fnhum.2012.00252

Williams, E. R., and Baker, S. N. (2009). Renshaw cell recurrent inhibition improves physiological tremor by reducing corticomuscular coupling at 10 Hz. *J. Neurosci.* 29, 6616–6624. doi: 10.1523/JNEUROSCI.0272-09.2009

Yang, Y., Dewald, J., Van Der Helm, F. C., and Schouten, A. C. (2018). Unveiling neural coupling within the sensorimotor system: directionality and nonlinearity. *Euro. J. Neurosci.* 48, 2407–2415. doi: 10.1111/ejn.13692

Yang, Y., Schouten, A. C., Solis-Escalante, T., and Van Der Helm, F. C. (2015). Probing the nonlinearity in neural systems using cross-frequency coherence framework. *IFAC-papersonline* 48, 1386–1390. doi: 10.1016/j.ifacol.2015.12.326

Yang, Y., Solis-Escalante, T., Van De Ruit, M., Van Der Helm, F. C., and Schouten, A. C. (2016a). Nonlinear coupling between cortical oscillations and muscle activity during isotonic wrist flexion. *Front. Comput. Neurosci.* 10:126. doi: 10.3389/fncom.2016.00126

Yang, Y., Solis-Escalante, T., Van Der Helm, F. C., and Schouten, A. C. (2016b). A generalized coherence framework for detecting and characterizing nonlinear interactions in the nervous system. *IEEE Trans. Biomed. Eng.* 63, 2629–2637. doi: 10.1109/TBME.2016.2585097

Yang, Y., Tian, R., Cummings, M., Hogenhuis, C. H. E. Y., Deol, J., Drogos, J., et al. (2019). *Determine the Usage of Indirect Motor Pathways Following a Hemiparetic Stroke: A Pilot Study.* Philadelphia, PA: Neuroscience 2019.

Conflict of Interest: The authors declare that the research was conducted in the absence of any commercial or financial relationships that could be construed as a potential conflict of interest.

Copyright © 2020 Sinha, Dewald, Heckman and Yang. This is an open-access article distributed under the terms of the Creative Commons Attribution License (CC BY). The use, distribution or reproduction in other forums is permitted, provided the original author(s) and the copyright owner(s) are credited and that the original publication in this journal is cited, in accordance with accepted academic practice. No use, distribution or reproduction is permitted which does not comply with these terms.

APPENDIX

Equilibrium Potentials

$E_{Na} = 55mV$; $E_K = -80mV$; $E_{Ca} = 80mV$;
$E_{L(S)} = -65mV \pm 0.3$; $E_{L(D)} = -65 \pm 0.15mV$ (motoneurons∗)
∗Motoneuron equilibrium potentials were assigned from uniform random distributions with mean ± S.D as given above to obtain firing rates in the range of 5–30 spikes/s as described in section Simulations.
∗ ∗ Interneuron equilibrium potentials were set as described in section Simulations.

Neuron Paramteres

Motoneurons:
$g_{Na(S)} = 120\ mS\ cm^{-2}$; $g_{NaP(S)} = 0.1\ mS\ cm^{-2}$; $g_{K(S)} = 100\ mS\ cm^{-2}$;
$g_{CaN(S)} = 14\ mS\ cm^{-2}$; $g_{K,Ca(S)} = 5\ mS\ cm^{-2}$; $g_{L(S)} = 0.51\ mS\ cm^{-2}$;
$g_{CaN(D)} = 0.3\ mS\ cm^{-2}$; $g_{CaL(D)} = 0.33\ mS\ cm^{-2}$; $g_{NaP(D)} = 0.1\ mS\ cm^{-2}$;
$g_{K,Ca(D)} = 1.1\ mS\ cm^{-2}$; $g_{L(D)} = 0.51\ mS\ cm^{-2}$; $g_c = 0.1\ mS\ cm^{-2}$;
$p = 0.1$; $f = 0.01$; $\alpha = 0.0009\ mol\ C^{-1}\ \mu m^{-1}$; $k_{Ca} = 2ms^{-1}$; $K_d = 0.2\mu M$

Interneurons:
$g_{Na} = 120\ mS\,cm^{-2}$; $g_K = 100\ mS\,cm^{-2}$; $g_L = 0.51\ mS\,cm^{-2}$;

Synapses:
$E_{synE} = -10mV$; $g_{synE} = 0.01mS\,cm^{-2}$; $\tau_{synE} = 5ms$;
$E_{synE} = -10mV$; $g_{synE} = 0.0075mS\,cm^{-2}$; $\tau_{synE} = 5ms$;

TABLE A1 | Steady-state activation and inactivation variables and time constants for voltage-dependent ionic channels (Rybak et al., 2006).

Ionic channels	$m_\infty(V)$, V *is in mV* $h_\infty(V)$, V *is in mV*	$\tau_m(V)$, *ms* $\tau_h(V)$, *ms*
Na^+	$m_{\infty Na} = \frac{1}{1+e^{-\frac{(V+35)}{7.8}}}$ $h_{\infty Na} = \frac{1}{1+e^{\frac{(V+55)}{7}}}$	$\tau_{mNa} = 0$ $\tau_{hNa} = \frac{30}{e^{\frac{(V+50)}{15}} + e^{-\frac{(V+50)}{16}}}$
NaP^+	$m_{\infty NaP} = \frac{1}{1+e^{-\frac{(V+47.1)}{3.1}}}$ $h_{\infty NaP} = \frac{1}{1+e^{-\frac{(V+59)}{8}}}$	$\tau_{mNaP} = 0$ $\tau_{hNaP} = \frac{1{,}200}{\cosh(\frac{(V+59)}{16})}$
K^+	$m_{\infty K} = \frac{1}{1+e^{-\frac{(V+28)}{15}}}$ $h_K = 1$	$\tau_{mK} = \frac{7}{e^{\frac{(V+40)}{40}} + e^{-\frac{(V+40)}{50}}}$
CaN^{2+}	$m_{\infty CaN} = \frac{1}{1+e^{-\frac{(V+30)}{5}}}$ $h_{\infty CaN} = \frac{1}{1+e^{-\frac{(V+45)}{5}}}$	$\tau_{mCaN} = 4$ $\tau_{hCaN} = 40$
CaL^{2+}	$m_{\infty CaL} = \frac{1}{1+e^{-\frac{(V+40)}{7}}}$ $h_{CaL} = 1$	$\tau_{mCaL} = 4$;

frontiers in Computational Neuroscience

ORIGINAL RESEARCH
published: 03 March 2020
doi: 10.3389/fncom.2020.00018

Neuronal Degeneration Impairs Rhythms Between Connected Microcircuits

*Samantha N. Schumm[1], David Gabrieli[1] and David F. Meaney[1,2]**

[1] Department of Bioengineering, School of Engineering and Applied Sciences, University of Pennsylvania, Philadelphia, PA, United States, [2] Penn Center for Brain Injury and Repair, Department of Neurosurgery, Perelman School of Medicine, University of Pennsylvania, Philadelphia, PA, United States

Synchronization of neural activity across brain regions is critical to processes that include perception, learning, and memory. After traumatic brain injury (TBI), neuronal degeneration is one possible effect and can alter communication between neural circuits. Consequently, synchronization between neurons may change and can contribute to both lasting changes in functional brain networks and cognitive impairment in patients. However, fundamental principles relating exactly how TBI at the cellular scale affects synchronization of mesoscale circuits are not well understood. In this work, we use computational networks of Izhikevich integrate-and-fire neurons to study synchronized, oscillatory activity between clusters of neurons, which also adapt according to spike-timing-dependent plasticity (STDP). We study how the connections within and between these neuronal clusters change as unidirectional connections form between the two neuronal populations. In turn, we examine how neuronal deletion, intended to mimic the temporary or permanent loss of neurons in the mesoscale circuit, affects these dynamics. We determine synchronization of two neuronal circuits requires very modest connectivity between these populations; approximately 10% of neurons projecting from one circuit to another circuit will result in high synchronization. In addition, we find that synchronization level inversely affects the strength of connection between neuronal microcircuits – moderately synchronized microcircuits develop stronger intercluster connections than do highly synchronized circuits. Finally, we find that highly synchronized circuits are largely protected against the effects of neuronal deletion but may display changes in frequency properties across circuits with targeted neuronal loss. Together, our results suggest that strongly and weakly connected regions differ in their inherent resilience to damage and may serve different roles in a larger network.

Keywords: neurodegeneration, microcircuit, network, synchronization, rhythms

OPEN ACCESS

Edited by:
Spase Petkoski, INSERM U 1106, Institut de Neurosciences des Systèmes, France

Reviewed by:
Federico Devalle, Centre de Recerca Matemàtica, Spain
Fernando Montani, National Scientific and Technical Research Council (CONICET), Argentina

***Correspondence:**
David F. Meaney
dmeaney@seas.upenn.edu

Received: *13 September 2019*
Accepted: *11 February 2020*
Published: *03 March 2020*

Citation:
Schumm SN, Gabrieli D and Meaney DF (2020) Neuronal Degeneration Impairs Rhythms Between Connected Microcircuits. Front. Comput. Neurosci. 14:18. doi: 10.3389/fncom.2020.00018

INTRODUCTION

Affecting as many as 3.8 million new patients each year (Langlois et al., 2006), traumatic brain injury (TBI) is a leading cause of disability in the U.S. population (Blennow et al., 2016; Pevzner et al., 2016). As such, TBI constitutes a substantial financial burden for both caregivers and healthcare systems (Coronado et al., 2012; Pevzner et al., 2016). Although TBI may occur during high-contact sports or from exposure to explosive military devices (Blennow et al., 2016), TBI is more frequently caused by motor vehicle accidents and falls (Blennow et al., 2016). In addition, TBI commonly affects the elderly, a growing demographic in the United States.

Due to its diverse array of causes, TBI has broad social impact across many demographics and continues to pose a challenge to researchers attempting to develop treatments. Although many recover completely from mild TBI, other patients suffer long-term consequences (Masel and DeWitt, 2010; Blennow et al., 2016; Hiploylee et al., 2017; Wilson et al., 2017), which include memory deficits, sleep disturbances, or mood disorders (Masel and DeWitt, 2010; Wilson et al., 2017). Recent work shows that some of these long-term effects are associated with lasting changes in brain networks. For instance, increased activation in the default mode network is linked to sustained attention deficits after TBI (Bonnelle et al., 2011). Additionally, alterations in functional brain connectivity are thought to explain motor impairments after mild TBI (Kasahara et al., 2010), can target regions involved in cognitive function (Stevens et al., 2012) and sensory processing (Sours et al., 2015), and can differentially target areas associated with episodic memory (Yan et al., 2016). With the well-known heterogeneity of injury patterns and TBI mechanisms, though, it is difficult to draw direct and consistent associations between an impact, the resulting network changes, and the corresponding behavioral impairments. One critically understudied area is how damage in TBI affects the coordination of circuits at the mesoscale level, where hundreds to thousands of neurons coordinate their relative activation pattern with other areas of the brain, leading to the periodic synchronization of areas throughout the brain during task execution, recall, and learning.

Coherence is an important concept across scales in neural communication and brain networks. When the brain is engaged in a task, anatomical regions exhibiting synchronous activity are believed to participate in executing that task (Logothetis and Wandell, 2004; Damoiseaux et al., 2006; Jilka et al., 2014). Most commonly, temporal correlations in hemodynamic fluctuations (functional MRI BOLD data) are used to determine networks of functionally connected brain regions (Fransson, 2006; Greicius et al., 2009). Beyond defining intrinsic brain networks, synchronization is important at the cellular scale for facilitating communication, as it temporarily binds neurons together into functional ensembles (Bastos et al., 2015; Bocchio et al., 2017). Likewise, learning and memory largely depend on coherence, which enables long-distance communication between brain regions (Dü Zel et al., 2010; Wang et al., 2010). Several human imaging studies demonstrate that TBI disrupts synchronization (Sharp et al., 2011; Venkatesan et al., 2015; Wang et al., 2017), leading to the likely increase or decrease in functional network connectivity that contributes to long-term cognitive effects.

Synchronization has been studied extensively at the whole brain scale, but it has also proved important in microscale neuronal networks (Eytan and Marom, 2006; Penn et al., 2016). Despite our understanding and visualization of whole brain activity, little is known about the way in which smaller scale dynamics give rise to high-level coherence. Although it is expected that cellular dysfunction at the beginning and over the course of neurological disorders will impact the coherence of neural activity throughout the brain, there is remarkably little known about how the structure of a network at the cellular scale can lead to coherence changes at the microcircuit level. Furthermore, macroscale synchronization may obscure greater dynamic variability at a smaller spatial scale. Few computational models have emphasized connections between physically separated neuronal clusters or the flow of information between them (Vicente et al., 2008), so there are many unanswered questions regarding how synchronization emerges in mesoscale circuits and how resilient that behavior is to damage.

In this report, we examine how disrupting an intermediate level of neural computation informs and affects the interpretation of large-scale synchrony. We use a computational model of a neuronal network to make precise manipulations that would not be possible experimentally, with the goal of uncovering the principles of mesoscale synchronization that occur when coupled neuronal networks are traumatically injured. There are few existing studies that examine coherence at this scale (Vicente et al., 2008; Gollo et al., 2014), and we are not aware of any similar efforts to examine the unique intersection between traumatic injury and coherence at the mesoscale. We find that our modeled networks synchronize easily despite relatively modest connections between two microcircuits. Upon simulating the effects of neuronal inactivation or degeneration, we find the simplest model of two connected neuronal populations – i.e. the directed projection of neuronal outputs from one cluster to another – reveals inherent advantages of two levels of interconnectivity between microcircuits. Broadly speaking, our results show that highly interconnected clusters are resilient and highly reliable and moderately interconnected clusters are less resilient and more flexible.

MATERIALS AND METHODS

Networks were constructed by assembling and connecting clusters consisting of 1000 neurons each. Two of these clusters were then connected. We prescribed the properties of each cluster independently before connecting the two together.

Properties of a Single Microcircuit

Each individual cluster consisted of 1000 neurons, 80% of which were excitatory and 20% of which were inhibitory, according to empirical evaluation of cortical tissue (Soriano et al., 2008). To create a network, neurons were represented as nodes placed randomly on the surface of a unit sphere, which eliminated the potential boundary effects of a planar geometry. Synaptic connections were represented as directed edges and added at random according to distributions of excitatory and inhibitory connections experimentally derived by Soriano et al. (2008). Neurons averaged 100 outputs and an average of 80 excitatory and 20 inhibitory inputs.

In networks with spike-timing-dependent plasticity (STDP), edge weights are known to follow a bimodal distribution with most connections pushed toward the lowest and highest possible strengths (Song et al., 2000). Accordingly, the initial synaptic strength of each connection was assigned from a bimodal distribution where networks with greater excitatory strength had a higher proportion of strong, high-weight connections. This distribution was scaled from a minimum strength of

0 to a maximum strength of 4 (peak mV/ms). Inhibitory neurons instead followed a Gaussian distribution of strength with 10% variance ranging from −14 to 0 (peak mV/ms). These ranges were selected such that post-synaptic potentials fell within the range of voltages observed empirically for cortical neurons (Ferster and Jagadeesh, 1992). Conduction delays between neurons were proportional to the distance between two neurons and ranged from 1–8 milliseconds (ms), as derived from experimental work by Swadlow (1985).

Connecting Multiple Neuronal Microcircuits

For more complex simulations, the individual microcircuits (clusters) were first created and then connections were added between them (**Figures 1A,B**). The parameters defining intercluster connections include the following: (1) the percentage of excitatory neurons in the upstream cluster ("Pre") that project to the downstream cluster ("Post"), (2) the percentage of excitatory neurons in the downstream cluster that receive connections from the upstream cluster, and (3) the number of connections per upstream projecting neuron (**Figure 1A**). We randomly selected neurons in the upstream network to connect to randomly selected neurons in the downstream cluster. The synaptic weights for these connections were selected from the weight distribution of the upstream cluster. Intercluster conduction delays were chosen from a uniform distribution in the range of 10 ± 2 ms. This delay corresponds to a separation distance between the two clusters of 2–3 mm. Finally, we maintained the total number of inputs on each excitatory neuron by removing intracluster connections to verify activity-related results are due to the two-cluster architecture and not to a change in the number of inputs a neuron receives. This approach of preserving the number of inputs to a neuron is referred to as "input-degree control." In a subset of simulations, we compared our results in non-degree controlled and output-degree controlled networks, finding no significant differences between their baseline synchronization behavior. In order to best interpret changes in activity and avoid an unrealistic number of connections, we proceeded with input-degree controlled simulations. Accordingly, we limited the potential number of intercluster connections such that the downstream neurons must receive >50% excitatory inputs from the downstream population, ensuring the downstream cluster remains distinct from the upstream.

To characterize the structural changes with more detail, we identified six subpopulations within the two-cluster topology. There is a total of four excitatory neuron populations defined based on cluster membership (Cluster 1 = presynaptic OR Cluster 2 = postsynaptic) and whether the neurons have intercluster connections. Neurons sending *inter*cluster connections in the upstream or *pre*synaptic cluster are referred to as the *Inter Pre* subpopulation. Neurons with *intra*cluster connections only in the *pre*synaptic cluster are the *Intra Pre* subpopulation. Those receiving *inter*cluster connections in the downstream or *post*synaptic cluster are the *Inter Post* neurons. Finally, neurons with *intra*cluster connections only in the downstream cluster are the *Intra Post* subgroup. There are also two inhibitory neuron populations, one per cluster. These are referred to as *Inhib Pre* and *Inhib Post*. We focused our analysis predominantly on the excitatory subpopulations because these are the neurons that may have intercluster connections and, thereby, shape synchronization most directly (see the section "Results").

Dynamics and Neural Activity

Neuron activity was modeled via a system of differential equations, which describe the membrane potential and the recovery potential (Izhikevich, 2003; Izhikevich et al., 2004; Izhikevich and Edelman, 2008; Wiles et al., 2017; Gabrieli et al., 2019). The dynamic equations are as follows:

$$v' = 0.04v^2 + 5v + 140 - u + I$$

$$u' = a(bv - u)$$

$$\text{if } v \geq 30\,\text{mV}, \text{ then } \begin{cases} v = c \\ u = u + d \end{cases}$$

where v is the membrane potential in millivolts and u is the recovery variable. I is the current and includes both synaptically driven and noise currents. The parameters a, b, c, and d shape the neuron spiking behavior. These parameters were used to create regular-spiking excitatory neurons and fast-spiking, low-threshold inhibitory neurons, according to Izhikevich (2003).

The model also incorporated primary ionic currents through AMPA and GABA receptors, which drove synaptic-based activity. As in our previous work (Gabrieli et al., 2019), the networks were driven with a contribution of 1 Hz noise according to a gamma distribution (k, θ = 2, 1/2) (Izhikevich and Edelman, 2008; Wiles et al., 2017). When neurons fired, the action potential propagated along synaptic connections with a delay depending on the distance the signal must travel. Neurons were desensitized to repeated action potential inputs at 40% attenuation (τ = 150 ms).

Our model also featured STDP in connections between excitatory neurons, according to the following equation:

$$\Delta w(w) = \begin{cases} A_+(w) \exp\left(-\frac{t_{\text{post}} - t_{\text{pre}}}{\tau}\right) & \text{if } t_{\text{post}} - t_{\text{pre}} > 0 \\ A_-(w) \exp\left(-\frac{t_{\text{post}} - t_{\text{pre}}}{\tau}\right) & \text{if } t_{\text{post}} - t_{\text{pre}} \leq 0 \end{cases}$$

where w is the weight of the connection between two neurons. A_+ and A_- set the maximum magnitude of synaptic change. τ is the plasticity time constant and equal to 20 ms. Finally, t_{pre} and t_{post} are the timing of pre- and post-synaptic spikes. By the process of STDP, synapses are strengthened when the post-synaptic neuron fires closely after receiving an input from the presynaptic neuron (Song et al., 2000; Effenberger et al., 2015). If, instead, the post-synaptic neuron fires before receiving a signal from the presynaptic neuron, the synapse is weakened (Song et al., 2000; Effenberger et al., 2015). This process is believed to contribute to learning and memory and to enable entrainment of information into neuronal networks (Song et al., 2000).

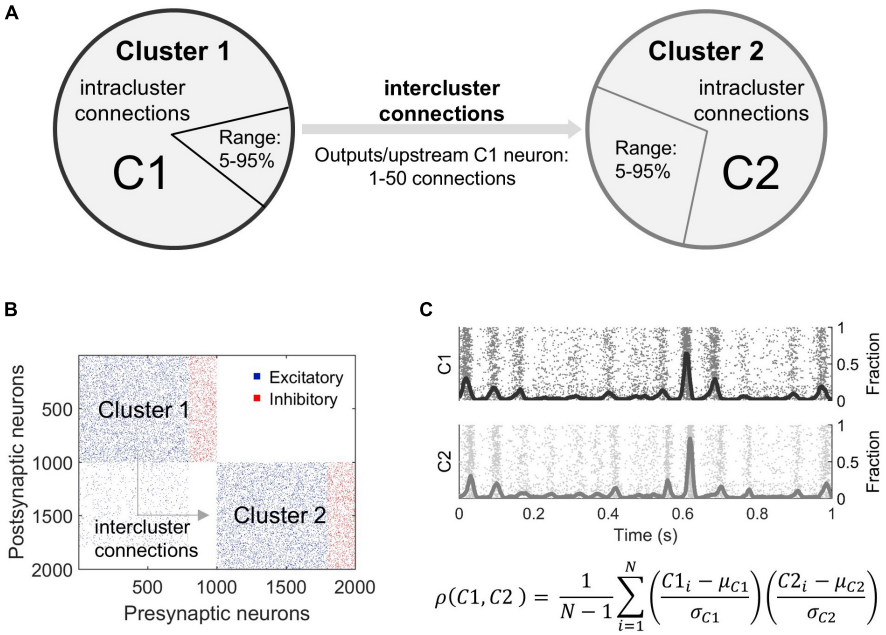


FIGURE 1 | Overview of modeling microcircuit synchronization. **(A)** Two microcircuits (Cluster 1, Cluster 2), each composed of 800 excitatory and 200 inhibitory neurons, were coupled by connecting some outputs of randomly selected neurons in upstream Cluster 1 to randomly selected neurons in downstream Cluster 2. These projections are termed intercluster connections. All neurons were also connected to other neurons within the same cluster via intracluster connections. The relative fraction of neurons in Cluster 1 that sent outputs to Cluster 2 varied from 5 to 95% of the excitatory neuron population in Cluster 1. Similarly, a fraction of excitatory neurons in Cluster 2 was targeted by these outputs (5–95% of excitatory neurons in Cluster 2). The number of intercluster connections from each projecting neuron in Cluster 1 ranged from 1 to 50 downstream connections. **(B)** A connectivity matrix of the overall network topology shows intercluster connections between excitatory neurons in the bottom left quadrant. To mimic *in vivo* connectivity patterns over long distances, only excitatory neurons projected outputs from Cluster 1 to excitatory neurons in Cluster 2. **(C)** Neurons were modeled using the Izhikevich integrate-and-fire formulation. Each simulation achieved a stable firing pattern before activity was analyzed. Raw neuron activity (raster plot) was summed into an aggregate activity trace (solid, oscillating lines) for each cluster and smoothed. Synchronization between the two clusters was calculated as a time-based correlation for 5 min of data. In this equation, ρ is correlation, C1 is Cluster 1, C2 is Cluster 2, μ is the mean, σ is the standard deviation, and N is the sample size or number of timesteps.

Convergence studies were performed by conducting a 24-h simulation and measuring the aggregate change in connectivity weights at each minute over the 24 h of simulation time. The network connectivity reached stable convergence after 90 min. Therefore, we ran all simulations for 2 h to allow adequate time for network activity and synaptic weights to stabilize. All activity and network measures were collected in the final 5 min of simulation time.

To determine synaptic strength parameters used in subsequent simulations, we tested all combinations of excitatory and inhibitory strength available with our model. Given the range of firing rates observed, we then selected one set of strength parameters each for approximately 4, 5, and 6 Hz (**Supplementary Figure S1**).

Analysis Metrics

Indeed, there are many ways to measure neural synchronization, ranging from phase locking to different forms of correlation, depending on the relevant time and spatial scales (Varela et al., 2001; Narayanan and Laubach, 2009; Cohen and Kohn, 2011). Here, synchronization of activity between the upstream and downstream clusters was evaluated as a time-based correlation because this methodology incorporated both activity timing and magnitude and was effective for our purposes. That is, we sought to precisely measure the extent to which the population-wide spike density of the downstream cluster matched that of the upstream cluster across minutes of simulated activity. To do so, spiking activity was summed for all neurons of each cluster every millisecond and smoothed with a 50 ms window averaging filter. A filter size of 50 ms was used because it corresponds to an intermediate temporal range of neural activity. This yielded an aggregate, smoothed signal for each cluster (**Figure 1C**). A time-based correlation was then computed between these two signals and used as a proxy for synchronization.

The rhythmic oscillations of network activity were analyzed with a similar aggregate signal approach. Spike counts were collected in 1 ms bins for the full network, and the resulting signal was then smoothed using a moving average filter (10 ms window) to produce a measure of temporal change in the network spiking activity. The magnitude (height) of the high activity periods (peak prominence ≥ 1) was calculated to represent the relative activation level of the network. The height of each activity peak was normalized by the number of neurons to yield a fraction, and these magnitudes were averaged to obtain a single value for each simulation. In addition, this smoothed, aggregate signal was analyzed in the frequency domain using Welch's method to generate the power spectral density. The power ratio was

computed as the ratio of power in a high frequency band (10–17 Hz) over the power in a low frequency band (1–4 Hz). To identify these bands, we found the highest two peaks in the frequency spectra for all networks considered and determined the range for these two dominant peaks across all spectra. (See **Supplementary Figure S2** for more detail and representative spectra for baseline networks).

We used network control theory to identify potentially important roles for subgroups of neurons in the network. Network control theory uses the concept of controllability to identify control points in a network for driving the network to alternative activity states. For example, in the brain, this could mean switching between states of daydreaming and active learning (Gu et al., 2015). Two mechanisms of control are average and modal. Nodes with high average controllability are predicted to be important for driving the network to nearby, easy-to-reach states (Gu et al., 2015). In contrast, nodes with high modal controllability are predicted to drive the network to difficult-to-reach states (Gu et al., 2015). (See **Supplementary Figure S3** for schematics). Since the metric relies on the underlying network connectivity to theoretically predict functional roles of nodes, controllability attempts to unite both network structure and function. Using established methods [see Wiles et al. (2017) for derivations] (Gu et al., 2015; Wiles et al., 2017), we calculated both average and modal controllability for each neuron in the network. The raw controllability values were then rank ordered such that 1 is the neuron with lowest controllability and N is the neuron with highest controllability.

Injury

To assess the impact of injury on the synchronization of these two neuronal populations, we selected a generic high correlation and moderate correlation network for further analysis. These networks were determined by analyzing the effect of adding intercluster connections in healthy networks. (See the section "Results" and **Figure 2** for how these correlation levels were determined). After each network ran for 2 h of simulation time to achieve stable synchronization levels, neurodegeneration was simulated by removing neurons and all their connections from the network. We focused on deleting neurons with a specific structural subtype (see the section "Materials and Methods" for detailed definitions), such that neurons were targeted from a single subtype for each injury simulation. With our interest in testing whether the controllability of a specific neuron was important to overall network synchronization, we first deleted neurons with the highest controllability ranking. For comparison, we deleted the same number of neurons randomly, again by subtype, in separate simulations and compared these results to the targeted deletion approach. After neurons were removed, we ran the simulation for another 2 h to stabilize connectivity weights before analyzing neural dynamics in the final 5 min of the simulation period. This process was repeated for five high correlation and five moderate correlation networks.

Statistical Analysis

One-way ANOVA was applied to compare the average strength of structural subtypes. A repeated measures model was used to differentiate neuron subpopulations based on nodal network measures. The Tukey–Kramer test was applied *post hoc* for multiple comparisons where relevant. To determine the effects of injuring different neuronal subtypes, we used paired Student's t-test to compare to uninjured baseline measures. Bonferroni corrections were used to determine significance when noted. To compare different neuron selection methods of injury, we applied analysis of covariance (ANCOVA) to control for the injury level covariate.

RESULTS

Unidirectional Connection of Two Neuronal Clusters

With our interest in studying how two independent neural circuits synchronize and change after injury, we first studied the physical connectivity requirements for two neural circuits to synchronize their activity. We added unidirectional connections from an upstream Cluster 1 to downstream Cluster 2 (**Figures 1A,B**) to understand the impact of intercluster connections on network dynamics, namely synchronization (**Figure 1C**). In general, we observed two phases: (1) a rapidly increasing linear phase of increasing synchronization at low levels of intercluster connection and (2) a more gradually increasing plateau phase at high levels of intercluster connection. We tested different combinations of basal firing rates in Cluster 1 and Cluster 2 and found that these results held for all conditions (**Figure 2C**). Furthermore, we examined a subset of simulations with 30% inhibitory and 70% excitatory neurons and, again, found this consistent synchronization behavior (**Supplementary Figure S4**). Importantly, the activity correlation was significantly related to the number of connections between the two clusters. We normalized this quantity as the proportion of excitatory inputs to downstream Cluster 2 that originated in upstream Cluster 1. Using the completely decoupled state of the circuits as the starting point (proportion of excitatory inputs = 0), we found the synchronization level below a proportion of inputs of 0.09 increased rapidly with more intercluster connections (linear regression, $Y = 7.53X + 0.10$, $R^2 = 0.78$, $p < 10^{-5}$). Above a physical coupling level of 0.09, the synchronization levels were also significantly correlated with the proportion of intercluster inputs, however more gradually (linear regression, $Y = 0.66X + 0.58$, $R^2 = 0.77$, $p < 10^{-5}$). The transition between these two phases occurred around 9% of inputs and was found by determining a cutoff that would produce approximately equal goodness of fit (R^2-values) for both phases. The intersection between the transition point (0.09) and the gradual phase regression line was used to set a threshold for identifying high correlation networks (correlation > 0.65). We also created a designation between moderate and low correlation networks to facilitate subsequent injury analysis where we were interested in networks that could display an appreciable decrease in synchronization. Lastly, we observed relatively modest coupling was required to cause a significant change in synchronization, learning that the downstream cluster needed only 0.3% of inputs from the upstream cluster to significantly

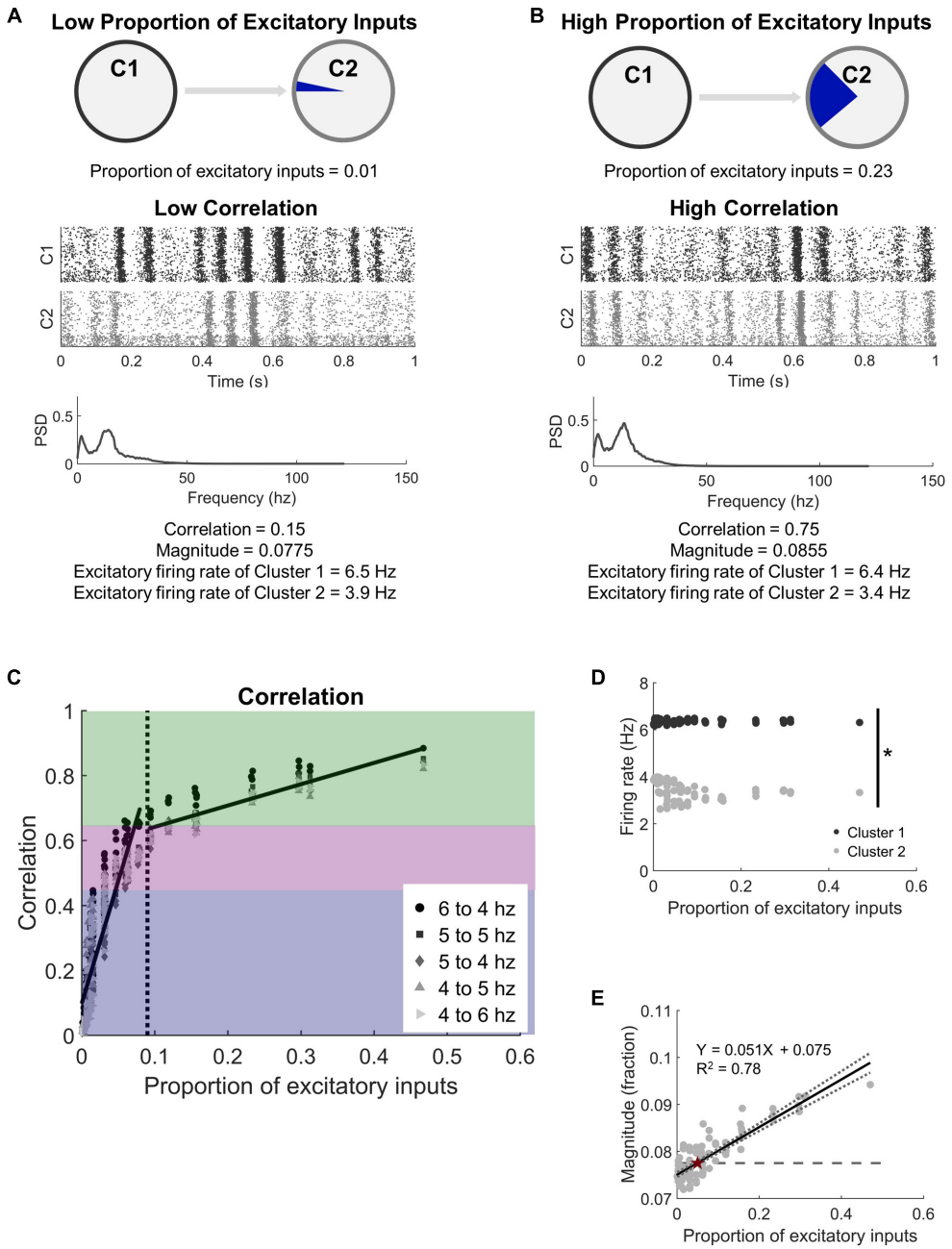


FIGURE 2 | Two microcircuits synchronize activity with relatively few intercluster connections. **(A)** Microcircuits were modeled as two distinct populations of neurons. They were coupled by progressively increasing the proportion of excitatory inputs received by Cluster 2 (C2) from the upstream Cluster 1 (C1). A low proportion of excitatory inputs was associated with low activity correlation between the microcircuits. A representative raster plot of neural activity in both microcircuits shows that periods of high and low activity were not coordinated across the two circuits at low correlation (correlation < 0.45). The corresponding frequency spectrum for low correlation networks has two distinct peaks (PSD = power spectral density). **(B)** In comparison, periods of high and low activity frequently occurred at the same time when the circuits were highly correlated (correlation > 0.65). **(C)** Increasing the proportion of inputs to one microcircuit (C2) from another (C1) led to a rapid increase in synchronization. We considered three regions of synchrony: low (correlation < 0.45; blue region), moderate ($0.45 <$ correlation < 0.65; purple region), and high (correlation > 0.65; green region). Legend indicates the average firing rates of neurons in each microcircuit when correlation is computed. The corresponding frequency spectrum for high correlation networks has two distinct peaks (PSD = power spectral density). **(D)** While the correlation between the two clusters increased with more intercluster connections, the two clusters maintained independent firing rates (*t*-test; $p < 10^{-5}$). While the correlation between the two microcircuits increased with more physical connections between them, average firing rates of neurons in each microcircuit were significantly different from each other (Student's *t*-test; $p < 10^{-5}$). **(E)** The magnitude (fraction of network participating) of the high activity oscillations continued to increase with more intercluster connections, showing a strong positive correlation (linear regression, $R^2 = 0.78$, $p < 10^{-5}$). The dashed line marks the baseline level of the null model, which has no intercluster connections. The intersection between the baseline and the regression line is marked with a red star.

change synchronization from baseline (Control networks with 0 intercluster connections: correlation = -0.008 ± 0.006 vs. Networks with 0.3% connection: correlation = 0.025 ± 0.010; paired Student's *t*-test, $p = 0.002$). For thoroughness, we investigated correlated activity within the excitatory populations of each cluster with similar methodology, finding that Cluster 1 populations (InterPre and IntraPre) are correlated at 0.98 ± 0.01 and Cluster 2 populations (InterPost and IntraPost) are correlated at 0.86 ± 0.09. This result verifies that the two follower populations in the downstream cluster remain coordinated with one another despite our removal of some intracluster connections due to input-degree control.

In addition to synchronization, another important feature of activity in the neural circuits was the rhythmic oscillations of high and low activity that would appear under normal conditions. We converted the signal to the frequency spectrum (**Figures 2A,B**) to characterize these rhythms and found oscillations of 12.6 ± 0.5 Hz in our uninjured networks. These rhythms are also addressed more formally in **Supplementary Figure S2**. Unlike synchronization, which plateaued above a specific proportion of intercluster connections, we observed that the rhythmic oscillations continued to include more neurons (higher magnitude) as the coupling of the networks increased (**Figure 2E**). Peak magnitude showed a strong positive correlation with the proportion of excitatory inputs into Cluster 2 that originate in Cluster 1 (linear regression, $Y = 0.051X + 0.075$, $R^2 = 0.78$, $p < 10^{-5}$). We tested whether these changes in synchronous, rhythmic activity were correlated with altered firing rates; however, we found no corresponding change in the average firing rates of the excitatory neurons in the network (Cluster 1: 6.4 ± 0.1 Hz vs. Cluster 2: 3.5 ± 0.4 Hz; paired Student's *t*-test, $p < 10^{-5}$) (**Figure 2D**). Therefore, the observed increase in correlation depended on a temporal shift in activity in Cluster 2, not increased activity.

With this clear change in synchronization that appeared as the network adapted with STDP, we next asked what sort of commensurate changes occur in the structural network to facilitate the observed synchronization. We expected that developing synchronous activity would necessitate strong intercluster connections. It is well-known that the STDP model implemented in our networks will lead to a bimodal synaptic weight distribution (Song et al., 2000), and we also saw a similar result in our stabilized networks (**Figures 3A,B**). From this distribution, we defined high strength connections as strengths $>50\%$ of the maximum (normalized strength > 0.5) and saw that a significantly higher fraction of intercluster connections were high strength than upstream intracluster outputs (intercluster: 0.822 ± 0.007 vs. intracluster: 0.521 ± 0.001; paired Student's *t*-test, $p < 10^{-5}$). In addition, the proportion of high strength intercluster connections increased rapidly and persisted for the duration of the simulation (**Figure 3C**). This remained true whether the network displayed high, moderate, or low levels of synchronization. Not only was the proportion of high strength intercluster connections stable, these connections themselves were highly stable. Among them, only $0.08 \pm 0.04\%$ change per minute was observed in the last 30 min of simulation time. As more intercluster connections were added (i.e. the proportion of excitatory inputs to downstream Cluster 2 from upstream Cluster 1 increased), the proportion of high strength intercluster connections decreased (linear regression, $R^2 = 0.58$, $p < 10^{-5}$) (**Figure 3D**). At low synchronization, when there were few intercluster connections, a larger proportion of those connections were high strength. As more intercluster connections were added, synchronization increased (**Figure 2C**), and the proportion of high strength intercluster connections decreased (linear regression, $R^2 = 0.58$, $p < 10^{-5}$) (**Figure 3D**). This suggests redundancy at maximal levels of coupling since it is unnecessary for as many connections to have high strength to achieve high synchronization.

Given the high strength intercluster connections, we considered whether intercluster projecting neurons (Inter Pre) are strong overall. To determine whether that was true, we assessed the average output strength of each excitatory population. The output strength of each neuron was summed and normalized by the total number of outputs. Contrary to our expectation, the Inter Pre population did not have high strength outputs as a whole, indicating that the outputs of these neurons to other neurons within the upstream population are rather weak. Instead, downstream neurons receiving connections from the upstream cluster (Inter Post) had significantly higher average output strength than other populations did (one-way ANOVA, $p < 10^{-5}$) (**Figure 3F**). Interestingly, upstream neurons with no downstream projections (Intra Pre) showed significantly lower average output strength than did the intercluster populations (one-way ANOVA, $p < 10^{-4}$) (**Figure 3F**). Notably, the Intra Pre neurons also had the least variance in strength, which suggests they respond minimally to the addition of intercluster connections (**Figure 3F**). Since the Intra Pre neurons also display relatively weak outputs, these findings show that Intra Pre neurons are the most isolated subpopulation and likely function primarily as drivers of activity in the upstream cluster.

Controllability

At this point, we knew that the network synchronized and adapted structurally. However, we did not know how this architecture might be described with higher level network metrics, and specifically, whether the neuron subtypes we defined could be identified with these metrics. In network science, there are many measures that characterize nodal importance and identify nodes as influential under different circumstances. One such nodal property, betweenness centrality, describes how often paths between two nodes in the network must pass through a given node. High betweenness centrality indicates that node is an important connector between other nodes. Commonly called hubs, nodes with high betweenness centrality are often affected after TBI due to axonal injury (Fagerholm et al., 2015). A second nodal property, controllability, predicts the importance of nodes for driving the network to a different energetic state. We examined two mechanisms of control – average and modal, which describe the ability to access easy-to-reach and difficult-to-reach states, respectively. We were interested in how the network control points identified by average and modal controllability reflected the known dynamics of the system, namely synchronization. From all tested combinations

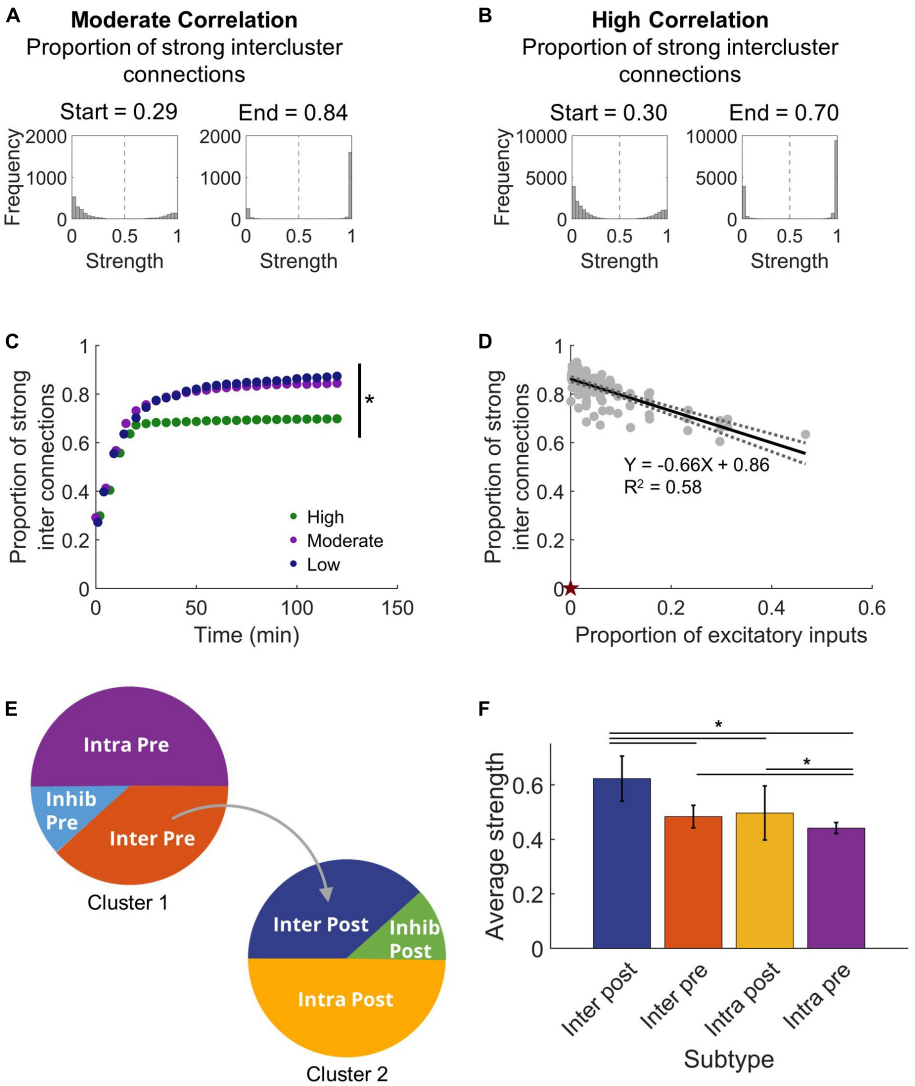


FIGURE 3 | Intercluster connections become strong connections. **(A)** Within either microcircuit, synaptic strength showed a bimodal distribution that is consistent with previous simulations that incorporate plasticity-based changes in synaptic strength. Once connections were made between the circuits, intercluster connections from Cluster 1 to Cluster 2 predominantly increased in synaptic strength. The proportion of strong intercluster connections is defined as the fraction of intercluster connections that have strength greater than half the maximum strength (marked by dashed vertical line in histograms). For a moderate correlation network, the proportion of strong connections was higher at the end time that at the start time. **(B)** Similarly, for a high correlation network, the proportion of strong connections increased from the start time to the end time. **(C)** The proportion of strong intercluster connections (strength > half maximum) increased as the simulation settled, and this proportion remained stable over time for all connected networks. In this representative example, the final proportion was significantly higher in low and moderate correlation networks than in high correlation networks (ANOVA with Tukey's *post hoc* comparison, $p < 0.001$). **(D)** The proportion of strong synaptic connections between microcircuits depended on the proportion of excitatory inputs. As the number of intercluster connections increased, the proportion of strong intercluster connections decreased (linear regression, $R^2 = 0.58$, $p < 10^{-5}$). The null model has 0 intercluster connections and, thereby, 0 strong intercluster connections (marked by red star). **(E)** We define four excitatory neuron subtypes in this architecture based on their participation in intercluster connections and two inhibitory neuron subtypes. **(F)** The Inter Post neurons had higher average output strength than the other excitatory subtypes (ANOVA with Tukey's *post hoc* comparison, $p < 10^{-4}$).

of a 6 Hz Cluster 1 projecting to 4 Hz Cluster 2 (**Figure 2C**), two representative networks (one each for moderate and high synchronization) were selected for this analysis, though similar results were found for a more extensive sample of networks. Low correlation networks were also considered but were structurally similar to moderate correlation networks in this analysis.

We found that controllability and betweenness centrality reveal distinct phenotypes in this two-cluster architecture that mirror the subtypes we know to exist and previously defined (**Figure 4**). The subtypes with intercluster connections (Inter Pre and Inter Post) had the highest betweenness centrality, underscoring their integral position in the network. Any signal passing from Cluster 1 to Cluster 2 must pass

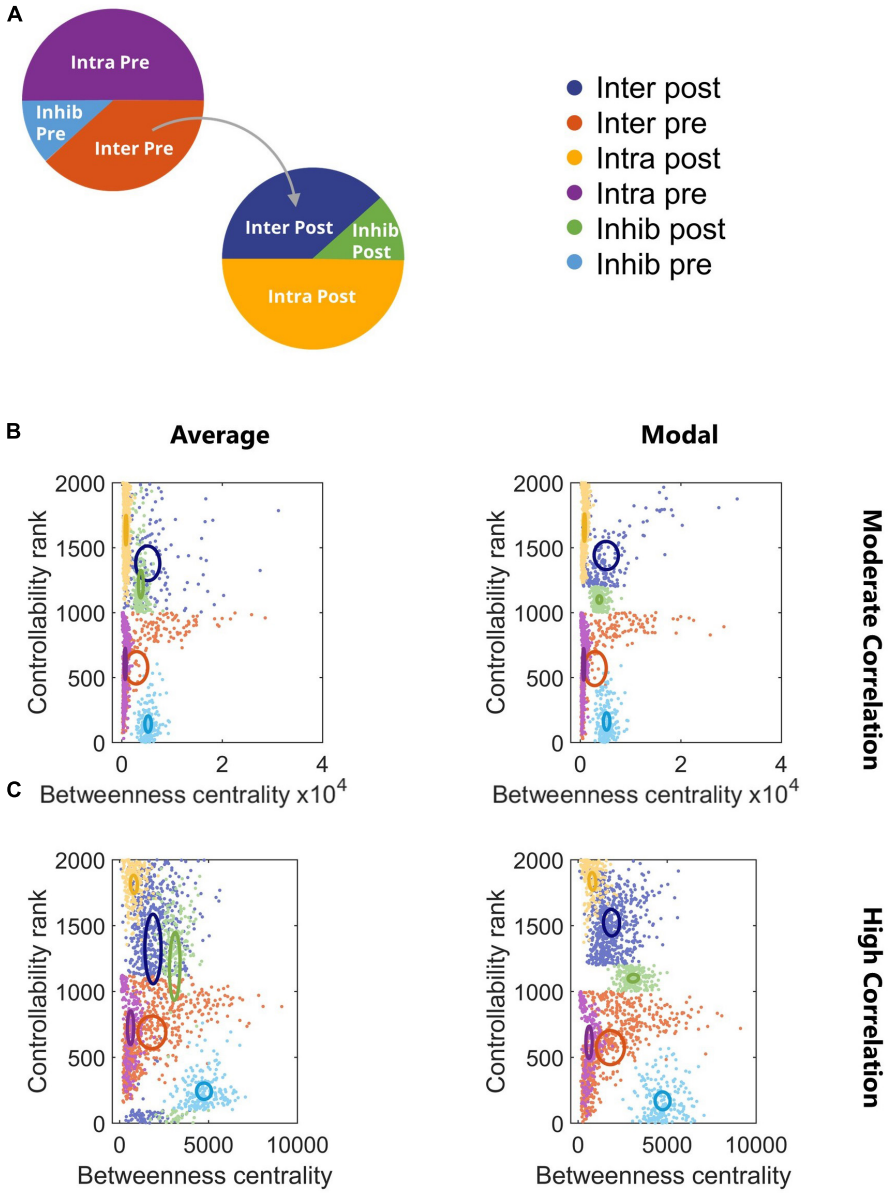


FIGURE 4 | Controllability and betweenness centrality reveal phenotypes of neuron subtypes. **(A)** Legend for subsequent panels. **(B)** Controllability and betweenness centrality differentiated the neuronal subtypes for all correlation levels. All subtype comparisons were significant (repeated measures model with Tukey–Kramer *post hoc*, $p < 10^{-4}$) with the exception of Inhib Post vs. Inhib Pre ($p = 0.075$). **(C)** All subtype comparisons were significant (repeated measures model with Tukey–Kramer *post hoc*, $p < 10^{-4}$) with the exception of Inter Pre vs. Intra Post. Ovals are centered at the group mean and represent 50% of the group standard deviation.

through Inter Pre and Inter Post neurons. The betweenness centrality of these populations decreased as more intercluster connections were added and the correlation of the network increased (**Figures 4B,C**). In contrast to betweenness centrality, controllability did not show a relationship with correlation (**Figures 4B,C**). In general, populations in the downstream cluster had higher controllability than populations in the upstream cluster. This result indicates that targeting the downstream cluster would be a more effective way to change the network state than targeting the upstream cluster. For the hypothetical example of attempting to change the network state by breaking synchronization, exogenous stimulation applied to the downstream cluster would likely be a more effective strategy because the upstream cluster is the driver while the downstream cluster is the follower. Controllability does depend on the strength of connections, so while this was generally the case, we did identify a network in which the upstream cluster had higher controllability (data not shown). Overall, the subtypes showed minimal overlap in controllability, which emphasizes the distinct roles neuronal subtypes play in this

two-cluster topology. Notably, average and modal controllability show similar trends, suggesting that the same populations would be important for driving the network to both easy-to-reach and difficult-to-reach states. Using a repeated measures model with Tukey–Kramer *post hoc* test for multiple comparisons, we found for high correlation networks all comparisons were significant (repeated measures model with Tukey–Kramer *post hoc*, $p < 10^{-4}$) except for Inter Pre vs. Intra Post (**Figure 4C**). For moderate correlation networks, all subtypes were significantly different (repeated measures model with Tukey–Kramer *post hoc*, $p < 10^{-4}$) with the exception of Inhib Post vs. Inhib Pre ($p = 0.075$).

Injuring Highly Controllable Neurons by Subtype

Given the emergence of nodal subtypes, we sought to better understand their functional roles by implementing a scheme of targeted neurodegeneration in which we removed neurons from the network. Neurons were selected from one subtype at a time to compare the effect of their removal on synchronization and activity oscillations. Since controllability is believed to link structure and function, enhancing the likelihood of activity changes due to damage, we interrogated the functional influence of removing highly controllable neurons. This is in contrast to previous work in which highly controllable neurons are stimulated (Betzel et al., 2016; Muldoon et al., 2016; Gu et al., 2017; Kim et al., 2018). We hypothesized that removing the most controllable neurons within a given subtype would be more detrimental to network function than removing random neurons from that subtype. The distributions of output weights from removed neurons vs. remaining neurons of the same subtype remain bimodal; however, for some cases of controllability-based removal, the removed neurons have many connections of relatively low output strength (**Supplementary Figure S5**). The representative high and moderate correlation networks used for our controllability analysis were also used in these studies ($N = 5$ networks per type). Low correlation networks were excluded because the baseline synchronization level could not drop further as a result of injury. We tested three injury levels (25, 50, and 75% removal) for each excitatory subtype (Inter Post, Inter Pre, Intra Post, and Intra Pre). While inhibitory neurons influence local spike timing and may thereby modulate synchronization indirectly, excitatory neurons directly affect synchronization and adapt according to STDP in our model. Thus, we focused our injury on excitatory subtypes. Finally, we found that the intercluster connection weights continued to follow the distributions shown in **Figures 3A,B** with predominantly strong connections (**Supplementary Figure S6**). Therefore, our subsequent analysis emphasizes the effects of injury on network activity.

We found that synchronization in high correlation networks was robust. When neurons were targeted according to their *controllability* ranking (average or modal), no level of deletion for any subtype reduced synchronization below the threshold for high synchronization (0.65 as determined in **Figure 2C**) (**Figure 5A**). We used paired *t*-tests with Bonferroni correction for multiple comparisons to evaluate each set of damaged networks compared to baseline uninjured networks. While there were a few significant decreases in synchronization (75% injury to Inter Pre neurons differed significantly from baseline for all targeting methods; $p < 0.0014$ for all), high correlation networks remained high correlation networks post-injury, with a single exception (**Figure 5A**). The one exception is *random* targeting of upstream neurons with intercluster connections (Inter Pre) at the highest injury level: 75% deletion yielded 0.6 ± 0.05 correlation. By applying ANCOVA to control for the injury level covariate, we also found that networks with damaged Inter Pre populations differed from one another based on the targeting strategy. Average and modal controllability targeting methods both differed from random deletion (ANCOVA with Bonferroni correction, $p < 0.001$); however, they did not differ from one another ($p > 0.8$). Lastly, we tested correlated activity within each cluster and found intracluster correlations remain high after injury (Cluster 1: 0.97 ± 0.04 and Cluster 2: 0.86 ± 0.07).

In contrast, the moderate correlation networks revealed a marked, dose-dependent vulnerability when the Inter Pre subtype (upstream neurons that send intercluster projections) was damaged (**Figure 5B**). While the changes were more modest than for Inter Pre, targeting the Inter Post population (downstream neurons that receive intercluster projections) also produced a dose-dependent decrease in synchronization. When comparing the results of Inter Pre deletion across the three methods, average and modal controllability-based deletion differed significantly from random (ANCOVA with Bonferroni correction, $p < 0.008$) but not from each other ($p > 0.8$). As for high correlation networks, intracluster correlated activity remained high (Cluster 1: 0.97 ± 0.03 and Cluster 2: 0.83 ± 0.06). For moderate correlation networks, we observed both significant decreases and increases in synchronization compared to baseline depending on the targeted subtype (paired *t*-test with Bonferroni correction, $p < 0.0014$) (**Figure 5B**). Notably, when Intra Post neurons were targeted, the resulting correlation increased. This is likely because achieving high synchronization is easier when there are fewer downstream neurons without direct inputs from the upstream cluster. In total, these results reveal a malleability of the synchronization of moderate correlation networks. Targeted injury could drive the network toward a state of either higher or lower synchrony.

While injury predominantly did not impact the synchronization of high correlation networks, we observed that the oscillation pattern of the high activity periods changed (**Figures 6A,B**). Therefore, we turned to the frequency spectrum to evaluate these rhythms. In undamaged networks, we routinely observed two prominent peaks in the power spectrum, corresponding to two primary oscillation frequencies that existed in the network activity (10–17 and 1–4 Hz; see the section "Materials and Methods," **Figures 2A,B**, and **Supplementary Figure S3** for further detail). The baseline power ratio between these two frequency bands (power in 10-14 Hz over power in 1-4 Hz) in high correlation networks was 2.6 ± 0.1 ($N = 5$). High correlation networks showed a rapid decline in this power ratio following selective damage to the Inter Pre population (paired *t*-tests with Bonferroni correction, $p < 0.0014$ for 50 and 75%

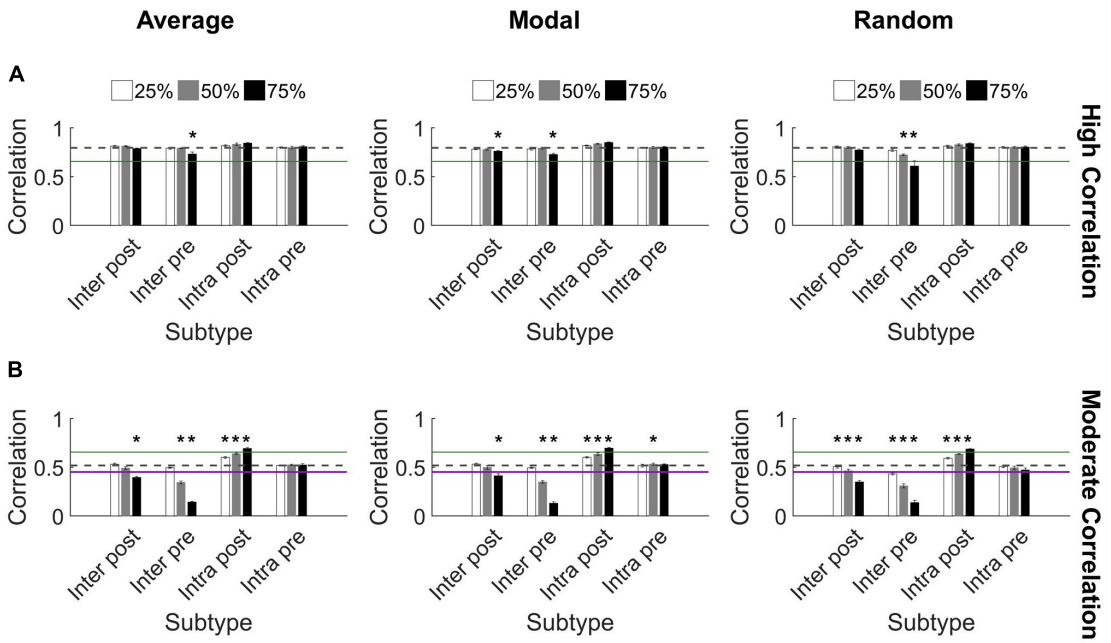


FIGURE 5 | Synchronization protects against damage to microcircuits. **(A)** Most highly synchronized networks (correlation > 0.65; green line marks threshold for high correlation) maintained high correlation when neurons from specific populations were deleted from the network. The dashed gray line denotes the baseline correlation prior to injury. Some injured networks remained high correlation while having significantly lower synchronization compared to baseline (one-sided paired *t*-test, Bonferroni corrected, $p < 0.0014$). **(B)** In comparison, networks with moderate correlation (0.45 < correlation < 0.65) prior to injury were more likely to change synchronization level after injury. The most harmful deletion strategy was targeting excitatory neurons from Cluster 1 that send projections to Cluster 2 (the Inter Pre subtype). The green line marks the threshold between moderate and high correlation networks (0.65). The purple line marks the threshold between low and moderate correlation networks (0.45) (**Figure 2**). The gray dashed line marks the baseline correlation prior to injury. Many injury networks had significantly higher or lower correlation compared to baseline (paired *t*-test, Bonferroni corrected, $p < 0.0014$). Damaging Inter Pre neurons decreased synchronization while damaging Intra Post neurons increased synchronization.

injury for all selection strategies) (**Figure 6C**). A decrease in power ratio indicates a reduction in high frequency components of the activity signal. As we observed for correlation post-injury, average and modal controllability-based deletion differed from random deletion of the Inter Pre subtype (ANCOVA with Bonferroni correction, $p < 0.005$) but did not differ from one another ($p > 0.8$). Of note, this decrease in high frequency signal occurs across both clusters (**Figure 6A**) and suggests that the upstream cluster is unable to generate higher frequencies. Since the upstream cluster serves as the driver for high correlation networks, the downstream cluster depends on receiving input from the upstream cluster. After adapting with STDP, these networks appear to prioritize synchronization over more varied frequency information.

The power ratio of moderate correlation networks varied after targeted neurodegeneration. The baseline power ratio for moderate correlation networks was 2.1 ± 0.1 ($N = 5$). Removing non-projecting neurons from the upstream cluster (Intra Pre) significantly reduced the power ratio for all targeting methods (paired *t*-tests with Bonferroni correction, $p < 0.0014$) (**Figure 6D**). This effect was more pronounced in response to controllability-based deletion. In contrast, removing neurons in the downstream cluster that lacked intercluster connections (Intra Post) increased the power ratio (significant at the 75% level with random or modal controllability-based removal; paired *t*-tests with Bonferroni correction, $p < 0.0014$) (**Figure 6D**). The power ratio was most resilient to damage in the downstream population with intercluster input (Inter Post). Of note, the power ratio increased when the Inter Pre subtype was injured at the 75% level despite these same networks showing a decrease in correlation (**Figure 5B**). Here, the frequency of high oscillation periods in Cluster 1 decreased while Cluster 2 retained higher frequency (**Figure 6B**). Thus, for the aggregate network activity, frequency was high while correlation was low. In this case, the results of removing Inter Pre neurons were not significantly different by targeting method.

DISCUSSION

In this work, we were interested in how the coherence of two model microcircuits was established by connecting one population to another. We were also interested in determining whether specific neuronal subpopulations would be more influential in changing the dynamics of these coupled circuits after traumatic injury. We found that the two clusters synchronized with relatively few intercluster connections. In addition, intercluster connections became significantly stronger than did those among neurons within each microcircuit, indicating that they are high priority connections within the

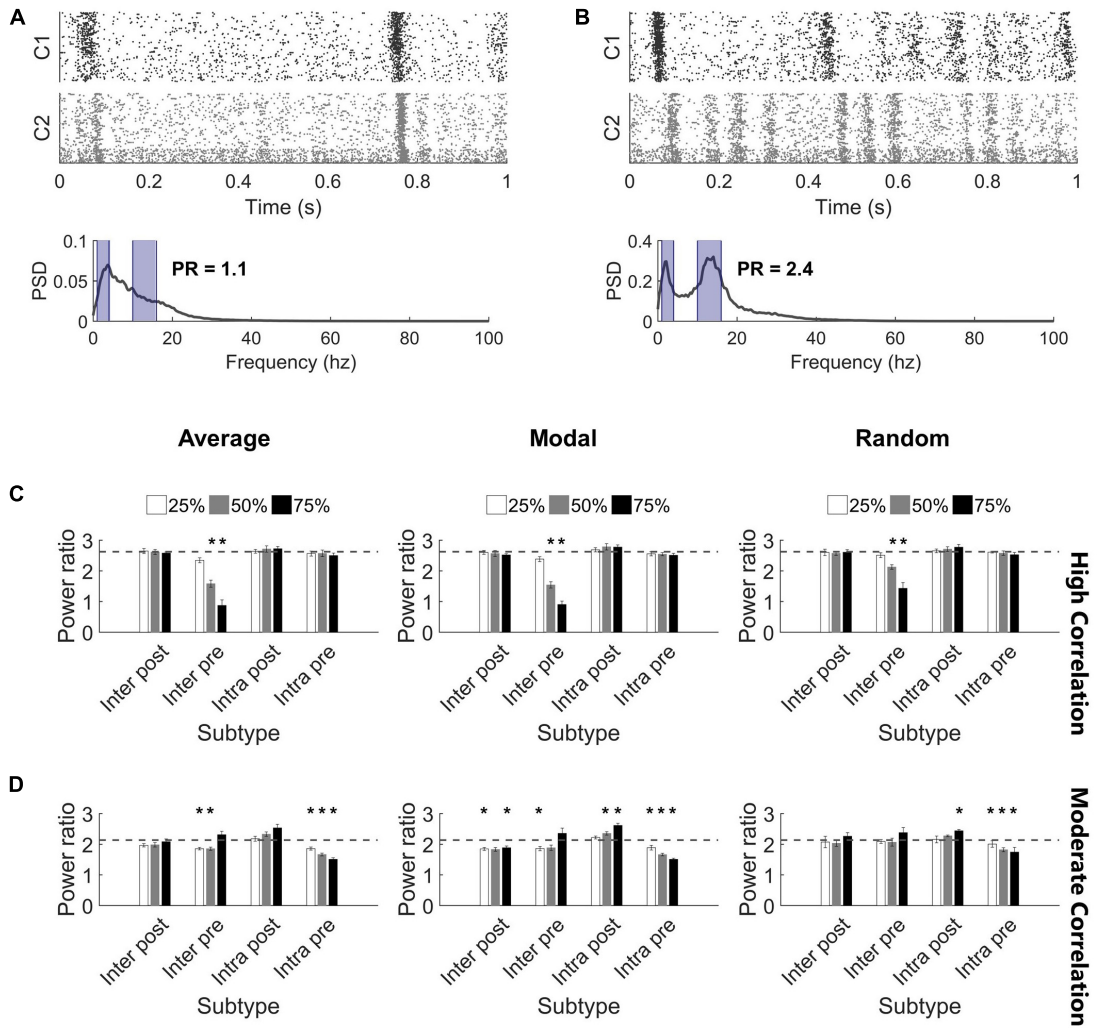
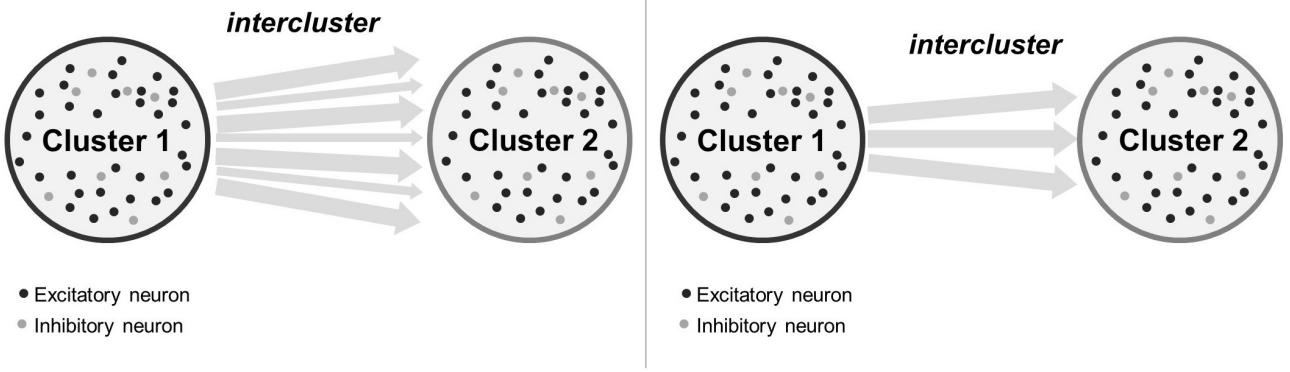


FIGURE 6 | Highly synchronized networks are prone to large decreases in power ratio after injury. **(A)** A raster plot and corresponding frequency spectrum of an injured network with *high correlation* and *low power ratio*. The blue overlays mark the portions of signal that contribute to the power ratio calculation. **(B)** A raster plot and corresponding frequency spectrum of an injured network with *low correlation* and *high power ratio*. The blue overlays mark the portions of signal that contribute to the power ratio calculation. **(C)** Removing Inter Pre neurons in a high correlation network reduced the power ratio at deletion levels 50% and above for all selection methods (paired *t*-test, Bonferroni corrected, $p < 0.0014$). The dashed gray line marks the baseline power ratio prior to injury. **(D)** Removing neurons in a moderately correlated network had variable effects. In most cases, networks had modest, though significant, reductions in the power ratio; however, there were also injured networks with higher power ratio than they had at baseline (paired *t*-test, Bonferroni corrected, $p < 0.0014$). Increased power ratio was typically observed after damage to Intra Post neurons whereas decreased power ratio was common after damage to other subtypes.

network. Finally, we employed targeted neurodegeneration to explore the influence of neuron subtypes on overall network behavior and showed that neuron controllability did not strongly influence injury response. However, neurons linking the two microcircuits were critical for maintaining both the broad power spectrum of activity communicated between the two networks and the coherence of this communication. Together, the results of targeted neurodegeneration reveal that densely connected microcircuits are resilient and highly reliable, even when injured, but these benefits may come at the cost of reduced signal flexibility (**Figure 7**). Conversely, moderately coupled microcircuits are more flexible than their densely coupled counterparts. However, because these networks have fewer intercluster connections, they are less resilient and may suffer greater effects of isolation after damage (**Figure 7**).

There are several assumptions we made throughout these studies. First, we used generic excitatory and inhibitory neurons based on the Izhikevich integrate-and-fire neuron model (Izhikevich, 2003). These model neurons are simplistic but versatile, well-verified, and adequate for our purposes. Several past studies employed these models to study polychronous neural computation (Izhikevich, 2006), autaptic neuronal connections (Wiles et al., 2017), and dopaminergic modulation of brain oscillations (Kobayashi et al., 2017). Second, we implemented only AMPA and GABA receptor currents as well as one type



Many intercluster connections	>	Fewer intercluster connections
Lower proportion of strong intercluster connections	<	Higher proportion of strong intercluster connections
Intercluster populations have lower betweenness centrality	<	Intercluster populations have higher betweenness centrality
Controllability rankings do not differ based on correlation	≈	Controllability rankings do not differ based on correlation
Correlation is robust and remains high after injury	>	Correlation is not stable after injury, changing based on the injured subpopulation
Power ratio decreases after injury to Inter Pre neurons	<	Power ratio is more stable after injury than correlation is
More resilient & More reliable		**Less resilient & More flexible**

FIGURE 7 | Summary comparison between high and moderate correlation networks. In the schematics showing network topology, black circles represent excitatory neurons and light gray circles represent inhibitory neurons. Not shown are the connections between them. Arrows between clusters stand for intercluster connections between excitatory neurons. Thicker arrows indicate stronger connections.

of plasticity (STDP). Although adding additional receptors or dynamics could affect the precise timing of neuron activation, these changes would not likely impact our broad findings, which indicate synchronization is a robust phenomenon in a unidirectional architecture. These simplifications were also made deliberately to produce a realistic, yet efficient and tractable, neuronal network model. A third simplification we made was connecting the two clusters by unidirectional connections only. It is often assumed that brain regions are reciprocally connected in diffusion tractography or functional MRI (Buckner et al., 2009; Bullmore and Sporns, 2009; Damoiseaux and Greicius, 2009; Nakamura et al., 2009; Cabral et al., 2011; Rubinov and Sporns, 2011; Horn et al., 2014; Fagerholm et al., 2015). Our goal was to build a more principled view of how groups of neurons interact to produce a composite network signal. To do so required beginning with a simplified architecture. Moreover, this unidirectional architecture does appear in larger, network-based descriptions of the brain. For example, the hippocampus is predominantly unidirectionally connected (Hummos et al., 2014; Wheeler et al., 2015), and other structures like the hypothalamus have a combination of bidirectional and unidirectional pathways, including afferent inputs as part of the sensory circuitry and outputs to the brainstem (Lechan and Toni, 2000; Card and Swanson, 2013). Given these limitations, however, we plan to pursue more complex and anatomically accurate network topologies in future work. In particular, it would be interesting to combine more diverse and specific neuron types with known connectivity features of anatomical regions like the hippocampus.

In healthy brain networks, it is known that synchronization or coherence between distant brain regions is important for

functions like attention, learning, and memory (Dü Zel et al., 2010; Clayton et al., 2015; Fries, 2015; Hanslmayr et al., 2016). Typically, coherence is discussed at the scale of whole brain imaging, such as fMRI BOLD, which has a temporal resolution on the order of seconds (Logothetis and Wandell, 2004). With this resolution, there are nuances of activity patterns which may not be observed, and synchronization remains important at intermediate spatial and temporal scales. Nonetheless, due to experimental constraints, early studies about local networks and neuron response focused on firing rate (Barlow, 1972; Newsome et al., 1989). Currently, with improved technology for measuring activity in multiple neurons or regions simultaneously (multielectrode arrays, *in vivo* calcium imaging), there is a growing emphasis on understanding the correlation of activity among neurons (Cohen and Kohn, 2011). There is an interest in what correlation might encode in comparison to firing rate alone and what it might mean at various timescales (Cohen and Kohn, 2011). It is valuable to consider how complex patterns may combine to generate the activity observed at larger spatial scales and longer time scales. This work aims to examine this phenomenon at an intermediate scale where subtle topology changes may impact synchronization.

Our general finding that clusters of neurons synchronize with a low proportion of intercluster connections finds support in the literature. For example, thalamic inputs are important drivers of activity in the primary visual cortex yet account for only 5% of synapses on cortical simple cells (Wang et al., 2010). The authors further suggest that spike synchrony may be a critical mechanism for ensuring reliable, efficient transmission when inputs comprise a small percentage of overall synaptic input. Within the context of TBI, it is well-known that diffuse axonal injury and white matter damage more broadly are associated with cognitive impairment (Sharp et al., 2011; Johnson et al., 2013; Fagerholm et al., 2015; Blennow et al., 2016). Our current work suggests that if two brain areas are connected with a high density of projections, a significant amount of axonal injury (disconnection) will be needed to disrupt synchronization between these areas. Conversely, our work also suggests a relatively rapid decline in synchronization if two brain areas are only weakly connected and the linking connections are damaged. By extension, our work predicts that TBI neurodegeneration is most problematic when it impacts long-range projections between brain regions, especially when these regions are not strongly connected. In addition to synchronization itself, our supporting result that intercluster connections become strong, stable connections corroborates evidence in the literature. It has been observed in dissociated cultures of hippocampal neurons that "loose synchrony" exists at weak connectivity (Penn et al., 2016). As connectivity strength increased, the mean phase shift between oscillations decreased as the network converged to a common oscillation frequency characterized by synchronous periodic bursts (Penn et al., 2016). More broadly interpreted, these changes in synaptic strength reinforce connections among brain areas and could protect against synchronization deficits that occur in disease or injury.

Our results studying the influence of neuron controllability on intercluster dynamics revealed a surprisingly consistent result – deleting nodes of either high average or high modal controllability achieved the same change in network dynamics. Controllability is frequently applied to undirected, symmetric networks at the full-brain scale (Gu et al., 2015, 2017; Betzel et al., 2016; Muldoon et al., 2016). In general, these past studies show that nodes with high average controllability drive the network to easy-to-reach energy states, whereas nodes with high modal controllability push the network into hard-to-reach states. In the brain, these types of controllability often pertain to different tasks and networks. For instance, high modal control is associated with cognitive control regions, and high average control is associated with the default mode network (Gu et al., 2015; Tang et al., 2017). Our results, though, predominantly showed no differential effect of deleting neurons with either high average or modal controllability. One possibility is that easy- and hard-to-reach states are near one another on the energy landscape, so this deletion process would produce indistinguishable results. However, our manipulation also fundamentally differs from previous control studies in macroscale brain networks because deleting neurons effectively subtracts energy from the system as evidenced by deficits in both firing rate (Gabrieli et al., 2019) and frequency power after injury. These changes indicate a global loss of energy after neurodegeneration. More often, controllability is used in the context of stimulation or adding energy to drive the network to a different energetic state (Betzel et al., 2016; Muldoon et al., 2016; Gu et al., 2017; Kim et al., 2018). Prior to neurodegeneration, our networks already exist in a stable energy basin, and subtracting energy by removing nodes does little to drive the network toward a different state. As such, it suggests that *a priori* controllability rankings may be limited in their ability to predict dynamic network changes from degenerating neurons.

Whereas controllability regulates network dynamics and state transitions, synchronization appears to operate ideally within a "sweet spot" regime. With excessive synchronization comes dysfunction, including seizures. Excessive synchronization also limits cognitive flexibility, an important component of switching between different task networks. Using blood flow to detect coordinated neural activity, fMRI determines which regions of the brain are functionally connected. Neurological diseases are known to impact functional connectivity, variably increasing or decreasing it. In general, hyperconnectivity is associated with cognitive dysfunction, including decreased cognitive flexibility (Mayer et al., 2011; Tang et al., 2011; Pang, 2015; Venkatesan et al., 2015), an attribute that enables the brain to attain and utilize diverse brain states (Tang et al., 2017). In contrast, hypoconnectivity is related to cognitive decline due to loss of neural resources, such as occurs in Alzheimer's disease (Sheline and Raichle, 2013; Hillary et al., 2015). A reasonable expectation is that traumatic injury – either from degenerating neurons or from disrupted connections between them – will only decrease functional connectivity in the brain. However, functional connectivity can both increase and decrease after TBI (Bullmore and Sporns, 2009; Mayer et al., 2011; Pandit et al., 2013; Sharp et al., 2014; Venkatesan et al., 2015). Our work studying the degeneration of specific neurons within each population raises an intriguing new mechanism at the

cellular scale that may help explain how TBI can promote either functional hyper- or hypoconnectivity. In our moderate networks subjected to neurodegeneration, we observed both increases and decreases in correlation depending on which neuron subtype was targeted. If injury affects predominantly neurons that send connections to other regions, we can expect coherence with those regions to decline and subsequent hypoconnectivity. We would expect a similar decrease in functional connectivity if the projections between two different brain areas declined, a potential effect of diffuse injury to the white matter tracts connecting these areas. However, if neurons with primarily local connections are damaged, the diversity of information in that region goes down and correlation increases, leading to hyperconnectivity and reduced cognitive flexibility. To our knowledge, we are not aware of previous work showing this bifurcating response within a single network, making this the first study to demonstrate both higher and lower synchronization as a result of differentially targeted injury.

Correlation, as we have defined it, is a robust metric with tight standard deviations and high consistency among simulations. Despite this, synchronization alone does not provide a full picture of network activity. The traditional metric of neuron firing rate also fails to add much to this picture because it does not account for the variability in action potential timing. Both our networks and more complex networks *in vitro* and *in vivo* develop oscillatory patterns with periods of high and low activity. These rhythms may themselves encode information or instead facilitate the flow of information (Sejnowski and Paulsen, 2006). *In vivo* oscillations contribute to many important cognitive functions, including the representation, consolidation, and retrieval processes of memory (Dü Zel et al., 2010; Hanslmayr et al., 2016). Oscillations are also believed to coordinate activity in different brain regions, dynamically shaping brain networks that have static structural connections (Dü Zel et al., 2010; Deco and Kringelbach, 2016). The coupling is hypothesized to occur via different frequencies. Theta-gamma coupling in the hippocampus is one well-studied example (Dü Zel et al., 2010; Lisman and Jensen, 2013; Colgin, 2015), in which gamma frequencies are coupled to phases of the theta signal to enable CA1 to coordinate with the entorhinal cortex via high frequency gamma and with CA3 via low frequency gamma (Dü Zel et al., 2010; Colgin, 2015). Similarly, coherent activity appears between the hippocampus and prefrontal cortex during certain behaviors in rodents (Jones and Wilson, 2005; Tamura et al., 2017). Thus, transmitting spike rate information across different frequency bands allows a single region to communicate with multiple regions or even participate in different networks simultaneously. As an approximation of the signal properties encoded in the network, we defined a power ratio of the total network activity. In a more complex topology, different features of the frequency spectra may synchronize more strongly than others between two regions. Our results indicate that weakly connected regions are more vulnerable to changes in synchronization post-injury while highly connected regions are more vulnerable to changes in frequency, though they may remain synchronized. As the brain is comprised of regions coupled by varied connectivity strength, our results imply that an injured brain may show altered synchrony or oscillation frequency between some brain regions and not others, with the difference due to the connection strength. Moreover, both phenomena may occur simultaneously for a given region, contributing to the response heterogeneity observed after TBI. We also note that the high frequency components were susceptible to neurodegeneration, showing the largest change when upstream projecting neurons were targeted in high correlation networks. This finding corroborates other reports of decreased broadband power in the CA1 region of the hippocampus (Paterno et al., 2016; Gagnon et al., 2019).

The changes in oscillatory rhythms in our model after damage lead us to consider ways to restore the original rhythms. One possibility is stimulation of neurons within each network, which would also enable us to further explore our insights about controllability in the framework of injury. At a larger scale, deep brain stimulation (DBS) has been implemented to treat neurological conditions including Parkinson's disease (de Hemptinne et al., 2015) and chronic pain (Owen et al., 2006) by modulating inappropriate brain activity (Kringelbach et al., 2007). While it has been used for years, the fundamental mechanisms of DBS are not well understood. In the context of TBI, DBS has been previously proposed to restore cognitive rhythms (Pevzner et al., 2016). At the scale of our network model, we can examine the principles of restorative stimulation protocols as a means of reestablishing disrupted rhythms. With the flexibility of our model, we can compare various stimulation strategies, including testing different frequencies and targeting highly controllable neurons, to study both effectiveness and structural network changes. Past work indicates the controllability type and rank for a network node will affect transition states for the network when energy is injected into this node (Betzel et al., 2016; Muldoon et al., 2016; Kim et al., 2018). As such, we expect that nodal stimulation will function differently than nodal deletion and will allow one to systematically reconstruct activity oscillations and re-establish information encoding properties across nodes in the network.

In closing, we find that a relatively simple injury, namely neurodegeneration, can cause complex outcomes that depend on the baseline coupling of microcircuits and on the function of damaged neurons (**Figure 7**). The communication abilities (synchronization) and information coding capacity (frequency content) of these networks may be impaired after traumatic injury. Densely connected microcircuits possess an inherent resilience to synchronization-related changes after damage while moderately coupled networks are more malleable. Our work underscores that upstream neurons sending downstream projections are highly valuable for maintaining both synchronization and frequency properties of the aggregate signal in a multi-regional network. More broadly, this work raises a new dimension of heterogeneity of TBI where the pattern of cellular damage may contribute to the specific outcome and impairment. In future work, this complexity could be explored with a multiscale approach which integrates local, time-varying signal information as inputs to oscillator-based models of macroscale brain connectivity (Váša et al., 2015; Lee et al., 2017).

Thus, this work facilitates integrative multiscale efforts for translating fundamental mechanisms of TBI to macroscale consequences by establishing principles which may be applied and tested in a larger scale model of the brain.

DATA AVAILABILITY STATEMENT

The datasets generated for this study are available on request to the corresponding author.

AUTHOR CONTRIBUTIONS

SS and DM conceived and designed the studies and analysis, and wrote the manuscript. SS performed the simulations and conducted the analysis. SS and DG contributed to the model and analysis tools. DG contributed to the manuscript discussion and revision.

FUNDING

This work was funded by grants from the Paul G. Allen Foundation and the National Institutes of Health (NIH) (RO1 NS088176).

ACKNOWLEDGMENTS

We would like to thank Lia Papadopoulos for careful reading of the manuscript and Danielle S. Bassett for aiding our understanding of network controllability.

SUPPLEMENTARY MATERIAL

The Supplementary Material for this article can be found online at: https://www.frontiersin.org/articles/10.3389/fncom.2020.00018/full#supplementary-material

REFERENCES

Barlow, H. B. (1972). Single units and sensation: a neuron doctrine for perceptual psychology? *Perception* 1, 371–394. doi: 10.1068/p010371

Bastos, A. M., Vezoli, J., and Fries, P. (2015). Communication through coherence with inter-areal delays. *Curr. Opin. Neurobiol.* 31, 173–180. doi: 10.1016/j.conb.2014.11.001

Betzel, R. F., Gu, S., Medaglia, J. D., Pasqualetti, F., and Bassett, D. S. (2016). Optimally controlling the human connectome: the role of network topology. *Sci. Rep.* 6:30770. doi: 10.1038/srep30770

Blennow, K., Brody, D. L., Kochanek, P. M., Levin, H., McKee, A., Ribbers, G. M., et al. (2016). Traumatic brain injuries. *Nat. Rev. Dis. Prim.* 2, doi: 10.1038/nrdp.2016.84

Bocchio, M., Nabavi, S., and Capogna, M. (2017). Synaptic plasticity, engrams, and network oscillations in amygdala circuits for storage and retrieval of emotional memories. *Neuron* 94, 731–743. doi: 10.1016/j.neuron.2017.03.022

Bonnelle, V., Leech, R., Kinnunen, K. M., Ham, T. E., Beckmann, C. F., De Boissezon, X., et al. (2011). Default mode network connectivity predicts sustained attention deficits after taumatic brain injury. *J. Neurosci.* 31, 13442–13451. doi: 10.1523/JNEUROSCI.1163-11.2011

Buckner, R. L., Sepulcre, J., Talukdar, T., Krienen, F. M., Liu, H., Hedden, T., et al. (2009). Cortical hubs revealed by intrinsic functional connectivity: mapping, assessment of stability, and relation to Alzheimer's disease. *J. Neurosci.* 29, 1860–1873. doi: 10.1523/JNEUROSCI.5062-08.2009

Bullmore, E., and Sporns, O. (2009). Complex brain networks: graph theoretical analysis of structural and functional systems. *Nat. Rev. Neurosci.* 10, 186–198. doi: 10.1038/nrn2575

Cabral, J., Hugues, E., Sporns, O., and Deco, G. (2011). Role of local network oscillations in resting-state functional connectivity. *Neuroimage* 57, 130–139. doi: 10.1016/j.neuroimage.2011.04.010

Card, J. P., and Swanson, L. W. (2013). "The hypothalamus: an overview of regulatory systems," in *Fundamental Neuroscience*, eds L. R. Squire, D. Berg, F. E. Bloom, S. du Lac, A. Ghosh, and N. C. Spitzer, (Waltham, MA: Elsevier), 717–727. doi: 10.1016/B978-0-12-385870-2.00033-0

Clayton, M. S., Yeung, N., and Kadosh, R. C. (2015). The roles of cortical oscillations in sustained attention. *Trends Cogn. Sci.* 19, 188–195. doi: 10.1016/j.tics.2015.02.004

Cohen, M. R., and Kohn, A. (2011). Measuring and interpreting neuronal correlations. *Nat. Neurosci.* 14, 811–819. doi: 10.1038/nn.2842

Colgin, L. L. (2015). Theta-gamma coupling in the entorhinal-hippocampal system. *Curr. Opin. Neurobiol.* 31, 45–50. doi: 10.1016/j.conb.2014.08.001

Coronado, V. G., Mcguire, L. C., Sarmiento, K., Bell, J., Lionbarger, M. R., Jones, C. D., et al. (2012). Trends in traumatic brain injury in the U.S. and the public health response: 1995–2009. *J. Safety Res.* 43, 1995–2009. doi: 10.1016/j.jsr.2012.08.011

Damoiseaux, J. S., and Greicius, M. D. (2009). Greater than the sum of its parts: a review of studies combining structural connectivity and resting-state functional connectivity. *Brain Struct. Funct.* 213, 525–533. doi: 10.1007/s00429-009-0208-6

Damoiseaux, J. S., Rombouts, S. A. R. B., Barkhof, F., Scheltens, P., Stam, C. J., Smith, S. M., et al. (2006). Consistent resting-state networks across healthy subjects. *Proc. Natl. Acad. Sci. U.S.A.* 103, 13848–13853. doi: 10.1073/pnas.0601417103

de Hemptinne, C., Swann, N. C., Ostrem, J. L., Ryapolova-Webb, E. S., San Luciano, M., Galifianakis, N. B., et al. (2015). Therapeutic deep brain stimulation reduces cortical phase-amplitude coupling in Parkinson's disease. *Nat. Neurosci.* 18, 779–786. doi: 10.1038/nn.3997

Deco, G., and Kringelbach, M. L. (2016). Metastability and coherence: extending the communication through coherence hypothesis using a whole-brain computational perspective. *Trends Neurosci.* 39, 125–135. doi: 10.1016/j.tins.2016.01.001

Dü Zel, E., Penny, W. D., and Burgess, N. (2010). Brain oscillations and memory. *Curr. Opin. Neurobiol.* 20, 143–149. doi: 10.1016/j.conb.2010.01.004

Effenberger, F., Jost, J., and Levina, A. (2015). Self-organization in balanced state networks by STDP and homeostatic plasticity. *PLoS Comput. Biol.* 11:e1004420. doi: 10.1371/journal.pcbi.1004420

Eytan, D., and Marom, S. (2006). Dynamics and effective topology underlying synchronization in networks of cortical neurons. *J. Neurosci.* 26, 8465–8476. doi: 10.1523/JNEUROSCI.1627-06.2006

Fagerholm, E. D., Hellyer, P. J., Scott, G., Leech, R., and Sharp, D. J. (2015). Disconnection of network hubs and cognitive impairment after traumatic brain injury. *Brain* 138, 1696–1709. doi: 10.1093/brain/awv075

Ferster, D., and Jagadeesh, B. (1992). EPSP-IPSP interactions in cat visual cortex studied with in vivo whole-cell patch recording. *J. Neurosci.* 12, 1262–1274. doi: 10.1523/jneurosci.12-04-01262.1992

Fransson, P. (2006). How default is the default mode of brain function? Further evidence from intrinsic BOLD signal fluctuations. *Neuropsychologia* 44, 2836–2845. doi: 10.1016/j.neuropsychologia.2006.06.017

Fries, P. (2015). Rhythms for cognition: communication through coherence. *Neuron* 88, 220–235. doi: 10.1016/j.neuron.2015.09.034

Gabrieli, D., Schumm, S. N., Parvesse, B., and Meaney, D. F. (2019). Neurodegeneration exposes firing rate dependent effects on oscillation dynamics in computational neural networks. *bioRxiv* doi: 10.1101/663187

Gagnon, K., Cottone, C., Adam, C., and Wolf, J. (2019). Disruptions in hippocampal circuitry involved in learning and memory following TBI. *J. Neurotrauma* 36:A-3. doi: 10.1089/neu.2019.29100.abstracts

Gollo, L. L., Mirasso, C., Sporns, O., and Breakspear, M. (2014). Mechanisms of zero-lag synchronization in cortical motifs. *PLoS Comput. Biol.* 10:e1003548. doi: 10.1371/journal.pcbi.1003548

Greicius, M. D., Supekar, K., Menon, V., and Dougherty, R. F. (2009). Resting-state functional connectivity reflects structural connectivity in the default mode network. *Cereb. cortex* 19, 72–78. doi: 10.1093/cercor/bhn059

Gu, S., Betzel, R. F., Mattar, M. G., Cieslak, M., Delio, P. R., Grafton, S. T., et al. (2017). Optimal trajectories of brain state transitions. *Neuroimage* 148, 305–317. doi: 10.1016/j.neuroimage.2017.01.003

Gu, S., Pasqualetti, F., Cieslak, M., Telesford, Q. K., Yu, A. B., Kahn, A. E., et al. (2015). Controllability of structural brain networks. *Nat. Commun.* 6:8414. doi: 10.1038/ncomms9414

Hanslmayr, S., Staresina, B. P., and Bowman, H. (2016). Oscillations and episodic memory: addressing the synchronization/desynchronization conundrum. *Trends Neurosci.* 39, 16–25. doi: 10.1016/j.tins.2015.11.004

Hillary, F. G., Roman, C. A., Venkatesan, U., Rajtmajer, S. M., Bajo, R., and Castellanos, N. D. (2015). Hyperconnectivity is a fundamental response to neurological disruption. *Neuropsychology* 29, 59–75. doi: 10.1037/neu0000110

Hiploylee, C., Dufort, P. A., Davis, H. S., Wennberg, R. A., Tartaglia, M. C., Mikulis, D., et al. (2017). Longitudinal study of postconcussion syndrome: not everyone recovers. *J. Neurotrauma* 34, 1511–1523. doi: 10.1089/neu.2016.4677

Horn, A., Ostwald, D., Reisert, M., and Blankenburg, F. (2014). The structural–functional connectome and the default mode network of the human brain. *Neuroimage* 102, 142–151. doi: 10.1016/j.neuroimage.2013.09.069

Hummos, A., Franklin, C. C., and Nair, S. S. (2014). Intrinsic mechanisms stabilize encoding and retrieval circuits differentially in a hippocampal network model. *Hippocampus* 24, 1430–1448. doi: 10.1002/hipo.22324

Izhikevich, E. M. (2003). Simple model of spiking neurons. *IEEE Trans. Neural Netw.* 14, 1569–1572. doi: 10.1109/TNN.2003.820440

Izhikevich, E. M. (2006). Polychronization: computation with spikes. *Neural Comput.* 18, 245–282. doi: 10.1162/089976606775093882

Izhikevich, E. M., and Edelman, G. M. (2008). Large-scale model of mammalian thalamocortical systems. *Proc. Natl. Acad. Sci. U.S.A.* 105, 3593–3598. doi: 10.1073/pnas.0712231105

Izhikevich, E. M., Gally, J. A., and Edelman, G. M. (2004). Spike-timing dynamics of neuronal groups. *Cereb. Cortex* 14, 933–944. doi: 10.1093/cercor/bhh053

Jilka, S. R., Scott, G., Ham, T., Pickering, A., Bonnelle, V., Braga, R. M., et al. (2014). Damage to the salience network and interactions with the default mode network. *J. Neurosci.* 34, 10798–10807. doi: 10.1523/JNEUROSCI.0518-14.2014

Johnson, V. E., Stewart, W., and Smith, D. H. (2013). Axonal pathology in traumatic brain injury. *Exp. Neurol.* 246, 35–43. doi: 10.1016/j.expneurol.2012.01.013

Jones, M. W., and Wilson, M. A. (2005). Theta rhythms coordinate hippocampal-prefrontal interactions in a spatial memory task. *PLoS Biol.* 3:e402. doi: 10.1371/journal.pbio.0030402

Kasahara, M., Menon, D. K., Salmond, C. H., Outtrim, J. G., Taylor Tavares, J. V., Carpenter, T. A., et al. (2010). Altered functional connectivity in the motor network after traumatic brain injury Background: a large proportion of survivors of traumatic brain injury (TBI) have persistent cognitive. *Neurology* 75, 168–176. doi: 10.1212/WNL.0b013e3181e7ca58

Kim, J. Z., Sooer, J. M., Kahn, A. E., Vettel, J. M., Pasqualetti, F., and Bassett, D. S. (2018). Role of graph architecture in controlling dynamical networks with applications to neural systems. *Nat. Phys.* 14, 91–98. doi: 10.1038/NPHYS4268

Kobayashi, T., Shimada, Y., Fujiwara, K., and Ikeguchi, T. (2017). Reproducing infra-slow oscillations with dopaminergic modulation. *Sci. Rep.* 7:2411. doi: 10.1038/s41598-017-02366-z

Kringelbach, M. L., Jenkinson, N., Owen, S. L. F., and Aziz, T. Z. (2007). Translational principles of deep brain stimulation. *Nat. Rev. Neurosci.* 8, 623–635. doi: 10.1038/nrn2196

Langlois, J. A., Rutland-Brown, W., and Wald, M. M. (2006). The epidemiology and impact of traumatic brain injury. *J. Head Trauma Rehabil.* 21, 375–378. doi: 10.1097/00001199-200609000-200609001

Lechan, R. M., and Toni, R. (2000). *Functional anatomy of the hypothalamus and pituitary*, eds K. Feingold, B. Anawalt, and A. Boyce South, (Darthmouth, MA: MDText.com, Inc).

Lee, W. H., Bullmore, E., and Frangou, S. (2017). Quantitative evaluation of simulated functional brain networks in graph theoretical analysis. *Neuroimage* 146, 724–733. doi: 10.1016/j.neuroimage.2016.08.050

Lisman, J. E., and Jensen, O. (2013). The theta-gamma neural code. *Neuron* 77, 1002–1016. doi: 10.1016/j.neuron.2013.03.007

Logothetis, N. K., and Wandell, B. A. (2004). Interpreting the BOLD signal. *Annu. Rev. Physiol.* 66, 735–769. doi: 10.1146/annurev.physiol.66.082602.092845

Masel, B. E., and DeWitt, D. S. (2010). Traumatic brain injury: a disease process, not an event. *J. Neurotrauma* 27, 1529–1540. doi: 10.1089/neu.2010.1358

Mayer, A. R., Mannell, M. V., Ling, J., Gasparovic, C., and Yeo, R. A. (2011). Functional connectivity in mild traumatic brain injury. *Hum. Brain Mapp.* 32, 1825–1835. doi: 10.1002/hbm.21151

Muldoon, S. F., Pasqualetti, F., Gu, S., Cieslak, M., Grafton, S. T., Vettel, J. M., et al. (2016). Stimulation-based control of dynamic brain networks. *PLoS Comput. Biol.* 12:e1005076. doi: 10.1371/journal.pcbi.1005076

Nakamura, T., Hillary, F. G., and Biswal, B. B. (2009). Resting network plasticity following brain injury. *PLoS One* 4:e8220. doi: 10.1371/journal.pone.0008220

Narayanan, N. S., and Laubach, M. (2009). Methods for studying functional interactions among neuronal populations. *Methods Mol. Biol.* 489, 135–165. doi: 10.1007/978-1-59745-543-5_7

Newsome, W. T., Britten, K. H., and Movshon, J. A. (1989). Neuronal correlates of a perceptual decision. *Nature* 341, 52–54. doi: 10.1038/341052a0

Owen, S. L. F., Green, A. L., Stein, J. F., and Aziz, T. Z. (2006). Deep brain stimulation for the alleviation of post-stroke neuropathic pain. *Pain* 120, 202–206. doi: 10.1016/j.pain.2005.09.035

Pandit, A. S., Expert, P., Lambiotte, R., Bonnelle, V., Leech, R., Turkheimer, F. E., et al. (2013). Traumatic brain injury impairs small-world topology. *Neurology* 80, 1826–1833. doi: 10.1212/WNL.0b013e3182929f38

Pang, E. W. (2015). Different neural mechanisms underlie deficits in mental flexibility in post-traumatic stress disorder compared to mild traumatic brain injury. *Front. Psychiatry* 6:170. doi: 10.3389/fpsyt.2015.00170

Paterno, R., Metheny, H., Xiong, G., Elkind, J., and Cohen, A. S. (2016). Mild traumatic brain injury decreases broadband power in area CA1. *J. Neurotrauma* 33, 1645–1649. doi: 10.1089/neu.2015.4107

Penn, Y., Segal, M., and Moses, E. (2016). Network synchronization in hippocampal neurons. *Proc. Natl. Acad. Sci. U.S.A.* 113, 3341–3346. doi: 10.1073/pnas.1515105113

Pevzner, A., Izadi, A., Lee, D. J., Shahlaie, K., and Gurkoff, G. G. (2016). Making waves in the brain: what are oscillations, and why modulating them makes sense for brain injury. *Front. Syst. Neurosci.* 10:30. doi: 10.3389/fnsys.2016.00030

Rubinov, M., and Sporns, O. (2011). Weight-conserving characterization of complex functional brain networks. *Neuroimage* 56, 2068–2079. doi: 10.1016/j.neuroimage.2011.03.069

Sejnowski, T. J., and Paulsen, O. (2006). Network oscillations: emerging computational principles. *J. Neurosci.* 26, 1673–1676. doi: 10.1523/JNEUROSCI.3737-05d.2006

Sharp, D. J., Beckmann, C. F., Greenwood, R., Kinnunen, K. M., Bonnelle, V., De Boissezon, X., et al. (2011). Default mode network functional and structural connectivity after traumatic brain injury. *Brain* 134, 2233–2247. doi: 10.1093/brain/awr175

Sharp, D. J., Scott, G., and Leech, R. (2014). Network dysfunction after traumatic brain injury. *Nat. Rev. Neurol.* 10, 156–166. doi: 10.1038/nrneurol.2014.15

Sheline, Y. I., and Raichle, M. E. (2013). Resting state functional connectivity in preclinical Alzheimer's disease. *Biol. Psychiatry* 74, 340–347. doi: 10.1016/j.biopsych.2012.11.028

Song, S., Miller, K. D., and Abbott, L. F. (2000). Competitive Hebbian learning through spike-timing-dependent synaptic plasticity. *Nat. Neurosci.* 3, 919–926. doi: 10.1038/78829

Soriano, J., Rodriguez Martinez, M., Tlusty, T., and Moses, E. (2008). Development of input connections in neural cultures. *Proc. Natl. Acad. Sci. U.S.A.* 105, 13758–13763. doi: 10.1073/pnas.0707492105

Sours, C., George, E. O., Zhuo, J., Roys, S., and Gullapalli, R. P. (2015). Hyper-connectivity of the thalamus in during early stages following mild traumatic brain injury. *Brain Imaging Behav.* 9, 550–563. doi: 10.1007/s11682-015-9424-2

Stevens, M. C., Lovejoy, D., Kim, J., Oakes, H., Kureshi, I., and Witt, S. T. (2012). Multiple resting state network functional connectivity abnormalities in mild traumatic brain injury. *Brain Imaging Behav.* 6, 293–318. doi: 10.1007/s11682-012-9157-4

Swadlow, H. A. (1985). Physiological properties of individual cerebral axons studied in vivo for as long as one year. *J. Neurophysiol.* 54, 1346–1362. doi: 10.1152/jn.1985.54.5.1346

Tamura, M., Spellman, T. J., Rosen, A. M., Gogos, J. A., and Gordon, J. A. (2017). Hippocampal-prefrontal theta-gamma coupling during performance of a spatial working memory task. *Nat. Commun.* 8:2182. doi: 10.1038/s41467-017-02108-9

Tang, E., Giusti, C., Baum, G. L., Gu, S., Pollock, E., Kahn, A. E., et al. (2017). Developmental increases in white matter network controllability support a growing diversity of brain dynamics. *Nat. Commun.* 8:1252. doi: 10.1038/s41467-017-01254-4

Tang, L., Ge, Y., Sodickson, D. K., Miles, L., Zhou, Y., Reaume, J., et al. (2011). Thalamic resting-state functional networks: disruption in patients with mild traumatic brain injury. *Radiology* 260, 831–840. doi: 10.1148/radiol.11110014

Varela, F., Lachaux, J. P., Rodriguez, E., and Martinerie, J. (2001). The brainweb: phase synchronization and large-scale integration. *Nat. Rev. Neurosci.* 2, 229–239. doi: 10.1038/35067550

Váša, F., Shanahan, M., Hellyer, P. J., Scott, G., Cabral, J., and Leech, R. (2015). Effects of lesions on synchrony and metastability in cortical networks. *Neuroimage* 118, 456–467. doi: 10.1016/J.NEUROIMAGE.2015.05.042

Venkatesan, U. M., Dennis, N. A., and Hillary, F. G. (2015). Chronology and chronicity of altered resting-state functional connectivity after traumatic brain injury. *J. Neurotrauma* 32, 252–264. doi: 10.1089/neu.2013.3318

Vicente, R., Gollo, L. L., Mirasso, C. R., Fischer, I., and Pipa, G. (2008). Dynamical relaying can yield zero time lag neuronal synchrony despite long conduction delays. *Proc. Natl. Acad. Sci. U.S.A.* 105, 17157–17162. doi: 10.1073/pnas.0809353105

Wang, C., Costanzo, M. E., Rapp, P. E., Darmon, D., Nathan, D. E., Bashirelahi, K., et al. (2017). Disrupted gamma synchrony after mild traumatic brain injury and its correlation with white matter abnormality. *Front. Neurol.* 8:571. doi: 10.3389/fneur.2017.00571

Wang, H.-P., Spencer, D., Fellous, J.-M., and Sejnowski, T. J. (2010). Synchrony of thalamocortical inputs maximizes cortical reliability. *Science* 328, 106–109. doi: 10.1126/science.1183108

Wheeler, D. W., White, C. M., Rees, C. L., Komendantov, A. O., Hamilton, D. J., and Ascoli, G. A. (2015). Hippocampome.org: a knowledge base of neuron types in the rodent hippocampus. *Elife* 4:e09960. doi: 10.7554/eLife.09960

Wiles, L., Gu, S., Pasqualetti, F., Parvesse, B., Gabrieli, D., Bassett, D. S., et al. (2017). Autaptic connections shift network excitability and bursting. *Sci. Rep.* 7:44006. doi: 10.1038/srep44006

Wilson, L., Stewart, W., Dams-O'Connor, K., Diaz-Arrastia, R., Horton, L., Menon, D. K., et al. (2017). The chronic and evolving neurological consequences of traumatic brain injury. *Lancet Neurol.* 16, 813–838. doi: 10.1016/S1474-4422(17)30279-X

Yan, H., Feng, Y., and Wang, Q. (2016). Altered effective connectivity of hippocampus-dependent episodic memory network in mTBI survivors. *Neural Plast.* 2016:6353845. doi: 10.1155/2016/6353845

Conflict of Interest: The authors declare that the research was conducted in the absence of any commercial or financial relationships that could be construed as a potential conflict of interest.

Copyright © 2020 Schumm, Gabrieli and Meaney. This is an open-access article distributed under the terms of the Creative Commons Attribution License (CC BY). The use, distribution or reproduction in other forums is permitted, provided the original author(s) and the copyright owner(s) are credited and that the original publication in this journal is cited, in accordance with accepted academic practice. No use, distribution or reproduction is permitted which does not comply with these terms.

frontiers in Physics

ORIGINAL RESEARCH
published: 31 March 2020
doi: 10.3389/fphy.2020.00082

Normal Aging: Alterations in Scalp EEG Using Broadband and Band-Resolved Topographic Maps

Ehtasham Javed, Pierpaolo Croce, Filippo Zappasodi and Cosimo Del Gratta*

Department of Neuroscience, Imaging and Clinical Sciences, Institute for Advanced Biomedical Technologies, Gabriele d'Annunzio University, Chieti, Italy

Given the majority of age-related diseases have been described as disconnection syndromes, understanding the functional connections of normal aging is of considerable importance. Here, an EEG-based scalp level analysis has been performed to identify the alterations in the synchronized brain regions in aged, compared to young persons. Two groups, aged and young subjects were studied, each consisting of 18 participants. First, conventionally extracted broadband topographic maps, also called microstate maps, were examined. The results showed an overall dominant alteration: a uniform decrease in synchronization of brain regions related to cognitive processing resources that was observed only when the maps C and D were characterized in temporal parameters. However, no remarkable change in the spatial distribution was found between the groups. This failure in identifying differences in the spatial distribution was hypothesized to be due to the presence of superimposed signals of several frequencies in the broadband signal that is used for the extraction of microstate maps. Second, spectrally resolved band-wise topographic maps, which we have shown, in a previous study, are able to detect spectral details associated with broadband microstates maps, were used to address this failure. The use of the instantaneous frequency concept is essential in the extraction of band-wise topographic maps, and represents a novelty compared to current studies. The method consists of three steps: (a) from EEG signal, the Empirical Mode Decomposition method is used to extract underlying oscillatory components; (b) these intrinsic oscillatory components are then amplitude demodulated and subjected to numerical equations for the calculation of instantaneous features, such as amplitude, and frequency; finally, (c) based on these instantaneous features, band-wise topographic maps are extracted. Here, as a first application to aging data, these band-wise topographic maps have shown the capability of capturing the age-related changes in both spatial distributions, and in temporal characterization. Spatially, the potential distribution in the aged and the young subject groups, respectively, showed differences, while, in temporal characterization, both increases and decreases were observed, suggesting the lengths of synchronized activities vary differentially, and in accordance with results from fMRI studies. These observed differences also support the dedifferentiation and compensation mechanisms.

Keywords: aging, microstate analysis, band-wise topographic analysis, empirical mode decomposition, instantaneous frequency

OPEN ACCESS

Edited by:
Nicola Toschi,
University of Rome Tor Vergata, Italy

Reviewed by:
Krasimira Tsaneva-Atanasova,
University of Exeter, United Kingdom
Luis Diambra,
National University of La Plata, Argentina
Maria Grazia Puxeddu,
Sapienza University of Rome, Italy

****Correspondence:***
Ehtasham Javed
rajaehti1@gmail.com;
ehtasham.javed@unich.it

Specialty section:
This article was submitted to Biophysics, a section of the journal Frontiers in Physics

Received: *16 December 2019*
Accepted: *09 March 2020*
Published: *31 March 2020*

Citation:
Javed E, Croce P, Zappasodi F and Del Gratta C (2020) Normal Aging: Alterations in Scalp EEG Using Broadband and Band-Resolved Topographic Maps. Front. Phys. 8:82. doi: 10.3389/fphy.2020.00082

INTRODUCTION

Numerous studies have shown age-related alterations in functional connectivity of brain regions while evaluating task-based performance as well as during rest, likely ensuing from a decline in cognitive performance. Intra and inter-networks changes in functional connectivity of resting-state networks have been recurrently reported [1]. The patterns of these alterations in functional connectivity are relatively complex i.e., both increases and decreases in number of connections have been found. For example, increase in anterior regions of DMN, subcortical and somatosensory/motor network, and decrease in posterior DMN regions, dorsal attention, and salience networks [2, 3]. In addition, the within-region functional connectivity in the somatosensory, and central visual areas, were found to be non-linearly related to aging, whereas other studies found results in contrast to the above mentioned [4].

In the literature, the complex nature of aging-related changes is based on two main hypotheses i.e., dedifferentiation and compensation. First, dedifferentiation is the term used to explain the loss of underlying functional resources required to perform the given task [5]. Biologically, it is referred to as the chain of processes affected by the deterioration of dopaminergic neuromodulation that result in a reduced specificity of involved cortical areas [6]. Second, the compensation hypothesis explains the involvement of newly recruited brain areas in a higher level of activity to overcome the decline in functional specificity [7]. The compensation process was first identified by Grady et al. [8] while investigating the performance metrics for memory tasks.

In recent years, research on brain changes related to aging increasingly relied on functional magnetic resonance imaging (fMRI). Numerous insights were provided e.g., key brain areas like the anterior cingulate cortex involved in emotional and cognitive processing has been found to be significantly affected by aging, even when its functional connections were investigated during rest [9]. Similarly, Roski et al. [10] found that the age-related resting-state functional connectivity alterations were correlated with behavioral changes. Despite advancements, in the existing literature, inconsistency of results in the aging-related resting-state functional connectivity alterations still persist [11]. Although fMRI data provide high spatial resolution, it has certain limitations. First, fMRI is primarily based on BOLD contrast which allows us to measure neuronal activity only indirectly, whereas non-neuronal factors such as metabolic rate and cerebral blood flow, influencing BOLD response, may hinder the correct assessment of aging-related functional connectivity alterations, aging being linked with several factors that include changes in dopaminergic neurotransmission [12], metabolism [13], alterations in brain structure [14], cerebral blood flow [15], and cognitive resources [16]. Second, due to low temporal resolution, fMRI is less efficient in the investigation of temporal dynamics of functional connectivity, and consequently, it is reasonable to mention that most of the existing aging studies assumed that functional connectivity is stationary during rest. However, a recent fMRI study by Chen et al. [11], inspired from the evidences in the studies of schizophrenia [17], cognition impairment [18], depression [19] and epilepsy [20], has examined the temporal dynamics of resting-state functional connectivity in young and elder subjects, and found it non-stationary. Moreover, they reported a decline in the modularization of dynamic functional connectivity in elderly subjects. Therefore, it is timely to further assess these observations with modalities providing a sufficiently high temporal resolution.

In EEG data analysis, several methods have been used to assess coupling and synchronizations among EEG signals [21]. However, one method, which has recently gained a wide interest of researchers aiming at assessing synchronization across signals, is capable of detecting short lived quasi stationary states. These EEG states are found useful to empirically analyze cognitive and sensory process [22]. Lehman et al. proposed this spatiotemporal method to keep track of quasi-stable neuronal processes at a fine resolution, and named it "*Microstate analysis*" [23]. In microstate analysis, short-lived functional states are referred to as microstates, which are topographic configurations representing the distribution of electric potential across the scalp [23]. An observation which made microstate analysis a strikingly influential tool for the assessment of neuronal activity in time domain was that the temporal sequence of these spatial maps is non-random, and does not change continuously. These topographic configurations are found to be stable for short duration before transiting abruptly into another. The average duration of microstate ranges from 40 to 120 ms [24]. These short-lived microstates are viewed as an electrophysiological signature of a global integrative process. A study by Lehmann et al. [25] in which microstate configurations and syntax were found significantly different for imagery, and abstract thoughts, respectively, is considered as a validation of their link with cognitive processes. In a clinical context, studies employing microstate analysis found substantial electrophysiological signatures for altered neuronal processes that differ between healthy controls and subjects with psychopathology [26], dementia [27], schizophrenia [28], and stroke [29], provide further evidence of their usefulness. Moreover, recent studies assessing resting state dynamics using simultaneous EEG and fMRI has shown that the imprints of abruptly changing short-lived states of brain calculated using multichannel electrode array are related to resting-state networks. The normative four states are reported to be associated with visual, verbal, interoceptive-autonomic processing and attention reorientation [30, 31]. On how the associations between dynamics of microstates derived from EEG at high temporal resolution and resting-state networks based on slow hemodynamic fluctuations are possible, Van De Ville et al. found that the temporal dynamics of microstates are scale-free dynamics over six dyadic cycles (256 ms-16 s), suggesting the same underlying neurophysiological phenomenon, and microstates being the probable candidate for electrophysiological signatures of slow fluctuations of brain activity as measured by methods relying on hemodynamics [32].

These considerations encouraged the present analysis to explicitly investigate aging-related resting-state alterations using microstate analysis. A related work in which microstates analysis was used to study developmental stages of brain was published in 2002 by Koenig et al. [33]. Temporal profiles of microstates were

investigated in subjects aged 6–80 years. They found microstate temporal parameters differ as the brain develops, but mainly had focus on the investigation of developmental changes in the brain of age 6–16 years. However, without going into details, they suggested that the changes in the brains of subjects over 50 years of age are due to aging. In short, their study provided the preliminary evidence that microstates can capture age-related changes. With the knowledge and insights provided by the studies in the last decade, we believe that it is the need of the hour to investigate whether the altered neuronal signatures due to aging observed (if any) using the microstate analysis at scalp support the hypotheses derived from the evidence of existing fMRI studies that are dedifferentiation and compensation. We expect that age-related alterations will not only be found in temporal parameters of microstates but also in their spatial configurations. We have also applied our recently published method of band-wise topographic analysis as a new application to aging data. It has shown great promise to capture further details that are not identifiable with conventional microstate analysis.

MATERIALS AND METHODS

Data and Pre-processing

Eyes closed resting-state EEG data were recorded in 36 healthy subjects equally divided into aged and young adults. The aged subjects group ranged between the ages of 62–85 years (mean age: 71.8 $\pm$ 5.6, 12 males), whereas, young subjects had age ranging from 19 to 31 years (mean age: 23.2 $\pm$ 4.1, 12 males). Scalp potentials were measured using Electrical Geodesics sensor net. No subject had a history of neurological disorders, head injuries causing loss of consciousness or mental illness. All subjects were right-handed, tested and confirmed by Edinburgh Manuality test. The acquisitions were performed at, and under the ethical guidelines of "Gabriele d'Annunzio" University of Chieti, after signed written informed consent. The subjects were instructed to close their eyes while staying conscious.

Data Analysis

The analysis has been performed for spatiotemporal assessment of the EEG data in two ways. First, the conventional microstate analysis was implemented using the well-established standardized procedure [34] over the whole bandwidth of the data i.e., 0.01–40 Hz. In this procedure, to start with, the standard deviation across channels also known as Global Field Potential (GFP) was calculated at each time point. It was calculated using the following formula

$$GFP(t) = \sqrt{\frac{1}{N}\left(\sum_{i=1}^{N}\left(V_i\left(t\right) - V_m\left(t\right)\right)^2\right)} \quad (1)$$

where N is the number of channels, $V_i(t)$ is the electric potential at the i_{th} electrode and $V_m(t)$ represents the instantaneous mean potential across electrodes. The *GFP(t)* is the array representing standard deviations across channels for all data samples. Afterwards, from *GFP(t)* waveform, the time points of local maxima were extracted to find out the optimal set of microstate maps. The intuitions to only include time points with local maxima were that these instances have high signal-to-noise ratio and reduce the computational complexity of clustering algorithm [35]. Moreover, microstate maps are found to be stable at local maxima of GFP waveform and transitioning from one to another topographical map occurs at local minima [22]. Therefore, in next step, the potentials of all electrodes (topographic maps) at these local maxima time points are subjected to the K-means algorithm for clustering.

For an optimal selection of a number of microstates, the cluster size (number of microstates in the cluster) was varied from 2 to 7. The optimality criteria consisted of Cross Validation (CV)—a modified version of the predictive residual variance [34], and of Explained Variance (EV)—the fit percentage of segmented data. The EV and CV values were calculated for each cluster size. Based on statistical significance between consecutive EV and CV values over the cluster size range, the following two cases were used to define optimality. First, if the increase in EV value by increasing the cluster size is not found statistically significant while CV value increased statistically, previous cluster size is said to be optimum. Second, if, both, the increase in EV value and in CV value is significant, the statistical increase in CV value (i.e., the high probability of having different spatial patterns when clustering is repeated) is given priority and previous cluster size is chosen as optimum. Else, the statistical analysis is performed for the next consecutive cluster size. Based on the criteria, optimal microstates were calculated for individual subjects. For group microstates, these individual microstates were averaged based on minimal topographic dissimilarity [33] for both groups of young and aged subjects. Furthermore, these microstate maps explaining maximal variance were extracted after 300 iterations to minimize error due to stochastic processing. In summary, the step wise procedure for extraction of microstate maps is as follows

1. Calculate GFP waveform by computing standard deviation across electrodes for each time point.
2. Find time points where GFP waveform has local peaks.
3. Input topographic maps of EEG potential at time points found in step 2 to a clustering algorithm.
4. Pre-assign cluster size or set criteria for optimal selection of microstate maps.
5. Repeat clustering algorithm for multiple time (300 iterations performed commonly) to identify microstate maps explaining maximum variance present in the data.

The EEG data were segmented into a topographic sequence of extracted group averaged four microstates as shown in **Figure 1**.

Second, the conventional microstate analysis was extended to spectrally resolved topographic analysis using band-wise topographic maps [36]. This is to investigate the age-related spatial changes which are limited to a narrow band oscillations. The wide-band [0.01 Hz−40 Hz] EEG data is transformed into five fundamental EEG bands (delta (δ) = [0.01Hz–4Hz), theta (θ) = [4 Hz–8Hz), 191 alpha (α) = [8Hz–12Hz), beta (β) = [12Hz–30Hz), gamma (γ) >= 30 Hz) via time-frequency method with a concept of instantaneous frequencies. This means that the method, unlike traditional frequency analysis approaches, does not require few time periods to calculate the EEG

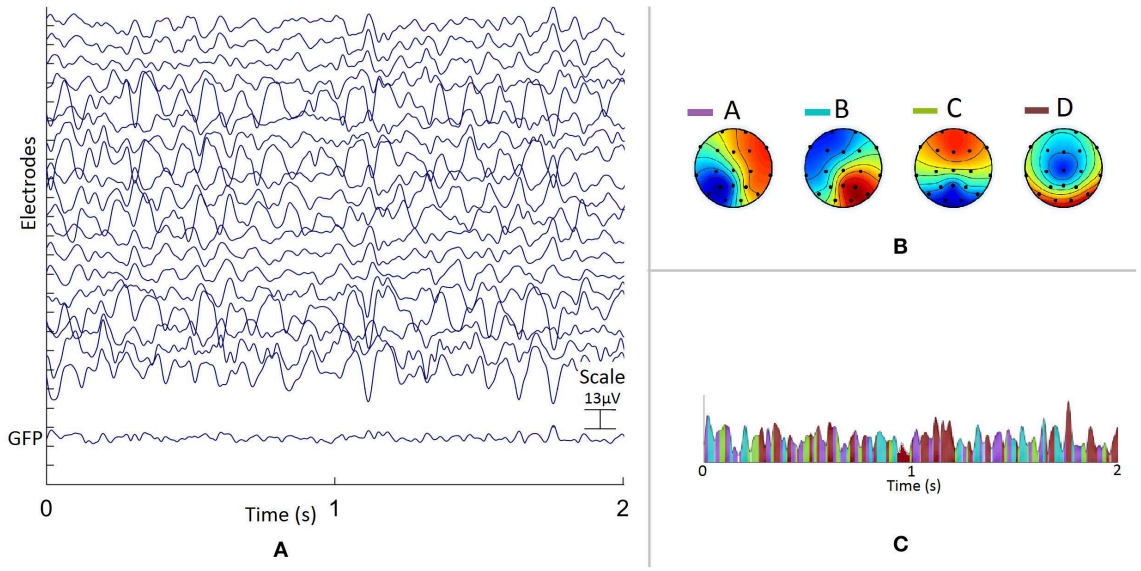


FIGURE 1 | Example of a representative young subject, **(A)** 2 s epoch of EEG recorded during eyes closed resting state (average referenced) for each of the 19 EEG sensors. The Global Field Power (GFP), standard deviation of EEG across sensors, computed for each time point is shown at the bottom of EEG data. Four averaged microstates labeled a, b, c, d are presented in **(B)** in a color scale representing the normalized potentials on scalp. In **(C)** the EEG data is segmented using these microstates: intervals of stability of different microstates are shown in their respective colors.

power/energy in a particular frequency band, instead it calculates Instantaneous Frequencies (IFs) and Instantaneous Amplitudes (IAs) for each data time-point. In the method, first, the EEG data is decomposed into bands using the modified Hilbert Huang Transform proposed by Sandoval and Leon [37]. Where, intrinsic oscillations named Intrinsic Mode Functions (IMFs) present in the data are extracted using Complete Ensemble Empirical Mode Decomposition (CEEMD). The CEEMD is an improved version of Empirical Mode Decomposition (EMD) that reduces the "mode-mixing" problem and help in preserving the completeness property of the decomposition. Mode-mixing is named after the drawback of EMD that consists in the leakage of a single physical oscillation across several IMFs. Based on the inherited property of IMFs i.e., local orthogonality, their IFs and IAs are estimated at each time-point using "amplitude demodulation and numerical equations." The data decomposed into IMFs can be represented as follows

$$\boldsymbol{x}(\boldsymbol{t}) = \sum_{n=1}^{k} \boldsymbol{C_n}(\boldsymbol{t}) + \boldsymbol{r}(\boldsymbol{t}) \tag{2}$$

where, $\{\boldsymbol{C_i}(\boldsymbol{t})\}_{i=1}^{k}$ are the $\boldsymbol{k}$ decomposed IMFs of $\boldsymbol{x}(\boldsymbol{t})$ and $\boldsymbol{r}(\boldsymbol{t})$ is the residue. The process to extract IMFs is called sifting process [38]. The formulae to estimate their IFs and IAs are shown in (3) and (5) respectively:

$$\hat{\boldsymbol{w}}(\boldsymbol{t}) = \boldsymbol{d}/\boldsymbol{dt}[\boldsymbol{arg}(\hat{\boldsymbol{s}}(\boldsymbol{t}) + \boldsymbol{j}\hat{\sigma}(\boldsymbol{t}))] \tag{3}$$

with $\hat{\boldsymbol{w}}(\boldsymbol{t})$ symbolizing IF estimated by calculating derivative $\frac{\boldsymbol{d}}{\boldsymbol{dt}}()$ of complex number in which real part $\hat{\boldsymbol{s}}(\boldsymbol{t})$ is an amplitude demodulated IMF ($\{\boldsymbol{C_i}(\boldsymbol{t})\}_{i=1}^{k}$) i.e., iteratively, dividing $\boldsymbol{C}(\boldsymbol{t})$ by its amplitude envelope until there are no oscillations in the envelope and the imaginary component $\hat{\sigma}(\mathbf{t})$ is calculated as in (3)

$$\hat{\sigma}(\boldsymbol{t}) = -\boldsymbol{sgn}[\boldsymbol{d}/\boldsymbol{dt}\hat{\boldsymbol{s}}(\boldsymbol{t})]\sqrt{\boldsymbol{1}-\hat{\boldsymbol{s}}^{\boldsymbol{2}}(\boldsymbol{t})} \tag{4}$$

where $\sqrt{\mathbf{1}-\hat{\boldsymbol{s}}^{\boldsymbol{2}}(\boldsymbol{t})}$, the magnitude of the imaginary component is calculated using Pythagorean Theorem in which the magnitude of the complex number is unity due to amplitude demodulation. The expression $-\boldsymbol{sgn}[\frac{\boldsymbol{d}}{\boldsymbol{dt}}\hat{\boldsymbol{s}}(\boldsymbol{t})]$ estimates the sign of the imaginary component, or, in other words, it identifies +ve or –ve plane of the imaginary axis. It is calculated empirically i.e., if $\hat{\boldsymbol{s}}(\boldsymbol{t})$ is decreasing, the sign of imaginary component will be positive whereas a negative sign of the imaginary component is for increasing $\hat{\boldsymbol{s}}(\boldsymbol{t})$. Hence, reversing the sign ($-\boldsymbol{sgn}[]$) of derivative $\frac{\boldsymbol{d}}{\boldsymbol{dt}}()$ of $\hat{\boldsymbol{s}}(\boldsymbol{t})$ will yield the sign of the imaginary component. While corresponding $\hat{\boldsymbol{a}}(\boldsymbol{t})$ is calculated by interpolating local maxima of respective IMF or simply by calculating the upper envelope as in (5):

$$\hat{\boldsymbol{a}}(\boldsymbol{t}) = \boldsymbol{interpolate}(\boldsymbol{t_p}, \boldsymbol{U_p}) \tag{5}$$

where, $\boldsymbol{t_p}$ are the times at which the local maxima occur and $\boldsymbol{U_p}$ is their magnitude (see details on these equations in [37]). The theoretical explanation along with the representation in algorithmic form can be found in our article in which the method was originally proposed [36]. That study also identifies the spectral details associated with wide-band microstates when the data is spectrally decomposed using the very method. Thus, based on an identified link between the band-wise topographic maps and conventional microstate maps, the use of the method

in this study not only provides further insights to differences among distinct age groups but also a step forward in the effectiveness of its use in EEG analysis of synchronized activities. Interested readers are also referred to the studies [37, 38] for more details on method. However, a stepwise overview of procedure for calculation of band-wise topographic maps is as follows

1. Extract IMFs for a pre-processed signal as in equation 2 by employing CEEMD algorithm.
2. Calculate instantaneous frequencies (IFs) and instantaneous amplitudes (IAs) for each IMF and for all time-samples using equation 3 and 5, respectively.
3. Define frequency bands (e.g. δ, θ, α, β, and γ) and construct their amplitude-time-series based on above calculated IAs and IFs i.e., by assigning IA of given sample to the frequency band determined by IF of that sample. This is repeated for all IMFs and resultants are summed up in respective frequency bands to get single amplitude-time-series.
4. Above steps are repeated for all electrodes in a data individually.
5. After construction of band's amplitude time series, conventional microstate procedure as explained above is applied to get topographic maps for each band.

Optimality criterion is applied for each band's topographic maps to get final set of band-wise topographic maps.

The EEG data were spectrally transformed into five fundamental EEG bands based on the estimated IFs at each time point, providing the same temporal resolution as in the time domain EEG data. As will be shown below, the preserved timescale allowed us to analyze spatial patterns at each frequency band and to identify the differences between young and aged subjects that could not be captured by conventional microstate analysis due to the use of full band data. The procedure [34] for the extraction of topographic maps was then applied to each frequency band data and the same optimality criteria (mentioned above) for all band-wise topographic maps from both young and aged subjects group was used.

Moreover, the differences between the aged and young subjects in temporal dynamics of the topographic sequence are quantitatively analyzed for both conventional and band-wise topographic analysis using the following parameters:

- Mean-duration (MD): average stability time of each microstate.
- Frequency-of-occurrence (FO): average number of appearances of each microstate within a window size of 1 min.
- Coverage (Cov): the ratio of time covered by each microstate per total time.
- Transition-probability-matrix: the probability of each microstate transiting into other microstates e.g., transition probability of microstate A to microstate B symbolized by A→ B. For example, in resting-state literature, it has been found that, on average, twelve transitions between microstates can occur in a second if the number of microstates is four.

In addition to these parameters, EV is also calculated to demonstrate the fit percentage of extracted microstate maps to the EEG data for both groups. Whereas, for spatial changes, the dissimilarity index has been calculated. The dissimilarity index represents the strength of spatial similarity, the value of which ranges from 0 to 2 with 0 representing the same spatial configuration with similar polarity and 2 for the same spatial configuration with inverted polarity. It should be noted that instead of strictly restricting the definition of similarity to these extremes, we used the range of 0–0.2 and 1.8–2 for similar and inverted polarity configuration, respectively, in our study to account for the variance induced due to averaging of maps across subjects (i.e., group averaged topographic maps).

RESULTS

As mentioned in above section, the analysis is performed in two ways and their results highlighting the differences between two groups in respective analysis are presented in separate subsections below.

Differences Between Groups in the Conventional Microstate Analysis

Based on optimality criteria, for the conventional microstate analysis, four microstate maps are found to be optimal for both young and aged subject group. Four microstate maps are also found to be consistent with the normative and existing literature of microstate analysis. Based on resemblance in the topographic configurations of extracted microstate maps from both groups with the existing literature, standard labels of A, B, C, and D are assigned as shown in **Figure 2**. Note that these spatial configurations are prototypical representations of potential distribution across electrodes, ignoring polarity inversion (as polarity is not taken in to account: (1) when unique clusters for these potential distribution are being computed using clustering algorithm and (2) when spatial correlations are computed for back-fitting of these maps to the EEG data. The back-fitting is elaborated in **Figure 1** where time series across electrodes presented in (a) are represented by topographic maps in (b) as a single time series of colored blocks in (c), whose amplitude is varied according to GFP waveform). The extracted microstate maps used to segment EEG data achieved Global Explained Variance (GEV) of 73.55 ± 3.7% for aged and 79.68 ± 4.1% for the young subjects group. The difference in GEVs is found statistically significant (independent t-test, $p < 0.05$). Moreover, an overall four microstate maps are also calculated by combining the data of both groups to investigate the need for separate microstate maps for longitudinal studies. The GEVs using overall microstate maps for both groups have decreased i.e., 71.64 ± 5.5% for aged and 78.72 ± 4.3% for the young subjects. Note that, although the differences in the explained variance between individual and combined microstate maps for each group are small, they are found statistical significant (independent t-test, $p < 0.05$).

The repeated measures ANOVA (rmANOVA) has been separately (2 × 4) conducted for the three metrics that

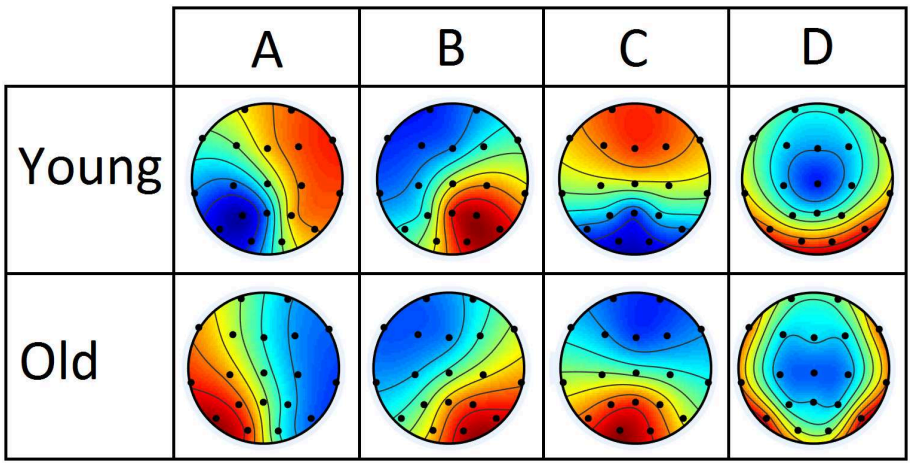


FIGURE 2 | Four group-microstate maps extracted from young and aged datasets separately. The maps are labeled conventionally based on maximum resemblance.

include duration, frequency of occurrence, and coverage. Each rmANOVA had one factor for groups (Aged, or Young) and one factor for microstate maps (A, B, C, or D). The difference in mean values for metrics presented in **Figure 3** are found to be significant ($p < 0.05$) with the exception of the frequency of occurrence, as presented in **Table 1**. The significance found in the full model of mean duration and coverage is further tested using reduced models (*post-hoc* analyses), which revealed that the dynamics of microstate C are dependent on age-related changes and the mean values of metrics for microstate C decrease in aged compared to young subjects group ($p < 0.0125$, Bonferroni corrected independent t-test). The significance level $p = 0.023$ for microstate C is found in the frequency of occurrence metrics suggesting marginally significant difference. However, no relation has been found between age and dynamics of the rest of the microstate maps (A, B, or D) in all metrics ($p > 0.02$, independent t-test).

Additionally, the syntax analysis, i.e., analyzing the non-randomness or directional dominance in the microstate transitioning, probabilities for each transition pair (in total: twelve pairs, e.g., X↔Y represents two pairs that are X→ Y and X←Y) of four microstates are calculated. Our analysis reports discernable patterns for aged and young subjects group i.e., directional dominance is always found opposite (i.e., for example, if aged subjects group has dominant transition from A to B, then young subjects group found having dominant transitions from B to A) for each pair as shown in **Figure 4**. However, this pattern was not statistically significant except for the transitions between microstates C and D ($p < 0.0125$, Bonferroni corrected independent t-test).

Apart from evaluation of age-related changes in the temporal parameters of conventional microstates, spatial changes across groups are also quantified using the dissimilarity index. The results are presented in **Table 2**. The results provide evidence that a change (if any) in spatial maps of scalp-level data can be detected effectively as in this case microstate map D found dissimilar across two groups while others are similar with inverted polarity.

Differences Between Groups in the Band-Wise Topographic Analysis

In this analysis, three topographic maps are found optimal for each band in both groups using the same optimal map selection procedure explained in conventional microstate analysis. The topographic maps of each band are presented in **Figure 5**. The segmentation of EEG data using these band-wise topographic maps yielded EV of 44.47 ± 3.4% in Delta, 49.15 ± 8.5% in Theta, 54.28 ± 7.3% in Alpha, 46.69 ± 6.7% in Beta, and 44.54 ± 5.5% in Gamma band for the young subjects group; While EV for the aged subjects group is: 61.52 ± 11.3% in Delta, 57.97 ± 9.7% in Theta, 56.79 ± 6.9% in Alpha, 56.48 ± 8.1% in Beta and 51.14 ± 6.5% in Gamma band. The difference in EVs in respective bands among groups has been found statistically significant (independent t-test, $p < 0.01$, Bonferroni corrected) for all bands except the alpha band.

Like conventional microstate analysis, the temporal dynamics of band-wise topographic segmentation are also analyzed. Same metrics: mean duration, frequency of occurrence, and coverage are calculated for all band maps i.e., D1, D2, D3 of the delta, T1, T2, T3 of theta, A1, A2, A3 of alpha, B1, B2, B3 of beta and G1, G2, G3 of gamma band. The results are presented in **Figure 6**. Statistical inferences for the changes among groups are drawn by conducting the repeated measures ANOVA (rmANOVA) separately (2 × 3) for these temporal metrics. Each rmANOVA had one factor for groups (Aged or Young) and one factor for band-wise topographic maps. In the full model i.e., **Table 3A**, the differences in the temporal characteristics of band-wise topographic segmentation have been found significant ($p < 0.05$) except for the theta band for the mean duration and for the beta band for the frequency of occurrence. To further analyze the relation found in the full model, *post hoc* analysis was performed (**Table 3B**) where, for every band-wise topographic map, at least one temporal metric is found significant (independent t-test, $p < 0.0167$, Bonferroni corrected).

In addition to the analysis of temporal dynamics, the dissimilarity index has been used to quantify the spatial changes between groups. The dissimilarity index has been calculated

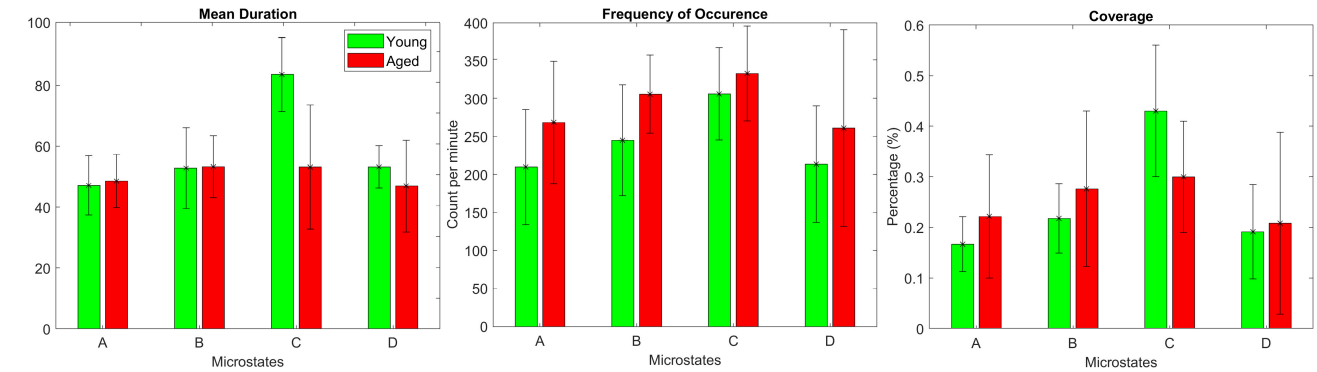


FIGURE 3 | Bars representing average values of microstate metrics calculated for both aged (red) and young (green) subject groups to visualize within group differences for each group-microstate maps.

TABLE 1 | Statistical comparison of microstate temporal dynamics in aged and young subjects.

	Repeated measure ANOVA			*Post-hoc* comparison—*p* level			
	df	**F**	***p* level**	**A**	**B**	**C**	**D**
Mean duration							
Group	1;36	5.538	**0.031**				
Map	3;72	16.143	**0.000**				
Group* Map	3;72	10.919	**0.002**	0.902	0.819	**0.001**	0.056
Frequency of occurrence							
Group							
Map	3;72	10.403	**0.000**				
Group* Map	3;72	1.684	0.182	0.232	0.339	0.023	0.913
Coverage							
Group							
Map	3;72	15.270	**0.000**				
Group* Map	3;72	7.732	**0.001**	0.025	0.058	**0.001**	0.636

Results of repeated measure ANOVA and post-hoc comparisons for microstate metrics. 'Group' describes between-subject factor as aged or young and within-subject factor i.e. 'Map' describes four microstate maps (A, B, C, or D). p-values highlighted in bold formatting are significant.

across the band-wise topographic maps to give us intra and inter-band similarities if there exist any between two groups. The results averaged across subjects are presented in **Figure 7** which quantitatively confirms the visual observations of **Figure 5** that narrow band topographies are not only unique with in the bands of same subject, but are also capable of capturing the differences across groups.

DISCUSSION

In this study, by means of band-wise microstate analysis, we have for the first time, to the best of our knowledge, observed age-related EEG differences in spectrally resolved, spatial domain, scalp EEG data. Conventional microstate analysis which constructs spatially synchronized topographies using the whole bandwidth of EEG data was also used. This conventional analysis served few purposes in the study. First, the extent to which age-related changes are identifiable using broad-band EEG data was still to be analyzed in detail. Second, this provided a reference for comparison of the band-wise topographic method which can be considered as a spectral extension of the former. Third, due to our recent study [36] identifying the link between band-wise topographic maps and conventional microstates, it allowed us to draw inferences and reasonably argue that the results observed using band-wise topographic maps could be linked with age related changes. Finally, on a similar note, to show how these observed results could possibly be related to the results of fMRI studies on normal aging i.e., dedifferentiation and compensation mechanisms. The interesting findings of this article are: (a) conventional microstate analysis was found to have limited effectiveness in identifying age-related changes compared to band-wise topographic analysis. That is, using the band-wise topographic method, the observed variations in temporal features could possibly represent the complex functional changes found in existing fMRI studies [4, 11], whereas conventional analysis failed in providing such details. (b) The relative increase or decrease in timing of synchronized activity between young and aged subject groups is observed at scalp level which among existing fMRI studies [4] has been well-reported. And, (c), the topographic maps of band-wise topographic analysis has shown

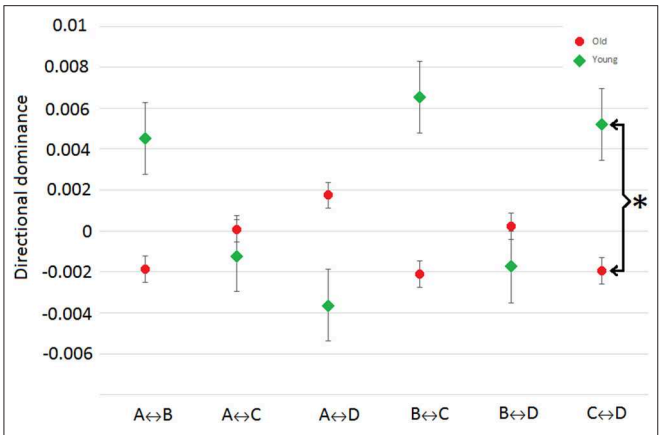


FIGURE 4 | Directional predominance: difference between transition probabilities of each pair i.e., X↔Y = (X→ Y)-(X←Y). The sign indicating dominant direction [+ve = (X→ Y) and –ve = (X←Y)]. The values are averaged across subjects in respective groups. Asterisk is for significant differences ($p < 0.0167$) between groups.

TABLE 2 | Dissimilarity index among the group averaged microstates of young and aged subjects group.

Young \ Aged	A	B	C	D
A	1.89	1.39	1.84	1.33
B		1.92	1.66	1.31
C			1.92	1.47
D				0.69

spatial changes among groups which is unlike conventional microstate analysis. Here, the findings are discussed in the light of the results described above, along with new insights provided by the band-wise topographic method.

Differences Between Groups in the Conventional Microstate Analysis

A relevant work of Koenig et al. [33] in which they studied developmental stages with microstate analysis, using data of subjects between age of 6 and 80 years. They suggested that changes in microstate dynamics in subjects above 50 years of age could possibly be age-related changes. However, the focus of the study being on developmental stages they did not evaluate age-related changes in detail. Therefore, we started our analysis by assessing what insights can be provided by conventional microstates in this regard. In the present work, four microstates were found optimal for both datasets. The Global Explained Variance (GEV) was evaluated to find out whether representing both groups with grouped-averaged microstate maps (extracted after concatenating data of both groups), like in Koenig et al. [33], constitutes a sufficient model, or if, conversely, separating the two groups with distinct averaged microstate maps for each group, yields a more explanatory model. Results demonstrate a significant increase in the GEV values in each group when distinct microstates maps are used for distinct groups. Although the change in GEV is not large, it is statistically significant, and therefore encourages the use of separate microstate maps for aged and young subject groups, respectively (at least in this study). This is to avoid any segmentation bias that may hinder age-related changes. Therefore, we have used separate microstate maps for each group for further analysis. The extracted microstate maps are shown in **Figure 2**.

Temporal parameters of microstate analysis have their own neurophysiologic significance. The Mean Duration (MD) is representative of stability in underlying neuronal patterns, the Frequency of Occurrence (FO) is representative of propensity of specific neuronal generators to be activated in a given time-period, and coverage is interpreted as the amount of time neuronal generators remain dominant [29]. For example, Seitzman et al. [39] observed that the coverage and FO of microstate B has increased significantly when analyzing open-eyes data compared to closed-eyes data for same subject across 24 healthy young subjects (age: 21.1 ± 4.5 years). Note that microstate B has been previously linked with the visual system [40]. Similarly, a few other studies have also found alterations in the temporal parameters of other microstates, such as C and D [31, 41, 42]. Therefore, to investigate if there are any age-related alterations to these parameters, the above-mentioned metrics were calculated (results in **Figure 3**) for both groups, and rmANOVA (**Table 1**) was performed to search for an overall difference among the four microstate maps. The metrics MD and coverage have been found to be statistically different. Further investigation using *post hoc* analysis revealed that the differences in the respective metrics are mainly due to the decreases in microstate C in aged compared to young subjects. The decrease in microstate C in aged subjects group is not surprising considering its relation to the hemodynamic counterpart: It has been found positively correlated with the BOLD signals of the anterior cingulate cortex (ACC), right anterior insula, inferior frontal gyri and left claustrum [40]. These areas are also said to be roughly related to resting state network (RSN 6) in Mantini et al. work [43]. Several fMRI studies identified age-related decline in functional connectivity involving these regions. As in Damoiseaux et al. [2], decrease in connectivity involving most frontal and parietal brain regions has been found. The ACC which is related to working memory has been found to have decreased activations in elderly people [44]. Additionally, not only in fMRI studies, Kalpouzos et al. [45] suggested decline in metabolic activity at ACC and prefrontal cortex using Positron Emission Tomography. Similarly, structural changes i.e., gray matter volume in ACC along with parietal cortex, insula, and cerebellum has been found to be reduced in aged people [46]. Therefore, decrease in temporal parameters has been in-line with existing studies analyzing data of different modalities, and possibly this observed change is due to the attention deficiency and limited emotional, cognitive, and perceptual brain processing in normal aging.

Furthermore, we have also computed the syntax of microstate-based segmentation of EEG. The results in **Figure 4** show that transitions in pairs is inverted between young and aged subjects but there is no statistically significant difference except for the pair of C↔D. This suggests an overall balance is maintained

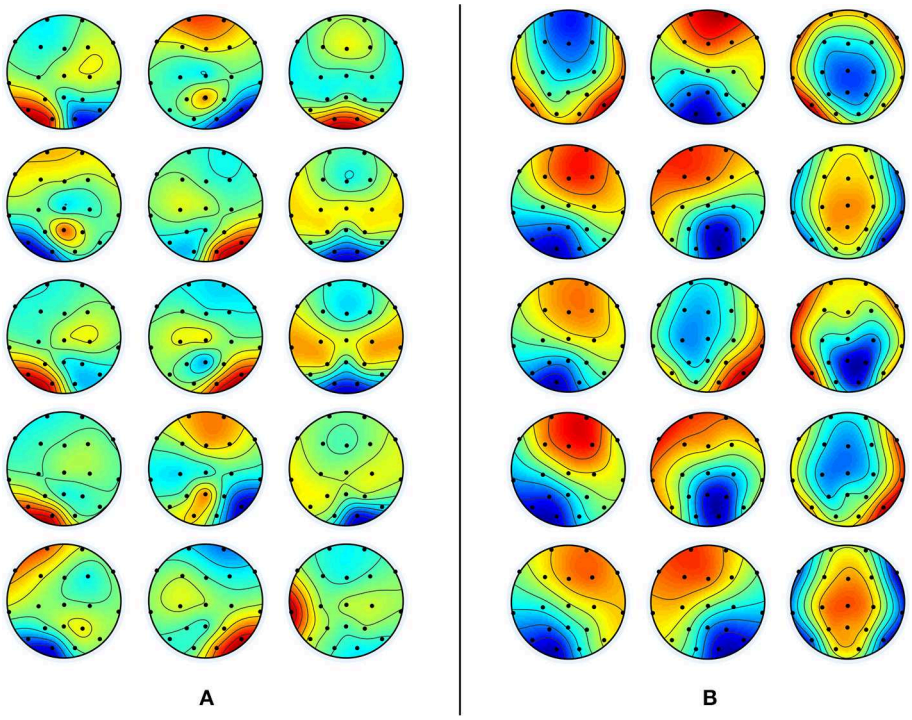


FIGURE 5 | Band-wise group averaged topographic maps of young subject data in **(A)** and aged subject data in **(B)**. From top to bottom are five frequency bands (δ, θ, α, β, and γ) with 3 maps for each band from left to right, labeled as D1, D2, D3 for delta, T1, T2, T3 for theta, A1, A2, A3 for alpha, B1, B2, B3 for beta, and G1, G2, G3 for gamma band. This sequence is the same for both panels.

in connectivity patterns in both groups. The balance in elder people is suggested to be due to the compensatory mechanism which fulfills the need of any reduced activity in performing a given task [11]. Despite the differences in connectivity of several regions involved in deficiency due to normal aging, several fMRI studies have reported the compensatory mechanisms. This compensation-related activity has been formulated using three cognitive models as reported by Sala-Llonch et al. [4]. One of these models named "Hemispheric Asymmetry Reduction in Old Adults" informs about the compensatory activity arising from decline in lateralized pattern of activity in frontal region in elder people [47]. And, Britz et al. [40] reported that microstate D is related to the BOLD signal of ventral and right-lateralized dorsal areas of parietal and frontal cortex which are responsible for reorientation and switching of attention. Therefore, it is reasonable to assume that the significant change in the syntax of pair C↔D are due to the microstate D.

Besides inferring that the change in microstate D is due to compensatory activity, to further support the link of observed changes in our conventional microstate analysis with the dedifferentiation and compensatory mechanisms, we highlight that, in **Figure 2**, microstate D appears visually dissimilar between the groups in spatial configuration, a result that is also supported quantitatively by the dissimilarity index in **Table 2**. However, except for microstate D, no other microstate map shows such dissimilarity. This could be acceptable for microstates A and B, as they were found similar in their temporal parameters as well. But the spatial similarity of microstate C (even though its temporal parameters have shown significant alterations) across groups raised concern about the possibility of visualizing the spatial changes at scalp level that occurred locally in normal aging due to dedifferentiation and compensatory mechanisms as observed in fMRI studies at the cortical level. Having said that, it is also observed from the existing fMRI studies that the age-related changes are not straightforward, i.e., both increases and decreases are found which are in abidance to the results of dynamic balancing of connectivity patterns of both young and elder brains [11]. Based on these results, it can be deduced that for dedifferentiation and compensation mechanisms to be true, if there is a decrease in connectivity of a certain region, there should be a compensatory increase in connectivity involving other regions. However, detecting such mechanisms topographically with scalp-level data may well be tricky as in our analysis of conventional microstate analysis, and might require adding constraints or transformations to the scalp data to be resolved.

One possible reason which we thought of to help us solve this issue of observing age-related changes spatially at scalp-level analysis, was to spectrally decompose the data. The intuition behind is that we did not observe the age-related changes occurring in local brain areas could be due to the amalgamation of signals of different frequencies into one signal which will consequently describe only the prominent change even if multiple changes have occurred at different frequencies. In such a case, it would be reasonable to assume that the failure

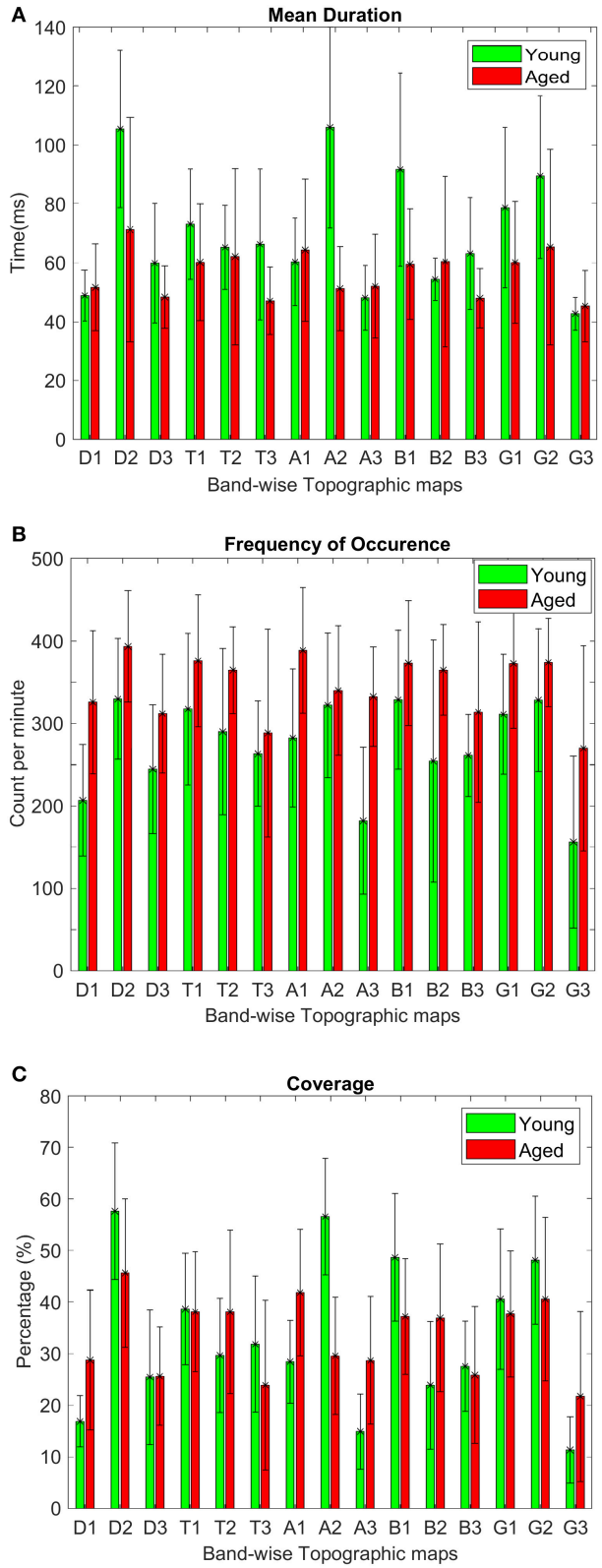


FIGURE 6 | Average values along with standard deviations of microstate metrics: **(A)** mean duration, **(B)** frequency of occurrence, and **(C)** coverage, calculated for both aged and young subject groups to assess within-group differences for each grouped band-wise topographic map.

in capturing such changes could be due to the use of broad-bandwidth of the signal for the extraction of the conventional microstate maps. Therefore, we hypothesized that decomposing spectrally the EEG signals, and then evaluating the spatial patterns could capture the complex changes which are already known from fMRI studies. This brings forth the need to apply the band-wise topographic analysis to investigate differences between young and aged subjects.

Differences Between Groups in the Band-Wise Topographic Analysis

To strengthen our point of using separate microstate maps for young and aged subjects, EV has been calculated for band-wise topographic maps at each frequency band using EEG data. The statistically significant ($p < 0.01$) differences in EV values suggest age-related changes should be considered a factor while examining spatial synchronicity. As expected, there are more differences in temporal and spatial characterization of band-wise analysis compared to broad-band analysis between the two groups. For the temporal characterization of band-wise topographic analysis, the metrics analogous to those used in the conventional analysis, evaluating stability, occurrence, and percentage of existence over time, were used. The results presented in **Figure 6** show a complex pattern of increase and decrease between groups. The rmANOVA (2×3) analysis (**Table 3A**) suggest a significant change between groups at each frequency band for each metric except for the theta band concerning MD, and for the beta band concerning FO. Further analysis (*Post hoc*: **Table 3B**) revealed that at least one metric is found to have statistically different values at each band between groups. The observed changes in temporal characteristics of band-wise topographic segmentation are in line with our hypothesis. That is, on one hand, in the temporal domain, both increases and decreases in MD are observed, however, the dynamic balance in synchronized activity across brain, which has been found in fMRI studies, is still maintained and can be noticed at scalp-level analysis. For example, the MD for A1 and A3 increased in aged compared to young subjects but a decrease in A2 compensate this. Similarly, other temporal parameters also adjusted themselves to maintain a dynamic balance.

On the other hand, in the spatial domain, from **Figure 5**, the spatial differences can also be visualized easily. The band-wise spatial maps of young subjects appear to be more localized than those of aged subjects. This spread in synchronized brain activity in the maps of aged subjects is not surprising because, in existing studies of fMRI data, increases in brain activity in aged subjects are reported, and these increases in activation have heterogeneous localization compared to young subjects [4]. At this point, we refrain from concluding that these spatial changes are a consequence of age-related dedifferentiation and compensation mechanisms, but the inferences that can be drawn from fMRI studies do highly support this notion. For example, a few studies also suggested that brain regions continue to reconfigure with age during rest to compensate for decline in other regions [48]. Moreover, the "Posterior-Anterior Shift with Aging (PASA)," experimentally proven model to describe age-related changes also support changes which

TABLE 3A | Statistical analysis of the temporal dynamics of band-wise topographic maps in aged and young subjects.

Repeated measure ANOVA

		Delta		Theta		Alpha		Beta		Gamma	
	df	**F**	**Sig.**	**F**	**Sig**	**F**	**Sig.**	**F**	**Sig.**	**F**	**Sig.**
Mean duration											
Group	1;36	10.2	0.005	6.1	0.024	10.3	0.005	10.3	0.005	7.4	0.014
Map	2;54	41.7	0.000	2.7	0.078*	30.9	0.000	30.9	0.000	17.3	0.000
Group* Map	2;54	10.8	0.000	2.9	0.064*	30.5	0.000	30.5	0.000	10.5	0.000
Frequency of occurrence											
Group	1;36	7.4	0.014	7.4	0.014	15.3	0.001	8.0	0.12	10.9	0.004
Map	2;54	17.3	0.000	17.3	0.000	30.9	0.000	9.6	0.000	49.6	0.000
Group* Map	2;54	10.5	0.000	10.5	0.000	15.5	0.000	2.6	0.089*	3.4	0.044
Coverage											
Group											
Map	2;54	49.5	0.000	48.5	0.000	38.8	0.00	18.0	0.00	32.3	0.00
Group* Map	2;54	3.4	0.044	9.5	0.001	35.5	0.00	7.2	0.03	5.6	0.08*

Results of repeated measure ANOVA.
"Group" describes between-subject factor as aged or young and within-subject factor i.e., "Map" describes three band-wise topographic maps.
Sig. represents p-level and values >0.05 are highlighted with asterisk at their end and are considered non-significant.

TABLE 3B | A *post-hoc* analysis of temporal dynamics of band-wise topographic maps in aged and young subjects.

		Mean duration (ms)	**Frequency of occurrence (FO/min)**	**Coverage (%)**
Delta	D1	**0.395**	0.00	0.000
	D2	0.001	0.005	0.005
	D3	**0.037**	0.005	**0.968**
Theta	T1	**0.028**	**0.028**	**0.883**
	T2	**0.625**	0.003	**0.113**
	T3	0.007	**0.432**	**0.186**
Alpha	A1	**0.461**	0.000	0.000
	A2	0.000	**0.758**	0.000
	A3	**0.330**	0.000	0.000
Beta	B1	0.001	**0.077**	0.003
	B2	**0.247**	0.001	0.002
	B3	0.004	**0.071**	**0.579**
Gamma	G1	**0.019**	0.013	**0.467**
	G2	0.009	**0.037**	**0.072**
	G3	**0.323**	0.003	0.004

The significance here is tested using independent t-test.
p > 0.0167 (Bonferroni corrected) are considered non-significant and are highlighted in bold formatting.

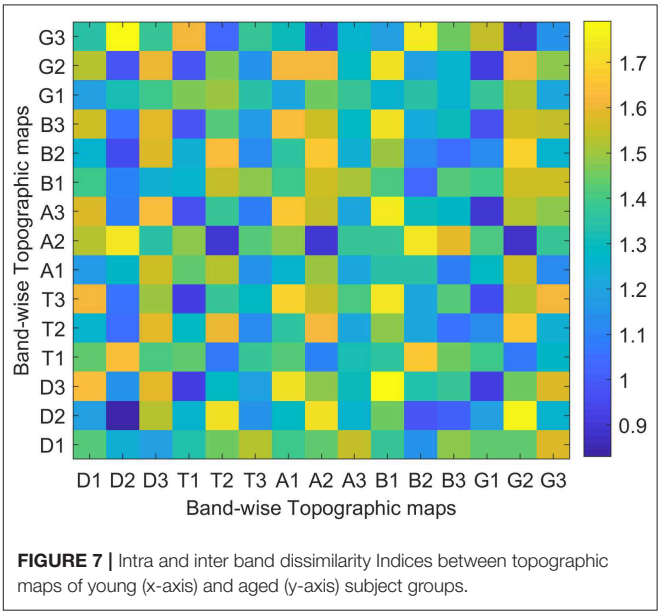


FIGURE 7 | Intra and inter band dissimilarity Indices between topographic maps of young (x-axis) and aged (y-axis) subject groups.

include both increases and decreases in connected regions along with the changes in spatial patterns [49]. As in PASA, Davis et al., have described the dedifferentiation mechanism with the decline in posterior midline cortex combined with the compensatory mechanism of increased activity in medial frontal cortex. However, to be sure that the spatial changes observed in band-wise topographic maps are due to age-related changes, one has to reconstruct the underlying sources at the time of their occurrences by utilizing some forward/inverse modeling. But, to further add support to our opinion, we would like to take advantage of recently identified associations between band-wise topographic maps and conventional microstate maps in one of our works [36]. It says that conventional microstates maps could well be represented by the combination of any of these five band-wise topographic maps (one from each band). This means that a meta-process described by one microstate map can be spectrally resolved into five sub-processes, which are described by five band-wise topographic maps, one from each band. Thus, these observed spatial and temporal changes

in band-wise topographic analysis can be linked to age-related changes observed in fMRI studies similar to the conventional microstate analysis in the above subsection. For example, in Javed et al. [36], band-wise topographies D2 and D3 are associated with conventional microstate C which is described above to be linked with ACC [40], and the ACC has been found to have decreased activations in elderly people [44]. Moreover, results of spatial dissimilarity index presented in **Figure 7** show intra and inter band dissimilarities among groups. No two band-wise topographic maps are found similar, which is unlike conventional microstate maps. Therefore, it is reasonable to suggest that the failure in identifying the spatial changes among groups using conventional microstate maps is due to the amalgamation of signals of different frequencies into one signal of broad-bandwidth. However, being one of the very first studies using band-wise topographic maps to investigate dedifferentiation and compensation mechanism at scalp-level, these findings reveal new and interesting directions that require further assessments.

CONCLUSION AND FUTURE WORK

One of the most frequently reported age-related factors is the change in cognitive and perceptual systems, which may consequently affect behavior. In turn, the majority of age-related diseases, including Alzheimer, which are related to these systems, are reported as disconnection syndromes. Therefore, the need to carry out this work lies in the importance of identifying the scalp-level electrophysiological correlates of fMRI findings. As it is believed that the results found via different modalities, more so with the one that directly measures neuronal potentials, and recent analysis tools, will be helpful in developing consensus over aging-related alterations; inching closer to the underlying mechanism which is still elusive, and consequently helping in limiting the differences between young and elder brain. In this work, we first showed that conventional microstate analysis can only identify the prominent changes in normal aging and is unable to detect complex changes. However, to conclude on results of conventional microstate analysis if one wants to use it for, let say, identification of any potential electrophysiological biomarkers of a given disease, we suggest using separate microstate maps for young and aged subject groups. Second, to get further insights, we applied our recently proposed band-wise topographic analysis which has shown more sensitivity in detecting the changes between the young and aged groups. However, we are constrained in drawing conclusions on their relevance since, to the best of our knowledge, this is the first study evaluating spectrally resolved spatial changes of aging. And unlike conventional microstate analysis where the corresponding resting state networks are known for each microstate map, a simultaneous study of EEG and fMRI is an imminent future prospect for band-wise topographic analysis to unfold its functional significance. Having said that, it is also important to mention that the band-wise topographic method has shown the glimpse of advancements that could converge the efforts of linking the results from different modalities to one another.

DATA AVAILABILITY STATEMENT

The datasets generated for this study are available on request to the corresponding author.

ETHICS STATEMENT

The studies involving human participants were reviewed and approved by Comitato di Bioetica Università Gabriele D'Annunzio, Chieti, Italy. The patients/participants provided their written informed consent to participate in this study.

AUTHOR CONTRIBUTIONS

EJ with the supervision of CD contributed to design, implementation, and writing of the manuscript. PC and FZ collected and pre-processed data. PC provided technical assistance during implementation phase. All authors contributed to the analysis and discussed results.

REFERENCES

1. Tomasi D, Volkow ND. Aging and functional brain networks. *Mol Psychiatr.* (2012) **17**:471–558. doi: 10.1038/mp.2012.27
2. Damoiseaux JS, Beckmann CF, Arigita EJ, Barkhof F, Scheltens P, Stam CJ, et al. Reduced resting-state brain activity in the 'Default Network' in normal aging. *Cereb Cortex.* (2008) **18**:1856–64. doi: 10.1093/cercor/bhm207
3. Andrews-Hanna JR, Snyder AZ, Vincent JL, Lustig C, Head D, Raichle ME, et al. Disruption of large-scale brain systems in advanced aging. *Neuron.* (2007) **56**:924–35. doi: 10.1016/j.neuron.2007.10.038
4. Sala-Llonch R, Bartrés-Faz D, Junqu é C. Reorganization of brain networks in aging: a review of functional connectivity studies. *Front Psychol.* (2015) **6**:663. doi: 10.3389/fpsyg.2015.00663
5. Park DC, Polk TA, Park R, Minear M, Savage A, Smith MR. Aging reduces neural specialization in ventral visual cortex. *Proc Natl Acad Sci USA.* (2004) **101**:13091–5. doi: 10.1073/pnas.0405148101
6. Li SC, Lindenberger U, Sikström S. Aging cognition: from neuromodulation to representation. *Trends Cognit Sci.* (2001) **5**:479–86. doi: 10.1016/S1364-6613(00)01769-1
7. Turner GR, Spreng RN. Executive functions and neurocognitive aging: dissociable patterns of brain activity. *Neurobiol Aging.* (2012) **33**:826.e1–826.e13. doi: 10.1016/j.neurobiolaging.2011.06.005
8. Grady CL, Maisog JM, Horwitz B, Ungerleider LG, Mentis MJ, Salerno JA, et al. Age-related changes in cortical blood flow activation during visual processing of faces and location. *J Neurosci.* (1994) **14**:1450–62. doi: 10.1523/JNEUROSCI.14-03-01450.1994
9. Cao W, Luo C, Zhu B, Zhang D, Dong L, Gong J, et al. Resting-state functional connectivity in anterior cingulate cortex in normal aging. *Front Aging Neurosci.* (2014) **6**:280. doi: 10.3389/fnagi.2014.00280
10. Roski C, Caspers S, Langner R, Laird AR, Fox PT, Zilles K, et al. Adult age-dependent differences in resting-state connectivity within and between visual-attention and sensorimotor networks. *Front Aging Neurosci.* (2013) **5**:67. doi: 10.3389/fnagi.2013.00067
11. Chen Y, Wang W, Zhao X, Sha M, Liu Y, Zhang X, et al. Age-related decline in the variation of dynamic functional connectivity: a resting state analysis. *Front Aging Neurosci.* (2017) **9**:203. doi: 10.3389/fnagi.2017.00203
12. Bäckman L, Lindenberger U, Li SC, Nyberg L. Linking cognitive aging to alterations in dopamine neurotransmitter functioning: recent

data and future avenues. *Neurosci Biobehav Rev.* (2010) **34**:670–7. doi: 10.1016/j.neubiorev.2009.12.008
13. Segobin S, La Joie R, Ritz L, Beaunieux H, Desgranges B, Chételat G, et al. FDG-PET contributions to the pathophysiology of memory impairment. *Neuropsychol Rev.* (2015) **25**:326–55. doi: 10.1007/s11065-015-9297-6
14. Salami A, Wåhlin A, Kaboodvand N, Lundquist A, Nyberg L. Longitudinal evidence for dissociation of anterior and posterior MTL resting-state connectivity in aging: links to perfusion and memory. *Cereb Cortex.* (2016) **26**:3953–63. doi: 10.1093/cercor/bhw233
15. Zarrinkoob L, Ambarki K, Wåhlin A, Birgander R, Eklund A, Malm J. Blood flow distribution in cerebral arteries. *J Cereb Blood Flow Metabol.* (2015) **35**:648–54. doi: 10.1038/jcbfm.2014.241
16. Nyberg L, Andersson M, Kauppi K, Lundquist A, Persson J, Pudas S, et al. Age-related and genetic modulation of frontal cortex efficiency. *J Cogn Neurosci.* (2014) **26**:746–54. doi: 10.1162/jocn_a_00521
17. Du Y, Pearlson GD, Yu Q, He H, Lin D, Sui J, et al. Interaction among subsystems within default mode network diminished in schizophrenia patients: a dynamic connectivity approach. *Schizophr Res.* (2016) **170**:55–65. doi: 10.1016/j.schres.2015.11.021
18. Wong WP, Hassed C, Chambers R, Coles J. The effects of mindfulness on persons with mild cognitive impairment: protocol for a mixed-methods longitudinal study. *Front Aging Neurosci.* (2016) **8**:156. doi: 10.3389/fnagi.2016.00156
19. Qin B, Zhou X, Michael KD, Liu Y, Whittington C, Cohen D, et al. Psychotherapy for depression in children and adolescents: study protocol for a systematic review and network meta-analysis. *BMJ Open.* (2015) **5**:e005918. doi: 10.1136/bmjopen-2014-005918
20. Liu S, Yu W, Lü Y. The causes of new-onset epilepsy and seizures in the elderly. *Neuropsychiatr Disease Treat.* (2016) **12**:1425–34. doi: 10.2147/NDT.S107905
21. Wen D, Zhou Y, Li X. A critical review: coupling and synchronization analysis methods of EEG signal with mild cognitive impairment. *Front Aging Neurosci.* (2015) **7**:54. doi: 10.3389/fnagi.2015.00054
22. Michel CM, Koenig T, Brandeis D, Gianotti LRR, Wackermann J. *Electrical Neuroimaging*. New York, NY: Cambridge University Press (2009).
23. Lehmann D, Ozaki H, Pal I. EEG alpha map series: brain micro-states by space-oriented adaptive segmentation. *Electroencephalogr Clin Neurophysiol.* (1987) **67**:271–88. doi: 10.1016/0013-4694(87)90025-3
24. Khanna A, Pascual-Leone A, Michel CM, Farzan F. Microstates in resting-state EEG: current status and future directions. *Neurosci Biobehav Rev.* (2015) **49**:105–13. doi: 10.1016/j.neubiorev.2014.12.010
25. Lehmann D, Strik WK, Henggeler B, Koenig T, Koukkou M. Brain electric microstates and momentary conscious mind states as building blocks of spontaneous thinking: I. visual imagery and abstract thoughts. *Int J Psychophysiol.* (1998) **29**:1–11. doi: 10.1016/S0167-8760(97)00098-6
26. Fingelkurts AA, Fingelkurts AA, Bagnato S, Boccagni C, Galardi G. EEG oscillatory states as neuro-phenomenology of consciousness as revealed from patients in vegetative and minimally conscious states. *Conscious Cogn.* (2012) **21**:149–69. doi: 10.1016/j.concog.2011.10.004
27. Strik WK, Chiaramonti R, Muscas GC, Paganini M, Mueller TJ, Fallgatter AJ, et al. Decreased EEG microstate duration and anteriorisation of the brain electrical fields in mild and moderate dementia of the alzheimer type. *Psychiatr Res Neuroimag.* (1997) **75**:183–91. doi: 10.1016/S0925-4927(97)00054-1
28. Andreou C, Faber PL, Leicht G, Schoettle D, Polomac N, Hanganu-Opatz IL, et al. Resting-state connectivity in the prodromal phase of schizophrenia: insights from EEG microstates. *Schizophren Res.* (2014) **152**:513–20. doi: 10.1016/j.schres.2013.12.008
29. Zappasodi F, Croce P, Giordani A, Assenza G, Giannantoni NM, Profice P, et al. Prognostic value of EEG microstates in acute stroke. *Brain Topogr.* (2017) **30**:698–710. doi: 10.1007/s10548-017-0572-0
30. Schwab S, Koenig T, Morishima Y, Dierks T, Federspiel A, Jann K. Discovering frequency sensitive thalamic nuclei from EEG microstate informed resting state FMRI. *NeuroImage.* (2015) **118**:368–75. doi: 10.1016/j.neuroimage.2015.06.001
31. Milz P, Faber PL, Lehmann D, Koenig T, Kochi K, Pascual-Marqui RD. The functional significance of EEG microstates-associations with modalities of thinking. *NeuroImage.* (2016) **125**:643–56. doi: 10.1016/j.neuroimage.2015.08.023
32. Van de Ville D, Britz J, Michel CM. EEG microstate sequences in healthy humans at rest reveal scale-free dynamics. *Proc Natl Acad Sci USA.* (2010) **107**:18179–84. doi: 10.1073/pnas.1007841107
33. Koenig T, Prichep L, Lehmann D, Sosa PV, Braeker E, Kleinlogel H, et al. Millisecond by millisecond, year by year: normative EEG microstates and developmental stages. *NeuroImage.* (2002) **16**:41–8. doi: 10.1006/nimg.2002.1070
34. Brunet D, Murray MM, Michel CM. *Spatiotemporal Analysis of Multichannel EEG: CARTOOL*. Computational Intelligence and Neuroscience (2011).
35. Murray MM, Brunet D, Michel CM. Topographic ERP analyses: a step-by-step tutorial review. *Brain Topogr.* (2008) **20**:249–64. doi: 10.1007/s10548-008-0054-5
36. Javed E, Croce P, Zappasodi F, Gratta CD. Hilbert spectral analysis of EEG data reveals spectral dynamics associated with microstates. *J Neurosci Methods.* (2019) **325**:108317. doi: 10.1016/j.jneumeth.2019.108317
37. Sandoval S, De Leon PL. Theory of the hilbert spectrum. *ArXiv.* (2015) 1–61. Available online at: https://arxiv.org/abs/1504.07554v4
38. Huang NE, Shen Z, Long SR, Wu MC, Shih HH, Zheng Q, et al. The empirical mode decomposition and the hilbert spectrum for nonlinear and non-stationary time series analysis. *Proc Royal Soc Lond A.* (1998) **495**:903–95. doi: 10.1098/rspa.1998.0193
39. Seitzman BA, Abell M, Bartley SC, Erickson MA, Bolbecker AR, Hetrick WP. Cognitive manipulation of brain electric microstates. *NeuroImage.* (2017) **146**:533–43. doi: 10.1016/j.neuroimage.2016.10.002
40. Britz J, Van De Ville D, Michel CM. BOLD correlates of EEG topography reveal rapid resting-state network dynamics. *NeuroImage.* (2010) **52**:1162–70. doi: 10.1016/j.neuroimage.2010.02.052
41. Katayama H, Gianotti LR, Isotani T, Faber PL, Sasada K, Kinoshita T, et al. Classes of multichannel EEG microstates in light and deep hypnotic conditions. *Brain Topogr.* (2007) **20**:7–14. doi: 10.1007/s10548-007-0024-3
42. Brodbeck V, Kuhn A, von Wegner F, Morzelewski A, Tagliazucchi E, Borisov S, et al. EEG microstates of wakefulness and NREM sleep. *NeuroImage.* (2012) **62**:2129–39. doi: 10.1016/j.neuroimage.2012.05.060
43. Mantini D, Perrucci MG, Del Gratta C, Romani GL, Corbetta M. Electrophysiological signatures of resting state networks in the human brain. *Proc Natl Acad Sci USA.* (2007) **104**:13170–75. doi: 10.1073/pnas.0700668104
44. Otsuka Y, Osaka N, Morishita M, Kondo H, Osaka M. Decreased activation of anterior cingulate cortex in the working memory of the elderly. *NeuroReport.* (2006) **17**:1479–82. doi: 10.1097/01.wnr.0000236852.63092.9f
45. Kalpouzos G, Chételat G, Baron JC, Landeau B, Mevel K, Godeau C, et al. Voxel-based mapping of brain gray matter volume and glucose metabolism profiles in normal aging. *Neurobiol Aging.* (2009) **30**:112–24. doi: 10.1016/j.neurobiolaging.2007.05.019
46. Good CD, Johnsrude IS, Ashburner J, Henson RN, Friston KJ, Frackowiak RS. A voxel-based morphometric study of ageing in 465 normal adult human brains. *NeuroImage.* (2001) **14**:21–36. doi: 10.1006/nimg.2001.0786
47. Cabeza R. Hemispheric asymmetry reduction in older adults: the HAROLD model. *Psychol Aging.* (2002) **17**:85–100. doi: 10.1037/0882-7974.17.1.85
48. Schaefer A, Margulies DS, Lohmann G, Gorgolewski KJ, Smallwood J, Kiebel SJ, et al. Dynamic network participation of functional connectivity hubs assessed by resting-state FMRI. *Front Hum Neurosci.* (2014) **8**:195. doi: 10.3389/fnhum.2014.00195
49. Davis SW, Dennis NA, Daselaar SM, Fleck MS, Cabeza R. Qué PASA? The posterior-anterior shift in aging. *Cereb Cortex.* (2008) **18**:1201–9. doi: 10.1093/cercor/bhm155

Conflict of Interest: The authors declare that the research has been conducted independent of any financial or commercial interests.

Copyright © 2020 Javed, Croce, Zappasodi and Del Gratta. This is an open-access article distributed under the terms of the Creative Commons Attribution License (CC BY). The use, distribution or reproduction in other forums is permitted, provided the original author(s) and the copyright owner(s) are credited and that the original publication in this journal is cited, in accordance with accepted academic practice. No use, distribution or reproduction is permitted which does not comply with these terms.

frontiers in Systems Neuroscience

ORIGINAL RESEARCH
published: 17 April 2020
doi: 10.3389/fnsys.2020.00020

Ghost Attractors in Spontaneous Brain Activity: Recurrent Excursions Into Functionally-Relevant BOLD Phase-Locking States

Jakub Vohryzek[1,2], Gustavo Deco[3,4,5,6], Bruno Cessac[7], Morten L. Kringelbach[1,2] and Joana Cabral[1,2,8]**

[1] Department of Psychiatry, University of Oxford, Oxford, United Kingdom, [2] Center for Music in the Brain, Department of Clinical Medicine, Aarhus University, Aarhus, Denmark, [3] Center for Brain and Cognition, Computational Neuroscience Group, Universitat Pompeu Fabra, Barcelona, Spain, [4] Department of Neuropsychology, Max Planck Institute for human Cognitive and Brain Sciences, Leipzig, Germany, [5] Institució Catalana de Recerca i Estudis Avançats (ICREA), Barcelona, Spain, [6] Turner Institute for Brain and Mental Health, Monash University, Melbourne, VIC, Australia, [7] Biovision Team, Université Côte d'Azur, Inria, France, [8] Life and Health Sciences Research Institute, School of Medicine, University of Minho, Braga, Portugal

OPEN ACCESS

Edited by:
Spase Petkoski, INSERM U1106 Institut de Neurosciences des Systèmes, France

Reviewed by:
Wesley Clawson, INSERM U1106 Institut de Neurosciences des Systèmes, France
Brandon Robert Munn, The University of Sydney, Australia

***Correspondence:**
Jakub Vohryzek
jakub.vohryzek@queens.ox.ac.uk
Joana Cabral
joanacabral@med.uminho.pt

Received: *07 December 2019*
Accepted: *25 March 2020*
Published: *17 April 2020*

Citation:
Vohryzek J, Deco G, Cessac B, Kringelbach ML and Cabral J (2020) Ghost Attractors in Spontaneous Brain Activity: Recurrent Excursions Into Functionally-Relevant BOLD Phase-Locking States. Front. Syst. Neurosci. 14:20. doi: 10.3389/fnsys.2020.00020

Functionally relevant network patterns form transiently in brain activity during rest, where a given subset of brain areas exhibits temporally synchronized BOLD signals. To adequately assess the biophysical mechanisms governing intrinsic brain activity, a detailed characterization of the dynamical features of functional networks is needed from the experimental side to constrain theoretical models. In this work, we use an open-source fMRI dataset from 100 healthy participants from the Human Connectome Project and analyze whole-brain activity using Leading Eigenvector Dynamics Analysis (LEiDA), which serves to characterize brain activity at each time point by its whole-brain BOLD phase-locking pattern. Clustering these BOLD phase-locking patterns into a set of k states, we demonstrate that the cluster centroids closely overlap with reference functional subsystems. Borrowing tools from dynamical systems theory, we characterize spontaneous brain activity in the form of trajectories within the state space, calculating the Fractional Occupancy and the Dwell Times of each state, as well as the Transition Probabilities between states. Finally, we demonstrate that within-subject reliability is maximized when including the high frequency components of the BOLD signal (>0.1 Hz), indicating the existence of individual fingerprints in dynamical patterns evolving at least as fast as the temporal resolution of acquisition (here $TR = 0.72$ s). Our results reinforce the mechanistic scenario that resting-state networks are the expression of erratic excursions from a baseline synchronous steady state into weakly-stable partially-synchronized states - which we term ghost attractors. To better understand the rules governing the transitions between ghost attractors, we use methods from dynamical systems theory, giving insights into high-order mechanisms underlying brain function.

Keywords: LEiDA, ghost attractors, dynamic functional connectivity, dynamical system theory, functional networks, resting-state

INTRODUCTION

For healthy human cognition, the brain needs to engage in functionally meaningful activity through an integration of information incoming from various segregated brain areas (Tononi and Edelman, 1998; Sporns et al., 2000). At rest, brain activity has been shown to reveal the spontaneous activation of meaningful functional subsystems, sharing spatial features with networks of brain areas typically activated during task (Beckmann et al., 2005; Fox et al., 2005; Damoiseaux et al., 2006). These spatially activated coalitions of brain regions, dubbed resting-state networks (RSNs), have been remarkably consistent across neuroimaging studies and utilized in describing functional changes in disruptions to the healthy brain functioning (Greicius, 2008; Fox and Greicius, 2010; van den Heuvel and Hulshoff Pol, 2010; Vargas et al., 2013; Kaiser et al., 2015). However, while RSNs represent spatially meaningful information, in order to further investigate the generative mechanisms of RSNs and their functional role, it is important to further characterize their behavior in the temporal domain (Preti et al., 2016; Cabral et al., 2017b).

Indeed, recent advances have focused on how these spatially coherent functional patterns can explain the complex brain dynamics evolving in time (Chang and Glover, 2010; Hutchison et al., 2013; Allen et al., 2014). However, the most appropriate way to characterize network dynamics at the whole brain level is still unclear. The most common approach to dynamic functional connectivity (dFC) has been the sliding-window method, which describes statistical relationship between brain regions in successive intervals of time and generates recurrent states of functional connectivity using unsupervised learning (Hutchison et al., 2013; Allen et al., 2014; Calhoun et al., 2014). However, the choice of the "window" size introduces limitations which hinders the temporal resolution as well as statistical validation (Hindriks et al., 2016; Preti et al., 2016). To overcome these caveats, recent development has focused on describing single frame functional connectivity [FC(t)] either by considering BOLD co-activations (Karahanoğlu and Van De Ville, 2015; Tagliazucchi et al., 2016) or BOLD phase coherence (Glerean et al., 2012; Cabral et al., 2017b). Framewise co-activation analysis considers the brain regions with BOLD signal above a certain threshold before clustering into distinct FC patterns (Karahanoğlu and Van De Ville, 2015; Tagliazucchi et al., 2016). While it allows for higher temporal resolution, it is still dependent on the choice of the threshold as well as limited to describing simultaneous (in-phase) activations. On the other hand, phase coherence techniques represent the time instances as relative phase relationships between brain regions and thus do not require thresholding and are sensitive to phase-shifted patterns (Glerean et al., 2012; Cabral et al., 2017b)

To overcome issues with high data dimensionality, Cabral and colleagues have proposed to represent the instantaneous relationships between brain regions using the largest magnitude eigenvector of BOLD phases (a *1xN* vector for each time point) instead of the *NxN* phase synchronization matrix (Cabral et al., 2017b). Notably, Leading Eigenvector Dynamic Analysis (LEiDA) has been shown not only to improve clustering performance, but to consistently capture meaningful BOLD phase-locking states (PL-states) that closely overlap with previously-described functional subsystems (Cabral et al., 2017b; Figueroa et al., 2019; Lord et al., 2019). By representing whole-brain activity over time as a succession of discrete PL states, it is possible to quantify the fractional occupancy, the probability of transition as well as the Dwell Time of individual states. Importantly, these measures have shown to be significantly related with cognitive performance (Cabral et al., 2017b), to be altered in clinical populations of patients suffering with major depressive disorder (Figueroa et al., 2019), as well as to describe the network-specific modulation of resting-state activity by the psychoactive compound psilocybin (Lord et al., 2019). As such, LEiDA opens up as a useful tool to quantitatively characterize individual fingerprints in dynamic functional connectivity, reinforcing a mechanistic scenario proposed by theoretical works where RSNs are the expression of a repertoire of BOLD FC configurations emerging from complex non-linear interactions in the whole-brain network (Ghosh et al., 2008; Cabral et al., 2011; Deco and Jirsa, 2012; Deco et al., 2013; Haimovici et al., 2013; Hansen et al., 2015).

Here, we explore this mechanistic hypothesis using the mathematical formalism from dynamical systems theory and Markov chains in order to characterize the spatio-temporal dynamics of spontaneous brain activity in terms of probabilistic trajectories between recurrent BOLD phase-locking patterns. We validate the functional role of the patterns obtained by comparing them with known RSNs. Furthermore, we evaluate the stability of BOLD phase locking states based on their Fractional Occupancy, Dwell Times and Transition probabilities. While previous works have applied LEiDA to condition-specific datasets, with reduced sample sizes, here we make secondary use of a large open source dataset of healthy participants, demonstrating the reliability of the yielded metrics across subjects and consecutive fMRI recording sessions.

MATERIALS AND METHODS

Data

All data used in this work comes from a publicly available database – the Human Connectome Project, WU-Minn Consortium (Principal Investigators: David Van Essene and Kamil Ugurbil; 1U54MH091657) with funding from the sixteen NIH Institutes and Centers supporting the NIH Blueprint for Neuroscience Research; and by the McDonell Center for Systems Neuroscience at Washington University.

Participants

100 unrelated subjects (mean age 29.5 years old, 55% females (Glasser et al., 2013)).

Neuroimaging HCP Acquisition

Each participant underwent four resting-state fMRI sessions lasting 14 min 30 s with a repetition time (TR) of 0.72 s, on a 3-T connectome Skyra scanner (Siemens) – two during the first

day and two during the second day. The 2 fMRI sessions acquired on the same day differ only in the oblique axial acquisition phase encoding, one being from Left to Right (LR) and the other from Right to Left (RL). The acquisition and pre-processing of the data is fully described in detail at the HCP website https://www.humanconnectome.org/. Here, we used the fMRI data acquired on the first day of scanning. One subject was excluded because one session was missing. In total, two same-day resting-state fMRI sessions from 99 of the 100 unrelated subjects' sessions were used for the analysis.

Parcellation

To reduce the dimensionality of the voxel-based data (Voxels × Time), the Anatomic Automatic Labeling (AAL) atlas was used to define N = 90 anatomically distinct cortical and sub-cortical regions covering the whole brain, excluding the cerebellum. Data was reduced to size N × Time, with Time = 1200 TR per session, by averaging the BOLD signals in all the voxels associated to each brain region (**Figure 1A**).

Analysis

BOLD Phase Dynamics

To compute the phase relationship between brain regions, for each region n with $n = 1...N$, a BOLD phase $\theta(n, t)$ varying in time t, was calculated via Hilbert transform (Glerean et al., 2012). The analytical signal expresses the regional signal $x(t)$ as $x(t) = A(t) * \theta(t))$ with A and θ representing the time-varying amplitude and phase respectively (**Figure 1C**). The first and last time points were removed from each time series, to exclude the boundary artifacts induced by the Hilbert transform. Subsequently, for every pair of brain regions n and m at time t the phase coherence matrix dPC is calculated as follows: $dPC\,(n, m, t) = cos(\theta\,(n, t) - \theta(m, t))$, where $cos\,(0) = 1$ represents the case when the two brain areas n and m are aligned at time t (**Figure 1E**). Conversely $cos\,(\pi) = -1$ indicates the two brain areas $nandm$ to be anti-aligned at time t. Lastly, $cos\,(\pi/2) = 0$ shows the two brain areas n and m at time t to be orthogonal to each other and therefore their phase relationship being 0.

Phase Dynamics Leading Eigenvector

We used LEiDA, where only the $1xN$ leading eigenvector $V_1(t)$ of the dPC is considered in the analysis, to describe the phase coherence pattern of the (NxN) $dPC(t)$ at every time-point t with reduced dimensionality. In other words, we calculated the eigendecomposition of dPC(t) at every time t [$dPC(t) = V(t)D(t)V^{-1}(t)$, where columns of $V(t)$ are the corresponding eigenvectors of $dPC(t)$ and $D(t)$ is the diagonal matrix of the eigenvalues of $dPC(t)$, and we took the first (most dominant) eigenvector$V_1(t)$ to represent the BOLD PL pattern at each time point with size $1xN$. Since $dPC(t)$ is symmetric, its eigenvectors are orthogonal ($V^{-1}(t) = V(t)^T$) and the eigenvalues are real. Each element in the eigenvector can be associated to a specific brain area (i.e., in **Figures 1B–D** each brain area is colored according to its sign in $V_1(t)$). The NxN dominant connectivity pattern at every time t captured by $V_1(t)$ can simply be retrieved by calculating the matrix product of the eigenvector with its transpose as $V_1(t) * V_1^T(t)$ (Cabral et al., 2017b).

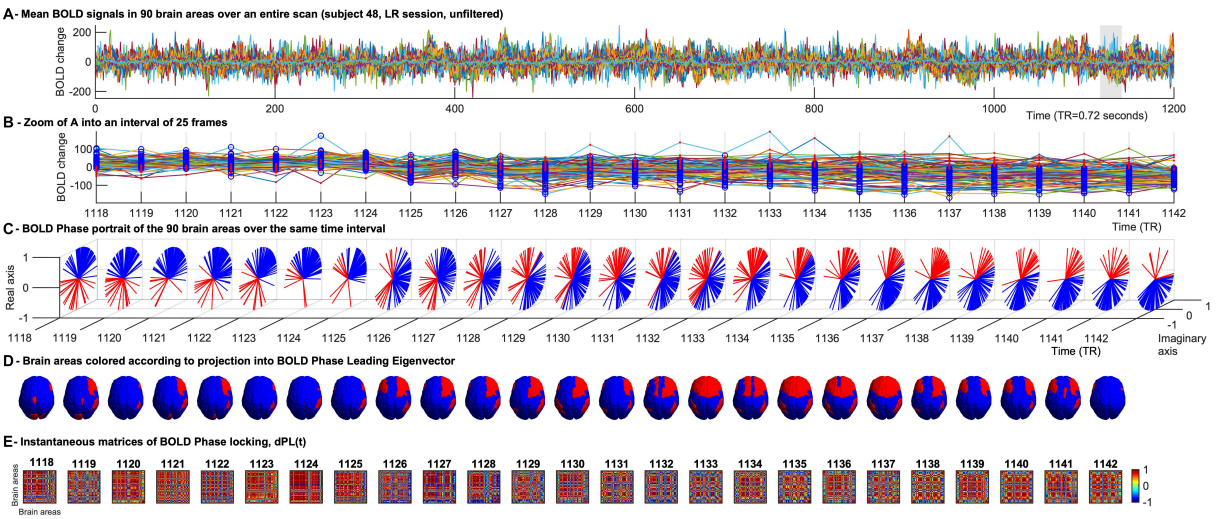


FIGURE 1 | Time-evolving patterns of BOLD Phase Dynamics. **(A)** BOLD signals from a representative fMRI scan of the HCP dataset averaged over all voxels within each region of interest (ROI). ROIs were defined using an anatomically-based parcellation scheme (AAL) covering the entire brain (here excluding the cerebellum). **(B)** To illustrate BOLD phase dynamics, we select a representative interval of TRs. At each TR, blue circles represent the brain areas whose BOLD phase projects into the main BOLD phase direction (captured by the leading eigenvector, see **(C)**, and red dots represent the brain areas whose BOLD phase project into the opposite direction of the main BOLD phase orientation. It serves to illustrate that the phase-shifted signals (in red) do not directly correspond to supra-threshold BOLD increases. **(C)** Phase portraits of the analytic BOLD signal at each TR, where the real and imaginary axis represent the cosines and sines of the Hilbert phase at each TR. **(D)** Representation of the brain patterns captured by the signs of the leading eigenvector at each TR, illustrating how phase-locking patterns evolve smoothly over several TRs, whereas the corresponding BOLD signals (shown in panel **B**) exhibit significantly different activation patterns over the same range of TRs. **(E)** Representation of the instantaneous phase coherence matrices obtained at each TR as the cosine of the phase difference at each instant of time.

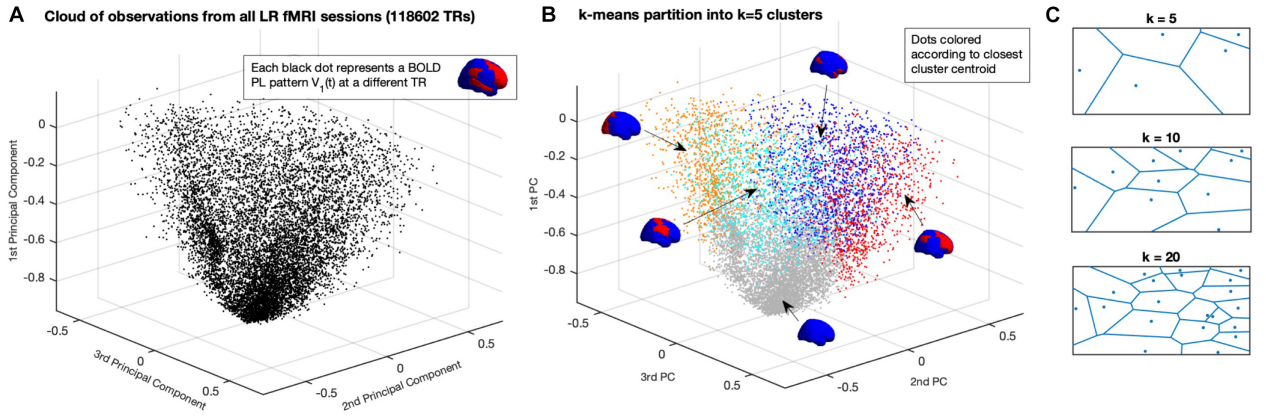


FIGURE 2 | Partition of the *N*-dimensional phase space into a K-dimensional state-based space. **(A)** Representation of all BOLD PL patterns captured at each TR in a reduced 3-dimensional perspective of the phase space. Since each observation is a 1xN vector - corresponding to the leading eigenvector of BOLD phases at each TR - the full phase space is *N*-dimensional, where $N = 90$ is the number of ROIs used to parcellate the brain). Each dot corresponds to one fMRI volume recorded over time (TR = Repetition Time = 0.72 s). Dots are placed according to their cosine distance with respect to the first three principal components (i.e., the first 3 eigenvectors of the covariance matrix) of all observations. **(B)** Partition of the Phase Space using *K*-means clustering decomposes the space of observations into k clusters, where each observation from an fMRI experiment is assigned to a cluster given its closest proximity to the corresponding centroid. The centroids obtained for K = 5 are represented by coloring each brain area using the same color scheme as in **Figure 1**, representing distinct whole-brain BOLD phase-locking patterns. **(C)** Illustration of the partition of a 2D plane into k Voronoi cells, where each point in a given cell is closer to its centroid than to any other centroid.

With the aforementioned reduction, whole-brain activity at each time point t is represented by a *1xN* vector, where N is the number of brain regions defined by the applied parcellation. Each vector $V_1(t)$ can be seen as an observation of the dynamical system and can be represented as a point in a N-dimensional space R^N (in **Figure 2A**, represented in R^3 for illustration). Each fMRI experiment is thus characterized by a trajectory of the leading eigenvector V_1 in this N-dimensional space. To get a graphical representation (**Figures 2A,B**), we project each vector $V_1(t)$ on the space determined by the first three principal components of all V_1s, (i.e., the x, y, and z coordinates are given by the cosine distance between each *1xN* $V_1(t)$ and the first 3 *Nx1* eigenvectors of the *NxN* covariance matrix of all V_1s (with size *NxT*).

Partition of Phase Space

In order to achieve a state-based representation, the leading eigenvectors obtained from all 99 participants in the Left-Right (LR) fMRI scanning session - corresponding to a total of $T = 118602$ observations (99×1198 TRs) with $N = 90$ dimensions each - are partitioned into a set of discrete states. Importantly, we do not include in this partition the Right-Left (RL) fMRI scanning sessions from the same 99 participants recorded on the same day, which will serve to test the validity and consistency of the results, as described in the following section.

Given the large number of observations in this dataset, clustering algorithms relying on the *TxT* similarity matrix had to be discarded because of limited computational resources (i.e., computing our *TxT* matrix requires >100 GB of RAM). Instead, we use the k-means algorithm, which relies on an iterative process to find the solution that minimizes the distance between each (*1xN*) observation and the closest 1xN cluster centroid (we note that, given the large number of dimensions, we use the Cosine distance, which significantly reduces the computation time with respect to City Block or Euclidean distances). As such, *k*-means algorithm is used to iteratively cluster the leading eigenvectors into $k = 2$ to $k = 20$ clusters (resulting in 19 partitions), repeating each calculation 100 times to ensure stability in the results. Since each observation represents a time point, the output vector of cluster assignments - where each observation is assigned to its closest *1xN* cluster centroid$\alpha = 1...k$ - can be approached as a trajectory $\underline{x}(t)$ in state space.

In **Figure 2** we show how the *k*-means clustering algorithm divides the phase-space (here represented in only three dimensions for illustration) into $k = 5$ (Voronoi) cells, where each location in the phase space is assigned to the closest centroid. Using colors to represent the regions of the phase space assigned to each cluster R^α, we represent in **Figure 2B** the same observations from panel A, but highlighting the cluster assignment at each time point. Although the 3-dimensional representation serves to illustrate the partition of the phase-space, there is a clear overlap of colors given that the phase-space, defined in $N = 90$ dimensions, cannot be adequately represented in three dimensions only. To illustrate the decomposition into k-means clustering algorithm we show, in **Figure 2C**, the partition of a 2D plane into k Voronoi cells, where each region in space is assigned to the closest centroid.

Each cluster R^α(with $\alpha = 1...k$) is now represented by its cluster centroid $V_{c\alpha}$, each corresponding to a distinct BOLD phase-locking state (which will be described in detail in the section "Results"). To assess the quality of the cluster separation, the silhouette value is computed for each k, which estimates how similar each observation $V_1(t)$ is to its own cluster compared to other clusters.

Comparison to Reference Intrinsic Functional Networks

The existence of functionally interconnected subsystems, where subsets of brains areas consistently activate together even during rest, has been widely explored in studies of resting-state functional connectivity. Intrinsic Functional Networks, typically assessed using correlation analysis, have been consistently detected in large cohorts of resting-state fMRI experiments (Yeo et al., 2011), but the analysis of their temporal dynamics has been hindered by the methods used to assess them, namely sliding window methods with their choice of the window over which connectivity is computed (Hindriks et al., 2016).

Here, we verify if the centroids obtained from clustering BOLD phase leading eigenvectors obtained at TR resolution share spatial similarities with the seven cerebral intrinsic functional networks estimated by Yeo et al. (2011) clustering correlation-based functional connectivity between 1175 regions of interest from 1000 participants.

To do so - and since our BOLD PL centroids V_α are defined in AAL parcellation - we take the mask of the Yeo parcellation into seven non-overlapping functional networks defined in MNI152 space[1] and the mask of the AAL parcellation in the same MNI152 space, and calculate, for each of the 90 AAL brain areas, the proportion of voxels assigned to each of the seven functional networks, obtaining in this way 7 1 × 90 vectors representing the intrinsic functional networks in AAL space.

Subsequently, we compute the Pearson's correlation (with associated p-values) between these seven networks and the centroids V_α obtained from our clustering analysis across the whole range of k explored (setting all negative values of the centroids' vectors to zero, to consider only the areas whose BOLD phase is shifted from the main orientation).

Projection of the Validation Dataset Into the Same State Space

We used the second fMRI scanning session from each of the 99 participants recorded on the same day as the primary dataset - differing only in the oblique axial acquisition phase encoding, being Right to Left (RL) instead of Left to Right (LR) - to verify the validity and consistency of the partition performed in the previous session. To do so, we obtained all the *1xN* leading eigenvectors from the the Right-Left (RL) scanning session - totaling 118602 observations (1198 TRs × 99 subjects) - using the same methodology as before, but instead of running the k-means algorithm, we compute the cosine distance between each *1xN* eigenvector $V_1(t)$ and the k *1xN* cluster centroids $V_{c\alpha}$ obtained from the previous analysis, and define the trajectory vector $\underline{x}(t)$ by assigning each $V_1(t)$ to its closest cluster centroid $V_{c\alpha}$.

Fractional Occupancy

Following the cluster partition into k PL states evolving in time t, the probabilities - or fractional occupancies - $\Pi_\alpha^{(S)}$ associated to each PL state α and each scan S, can be calculated as follows:

$$\Pi_\alpha^{(S)} = \frac{1}{T}\sum_{t=1}^{T} \chi\left[\underline{x}(t) \in R^\alpha\right] \quad (1)$$

where χ is the indicator function - $\chi(A) = 1$ if the event A is true, and $\chi(A) = 0$ otherwise, and T = 1198 is the number of time points (TRs) corresponding to each fMRI scan *(S)*. In other words, the equation counts the number of times when the trajectory $\underline{x}(t)$ is assigned to each of the defined clusters $R^{(\alpha)}$, divided by the total number of time points T. Furthermore, given that participants are constantly in resting state - i.e. without performing any task -, we assume stationarity in the data within each scan (justifying the time average in Eq. 1). Cluster probabilities are estimated separately for each individual fMRI scan.

Dwell Time

To describe the average time periods when a given PL state α is being visited in each fMRI scan S, the Dwell Time $DT_\alpha^{(S)}$ is defined as the mean of all the consecutive periods of each state, i.e.,

$$DT_\alpha^{(S)} = \frac{1}{p_\alpha}\sum_{1}^{p_\alpha} C_{p_\alpha} \quad (2)$$

where DT_α is the Dwell Time of PL state α, p_α is the number of consecutive periods assigned to PL state α and C_{p_α} is the duration of each consecutive period.

Markov Chain Transition Probabilities

Following the same rational as in Eq.1, the definition of the probability $\Pi_{\alpha\beta}$ to be in the PL state α at time bin t and in the PL state β at time bin t + 1 can be written as follows:

$$\Pi_{\alpha\beta}^{(S)} = \frac{1}{T-1}\sum_{t=1}^{T-1} \chi[\underline{x}(t) \in R^\alpha, \underline{x}(t+1) \in R^\beta] \quad (3)$$

and thus, the transition probability matrix $W_{\alpha\beta}^{(S)}$ of each fMRI scan S is defined as:

$$W_{\alpha\beta}^{(S)} = P[\underline{x}(t+1) \in R^\beta \mid \underline{x}(t) \in R^\alpha] = \frac{\Pi_{\alpha\beta}^{(S)}}{\Pi_\alpha^{(S)}}. \quad (4)$$

$W_{\alpha\beta}$ defines the transition matrix from state alpha to state beta. This defines an homogeneous Markov chain, characterizing the transition between BOLD phase locking states. The transition probability matrix $W_{\alpha\beta}^{(S)}$ is estimated separately for each scan S. To each matrix $W_{\alpha\beta}^{(S)}$ is associated a transition graph with an oriented arrow from α to β if $W_{\alpha\beta}^{(S)} > 0$ (see **Supplementary Figures S2–S4**). To illustrate the transitions at the group level, we represent the transition graph of the average transition matrix $W_{\alpha\beta}$ across all scans in the LR sessions.

Intra-Class Correlation

In order to calculate the reliability of the computed measures between the LR and RL fMRI sessions recorded on the same day, we calculated the Inter-Class Correlation (ICC) (Landis and

[1] surfer.nmr.mgh.harvard.edu/fswiki/CorticalParcellation_Yeo2011

Koch, 1977; Xing and Zuo, 2018). ICC describes the proportion of within-subject variability versus between-subject variability across recording conditions as follows:

$$ICC = \frac{MSE_b - MSE_w}{MSE_b + MSE_w}, \quad (5)$$

where MSE_w and MSE_b are the within-subject and between-subject mean squared errors, respectively (Xing and Zuo, 2018). Positive ICC values (i.e., when within-subject MSE is smaller than the between-subject MSE) indicate individual reliability, which, depending on its value, is categorized as low ($0 < ICC < 0.2$), fair ($0.2 < ICC < 0.4$), moderate ($0.4 < ICC < 0.6$), substantial ($0.6 < ICC < 0.8$) and almost perfect ($0.8 < ICC < 1$) (Landis and Koch, 1977).

Effects of Low-Pass Temporal Filtering

A typical step in the pre-procession of fMRI resting-state data is the application of a low-pass filter to exclude high frequency noise in the BOLD signal (typically < 0.1 Hz). However, given that BOLD signals are already averaged over all voxels within each brain area - which should improve the signal-to-noise ratio-, and given the instantaneous nature of our dynamic analysis, we performed our first analysis directly on the unfiltered BOLD signals recorded at a TR of 0.72 s, corresponding to a Nyquist frequency of fNq = 1/2TR = 0.694 Hz.

To verify whether the higher frequency components in the BOLD signal are meaningful for the dynamic analysis of functional networks, we apply a 2nd order Butterworth band-pass filter to the ROI-averaged BOLD signals - before computing LEiDA and clustering into $k = 5$ states - varying the low-pass cut-off frequency to 0.07, 0.1, 0.2 or 0.6944 Hz, while keeping the lower high-pass frequency limit at 0.01 Hz (to exclude only the ultra-slow signal drifts from the scanner). ICC measures were subsequently calculated for the corresponding Dwell Times, Fractional Occupancy and Transition Probabilities obtained.

RESULTS

Phase-Locking States Reveal Relevant Functional Networks

We obtain a set of BOLD phase-locking patterns from the first session of resting-state fMRI of 99 unrelated subjects using the LEiDA approach (see section "Materials and Methods" for details). Each BOLD phase-locking pattern is represented as a vector with N elements, each element representing the projection of the BOLD phase of a brain area into the leading eigenvector of all BOLD phases (here $N = 90$ since we use the 90 non-cerebellar brain regions from the AAL atlas).

Firstly, we verify the overlap between the BOLD phase-locking states obtained across clustering solutions (with $2 < k < 20$) to seven intrinsic functional networks defined in the literature (Yeo et al., 2011). In **Figure 3**, we report for all partitions into k states (rows), the k cluster centroids obtained (columns). The cluster centroids $V_{c\alpha}$(representing BOLD phase-locking states) are represented in the brain by coloring only the brain areas whose BOLD phase projects in the opposite direction from the main orientation of BOLD phases (negative elements in $V_{c\alpha}$). BOLD phase locking states are color-coded according to the most significantly correlated RSN used as reference (shown in panel B), given a corrected threshold of $p < 0.05/k$, and in black otherwise. The same Figure is shown from a top view perspective in **Supplementary Figure S1**.

Sorting the states according to their probability of occurrence, we find consistently across clustering solutions a most prevalent state, occupying the first column of **Figure 3**, in which the BOLD phase of all brain areas project into the same direction. Since it does not reveal the separation of any particular subsystem, and does not significantly overlap with any reference functional network, this so-called global state (state 1) is represented as a transparent brain.

The remaining states are all characterized by a phase shift in the BOLD signal of a given subset of brain areas, which are highlighted as colored patches. Notably, most of the obtained cluster centroids demonstrate a close statistical similarity to reference functional networks, revealing a strong and highly significant overlap (up to $r = 0.89$, with p-values down to10^{-30}) with the different RSNs used as reference. We also find that some partitions show different PL states overlapping with the same reference RSN. When no significant overlap is found, the patches are colored in black. One example is the second most prominent state appearing in all clustering solutions with $k > 7$, which involves regions of basal ganglia, which have been omitted in the analysis of functional networks from Yeo et al. (2011).

We chose to focus on the clustering solution with $k = 5$ within the range of best clustering performance according to the silhouette value (**Figure 3C**), as it reveals a meaningful partition of the BOLD PL patterns into four representative functional networks. For $k = 5$ we found State 2 to correlate with the Default Mode Network ($r = 0.71$, $p = 10^{-14}$), State 3 to correlate with the Fronto-parietal Network ($r = 0.84$, $p = 10^{-21}$), State 4 to correlate with the Visual Network ($r = 0.88$, $p = 10^{-29}$) and finally State 5 to mostly correlate with the Ventral Attention Network ($r = 0.71$, $p = 10^{-14}$). In **Supplementary Figures S5, S6**, we also report the overlap of cluster centroids with reference functional brain networks obtained for the filtered series (0.04–0.07 Hz) both from top and side view.

Exploration of a Repertoire of BOLD Phase Locking States

In **Figure 4**, we show the different representations of the BOLD PL states and their properties. Each PL state is represented in two ways: on the left we plot the $N = 90$ vector elements as arrows representing the magnitude of projection of each brain area into the leading eigenvector of BOLD phases V_1 and on the right by rendering and coloring the brain regions shifted from the main orientation (corresponding to the red arrows on the left) according to the relevant functional system to which they maximally overlap with (**Figures 4A,E**).

The PL states can also be represented in the form of a matrix by computing the matrix product of each centroid's vector $V_{c\alpha}$ and its transpose, describing the pairwise relationship between individual brain regions in each PL state (**Figure 4B**).

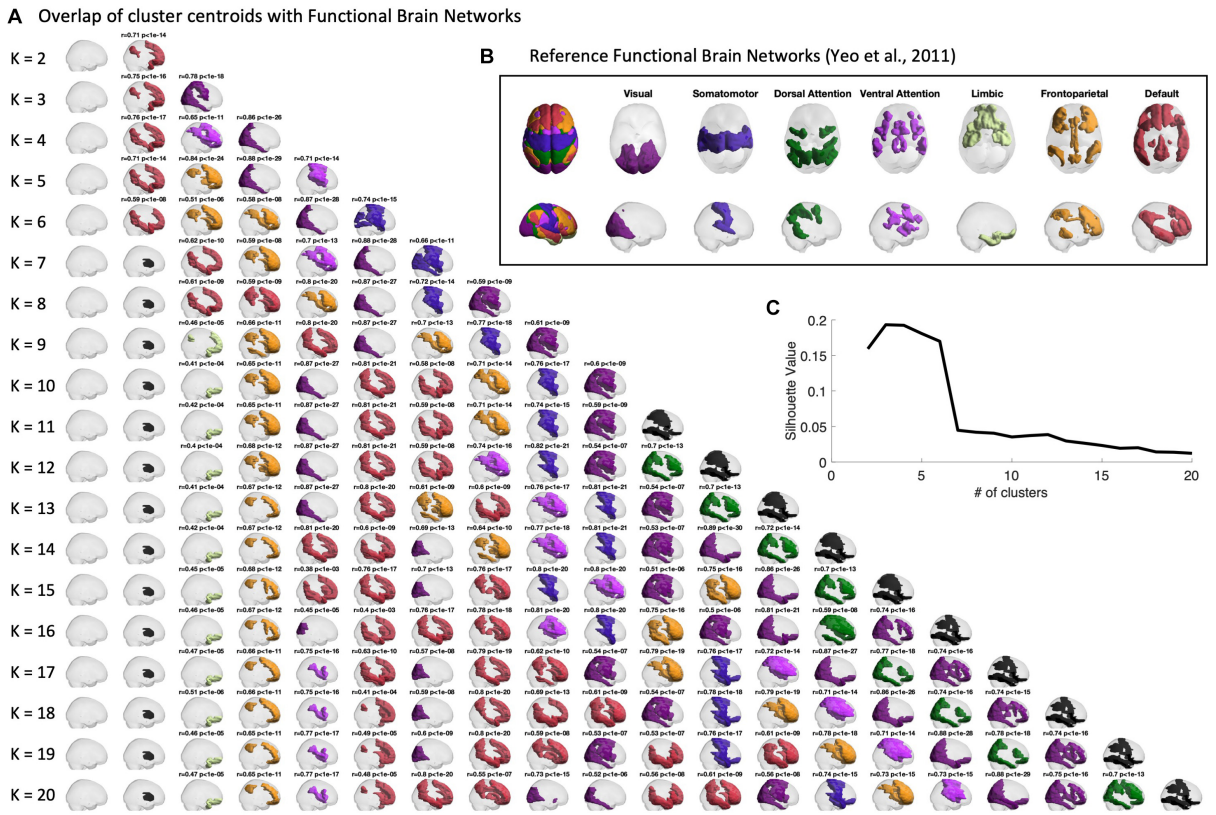


FIGURE 3 | Centroids overlap with Functional Brain Networks. **(A)** Representation of the centroids obtained for each k-means clustering solution with K ranging between 2 and 20. Centroids are represented in cortical space, rendering only the ROIs whose BOLD phase is shifted $> \pm\pi/2$ with respect to the leading direction. ROIs are colored according to the reference Functional Brain Network (shown in panel **B**) to which they most significantly relate with. Pearson's r and corresponding *p*-value are reported as a title only when surviving a conservative threshold of $p < 0.05/K$, to correct for the number of independent hypotheses tested in each partition model. Centroids not significantly overlapping with any of the reference functional networks are colored in black. Side views of the same centroids are reported in **Supplementary Figure S1**. **(B)** Reference functional brain networks estimated from 1000 subjects from correlation-based intrinsic functional connectivity (Yeo et al., 2011). **(C)** Silhouette value, used to evaluate clustering performance, shows a peak for partitions into 2 to 6 clusters.

Assuming stationarity of the brain's dynamical regime during rest, we compute the probability of occurrence of PL states as well as their mean Dwell Time within each fMRI scan (see section "Materials and Methods"). In **Figures 4C,D**, we show the probabilities of occurrence and mean Dwell Times of each PL state obtained for each participant, plotting the values obtained from the first fMRI session (LR) versus the values obtained from the second same-day fMRI session (RL). We find that, in both LR and RL sessions, State 1 shows high variability both in terms of probability of occurrence (mean = 0.51, standard deviation (std) = 0.16) and Dwell Times (mean = 3.94 s, std = 1.73 s), with some subjects spending as little as 20% of the time in this globally coherent state, whereas others spend up to 80% of the time, with some occurrences lasting up to 10 s (the reliability of metrics across recordings will be addressed in a following section). Interestingly, the other 4 states show consistently lower probabilities of occurrence, with state 2 (overlapping with the DMN) occurring on average 16.6 ± 7.6% of the time (mean ± std), being slightly more prevalent than the other states (state 3: 12.7 ± 6.2%; state 4: 9.9 ± 4.7%; state 5: 9.5 ± 5.5%). Not only do these functionally relevant PL patterns occur less often, but they also show, consistently across subjects, much shorter Dwell Times, lasting on average around 2 TRs (state 2, 1.71 ± 0.34 s; state 3 1.57 ± 0.37 s; state 4, 1.4 ± 0.34 s; state 5, 1.3 ± 0.22 s).

In **Figure 4E**, we report the correlation between each PL state and the seven intrinsic functional networks used as reference (see section "Materials and Methods"). We observed State 2 to correlate only with the Default Mode Network ($r = 0.71$, $p = 10^{-14}$), State 3 to correlate with the Fronto-parietal Network ($r = 0.84$, $p = 10^{-24}$), State 4 to correlate with the Visual Network ($r = 0.88$, $p = 10^{-29}$) and finally State 5 to mostly correlate with the Ventral Attention Network ($r = 0.71$, $p = 10^{-14}$) but also with the Somatomotor Network ($r = 0.53$, $p = 10^{-8}$). **Supplementary Figure S7** of the states' measures for the filtered data (0.04–0.07 Hz) is added in the **Supplementary Material**.

Recurrent Excursions Into BOLD PL States

Similar to the probability of occurrence of a given state, we can quantitatively characterize the temporal trajectories by the

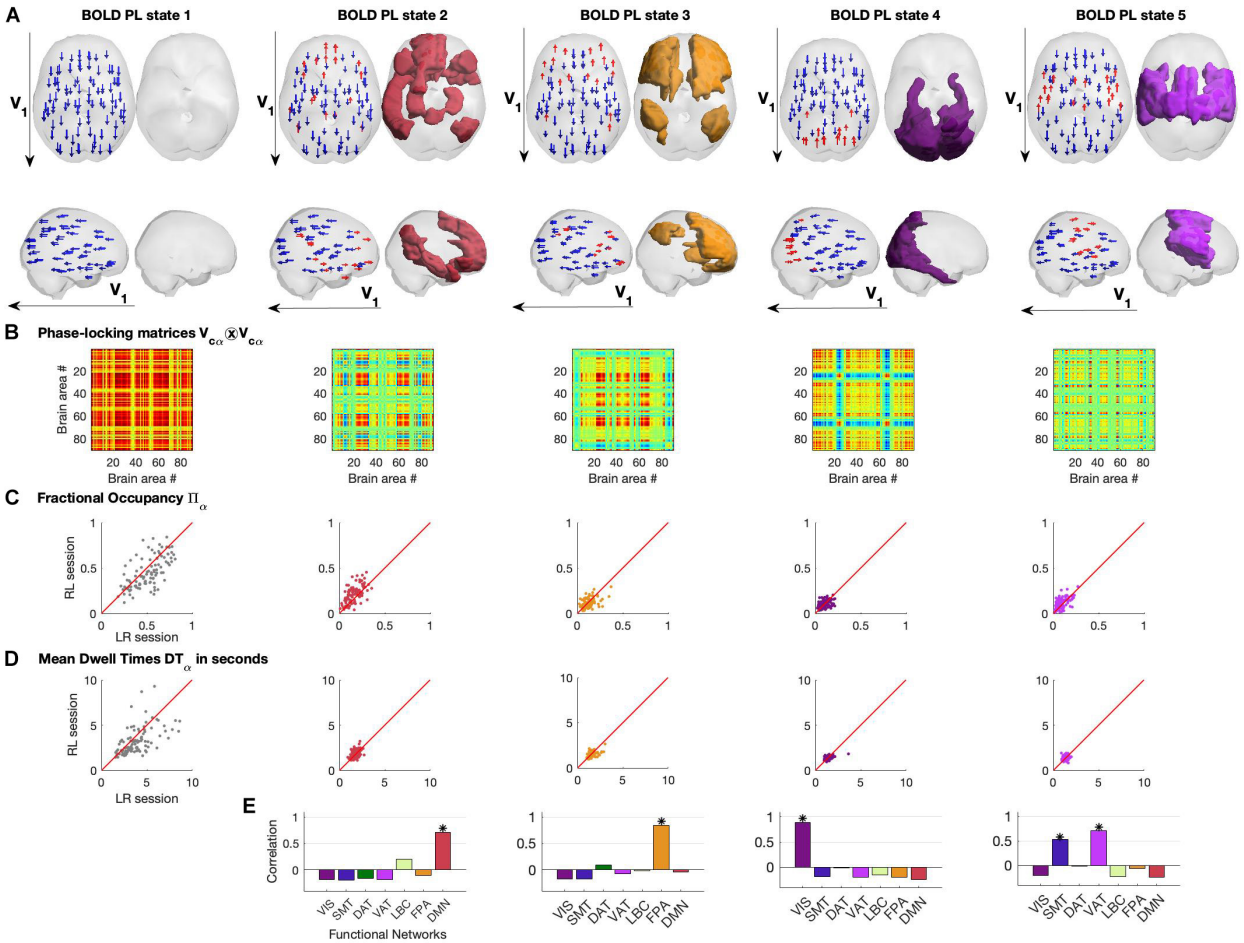


FIGURE 4 | Repertoire of BOLD Phase Locking States obtained using $K = 5$. **(A)** BOLD Phase Locking states represent recurrent patterns of BOLD phase alignment across the whole brain. Each centroid is a vector V_C of size 1xN whose elements indicate how each brain area projects into it. Each centroid is represented in the brain in two different ways: (left) by placing an arrow at the centre of gravity of each brain area and setting its size, direction and color according to the magnitude and sign of the corresponding element in V_C (coloring in red for positive projections into V_C, and blue otherwise). (right) Rendering all brain areas with positive values in V_C colored according to the functional network to which they show maximal overlap (see **Figure 3** and/or panel **E** below). **(B)** Phase-locking matrices computed as the outer product of the centroid vectors V_C. **(C)** Scatter plots of state Fractional Occupancy, plotting the values obtained for the 99 fMRI scans in the LR scanning session versus the values from the RL session. **(D)** Scatter plots of mean state Dwell Times, plotting the values obtained for the 99 fMRI scans in the LR scanning session versus the values from the RL session. **(E)** Correlation between each BOLD PL state and the seven networks of intrinsic functional connectivity from Yeo et al. (2011). * indicates significance corrected for multiple comparisons with Pearson's p-value $< 0.05/7$.

probabilities of transition between the different BOLD PL states. In **Figure 5A** we show the average transition matrix, $W_{\alpha\beta}$, as the probability of switching from state α to state β. We noted that the highest probabilities of transition ($W_{\alpha\beta} > 0.5$) were along the diagonal (representing the probability to remain in the same state) as well as along the first column (representing the transitions back to the state 1). The characteristic self-transitions ($\alpha \rightarrow \alpha$) along the diagonal are a distinctive feature of the system, indicating the relative stability of each state. State 1 reveals the highest stability (with 77% probability of remaining in it in the following TR), whereas the probability of remaining in the other states is close to chance levels. The scatter plots in **Figure 5B** show the transition probabilities obtained for each of the 99 participants (LR session vs. RL session), revealing consistency of the results across participants and scanning sessions.

Another relevant feature is the asymmetry of the transition matrix, which is indicative of an imbalance in the reciprocity of transitions both to and from a given state, as can be observed with the apparent proclivity for switching into the (global) state 1, whereas the probability to leave from it is much smaller.

In **Figure 5C**, a Transition Graph is constructed from the transition matrix W shown in panel A, where edges $\alpha \rightarrow \beta$ are directed and weighted with weight $W_{\alpha\beta}$. This gives a good insight into the spontaneous transition dynamics and motivates the use of the Markov chain transition matrix beyond the probability of occurrence alone. **Supplementary Figure S8** of the transition graph and matrix for the filtered data (0.04–0.07) is added in the **Supplementary Material**. Furthermore, the comparison of LR and RL sessions for the probabilities of transition is added in **Supplementary Figure S10**.

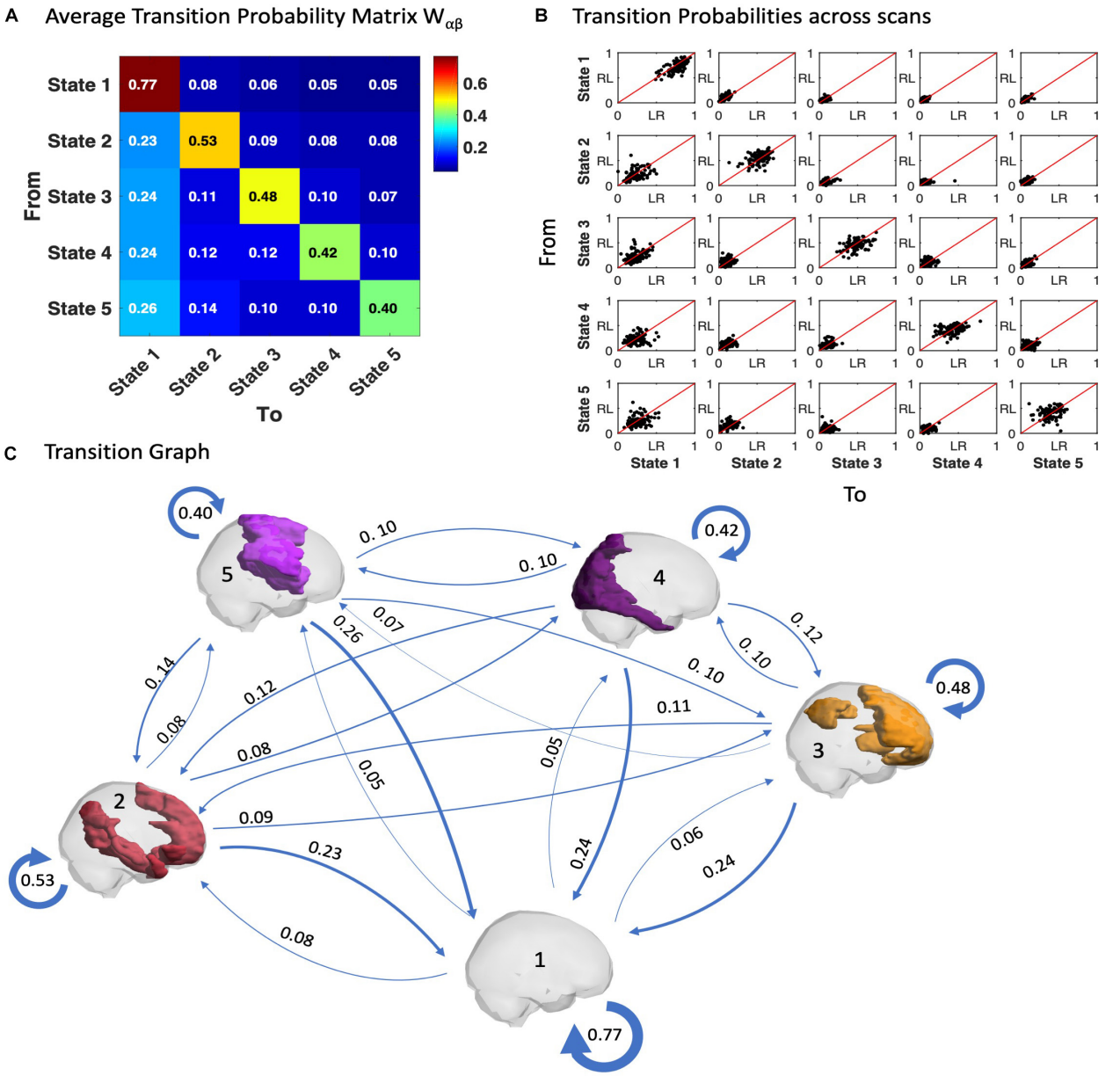


FIGURE 5 | Trajectories of brain activity in state space. **(A)** Transition matrix quantifying the probability of the trajectory transiting from one state to another as defined in Equation 5, averaged across the scans from all 99 participants in the LR session. **(B)** Transition probabilities estimated for each fMRI scan, each dot corresponding to one participant, plotting the probabilities of switching in the LR fMRI session versus the RL fMRI session. **(C)** Transition Graph is constructed from transition matrix W where edges $\alpha \rightarrow \beta$ are directed and weighted with weight $W_{\alpha\beta}$.

Reliability of Individual Metrics

To assess the metric's reliability across same-subject same-day recordings when compared to other subjects, we computed the Intra-Class Correlation (see section "Materials and Methods") for each measure above, namely, the Fractional Occupancies, the Dwell Times and the Transition Probabilities. In **Figure 6A**, we show the Fractional Occupancy for all 5 states to have moderate reliability values (State1: ICC = 0.59, State 2: ICC = 0.47, State 3: ICC = 0.42, State 4: ICC = 0.39 and State 5: ICC = 0.51). The Dwell Times for the first three states had moderate values of ICC and States 4 and 5 showed poor values (State1: ICC = 0.55, State 2: ICC = 0.37, State 3: ICC = 0.4, State 4: ICC = 0.32, and State 5: ICC = 0.28, **Figure 6B**).

Regarding the transition matrix, **Figure 6C** shows that the probability of remaining in the (global) State 1 has one of the highest ICC values (ICC = 0.61), with most of the transition to and from the State 1 showing a range of fair to moderate ICC values ($0.29 < ICC < 0.62$). States 2 and 3 have border-line

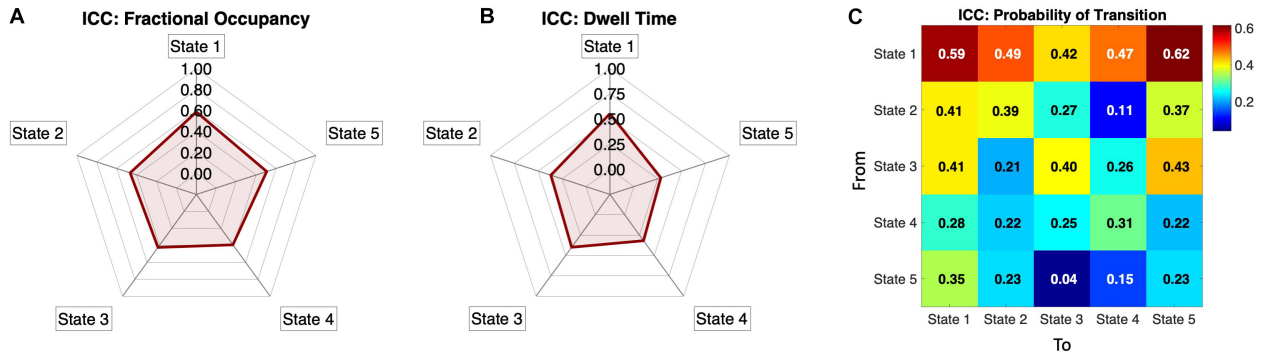


FIGURE 6 | Individual reliability of the Phase-locking states' measures: **(A)** Intra-Class Correlation (ICC) calculated for the Fractional Occupancy, showing positive ICC values for all five PL states, meaning that the within-subject error is smaller than the between-subject error. All values are within a moderate range of within-subject reliability (i.e., 0.4 < ICC < 0.6) according to the categorization by (Landis and Koch, 1977). **(B)** Intra-Class Correlation for Dwell Times for all five states showing the states 1,2 and 3 to be in the moderate reliability range. **(C)** ICC for the normalized Probability Transition Matrix showing positive ICC values in all transitions, with the probabilities of transition from state 1 being the most reliable, whereas other transitions, particularly between states 2 to 5, showing lower reliability. The ICC is categorized, based on (Landis and Koch, 1977) as low (0 < ICC < 0.2), fair (0.2 < ICC < 0.4), moderate (0.4 < ICC < 0.6), substantial (0.6 < ICC < 0.8) and almost perfect (0.8 < ICC < 1)

moderate values of ICC in the self-transitions (State 2: ICC = 0.39, State 3: ICC = 0.40) and some of the transitions to other states were also in the moderate range. States 4 and 5 seem to have relatively poor, but still positive, ICC values for the probability of transitions metric (**Figure 6C**).

Taken overall, the ICC results show that all the measures evaluated have smaller within-subject error than the between-subject error (given ICC values are positive for all measures), indicating that the measures proposed herein capture individual fingerprints of dynamic functional connectivity. To improve the assertion of individual landscapes and reliability of the methodology we added scatter plots for all the three measures (Fractional Occupancy, Dwell Times and Transition Probabilities) of the two sessions (LR and RL) in **Figures 4**, **5**.

Effect of the Temporal Filtering

All the results shown so far were obtained directly from the ROI-averaged BOLD signals from the HCP dataset, without applying any temporal frequency filter. Temporal filtering is a typical pre-processing step in resting-state fMRI analysis to remove frequency components regarded as noise. In this section, we evaluate whether the inclusion of the higher frequency components in the BOLD signal improve the analysis of dynamic functional connectivity by evaluating its effects on the reliability (ICC) of the measures across sessions, which should be maximized if assuming stationarity in individual resting-state dynamics.

As shown in **Figures 7A,C**, filtering has a crucial effect on the Dwell Times, with lower cut-off frequencies leading to longer Dwell Times for all states, and especially for state 1. Notably, when reaching up to the Nyquist frequency, the mean Dwell Times of states 2 to 5 approach the duration of 2TRs consistently for all subjects and in both LR and RL fMRI sessions, while state 1 lasts for slightly longer periods. When evaluating the Dwell Times ICC (**Figure 7E**), we find that the ICC is maximal for states 1, 2, and 3 when the high frequency components of the BOLD signal are included. However, it is important to take into account that the accurate estimation of Dwell Times is limited by the temporal resolution of the current fMRI dataset, minimizing the difference between subjects and hence affecting the ICC estimation.

Regarding the Fractional Occupancy of the states, it appears from **Figures 7B,D** that filtering does not affect the overall values estimated across subjects and in the different sessions. However, when looking at the ICC values for Fractional Occupancy (**Figure 7F**), we find that this measure is much more reliable within individuals (and across all states) when the high frequency components of the BOLD signal are included. Similarly, the ICC of the Transition Probabilities (shown in **Supplementary Figure S9**) shows a slight improvement in the reliability of most transitions. Actually, when considering only frequencies <0.2 Hz, a few transition probabilities have even a negative ICC, indicating no individual reliability at all. Overall, these findings point to the direction that it is important to consider the high frequency components of resting-state BOLD signals when assessing individual fingerprints in dynamic functional connectivity.

DISCUSSION

The challenge of describing dynamic functional connectivity for a mechanistic understanding of the brain processing as well as for its potential use in clinical research, has been of great interest to the neuroimaging community (Hutchison et al., 2013; Preti et al., 2016). With the advent of open multimodal neuroimaging data, it is possible to address and validate these approaches in representative datasets (Van Essen et al., 2013; Poldrack and Gorgolewski, 2014). In this work, we apply, formalize and validate the Leading Eigenvector Dynamics Analysis (LEiDA) to a large cohort of 99 healthy unrelated HCP subjects (Glasser et al., 2013). We describe brain activity during rest as a time evolving trajectory in a low-dimensional state space, where states are defined according to characteristic whole-brain configurations

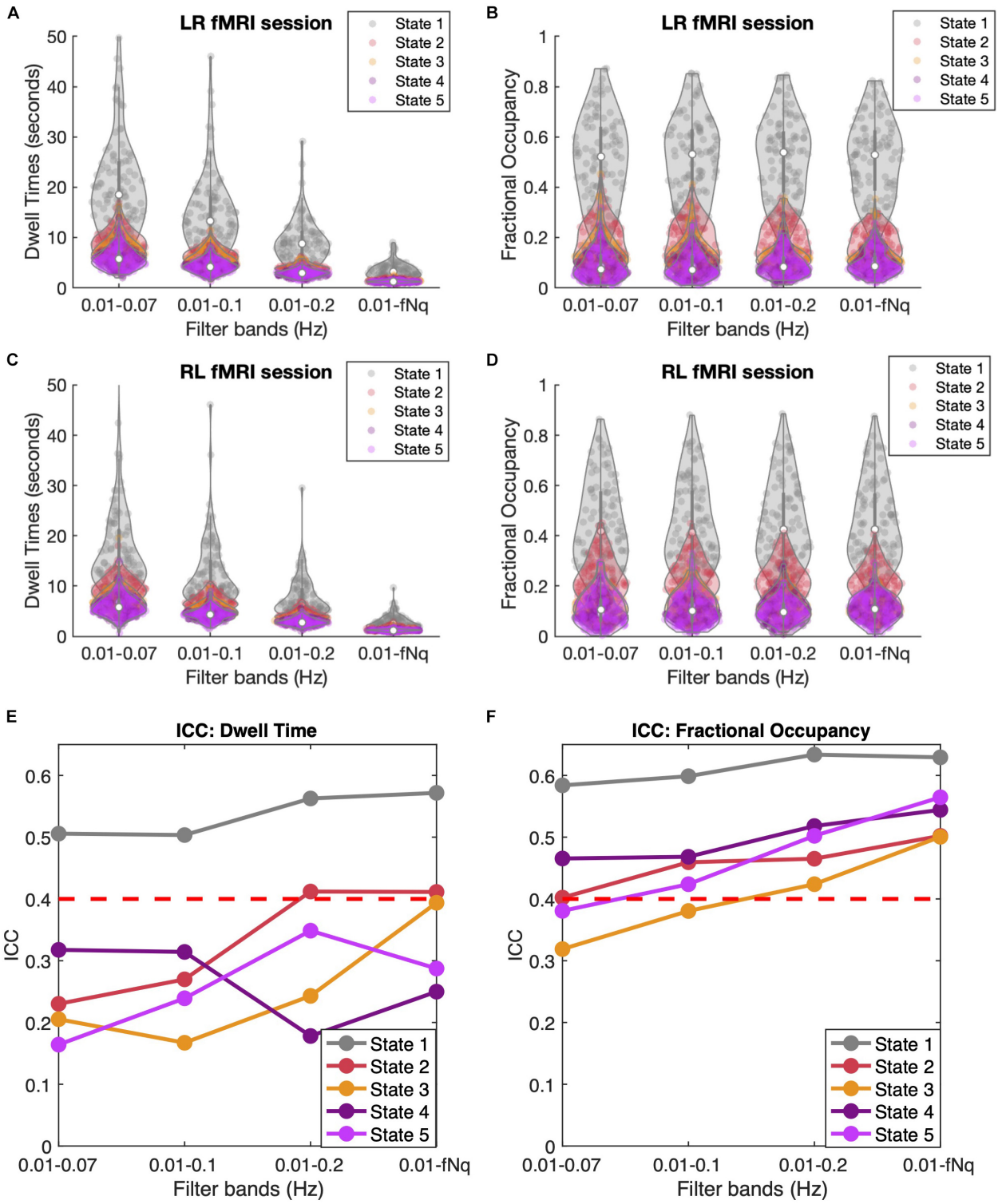


FIGURE 7 | Temporal Filtering effect on Dwell Time and Fractional Occupancy. **(A,C)** Dwell Times obtained across four different band-pass filters applied to the BOLD signals, keeping the lower bound fixed at 0.01 Hz and varying the higher (lowpass) cutoff frequency between 0.07, 0.1, 0.2, and 0.6944 Hz, which corresponds to the Nyquist frequency fNq = 1/(2TR). Results are shown for LR **(A)** and RL **(C)** recording sessions. **(B,D)** Fractional Occupancies across the four different filtrations for LR **(B)** and RL **(D)** recording sessions. **(E,F)** Inter-Class Correlation (ICC) across four different filtrations for Dwell Times **(E)** and Fractional Occupancy **(F)**. The red dashed line represents the threshold for moderate reliability based on the Landis and Koch (1977) ICC scale.

of BOLD phase-locking. Furthermore, we validate these BOLD phase-locking states to reference networks of intrinsic functional connectivity (Yeo et al., 2011) and compute their properties of fractional occupancy, Dwell Times and transition probabilities. We subsequently assess the reliability of these measures across the two same-day fMRI recordings (using Intra-Class Correlation) and show that all measures have a smaller within-subject error than the between-subject error (ICC values > 0), with the highest reliability values being detected when including the high frequency components (>0.1 Hz) of ROI-averaged BOLD signals in the analysis. We argue that such interpretation of brain activity, validated with reliability analysis, has the potential to identify individual-specific fingerprints in the brain's dynamical landscape and thus serve personalized clinical applications in diagnostics and therapeutics of patients with cognitive disorders.

Concepts and methods from dynamical systems theory are proving useful in the analysis of brain activity at the macroscopic scale, as they serve to formally characterize the complex dynamics emerging from the collective behavior of billions of interacting neurons, exhibiting features such as multi-stability, meta-stability and self-organized criticality, that may serve helpful to identify the underlying principles coordinating cognition at the whole-brain level (Deco and Jirsa, 2012; Tognoli and Kelso, 2014; Cocchi et al., 2017; Roberts et al., 2019). Here, we aimed at a different characterization of the dynamical properties of the intrinsic functional networks emerging spontaneously and consistently during rest. Our analysis revealed a repertoire of BOLD phase-locking states through which the trajectory of brain activity consistently returns in time and across subjects.

By analyzing the PL state's fractional occupancy, Dwell Time and probability of transitions, our results revealed that the BOLD phase-locking states can be divided in two groups according to their dynamical properties: On one hand, our algorithm consistently detects a state where all the ROI-averaged BOLD signals project into the same direction captured by the leading eigenvector (state 1 for all clustering solutions). This state exhibits longer Dwell Times and shows high between-subject variability but also high within-subject reliability. On the other hand, we detect for all k-means clustering solutions, a set of k-1 states where the BOLD signals of some brain areas project into the opposite direction from the main BOLD phase orientation. These states occur consistently less often and last for shorter times than the global state, but reoccur consistently across subjects and sessions. Given the reduced stability of these BOLD phase-locking states with respect to the meta-stable globally synchronized state, we refer to this second group as "ghost" attractor states. In other words, ghost attractors in this framework refer to short-lived (or weakly stable) network configurations that consistently reoccur across fMRI recordings.

Regarding the functional relevance of these "ghost" phase-locking states, our results show a clear and highly significant overlap of most cluster centroids (obtained for the whole range of partitions explored) with a set of seven previously identified networks of intrinsic functional connectivity used as reference. This finding indicates that these patterns of BOLD phase locking, despite being obtained from a different analytic perspective than more conventional correlation-based analyzes, are closely related to the so-called resting-state networks. Yet, unlike correlation-based analyses that reveal only the spatial map of these functional networks, the LEiDA approach allows characterizing their properties over the temporal dimension. As the reference RSNs are computed from the correlation-based static functional connectivity, a perfect match to the BOLD phase-locking states detected herein is not expected. Rather, they can be considered for validation of the functional relevance of the PL states and served to guide the choice of the number of states or further analysis. The number of states chosen is a trade-off between more fine-grained but less robust state solutions as demonstrated by the increasing specificity of functional subsystems for higher k. Here, the clustering solution with $k = 5$ was chosen for being within the range of maximal Silhouette value and for revealing a separation into distinct functionally meaningful systems such as the Default Mode Network, the Frontoparietal Network, the Ventral Attention Network and the Visual Network. However, a partition into a higher number of states may prove necessary when addressing particular conditions that affects a particular subsystem optimally defined for higher k. For instance, in a previous work using LEiDA, the partition into $k = 10$ was chosen for detecting the network that most significantly distinguished patients in remission from major depressive disorder and controls (Figueroa et al., 2019), whereas another study found the solution with $k = 7$ to optimally highlight the effects of psilocybin (Lord et al., 2019).

For all partitions into $k > 7$, our algorithm consistently detected a functional subsystem involving the basal ganglia (colored in black in **Figure 3** and **Supplementary Figure S1**) for not overlapping with any of the reference RSNs) as the second most prevalent BOLD PL state. This indicates that resting-state activity also involves connectivity to subcortical areas, which appears particularly important for the study of psychiatric disorders, such as anxiety-related disorders involving the basal ganglia. Following previous LEiDA studies, we chose here a coarse parcellation into N = 90 brain areas and did not include the BOLD signal detected in the cerebellum. The Anatomic Automatic Labeling Atlas has been validated in many studies and has shown consistency in the LEiDA results across datasets (Cabral et al., 2017b; Figueroa et al., 2019; Lord et al., 2019). However, it is based on an anatomic definition of the brain regions and as such might not generalize adequately to the dynamic functional connectivity analysis. We expect to extend to finer-grained and fMRI-derived parcellations in future studies, potentially including other substructures such as the cerebellum, in order to gain a wider insight into the network configurations observed in brain activity at the macroscopic scale (Cammoun et al., 2012; Glasser et al., 2016; Schaefer et al., 2018).

The mechanistic interpretation of the empirical data proposed herein serves as a great candidate for further theoretical exploration by whole-brain computational models (Ghosh et al., 2008; Deco et al., 2009; Honey et al., 2009). To this date, many models have demonstrated well-matched dynamics to the brain activity as represented by static functional connectivity in a critical range of parameters where the brain is poised between noisy and oscillatory activity. Furthermore, different properties were shown to have an impact on the emerging dynamics

such as propagation delays, local vs. global connections, signal-to-noise ratio, and local inhibitory rules (Deco et al., 2009, 2014; Honey et al., 2009; Cabral et al., 2011). Extending such modeling endeavors away from static functional connectivity to a dynamic representation of the experimental data is currently becoming a possible new avenue into understanding the underlying principles governing dynamic functional connectivity (Hansen et al., 2015; Cabral et al., 2017a; Deco et al., 2018, 2019). Recently, Deco et al. have shown how the dynamic representation of resting-state data in wakefulness and sleep (characterized using LEiDA) can serve to explore how a whole-brain model can be perturbed to identify the brain regions responsible for the transition between awake and sleep state (Deco et al., 2019).

Representing dynamic functional connectivity through the prism of dynamical system theory hypothesizes the existence of attractors in *N*-dimensional space through which the functional activity evolves in time. Assuming this hypothetical scenario, it describes a state-based propagation of the data, rendering the underlying dynamics in a discrete sense (Baker et al., 2014; Karahanoğlu and Van De Ville, 2015; Preti et al., 2016; Cabral et al., 2017a). However, other methods have considered dynamic functional connectivity from a continuous point-of-view, such as the spatio-temporal connectome where brain activity is described as a temporal graph (Griffa et al., 2017; Vohryzek et al., 2019) and auto-regressive models (Liégeois et al., 2017). We acknowledge that looking at the brain activity in a discrete sense is only one of the interpretations currently proposed in trying to describe the emergent complex phenomena observed in whole-brain dynamics.

It is to be noted that the applied clustering algorithm is just one amongst many decomposition methods that can partition the LEiDA results into meaningful states. Indeed, (Cabral et al., 2017b) compared the results from k-means algorithm to the Hidden Markov Model (HMM), in their paper on cognitive performance of patients, showing similar results with both approaches (Cabral et al., 2017b). However, k-means was chosen here for its relatively simple implementation and its relatively low computational cost, revealing functionally meaningful cluster centroids.

New imaging methods benefit greatly from the reliability analysis that investigates individual variabilities across recordings sessions. Especially in clinical applications, reliability is crucial to obtain stable measures across time for individual subjects (i.e., low within-subject variability) and at the same time distinguishable differences between subjects (i.e., high between-subject variability) (Xing and Zuo, 2018; Zuo et al., 2019). In this work, Intra-Class Correlation is used to calculate the desirable ratio between between-subject variability and within-subject variability across recording sessions. One of the Intra-Class Correlation scales proposed by Landis and Koch (1977) to assess reliability for clinical applications suggests that values $1.0 > ICC > 0.8$ have excellent reliability, $0.8 > ICC > 0.6$ substantial reliability, $0.6 > ICC > 0.4$ have moderate reliability and, $0.4 > ICC > 0.2$ poor substantial reliability. In other words, it is desirable to obtain high reliability values for the method's possible clinical application.

In the last part of our study, we show that including the high frequency components up to the Nyquist frequency maximizes the ICC values (reaching a mainly moderate range of ICC values). As such, it is likely that the temporal resolution of the fMRI acquisition might have hindered further increase in reliability. Although the Dwell Times become significantly shorter if no smoothing is applied - which may decrease the detection of RSNs in correlation-based analysis - we find that the occurrence of these states is intrinsically short, given that the measures become more reliable. Although the hemodynamic response function (HRF) is intrinsically slow, the capacity of the BOLD signal to detect faster frequency components is still highly debated in the literature (Glerean et al., 2012; Deco et al., 2019). Nevertheless, it is likely that resting-state dynamics occurs at a faster time scale than captured with the BOLD signal, as suggested by MEG studies that point to a duration of around 200 ms (Baker et al., 2014; Vidaurre et al., 2016). Here, we show that LEiDA allows detecting meaningful dynamic network configurations occurring at relatively short time-scales for fMRI analysis, which may serve useful not only for resting-state analysis but also for the detection of task related patterns [as in Stark et al. (2019)], that may not be captured with conventional general linear models using the HRF. Overall, we expect that novel insights into BOLD signal temporal characteristics and improvements in fMRI temporal resolution might increase the ICC reliability of these measures.

CONCLUSION

In summary, we combine novel analytic tools to quantitatively characterize brain activity in each fMRI scan as a trajectory through a discrete set of BOLD phase-locking states. Given the dynamical properties of these states (fractional occupancy, Dwell Time and transition probability) we propose that RSNs behave as ghost attractors, emerging spontaneously and for brief periods, but recurring consistently across subjects and sessions. Our study corroborates previous theoretical works that put forward an interpretation of brain activity as a trajectory evolving in time in an energy landscape (Deco et al., 2011; Ashourvan et al., 2017). By demonstrating the functional relevance of the BOLD phase-locking states detected and the reliability of the measures across same-subject sessions we go further by revealing the existence of individual-specific energy landscapes in brain activity with potential application in patient-specific diagnostics and therapeutics.

DATA AVAILABILITY STATEMENT

All data and codes used in this study are publicly available on https://github.com/jvohryzek/GhostAttractors.

ETHICS STATEMENT

The studies involving human participants were reviewed and approved by The Washington University review board including all study protocols. Informed consent was obtained for all

participants. The participants provided their written informed consent to participate in this study.

AUTHOR CONTRIBUTIONS

JV and JC carried out the analysis, wrote the main manuscript and came up with the paper's ideas. BC and GD verified and advised the theoretical methods. MK and JC supervised the whole project. All authors participated in the discussion of the ideas and contributed in the final writing of the manuscript.

FUNDING

This work has been funded by FEDER through the Competitiveness Factors Operational Program (COMPETE), by National funds through the Foundation for Science and Technology (FCT) under the scope of the project UID/Multi/50026; and by the projects NORTE-01-0145-FEDER-000013 and NORTE-01-0145-FEDER-000023, supported by the Northern Portugal Regional Operational Programme (NORTE 2020), under the Portugal 2020 Partnership Agreement, through the European Regional Development Fund (FEDER). JC was supported by Portuguese Foundation for Science and Technology CEECIND/03325/2017, Portugal. GD acknowledges funding from the European Union's Horizon 2020 FET Flagship Human Brain Project under Grant Agreement 785907 HBP SGA2, the Spanish Ministry Project PSI2016-75688-P (AEI/FEDER) and the Catalan Research Group Support 2017 SGR 1545. MK was supported by the European Research Council Consolidator Grant: CAREGIVING (615539), Pettit Foundation, Carlsberg Foundation and Center for Music in the Brain, funded by the Danish National Research Foundation (DNRF117). BC was supported by the French Government through the UCA-Jedi project managed by the National Research Agency (ANR-15-IDEX-01) and, in particular, by the interdisciplinary Institute for Modeling in Neuroscience and Cognition (NeuroMod) of the Université Côte d'Azur.

SUPPLEMENTARY MATERIAL

The Supplementary Material for this article can be found online at: https://www.frontiersin.org/articles/10.3389/fnsys.2020.00020/full#supplementary-material

REFERENCES

Allen, E. A., Damaraju, E., Plis, S. M., Erhardt, E. B., Eichele, T., and Calhoun, V. D. (2014). Tracking whole-brain connectivity dynamics in the resting state. *Cerebral. Cortex* 24, 663–676. doi: 10.1093/cercor/bhs352

Ashourvan, A., Gu, S., Mattar, M. G., Vettel, J. M., and Bassett, D. S. (2017). The energy landscape underpinning module dynamics in the human brain connectome. *NeuroImage* 157, 364–380. doi: 10.1016/j.neuroimage.2017.05.067

Baker, A. P., Brookes, M. J., Rezek, I. A., Smith, S. M., Behrens, T., Smith, P. J. P., et al. (2014). Fast transient networks in spontaneous human brain activity. *ELife* 2014, 1–18. doi: 10.7554/eLife.01867

Beckmann, C. F., DeLuca, M., Devlin, J. T., and Smith, S. M. (2005). Investigations into resting-state connectivity using independent component analysis. *Philos. Trans. R. Soc. BBiol. Sci.* 360, 1001–1013. doi: 10.1098/rstb.2005.1634

Cabral, J., Hugues, E., Sporns, O., and Deco, G. (2011). Role of local network oscillations in resting-state functional connectivity. *NeuroImage* 57, 130–139. doi: 10.1016/j.neuroimage.2011.04.010

Cabral, J., Kringelbach, M. L., and Deco, G. (2017a). Functional connectivity dynamically evolves on multiple time-scales over a static structural connectome: models and mechanisms. *NeuroImage* 160, 84–96. doi: 10.1016/j.neuroimage.2017.03.045

Cabral, J., Vidaurre, D., Marques, P., Magalhães, R., Silva Moreira, P., Miguel Soares, J., et al. (2017b). Cognitive performance in healthy older adults relates to spontaneous switching between states of functional connectivity during rest. *Sci. Rep.* 7:5135. doi: 10.1038/s41598-017-05425-7

Calhoun, V. D., Miller, R., Pearlson, G., and Adali, T. (2014). The chronnectome: time-varying connectivity networks as the next frontier in fmri data discovery. *Neuron* 84, 262–274. doi: 10.1016/j.neuron.2014.10.015

Cammoun, L., Gigandet, X., Meskaldji, D., Thiran, J. P., Sporns, O., Do, K. Q., et al. (2012). Mapping the human connectome at multiple scales with diffusion spectrum MRI. *J. Neurosci. Methods* 203, 386–397. doi: 10.1016/j.jneumeth.2011.09.031

Chang, C., and Glover, G. H. (2010). Time-frequency dynamics of resting-state brain connectivity measured with fMRI. *NeuroImage* 50, 81–98. doi: 10.1016/j.neuroimage.2009.12.011

Cocchi, L., Gollo, L. L., Zalesky, A., and Breakspear, M. (2017). Criticality in the brain: a synthesis of neurobiology, models and cognition. *Prog. Neurobiol.* 158, 132–152. doi: 10.1016/j.pneurobio.2017.07.002

Damoiseaux, J. S., Rombouts, S. A. R. B., Barkhof, F., Scheltens, P., Stam, C. J., Smith, S. M., et al. (2006). Consistent resting-state networks across healthy subjects. *Proc. Natl. Acad. Sci. U.S.A.* 103, 13848–13853. doi: 10.1073/pnas.0601417103

Deco, G., Cruzat, J., Cabral, J., Tagliazucchi, E., Laufs, H., Logothetis, N. K., et al. (2019). Awakening: predicting external stimulation to force transitions between different brain states. *Proc. Natl. Acad. Sci. U.S.A.* 116, 18088–18097. doi: 10.1073/pnas.1905534116

Deco, G., Cruzat, J., and Kringelbach, M. L. (2019). *Brain Songs: Discovering the Relevant Timescale of the Human Brain. Nature Communications*. Berlin: Nature Publishing Group.

Deco, G., Jirsa, V., Mcintosh, A. R., Sporns, O., and Kotter, R. (2009). Key role of coupling, delay, and noise in resting brain fluctuations. *Proc. Natl. Acad. Sci. U.S.A.* 106, 10302–10307. doi: 10.1073/pnas.0901831106

Deco, G., and Jirsa, V. K. (2012). Ongoing cortical activity at rest: criticality, multistability, and ghost attractors. *J. Neurosci.* 32, 3366–3375. doi: 10.1523/JNEUROSCI.2523-11.2012

Deco, G., Jirsa, V. K., and McIntosh, A. R. (2011). Emerging concepts for the dynamical organization of resting-state activity in the brain. *Nat. Rev. Neurosci.* 12, 43–56. doi: 10.1038/nrn2961

Deco, G., Ponce-Alvarez, A., Hagmann, P., Romani, G., Mantini, D., and Corbetta, M. (2014). How local excitation-inhibition ratio impacts the whole brain dynamics. *J. Neurosci.* 34, 7886–7898. doi: 10.1523/JNEUROSCI.5068-13.2014

Deco, G., Ponce-Alvarez, A., Mantini, D., Romani, G. L., Hagmann, P., and Corbetta, M. (2013). Resting-state functional connectivity emerges from structurally and dynamically shaped slow linear fluctuations. *J. Neurosci.* 33, 11239–11252. doi: 10.1523/JNEUROSCI.1091-13.2013

Deco, G., Vidaurre, D., and Kringelbach, M. L. (2019). Revisiting the global workspace: orchestration of the functional hierarchical organisation of the human brain. *BioRxiv* [preprint]. doi: 10.1101/859579

Deco, G., Cruzat, J., Cabral, J., Knudsen, G. M., Carhart-Harris, R. L., Whybrow, P. C., et al. (2018). Whole-brain multimodal neuroimaging model using serotonin receptor maps explains non-linear functional effects of LSD. *Curr. Biol.* 28, 3065.e6–3074.e6. doi: 10.1016/j.cub.2018.07.083

Figueroa, C. A., Cabral, J., Roel, M. J. T., Rapuano, K. M., Van Hartevelt, T. J., and Ruhé, H. G. (2019). Altered ability to access a clinically relevant control network in patients remitted from major depressive disorder. *Hum. Brain Mapp.* 40, 2771–2786. doi: 10.1002/hbm.24559

Fox, M. D., and Greicius, M. (2010). Clinical applications of resting state functional connectivity. *Front. in Syst. Neurosci.* 4:19. doi: 10.3389/fnsys.2010.00019

Fox, M. D., Snyder, A. Z., Vincent, J. L., Corbetta, M., Van Essen, D. C., and Raichle, M. E. (2005). The human brain is intrinsically organized into dynamic, anticorrelated functional networks. *Proc. Natl. Acad. Sci. U.S.A.* 102, 9673–9678. doi: 10.1073/pnas.0504136102

Ghosh, A., Rho, Y., Mcintosh, A. R., Kö Tter, R., and Jirsa, V. K. (2008). Noise during rest enables the exploration of the brain's dynamic repertoire. *PLoS Comput. Biol.* 4:1000196. doi: 10.1371/journal.pcbi.1000196

Glasser, M. F., Coalson, T. S., Robinson, E. C., Hacker, C. D., Harwell, J., Yacoub, E., et al. (2016). A multi-modal parcellation of human cerebral cortex. *Nature* 536, 171–178. doi: 10.1038/nature18933

Glasser, M. F., Sotiropoulos, S. N., Wilson, J. A., Coalson, T. S., Fischl, B., Andersson, J. L., et al. (2013). The minimal preprocessing pipelines for the human connectome project. *NeuroImage* 80, 105–124. doi: 10.1016/j.neuroimage.2013.04.127

Glerean, E., Salmi, J., Lahnakoski, J. M., Jääskeläinen, I. P., and Sams, M. (2012). Functional magnetic resonance imaging phase synchronization as a measure of dynamic functional connectivity. *Brain Connectivity* 2, 91–101. doi: 10.1089/brain.2011.0068

Greicius, M. (2008). Resting-state functional connectivity in neuropsychiatric disorders. *Curr. Opin. Neurol.* 21, 424–430. doi: 10.1097/WCO.0b013e328306f2c5

Griffa, A., Ricaud, B., Benzi, K., Bresson, X., Daducci, A., Vandergheynst, P., et al. (2017). Transient networks of spatio-temporal connectivity map communication pathways in brain functional systems. *NeuroImage* 155, 490–502. doi: 10.1016/j.neuroimage.2017.04.015

Haimovici, A., Tagliazucchi, E., Balenzuela, P., and Chialvo, D. R. (2013). Brain organization into resting state networks emerges at criticality on a model of the human connectome. *Physical. Rev. Lett.* 110:178101. doi: 10.1103/PhysRevLett.110.178101

Hansen, E. C. A., Battaglia, D., Spiegler, A., Deco, G., and Jirsa, V. K. (2015). Functional connectivity dynamics: modeling the switching behavior of the resting state. *NeuroImage* 105, 525–535. doi: 10.1016/j.neuroimage.2014.11.001

Hindriks, R., Adhikari, M. H., Murayama, Y., Ganzetti, M., Mantini, D., Logothetis, N. K., et al. (2016). Can sliding-window correlations reveal dynamic functional connectivity in resting-state fMRI? *NeuroImage* 127, 242–256. doi: 10.1016/j.neuroimage.2015.11.055

Honey, C. J., Sporns, O., Cammoun, L., Gigandet, X., Thiran, J.-P., Meuli, R., et al. (2009). Predicting human resting-state functional connectivity from structural connectivity. *Proc. Natil. Acad. Sci. U.S.A.* 106, 2035–2040. doi: 10.1073/pnas.0811168106

Hutchison, R. M., Womelsdorf, T., Allen, E. A., Bandettini, P. A., Calhoun, V. D., Corbetta, M., et al. (2013). Dynamic functional connectivity: promise, issues, and interpretations. *NeuroImage* 80, 360–378. doi: 10.1016/j.neuroimage.2013.05.079

Kaiser, R. H., Andrews-Hanna, J. R., Wager, T. D., and Pizzagalli, D. A. (2015). Large-scale network dysfunction in major depressive disorder. *JAMA Psychiatry* 72, 603611. doi: 10.1001/jamapsychiatry.2015.0071

Karahanoğlu, F. I., and Van De Ville, D. (2015). Transient brain activity disentangles fMRI resting-state dynamics in terms of spatially and temporally overlapping networks. *Nat. Commun.* 6:7751. doi: 10.1038/ncomms8751

Landis, J. R., and Koch, G. G. (1977). The measurement of observer agreement for categorical data. *Biometrics* 33, 159–174. doi: 10.2307/2529310

Liégeois, R., Laumann, T. O., Snyder, A. Z., Zhou, J., and Yeo, B. T. T. (2017). Interpreting temporal fluctuations in resting-state functional connectivity MRI. *NeuroImage* 163, 437–455. doi: 10.1016/J.NEUROIMAGE.2017.09.012

Lord, L. D., Expert, P., Atasoy, S., Roseman, L., Rapuano, K., Lambiotte, R., et al. (2019). Dynamical exploration of the repertoire of brain networks at rest is modulated by psilocybin. *NeuroImage* 199, 127–142. doi: 10.1016/j.neuroimage.2019.05.060

Poldrack, R. A., and Gorgolewski, K. J. (2014). Making big data open: data sharing in neuroimaging. *Nat. Neurosci.* 17, 1510–1517. doi: 10.1038/nn.3818

Preti, M. G., Bolton, T. A., and Ville, V. D. D. (2016). The dynamic functional connectome: state-of-the-art and perspectives. *NeuroImage* 160, 41–45. doi: 10.1016/j.neuroimage.2016.12.061

Roberts, J. A., Gollo, L. L., Abeysuriya, R. G., Roberts, G., Mitchell, P. B., Woolrich, M. W., et al. (2019). Metastable brain waves. *Nat. Commun.* 10:1056. doi: 10.1038/s41467-019-08999-0

Schaefer, A., Kong, R., Gordon, E. M., Laumann, T. O., Zuo, X.-N., Holmes, A. J., et al. (2018). Local-global parcellation of the human cerebral cortex from intrinsic functional connectivity MRI. *Cerebral. Cortex* 28, 3095–3114. doi: 10.1093/cercor/bhx179

Sporns, O., Tononi, G., and Edelman, G. M. (2000). *Connectivity and Complexity: The Relationship Between Neuroanatomy and Brain Dynamics. Neural Networks*. Amsterdam: Elsevier Science Ltd.

Stark, E. A., Cabral, J., Riem, M. M. E., Van Ijzendoorn, M. H., Stein, A., and Kringelbach, M. L. (2019). The power of smiling: the adult brain networks underlying learned infant emotionality. *Cerebral. Cortex* 00, 1–11. doi: 10.1093/cercor/bhz219

Tagliazucchi, E., Siniatchkin, M., Laufs, H., and Chialvo, D. R. (2016). The voxel-wise functional connectome can be efficiently derived from co-activations in a sparse spatio-temporal point-process. *Front. Neurosci.* 10:38. doi: 10.3389/fnins.2016.00381

Tognoli, E., and Kelso, J. A. S. (2014). The metastable brain. *Neuron* 81, 35–48. doi: 10.1016/j.neuron.2013.12.022

Tononi, G., and Edelman, G. M. (1998). Consciousness and complexity. *Science* 282, 1846–1851. doi: 10.1126/science.282.5395.1846

van den Heuvel, M. P., and Hulshoff Pol, H. E. (2010). Exploring the brain network: a review on resting-state fMRI functional connectivity. *Eur. Neuropsychopharmacol.* 20, 519–534. doi: 10.1016/j.euroneuro.2010.03.008

Van Essen, D. C., Smith, S. M., Barch, D. M., Behrens, T. E. J., Yacoub, E., and Ugurbil, K. (2013). The WU-minn human connectome project: an overview. *NeuroImage* 80, 62–79. doi: 10.1016/j.neuroimage.2013.05.041

Vargas, C., López-Jaramillo, C., and Vieta, E. (2013). A systematic literature review of resting state network-functional MRI in bipolar disorder. J. Affect. Disord.. 150, 727–735. doi: 10.1016/j.jad.2013.05.083

Vidaurre, D., Quinn, A. J., Baker, A. P., Dupret, D., Tejero-Cantero, A., and Woolrich, M. W. (2016). Spectrally resolved fast transient brain states in electrophysiological data. *NeuroImage* 126, 81–95. doi: 10.1016/j.neuroimage.2015.11.047

Vohryzek, J., Griffa, A., Mullier, E., Friedrichs-Maeder, C., Sandini, C., Schaer, M., et al. (2019). Dynamic spatio-temporal patterns of brain connectivity reorganize across development. *Network Neurosci.* 4, 115–133. doi: 10.1162/netn_a_00111

Xing, X. X., and Zuo, X. N. (2018). The anatomy of reliability: a must read for future human brain mapping. *Sci. Bull.* 63, 1606–1607. doi: 10.1016/j.scib.2018.12.010

Yeo, B. T. T., Krienen, F. M., Sepulcre, J., Sabuncu, M. R., Lashkari, D., Hollinshead, M., et al. (2011). The organization of the human cerebral cortex estimated by intrinsic functional connectivity. *J. Neurophysiol.* 106, 1125–1165. doi: 10.1152/jn.00338.2011

Zuo, X. N., Xu, T., and Milham, M. P. (2019). Harnessing reliability for neuroscience research. *Nat. Hum. Behav.* 3, 768–771. doi: 10.1038/s41562-019-0655-x

Conflict of Interest: The authors declare that the research was conducted in the absence of any commercial or financial relationships that could be construed as a potential conflict of interest.

Copyright © 2020 Vohryzek, Deco, Cessac, Kringelbach and Cabral. This is an open-access article distributed under the terms of the Creative Commons Attribution License (CC BY). The use, distribution or reproduction in other forums is permitted, provided the original author(s) and the copyright owner(s) are credited and that the original publication in this journal is cited, in accordance with accepted academic practice. No use, distribution or reproduction is permitted which does not comply with these terms.

frontiers in Computational Neuroscience

ORIGINAL RESEARCH
published: 26 May 2020
doi: 10.3389/fncom.2020.00044

Synaptic Diversity Suppresses Complex Collective Behavior in Networks of Theta Neurons

Lucas Lin[1], *Ernest Barreto*[2]* *and Paul So*[2]

[1] Department of Computer Science, Stanford University, Stanford, CA, United States, [2] Department of Physics and Astronomy and Interdisciplinary Program in Neuroscience, George Mason University, Fairfax, VA, United States

Comprehending how the brain functions requires an understanding of the dynamics of neuronal assemblies. Previous work used a mean-field reduction method to determine the collective dynamics of a large heterogeneous network of uniformly and globally coupled theta neurons, which are a canonical formulation of Type I neurons. However, in modeling neuronal networks, it is unreasonable to assume that the coupling strength between every pair of neurons is identical. The goal in the present work is to analytically examine the collective macroscopic behavior of a network of theta neurons that is more realistic in that it includes heterogeneity in the coupling strength as well as in neuronal excitability. We consider the occurrence of dynamical structures that give rise to complicated dynamics via bifurcations of macroscopic collective quantities, concentrating on two biophysically relevant cases: (1) predominantly excitable neurons with mostly excitatory connections, and (2) predominantly spiking neurons with inhibitory connections. We find that increasing the synaptic diversity moves these dynamical structures to distant extremes of parameter space, leaving simple collective equilibrium states in the physiologically relevant region. We also study the node vs. focus nature of stable macroscopic equilibrium solutions and discuss our results in the context of recent literature.

Keywords: network, synaptic diversity, theta neuron, oscillations, synchronization, heterogeneity

OPEN ACCESS

Edited by:
Tomislav Stankovski,
Saints Cyril and Methodius University of Skopje, North Macedonia

Reviewed by:
Alessandro Torcini,
Université de Cergy-Pontoise, France
Ernest Montbrió,
Pompeu Fabra University, Spain
Carlo Laing,
Massey University, New Zealand

***Correspondence:**
Ernest Barreto
ebarreto@gmu.edu

Received: *16 December 2019*
Accepted: *29 April 2020*
Published: *26 May 2020*

Citation:
Lin L, Barreto E and So P (2020) Synaptic Diversity Suppresses Complex Collective Behavior in Networks of Theta Neurons. Front. Comput. Neurosci. 14:44. doi: 10.3389/fncom.2020.00044

1. INTRODUCTION

In 1949, Hebb (1949) proposed that cell assemblies are the true functional unit of the nervous system. The cerebral cortex contains networks of neuronal assemblies that comprise a large number of interacting neurons (Harris, 2005; Sporns et al., 2005). Individual neuronal assemblies organize via transient synchronization to generate collective behavior that is critical to communication between the neuronal assemblies themselves. Furthermore, it has been suggested that this synchronous neural activity, as well as average spatiotemporal firing patterns that emerge from these populations, are important coding mechanisms (Harris, 2005).

In developing an analytical understanding of the behavior of large neuronal assemblies, it is prohibitively challenging to use realistic models of actual neurons. To make progress, it is useful to use a canonical model that can represent the general behavior of a whole class of neurons (Izhikevich, 2000). A model can be considered canonical for a family of models if a continuous change of variables can transform any instance of that family into the canonical model. Such a model is advantageous due to its universality since any behavior exhibited by the canonical

model informs the behavior of the entire family of neurons. In approaching the characterization of neuronal populations specifically, the use of a canonical model is beneficial in that it may be amenable to a complete analytical treatment.

Physiologically, excitable neurons are typically classified into two types (Hodgkin, 1948; Izhikevich, 2007). Here, we are concerned with Type I neurons, which represent a category that includes cortical excitatory pyramidal neurons that generate action potentials at an arbitrarily low rate when a sufficiently large input stimulus is applied. Ermentrout and Kopell derived a one-dimensional neuronal model that includes a saddle-node bifurcation on an invariant circle, or SNIC bifurcation, and demonstrated that it is canonical for Type I neurons near the firing threshold (Ermentrout and Kopell, 1986). We use this model, also termed the theta neuron, to analyze the collective dynamics of a large population of Type I neurons.

Instead of being concerned with the exact values of all neuronal state variables in a large network of model neurons, we look to classify the macroscopic or collective behaviors that describe the activity of a population as a whole. Much early work studied such collective behaviors in terms of mean firing rates. Famously, the Wilson–Cowan equations consider a homogeneous population of interconnected excitatory and inhibitory neurons (Wilson and Cowan, 1972, 1973; Coombes, 2006). But, in recent years, many authors have employed the groundbreaking techniques of Ott and Antonsen (2008, 2009), which yield an understanding of the collective dynamics from the asymptotic behavior of a low-dimensional set of reduced equations for an appropriate set of macroscopic variables.

Luke et al. (2013) used these methods to analyze a network of globally-coupled theta neurons (see also Luke et al., 2014; So et al., 2014). These authors analytically obtained the asymptotic dynamics of a Kuramoto-type order parameter that quantifies the collective network dynamics. This work was later adapted to a spatiotemporal context by Laing (2014, 2015) and used to make a connection between the microscopic theta neuron steady states and the corresponding mean-field firing-rate-based model. At about the same time, similar work was pursued independently by Pazó and Montbrió (2014) for pulse-coupled Winfree networks. Then, Montbrió et al. (2015) used similar analytic techniques to describe the collective dynamics of a population of quadratic integrate-and-fire (QIF) neurons in terms of the network firing rate and average membrane potential. It is important to note that the theta neuron can be transformed into a QIF neuron by an appropriate change of variable. Montbrió et al. (2015) went further, linking networks of these neurons by identifying a conformal mapping between the two macroscopic variables for the QIF network (i.e., firing rate and mean membrane potential) and the Kuramoto order parameter for the theta neuron system.

The current work builds directly on the results of Luke et al. (2013), which included heterogeneity in the excitability parameter of the theta neuron in order to model this obviously significant feature of real neuronal ensembles. However, the neurons were assumed to be linked together with a single value of coupling strength. In the current work, we extend this analysis to also include synaptic diversity, modeled as heterogeneity in the coupling strength parameter. Our aim is to determine how this additional and realistic feature of the network model affects the macroscopic patterns produced by the population as a whole. We note that in Appendix E1 of Montbrió et al. (2015), this situation was also considered for QIF networks, and we comment on the relationship of our work to theirs in section 4.

We also take interest in the nature of equilibrium solutions of the macroscopic network variables. Luke et al. (2013) noted that collective stable node and stable focus solutions exist, and that their nature can be identified by observing the collective network response to a perturbation (see their Figure 5), since the relaxation back to a focus solution involves oscillatory behavior in the macroscopic variable. Recently, di Volo and Torcini (2018) (see also Bi et al., 2020) argued that collective oscillations in balanced spiking inhibitory networks can arise via this mechanism when driven by appropriate fluctuations. They showed using a model based on Montbrió et al. (2015) that the frequency of such collective oscillations match the relaxation dynamics around a stable focus equilibrium. Thus we are also interested in examining how introducing synaptic diversity affects the node vs. focus nature of macroscopic equilibrium solutions.

2. METHODS

2.1. Microscopic Formulation

The theta neuron model is a canonical representation of a Type-1 neuron (Ermentrout, 2008) and is given by

$$\dot{\theta} = (1 - cos\theta) + \eta(1 + cos\theta),$$

where the phase angle θ characterizes the state of the neuron. The neuron is considered to "spike," or produce an action potential, when θ crosses π while increasing. We call η the "excitability parameter" and think of it as playing the role of a fixed input current. If $\eta < 0$, then the model has a stable and an unstable equilibrium which we call the resting state and the threshold, respectively. In this situation, the neuron is excitable, as a sufficiently large external stimulus could push the phase of the neuron across the unstable equilibrium, where upon θ would travel around the circle, pass $\theta = \pi$ and spike, and then approach the stable equilibrium from the other side. As η increases, the stable and unstable equilibria get closer together, merge in a SNIC bifurcation at $\eta = 0$, and disappear. For $\eta > 0$, the neuron's dynamics is that of a limit cycle, representing a periodically spiking neuron.

We consider a network of N theta neurons,

$$\dot{\theta}_j = (1 - cos\theta_j) + [\eta_j + I_{syn,j}](1 + cos\theta_j), \tag{1}$$

where $j = 1, ..., N$ is the index of the j-th neuron. The theta neurons are coupled together via a pulse-like synaptic current $I_{syn,j}$ given by

$$I_{syn,j} = \frac{k_j}{N} \sum_{i=1}^{N} P_n(\theta_i), \tag{2}$$

where $P_n(\theta) = a_n(1 - cos\theta)^n, n \in \mathbb{N}$, k_j is the coupling strength, and a_n is a normalization constant such that

$$\int_0^{2\pi} P_n(\theta)d\theta = 2\pi.$$

In this model, the parameters η_j, k_j, and n represent biological features. η_j determines either the degree to which neuron j is excitable (for $\eta_j < 0$), or the frequency of regular spiking (for $\eta_j > 0$). k_j describes the strength of coupling between neuron j and its presynaptic partners, and can be inhibitory ($k_j < 0$) or excitatory ($k_j > 0$). The parameter n determines the shape of the synaptic current. As n increases, the current pulse becomes more sharply peaked. Throughout most of this paper, we set $n = 2$, but we also consider $n = 9$ as noted.

To quantify the macroscopic collective behavior of the network, we use the usual Kuramoto complex order parameter $z(t)$:

$$z(t) = \frac{1}{N}\sum_{j=1}^{N} e^{i\theta_j}.$$

This is the centroid of the phase distribution. Perfect phase synchrony corresponds to $|z| = 1$, and partial phase synchrony to $0 < |z| < 1$. Note, however, that because the angular speed of a spiking theta neuron is not uniform in θ, a population of such neurons exhibits a degree of phase synchrony with $|z| \neq 0$ when completely uncoupled.

Since neurons in real biological networks exhibit a range of intrinsic excitabilities, the parameter η_j is typically different for each neuron. New in this work, we also allow for diversity in the coupling strengths k_j. We model this by drawing these parameters at random from two independent Cauchy–Lorentz distribution functions $g_\eta(\eta)$ and $g_k(k)$ given by

$$g_\eta(\eta) = \frac{1}{\pi}\frac{\Delta_\eta}{(\eta - \eta_0)^2 + \Delta_\eta^2}, \quad g_k(k) = \frac{1}{\pi}\frac{\Delta_k}{(k - k_0)^2 + \Delta_k^2}, \quad (3)$$

where η_0 and k_0 are the centers of the distributions, and Δ_η and Δ_k are their half-widths at half-maximum. The latter two parameters describe the degree of heterogeneity in the excitability parameter and the coupling strength, respectively. This particular choice of distribution function permits analytical solutions. Because the distribution has infinite support, the infinitely large networks include both positive and negative η's and k's, meaning that the network contains a mixture of excitable and spiking neurons as well as inhibitory and excitatory connections. The ratios of these depend on the values of η_0 and k_0, i.e., where the distributions are centered.

2.2. Mean Field Reduction

We adopt a mean-field continuum description of our network (Kuramoto, 1975, 1984) by considering the limit $N \to \infty$ such that the network is described by a probability density function $F(\theta, \eta, k, t)$, where $F(\theta, \eta, k, t)d\theta d\eta dk$ gives the probability at time t of finding an oscillator with phase in $[\theta, \theta + d\theta]$ and parameters in $[\eta, \eta + d\eta]$ and $[k, k + dk]$. The total number of neurons is conserved and we assume that the marginal probability distribution functions $g_\eta(\eta)$ and $g_k(k)$ are both time-independent and independent of each other. Thus, F satisfies the continuity equation,

$$\frac{\partial F}{\partial t} + \frac{\partial}{\partial \theta}(Fv_\theta) = 0, \quad (4)$$

where v_θ represents the velocity of a neuron and is given by the continuum version of the single neuron equation,

$$v_\theta = (1 - cos\theta) + \Big[\eta + ka_n \int_{-\infty}^{\infty}\int_{-\infty}^{\infty}\int_0^{2\pi} F(\theta', \eta', k', t) (1 - cos\theta')^n d\eta' dk' d\theta'\Big](1 + cos\theta). \quad (5)$$

We also define the order parameter $z(t)$ in the continuum limit,

$$z(t) \equiv \int_0^{2\pi} d\theta \int_{-\infty}^{\infty} d\eta \int_{-\infty}^{\infty} dk F(\theta, \eta, k, t)e^{i\theta}. \quad (6)$$

This describes the collective behavior of the infinite network.

Ott and Antonsen showed that in the continuum limit, the macroscopic behavior of Kuramoto-type populations of globally coupled and heterogeneous phase oscillators displays low-dimensional dynamics (Ott and Antonsen, 2008, 2009). They adopted the ansatz that the probability density function describing the network can be written as a Fourier expansion in the phase variable whose coefficients are powers of a single complex function. Using the continuity equation and a self-consistency argument, they derived an equation that this complex function must satisfy. Ultimately, with appropriate choices of g_η and g_k (such as Equation 3), this procedure leads to a low-dimensional ordinary differential equation (ODE) whose asymptotic dynamics coincides with that of the order parameter $z(t)$ of the infinite discrete network. Thus, the asymptotic collective dynamics of the infinite discrete network can be obtained by solving that low-dimensional ODE instead of the infinitely many coupled ODEs of the discrete network (i.e., Equation 1), or the partial differential equation that describes the network in the continuum description (i.e., Equation 4). Later, Marvel et al. (2009) showed that the Ott-Antonsen (OA) approach applies more generally to other oscillator-type systems for which the velocity field v_θ can be written in "sinusoidally coupled form," i.e., $v_\theta = fe^{i\theta} + h + f^*e^{-i\theta}$, where the dependence on the individual oscillator's phase occurs only through the first harmonics $e^{i\theta}$ and $e^{-i\theta}$.

These methods were applied to a globally-coupled population of theta neurons with heterogeneity in the excitability parameter, which can be written in the sinusoidally-coupled form described above, by Luke et al. (2013). The result was a two-dimensional (i.e., complex) ordinary differential equation for $z(t)$ which identifies the asymptotic collective dynamics of the infinite discrete network. The equation admits three possible asymptotic states: equilibrium solutions with either real (node) or complex-conjugate (focus) eigenvalues, and limit cycles. The authors confirmed by numerical simulation that the reduced model accurately captures the collective behavior of discrete networks of 10,000 neurons.

Note that there is considerable discussion in the literature regarding the interesting question of the marginal stability of the OA manifold and its relation to earlier work. See, for example, Pikovsky and Rosenblum (2015), Mirollo (2012), Watanabe and Strogatz (1994), Watanabe and Strogatz (1993), and Goldobin and Dolmatova (2019), and for networks with parameter-dependent oscillators, such as our theta neuron network, see Pietras and Daffertshofer, 2016.

In the following, we follow the approach in Luke et al. (2013), but include heterogeneity in the coupling strength k as in Equation (3). We comment on the relationship between our results and those in Appendix E1 of Montbrió et al. (2015) in section 4.

2.3. Bifurcation Analysis Methods

In addition to constructing standard one-dimensional bifurcation diagrams, we employ the following less-common approach to bifurcation analysis (Luke et al., 2013). With $z(t) = x(t) + iy(t)$ and fixed values of n and Δ_k, we think of the conditions for an equilibrium solution (x_e, y_e),

$$\begin{aligned} \dot{x}(t) &= f(n, \Delta_k; x_e, y_e, \eta_0, \Delta_\eta, k_0) = 0 \\ \dot{y}(t) &= g(n, \Delta_k; x_e, y_e, \eta_0, \Delta_\eta, k_0) = 0, \end{aligned} \tag{7}$$

as being two constraints on the five independent variables x_e, y_e, η_0, Δ_η, and k_0. A saddle-node bifurcation occurs when one of the eigenvalues of the Jacobian J of the equations of motion (Equations 7) is zero. Thus, it is sufficient to require

$$det[J(x_e, y_e, \eta_0, \Delta_\eta, k_0)] = 0. \tag{8}$$

With this equation, we have three constraints on five variables, thus defining two-dimensional surfaces. We manipulate these equations to find expressions for η_0, Δ_η, and k_0, each in terms of x_e and y_e. This then allows us to parametrically plot the saddle-node bifurcation surfaces in the three-dimensional parameter space $(\eta_0, \Delta_\eta, k_0)$ by scanning over (x_e, y_e). In other words, we construct plots of two-dimensional surfaces in the parameter space $(\eta_0, \Delta_\eta, k_0)$ such that points on these surfaces correspond to parameter values at which an (unspecified) equilibrium undergoes a saddle-node bifurcation.

Since our reduced system is two-dimensional, surfaces of Hopf bifurcations can be obtained in the same way by replacing Equation (8) with

$$tr[J(x_e, y_e, \eta_0, \Delta_\eta, k_0, \Delta_k)] = 0 \tag{9}$$

subject to

$$det[J(x_e, y_e, \eta_0, \Delta_\eta, k_0, \Delta_k)] > 0. \tag{10}$$

Finally, surfaces corresponding to node-focus (NF) transitions can be obtained, for two-dimensional systems, using the condition

$$tr[J]^2 - 4det[J] = 0. \tag{11}$$

In the following, we examine how the saddle-node, Hopf, and node-focus transition surfaces evolve as Δ_k changes.

2.4. Computational Methods

One-dimensional bifurcation diagrams of the reduced equations were calculated using XPPAUT (Ermentrout, 2002), and three-dimensional diagrams were generated with custom-made code using the ParametricPlot3D function in Mathematica Version 12.0 (Wolfram Research, 2019). In addition, simulations of the discrete network were carried out to confirm the validity of our results, but are not reported here.

3. RESULTS

3.1. The Reduced System

To derive the reduced dynamical system for our network, we follow the methods of Ott and Antonsen (2008, 2009), Marvel et al. (2009), and Luke et al. (2013), but include heterogeneity in the coupling strength according to Equation (3). We sketch the procedure here.

We first write the velocity equation in sinusoidally coupled form, $v_\theta = fe^{i\theta} + h + f^* e^{-i\theta}$, with

$$\begin{aligned} f &= -\frac{1}{2}[(1-\eta) - kH(z,n)] \\ h &= (1 + \eta + kH(z,n)), \end{aligned} \tag{12}$$

where $H(z,n)$ is the rescaled synaptic current (Luke et al., 2013)

$$\begin{aligned} H(z,n) &= a_n(A_0 + \sum_{q=1}^{n} A_q(z^q + z^{*q})) \\ A_q &= \sum_{j,m=0}^{n} \delta_{j-2m,q} Q_{jm} \\ Q_{jm} &= \frac{(-1)^{j-2m} n!}{2^j m!(n-j)!(j-m)!}. \end{aligned}$$

Next we adopt the OA ansatz that the solution to the continuity equation, F, can be written as a Fourier series,

$$F(\theta, \eta, k, t) = \frac{g(\eta, k)}{2\pi} \left\{ 1 + \sum_{q=1}^{\infty} \left(\alpha^*(\eta, k, t)^q e^{iq\theta} + \alpha(\eta, k, t)^q e^{-iq\theta} \right) \right\}, \tag{13}$$

where $g(\eta, k) = g_\eta(\eta) * g_k(k)$ is the joint probability distribution for the two independent random variables. At this point, the complex function $\alpha(\eta, k, t)$ is yet to be determined. This manifold is invariant if and only if $|\alpha(\eta, k, t)| < 1$ and α satisfies

$$\dot{\alpha} = i(f\alpha^2 + h\alpha + f^*). \tag{14}$$

Substituting Equation (13) into Equation (6) [which defines the order parameter $z(t)$] then gives

$$z(t) = \int_{-\infty}^{\infty} \int_{-\infty}^{\infty} \alpha(\eta, k, t) g(\eta, k) d\eta dk,$$

which can be evaluated using analytic continuation and the residue theorem, resulting in

$$z(t) = \alpha(\eta_0 + i\Delta_\eta, k_0 + i\Delta_k, t). \tag{15}$$

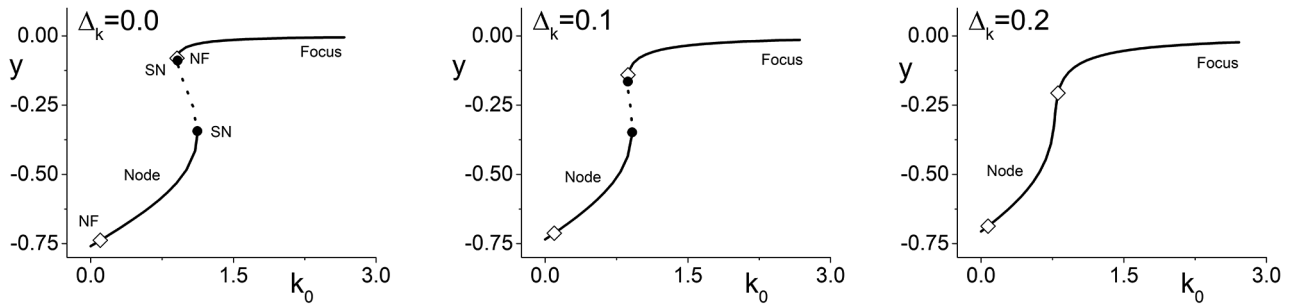


FIGURE 1 | Case 1: One-dimensional bifurcation diagrams showing $y = Im(z)$ vs. the parameter k_0, which is the center of the coupling strength distribution. The panels show the diagrams for increasing values of Δ_k, the width of the coupling strength distribution. Stable (unstable) equilibria are represented by solid (dotted) lines, and are nodes or foci as indicated. Open diamonds are node-focus transitions. For $\Delta_k = 0.0$, two saddle-node bifurcations are seen (solid black circles). These merge and disappear as Δ_k increases, but the node-focus transitions remain. The other parameters are $\eta_0 = -0.3$, $\Delta_\eta = 0.08$, and $n = 2$.

Substituting Equations (12) for f and h into Equation (14), combining with Equation (15), and evaluating at the residue, the reduced dynamical system is obtained:

$$\dot{z} = -i\frac{(z-1)^2}{2} + \frac{(z+1)^2}{2}\left[-\left(\Delta_\eta + \Delta_k H(z,n)\right) + i\left(\eta_0 + k_0 H(z,n)\right)\right]. \quad (16)$$

This result is similar to the result in Luke et al. (2013), but the incorporation of heterogeneity in the parameter k adds the relatively simple extra term that involves Δ_k. We numerically verified that predictions obtained with Equation (16) match the asymptotic collective behavior exhibited by a large discrete network of theta neurons. In fact, we find that the predictions from the reduced system are quite valid for networks with as few as 10,000 neurons (see also Luke et al., 2013). Note that we only consider solutions to Equation (16) with $|z| \leq 1$.

3.2. The Effects of Synaptic Diversity

As the title suggests, our main result is that increasing the synaptic diversity by increasing the parameter Δ_k, which is the width of the coupling strength distribution given in Equation (3), reduces the complexity of the collective dynamics of the network. We illustrate this result by using Equation (16) to construct series of one-dimensional bifurcation diagrams with increasing Δ_k. We then provide a more comprehensive perspective by using sequences of three-dimensional bifurcation diagrams.

Luke et al. (2013) argued that typically, interesting dynamics happen—by which we mean the occurrence of bifurcations of macroscopic quantities—when there is a competition between the intrinsic dynamics of individual neurons and the synaptic input. Thus, we concentrate attention on two generic cases. In our Case 1, we consider the situation in which most neurons are excitable ($\eta_0 < 0$) and are coupled by mostly excitatory synapses ($k_0 > 0$). Case 2 considers predominantly spiking neurons ($\eta_0 > 0$) with mostly inhibitory coupling ($k_0 < 0$). We keep $n = 2$ until the end, where we check the effects of setting $n = 9$.

3.2.1. One-Dimensional Bifurcation Diagrams

We begin by considering Case 1 (excitable neurons with excitatory coupling). **Figure 1** (left) shows a bifurcation diagram of $y = Im(z)$ vs. the parameter k_0 for $\Delta_k = 0$, i.e., no diversity in the coupling strength between neurons. The solid lines represent stable equilibria. Equilibria on the lower branch are nodes, and most of the upper branch are foci. The dotted line indicates unstable equilibria, and the solid circles are saddle-node bifurcations. The stable node that emerges from the upper saddle-node bifurcation almost immediately transitions into a stable focus at the location marked with an open diamond (NF). (Observe also that there is another node-focus transition near $k_0 = 0.0$.) Thus, throughout this range of k_0, the collective dynamics of the network is attracted to an equilibrium state. Interestingly, however, there is an interval of k_0 for which different equilibrium states coexist.

The middle and right panels of **Figure 1** show the same diagram but for $\Delta_k = 0.1$ and 0.2, respectively. We see the saddle-node points merge and disappear, thus removing the interval of multistability from these diagrams (with other parameters fixed). In this sense, introducing synaptic diversity removes an interesting dynamical feature from the network's behavior. Below we examine if this is true more globally. Note, however, that the node-focus transition points remain.

Figure 2 illustrates the more complicated situation that arises in Case 2 (spiking neurons with inhibitory coupling). Here, the upper left panel shows the one-dimensional bifurcation diagram of $x = Re(z)$ vs. η_0 for $\Delta_k = 0$ (no coupling strength diversity). We see a structure of lines representing stable and unstable equilibria (nodes and foci as indicated) with saddle-node bifurcations and a node-focus transition, which is very similar to that in **Figure 1**. In addition, however, there is a supercritical Hopf bifurcation depicted by the open circle, along with the limit cycle that emerges from it as η_0 decreases. This attracting limit cycle indicates that the network can exhibit collective time-dependent behavior with a degree of phase synchrony that oscillates in time. In the diagram, the red lines are the maximum and minimum values of x on this limit cycle. At its largest extent, the limit cycle collides with an unstable equilibrium in a homoclinic bifurcation. Note also that there is again an interval of multistability. In this case, the lower stable equilibrium (node) coexists with either the limit cycle or the upper equilibrium (focus), depending on η_0.

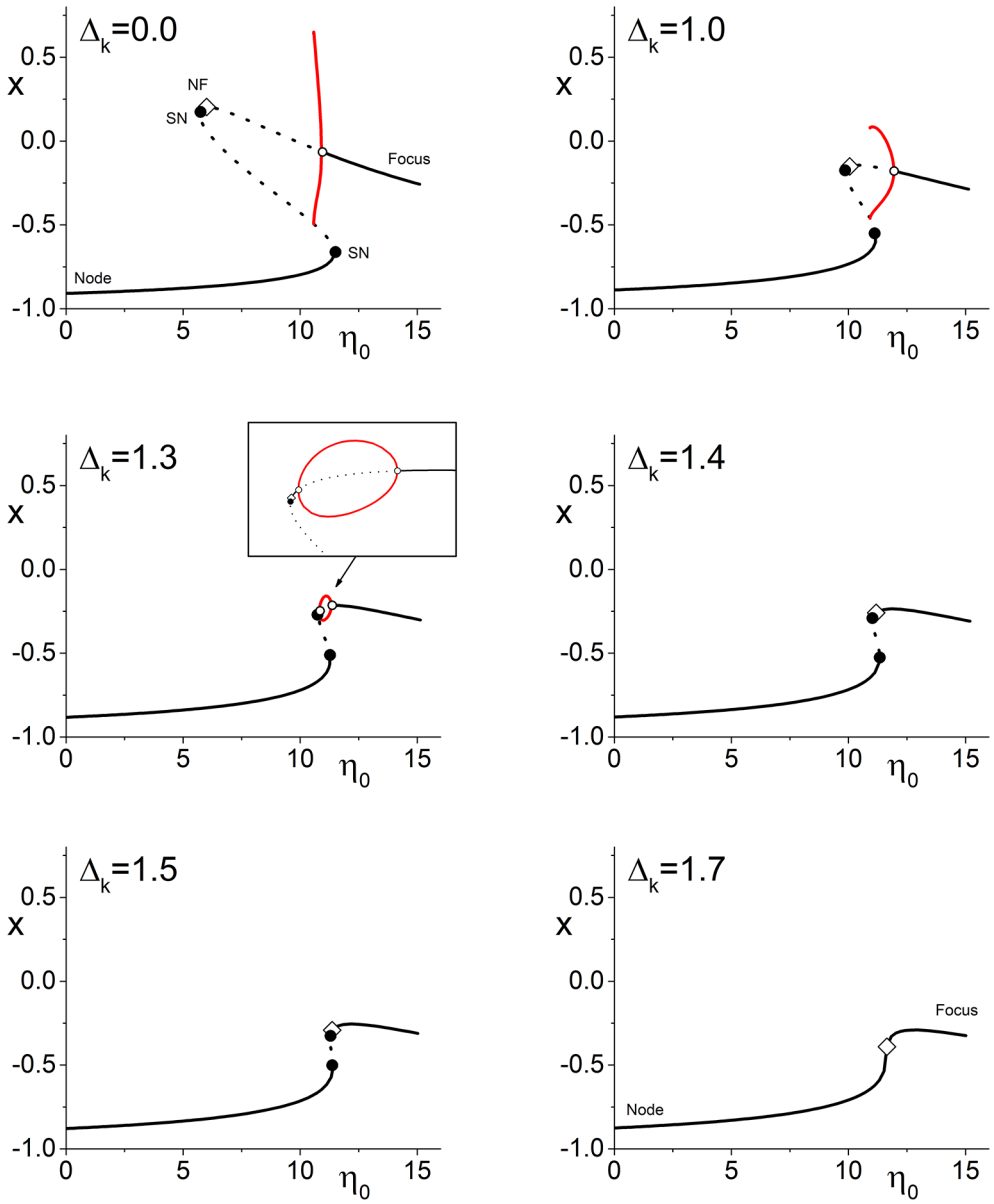


FIGURE 2 | Case 2: One-dimensional bifurcation diagrams showing $x = Re(z)$ vs. the parameter η_0. The panels show the diagram for increasing values of Δ_k, the width of the coupling strength distribution. Stable (unstable) equilibria are represented by solid (dotted) black lines, and are nodes or foci as indicated. Open diamonds are node-focus transitions. The maximal and minimal values of x on stable limit cycles are represented by the red lines. Solid black circles are saddle-node bifurcations, and open circles are Hopf bifurcations. As Δ_k increases, the various bifurcations merge and disappear, but the node-focus transition remains. The other parameters are $k_0 = -9.0$, $\Delta_\eta = 0.5$, and $n = 2$.

The subsequent panels show the same diagram but for increasing values of the coupling strength diversity parameter Δ_k as indicated. Again, we see that the various bifurcation points approach each other as Δ_k increases. An interesting phenomenon is how the homoclinic point approaches the upper saddle-node bifurcation. By $\Delta_k = 1.3$, it has disappeared, and a new Hopf bifurcation is seen on the upper branch (this sequence of events indicates that we are near a Bagdanov–Takens point, where the saddle-node, homoclinic, and left Hopf bifurcation coincide). The limit cycle now forms a loop linking the two Hopf points—see the magnified view in the inset.

As before, we observe that all these complexities merge and annihilate as Δ_k increases further. The two Hopf points coalesce, eliminating the limit cycle and the unstable equilibrium sandwiched between them. Subsequently the two remaining saddle-node points merge and disappear. Thus we see again that introducing synaptic diversity diminishes the dynamical repertoire of the network (at least when

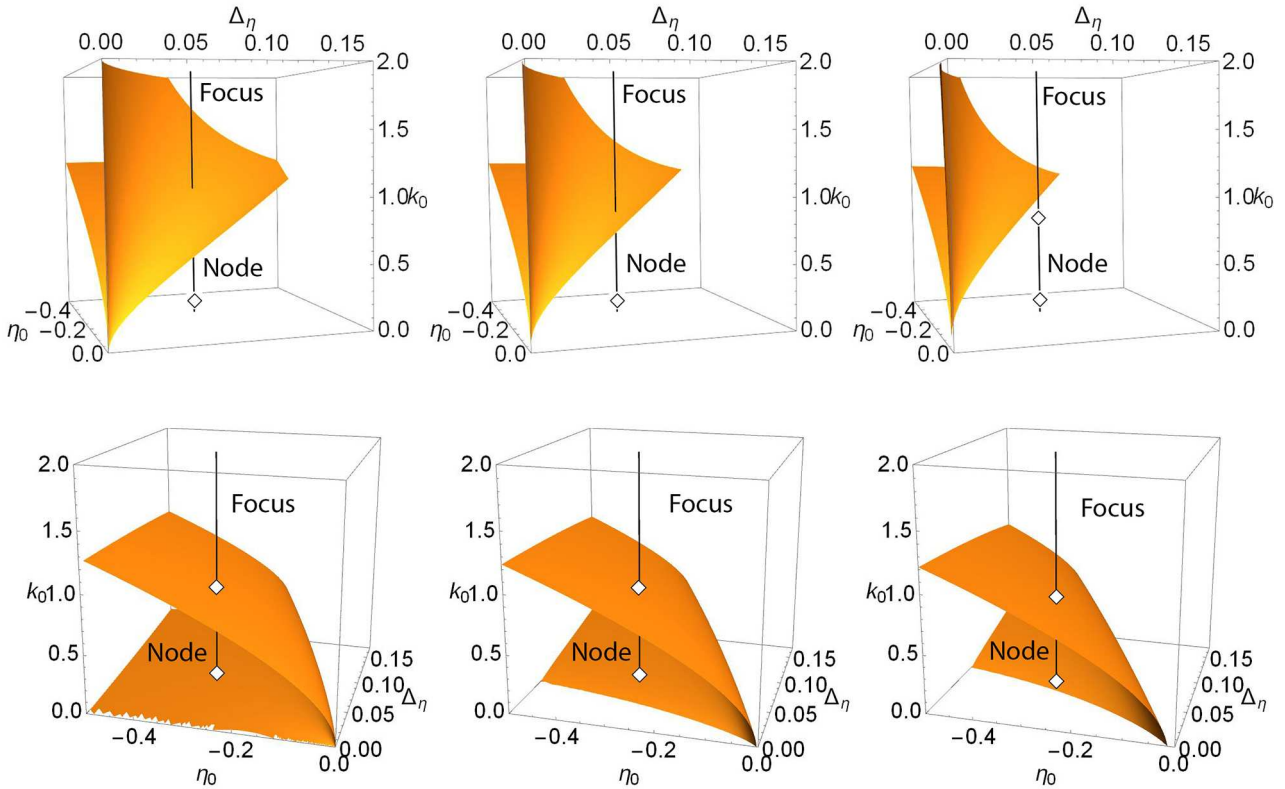


FIGURE 3 | Case 1: Plots of the saddle-node surface (top) and the node-focus surface (bottom) for $\Delta_k = 0.0$ (left), 0.1 (middle), and 0.2 (right), with $n = 2$. The black lines correspond to $\eta_0 = -0.3$ and $\Delta_\eta = 0.08$, and show the path traversed along k_0 in the bifurcation diagrams shown in **Figure 1**. Equilibria along the lines are labeled node or focus; see the discussion in the text. In the upper sequence, a hidden node-focus transition (open diamond) emerges in the right panel.

holding other parameters fixed). But, as before, the node-focus transition persists.

3.2.2. Three-Dimensional Bifurcation Diagrams

A reasonable question is whether or not this "decomplexification" by increasing synaptic diversity is something that happens locally in a particular region of parameter space, or if it is a more global phenomenon. We address this by showing three-dimensional bifurcation diagrams that incorporate the structures shown in **Figures 1** and **2**.

For example, the upper panels in **Figure 3** show a more general view of Case 1. The top left panel shows a locus of saddle-node points embedded in the $(\eta_0, \Delta_\eta, k_0)$ parameter space for $\Delta_k = 0$. This appears as a V-shaped folded sheet with a sharp crease. The black line corresponds to $\eta_0 = -0.3$ and $\Delta_\eta = 0.08$ and is the path traversed along k_0 in the one-dimensional bifurcation diagram shown in **Figure 1** (left). Node and focus equilibria along the black line are as indicated. This black line can be seen to intersect the saddle-node surfaces in two points; these are the same two saddle-node points shown in **Figure 1** (left). The remaining upper panels of **Figure 3** match those of **Figure 1**, and one can see that by increasing Δ_k, the saddle-node surface moves to the left (i.e, toward more negative η_0 and smaller Δ_η). In so doing, the creased fold in the surface approaches the fixed black line and then moves beyond it, so that the intersection points merge and then disappear. In the right panel, there is no longer any intersection.

Recall that in **Figure 1**, a node-focus point occurs very close to the upper saddle-node bifurcation. In the perspectives shown in the upper left and middle panels of **Figure 3**, this point is not visible, but it emerges in the right panel for $\Delta_k = 0.2$.

The lower panels in **Figure 3** show the node-focus surface for the same situation, but rotated to better show the folded shape. The diamonds show where the black line intersects this surface, and are the same diamonds that mark the NF transitions on the black lines in the upper panels. Within the region of parameter space shown, one generally finds a single attracting focus above (higher k_0) the NF surface, and an attracting node within the fold. However, multistability can occur.

For Case 2, a similar sequence of events can be seen in the upper three panels of **Figure 4**. These show the saddle-node surfaces corresponding to the $\Delta_k = 0.0$, 1.3, and 1.7 panels of **Figure 2**. Here, the black line is fixed at $k_0 = -0.9$ and $\Delta_\eta = 0.5$, representing the path traversed along η_0 in the one-dimensional bifurcation diagrams of **Figure 2**. Again we see a folded and creased saddle-node surface that migrates toward the unphysical negative Δ_η region with increasing Δ_k until it no longer intersects the black line. Note that in the right panel, the view has been rotated to show the lack of intersection.

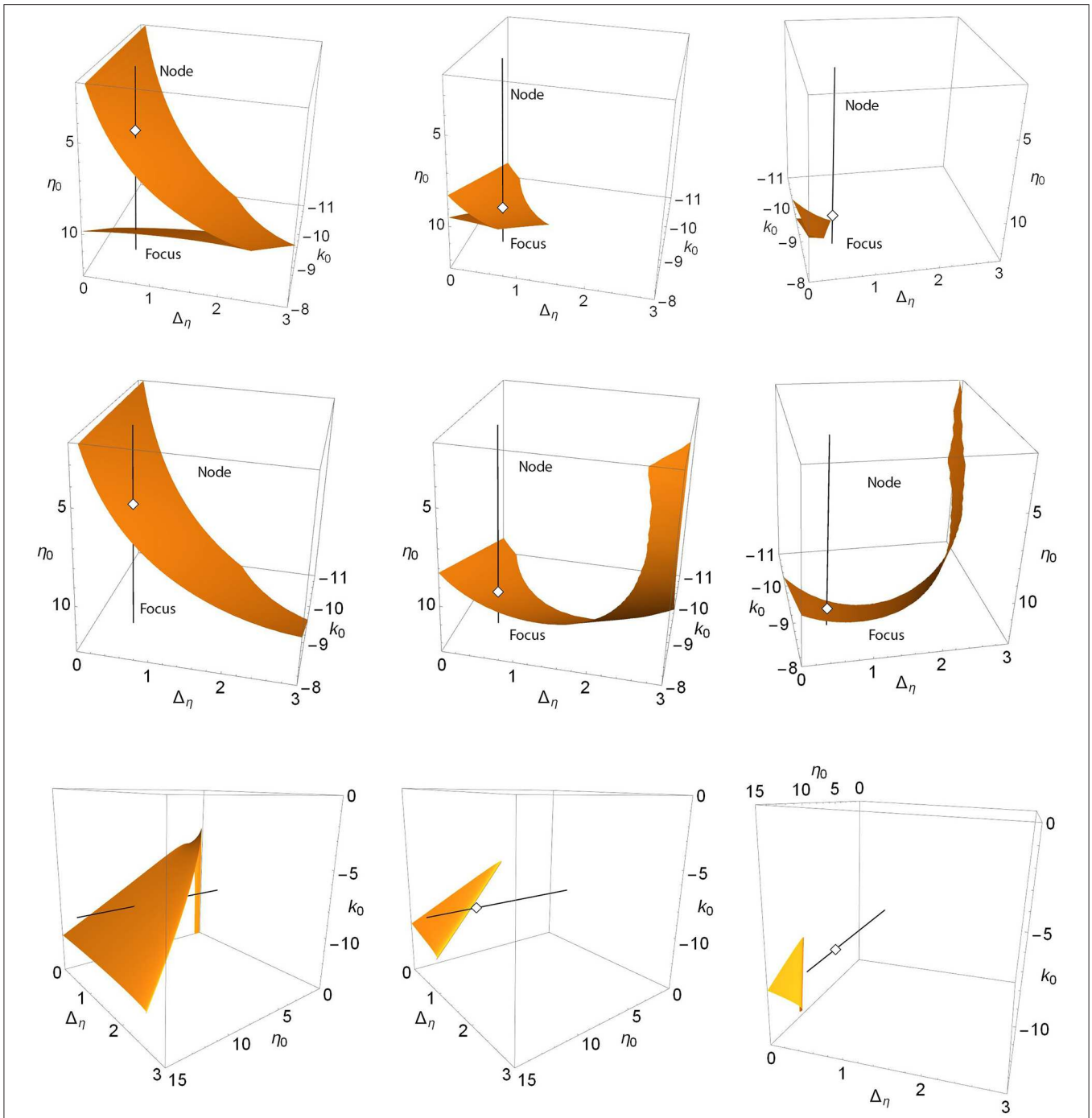


FIGURE 4 | Case 2: Plots of the saddle-node surface (top), the node-focus surface (middle), and the Hopf surface (bottom) for $\Delta_k = 0.0$ (left), 1.3 (middle), and 1.7 (right), with $n = 2$. The black line corresponds to $k_0 = -9.0$ and $\Delta_\eta = 0.5$, and is the path traversed along η_0 in the bifurcation diagrams shown in **Figure 2**. Open diamonds are node-focus transitions. The views in the upper and middle right panels have been rotated for clarity. In particular, the black line does not intersect the SN surface for $\Delta_k = 1.7$. The view in the lower panels is also rotated to better show the structure.

The middle panels show the node-focus surface. As Δ_k increases, the surface lowers and twists, but remains present. The larger structure, of which we only see limited portions here, is difficult to discern from these images. Below we examine a more comprehensive view.

The lower panels of **Figure 4** show the corresponding Hopf surfaces. The view has been rotated to give an easier-to-understand perspective. In the left panel, this surface resembles a high-heeled shoe, and we see a single intersection with the black line. This intersection point is the same Hopf bifurcation denoted

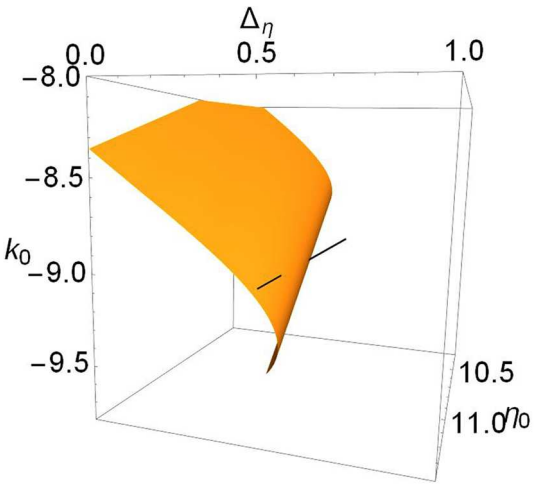


FIGURE 5 | Magnified view of the Hopf surface shown in the lower middle panel of **Figure 4**, for $\Delta_k = 1.3$, showing two intersections.

with the open circle in **Figure 2** for $\Delta_k = 0$. As Δ_k increases, the "shoe" migrates into the unphysical negative-Δ_η region, leaving the black line without intersections. Note that the NF transition point, hidden behind the surface in the left panel, emerges in the middle and right panels.

Recall that for $\Delta_k = 1.3$, we saw the interesting structure with the two Hopf bifurcation points in **Figure 2**. This case corresponds to the lower middle panel of **Figure 4**. Since it is hard to see, we present in **Figure 5** a magnification of the region where the black line intersects the surface. We see that the Hopf surface has a gentle curl at the edge such that as the surface migrates away, the approaching curl gives rise to a second intersection point before the surface goes away entirely. In fact, the lower edge of the Hopf surface seen here is a line of Bagdanov–Takens bifurcations.

To complete the story, we show in **Figures 6**, **7**, and **9** views of the saddle-node, Hopf, and node-focus surfaces with the ranges of η_0, k_0, and Δ_k greatly expanded. For visual clarity, we did not expand the Δ_η range, but our conclusions still hold. Recall also that Δ_η is the half-width at half-maximum of the distribution g_η in Equation (3). Therefore, negative values of this parameter are not considered.

In **Figure 6**, we see that the saddle-node surfaces are actually two V-shaped sharply-creased sheets corresponding our two cases. One surface occurs in the negative-η_0/positive-k_0 region, matching Case 1 (excitable neurons coupled with excitation), and the other occurs in the positive-η_0/negative-k_0 region, matching Case 2 (spiking neurons coupled with inhibition). Note also that the edges of the creased folds bend away toward $\pm\eta_0$ as Δ_η increases. As Δ_k increases, the two folded sheets migrate away from each other until essentially nothing is left within the view shown.

In contrast, we see in **Figure 7** that there is only one Hopf surface. It resides entirely within the Case 2 region (positive-η_0/negative-k_0). There is no corresponding Hopf surface in the Case 1 region (negative-η_0/positive-k_0).

The gray curved line in the top-left panel of **Figure 7** is the boundary between the subcritical and supercritical Hopf bifurcations. The supercritical versions occur on the side with larger values of η_0. In all the other panels, only supercritical bifurcations are found. The black lines correspond to paths used to calculate the one-dimensional bifurcation diagrams shown in **Figure 8**. This latter figure shows the periodic orbits that emerge from the Hopf bifurcations. On the left we see a subcritical bifurcation, where the dotted blue line denotes an unstable periodic orbit. Note that as this unstable orbit grows with increasing k_0, it collides with a stable periodic orbit (red line) at a saddle-node-of-periodic-orbits bifurcation (triangle). From this point, the stable orbit grows with decreasing k_0 until it collides with the lower unstable equilibrium and disappears in a homoclinic bifurcation. The right panel shows a supercritical Hopf bifurcation, with a stable periodic orbit (red) emerging and growing with decreasing k_0 until it too disappears in a homoclinic bifurcation.

Returning to the more comprehensive view of **Figure 7**, we see that as Δ_k increases, the surface disappears into the unphysical negative Δ_η region. Thus, increasing the synaptic diversity also removes the Hopf bifurcation structure such that by $\Delta_k = 3.0$, essentially nothing is left within the view shown. Interestingly, we find that subcritical Hopf bifurcations only occur for small values of Δ_k, i.e., little synaptic strength diversity. For example, the subcritical Hopf bifurcation shown in **Figure 8** (left) for $\Delta_k = 0.0$ remains subcritical as Δ_k increases to 0.114, where it merges with the saddle-node-of-periodic-orbits bifurcation at a Bautin point. Increasing Δ_k further, the bifurcation becomes supercritical, and goes on to follow a scenario similar to that shown in **Figure 2**, until it disappears at $\Delta_k = 0.864$.

Finally, we show the node-focus transition surfaces as Δ_k increases in **Figure 9**. The structure looks complicated for $\Delta_k = 0.0$, but its overall shape becomes clear as Δ_k increases and its various components separate. The surfaces occur in two pieces. There is a folded-over sheet in the Case 1 region of excitable neurons ($\eta_0 < 0$) with excitation ($k_0 > 0$), and another sheet that covers the entire η_0-Δ_η region shown and which, for $\Delta_k = 0.0$, dips sharply down toward negative k_0 in the Case 2 region ($\eta_0 > 0$ and $k_0 < 0$; spiking neurons with inhibition). As Δ_k increases, two things happen: the folded sheet in the Case 1 region migrates away toward the negative-η_0 direction, and the other sheet flattens out (i.e., occurs within a more restricted range of k_0 within the view shown).

To understand the nature of the equilibrium solutions that correspond to this region of parameter space, we identified and followed the equilibria along the black lines seen in the upper right panel of **Figure 9**. Generally, for parameters corresponding to the region above (meaning higher values of k_0) the surfaces shown, there exists a single stable focus equilibrium (recall that we restrict attention to solutions with $|z| \leq 1$). For the line with positive η_0, the NF surface is crossed only once as k_0 decreases, and below it we find a stable node. For the line with negative η_0, there are three surface crossings as k_0 decreases. We observe the following sequence of equilibria: Stable focus, stable node (within the folded upper surface), stable focus (between the folded surface and the lower sheet), and stable node (below

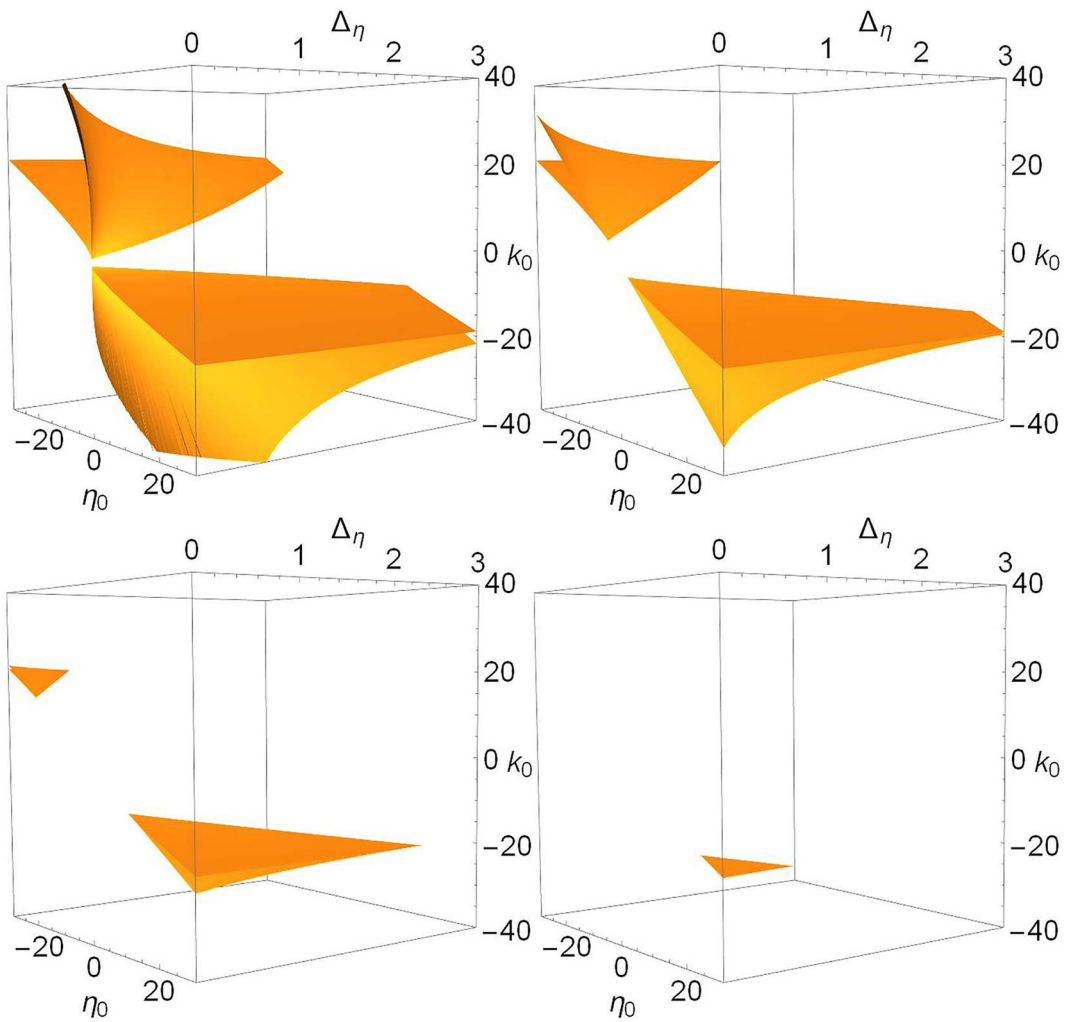


FIGURE 6 | The saddle-node surfaces disappear from view as Δ_k increases. $n = 2$ and $\Delta_k = 0.0$ **(top left)**, 1.0 **(top right)**, 2.0 **(lower left)**, and 3.0 **(lower right)**.

the lower sheet). The same scenarios were observed along lines shifted to $\Delta_\eta = 0.5$, and for the different values of Δ_k of the other panels (not shown). Note, however, that in some cases saddle-node bifurcations create other coexisting equilibria—compare **Figure 6**—so it is not entirely clear from **Figure 9** alone which equilibrium transitions as the NF surface is crossed. (One may resolve this issue with one-dimensional bifurcation diagrams such as those in **Figures 1** and **2**.) However, as we have seen, the other bifurcation surfaces leave this region of parameter space as Δ_k increases, and the situation becomes simpler.

It is interesting to compare our two cases in this context. In the Case 1 region, the folded sheet introduces more node-focus transitions. And as the synaptic diversity Δ_k increases, this folded surface moves away toward negative η_0, thus leading to reduced complexity within the view shown. However, the lower sheet persists, and covers the entire η_0-Δ_η plane. It shifts to be within a more restricted interval of k_0 (i.e., it flattens), but it remains.

Finally, we consider the effect of changing $n = 2$ to $n = 9$ in Equation (2), which results in a much narrower synaptic pulse. **Figure 10** shows (top to bottom) the saddle-node, Hopf, and node-focus surfaces for increasing values of Δ_k (right to left). In general, the surfaces are very similar to those shown in **Figures 6**, **7**, and **9**. The most obvious difference is in the Hopf surface for $\Delta_k = 0.0$. Comparing this panel to the upper right panel in **Figure 7**, we see that the downward spike seen for $n = 2$ opens up, becomes wider, and moves toward more negative values of k_0 for $n = 9$. A more subtle observation is that the migration of the surfaces in all the panels seems to occur slightly slower with respect to Δ_k. By this we mean that for equal surface migration, the $n = 9$ case may require a slightly higher value of Δ_k than for the $n = 2$ case. Overall, however, we see qualitative agreement with our results for $n = 2$. Specifically, our observation that increasing the synaptic strength diversity causes the various surfaces to migrate toward regions of the parameter

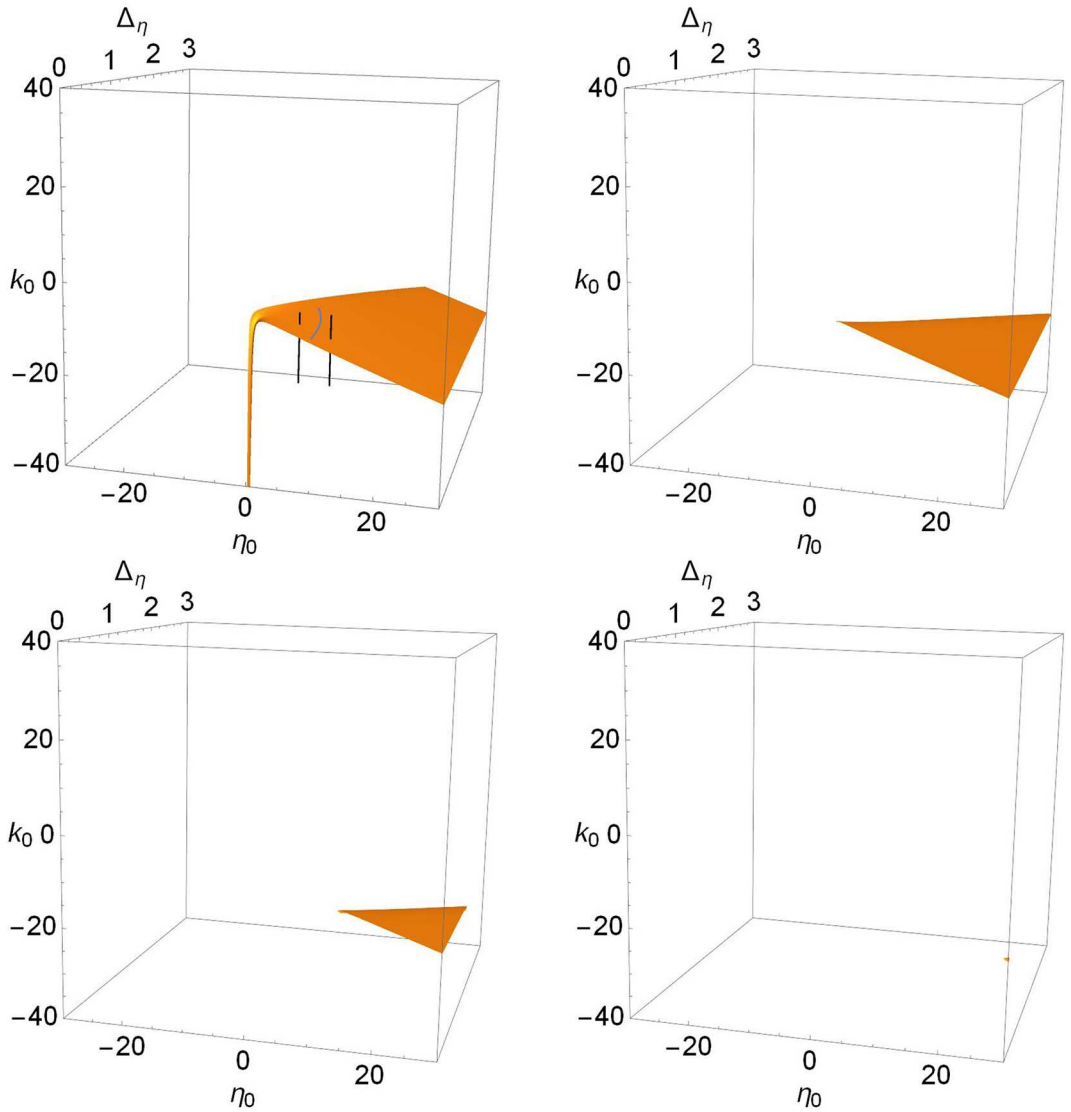


FIGURE 7 | The Hopf surfaces disappear from view as Δ_k increases. $n = 2$ and $\Delta_k = 0.0$ **(top left)**, 1.0 **(top right)**, 2.0 **(lower left)**, and 3.0 **(lower right)**. The gray line on the surface in the top left panel marks the boundary between sub- and super-critical Hopf bifurcations, and the black lines correspond to paths taken to create the one-dimensional bifurcation diagrams shown in **Figure 8**. Super-critical bifurcations occur on the side with larger η_0, and in all the other panels.

space with larger and/or non-physical values of the parameters is consistent with the $n = 9$ results shown in **Figure 10**.

4. DISCUSSION

We constructed a large network of theta neurons that included diversity in the excitability parameters as well as connections with diversity in their coupling strengths. Our aim was to examine the effects of adding this synaptic diversity. Extending previous work in Luke et al. (2013), we applied the OA reduction technique to derive a surprisingly simple ordinary differential equation that we used to identify the asymptotic behavior of the order parameter, which quantifies the macroscopic collective behavior of the network. Setting the synaptic diversity to zero, we constructed one-dimensional bifurcation diagrams and found dynamical structures that underlie the repertoire of collective behaviors that the network exhibits: equilibrium states—both nodes and foci—corresponding to states of partial synchrony of the network, limit-cycle states of temporally-evolving partial synchrony, saddle-node, Hopf, and homoclinic bifurcations, node-focus transitions, and different versions of multistability (Luke et al., 2013). We then increased the synaptic diversity and found that these rich dynamical structures migrated away toward unphysical and/or extreme regions of parameter space, except for one portion of the node-focus transition surface.

It is interesting to note that Ott and Antonsen's analysis revealed how the potentially high-dimensional behavior of a population of phase oscillators collapses onto a low-dimensional

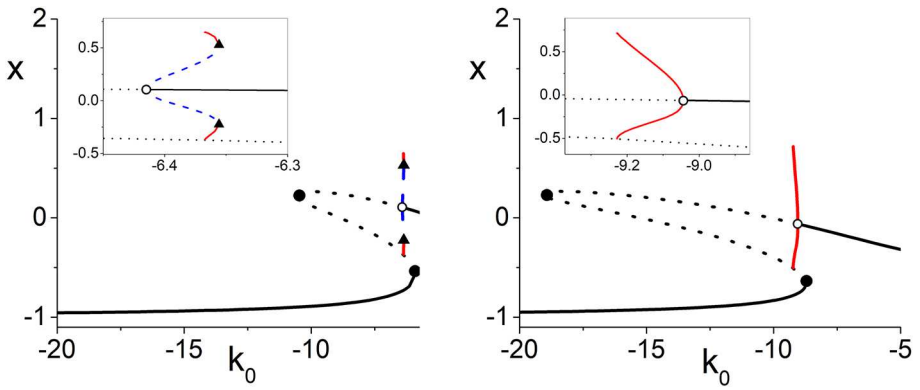


FIGURE 8 | One-dimensional bifurcation diagrams showing $x = Re(z)$ vs. k_0 illustrating subcritical **(left)** and supercritical **(right)** Hopf bifurcations (open circles). The insets are magnifications. These diagrams correspond to paths along the black lines in the top left panel of **Figure 7**. Here, black solid (dotted) lines are stable (unstable) equilibria, red (dotted blue) lines indicate stable (unstable) limit cycles, solid circles are saddle-node bifurcations, and triangles are saddle-node-of-periodic-orbits bifurcations. The other parameters are $\Delta_k = 0.0$, $n = 2$, $\Delta_\eta = 0.4$, and $\eta_0 = 6.0$ **(left)** and 11.0 **(right)**.

"OA manifold" defined by their ansatz (Equation 13) (Ott and Antonsen, 2008). But this does not happen in networks of identical phase oscillators. In fact, the OA manifold is only attracting when the oscillator population is heterogeneous (Ott and Antonsen, 2009; see also Pietras and Daffertshofer, 2016, which addresses this issue for systems such as our theta neuron network). Indeed, it becomes more attracting with increasing parameter heterogeneity. Accordingly, we found that incorporating an additional dimension of diversity into our network resulted in even simpler behavior than we already had.

Our sequences of one- and three-dimensional bifurcation diagrams allow us to interpret this somewhat abstract description of the complexity collapse within the more concrete context of our specific network, and draw inferences in biophysical terms. Dynamical complexity arises from macroscopic bifurcations, which require the right mix of parameters such that different dynamical tendencies compete against each other (Luke et al., 2013). We grossly categorized these into two cases: Case 1 corresponds to predominantly resting but excitable neurons connected mostly by excitation, and Case 2 corresponds to predominantly spiking neurons connected mostly by inhibition (the qualifying adjectives are necessary because the Cauchy–Lorentz distribution has infinite support). These scenarios have been studied for decades; for a small sampling, see, e.g., (Van Vreeswijk et al., 1994; Hansel et al., 1995; Brunel and Hakim, 2008), and some recent works (Devalle et al., 2017; di Volo and Torcini, 2018; Bi et al., 2020) that have investigated mechanisms for the emergence of collective oscillations in Case 2, as we discuss below. Note that our two cases suffice: parameter space regions corresponding to other mixtures of parameters were less interesting in that they did not contain bifurcations.

With $\Delta_k = 0$, we see from the first panels in **Figures 1**, **2**, and **6** that saddle-node bifurcations, unstable equilibria, and multistability between different equilibria occur in both Cases 1 and 2. In addition, the region inside the V-shape of the folded saddle-node surfaces, where multistability occurs, is wider if Δ_η is smaller, meaning that in both cases, a narrower distribution of neuronal excitability favors multistability. Most importantly, adding diversity by increasing Δ_k causes the two saddle-node surfaces to move away from each other, deeper into their own regions. That is, the Case 1 surface moves toward negative η_0 and positive k_0, and the Case 2 surface moves toward positive η_0 and negative k_0. In both cases, they also move toward the unphysical region of negative Δ_η. This migration is quite significant: within the parameter space shown in **Figure 6** (i.e., $\eta_0 \in [-30, 30], k_0 \in [-40, 40], \Delta_\eta \in [0, 3]$), only a tiny sliver of the Case 2 saddle-node surface remains for $\Delta_k = 3.0$. This suggests that the Case 1 surface moves away more quickly with respect to Δ_k. Indeed, for $\Delta_k = 6.0$, to see only small slivers of both surfaces requires the much larger and asymmetric parameter space region defined by $\eta_0 \in [-200, 100], k_0 \in [-60, 120]$, and $\Delta_\eta \in [0, 3]$ (not shown). All this means that with substantial synaptic diversity, complexity in the sense of finding saddle-node bifurcations requires very carefully tuned parameters at *extreme* values.

Similarly, we see in **Figure 7** that Hopf bifurcations occur only in Case 2, i.e., with predominantly spiking neurons ($\eta_0 > 0$) and inhibitory synapses ($k_0 < 0$), as is generally well-known (Van Vreeswijk et al., 1994; Hansel et al., 1995; Ermentrout, 1996; Brunel and Hakim, 2008; Devalle et al., 2017). We also find that Hopf bifurcations occur preferentially for more uniform networks (Δ_η small). In our theta neuron network, the vast majority of these are of the super-critical variety, but sub-critical bifurcations do occur in a small region of parameter space corresponding to weakly active neurons (small η_0) and little synaptic diversity (small Δ_k). And again, we see that with increasing synaptic diversity, the Hopf surface moves away such that this bifurcation requires more removed ($\eta_0 \gg 0$) and narrower ($\Delta_\eta \gtrsim 0$) distributions of the excitability parameter, as well as stronger inhibitory coupling ($k_0 \ll 0$).

Hopf bifurcations are currently of particular interest as they give rise to periodic orbits that are thought to underlie the emergence of fast gamma oscillations in inhibitory QIF networks, as has been recently investigated (Devalle et al., 2017; Bi et al., 2020). Interestingly, Bi et al. (2020) considered QIF

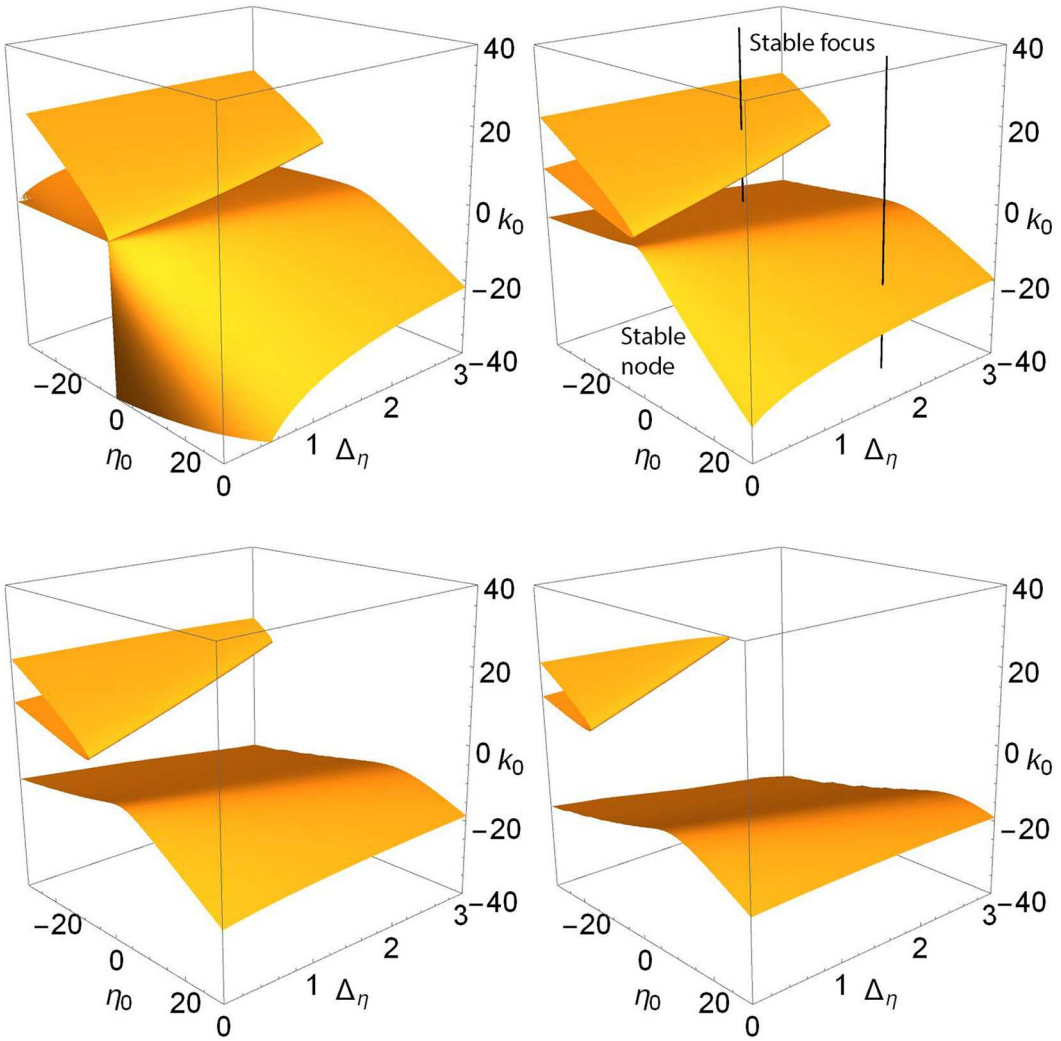


FIGURE 9 | The node-focus surfaces as Δ_k increases. $n = 2$ and $\Delta_k = 0.0$ **(top left)**, 1.0 **(top right)**, 2.0 **(lower left)**, and 3.0 **(lower right)**. Along the black lines in the upper right panels, we find a stable focus for k_0 above the surfaces, and a stable node below; see the discussion in the text.

networks with diversity in the synaptic strengths but not in the neurons' excitabilities, and found both sub- and supercritical Hopf bifurcations. In contrast, Devalle et al. (2017) considered QIF networks with diversity in the neurons' excitabilities but not in the synaptic strengths, and found only super-critical Hopf bifurcations. Recalling the equivalence between the QIF neuron and the theta neuron, it is interesting that in our theta neuron network, which includes both kinds of diversity, we find both kinds of Hopf bifurcations. However, as noted above, the sub-critical ones occur only in a small region of parameter space and with little synaptic diversity. Also interestingly, none of the works cited above report the termination of a limit cycle via homoclinic bifurcation, as we do.

But there is another important difference between the QIF models cited above and our theta neuron network that complicates the question: the synaptic connections are modeled differently. Montbrió et al. (2015) and di Volo and Torcini (2018) used delta-function pulses and included excitability but not synaptic diversity, and did not find Hopf bifurcations[1]. Bi et al. (2020) included exponentially-decaying post-synaptic currents with a non-zero time constant τ. They found both sub- and super-critical Hopf bifurcations. Devalle et al. (2017) included excitability but not synaptic diversity, and found that supercritical Hopf bifurcations only occur with τ within a finite range greater than zero, and that sub-critical Hopf bifurcations do not occur at all. In contrast to these works, we included both excitability and synaptic diversity, and we modeled our synapse by the pulse in Equation (2) with $n = 2$ (or 9). Since this is a wide pulse, we effectively have a non-zero synaptic time constant, but note that unlike (Devalle et al., 2017; Bi et al., 2020), we do not have an additional equation

[1]Montbrió et al. (2015) included synaptic diversity in their Appendix E1, but did not consider inhibitory coupling, necessary for Hopf bifurcations.

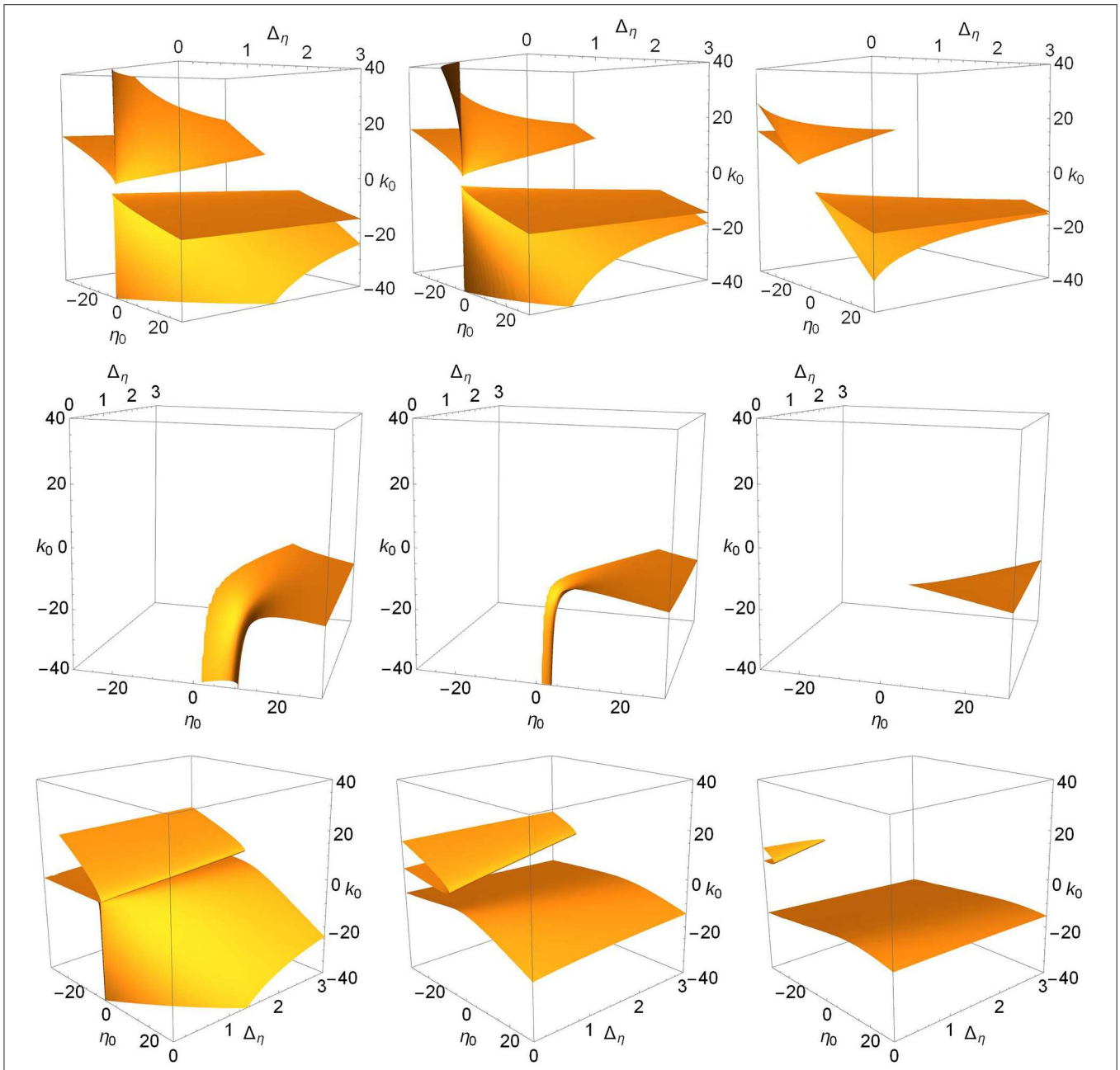


FIGURE 10 | The surfaces for $n = 9$, for which the synaptic pulse (Equation 2) is much narrower. **(Top)** The saddle-node surfaces for $\Delta_k = 0.0, 1.0, 2.0$. **(Middle)** The Hopf surfaces for $\Delta_k = 0.0, 1.0, 2.0$. **(Bottom)** The node-focus surfaces for $\Delta_k = 0.0, 3.0, 5.0$ (values chosen for visual clarity).

governing our synaptic dynamics. Thus our network is different from any of the ones considered above. We found both sub- and super-critical Hopf bifurcations, but our subcritical ones required low excitability diversity (i.e., small Δ_η). All of this might suggest that in addition to the requirement for a non-zero synaptic time constant, diversity in excitability might favor the occurrence of supercritical Hopf bifurcations, and synaptic diversity might favor subcritical Hopf bifurcations. But this is not clear, since in our case, the subcritical variety only occurred with small amounts of synaptic diversity. Furthermore, O'Keeffe and Strogatz (2016) studied a mixed system of excitable and active oscillators analogous to our theta neurons, and compared the effects of using a broad pulse vs. a delta-function pulse for the coupling. They found *only* subcritical Hopf bifurcations for the broad pulse coupling, and only supercritical Hopf bifurcations for the delta-function coupling.

It would be interesting to examine the limit $n \to \infty$, for which our pulse approaches a delta function. Given the results

in Devalle et al. (2017), we might expect the Hopf bifurcation surface to disappear in this limit. Our results for the Hopf surface with $n = 9$ (a narrower pulse), shown in the middle row of **Figure 10**, perhaps hints at this. Compared to the $n = 2$ case, the Hopf surface for $\Delta_k = 0.0$ has shifted toward more negative values of k_0 (stronger inhibitory coupling), especially for small Δ_η (narrower excitability distributions). Interestingly, however, no such overall shift appears to occur for the saddle-node or node-focus surfaces. In any case, a more complete study would certainly be needed before drawing any confident conclusions.

di Volo and Torcini (2018) and Bi et al. (2020) identified another mechanism that may give rise to slow gamma oscillations, namely fluctuation-driven oscillations that circulate around a stable focus. Since this mechanism does not work with a node, this is relevant to our study of the node-focus transition. This transition is not a true bifurcation in that it does not involve changes in either the existence or stability of a solution. Nevertheless, we identified the corresponding surfaces in parameter space, and observed that, as the synaptic diversity is increased, they behave both similarly and differently as compared to surfaces of the true bifurcations discussed above. We found (**Figure 9**) that in the parameter space corresponding to our Case 1, there are essentially three NF surfaces that are crossed as k_0 changes—a folded upper surface with two intersections and a lower surface—thus introducing complexity in the possible network behavior. However, the upper (higher k_0) folded sheet migrates away toward extreme values of negative-η_0 as synaptic diversity increases. In contrast, the increased synaptic diversity does not cause the lower NF surface, which occurs for negative k_0, to migrate away. It persists. For Case 2, only this lower NF surface occurs. Furthermore, as Δ_k increases and the saddle-node and Hopf surfaces move away, we find that the central parameter space rather neatly splits into a region for which a stable focus equilibrium exists for k_0 larger than a critical value (which depends increasingly weakly on η_0 and Δ_η), and a stable node exists for k_0 more negative than this critical value. This suggests that for non-extreme, physiologically "reasonable" parameter sets and sufficiently large fluctuations, the occurrence of fluctuation-driven collective network oscillations in networks of theta neurons with significant diversity in the connection weights depends quite simply on the value of the center of the connection weight distribution.

It is important to note that in Appendix E1 of Montbrió et al. (2015), the authors considered the same issue—the effect of introducing synaptic diversity—that we examine here. There are some differences in our formulations of the problem, however. We constructed our network using theta neurons, and they used quadratic integrate-and-fire neurons. This is not a major difference because, as was noted previously, these systems are related by a change of variable. Furthermore, we both used independent Cauchy–Lorentz distributions for the excitability parameters and synaptic strengths (i.e, Equation 3). A more important difference lies in the synaptic models. Montbrió et al. (2015) used delta function pulses, whereas we use the continuous pulse of Equation (2) with $n = 2$ (or 9), which is wide with respect to the state of the pre-synaptic neuron and is always "on" (see also O'Keeffe and Strogatz, 2016, which used a similar pulse). Also different are the macroscopic variables used to describe the collective network dynamics: We used the Kuramoto order parameter, and Montbrió et al. (2015) used the more directly interpretable quantities of firing rate and mean membrane potential. But we both found that the macroscopic equations, when extended to the case with heterogeneous coupling strengths, simply involves a single additional term proportional to the width of the coupling strength distribution.

Montbrió et al. (2015) reported their results in their Figure 9, which shows a family of saddle-node bifurcation curves parameterized by $\Gamma/\Delta^{1/2}$ on a two-dimensional plot of their rescaled parameters $\bar{J}/\Delta^{1/2}$ vs. $\bar{\eta}/\Delta$, where $\bar{J}$ and $\bar{\eta}$ are the center values of their current and synaptic weight distributions, and Δ and Γ are their widths, respectively. The saddle-node curves identify regions of bistability, and these are seen to shift toward lower values of $\bar{\eta}/\Delta$ and higher values of $\bar{J}/\Delta^{1/2}$ as $\Gamma/\Delta^{1/2}$ increases. We note that their graph is restricted to what is the equivalent of our Case 1: mostly excitable neurons with mostly excitatory connections ($\bar{\eta}/\Delta < 0$ and $\bar{J}/\Delta^{1/2} > 0$).

We see qualitatively equivalent behavior in our formulation: a careful study of appropriate slices of the surfaces shown in the upper panels of our **Figure 3** reveals that our results are consistent with those already published in Figure 9 of Montbrió et al. (2015). However, we do not rescale our parameters as they do, and this allows us to observe that the saddle-node surfaces move toward extreme values of $\pm\eta_0$ and $\pm k_0$, and into the unphysical negative-Δ_η region, as we increase the synaptic strength diversity Δ_k. We believe that it is appropriate to assume that the parameters η_0, k_0, and Δ_η have a somewhat restricted range of "reasonable" values. In this sense, our main result can be taken to mean that with increasing synaptic diversity, parameter values that correspond to interesting bifurcations of macroscopic variables move toward extreme and "unreasonable" regions of parameter space, and in this sense, are not likely to be encountered under "reasonable" circumstances. This conclusion is not evident in Figure 9 of Montbrió et al. (2015).

Furthermore, we adopt a more comprehensive view of the parameter space as compared to Montbrió et al. (2015) that includes our Case 2, i.e., networks of spiking neurons ($\eta_0 > 0$) coupled by inhibition ($k_0 < 0$), as well as the rest of the parameter space. In addition, we also consider saddle-node and Hopf bifurcations as well as the node-focus transition. See **Figures 6**, **7**, and **9**, respectively. It is interesting to note that the occurrence of saddle-node bifurcations are essentially restricted to Cases 1 and 2, and Hopf bifurcations just to Case 2, whereas the "off-diagonal" regions do not contain any bifurcation structures. We also observed that for small values of Δ_k, a folded surface of node-focus transitions occurs within the "reasonable" Case 1 region of parameter space, thus adding an additional measure of complexity which shifts away to "unreasonable" regions as Δ_k increases.

In a biological sense, a rich dynamical structure represents the means by which the firing patterns of neural assemblies in the brain can be dynamic and change states in response to external stimuli. Such differences in macroscopic patterns have been shown to strongly correlate with the function of different brain regions (Shinomoto et al., 2009). At the same

time, our findings are consistent with an *in vitro* study of how intrinsic heterogeneity in the phase response curve (PRC) characteristics of olfactory bulb mitral cells limits correlation-induced synchronous neural oscillations (Burton et al., 2012). See also the theoretical analysis of Pazó et al. (2019), which finds that beyond a critical level of PRC heterogeneity, the incoherent state—a simple equilibrium—is always stable. These works, and our observations reported here, suggest that evolution tunes the diversity of neuronal populations to achieve an appropriate balance between dynamical complexity and simplicity, depending on function.

Several avenues for future work suggest themselves. First, the assumption of global coupling may or may not be realistic, depending on the level of description that is desired. Interestingly, however, our network formulation includes a kind of sparsely-connected network in the case $k_0 = 0$, in which the majority of synaptic connections are very weak, regardless of the chosen spread Δ_k. This observation was used explicitly in di Volo and Torcini (2018) to relate collective oscillations in a network with a Cauchy–Lorentz distribution of in-degrees to the occurrence of a collective stable focus in the analogous globally-coupled network of Montbrió et al. (2015). In our work, we find in **Figures 6**, **7**, and **9** that the $k_0 = 0$ plane is the very boundary between the regions of interesting and simple dynamical structures. Second, our formulation allows a study of the role of the synaptic sharpness parameter n, particularly with respect to the occurrence of Hopf bifurcations, as described above. Third, it would be interesting to examine in greater depth the consequences of the different synapse models used in our work and in the various QIF networks cited above. Fourth, we assumed that the probability distributions g_η and g_k were independent, largely for mathematical convenience. However, fast-spiking neurons are typically inhibitory, and regularly-spiking neurons are typically excitatory, suggesting that it would be interesting to analyze our network with a more complicated joint probability distribution $g(\eta, k)$. Fifth, Pazó and Montbrió (2014) applied the OA technique to study pulse-coupled oscillators described by phase response curves, an approach that makes it possible to study the role of synaptic diversity in networks of Type II neurons (Pazó et al., 2019). Sixth, previous work has shown that in populations of coupled excitable systems subjected to an external periodic driving and/or noise, a resonance effect can occur for an optimal degree of oscillator diversity (Tessone et al., 2006, 2007). Thus, extending our autonomous network to include these kinds of external inputs might yield interesting insights about the interplay between this resonance effect and our observation that diversity leads to simpler dynamics. Finally, it would be interesting to allow the coupling strength between particular neurons to evolve dynamically based on activity, and to study the conditions on the synaptic plasticity rule that lead to simple or complex dynamical structures for the network's behavior.

Understanding the brain requires studying models of neuronal network dynamics with a balance between accurate biological description and analytical tractability. Real biological networks are typically studied by recording from several neurons and studying correlations (Gerstein and Kirkland, 2001). On the other hand, mathematical studies such as ours give a quantitative understanding of the dynamical and behavioral repertoire of what these networks can do, and suggest what to look for in the laboratory.

DATA AVAILABILITY STATEMENT

Codes used to generate data for this study are available upon request to the corresponding author.

AUTHOR CONTRIBUTIONS

EB and PS conceived the project. LL, EB, and PS carried out the mathematical analysis and numerical simulations, and constructed the figures. LL wrote the initial manuscript. EB and PS subsequently revised it.

FUNDING

Publication of this article was funded in part by the George Mason University Libraries Open Access Publishing Fund.

ACKNOWLEDGMENTS

We thank the reviewers for extensive and helpful feedback which significantly improved our paper. We also thank Thomas Jefferson High School for Science and Technology in Alexandria, Virginia. Preliminary portions of this work were presented in poster form at the 2015 SIAM Conference on Applications of Dynamical Systems, where it won a Red Sock Award.

REFERENCES

Bi, H., Segneri, M., di Volo, M., and Torcini, A. (2020). Coexistence of fast and slow gamma oscillations in one population of inhibitory spiking neurons. *Phys. Rev. Res.* 2:013042. doi: 10.1103/PhysRevResearch.2.013042

Brunel, N., and Hakim, V. (2008). Sparsely synchronized neuronal oscillations. *Chaos* 18:015113. doi: 10.1063/1.2779858

Burton, S. D., Ermentrout, G. B., and Urban, N. N. (2012). Intrinsic heterogeneity in oscillatory dynamics limits correlation-induced neural synchronization. *J. Neurophysiol.* 108, 2115–2133. doi: 10.1152/jn.00362.2012

Coombes, S. (2006). Neural fields. *Scholarpedia* 1:1373. doi: 10.4249/scholarpedia.1373

Devalle, F., Roxin, A., and Montbrió, E. (2017). Firing rate equations require a spike synchrony mechanism to correctly describe fast oscillations in inhibitory networks. *PLoS Comput. Biol.* 13:e1005881. doi: 10.1371/journal.pcbi.1005881

di Volo, M., and Torcini, A. (2018). Transition from asynchronous to oscillatory dynamics in balanced spiking networks with instantaneous synapses. *Phys. Rev. Lett.* 121:128301. doi: 10.1103/PhysRevLett.121.128301

Ermentrout, B. (1996). Type I membranes, phase resetting curves, and synchrony. *Neural Comput.* 8, 979–1001. doi: 10.1162/neco.1996.8.5.979

Ermentrout, B. (2002). *Simulating, Analyzing, and Animating Dynamical Systems*. Society for Industrial and Applied Mathematics. Philadelphia, PA: SIAM. doi: 10.1137/1.9780898718195

Ermentrout, B. (2008). Ermentrout-Kopell canonical model. Scholarpedia 3:1398. doi: 10.4249/scholarpedia.1398

Ermentrout, G., and Kopell, N. (1986). Parabolic bursting in an excitable system coupled with a slow oscillation. *SIAM J. Appl. Math.* 46, 233–253. doi: 10.1137/0146017

Gerstein, G. L., and Kirkland, K. L. (2001). Neural assemblies: technical issues, analysis, and modeling. *Neural Netw.* 14, 589–598. doi: 10.1016/S0893-6080(01)00042-9

Goldobin, D. S., and Dolmatova, A. V. (2019). Ott-antonsen ansatz truncation of a circular cumulant series. *Phys. Rev. Res.* 1:033139. doi: 10.1103/PhysRevResearch.1.033139

Hansel, D., Mato, G., and Meunier, C. (1995). Synchrony in excitatory neural networks. *Neural Comput.* 7, 307–337. doi: 10.1162/neco.1995.7.2.307

Harris, K. D. (2005). Neural signatures of cell assembly organization. *Nat. Rev. Neurosci.* 6, 399–407. doi: 10.1038/nrn1669

Hebb, D. O. (1949). *The Organization of Behavior; A Neuropsychological Theory*. Oxford: Wiley.

Hodgkin, A. (1948). The local electric changes associated with repetitive action in a non-medulated axon. *J. Physiol.* 107, 165–181. doi: 10.1113/jphysiol.1948.sp004260

Izhikevich, E. (2007). *Dynamical Systems in Neuroscience: The Geometry of Excitability and Bursting*. Cambridge, MA: MIT Press. doi: 10.7551/mitpress/2526.001.0001

Izhikevich, E. M. (2000). Neural excitability, spiking and bursting. *Int. J. Bifurcation Chaos* 10, 1171–1266. doi: 10.1142/S0218127400000840

Kuramoto, Y. (1975). Self-entrainment of a population of coupled non-linear oscillators," in *International Symposium on Mathematical Problems in Theoretical Physics*, ed H. Araki (Berlin; Heidelberg: Springer), 420–422. doi: 10.1007/BFb0013365

Kuramoto, Y. (1984). *Chemical Oscillations, Waves and Turbulence*. New York, NY: Springer. doi: 10.1007/978-3-642-69689-3

Laing, C. R. (2014). Derivation of a neural field model from a network of theta neurons. *Phys. Rev. E* 90:010901. doi: 10.1103/PhysRevE.90.010901

Laing, C. R. (2015). Exact neural fields incorporating gap junction. *SIAM J. Appl. Dyn. Syst.* 14, 1899–1929. doi: 10.1137/15M1011287

Luke, T. B., Barreto, E., and So, P. (2013). Complete classification of the macroscopic behavior of a heterogeneous network of theta neurons. *Neural Comput.* 25, 3207–3234. doi: 10.1162/NECO_a_00525

Luke, T. B., Barreto, E., and So, P. (2014). Macroscopic complexity from an autonomous network of networks of theta neurons. *Front. Comput. Neurosci.* 8:145. doi: 10.3389/fncom.2014.00145

Marvel, S. A., Mirollo, R. E., and Strogatz, S. H. (2009). Identical phase oscillators with global sinusoidal coupling evolve by möbius group action. *Chaos* 19:043104. doi: 10.1063/1.3247089

Mirollo, R. E. (2012). The asymptotic behavior of the order parameter for the infinite-n Kuramoto model. *Chaos* 22:043118. doi: 10.1063/1.4766596

Montbrió, E., Pazó, D., and Roxin, A. (2015). Macroscopic description for networks of spiking neurons. *Phys. Rev. X* 5:021028. doi: 10.1103/PhysRevX.5.021028

O'Keeffe, K. P., and Strogatz, S. H. (2016). Dynamics of a population of oscillatory and excitable elements. *Phys. Rev. E* 93:062203. doi: 10.1103/PhysRevE.93.062203

Ott, E., and Antonsen, T. M. (2008). Low dimensional behavior of large systems of globally coupled oscillators. *Chaos* 18:037113. doi: 10.1063/1.2930766

Ott, E., and Antonsen, T. M. (2009). Long time evolution of phase oscillator systems. *Chaos* 19:023117. doi: 10.1063/1.3136851

Pazó, D., and Montbrió, E. (2014). Low-dimensional dynamics of populations of pulse-coupled oscillators. *Phys. Rev. X* 4:011009. doi: 10.1103/PhysRevX.4.011009

Pazó, D., Montbrió, E., and Gallego, R. (2019). The winfree model with heterogeneous phase-response curves: analytical results. *J. Phys. A Math. Theor.* 52:154001. doi: 10.1088/1751-8121/ab0b4c

Pietras, B., and Daffertshofer, A. (2016). Ott-antonsen attractiveness for parameter-dependent oscillatory systems. *Chaos* 26:103101. doi: 10.1063/1.4963371

Pikovsky, A., and Rosenblum, M. (2015). Dynamics of globally coupled oscillators: progress and perspectives. *Chaos* 25:097616. doi: 10.1063/1.4922971

Shinomoto, S., Kim, H., Shimokawa, T., Matsuno, N., Funahashi, S., Shima, K., et al. (2009). Relating neuronal firing patterns to functional differentiation of cerebral cortex. *PLoS Comput. Biol.* 5:e1000433. doi: 10.1371/journal.pcbi.1000433

So, P., Luke, T. B., and Barreto, E. (2014). Networks of theta neurons with time-varying excitability: macroscopic chaos, multistability, and final-state uncertainty. *Phys. D Nonlinear Phenomena* 267, 16–26. doi: 10.1016/j.physd.2013.04.009

Sporns, O., Tononi, G., and Kötter, R. (2005). The human connectome: a structural description of the human brain. *PLoS Comput. Biol.* 1:e42. doi: 10.1371/journal.pcbi.0010042

Tessone, C. J., Mirasso, C. R., Toral, R., and Gunton, J. D. (2006). Diversity-induced resonance. *Phys. Rev. Lett.* 97:194101. doi: 10.1103/PhysRevLett.97.194101

Tessone, C. J., Sciré, A., Toral, R., and Colet, P. (2007). Theory of collective firing induced by noise or diversity in excitable media. *Phys. Rev. E* 75:016203. doi: 10.1103/PhysRevE.75.016203

Van Vreeswijk, C., Abbott, L. F., and Bard Ermentrout, G. (1994). When inhibition not excitation synchronizes neural firing. *J. Comput. Neurosci.* 1, 313–321. doi: 10.1007/BF00961879

Watanabe, S., and Strogatz, S. H. (1993). Integrability of a globally coupled oscillator array. *Phys. Rev. Lett.* 70, 2391–2394. doi: 10.1103/PhysRevLett.70.2391

Watanabe, S., and Strogatz, S. H. (1994). Constants of motion for superconducting Josephson arrays. *Phys. D Nonlinear Phenomena* 74, 197–253. doi: 10.1016/0167-2789(94)90196-1

Wilson, H. R., and Cowan, J. D. (1972). Excitatory and inhibitory interactions in localized populations of model neurons. *Biophys. J.* 12, 1–24. doi: 10.1016/S0006-3495(72)86068-5

Wilson, H. R., and Cowan, J. D. (1973). A mathematical theory of the functional dynamics of cortical and thalamic nervous tissue. *Kybernetik* 13, 55–80. doi: 10.1007/BF00288786

Wolfram Research, Inc. (2019). *Mathematica*. Version 12.0. Champaign, IL.

Conflict of Interest: The authors declare that the research was conducted in the absence of any commercial or financial relationships that could be construed as a potential conflict of interest.

Copyright © 2020 Lin, Barreto and So. This is an open-access article distributed under the terms of the Creative Commons Attribution License (CC BY). The use, distribution or reproduction in other forums is permitted, provided the original author(s) and the copyright owner(s) are credited and that the original publication in this journal is cited, in accordance with accepted academic practice. No use, distribution or reproduction is permitted which does not comply with these terms.

frontiers in Computational Neuroscience

ORIGINAL RESEARCH
published: 28 May 2020
doi: 10.3389/fncom.2020.00047

Theta-Nested Gamma Oscillations in Next Generation Neural Mass Models

Marco Segneri[1], *Hongjie Bi*[1,2], *Simona Olmi*[3,4] *and Alessandro Torcini*[1,4]*

[1] *Laboratoire de Physique Théorique et Modélisation, Université de Cergy-Pontoise,CNRS, UMR 8089, Cergy-Pontoise, France,* [2] *Okinawa Institute of Science and Technology Graduate University, Okinawa, Japan,* [3] *Inria Sophia Antipolis Méditerranée Research Centre, Valbonne, France,* [4] *CNR—Consiglio Nazionale delle Ricerche—Istituto dei Sistemi Complessi, Sesto Fiorentino, Italy*

Theta-nested gamma oscillations have been reported in many areas of the brain and are believed to represent a fundamental mechanism to transfer information across spatial and temporal scales. In a series of recent experiments *in vitro* it has been possible to replicate with an optogenetic theta frequency stimulation several features of cross-frequency coupling (CFC) among theta and gamma rhythms observed in behaving animals. In order to reproduce the main findings of these experiments we have considered a new class of neural mass models able to reproduce exactly the macroscopic dynamics of spiking neural networks. In this framework, we have examined two set-ups able to support collective gamma oscillations: namely, the pyramidal interneuronal network gamma (PING) and the interneuronal network gamma (ING). In both set-ups we observe the emergence of theta-nested gamma oscillations by driving the system with a sinusoidal theta-forcing in proximity of a Hopf bifurcation. These mixed rhythms always display phase amplitude coupling. However, two different types of nested oscillations can be identified: one characterized by a perfect phase locking between theta and gamma rhythms, corresponding to an overall periodic behavior; another one where the locking is imperfect and the dynamics is quasi-periodic or even chaotic. From our analysis it emerges that the locked states are more frequent in the ING set-up. In agreement with the experiments, we find theta-nested gamma oscillations for forcing frequencies in the range [1:10] Hz, whose amplitudes grow proportionally to the forcing intensity and which are clearly modulated by the theta phase. Furthermore, analogously to the experiments, the gamma power and the frequency of the gamma-power peak increase with the forcing amplitude. At variance with experimental findings, the gamma-power peak does not shift to higher frequencies by increasing the theta frequency. This effect can be obtained, in our model, only by incrementing, at the same time, also the stimulation power. An effect achieved by increasing the amplitude either of the noise or of the forcing term proportionally to the theta frequency. On the basis of our analysis both the PING and the ING mechanism give rise to theta-nested gamma oscillations with almost identical features.

Keywords: neural oscillations, neural mass models, cross-frequency coupling, hippocampus, quadratic integrate-and-fire neuron, phase-amplitude coupling

OPEN ACCESS

Edited by:
Spase Petkoski,
INSERM U1106 Institut de Neurosciences des Systèmes, France

Reviewed by:
Carlo Laing,
Massey University, New Zealand
Ernest Barreto,
George Mason University, United States

***Correspondence:**
Alessandro Torcini
alessandro.torcini@u-cergy.fr

Received: *05 March 2020*
Accepted: *30 April 2020*
Published: *28 May 2020*

Citation:
Segneri M, Bi H, Olmi S and Torcini A (2020) Theta-Nested Gamma Oscillations in Next Generation Neural Mass Models. Front. Comput. Neurosci. 14:47. doi: 10.3389/fncom.2020.00047

1. INTRODUCTION

Oscillations in the brain, reflecting the underlying dynamics of neural populations, have been measured over a broad frequency range (Buzsaki, 2006). Particularly studied are γ-rhythms (30–120 Hz), due to their ubiquitous presence in many regions of the brain, irrespectively of the species (Buzsáki and Wang, 2012), and for their relevance for cognitive tasks (Fries et al., 2007) and neuronal diseases (Uhlhaas and Singer, 2006; Williams and Boksa, 2010).

Inhibitory networks have been shown to represent a fundamental ingredient for the emergence of γ oscillations (Bartos et al., 2007; Buzsáki and Wang, 2012). Indeed, inhibition is at the basis of the two most known mechanisms: pyramidal interneuronal network gamma (PING) and interneuronal network gamma (ING) (Tiesinga and Sejnowski, 2009). The ING mechanism is observable in purely inhibitory networks in the presence of few ingredients: recurrent connections, a time scale associated with the synaptic $GABA_A$ receptors and an excitatory drive sufficiently strong to lead the neurons supra-threshold (Buzsáki and Wang, 2012). The collective oscillations (COs) emerge when a sufficient number of neurons begins to fire within a short time window and generate almost synchronous inhibitory post-synaptic potentials (IPSPs) in the post-synaptic interneurons. The inhibited neurons fire again when the IPSPs have sufficiently decayed and the cycle will repeat. Thus, the main ingredients dictating the frequency of the COs in the ING set-up are: the kinetics of the IPSPs and the excitatory drive (Whittington et al., 1995). On the other hand the PING mechanism is related to the presence of an excitatory and an inhibitory population, in this case COs emerge whenever the drive on the excitatory neurons is sufficiently strong to induce an almost synchronous excitatory volley that in turn elicits an inhibitory one. The period of the COs is thus determined by the recovery time of the pyramidal neurons from the stimulus received from the inhibitory population (Wilson and Cowan, 1972). A peculiarity of this mechanism, observed both *in vivo* and *in vitro* experiments, is that there is a delay between the firing of the pyramidal cells and the interneuronal burst (Buzsáki and Wang, 2012).

In several parts of the brain, one can observe that γ oscillations are modulated by θ oscillations, with θ frequencies corresponding to 4–12 Hz in rodents and to 1–4 Hz in humans. Specific examples have been reported for the hippocampus of rodents in behaving animals and during rapid eye movement (REM) sleep (Lisman, 2005; Colgin et al., 2009; Belluscio et al., 2012; Pernía-Andrade and Jonas, 2014; Colgin, 2015), for the visual cortex in alert monkeys (Whittingstall and Logothetis, 2009), for the neocortex in humans (Canolty et al., 2006) etc. This is an example of a more general mechanism of cross-frequency coupling (CFC) between a low and a high frequency rhythm, which is believed to have a functional role in the brain (Canolty and Knight, 2010). In particular, low frequency rhythms (such as θ) are usually involving broad brain regions and are entrained to external inputs and/or to cognitive events; on the other hand the high frequency activity (e.g., the γ-rhythm) reflects local computation activity. Thus CFC can represent an effective mechanism to transfer information across spatial and temporal scales (Canolty and Knight, 2010; Lisman and Jensen, 2013). Four different types of CFC of interest for electrophysiology, have been listed in Jensen and Colgin (2007): phase-phase, phase-frequency, phase-amplitude and amplitude-amplitude couplings (PPC, PFC, PAC, and AAC). Two more types of CFCs have later been added as emerging from the analysis of coupled non-linear oscillators (Witte et al., 2008) and coupled neural mass models (Chehelcheraghi et al., 2017): frequency-frequency and amplitude-frequency coupling (FFC and AFC).

In this paper, we will consider θ-nested γ oscillations, where specific features of the γ oscillations are correlated to the θ phase. In particular, we will analyze PPC, PFC, and PAC between θ and γ rhythms. The most studied CFC mechanism is the PAC, which corresponds to the modification of the amplitude (or power) of γ-waves induced by the phase of the θ-oscillations. This mechanism has been reported in the primary visual cortex of anaesthetized macaques subject to naturalistic visual stimulation (Mazzoni et al., 2011), as well as during the formation of new episodic memories in the human hippocampus (Lega et al., 2016). As discussed in Jensen and Colgin (2007), the θ phase can often modulate both amplitude (PAC) and frequency (PFC) of the γ oscillations, therefore these two mechanisms can occur at the same time. PPC, which refers to n:m phase locking between γ and θ phase oscillations (Tass et al., 1998), has been identified in the rodent hippocampus during maze exploration (Belluscio et al., 2012).

Our study is mostly motivated by recent optogenetic experiments revealing PAC in areas CA1 and CA3 of the hippocampus and in the medial enthorinal cortex (MEC) (Akam et al., 2012; Pastoll et al., 2013; Butler et al., 2016, 2018). These experiments have shown that a sinusoidal optogenetic stimulation at θ-frequency of the circuits *in vitro* is able to reproduce several features of θ-nested γ oscillations, usually observed in behaving rats (Bragin et al., 1995). All these experiments suggest that inhibition has a key role in generating this cross-frequency rhythm; however both ING (Pastoll et al., 2013) and PING (Butler et al., 2016, 2018) mechanisms have been invoked to explain locally generated γ oscillations.

PING and ING oscillation mechanisms have been qualitatively reproduced by employing heuristic neural mass models (Wilson and Cowan, 1972; Gerstner et al., 2014). However, these standard firing rate models do not properly describe the synchronization and desynchronizaton phenomena occurring in neural populations (Devalle et al., 2017; Laing, 2017; Coombes and Byrne, 2019). Recently a new generation of neural mass models has been designed, which are able to exactly reproduce the network dynamics of spiking neurons of class I, for any degree of synchronization among the neurons (Luke et al., 2013; Laing, 2014; So et al., 2014; Montbrió et al., 2015). In particular, for purely inhibitory networks, these mean-field models have been able to reproduce the emergence of COs, observed in the corresponding networks,

without the inclusion of an extra time delay (Devalle et al., 2017), as well as the phenomenon of event related synchronization and desynchronization (Coombes and Byrne, 2019).

Our main aim is to understand how θ-nested γ oscillations can emerge when a PING or ING mechanism is responsible for the fast oscillations and which differences can be expected in the population dynamics in the two cases. Therefore we will consider the new class of neural mass models introduced in Montbrió et al. (2015) in two configurations: namely, a purely inhibitory population (ING set-up) and two coupled excitatory-inhibitory populations (PING set-up). In both configurations we will examine the system response to an external sinusoidal θ-drive.

Section 2 is devoted to the introduction of different spiking network configurations of Quadratic Integrate-and-Fire (QIF) neurons able to generate γ COs via PING and ING mechanisms and to the introduction of their corresponding exact neural mass formulations. A detailed bifurcation analysis of the neural mass models for the PING and ING set-ups, in the absence of any external forcing, is reported in section 3. The PAC mechanism is analyzed and discussed in section 4. First, by considering different types of PAC states (namely, phase locked or unlocked) and second, by comparing our numerical results for PAC dynamics with experimental findings reported in Butler et al. (2016, 2018), for the CA1 region of the hippocampus under sinusoidal optogenetic stimulations. Finally, a discussion of our results and of their implications, as well as of possible future developments, will be presented in section 5. The results reported in the paper are mostly devoted to super-critical Hopf bifurcations, however a specific example of a sub-critical Hopf bifurcation leading to COs is discussed for the PING set-up in **Appendix A**. Further network configurations ensuring the emergence of COs via PING mechanism are presented in **Appendix B**.

2. MODELS AND BIFURCATION ANALYSIS

2.1. Network Models

In this paper we want to compare the two principal mechanisms at the basis of the emergence of collective oscillatory dynamics in neural networks: namely, the PING and ING mechanisms. Therefore we will consider QIF neurons in the two following set-ups: an excitatory and an inhibitory population coupled via instantaneous synapses (PING configuration) and a single inhibitory population interacting via post-synaptic potentials (PSPs) with exponential profile (ING configuration). The corresponding network configurations are shown in **Figure 1**. Moreover, the neurons are assumed to be fully coupled. As we will show in the following, both these two configurations support the emergence of COs.

The dynamics of the membrane potentials of the QIF neurons in the PING configuration is given by

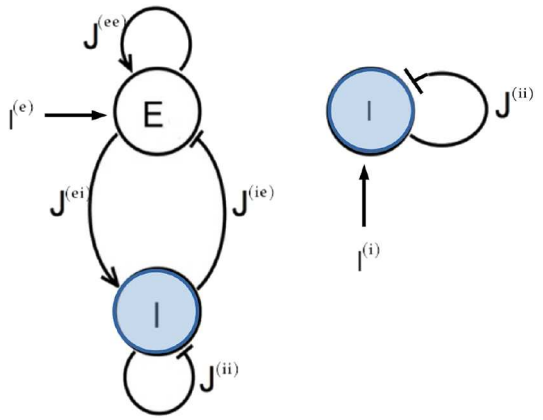


FIGURE 1 | Network topologies. Two different network configurations have been investigated: on the left side, an excitatory population (E) and an inhibitory population (I) form a circuit that can generate oscillatory output (PING set-up); on the right side one inhibitory population (I) is coupled to itself with an inhibitory coupling (ING set-up). In both cases an external current $I^{(l)}$ impinging on one single population has been considered.

$$\begin{aligned}
\tau_m^{(e)}\dot{V}_k^{(e)} &= \left(V_k^{(e)}\right)^2 + \eta_k^{(e)} + \tau_m^{(e)}\left[J^{(ee)}s^{(e)} - J^{(ie)}s^{(i)}\right] \\
&\quad + I^{(e)}(t) \quad k = 1, \ldots, N^{(e)} \\
\tau_m^{(i)}\dot{V}_j^{(i)} &= \left(V_j^{(i)}\right)^2 + \eta_j^{(i)} + \tau_m^{(i)}\left[J^{(ei)}s^{(e)} - J^{(ii)}s^{(i)}\right] \\
&\quad + I^{(i)}(t) \quad j = 1, \ldots, N^{(i)} \\
s^{(l)} &= \frac{1}{N^{(l)}}\sum_{t_m^{(l)}} \delta(t - t_m^{(l)}) \quad l \in \{e, i\} \qquad ;
\end{aligned} \tag{1}$$

where the super-scripts e (i) denote the excitatory (inhibitory) population, $\tau_m^{(e)} = 20$ ms ($\tau_m^{(i)} = 10$ ms) is the excitatory (inhibitory) membrane time constant, $\eta_k^{(l)}$ is the excitability of the k-th neuron of population l, $J^{(ln)}$ is the strength of the synaptic coupling of population l acting on population n. The term $I^{(l)}(t)$ represents a time-dependent external current applied to the population l; usually we have considered the external drive to be applied to the excitatory population only, i.e., $I^{(e)}(t) \neq 0$ and $I^{(i)}(t) = 0$. The synaptic field $s^{(l)}(t)$ is the linear super-position of all the pulses $p(t)$ emitted in the past within the l population, $p(t)$ being δ-functions in the present case. Furthermore, since the neurons are fully coupled, each neuron will be subject to the same synaptic field (Olmi et al., 2010). The emission of the m-th spike in the network occurs at time $t_m^{(l)}$ whenever the membrane potential of a generic neuron j reaches infinity, i.e., $V_j^{(l)}(t_m^{(l)-}) \to +\infty$, while the reset mechanism is modeled by setting $V_j^{(l)}(t_j^{(l)+}) \to -\infty$, immediately after the spike emission.

The main part of our analysis of the PING set-up will be devoted to networks with self-activation only (i.e., where $J^{(ii)} = 0$), a configuration which is known to favor the emergence of collective oscillations (Wilson and Cowan, 1972; Kilpatrick, 2015;

Onslow et al., 2014). However, as discussed in **Appendix B**, we have found that COs can arise in different PING set-ups: in the presence of self-inhibition only (i.e., with $J^{(ii)} \neq 0$ and $J^{(ee)} = 0$) and in the absence of both self-activation and inhibition (i.e., with $J^{(ee)} = J^{(ii)} = 0$).

For what concerns the purely inhibitory network, the membrane potential dynamics of the j-th neuron is ruled by the following equations:

$$\begin{aligned} \tau_m^{(i)} \dot{V}_j^{(i)} &= \left(V_j^{(i)}\right)^2 + \eta_j^{(i)} - \tau_m^{(i)} J^{(ii)} s^{(i)} + I^{(i)}(t) \\ \tau_d \dot{s}^{(i)} &= -s^{(i)} + \frac{1}{N^{(i)}} \sum_{t_m^{(l)}} \delta(t - t_m^{(i)}) \quad , \end{aligned} \tag{2}$$

where $\tau_m^{(i)} = 10$ ms. In this case the synaptic field $s^{(i)}(t)$ is the super-position of the exponential IPSPs $p(t) = \mathrm{e}^{-t/\tau_d}/\tau_d$ emitted in the past, where we set $\tau_d = 10$ ms.

For reasons that will become clear in the next paragraph, we assume that the neuron excitabilities $\eta_i^{(l)}$ are randomly distributed according to a Lorentzian probability density function (PDF)

$$g^{(l)}(\eta) = \frac{1}{\pi} \frac{\Delta^{(l)}}{(\eta - H^{(l)})^2 + (\Delta^{(l)})^2} \, , \tag{3}$$

where $H^{(l)}$ is the median and $\Delta^{(l)}$ is the half-width half-maximum (HWHM) of the PDF. Therefore each population will be composed of neurons supra- (with $\eta_j^{(l)} > 0$) and sub-threshold (with $\eta_j^{(l)} < 0$), the percentage of one group with respect to the other being determined by the Lorentzian parameters. For the PING set-up we fix $\Delta^{(e)} = \Delta^{(i)} = 1$, whereas varying $H^{(e)}$ and $H^{(i)}$. For the ING set-up we fix $\Delta^{(i)} = 0.3$ and analyze the dynamics by varying $H^{(i)}$.

The dynamical equations are integrated by employing a 4th order Runge-Kutta method in the absence of noise with a time step $dt = 0.002$ ms ($dt = 0.001$ ms) for the PING (ING) set-up. Moreover, we define a threshold $V_p = 100$ and a reset value $V_r = -100$. Whenever the membrane potential V_j of the j-th neuron overcomes V_p at a time t_p, it is reset to V_r for a refractory period equal to $2/V_j$. At the same time the firing time is estimated as $t_p + 1/V_j$; for more details see Montbrió et al. (2015). The membrane potentials are initialized from a random flat distribution defined over the range $[-100 : 100]$, while the excitabilities are randomly chosen from the Lorentzian distribution (3).

For instantaneous synapses, we will only employ the following two indicators to characterize the macroscopic dynamics:

$$r^{(l)}(t) = \frac{M^{(l)}(\Delta t)}{N^{(l)} \Delta t} \quad , \quad v^{(l)}(t) = \frac{1}{N^{(l)}} \sum_j^{N^{(l)}} V_j^{(l)}(t), \tag{4}$$

which represent the average population activity and the average membrane potential of the l-th population, respectively. In particular, the average population activity of the $l-$network $r^{(l)}(t)$ is given by the number of spikes $M^{(l)}(\Delta t)$ emitted in a time window Δt, divided by the total number of neurons in such population. For finite IPSPs we also consider the synaptic field $s^{(l)}(t)$. Furthermore, the emergence of COs, corresponding to periodic motions of $r^{(l)}(t)$ and $v^{(l)}(t)$, are characterized in terms of their frequencies $\nu^{(l)}$.

We assume that the driving current, mimicking the θ-stimulation in the optogenetic experiments, is a purely sinusoidal excitatory current of the following form

$$I_\theta(t) = \frac{I_0}{2}[1 - \cos(2\pi \nu_\theta t)] \tag{5}$$

where ν_θ is the forcing frequency, usually considered within the θ-range, i.e., $\nu_\theta \in [1 : 10]$ Hz. In this context a theta phase associated with the forcing field can be defined as $\theta(t) = \mathrm{mod}(2\pi \nu_\theta t, 2\pi)$. For the PING configuration we set $I^{(e)}(t) = I_\theta(t)$ and $I^{(i)}(t) \equiv 0$ and for the ING set-up $I^{(i)}(t) = I_\theta(t)$.

2.2. Neural mass models

As already mentioned, an exact neural mass model has been derived in Montbrió et al. (2015) for a fully coupled network of QIF neurons with instantaneous synapses and with Lorentzian distributed neuronal excitabilities. In this case the macroscopic neural dynamics of a population l is described by two collective variables: the mean field potential $v^{(l)}(t)$ and the instantaneous firing rate $r^{(l)}(t)$. In this context, the neural mass model for two coupled $E - I$ populations with instantaneous synapses, corresponding to the microscopic model reported in Equation (1), can be written as

$$\begin{aligned} \dot{r}^{(e)} &= \frac{\Delta^{(e)}}{\left(\tau_m^{(e)}\right)^2 \pi} + \frac{2 r^{(e)} v^{(e)}}{\tau_m^{(e)}} \\ \dot{v}^{(e)} &= \frac{\left(v^{(e)}\right)^2 + H^{(e)} + I^{(e)}(t)}{\tau_m^{(e)}} - \tau_m^{(e)} \left(\pi r^{(e)}\right)^2 \\ &\quad + J^{(ee)} r^{(e)} - J^{(ie)} r^{(i)} + A\xi^{(e)} \\ \dot{r}^{(i)} &= \frac{\Delta^{(i)}}{\left(\tau_m^{(i)}\right)^2 \pi} + \frac{2 r^{(i)} v^{(i)}}{\tau_m^{(i)}} \\ \dot{v}^{(i)} &= \frac{\left(v^{(i)}\right)^2 + H^{(i)} + I^{(i)}(t)}{\tau_m^{(i)}} - \tau_m^{(i)} \left(\pi r^{(i)}\right)^2 \\ &\quad + J^{(ei)} r^{(e)} - J^{(ii)} r^{(i)} + A\xi^{(i)} \quad . \end{aligned} \tag{6}$$

In the equations for the evolution of the average membrane potentials we have also inserted an additive noise term of amplitude A, employed in some of the analysis to mimic the many noise sources present in the brain dynamics. In particular, the noise terms $\xi^{(e)}$ and $\xi^{(i)}$ are both δ-correlated and uniformly distributed in the interval $[-1 : 1]$.

In case of finite synapses, the exact derivation of the corresponding neural mass model is still feasible for QIF neurons, but the macroscopic evolution now contains further equations describing the dynamics of the synaptic field characterizing the considered synapses (Devalle et al., 2017; Coombes and Byrne, 2019). In particular, for a single inhibitory population

with exponential synapses, the corresponding neural mass model reads as:

$$\begin{aligned}\dot{r}^{(i)} &= \frac{\Delta^{(i)}}{(\tau_m^{(i)})^2\pi} + \frac{2r^{(i)}v^{(i)}}{\tau_m^{(i)}} \\ \dot{v}^{(i)} &= \frac{(v^{(i)})^2 + H^{(i)} + I^{(i)}(t)}{\tau_m^{(i)}} - \tau_m^{(i)}(\pi r^{(i)})^2 \\ &- J^{(ii)}s^{(i)} + A\xi^{(i)} \\ \dot{s}^{(i)} &= \frac{1}{\tau_d}[-s^{(i)} + r^{(i)}].\end{aligned} \tag{7}$$

In the present case the equation for the average membrane potential contains, as already shown before in Equation (6), an additive noise term of amplitude A.

It should be noticed that in Equations (6) and (7) the noise has been added in an effective manner and not with a consistent procedure, that would amount to take into account the effect of microscopic noise on the mean-field formulation. This can be achieved by considering a Fokker-Planck description for the distribution of the membrane potentials, e.g., as done in Brunel and Hakim (1999), or by considering a reduced approach in terms of circular cumulants (Tyulkina et al., 2018; Goldobin et al., 2018). However, all these formulations will lead to much more complicated evolution equations for the macroscopic quantities.

To analyse the stability of the macroscopic solutions of Equations (6) and (7), one should estimate the corresponding Lyapunov spectrum (LS) (Pikovsky and Politi, 2016). This can be done by considering the time evolution of the tangent vector, which for the PING set-up turns out to be four dimensional, i.e., $\delta = \left\{\delta r^{(e)}, \delta v^{(e)}, \delta r^{(i)} \delta v^{(i)}\right\}$. The dynamics of the tangent vector is ruled by the linearization of the Equation (6), namely

$$\begin{aligned}\delta\dot{r}^{(e)} &= \frac{2\left(r^{(e)}\delta v^{(e)} + v^{(e)}\delta r^{(e)}\right)}{\tau_m^{(e)}} \\ \delta\dot{v}^{(e)} &= \frac{2v^{(e)}\delta v^{(e)}}{\tau_m^{(e)}} - 2\tau_m^{(e)}\pi^2 r^{(e)}\delta r^{(e)} + J^{(ee)}\delta r^{(e)} - J^{(ie)}\delta r^{(i)} \\ \delta\dot{r}^{(i)} &= \frac{2\left(r^{(i)}\delta v^{(i)} + v^{(i)}\delta r^{(i)}\right)}{\tau_m^{(i)}} \\ \delta\dot{v}^{(i)} &= \frac{2v^{(i)}\delta v^{(i)}}{\tau_m^{(i)}} - 2\tau_m^{(i)}\pi^2 r^{(i)}\delta r^{(i)} + J^{(ei)}\delta r^{(e)} - J^{(ii)}\delta r^{(i)} \quad .\end{aligned} \tag{8}$$

For the ING set-up the tangent vector is three dimensional, $\delta = \left\{\delta r^{(i)}, \delta v^{(i)}, \delta s^{(i)}\right\}$, and its time evolution can be obtained by the linearization of Equation (7), which reads as

$$\begin{aligned}\delta\dot{r}^{(i)} &= \frac{2\left(r^{(i)}\delta v^{(i)} + v^{(i)}\delta r^{(i)}\right)}{\tau_m^{(i)}} \\ \delta\dot{v}^{(i)} &= \frac{2v^{(i)}\delta v^{(i)}}{\tau_m^{(i)}} - 2\tau_m^{(i)}\pi^2 r^{(i)}\delta r^{(i)} - J^{(ii)}\delta s^{(i)} \\ \delta\dot{s}^{(i)} &= \frac{1}{\tau_d}[-\delta s^{(i)} + \delta r^{(i)}] \quad .\end{aligned} \tag{9}$$

Please notice that the presence of additive external noise or of forcing terms in Equations (6) and (7) does not modify the evolution equations in the tangent space Equations (8) and (9).

The LS is composed by 4 (3) Lyapunov exponents (LEs) $\{\lambda_i\}$ for the PING (ING) set-ups, which quantify the average growth rates of infinitesimal perturbations along the orthogonal manifolds. In details, LEs are estimated as follows

$$\lambda_i = \lim_{t\to\infty} \frac{1}{t} \log \frac{|\delta_{\mathbf{i}}(t)|}{|\delta_{\mathbf{i}}(0)|} \quad , \tag{10}$$

where the technique described in Benettin et al. (1980) to maintain the tangent vectors δ_i orthonormal during the evolution is employed. The autonomous system will be chaotic for $\lambda_1 > 0$, while a periodic (quasi-periodic) dynamics will be characterized by $\lambda_1 = 0$ ($\lambda_1 = \lambda_2 = 0$) and a fixed point by $\lambda_1 < 0$. In a non-autonomous system in the presence of an external forcing, one Lyapunov exponent will be necessarily zero, therefore a periodic behavior corresponds to $\lambda_1 < 0$ and a quasi-periodic dynamics to $\lambda_1 = 0$ (Pikovsky and Politi, 2016).

In the absence of noise, neural mass models have been directly integrated by employing a Runge-Kutta 4th order integration scheme, while in the presence of additive noise with a Heun scheme. In both cases the time step has been set to $dt = 0.01$ ms. In order to estimate the Lyapunov spectra we have integrated the direct and tangent space evolution with a Runge-Kutta 4th order integration scheme with $dt = 0.001$ ms, for a duration of 200 s, after discarding a transient of 10 s.

Besides LEs, in order to characterize the macroscopic dynamics of the model, we have estimated the frequency power spectra $P_S^{(e)}(F)$ ($P_S^{(i)}(F)$) of the mean excitatory (inhibitory) membrane potential $v^{(e)}(t)$ ($v^{(i)}(t)$) for the PING (ING) set-up. The power spectra have been obtained by calculating the temporal Fourier transform of the mean membrane potentials sampled at time intervals of 2 ms. In the deterministic (noisy) case, time traces composed of 2048 (1024) consecutive intervals have been considered to estimate the spectra, which are obtained at a frequency resolution of $\Delta F = 0.244$ Hz ($\Delta F = 0.488$ Hz). Finally, the power spectra have been averaged over 12 (488) independent realizations for the deterministic (noisy) dynamics. To compare our numerical findings with the experimental results reported in Butler et al. (2016), as a measure of the power of the γ oscillations, we have estimated the area of the power spectrum P_γ in an interval ± 15 Hz around the main peak position F_r of the corresponding power spectrum.

3. DYNAMICS IN THE ABSENCE OF FORCING

Due to the low dimensionality of the neural mass models we have been able to obtain the corresponding bifurcation diagrams by employing the software MATCONT developed for orbit continuation (Govaerts et al., 2006).

In particular, we have derived the bifurcation diagrams in the absence of forcing [$I^{(e)} = I^{(i)} \equiv 0$] as a function of the medians $H^{(e)}$ and $H^{(i)}$ of the excitability distributions for the PING and ING configuration. In general, we observe either asynchronous

dynamics, corresponding to a stable fixed point (a focus) of the neural mass equations, or COs, corresponding to stable limit cycles for the same set of equations.

3.1. PING set-up

For the excitatory-inhibitory set-up, as already mentioned, we usually fix $H^{(i)} = -5$ and we vary $H^{(e)}$. In this case the inhibitory neurons are mostly below threshold (apart from 6 to 7% of them) and they can be driven supra-threshold from the activity of the excitatory population for sufficiently large values of $H^{(e)}$. COs emerge when a sufficient number of neurons is supra-threshold, i.e., when $H^{(e)}$ becomes positive enough, Indeed, as shown in **Figure 2A**, at negative or low values of $H^{(e)}$, one can observe asynchronous dynamics, where the neurons fire independently and without any collective behavior (as an example see **Figure 2C**). By increasing $H^{(e)}$, a supercritical Hopf bifurcation occurs at $H_c^{(e)} \simeq 1.5$ leading to the emergence of COs. The COs regime is characterized in the network by almost periodic population bursts, where the neurons in one population partially synchronize over a short time window in the order of a few milliseconds. An example for $H^{(e)} = 5$ is shown in **Figure 2D**, where one can observe two salient characteristics of the oscillatory dynamics. Firstly, the excitatory anticipates always the inhibitory burst by a certain time interval T_a (in this case $T_a \simeq 5$ ms), as usually observed for the PING mechanism (Tiesinga and Sejnowski, 2009). Secondly, the bursts of the excitatory population have a temporal width ($\simeq 8$ ms) which is two or three times larger than those of the inhibitory ones ($\simeq 2-3$ ms). This is also due to the fact that a large part of the inhibitory neurons is sub-threshold, therefore most of them fire within a short time window, irrespective of their excitabilities, due to the arrival of the synaptic stimulation from the excitatory population. Instead, the excitatory neurons, which are mostly supra-threshold, recover from silence, due to the inhibitory stimulation received during the inhibitory burst, over a wider time interval, driven by their own excitabilities. It is evident that the CO frequency of the excitatory and inhibitory population coincide in this set-up.

Moreover, it is important to investigate the bifurcation diagram of the system at fixed median excitatory drive by varying $H^{(i)}$. The corresponding bifurcation diagram is displayed in **Figure 2B** for $H^{(e)} = 10$. By increasing $H^{(i)}$, COs emerge from the asynchronous state via a sub-critical Hopf bifurcation at $H_{c1}^{(i)} \simeq -8.4$ and they disappear via a super-critical Hopf bifurcation at $H_{c2}^{(i)} \simeq 0.20$. Since the first transition is hysteretical, COs disappear via a saddle-node of the limit cycles at a value $H_{SN}^{(i)} \simeq -10.00$ lower than $H_{c1}^{(i)}$. Indeed, in the interval $[H_{SN}^{(i)}; H_{c1}^{(i)}]$ we have the coexistence of a stable focus with a stable limit cycle. In summary, COs are clearly observable as long as $H^{(i)}$ is negative or sufficiently small. If the inhibitory neurons become mostly supra-threshold, this destroys the collective behavior associated with the PING mechanism.

It is worth noticing that the frequencies of the COs are in the γ-range, namely $\nu^{(e)} \in [22:71]$ Hz (as shown in the inset of **Figure 2A**): in this set-up the maximum achievable frequency $\simeq 100$ Hz, since the decay time of inhibition is dictated by $\tau_m^{(i)} = 10$ ms (Tiesinga and Sejnowski, 2009). On the other hand, the influence of $H^{(i)}$ on the frequency of the COs is quite limited. As shown in the inset of **Figure 2B** for a specific case corresponding to $H^{(e)} = 10.0$, $\nu^{(i)} \equiv \nu^{(e)}$ varies by few Hz (namely, from 42.8 to 46.9 Hz), when $H^{(i)}$ is varied by an order of magnitude.

For what concerns the delay T_a between the excitatory and inhibitory bursts, we observe a decrease of T_a with the increase of the excitatory drive $H^{(e)}$, from $T_a \simeq 10$ ms at the Hopf bifurcation, toward 2 ms for large $H^{(e)}$ value, see **Figure 2E**. The largest value of T_a is of the order of $\tau_m^{(i)}$. This can be explained by the fact that the excitatory stimulations should reach the inhibitory population within a time interval of (at most) $\simeq \tau_m^{(i)}$ to be able to sum up in an effective manner and to ignite the inhibitory burst. As shown in the inset of **Figure 2E**, the increase of $H^{(i)}$ has in general the effect to reduce T_a; this should be expected since for larger excitabilities [larger $H^{(i)}$], the inhibitory neurons are faster in responding to the excitatory stimulations. However, this is not the case in proximity of the saddle-node bifurcation at $H_{SN}^{(i)}$ and for positive $H^{(i)}$, where the effect is reversed and T_a increases with $H^{(i)}$. It is worth noticing that the same parameters as in **Figure 2A** are used for the main panel **Figure 2E**, while in the inset of **Figure 2E**, the data shown are calculated for the same parameters as in **Figure 2B**.

For the PING set-up we can also observe sub-critical Hopf bifurcations. A specific example is discussed in some detail in **Appendix A**.

3.2. ING set-up

As shown in Devalle et al. (2017), in order to observe COs in globally coupled inhibitory QIF networks and in the corresponding neural mass models, it is sufficient to include a finite synaptic time scale τ_d. On the other hand, in sparse balanced QIF networks, COs are observable even for instantaneous synapses (di Volo and Torcini, 2018). Indeed, for the set of parameters here employed, by varying the median of the inhibitory excitabilities $H^{(i)}$, we observe a super-critical Hopf bifurcation at $H_c^{(i)} \simeq 2.4$, from an asynchronous state to COs (see **Figure 3A**). Analogously to the PING set-up, the frequencies of the COs observable in the ING set-up are within the γ-range, namely $\nu^{(i)} \in [26:83]$ Hz. In particular, we observe an almost linear increase of $\nu^{(i)}$ with $H^{(i)}$. An example of the observed dynamics is shown in **Figure 3B** (**Figure 3C**) where the raster plot of the inhibitory network is calculated for $H^{(i)} = 0$ ($H^{(i)} = 10$).

Therefore, the PING and ING set-ups considered here are ideal candidates to analyse the influence of θ-forcing on γ-oscillatory populations, which represents the main focus of this paper. In particular, the response of the system to the excitatory θ-forcing current (5) can be interpreted in terms of the bifurcation diagrams for the model in the absence of forcing shown, respectively, in **Figure 2A** for the PING set-up and in **Figure 3A** for the ING set-up. The interpretation is possible due to the fact that the response of the system to the sinusoidal current (5) can be considered as almost adiabatic, because the forcing frequencies $\nu_\theta \in [1:10]$ Hz are definitely slower than those of the COs [$\nu^{(e)}$ and $\nu^{(i)}$], which lie in the γ-range.

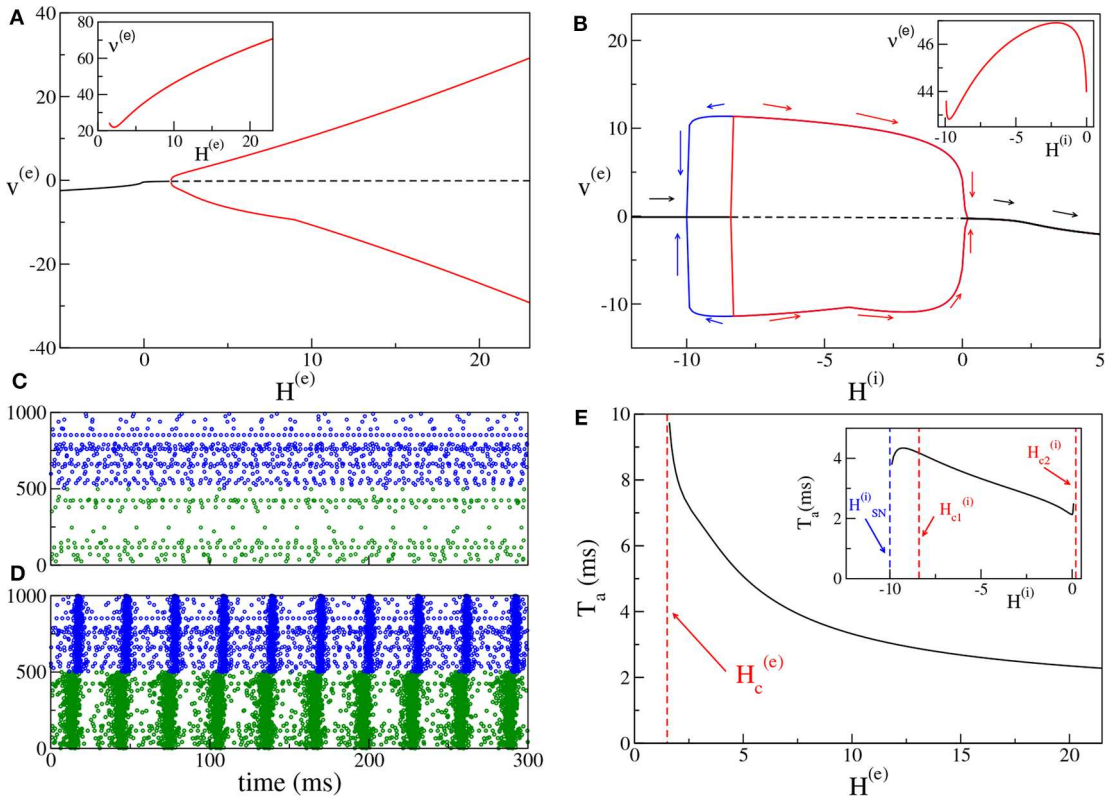


FIGURE 2 | (PING set-up) **(A)** Bifurcation diagram of the average membrane potential $v^{(e)}$ as a function of $H^{(e)}$, for $H^{(i)} = -5.0$. The black continuous (dashed) line identifies the stable (unstable) fixed point. The red lines denote the maxima and minima of the limit cycles. The supercritical Hopf bifurcation occurs at $H_c^{(e)} = 1.5$. The inset shows the frequency $\nu^{(e)}$ of the COs vs. $H^{(e)}$. **(B)** Bifurcation diagram of the average membrane potential $v^{(e)}$ vs. $H^{(i)}$ for $H^{(e)} = 10$. The Hopf bifurcations are located at $H_{c1}^{(i)} = -8.4$ and $H_{c2}^{(i)} = 0.20$, while the saddle-node bifurcation of limit cycles occurs at $H_{SN}^{(i)} = -10.0$. The inset show the frequency $\nu^{(i)} \equiv \nu^{(e)}$ of the COs vs. $H^{(i)}$. **(C,D)** Raster plots of the excitatory (green dots) and inhibitory (blue dots) networks are calculated in correspondence with the stable fixed point for $H^{(e)} = -5.0$ **(C)** and with the limit cycle for $H^{(e)} = +5.0$ (d) for the case analyzed in **(A)**. For a better visualization, the activity of only 500 neurons of each population is shown. **(E)** Delay T_a as a function of $H^{(e)}$. The red dashed line denotes $H_c^{(e)}$. Here we have used the same parameters as in **(A)**. In the inset is reported the dependence of T_a vs. $H^{(i)}$ for the parameters in **(B)**. The other parameters of the system are $J^{(ee)} = 8$, $J^{(ie)} = J^{(ei)} = 10$, $J^{(ii)} = 0$ and the sizes of the networks are $N^{(e)} = 5{,}000$, $N^{(i)} = 5{,}000$.

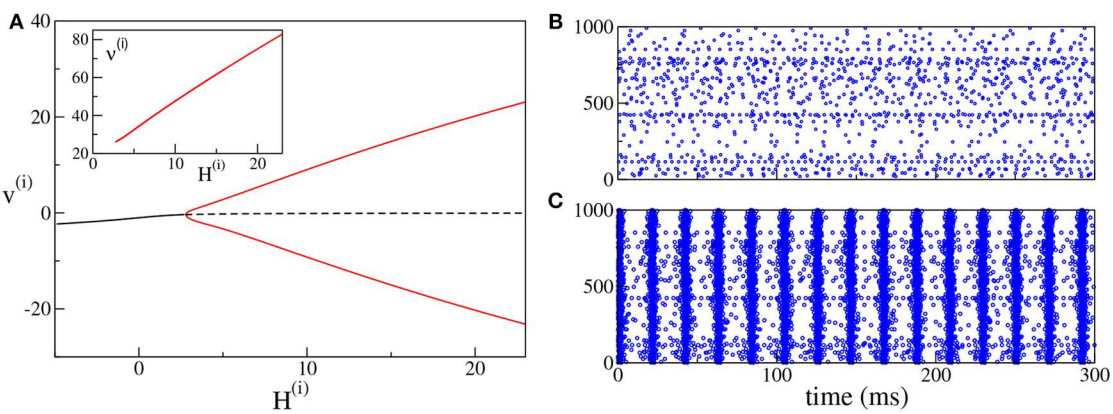


FIGURE 3 | (ING set-up) **(A)** Bifurcation diagram of the average membrane potential $v^{(i)}$ as a function of $H^{(i)}$. The black continuous (dashed) line identifies the stable (unstable) fixed point. The red lines denote the maxima and minima of the limit cycles. The supercritical Hopf bifurcation occurs at $H_c^{(i)} \simeq 2.4$. The inset shows the COs' frequency $\nu^{(i)}$ of the inhibitory population as a function of $H^{(i)}$. **(B,C)** Raster plots of the inhibitory network (blue dots) are calculated in correspondence with the stable fixed point at $H^{(i)} = 0.0$ **(B)** and with the limit cycle at $H^{(i)} = +10.0$ **(C)**. Only the firing activity of 1,000 neurons is displayed. Parameters of the system: $J^{(ii)} = 21.0$, $\bar{\eta}^{(i)} = 2.0$, $\Delta^{(i)} = 0.3$, $\tau_m^{(i)} = 10.0$ ms, $\tau_d = 10.0$ ms, $A = 0$. The system size for the purely inhibitory network is $N^{(i)} = 10,000$.

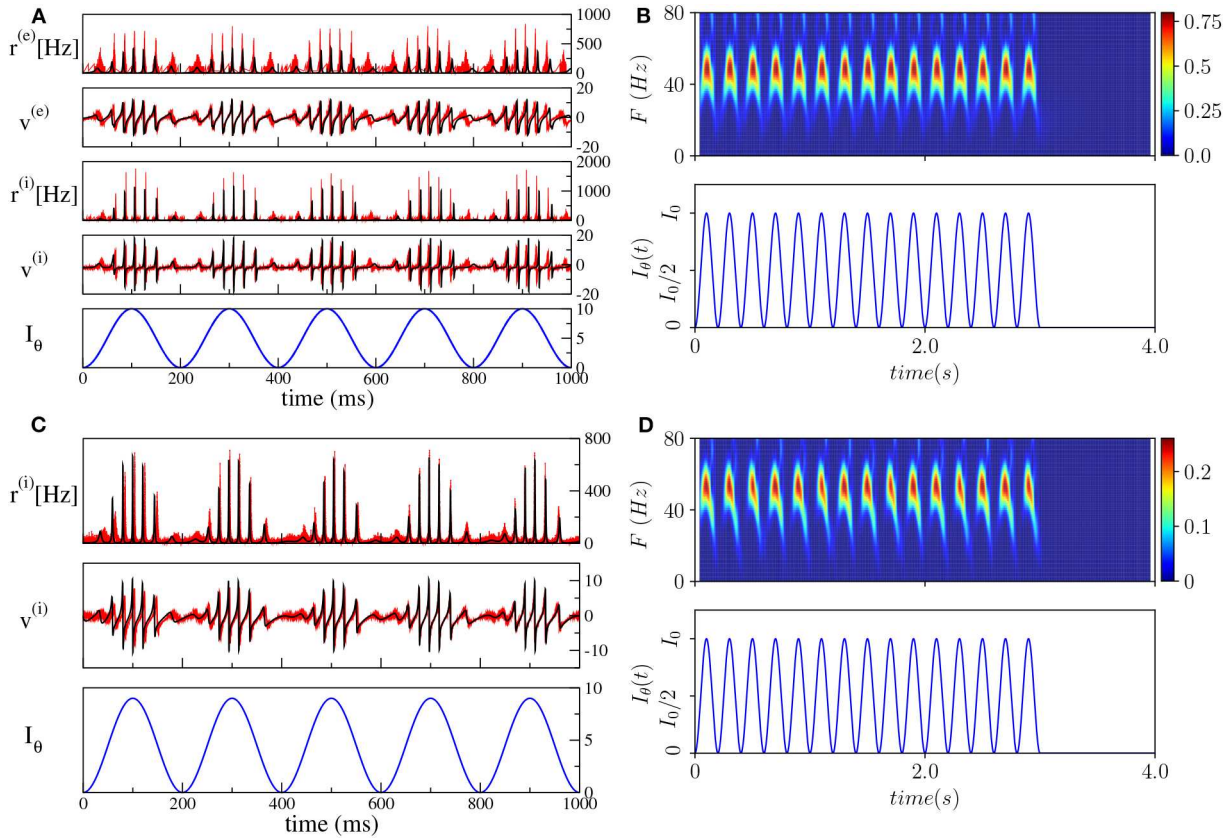


FIGURE 4 | Theta-nested gamma oscillations (PING set-up). **(A)** From top to bottom: temporal traces of $r^{(e)}$, $v^{(e)}$, $r^{(i)}$, $v^{(i)}$, for the spiking network (red curves) and the neural mass model (black curves). I_θ, reported in the bottom panel in blue, is the external current (5). For the neural mass model the average rates and membrane potentials are solutions of Equation (6), while for the network they are calculated according to Equation (4). **(B)** Spectrogram of the mean membrane potential $v^{(e)}$ (top) as a function of the external forcing (bottom). The amplitude of the forcing is $I_0 = 10$ and its frequency is $\nu_\theta = 5$ Hz. Parameters of the system: $J^{(ee)} = 8$, $J^{(ie)} = J^{(ei)} = 10$, $J^{(ii)} = 0$, $H_0^{(e)} = 1.3$, $H_0^{(i)} = -5.0$, $\Delta^{(e)} = 1$, $\tau_m^{(e)} = 20$, $\Delta^{(i)} = 1$, $\tau_m^{(i)} = 10.0$, $A = 0$, network size $N^{(e)} = N^{(i)} = 5,000$. The average firing rates are $\bar{R}^{(e)} \simeq 37$ Hz, $\bar{R}^{(i)} \simeq 36$ Hz. (ING set-up) **(C)** From top to bottom: temporal traces of $r^{(i)}$, $v^{(i)}$ where the line colors have the same meaning as in **(A)**. For the neural mass model, average rates and membrane potentials are solutions of Equation (7). **(D)** Spectrogram of the mean membrane potential $v^{(i)}$ (top) as a function of the external forcing (bottom). The amplitude of the forcing is $I_0 = 9$ and its frequency is $\nu_\theta = 5$ Hz. Parameters of the system: $J^{(ii)} = 21.0$, $H_0^{(i)} = 2.0$, $\Delta^{(i)} = 0.3$, $\tau_m^{(i)} = 10.0$ ms, $\tau_d = 10.0$ ms, $A = 0$, system size for the purely inhibitory network $N^{(i)} = 10,000$. The corresponding average firing rate is $\bar{R}^{(i)} \simeq 28$ Hz.

4. DYNAMICS UNDER θ-FORCING

As a first step, we have verified that the reduced mean-field models are able to reproduce the macroscopic evolution of the spiking network in both considered set-ups, under the external forcing (5). In particular, we set the unforced systems in the asynchronous regime in proximity of a super-critical Hopf bifurcation, by choosing $H_0^{(e)} = 1.3 < H_c^{(e)}$ and $H_0^{(i)} = -5$ ($H_0^{(i)} = 2.0 < H_c^{(i)}$) and considered a forcing term with frequency $\nu_\theta = 5$ Hz and amplitude $I_0 = 10$ ($I_0 = 9$) for the PING (ING) set-up.

The comparisons, reported in **Figures 4A,C**, reveal a very good agreement in both set-ups between the network and the neural mass simulations, for the mean membrane voltages and the instantaneous firing rates. Furthermore, in both cases, we clearly observe COs, whose amplitudes are modulated by the amplitude of the θ-forcing term (5), suggesting that we are in the presence of a Phase-Amplitude Coupling (PAC) mechanism (Hyafil et al., 2015). The corresponding spectrograms shown in **Figures 4B,D** reveal that the frequencies of the COs are in the γ-range with the maximum power localized around 50–60 Hz. Moreover, the spectrograms indicate that the process is stationary and due to the external stimulation. The gamma oscillations repeat during each θ-cycle and they arrest when the external stimulation is stopped. The characteristics of these COs resemble θ-nested γ-oscillations reported in many experiments for neural systems *in vitro* under optogenetic stimulation (Akam et al., 2012; Pastoll et al., 2013; Butler et al., 2016, 2018) as well as in behaving animals (Chrobak and Buzsáki, 1998).

4.1. Wavelet Analysis

To get a deeper insight into these dynamics we have estimated the continuous wavelet transform of the average membrane potential on each θ-cycle. As an example, we report in **Figure 5** the wavelet spectrogram of the mean potential within a single θ-cycle for the previously examined PING (**Figure 5A**) and ING (**Figure 5B**)

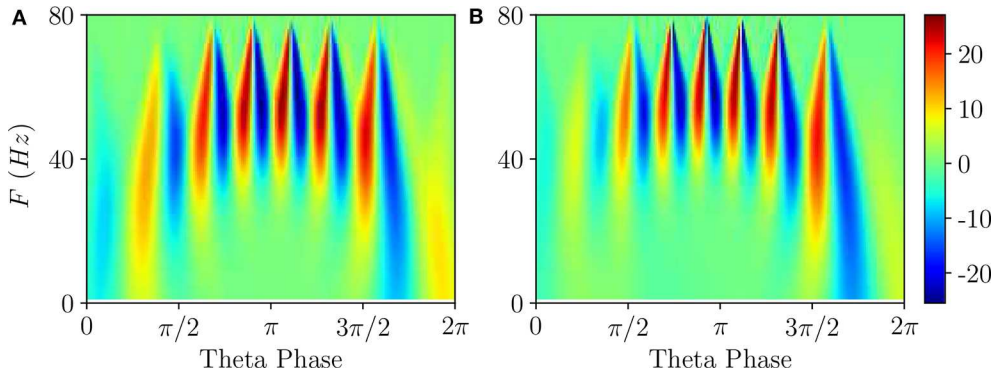


FIGURE 5 | Wavelet analysis. Continuous wavelet transform over a single θ-cycle of the mean membrane potentials $v^{(e)}$ and $v^{(i)}$ appearing in the neural mass models for PING **(A)** and ING **(B)** set-up, respectively. This analysis allows for accurate automated detection and extraction of γ activity without the need for bandpass filtering. Parameters as in **Figure 4**.

set-ups. Indeed, from the comparison of **Figures 5A,B**, we practically do not observe any difference: the system responds with COs in the range [40, 80] Hz and it exhibits alternating maxima and minima in the wavelet spectrogram as a function of the θ-phase. Similar results have been reported in Figure 4G in Butler et al. (2016) for the CA1-region of rat hippocampus under optogenetic sinusoidal θ-stimulation.

Differences among the two cases appear when one considers the wavelet spectrograms averaged over many θ-periods: for the PING case the spectrogram remains unchanged, instead for the ING set-up the spectrogram smears out and it does not present anymore the clear oscillations reported in **Figure 5B**. This difference indicates that, in the PING case, the observed pattern repeats exactly over each cycle: γ-oscillations and θ-oscillations are perfectly phase locked. This is not the case for the ING set-up: although the PAC patterns appear quite similar in successive cycles, as shown in **Figure 4C**, indeed they do not repeat exactly. From the point of view of non-linear dynamics, the PING case would correspond to a perfectly periodic case, while the other case could be quasi-periodic or even chaotic. Therefore, we can observe PAC with an associated phase locking, but also in the absence of phase locking.

Furthermore, according to the data shown in **Figure 5**, this can also represent an example of PFC, since COs with frequencies $\simeq$ 40 Hz occur at small and large θ-phases, while in the middle range $\pi/2 < \theta < 3\pi/2$ one observes similar oscillations with $F \simeq 60$ Hz.

For what concerns the wavelet analysis obtained from optogenetic experiments and shown in Figure 4G in Butler et al. (2016), we should stress two important aspects: (i) the wavelet spectrogram, averaged over several θ cycles (namely 30), displays clear correlations among the θ-phase and the γ-oscillations; (ii) the spectrogram is highly asymmetric indicating that γ-oscillations emerge in proximity of θ-phase $\simeq \pi$ and disappear $\simeq 3/2\pi$. The former aspect reveals that θ and γ oscillations were perfectly locked in the experiment, while the latter suggests that the bifurcation associated with the emergence of COs in the experiment is probably hysteretic. This would explain the asymmetry that we do not observe here for super-critical Hopf bifurcations in **Figure 5**, but that emerges for sub-critical Hopf bifurcations, as discussed in **Appendix A**.

4.2. Phase-Amplitude Locked and Unlocked States

To better examine the dynamical regimes emerging in our set-ups, we have first estimated the maximal Lyapunov exponent λ_1 associated with the neural mass models, for the same parameters considered in **Figure 4**, over a wide range of forcing amplitudes, that is $0 \leq I_0 \leq 20$. From the results reported in **Figures 6A,B**, it is clear that λ_1 is almost always zero, apart from some limited intervals where it is negative and a few values of I_0 for the ING set-up, where it can be even positive. This means that the dynamics is usually quasi-periodic, apart from some Arnold tongues where there is perfect locking between the external forcing and the forced system.

We notice that for small amplitudes the forcing entrains the system in a 1 : 1 periodic locking, therefore the instantaneous firing rate displays one peak for each θ-period with the same frequency as the forcing ν_θ. This locking is present in a wider region in the ING case (namely, $I_0 < 1.70$) with respect to the PING set-up (namely, $I_0 < 0.40$). More interesting locking regimes, where the forced populations oscillate in the γ-range, emerge at larger I_0. These locking regimes can be considered as θ-nested γ-oscillations; most of them are of the type $m : 1$, with $m \in [5 : 10]$, which means that, for each θ-period, the firing rate of the forced populations has m maxima (for specific examples see the insets of **Figures 6A,B**). In extremely narrow parameter intervals other, more complex, kinds of locking of the type $m : n$ emerge, where exactly m maxima in the population activity appear for every n θ-oscillations. In the examined cases we have identified locked patterns with n up to four. Moreover, for the ING case, we have even observed a chaotic region (see **Figure 6B**), which emerges at quite large forcing amplitude $I_0 \simeq 19$. On the basis of our analysis we cannot exclude that chaos could emerge also in the PING set-up, for sufficiently strong forcing.

Let us now focus on the $m : 1$ perfectly locked states with $m > 1$, which are worth investigating due to their relevance for

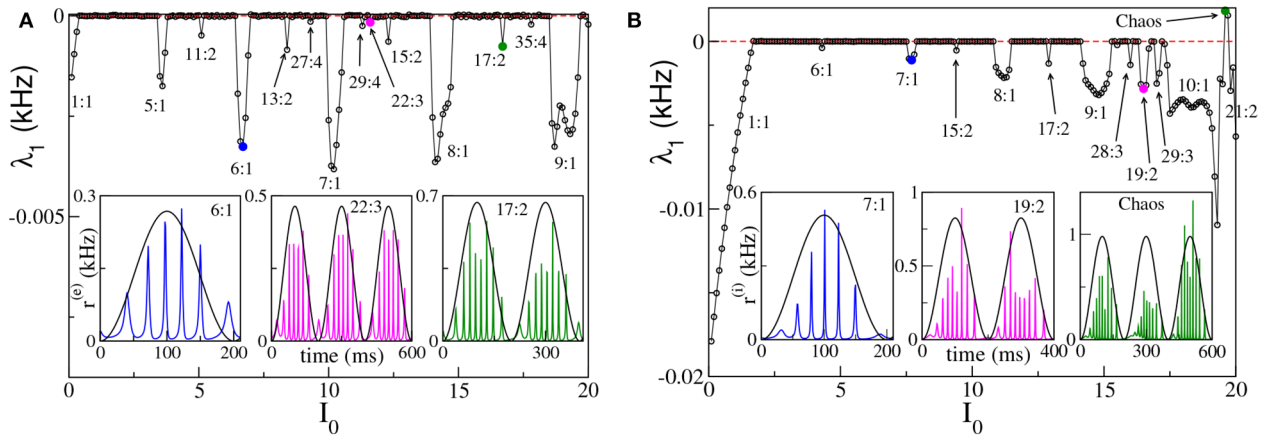


FIGURE 6 | Maximal Lyapunov exponent λ_1 estimated for the neural mass models as a function of the forcing amplitude I_0, for the PING **(A)** and ING **(B)** set-ups. In both cases the system is subject to a forcing frequency $\nu_\theta = 5$ Hz. Insets in **(A,B)** report the instantaneous firing rate $r^{(e)}(t)$ ($r^{(i)}(t)$) vs. time for the PING (ING) set-up, respectively. The three cases shown are representative of the states identified by circles in the main panels. The color code is the same, i.e., the color used in the inset identifies the corresponding circle in the main panel. The black continuous lines in the inset correspond to I_θ in arbitrary units. Parameters are the same as in **Figure 4**.

θ-γ mixed oscillations, as well as to their relative large frequency of occurrence with respect to more complex $m:n$ locked states. In particular, we have examined the response of the system to different forcing amplitudes $I_0 \in [0:20]$ and frequencies $\nu_\theta \in [1:10]$ Hz. The $m:1$ locked oscillations are reported in **Figures 7A,B** and characterized by the number m of oscillations displayed within a single θ-cycle.

These locked states appear only for $\nu_\theta > 2-3$ Hz. Moreover, the states with equal m are arranged in stripes in the (ν_θ, I_0)-plane. Locked states in the PING configuration occur in separated stripes whose order m increases for increasing I_0; in particular, states with $3 \leq m \leq 10$ are clearly identifiable. In the ING set-up, for sufficiently large ν_θ and I_0, we have a continuum of locked states, thus indicating that, for the ING set-up, phase locking to the forcing frequency is easier to achieve. In this case the order of occurrence of m-order states is not clearly related to the forcing amplitude; however locked states with order m and $2m$ are often nested within each other as shown in **Figure 7B**.

To examine which frequencies are excited in these states we have measured for each amplitude I_0 the minimal, the maximal and the average frequency of the COs associated with $m:1$ locked states over the whole range of examined forcing frequencies ν_θ. These frequencies are reported in **Figures 7C,D**. The analysis clearly reveals that the minimal CO frequency is essentially independent from I_0 and its value is around 20 Hz, while the maximal and the average grow with I_0. However all these frequencies stay within the γ-range for the examined forcing amplitudes.

To better understand the mechanism underlying the emergence of θ-nested γ oscillations, we have reported in **Figures 7C,D** the COs frequencies $\nu^{(e)}$ ($\nu^{(i)}$) (green solid lines) obtained from the adiabatic bifurcation analysis of the neural mass models (these frequencies are also shown in the insets of **Figures 2A**, **3A**). The very good agreement between $\nu^{(e)}$ and $\nu^{(i)}$ and the maximal frequency measured for the locked states suggests that the nested COs are induced by the crossing of the super-critical Hopf bifurcation during the periodic stimulation. In particular, during forcing, the maximal achievable γ-frequency is the one corresponding to the maximal stimulation current $I_0 + H_0^{(e)}$ ($I_0 + H_0^{(i)}$) for the unforced PING (ING) set-ups. Furthermore, under sinusoidal forcing, the system spends a longer time in proximity of the maximal stimulation value, since it is a turning point. This explains why this frequency is always present in the response of the driven system for the considered locked states.

4.3. Comparison with Experimental Findings

In a series of recent optogenetic experiments on the mouse enthorinal-hippocampal system, clear evidence has been reported that phase-amplitude coupled γ-rhythms can be generated locally in brain slices *ex vivo* in the CA1-region, as well as in the CA3 and MEC, under sinusoidal θ stimulations (Akam et al., 2012; Pastoll et al., 2013; Butler et al., 2016, 2018). In particular, in Butler et al. (2018) the authors reported evidence that, for all the regions CA1, CA3 and MEC, the generation of the γ-rhythms, under θ-rhythmic activation of pyramidal neurons, is due to a PING mechanism.

However, due to the fact that pyramidal neurons are directly activated during experiments, their result cannot exclude that tonic activation of interneurons contributes to θ–γ oscillations *in vivo*. Furthermore, in Pastoll et al. (2013) the authors affirm that θ-nested γ-oscillations due to the optogenetic θ-frequency drive, are generated, in MEC, by local feedback inhibition without recurrent excitation, therefore by a ING mechanism. In this section, we try to reproduce some of the analyses reported in these experimental studies by employing both the PING and ING set-ups, in order to understand if these two set-ups give rise to different dynamical behaviors.

By following the analysis performed in Butler et al. (2016, 2018), we have considered the response of the two set-ups

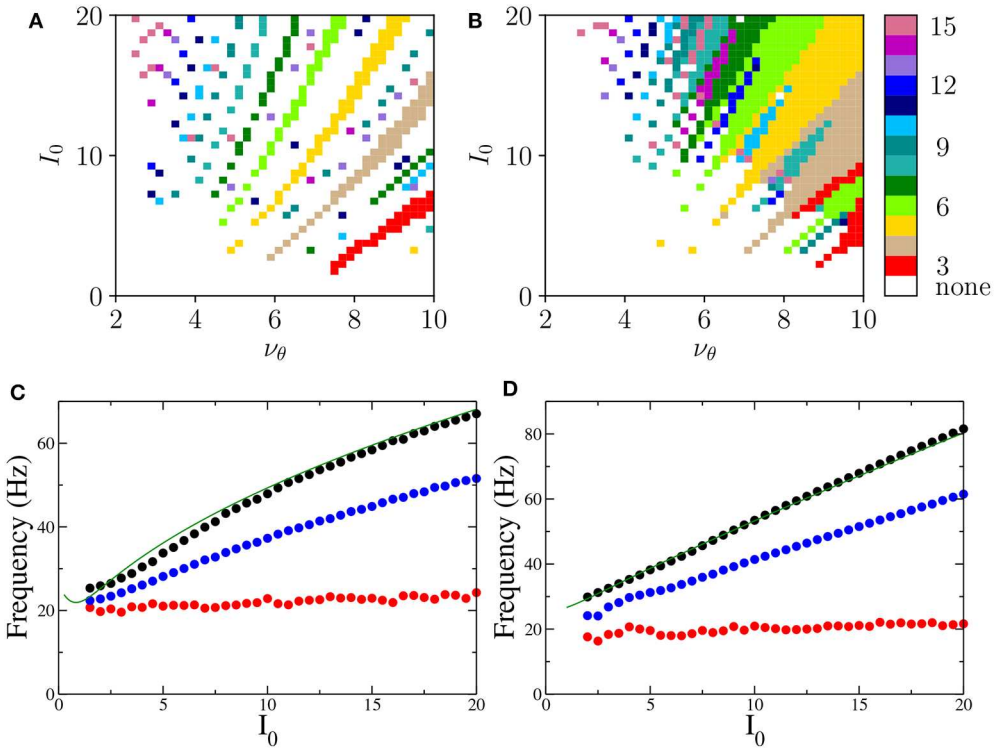


FIGURE 7 | Phase locked $m:1$ states Locked states for the neural mass models are displayed in **(A,B)** for the PING and ING set-ups, respectively. The color code identifies the locked states according to the value of m, from 3 to 15. **(C,D)** Minimal (red circles), average (blue circles), and maximal (black circles) frequencies of the COs as a function of the forcing amplitude I_0 for PING **(C)** and ING **(D)** set-ups. These values are obtained by considering all possible $m:1$ locked states corresponding to the examined I_0. The frequencies $\nu^{(e)}$ ($\nu^{(i)}$) (green solid lines) of the COs obtained from the bifurcation analysis in the adiabatic set-up are reported as a function of $H^{(e)} - H_0^{(e)}$ ($H^{(i)} - H_0^{(i)}$) for the PING (ING). Parameters are the same as in **Figure 4**.

to forcing of different frequencies ν_θ and amplitudes I_0. The results reported in **Figure 8** reveal that the phenomenon of PAC is present for all the considered frequencies $\nu_\theta \in [1, 10]$ Hz and amplitudes $I_0 \in [1, 20]$ in both set-ups. Moreover, analogously to what was reported in Butler et al. (2016, 2018), the amplitude of the γ-oscillations increases proportionally to I_0, while the number of nested oscillations in each cycle increases for decreasing ν_θ. On the basis of this comparison, the forced PING and ING set-ups display essentially the same dynamics.

To get a more detailed information about the dynamics in the two set-ups, we will now consider the features of the power spectra $P_S^{(e)}$ ($P_S^{(i)}$) of the mean excitatory (inhibitory) potential for the PING (ING) set-up. These features are obtained for different forcing amplitudes and frequencies, somehow similar to the analysis performed for the power spectra of the Local Field Potential (LFP) in Butler et al. (2016, 2018).

Let us first consider, as an example of the obtained power spectra, the case corresponding to the PING set-up with a forcing characterized by $\nu_\theta = 5$ Hz and amplitude $I_0 = 10$, shown in **Figure 9A**. In the spectrum we observe very well defined spectral lines located at frequencies which can be obtained as a linear combination of the forcing frequency $\nu_\theta = 5$ Hz and of the response frequency $F_r = 45$ Hz. In particular F_r is associated with the main peak and should correspond to the intrinsic frequency of the forced system. In the present case, the adiabatic bifurcation diagram reported in **Figure 2A** tells us that the maximal achievable frequency is $\nu_{max}^{(e)} \simeq 49.3$ Hz, corresponding to $H^{(e)} = I_0 + H_0^{(e)} = 11.3$. Indeed $F_r < \nu_{max}^{(e)}$ due to the interaction with the forcing current that eventually induces a locking phenomenon at a frequency that is exactly a multiple of ν_θ, as it happens in the present case. However, in general, a spectrum as the one shown in **Figure 9A**, is the emblem of a quasi-periodic motion characterized by two incommensurate frequencies. This can be easily observable in most cases in our system, where ν_θ and F_r are usually incommensurate.

The spectra obtained from optogenetic stimulation, reported in Butler et al. (2016, 2018), do not resemble the one shown in **Figure 9A**; indeed they present only two peaks: one corresponding to the stimulation frequency and one, quite broad, associated with the γ-oscillations. We can expect that the difference is due to the multiple noise sources that are always present in an experimental analysis (in particular for neurophysiological data), but that are absent in our model. Indeed, by considering the neural mass model for the PING set-up with additive noise on the membrane potentials of suitable amplitude, that is $A = 1.4$, we get a power spectrum resembling the experimental one, as shown in **Figure 9B**. The presence of noise induces the merging of the principal peaks in a unique broad one and the shift of the position of the main peak toward some larger values ($F_r = 54$ Hz in the present case) with respect to the fully deterministic case.

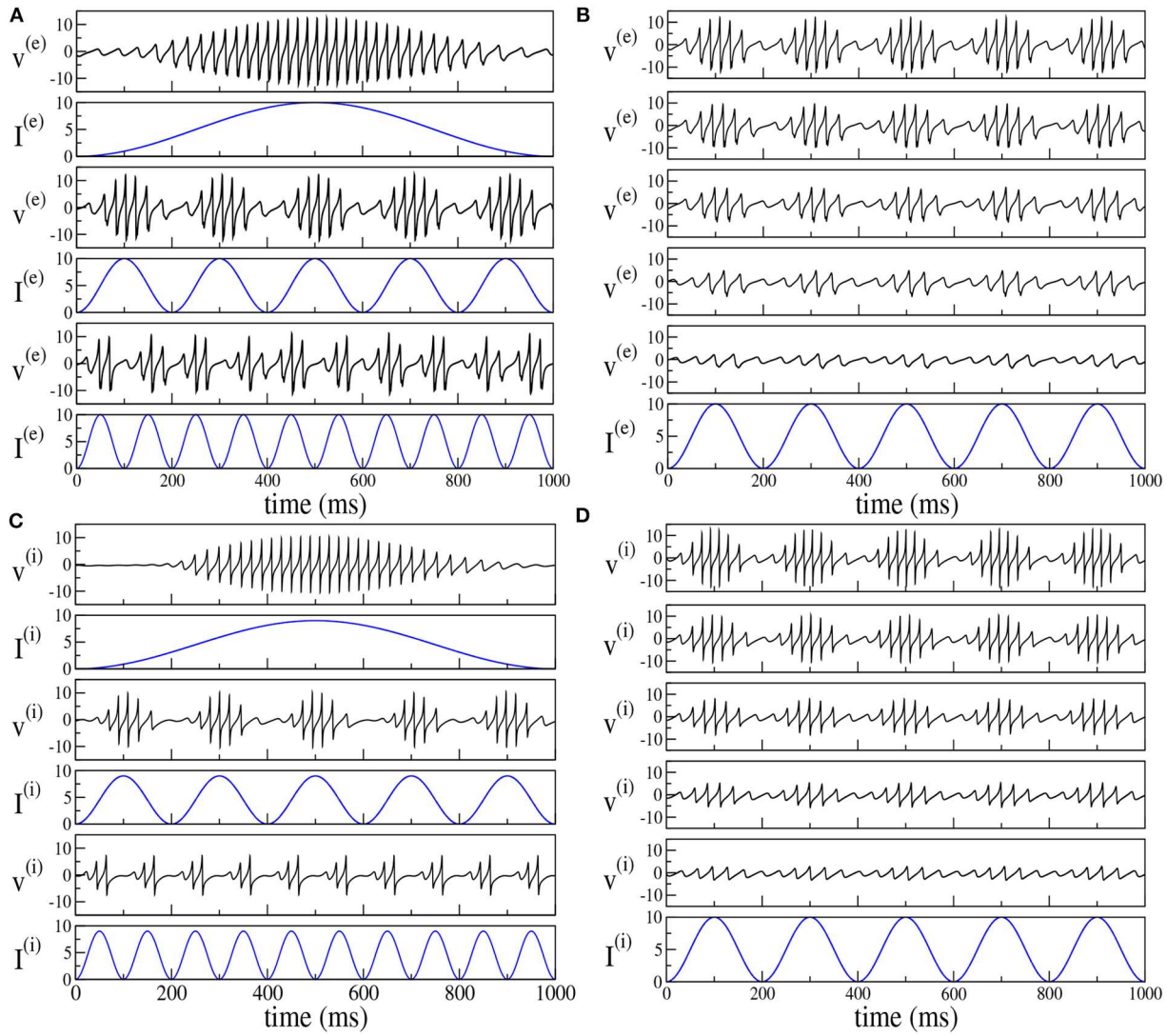


FIGURE 8 | Theta-nested gamma COs for PING **(A,B)** and ING set-up **(C,D)**. Left column: dependence of the mean membrane potential of the excitatory (inhibitory) population $v^{(e)}$ ($v^{(i)}$) on the frequency ν_θ of the external forcing $I^{(e)} = I_\theta$ ($I^{(i)} = I_\theta$) with $I_0 = 10$ ($I_0 = 9$) for the PING (ING) set-up. The current profiles (blue lines) are displayed immediately below the corresponding membrane potential evolution. From top to bottom, the frequency ν_θ is 1, 5, and 10 Hz. Right column: dependence of the mean membrane potential $v^{(e)}$ ($v^{(i)}$) on the amplitude I_0 of the external current. Here the forcing frequency is kept constant at the value $\nu_\theta = 5Hz$. The amplitude is changed from 100% of maximum (top) to 20% of maximum (bottom) in 20% increments, the maximum being given by $I_0 = 10$. The data refer to the evolution of neural mass models, the parameters are the same as in **Figure 4**.

Let us now consider the power spectra obtained for different forcing frequencies $\nu_\theta \in [1:10]$ Hz in the θ-range, in case of fixed forcing amplitude and in the absence of noise. The position of the main and auxiliary peaks are shown in **Figure 10A** (**Figure 10C**) for the PING (ING) set-up and compared with the experimental results (red circles) obtained for the CA1 region of the hippocampus in Butler et al. (2016). It is clear that, for both set-ups, the position of the main peak F_r (green squares) has a value $\simeq$ 50 Hz and it does not show any clear dependence on ν_θ. This is in contrast with the experimental data, which reveal an increase proportional to ν_θ from 49 to 60 Hz. The same trend is displayed in our simulation from the subsidiary peak located at $F_r + \nu_\theta$ (black stars), showing an increase with ν_θ.

Let us now take into account the power of the γ oscillations P_γ as defined in section 2.2. As shown in the insets of **Figures 10B,D**, this quantity remains essentially constant for low frequencies (namely, for $\nu_\theta \leq 5$ Hz in the PING and for $\nu_\theta \leq 7$ Hz in the ING), while it drops to smaller values at larger frequencies. On the other hand, the experimental results (red circles) reveal a similar decrease at frequencies $\nu_\theta > 5$ Hz, but they also reveal an increase at low frequencies, not present in our numerical data, thus suggesting a sort of resonance at 5 Hz. For what concerns the dependence of P_γ on the forcing amplitude, we have fixed $\nu_\theta = 5$

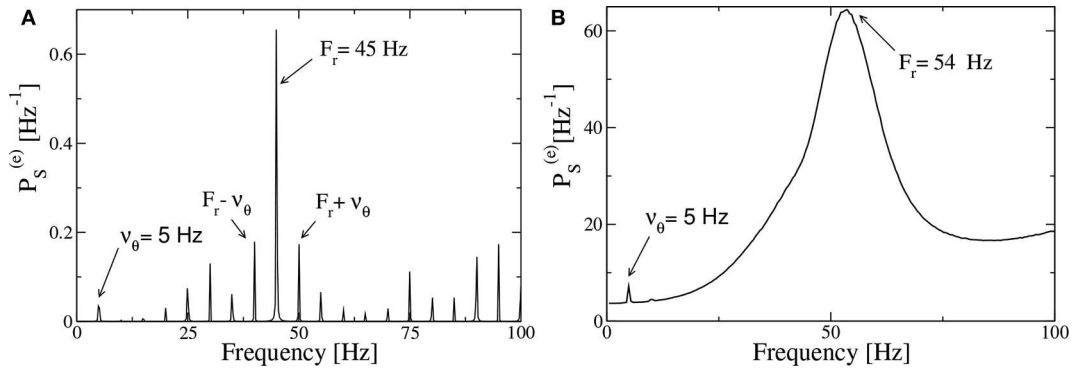


FIGURE 9 | Power spectra for the PING set-up. Spectra $P_S^{(e)}$ of the mean membrane potential $v^{(e)}$ of the neural mass model estimated when the excitatory population is subject to an external drive with frequency ν_θ = 5 Hz and amplitude $I_0 = 10$, in the absence of noise **(A)** and for additive noise with amplitude $A = 1.4$ **(B)**. The data refer to the evolution of neural mass models, the parameters are as in **Figure 4**.

Hz and varied I_0 in the range [4 : 10] ([8 : 20]) for the PING (ING) set-up. In both cases and analogously to experimental data, P_γ increases proportionally to I_0, see **Figures 10B,D**.

In both set-ups, our model is unable to reproduce, in the absence of noise and for fixed forcing amplitude I_0, the steady increase of F_r with ν_θ reported in the experiments for the mice CA1 in Butler et al. (2016). Therefore, in order to cope with this problem, we will now investigate how a similar trend can emerge in our data. In particular, in the remaining part of the paper we consider noisy dynamics, to have a better match with experiments where is unavoidable. In **Figure 11A** we report, for the PING set-up, the estimated power spectra for different noise levels, under constant external sinusoidal forcing. The effect of noise is to render the spectrum more flat and to shift the position of the peak in the γ-range toward higher frequencies. As shown in the inset of **Figure 11A**, the frequency F_r is almost insensitive to the noise up to amplitudes $A \simeq 1.0$, then it increases steadily with A from $\simeq$ 45 Hz to $\simeq$ 62 Hz. The effect of varying the forcing amplitude I_0, for constant forcing frequency $\nu_\theta = 5$ Hz and noise amplitude $A = 1.4$, is shown in **Figure 11B**. In this case the amplitude increase of the forcing leads to more defined peaks in the γ-range and to an almost linear increase with I_0 of F_r, as reported in the inset. In the same inset we also have reported the results related to two optogenetic experiments for the CA1-region of the mice hippocampus. In particular, the data-sets refer to two successive experiments performed by the same group: namely, red filled circles refer to Butler et al. (2016) and red open circles to Butler et al. (2018). While in one experiment (red open circles) a constant increase of F_r with the forcing amplitude is observable from 60 to 70 Hz, in the other one (red filled circles) the frequency initially increases with I_0 and then decreases with it. As a matter of fact in the latter case, F_r remains around 45–50 Hz for a variation of I_0 from 40 to 100 % of the maximal amplitude I_0^{max}. From the comparison with our results, we can affirm that our data reproduce the correct range of frequencies in both experiments and also the dependence on the forcing amplitude for $I_0/I_0^{max} \geq 60\%$ reported in Butler et al. (2018). The decrease of F_r for I_0/I_0^{max} larger than the 50% reported in Butler et al. (2016) is inconsistent with our data, but also with the experimental results of the same group published in Butler et al. (2018).

From this last analysis we have understood that, for constant forcing frequency, the γ-peak shifts toward higher frequencies by increasing the forcing amplitude or the noise level, i.e., by increasing the stimulation power.

Therefore, to obtain an increase of F_r with the forcing frequency ν_θ, analogously to the results reported in Butler et al. (2016) (and displayed as filled red circles in **Figures 10A,C**), we perform numerical experiments where ν_θ increases together with A or I_0. The simplest protocol is to assume that A (I_0) will increase linearly with ν_θ. The results obtained for the PING (ING) set-up are reported in **Figure 12A** (**Figure 12B**). As evident from the figures, in both set-ups and for both protocols we obtain results in reasonable agreement with the experiments. In the present framework, we have also analyzed the dependence of the γ-power P_γ on ν_θ. In particular, this quantity increases almost linearly with the forcing frequency, at variance with the experimental results in Butler et al. (2016) which revealed a sort of resonance with an associated maximal γ-power around $\nu_\theta = 5$ Hz (the experimental data are displayed as red circles in the insets of **Figures 10B,D**).

5. DISCUSSION AND CONCLUSIONS

In this paper we have analyzed the dynamics of a new class of neural mass models arranged in two different set-ups: an excitatory-inhibitory network (or PING set-up) and a purely inhibitory network (or ING set-up). These neural mass models are extremely relevant to mimick neural dynamics for two reasons. On one side, because they are not derived heuristically, since they reproduce exactly the dynamics of excitatory and inhibitory networks of spiking neurons for any degree of synchronization (Montbrió et al., 2015; Devalle et al., 2017; Ceni et al., 2019). On another side, these neural masses reproduce the macroscopic dynamics of quadratic integrate-and-fire neurons, which are normal forms of class I neurons, therefore they are

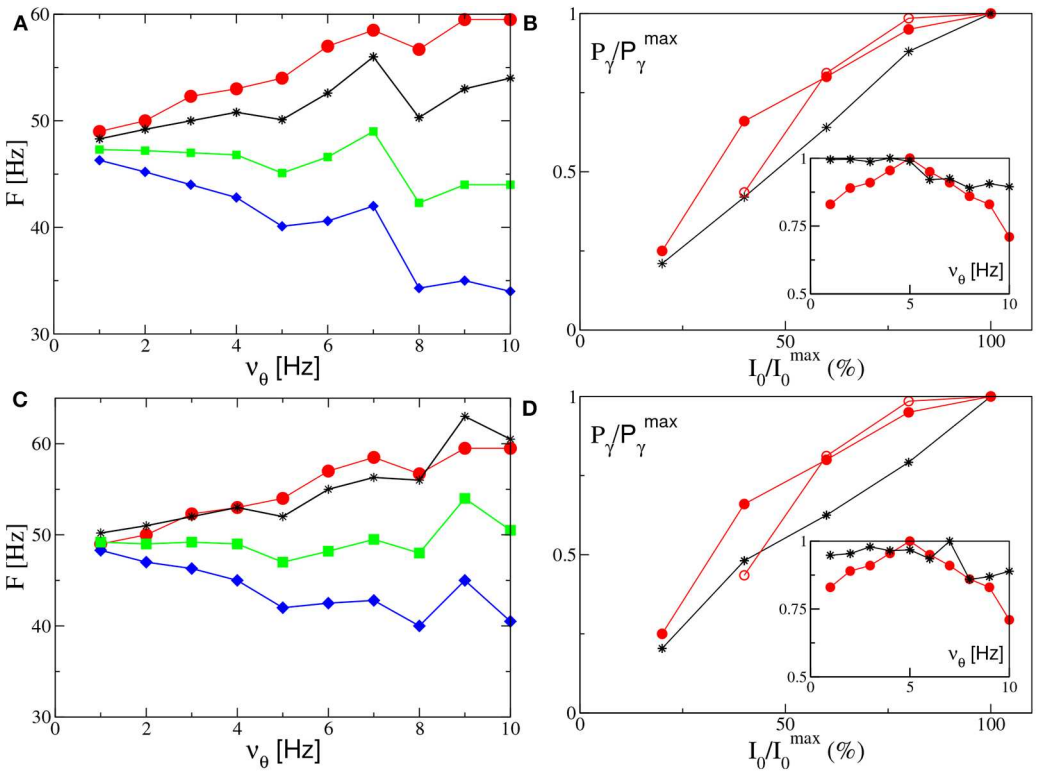


FIGURE 10 | Power spectra features (PING set-up). **(A)** Frequencies of the peaks of the power spectrum $P_S^{(e)}$ as a function of the stimulation frequency ν_θ. Green squares correspond to the main peak frequency F_r, while the black stars to $F_r + \nu_\theta$ and the blue diamonds to $F_r - \nu_\theta$. The red circles are the experimental data extrapolated from Figure 4C of Butler et al. (2016). The amplitude of the forcing is $I_0 = 10$. **(B)** Normalized power of the γ oscillations P_γ/P_γ^{max} associated with the signal $v^{(e)}$ as a function of the amplitude stimulation, where we set $I_0^{max} = 20$ and the frequency of stimulation at $\nu_\theta = 5$ Hz. In the inset we report the same quantity as a function of the frequency stimulation ν_θ for $I_0 = 10$. The black stars correspond to our simulations, while the red circles to experimental data extrapolated from Figure 4E (**Figure 4B** for the inset) of Butler et al. (2016) (filled circles) and from Figure 4C of Butler et al. (2018) (empty circles). The other parameters are as in **Figure 4**. (ING set-up) **(C)** Same as in **(A)** for the power spectrum $P_S^{(i)}$ with $I_0 = 9$. **(D)** Same as **(B)** for the signal $v^{(i)}$ with $I_0^{max} = 40$. The data refer to the evolution of neural mass models. For the inset we set $I_0 = 9$, other parameters as in **Figure 4**.

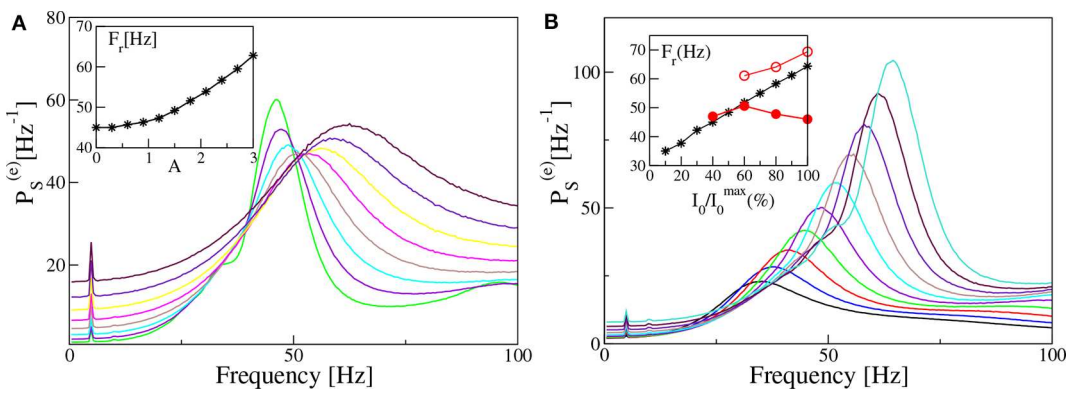


FIGURE 11 | Power spectra dependency on noise and forcing amplitudes (PING set-up). Power spectra $P_S^{(e)}$ for different noise level A **(A)** and different amplitude of the external input I_0 **(B)**, for a fixed forcing frequency $\nu_\theta = 5$ Hz. In the insets are reported the frequencies F_r of the main peak as a function of the noise level **(A)** and of the amplitude of the external drive I_0 **(B)**. In the inset of **(B)** are also reported experimental data extracted from Figure 4F of Butler et al. (2016) (filled red circles) and from Figure 4D of Butler et al. (2018) (open red circles). The curves in **(A)** are obtained by varying the noise amplitude $A \in [0.9 : 3.0]$ with a step of 0.3, while keeping $I_0 = 10$ fixed. On the other hand the curves in **(B)** refer to different forcing amplitudes $2 \leq I_0 \leq 20$, varied in steps of 0.2, with fixed noise amplitude $A = 1.4$. The other parameters are as in **Figure 4**. Data have been obtained by the integration of neural mass models.

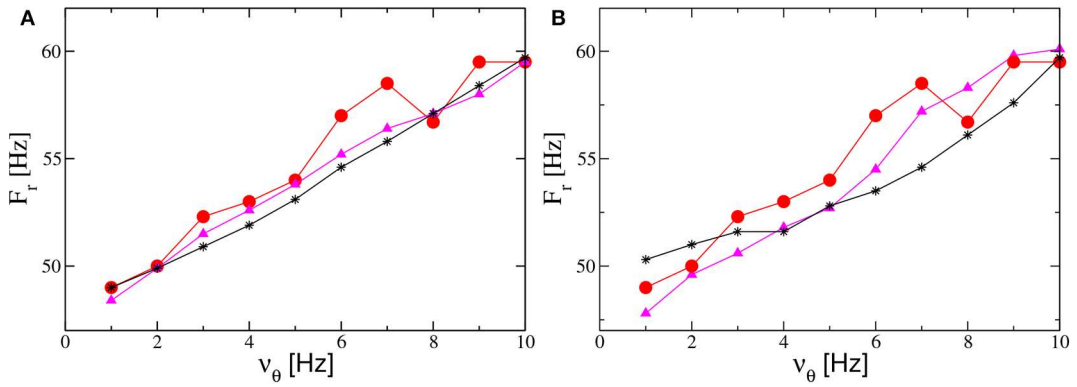


FIGURE 12 | Influence of the theta frequency on the gamma oscillations. Frequency F_r of the main peak of the power spectrum $P_S^{(e)}$ vs. ν_θ for the PING **(A)** and ING **(B)** set-ups. Red filled circles represent the experimental data extrapolated from Figure 4C in Butler et al. (2016). Black stars (magenta triangles) refer to numerical data obtained by varying linearly the noise amplitude A (the forcing amplitude I_0) as a function of ν_θ and maintaining the forcing amplitude I_0 (the noise amplitude A) constant. The data shown as black stars for the PING (ING) set-up in **(A)** (panel **B**) are obtained by adding white noise to the evolution of the mean membrane potentials and by varying linearly its amplitude in the interval $A \in [1.4 : 2.9]$ as a function of ν_θ with $I_0 = 10$ ($I_0 = 9$). The magenta triangles refer to data obtained by keeping fixed the noise amplitude at the value $A = 1.4$ and by varying linearly with ν_θ the forcing amplitude I_0 in the range $[9.5 : 18]$ ($[8 : 14]$) for the PING (ING) set-up in **(a)** (panel **B**). Other parameters for as in **Figure 4**. Data are obtained from neural mass models integration.

expected to represent the dynamics of this large class of neurons (Ermentrout and Kopell, 1986).

In this present work we have shown that θ-nested γ oscillations can emerge both in the PING and ING set-up under an external excitatory θ-drive whenever the system, in the absence of forcing, is in a regime of asynchronous dynamics, but in proximity of a Hopf bifurcation toward collective γ oscillations. The external forcing drives the system across the bifurcation inside the oscillatory regime, thus leading to the emergence of γ oscillations. The amplitude of these collective oscillations is related to the distance from the bifurcation point, therefore it depends on the phase of the θ-forcing term. These nested oscillations can arise in proximity of a super-critical and also a sub-critical Hopf bifurcations. As shown in **Appendix A**, in the latter case the amplitudes are no more symmetric with respect to the maximum value of the theta stimulation, analogously to the experimental findings reported in Butler et al. (2016).

Equivalent results have been reported for an excitatory-inhibitory network with a recurrent coupling among the excitatory neurons, by considering the Wilson-Cowan rate model (Onslow et al., 2014). However, at variance with our neural mass model, the Wilson-Cowan model fails to reproduce the emergence of γ-oscillations, displayed by the corresponding spiking networks, in several other set-ups. In particular, the Wilson-Cowan model is unable to display COs for purely inhibitory populations (the ING set-up), without the addition of a delay in the IPSPs transmission, delay that is not required in the network model. Moreover, the Wilson-Cowan model is unable to display COs even for excitatory-inhibitory coupled populations in the absence of a recurrent excitation (Onslow et al., 2014; Devalle et al., 2017). As shown in **Appendix B**, the considered neural mass model in the PING set-up displays clear θ-nested γ-oscillations in the absence of any recurrent coupling or with recurrent couplings only among the inhibitory neurons.

Furthermore, we have identified two different types of phase amplitude couplings. One characterized by a perfect locking between θ and γ-rhythms, corresponding to an overall periodic behavior dictated by the slow forcing. The other one where the locking is imperfect and the dynamics is quasi-periodic or even chaotic. The perfectly locked θ-nested γ oscillations display in turn two types of CFC: phase-phase and phase amplitude coupling (Hyafil et al., 2015). These states arise for ν_θ larger than 2–3 Hz and for sufficiently large forcing amplitudes. From the results reported in Butler et al. (2016) for the CA1-region of the hippocampus under sinusoidal forcing *in vitro*, it is evident that perfectly phase locked PACs have been observed in each single slice. However, *in vivo* this perfect phase-phase locking cannot be expected, see the detailed discussion of phase-phase coupling reported in Scheffer-Teixeira and Tort (2016), where the authors clarify that phase locking is indeed observable, but only over a limited number of successive θ-cycles. Therefore, PAC with an underlying chaotic (or noisy) dynamics is the scenario usually expected in behaving animals.

From our analysis it also emerges that locked states are more frequent in the ING set-up. The purely inhibitory population is more easily entrained by the forcing with respect to the coupled excitatory-inhibitory population system, where the forcing is applied to the excitatory population. This result is somehow in agreement with recent findings based on the analysis of phase response curves, which suggest that stimulating the inhibitory population facilitates the entrainment of the gamma-bands with an almost resonant frequency (Akao et al., 2018; Dumont and Gutkin, 2019). However, these analyses do not consider θ-γ entrainment: this will be a subject of future studies based on exact macroscopic phase response curves (Dumont et al., 2017; Dumont and Gutkin, 2019).

Our modelization of the PAC mechanism induced by an external θ-forcing is able to reproduce several experimental features reported for optogenetic experiments concerning the region CA1, CA3 of the hippocampus, as well as MEC (Akam et al., 2012; Pastoll et al., 2013; Butler et al., 2016, 2018). In agreement with the experiments, we observe nested γ COs for forcing frequencies in the range $[1:10]$ Hz, whose amplitude grows proportionally to the forcing one. Furthermore, the γ-power and the frequency of the γ peak increase almost linearly with the forcing amplitude, i.e., with the input θ-power. Moreover these findings are consistent with recent results for behaving rats, where it has been shown that hippocampal γ-frequency and the associated power increase proportionally to the animal speed (Ahmed and Mehta, 2012; Sheremet et al., 2019). In addition, in Richard et al. (2013), the authors have clearly demonstrated that the hippocampal θ-power and the mouse speed are positively correlated. This proportionality between the θ-power and the mouse speed has been recently employed to develop a computational model able to successfully reproduce CA1 network activity (Haimerl et al., 2019).

However, the neural mass model in all the examined PING and ING set-ups is unable to reproduce the increase in frequency of the γ-power peak with ν_θ reported in Butler et al. (2016). Indeed, such effect was expected by the observation that during movement, both the frequencies of hippocampal θ oscillations (Sławińska and Kasicki, 1998) and γ oscillations (Ahmed and Mehta, 2012) increase with the running speed of the animal. However, the variation of the γ frequency reported in Ahmed and Mehta (2012) for behaving animals amounts to 40–60 Hz, while in the optogenetic experiment by Butler et al. (2016), the increase was limited to $\simeq$ 10 Hz. In order to get a similar increase in the neural mass model, we have been obliged to assume that the stimulation power (namely, the noise or the forcing amplitude) increases proportionally to ν_θ. On one side, further experiments are required to clarify if, during optogenetic experiments, the forcing (or noise amplitude) affecting the neural dynamics is indeed dependent on ν_θ. This could be due to a reinforcement of the synaptic strengths for increasing forcing frequencies, or to the fact that higher θ frequencies can favor neural discharges in regions different from CA1, thus being assimilated to external noise. On another side it should be analyzed if other bifurcation mechanisms, beside the Hopf one, here considered, can give rise to such a dependence of γ power on θ forcing.

Finally, experiments on behaving rodents report clear evidence that θ-power and ν_θ, as well as the power of the γ-peak and the corresponding frequency, increase all proportionally to the animal speed (Sławińska and Kasicki, 1998; Ahmed and Mehta, 2012; Richard et al., 2013; Sheremet et al., 2019). Furthermore, in Sheremet et al. (2019) the authors report evidence of the increase of the phase-amplitude coupling with the speed. This scenario is consistent with the results reported in our analysis, where we have shown that an increase of ν_θ and of the stimulation power leads to an increase of P_γ and of the frequency of the γ peak as well as of the PAC.

DATA AVAILABILITY STATEMENT

The datasets generated for this study are available on request to the corresponding author.

AUTHOR CONTRIBUTIONS

MS, HB, and SO performed the simulations and data analysis. SO and AT were responsible for the state-of-the-art review and the paper write-up. All the authors conceived and planned the research.

FUNDING

AT received financial support by the Excellence Initiative I-Site Paris Seine (Grant No ANR-16-IDEX-008) (together with HB and MS), by the Labex MME-DII (Grant No ANR-11-LBX-0023-01) (together with SO) and by the ANR Project ERMUNDY (Grant No ANR-18-CE37-0014), all part of the French programme Investissements d'Avenir.

ACKNOWLEDGMENTS

This work has been initiated during the Advanced Study Group 2016/17 From Microscopic to Collective Dynamics in Neural Circuits at the Max-Planck Institute for Physics of Complex System in Dresden (Germany), where SO and AT had extremely useful interactions with E. Montbrió and H. P. Robinson. We also acknowledge fruitful discussions with D. Angulo-Garcia, F. Devalle, G. Dumont, M. di Volo, A. Pikovsky and we thank T. Kreuz for a carefully reading of the final manuscript. We would also like to thank A.P. Maureer for pointing out recent experimental findings on the Hippocampus of behaving rodents.

SUPPLEMENTARY MATERIAL

The Supplementary Material for this article can be found online at: https://www.frontiersin.org/articles/10.3389/fncom.2020.00047/full#supplementary-material

REFERENCES

Ahmed, O. J., and Mehta, M. R. (2012). Running speed alters the frequency of hippocampal gamma oscillations. *J. Neurosci.* 32, 7373–7383. doi: 10.1523/JNEUROSCI.5110-11.2012

Akam, T., Oren, I., Mantoan, L., Ferenczi, E., and Kullmann, D. M. (2012). Oscillatory dynamics in the hippocampus support dentate gyrus-ca3 coupling. *Nat. Neurosci.* 15:763. doi: 10.1038/nn.3081

Akao, A., Ogawa, Y., Jimbo, Y., Ermentrout, G. B., and Kotani, K. (2018). Relationship between the mechanisms of gamma rhythm generation and the magnitude of the macroscopic phase response function in a population of excitatory and inhibitory modified quadratic integrate-and-fire neurons. *Phys. Rev. E* 97:012209. doi: 10.1103/PhysRevE.97.012209

Bartos, M., Vida, I., and Jonas, P. (2007). Synaptic mechanisms of synchronized gamma oscillations in inhibitory interneuron networks. *Nat. Rev. Neurosci.* 8:45. doi: 10.1038/nrn2044

Belluscio, M. A., Mizuseki, K., Schmidt, R., Kempter, R., and Buzsáki, G. (2012). Cross-frequency phase-phase coupling between theta and gamma oscillations in the hippocampus. *J. Neurosci.* 32, 423–435. doi: 10.1523/JNEUROSCI.4122-11.2012

Benettin, G., Galgani, L., Giorgilli, A., and Strelcyn, J.-M. (1980). Lyapunov characteristic exponents for smooth dynamical systems and for Hamiltonian systems; a method for computing all of them. Part 1: Theory. *Meccanica* 15, 9–20. doi: 10.1007/BF02128236

Bragin, A., Jandó, G., Nádasdy, Z., Hetke, J., Wise, K., and Buzsáki, G. (1995). Gamma (40-100 hz) oscillation in the hippocampus of the behaving rat. *J. Neurosci.* 15, 47–60. doi: 10.1523/JNEUROSCI.15-01-00047.1995

Brunel, N., and Hakim, V. (1999). Fast global oscillations in networks of integrate-and-fire neurons with low firing rates. *Neural Comput.* 11, 1621–1671. doi: 10.1162/089976699300016179

Butler, J. L., Hay, Y. A., and Paulsen, O. (2018). Comparison of three gamma oscillations in the mouse entorhinal-hippocampal system. *Eur. J. Neurosci.* 48, 2795–2806. doi: 10.1111/ejn.13831

Butler, J. L., Mendonça, P. R., Robinson, H. P., and Paulsen, O. (2016). Intrinsic cornu ammonis area 1 theta-nested gamma oscillations induced by optogenetic theta frequency stimulation. *J. Neurosci.* 36, 4155–4169. doi: 10.1523/JNEUROSCI.3150-15.2016

Buzsaki, G. (2006). *Rhythms of the Brain*. New York, NY: Oxford University Press. doi: 10.1093/acprof:oso/9780195301069.001.0001

Buzsáki, G., and Wang, X.-J. (2012). Mechanisms of gamma oscillations. *Annu. Rev. Neurosci.* 35, 203–225. doi: 10.1146/annurev-neuro-062111-150444

Canolty, R. T., Edwards, E., Dalal, S. S., Soltani, M., Nagarajan, S. S., Kirsch, H. E., et al. (2006). High gamma power is phase-locked to theta oscillations in human neocortex. *Science* 313, 1626–1628. doi: 10.1126/science.1128115

Canolty, R. T., and Knight, R. T. (2010). The functional role of cross-frequency coupling. *Trends Cogn. Sci.* 14, 506–515. doi: 10.1016/j.tics.2010.09.001

Ceni, A., Olmi, S., Torcini, A., and Angulo-Garcia, D. (2019). Cross frequency coupling in next generation inhibitory neural mass models. *arXiv preprint arXiv:1908.07954*. doi: 10.1101/745828

Chehelcheraghi, M., van Leeuwen, C., Steur, E., and Nakatani, C. (2017). A neural mass model of cross frequency coupling. *PLoS ONE* 12:e0173776. doi: 10.1371/journal.pone.0173776

Chrobak, J., and Buzsáki, G. (1998). Gamma oscillations in the entorhinal cortex of the freely behaving rat. *J. Neurosci.* 18, 388–398. doi: 10.1523/JNEUROSCI.18-01-00388.1998

Colgin, L. L. (2015). Theta-gamma coupling in the entorhinal-hippocampal system. *Curr. Opin. Neurobiol.* 31, 45–50. doi: 10.1016/j.conb.2014.08.001

Colgin, L. L., Denninger, T., Fyhn, M., Hafting, T., Bonnevie, T., Jensen, O., et al. (2009). Frequency of gamma oscillations routes flow of information in the hippocampus. *Nature* 462:353. doi: 10.1038/nature08573

Coombes, S., and Byrne, Á. (2019). "Next generation neural mass models," in *Nonlinear Dynamics in Computational Neuroscience*, eds F. Corinto and A. Torcini (Cham: Springer), 1–16. doi: 10.1007/978-3-319-71048-8_1

Devalle, F., Roxin, A., and Montbrió, E. (2017). Firing rate equations require a spike synchrony mechanism to correctly describe fast oscillations in inhibitory networks. *PLoS Comput. Biol.* 13:e1005881. doi: 10.1371/journal.pcbi.1005881

di Volo, M., and Torcini, A. (2018). Transition from asynchronous to oscillatory dynamics in balanced spiking networks with instantaneous synapses. *Phys. Rev. Lett.* 121:128301. doi: 10.1103/PhysRevLett.121.128301

Dumont, G., Ermentrout, G. B., and Gutkin, B. (2017). Macroscopic phase-resetting curves for spiking neural networks. *Phys. Rev. E* 96:042311. doi: 10.1103/PhysRevE.96.042311

Dumont, G., and Gutkin, B. (2019). Macroscopic phase resetting-curves determine oscillatory coherence and signal transfer in inter-coupled neural circuits. *PLoS Comput. Biol.* 15:e1007019. doi: 10.1371/journal.pcbi.1007019

Ermentrout, G. B., and Kopell, N. (1986). Parabolic bursting in an excitable system coupled with a slow oscillation. *SIAM J. Appl. Math.* 46, 233–253. doi: 10.1137/0146017

Fries, P., Nikolić, D., and Singer, W. (2007). The gamma cycle. *Trends Neurosci.* 30, 309–316. doi: 10.1016/j.tins.2007.05.005

Gerstner, W., Kistler, W. M., Naud, R., and Paninski, L. (2014). *Neuronal Dynamics: From Single Neurons to Networks and Models of Cognition*. Cambridge: Cambridge University Press. doi: 10.1017/CBO9781107447615

Goldobin, D. S., Tyulkina, I. V., Klimenko, L. S., and Pikovsky, A. (2018). Collective mode reductions for populations of coupled noisy oscillators. *Chaos* 28:101101. doi: 10.1063/1.5053576

Govaerts, W., Kuznetsov, Y. A., and Sautois, B. (2006). Matcont. *Scholarpedia* 1:1375. doi: 10.4249/scholarpedia.1375

Haimerl, C., Angulo-Garcia, D., Villette, V., Reichinnek, S., Torcini, A., Cossart, R., and Malvache, A. (2019). Internal representation of hippocampal neuronal population spans a time-distance continuum. *Proc. Natl. Acad. Sci. U.S.A.* 116, 7477–7482. doi: 10.1073/pnas.1718518116

Hyafil, A., Giraud, A.-L., Fontolan, L., and Gutkin, B. (2015). Neural cross-frequency coupling: connecting architectures, mechanisms, and functions. *Trends Neurosci.* 38, 725–740. doi: 10.1016/j.tins.2015.09.001

Jensen, O., and Colgin, L. L. (2007). Cross-frequency coupling between neuronal oscillations. *Trends Cogn. Sci.* 11, 267–269. doi: 10.1016/j.tics.2007.05.003

Kilpatrick, Z. P. (2015). "Wilson-Cowan model," in *Encyclopedia of Computational Neuroscience,* eds D. Jaeger and R. Jung (New York, NY: Springer), 3159–3163. doi: 10.1007/978-1-4614-6675-8_80

Laing, C. R. (2014). Derivation of a neural field model from a network of theta neurons. *Phys. Rev. E* 90:010901. doi: 10.1103/PhysRevE.90.010901

Laing, C. R. (2017). "Phase oscillator network models of brain dynamics," in *Computational Models of Brain and Behavior, 1st ed,* ed A. Moustafa (Hoboken, NJ: WILEY Blackwell), 505–517. doi: 10.1002/9781119159193.ch37

Lega, B., Burke, J., Jacobs, J., and Kahana, M. J. (2016). Slow-theta-to-gamma phase-amplitude coupling in human hippocampus supports the formation of new episodic memories. *Cereb. Cortex* 26, 268–278. doi: 10.1093/cercor/bhu232

Lisman, J. (2005). The theta/gamma discrete phase code occuring during the hippocampal phase precession may be a more general brain coding scheme. *Hippocampus* 15, 913–922. doi: 10.1002/hipo.20121

Lisman, J. E., and Jensen, O. (2013). The theta-gamma neural code. *Neuron* 77, 1002–1016. doi: 10.1016/j.neuron.2013.03.007

Luke, T. B., Barreto, E., and So, P. (2013). Complete classification of the macroscopic behavior of a heterogeneous network of theta neurons. *Neural Comput.* 25, 3207–3234. doi: 10.1162/NECO_a_00525

Mazzoni, A., Brunel, N., Cavallari, S., Logothetis, N. K., and Panzeri, S. (2011). Cortical dynamics during naturalistic sensory stimulations: experiments and models. *J. Physiol. Paris* 105, 2–15. doi: 10.1016/j.jphysparis.2011.07.014

Montbrió, E., Pazó, D., and Roxin, A. (2015). Macroscopic description for networks of spiking neurons. *Phys. Rev. X* 5:021028. doi: 10.1103/PhysRevX.5.021028

Olmi, S., Livi, R., Politi, A., and Torcini, A. (2010). Collective oscillations in disordered neural networks. *Phys. Rev. E* 81:046119. doi: 10.1103/PhysRevE.81.046119

Onslow, A. C., Jones, M. W., and Bogacz, R. (2014). A canonical circuit for generating phase-amplitude coupling. *PLoS ONE* 9:e102591. doi: 10.1371/journal.pone.0102591

Pastoll, H., Solanka, L., van Rossum, M. C., and Nolan, M. F. (2013). Feedback inhibition enables theta-nested gamma oscillations and grid firing fields. *Neuron* 77, 141–154. doi: 10.1016/j.neuron.2012.11.032

Pernía-Andrade, A. J., and Jonas, P. (2014). Theta-gamma-modulated synaptic currents in hippocampal granule cells *in vivo* define a mechanism for network oscillations. *Neuron* 81, 140–152. doi: 10.1016/j.neuron.2013.09.046

Pikovsky, A., and Politi, A. (2016). *Lyapunov Exponents: A Tool to Explore Complex Dynamics*. Cambridge: Cambridge University Press. doi: 10.1017/CBO9781139343473

Richard, G. R., Titiz, A., Tyler, A., Holmes, G. L., Scott, R. C., and Lenck-Santini, P.-P. (2013). Speed modulation of hippocampal theta frequency correlates with spatial memory performance. *Hippocampus* 23, 1269–1279. doi: 10.1002/hipo.22164

Scheffer-Teixeira, R., and Tort, A. B. (2016). On cross-frequency phase-phase coupling between theta and gamma oscillations in the hippocampus. *Elife* 5:e20515. doi: 10.7554/eLife.20515

Sheremet, A., Kennedy, J., Qin, Y., Zhou, Y., Lovett, S. D., Burke, S. N., et al. (2019). Theta-gamma cascades and running speed. *J. Neurophysiol.* 121, 444–458. doi: 10.1152/jn.00636.2018

Sławińska, U., and Kasicki, S. (1998). The frequency of rat's hippocampal theta rhythm is related to the speed of locomotion. *Brain Res.* 796, 327–331. doi: 10.1016/S0006-8993(98)00390-4

So, P., Luke, T. B., and Barreto, E. (2014). Networks of theta neurons with time-varying excitability: macroscopic chaos, multistability, and final-state uncertainty. *Phys. D Nonlinear Phenomena* 267, 16–26. doi: 10.1016/j.physd.2013.04.009

Tass, P., Rosenblum, M. G., Weule, J., Kurths, J., Pikovsky, A., Volkmann, J., et al. (1998). Detection of $n:m$ phase locking from noisy data: application to magnetoencephalography. *Phys. Rev. Lett*. 81, 3291–3294. doi: 10.1103/PhysRevLett.81.3291

Tiesinga, P., and Sejnowski, T. J. (2009). Cortical enlightenment: are attentional gamma oscillations driven by ING or PING? *Neuron* 63, 727–732. doi: 10.1016/j.neuron.2009.09.009

Tyulkina, I. V., Goldobin, D. S., Klimenko, L. S., and Pikovsky, A. (2018). Dynamics of noisy oscillator populations beyond the ott-antonsen ansatz. *Phys. Rev. Lett*. 120:264101. doi: 10.1103/PhysRevLett.120.264101

Uhlhaas, P. J., and Singer, W. (2006). Neural synchrony in brain disorders: relevance for cognitive dysfunctions and pathophysiology. *Neuron* 52, 155–168. doi: 10.1016/j.neuron.2006.09.020

Whittingstall, K., and Logothetis, N. K. (2009). Frequency-band coupling in surface EEG reflects spiking activity in monkey visual cortex. *Neuron* 64, 281–289. doi: 10.1016/j.neuron.2009.08.016

Whittington, M. A., Traub, R. D., and Jefferys, J. G. (1995). Synchronized oscillations in interneuron networks driven by metabotropic glutamate receptor activation. *Nature* 373, 612–615. doi: 10.1038/373612a0

Williams, S., and Boksa, P. (2010). Gamma oscillations and schizophrenia. *J. Psychiatry Neurosci*. 35:75. doi: 10.1503/jpn.100021

Wilson, H. R., and Cowan, J. D. (1972). Excitatory and inhibitory interactions in localized populations of model neurons. *Biophys. J*. 12, 1–24. doi: 10.1016/S0006-3495(72)86068-5

Witte, H., Putsche, P., Hemmelmann, C., Schelenz, C., and Leistritz, L. (2008). Analysis and modeling of time-variant amplitude-frequency couplings of and between oscillations of EEG bursts. *Biol. Cybernet*. 99, 139–157. doi: 10.1007/s00422-008-0245-x

Conflict of Interest: The authors declare that the research was conducted in the absence of any commercial or financial relationships that could be construed as a potential conflict of interest.

Copyright © 2020 Segneri, Bi, Olmi and Torcini. This is an open-access article distributed under the terms of the Creative Commons Attribution License (CC BY). The use, distribution or reproduction in other forums is permitted, provided the original author(s) and the copyright owner(s) are credited and that the original publication in this journal is cited, in accordance with accepted academic practice. No use, distribution or reproduction is permitted which does not comply with these terms.

frontiers in Computational Neuroscience

ORIGINAL RESEARCH
published: 08 June 2020
doi: 10.3389/fncom.2020.00049

Emergence of Mixed Mode Oscillations in Random Networks of Diverse Excitable Neurons: The Role of Neighbors and Electrical Coupling

Subrata Ghosh[1], *Argha Mondal*[1], *Peng Ji*[2]*, *Arindam Mishra*[3], *Syamal K. Dana*[3,4], *Chris G. Antonopoulos*[5] *and Chittaranjan Hens*[1]*

[1] *Physics and Applied Mathematics Unit, Indian Statistical Institute, Kolkata, India,* [2] *The Institute of Science and Technology for Brain-Inspired Intelligence, Fudan University, Shanghai, China,* [3] *Department of Mathematics, Centre for Mathematical Biology and Ecology, Jadavpur University, Kolkata, India,* [4] *Division of Dynamics, Faculty of Mechanical Engineering, Lodz University of Technology, Lodz, Poland,* [5] *Department of Mathematical Sciences, University of Essex, Colchester, United Kingdom*

In this paper, we focus on the emergence of diverse neuronal oscillations arising in a mixed population of neurons with different excitability properties. These properties produce mixed mode oscillations (MMOs) characterized by the combination of large amplitudes and alternate subthreshold or small amplitude oscillations. Considering the biophysically plausible, Izhikevich neuron model, we demonstrate that various MMOs, including MMBOs (mixed mode bursting oscillations) and synchronized tonic spiking appear in a randomly connected network of neurons, where a fraction of them is in a quiescent (silent) state and the rest in self-oscillatory (firing) states. We show that MMOs and other patterns of neural activity depend on the number of oscillatory neighbors of quiescent nodes and on electrical coupling strengths. Our results are verified by constructing a reduced-order network model and supported by systematic bifurcation diagrams as well as for a small-world network. Our results suggest that, for weak couplings, MMOs appear due to the de-synchronization of a large number of quiescent neurons in the networks. The quiescent neurons together with the firing neurons produce high frequency oscillations and bursting activity. The overarching goal is to uncover a favorable network architecture and suitable parameter spaces where Izhikevich model neurons generate diverse responses ranging from MMOs to tonic spiking.

Keywords: Izhikevich neuron model, random networks, bicurcation scenaria, mixed mode oscillations (MMOs), mixed mode bursting oscillations (MMBOs), excitable neurons, electrical coupling

OPEN ACCESS

Edited by:
Spase Petkoski,
INSERM U1106 Institut de Neurosciences des Systèmes, France

Reviewed by:
Guosheng Yi,
Duke University, United States
Ergin Yilmaz,
Bulent Ecevit University, Turkey

***Correspondence:**
Chittaranjan Hens
chittaranjanhens@gmail.com
Peng Ji
pengji@fudan.edu.cn

Received: *31 January 2020*
Accepted: *04 May 2020*
Published: *08 June 2020*

Citation:
Ghosh S, Mondal A, Ji P, Mishra A, Dana SK, Antonopoulos CG and Hens C (2020) Emergence of Mixed Mode Oscillations in Random Networks of Diverse Excitable Neurons: The Role of Neighbors and Electrical Coupling. Front. Comput. Neurosci. 14:49. doi: 10.3389/fncom.2020.00049

1. INTRODUCTION

Diverse spiking oscillations and bursting phenomena of electrical activity in single neurons or neuronal networks play an important role in information processing and transmission across different brain areas (Connors and Gutnick, 1990; Izhikevich, 2003, 2004, 2007; Coombes and Bressloff, 2005; Antonopoulos et al., 2015, 2019; Ma and Tang, 2017; Mondal and Upadhyay, 2018; Teka et al., 2018). The underlying mechanism of signal processing in neurons depends on the variations of membrane voltages called spikes (Izhikevich, 2003, 2004, 2007). The complexity of

spikes or trains of spikes can be controlled by external stimuli, e.g., by injected electrical currents. In a common scenario, a bunch of spikes (called a burst) may emerge in the activity of single neurons or in neural populations (Izhikevich, 2000; Coombes and Bressloff, 2005; Constantinou et al., 2016; Zeldenrust et al., 2018). Such oscillatory patterns of membrane voltages can be modeled mathematically by biophysical dynamics (with realistic parameters) such as the (un)coupled Izikevich neuron model (Khoshkhou and Montakhab, 2018), described in the next section. Our goal is to study the firing and collective activities of coupled neurons in an environment of heterogeneous excitabilities. Neural networks support functional mechanisms within brain areas. For example, such diverse groups of neurons in the cortex are responsible for many complex neuronal mechanisms (Izhikevich, 2000, 2004, 2007).

Most of the neurons are excitable, i.e., they show quiescent behavior however, they can also fire spikes when they are stimulated by input stimuli. In neural computations, the neurons continue to fire a train of spikes when there is an input by injecting a pulse of direct current (DC) and this is called tonic spiking. There exist different types of spiking patterns depending on the nature of the intrinsic dynamics. Bursting follows a dynamic state in a neuron where it repeatedly fires discrete groups or bursts of spikes, i.e., when the activity alternates between a quiescent state and repetitive spiking (a bunch of spikes appear together). This might be regular or chaotic, depending on the dynamics of the system and excitabilities or couplings (Izhikevich, 2000, 2004, 2007). Apart from spiking and bursting activities, one of the interesting complex firing patterns emerge from the activity of neurons is the mixed-mode oscillations (MMOs) (Brøns et al., 2008; Desroches et al., 2012; Bacak et al., 2016), what is the main focus here. In MMOs, the oscillations are distributed with different amplitudes where the firings alternate between large and small amplitude oscillations (Brøns et al., 2008) (i.e., the so called *LAO*s and *SAO*s, respectively) reflecting different rhythmic activities such as locomotion or breathing (Bacak et al., 2016). The multiple time scales (e.g., fast potassium channels with slow kinetics; Ghaffari et al., 2015) of voltage variables or controlled noise can induce MMOs in neuronal systems (Muratov and Vanden-Eijnden, 2008; Upadhyay et al., 2017). MMOs were first observed in chemical reaction systems (Ostwald, 1900). They were also observed in Belouzov-Zhabotinsky reactions (Schmitz et al., 1977; Showalter et al., 1978; Brøns and Bar-Eli, 1991), calcium dynamics and electrocardiac systems (Kummer et al., 2000; Rotstein and Kuske, 2006). We note that, from a dynamical perspective, the generation of MMOs can be analyzed through the canard phenomenon (Eckhaus, 1983; Drover et al., 2004; Rubin and Wechselberger, 2008) and also via homoclinic bifurcations (Chakraborty and Dana, 2010). Krupa et al. (2008) analyzed the mechanism of MMOs in a two-compartmental model of dopaminergic neurons in the mammalian brain stem. To investigate the generation of MMOs in a self-coupled, FitzHugh-Nagumo model, Desroches et al. (2008) developed a computational method and Guckenheimer (2008) examined how chaotic dynamics and MMOs arise near folded nodes and folded saddle-nodes on slow manifolds. Vo et al. (2010) demonstrated that MMOs can generate a type of bursting that can be reflected in a biophysical model of pituitary lactotroph (Toporikova et al., 2008). MMOs were also observed in stellate cells of the medial entorhinal cortex (layer II) and Rotstein et al. (2008) analyzed the mechanism of such patterns in a biophysical, conductance-based, model. Apart from MMOs, mixed-mode bursting oscillations (MMBOs) (Desroches et al., 2013) were also observed when a bunch of spikes in a single burst appears with *SAO*s. In MMBOs, burst activity appears instead of single spikes within LAOs. Our study on network dynamics sheds more light on such interesting patterns.

In this paper, we explore the emergence of spiking and MMOs in a random network of diffusively coupled (through the membrane voltage variable) Izhikevich neurons in a backdrop of diverse excitabilities. The role of network structure and arrangement of mixed neural populations in the network are the main objectives for the study of the emergence of MMOs. In network neuroscience, researchers investigate the firing activities and collective patterns of neural activity where neurons are connected in a complex-network topology (Brøns et al., 2008; Desroches et al., 2008; Erchova and McGonigle, 2008; Postnov et al., 2008; Krupa et al., 2014; Malagarriga et al., 2015; Antonopoulos, 2016; Borges et al., 2017, 2020; Khoshkhou and Montakhab, 2018). For instance, a correlated synchronous firing appears in neuronal cells with the adaptive exponential integrate-and-fire model with excitatory-inhibitory synapses that can be associated with epileptic seizures (Protachevicz et al., 2019). Bittner et al. (2017) showed that balanced excitatory and inhibitory input currents in clustered (non-clustered) networks of neurons may reflect spiking activities in which inhibitory neurons share more coherent activities. Recently, MMOs have also been observed in pre-Bötzinger complex networks (Bacak et al., 2016) (a medullary region that controls breathing in mammals) in the presence of heterogeneous excitable parameters. In both studies, a three-coupled reduced model was proposed to understand the behavior of collective spiking patterns and the conditions for the emergence of *LAO*s and *SAO*s were studied.

However, the role of network architecture and different excitabilities in the emergence of MMOs are not well-understood. In this paper, we have affirmative answer to the question related to the emergence of MMOs. We reveal how such MMOs can be distinguished from other firing patterns, supported by their relevant biophysical significance (Golomb, 2014). Moreover, the neurons in the paper are placed on the nodes of a random network and transfer signals through its links. In the absence of coupling, the activity of the considered neuronal population reveals two types of dynamical states (or excitabilities), ranging from spike-bursting to subthreshold to quiescent states. The key question that arises here is the following: considering a mixed/heterogeneous neural population (neighboring neurons of self-sustained spiking neurons might have subthreshold oscillations), can we design a random network of neurons (with Poissonian neighbor node-degree-distribution) that will give rise to collective firings where subthreshold or quiescent neurons are compelled to show high amplitude activities? We want to uncover the coupling parameter space and the ratio of mixed populations

where MMOs and fast tonic spiking behavior emerge. In this context, by mixed/heterogeneous neural population we mean that neurons with different excitability properties i.e., the non-identical neurons with different firing patterns are connected in a complex network. At weak couplings and a diluted random network setting, we show that desynchronized subthreshold neurons exhibit MMOs. With the increase of the coupling, all subthreshold neurons fire in a mixed-mode state. In both cases, MMOs are not prominent in oscillatory neurons and eventually disappear as the coupling strength increases. Consequently, neural subpopulations emerge as synchronous clusters exhibiting tonic spiking behavior. For diluted random and homogeneous networks, where the electrical coupling strength is constant, we show that neighbors exhibiting self-sustained oscillations, determine the structural patterns of MMOs. Based on the synchronized cluster over a certain coupling range, we can reduce the random network to a low dimensional, reduced-order network, i.e., to two coupled oscillators which reflect and predict the diverse dynamical patterns that appear in the random network. Additional to the random network, we have validated our results in small-world network of 500 nodes. In particular, our results for both types of networks confirm that the emerging features observed in the random network can also be found in the small-world network.

The paper is organized as follows: in section 2, we describe the Izhikevich neuron model and discuss its dynamical properties. The model displays various electrical activities (i.e., different spiking and bursting patterns) for fixed parameter values and for a range of injected currents, I. Then, we investigate the dynamical behavior on a random network (see section 2.2) based on single Izhikevich neurons with various firing responses. In particular, we identify the parameter region and coupling strategy where MMOs and MMBOs exist, and analyze the transition phases of firing responses (sections 2.2.1 and 2.2.2). In section 3, the reduced-order network model is constructed to verify the results obtained for the random network. A bifurcation analysis is also performed to show the mixed mode states and other phases of oscillations. In section 4, the MMOs are further tested in a small-world network. Finally, we conclude our work in section 5, followed by a discussion.

2. BIOPHYSICAL MODEL AND RANDOM NETWORK

2.1. Model Description

Our work focuses on the analysis of the complex dynamical behavior in the 2-dimensional nonlinear Izhikevich model that captures neuronal membrane voltages (Izhikevich, 2003, 2004). It produces spiking and bursting patterns distributed over a range of parameter values. It is a biophysically plausible and computationally efficient mathematical model that takes into account continuous spike generation and a discontinuous resetting process following the spikes. It has two state variables; the membrane voltage, v and recovery variable, u, which measure the activation of K^+ and inactivation of Na^+ ionic currents, respectively. The dynamical activity of an Izhikevich neuron is captured by the set of equations

$$\dot{v} = 0.04v^2 + 5v + 140 - u + I, \tag{1}$$

$$\dot{u} = a(bv - u), \tag{2}$$

with an after-spike resetting constraint, i.e., when the membrane voltage v reaches a peak value v_{pk}, the following relation is applied: if $v \geq v_{pk}(= 30)$, then $v \leftarrow c$ and $u \leftarrow u + d$. The parameters a, b, c, and d are dimensionless. The resting potential ranges in the interval -70 to -60mV and depends on b that indicates the sensitivity of u to the subthreshold fluctuations of the membrane potential, v. The parameter a measures the timescale of the recovery variable u. The parameters c and d control the after-spike reset value of v and u, respectively, caused by fast high-threshold K^+ channel conductances and slow Na^+ and K^+ conductances. The function $(0.04v^2 + 5v + 140)$ was derived using the spike initiation dynamics of a cortical neuron. The different suitable choices of parameters generate various types of oscillations, often found in neocortical and thalamic neurons (Connors and Gutnick, 1990; Gray and McCormick, 1996; Izhikevich, 2000). The initial conditions are set to $v = -63$ and $u = bv$. Synaptic currents or injected DC-currents are delivered via I. We consider a fixed parameter regime that produces different firings for a single Izhikevich neuron (Izhikevich, 2003, 2004), i.e., $a = 0.1$, $b = 0.2$ with reset parameters $c = -65$ and $d = 8$, what we call set I. We note that for $I < 4$, the system of Eqs. (1) and (2) does not show any spiking or bursting behavior. Thus, the firing patterns can be obtained for $I \geq 4$. Simulations of the systems of ordinary differential equations were performed using the fourth-order Runge-Kutta method with a fixed time step of 0.01, as the simulation results with a smaller time step did not show any significant differences. Bifurcation diagrams of the deterministic dynamical model in the reduced-order network were computed using the MatCont software package (Dhooge et al., 2003).

2.2. Formulation of the Network of Model Neurons

We construct an Erdős-Rényi (ER) random network of $N = 500$ nodes with average node-degree 5. Then, we set up a mixed population of Izhikevich neurons to model neural activity on the nodes of the random network, where 70% of them exhibit oscillatory behavior (self-sustained spiking oscillations, for $I = 10$) as shown in **Figure 1B** (in blue) and 30% are in quiescent states (for $I = 3$), shown in **Figure 1B** (in red) by setting all the parameters in the tonic spiking condition (see set I). The system is coupled via the membrane voltage v with a mean-field diffusive coupling. In particular, the equations of the N coupled neurons $(i = 1, 2, \ldots, N)$ in the network are described by

$$\dot{v}_i = 0.04v_i^2 + 5v_i + 140 - u_i + I_i + \frac{K}{\sum_{j=1}^{N} A_{ij}} \sum_{j=1}^{N} A_{ij}(v_j - v_i),$$

$$\dot{u}_i = a(bv_i - u_i),$$

with the constraint that if $v_i \geq 30$, then, $v_i \leftarrow c$ and $u_i \leftarrow u_i + d$. A is the adjacency matrix of the random network, K

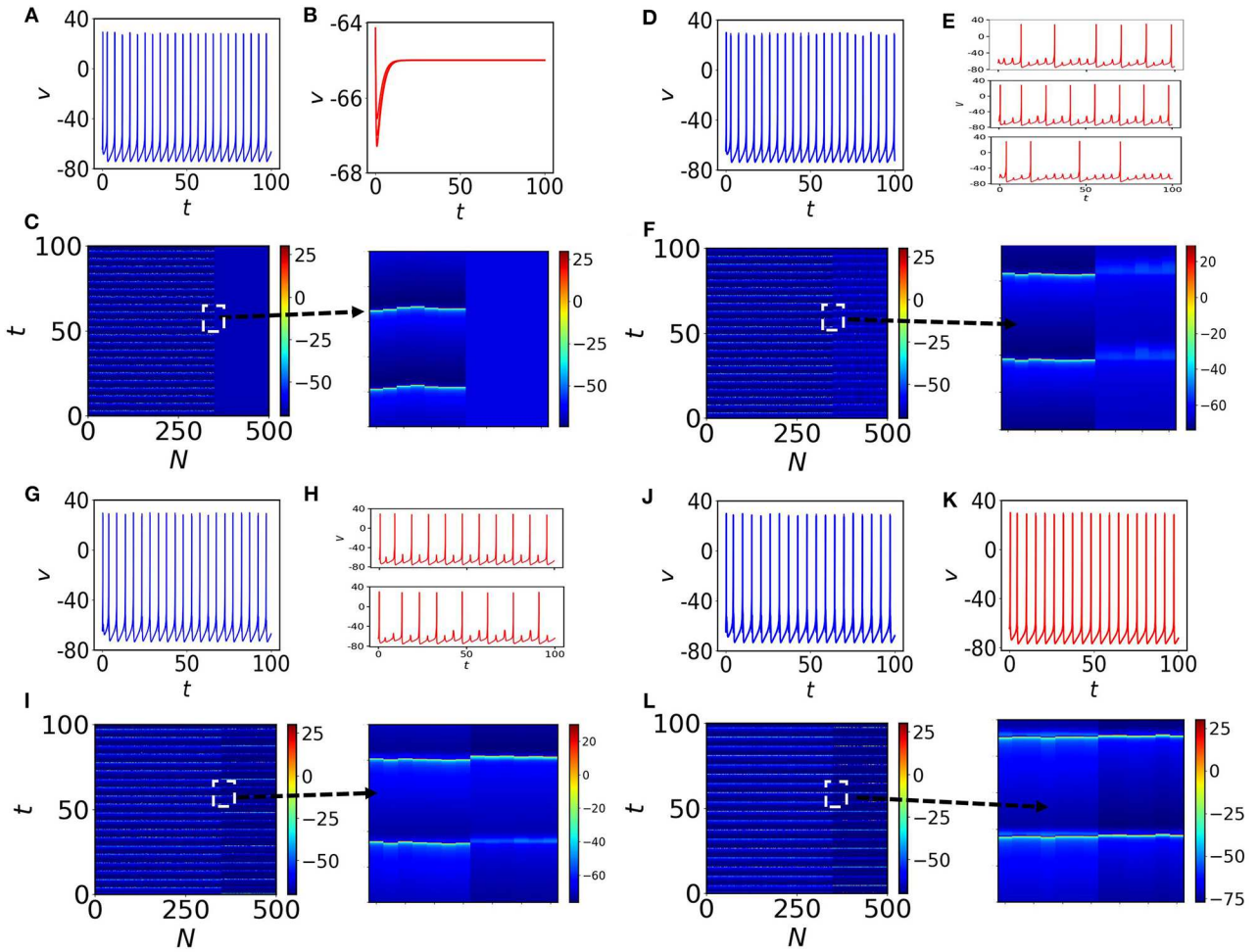


FIGURE 1 | Membrane potential v and spatiotemporal plots. **(A)** One self-oscillatory spiking neuron in the absence of coupling ($K = 0$) and a time-series of a quiescent node is shown in **(B)**. **(C)** The spatiotemporal plot for all neurons in the random network. The first 350 nodes are self-oscillatory. Nodes from 351 to 500 are in steady states (see the 4 zoom-ins). **(D,E)** The coupling is increased to $K = 0.3$. There are several types of MMOs observed in the quiescent subpopulation. Three nodes from the quiescent subpopulation are marked and the time series of each node over the course of time is shown in **(E)**. **(F)** Spatiotemporal plot of all neurons in the random network. The quiescent nodes are desynchronized with each other. **(G,H)** The coupling is increased to $K = 0.4$. *ISI* of spiking nodes are increased and decreased for quiescent nodes. Desynchronized MMOs (shown in **(H)**, where two quiescent nodes have been randomly chosen) are still visible in the quiescent population. **(I)** Spatiotemporal plot that shows the variation in spikes for all nodes in the random network. **(J–L)** are for $K = 1$. The entire population fires (without any MMOs appearing) with almost the same frequencies. Clearly two subpopulation are separately synchronized.

the coupling strength and $S_i = \sum_{j=1}^{N} A_{ij}$ the degree of the ith node. We consider $I_1 = \ldots = I_p = 3$, where $\frac{p}{N} = 0.3$ and $I_{p+1} = \ldots = I_N = 10$, where $q = 1 - \frac{p}{N} = 0.7$ that lead to the time evolution shown in **Figures 1A,B**. In the absence of coupling, the oscillatory nodes (70%) show desynchronized spiking and the rest of them (30%) converge to fixed points (see spatiotemporal plot in **Figure 1C**, where the inset is a zoom-in). With the increase of the coupling strength K, the quiescent neural subpopulation exhibits different transitions to oscillatory behavior. Generally, for weak coupling, this subpopulation generates MMOs and subthreshold oscillations. One type of MMOs shows that between two consecutive *LAO*s, there exist two *SAO*s. Interestingly, other aperiodic MMOs may coexist in this subpopulation. Interspike intervals (*ISI*) are not identical and the number of small amplitude spikes in *SAO*s within two large amplitude spikes may vary in the entire signal. We have found three types of MMOs shown in **Figure 1E**, randomly picked from the quiescent subpopulation in which the average interspike intervals, $\langle ISI \rangle$, differ significantly. We will analyze such mixed MMOs behavior and variation of *SAO*s between *LAO*s in the next subsections. This study unveils the generation and annihilation of MMOs within a subpopulation of neurons. We note that, the oscillatory subpopulation shows almost coherent tonic spiking (**Figure 1D**). The spatiotemporal plot of all nodes is shown in **Figure 1F**, where quiescent nodes are desynchronized (a zoom-in is shown on the right). With further increase of the coupling ($K = 0.4$), the quiescent subpopulation exhibits MMOs, however the number of *LAO*s between two spikes is considerably decreased.

The distance between two consecutive spikes is also decreased compared to the previous coupling case, therefore, $\langle ISI \rangle$ is also decreased (see **Figure 1H**, where two randomly chosen nodes have been depicted in the panels of the figures. Interestingly, the oscillatory subpopulation remains in the same firing regime and the network shows asynchronous behavior (**Figures 1G,I**) for all nodes. Finally, for $K = 1$, the complete population switches to tonic spiking (**Figures 1J–L**) with almost identical $\langle ISI \rangle$, and the two subpopulations form two clusters when they are separately synchronized.

2.2.1. MMOs in the Quiescent Subpopulation: Impact of Spiking Neighbors of Quiescent Nodes

Here, we elaborate on the quiescent population and on several coexisting MMOs that emerge. **Figure 2A** shows the network structure with a mixed population (spiking neurons are shown with blue filled circles and quiescent nodes with red filled circles). We first observe the emergence of MMOs in the quiescent nodes at weak coupling. At $K = 0.3$, we have isolated three red nodes with different neighbor distributions. The red node (left) with 7 neighbors shows MMOs in which three large amplitude spikes exist within 100 time units (see **Figure 2B**). *ISI* are not constant and the number of small amplitude spikes between two large amplitude consecutive spikes is also varied in *SAO*s. The neighbors of this node have two silent (blue) and five oscillatory nodes (red). The number of spikes is slightly increased for another neuron originally in a quiescent state (**Figure 2C**) and the number of small amplitude spikes in *LAO*s is varied from 4 to 5. This neuron has 11 neighbors in which 7 nodes are self-oscillatory (blue) in the absence of coupling.

Next, we define the parameter r_i to search for the presence of oscillatory nodes in the neighborhood of quiescent node (i) by

$$r_i = \frac{N_{oi}}{\sum_{j=1}^{N} A_{ij}} = \frac{N_{oi}}{S_i}, \tag{3}$$

where N_{oi} is the number of spiking oscillators connected with the ith quiescent node and S_i the degree of the ith node. The neighbors of a third selected node are all oscillatory ($r = 1$) and the node reveals lower *ISI* as there is comparably fast switching from *SAO*s to *LAO*s (see **Figure 2D**). Therefore, the ratio of adjacent spiking nodes (blue) with respect to neighbors, S_i, determines the effect of the average *ISI*, $\langle ISI \rangle$, on the ith quiescent node (red). To understand the effect of the average r on $\langle ISI \rangle$, we have considered three couplings: $K = 0.3$, 0.4, and 0.6, shown in **Figure 2E** with upper red line (filled circle), middle red line (filled diamond) and lower red line (star), respectively. For the weaker couplings $K = 0.3$ and $K = 0.4$, and for small r, $\langle ISI \rangle$ exhibits significantly higher values (25 time units with high fluctuations). For higher values of $r \approx 1$, $\langle ISI \rangle$ is decreased by 10 time units. The results confirm that, a red node with smaller r (where the presence of red (quiescent) neighbors is significantly larger, have strong impact on the red node) reduces the number of spikes compared to the case where $r \approx 1$. For even higher couplings ($K = 0.6$, red line with star marker), $\langle ISI \rangle$ decreases to around 5 and the impact of r on $\langle ISI \rangle$ is not prominent at even higher couplings (not shown herein). We note that, as we have seen in **Figures 2B–D**, smaller changes in r ($r = \frac{2}{7} \approx 0.28$, $r = \frac{7}{11} \approx 0.63$ and $r = 1$ for (b), (c) and (d), respectively) result in small amplitude spikes in *SAO*s between two large amplitude spikes (*LAO*s). $\langle ISI \rangle$ and

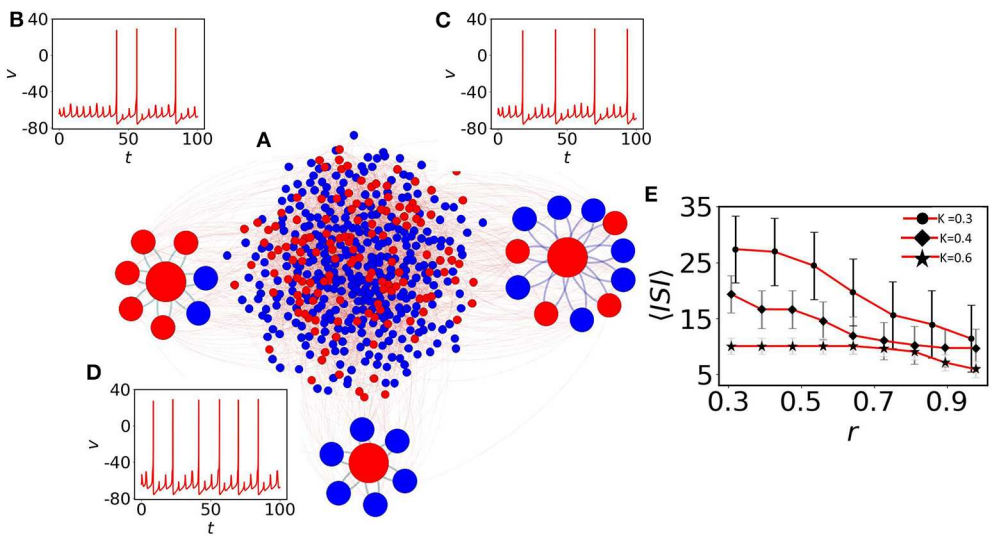


FIGURE 2 | The impact of neighbors of MMOs on quiescent nodes. **(A)** The random network of 500 nodes (Bastian et al., 2009). Red nodes are in quiescent and blue in self-oscillatory states. **(B)** One red node is identified with degree 7. Five of them are spiking oscillators ($r \approx 0.28$). Irregular MMOs are observed here. **(C)** The second red node with $r \approx 0.63$. MMOs with considerably lower *ISI* are shown. **(D)** All neighbors are self-oscillatory ($r = 1$), MMOs with highly frequent spikes are observed. For **(B–D)**, the coupling strength is fixed at $K = 0.3$. **(E)** Impact of r on $\langle ISI \rangle$. The $\langle ISI \rangle$ is continuously decreased if we check for higher values of r and the average value saturates below 15 (red curve with black filled circles, red curve with black filled diamonds) for $K = 0.3$ and 0.4, respectively. For even higher coupling ($K = 0.6$, red curve with black filled stars), r contributes less to $\langle ISI \rangle$ with the value fluctuating between 5 and 10.

spikes in *SAO*s of quiescent nodes are determined by two key factors: the number of neighboring spiking neurons and the coupling strength. Therefore, we conclude that $\langle ISI \rangle$ decreases if the number of oscillatory nodes in the neighbor increases.

2.2.2. MMOs of Quiescent Nodes: The Role of Electrical Coupling

Next, we choose randomly a quiescent node (red) and check the effect of electrical coupling strength on MMOs connected to that node. At the lower coupling $K = 0.3$, the node exhibits three small amplitude spikes (*SAO*s) between two large amplitude spikes (**Figure 3B**). To quantify the spike distribution, we define

$$f_{SAO} = \frac{S_{SAO}}{S_{all}},$$
$$f_{LAO} = \frac{S_{LAO}}{S_{all}},$$

where S_{SAO}, S_{LAO} are the numbers of small and large amplitude spikes, respectively, and S_{all} the count of all spike amplitudes in the same interval. In **Figure 3B**, three small amplitude spikes appear consecutively and are shown by star, triangle, and hexagon markers, respectively. They are distributed with almost similar amplitudes (see left part of **Figure 3A** shown in light blue). As the membrane voltage is periodic, f_{LAO} shares almost equal probability with f_{SAO}. We note that, we have used f in **Figure 3B** instead of f_{SAO} or f_{LAO} to accumulate the information of the entire spiking frequency set. If we increase the coupling to $K = 0.4$, we see that three small amplitude spikes converge to a single one (**Figure 3C**, diamond marker), the oscillatory neighbors influence the oscillation of the quiescent node and they are equiprobable (the light and deep blue bars in **Figure 3A** are almost of the same amplitudes). At $K = 0.6$, the small amplitude spikes appear recurrently (circle marker in **Figure 3D**) after two large amplitude spikes and give rise to MMBOs. Interestingly, simple MMOs change into more complex dynamics, i.e., MMBOs. Therefore, f_{LAO} (deep blue bar) is higher than f_{SAO} for small amplitude spikes (light blue bar). When the coupling is set to 1, the MMOs are completely lost (no light blue bar appears in the right-hand side of **Figure 3A**, see also the spiking behavior in **Figure 3E**). The quiescent neighbors at weak coupling contribute strongly to the generation of mixed-mode oscillations. When we increase the coupling, more information is shared among nearest neighbor nodes and long distant neighbors. The dynamics in the network, including that of quiescent nodes, is characterized by large amplitude spikes. We note that, the nodes in the random network are dominated by self-oscillatory neurons (70%) and for higher coupling, they control the spiking behavior in the entire network, therefore quiescent nodes cannot reflect MMOs for higher couplings.

2.2.3. Average *ISI* vs. Coupling Strength *K* in Neural Subpopulations

Here, we scan the average *ISI*, $\langle ISI \rangle$, interval of the entire subpopulation varying the coupling strength K. The $\langle ISI \rangle$ of oscillatory (blue) nodes in the network is slightly increased (see **Figure 4A** with filled blue circles) for weaker couplings and saturates around 5.6 time units when it is increased (for $K > 1.2$). On the other hand, the $\langle ISI \rangle$ of red quiescent nodes is decreased when the coupling is increased. For small couplings, $\langle ISI \rangle$ shows strong fluctuations (shown by black lines with error bars in the backdrop of red filled circles, **Figure 4B**) due to

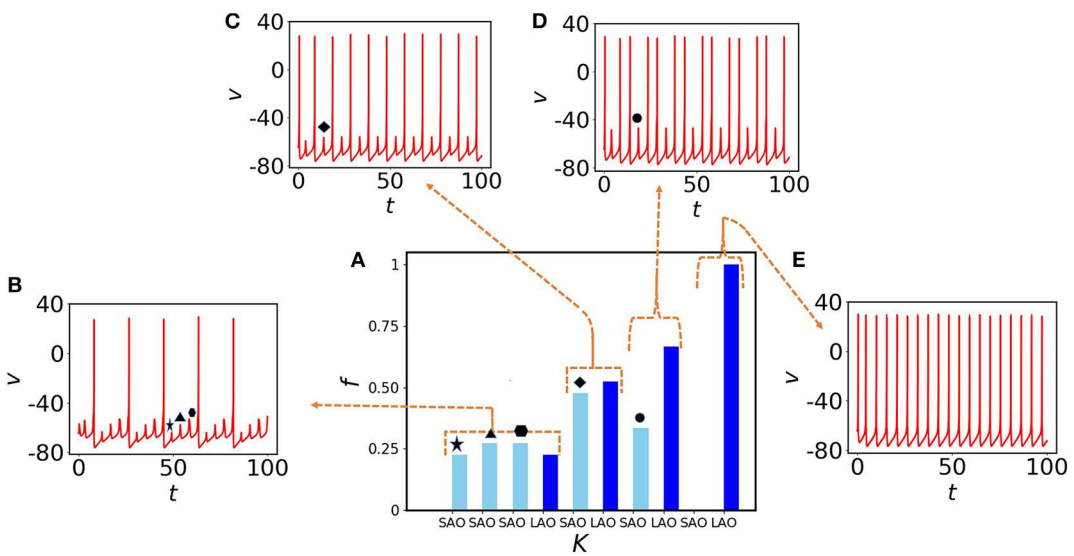


FIGURE 3 | Impact of coupling K on MMOs of a quiescent (red) node. **(A)** Probability distribution of spikes in *SAO*s (light blue) and *LAO*s (deep blue) for $K = 0.3$, 0.4, 0.6, and 1 from left to right, respectively. **(B)** The time evolution for $K = 0.3$. Three small amplitude oscillations (star, triangle, and hexagon) appear between two consecutive large amplitude spikes. **(C)** One small amplitude spike (diamond) appears between two large amplitude spikes at $K = 0.4$. **(D)** One small amplitude spike (black circle) appears after two spikes emerging together for $K = 0.6$. Therefore, the probability of small amplitude spikes is decreased [third part of **(A)**] and results to the emergence of MMBOs. **(E)** Small spikes vanish at higher coupling ($K = 1$), therefore MMOs are lost and tonic spikes are generated, instead.

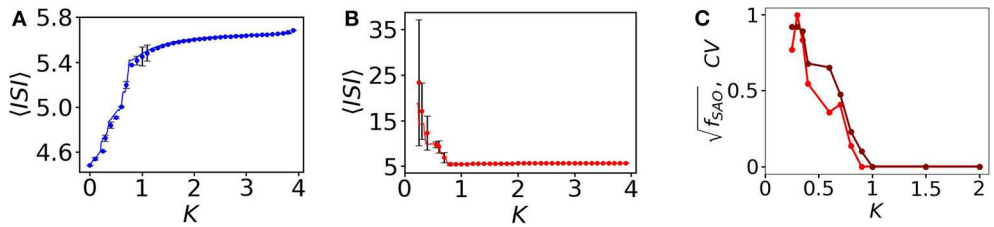


FIGURE 4 | $\langle ISI \rangle$, $\sqrt{f_{SAO}}$ and CV as a function of coupling K. **(A)** $\langle ISI \rangle$ for all spiking oscillators (in total 350). At small coupling, $\langle ISI \rangle$ is smaller, i.e., the spike frequencies are comparatively higher and it saturates around 5.6 for higher couplings. The fluctuations are negligible here, i.e., all spiking nodes have common frequencies for all couplings considered. **(B)** Quiescent nodes. For small couplings, the nodes exhibit diverse desynchronized MMOs (shown in black, with error bars). $\langle ISI \rangle$ saturates at higher couplings. **(C)** Relation between CV (red line with marker) and $\sqrt{f_{SAO}}$ (brown line with marker) as a function of the coupling strength K.

the desynchronized $\langle ISI \rangle$ in MMOs of the quiescent nodes. The red and blue lines in **Figures 4A,B** are plotted from the two coupled reduced models derived from the collective behavior of the connected network described in the next section. For small couplings, we see that the $\langle ISI \rangle$ of each quiescent node are dissimilar (see **Figure 2**), i.e., the firing rate varies from one node to another. We scan the entire average ISI interval of the quiescent subpopulation for a range of coupling strengths to understand the fluctuations in ISI. To quantify these fluctuations, we calculate the coefficient of variation, CV, of ISI of the quiescent subpopulation calculated from the numerical data (**Figure 4C**, red line with dots). CV becomes zero after a certain coupling strength, as there is no variation in spike sequences and SAOs completely vanish. The brown line in **Figure 4C** reflects the frequency of peaks in the SAOs, which is zero for higher couplings, where CV is also zero, thus revealing a close relation between CV^2 and f_{SAO}. In the **Supplementary Material**, we present an analytical approach that relates the two quantities and offer a plausible explanation for the discrepancy observed for small coupling strengths.

3. REDUCED MODEL DESCRIPTION

It is clear from **Figure 1** that neurons within subpopulations are synchronized for higher couplings, and cluster synchronization appears within subpopulations. This motivates us to pursue further an approach to construct a reduced model of two coupled systems which is able to encode the information in the large network. Since we have considered a random network in which the node-degrees follow the Poisson distribution, we can approximate the degree of each node/neuron by the average degree of the considered network (Hens et al., 2015; Sasai et al., 2015). Therefore, we can assume that $S_j = \langle S \rangle$ for $j = 1, \ldots, N$. The number of spiking oscillators in the neighborhood of each oscillator is expected to be $(1 - \frac{p}{N})S = \frac{q}{N}S$ and that of quiescent oscillators, $\frac{p}{N}S$, where p is the number of quiescent oscillators in the network. We set $v_j = V_Q$ for $j = 1, \ldots, p$ and $v_l = V_S$ for $l = p + 1, \ldots, N$. Over a certain coupling strength, within different clusters, the quiescent and spiking oscillators are synchronized separately. Therefore, by representing the two clustered subpopulations by two nodes, we obtain the following reduced system of coupled equations

$$\dot{V}_S = 0.04V_S^2 + 5V_S + 140 - U_S + I_S + Kp(V_Q - V_S), \quad (4)$$

$$\dot{U}_S = a(bV_S - U_S), \quad (5)$$

$$\dot{V}_Q = 0.04V_Q^2 + 5V_Q + 140 - U_Q + I_Q + Kq(V_S - V_Q), \quad (6)$$

$$\dot{U}_Q = a(bV_Q - U_Q), \quad (7)$$

with the constraint equation that if $V_Q \geq 30$, then $V_Q \leftarrow c$ and $U_Q \leftarrow U_Q + d$. These conditions are also valid for spiking nodes, i.e., for Eqs. (4) and (5) for spike oscillators with $I_S = 10$ and for Eqs. (6) and (7) for quiescent oscillators with $I_Q = 3$. We note that, for homogeneous networks, there will be no effect of the assortativity (degree-degree correlation) on MMOs or on collective firing states as the number of quiescent oscillators in the neighborhood of each oscillator will not be affected. The $\langle ISI \rangle$ plotted for V_S and V_Q as a function of K is shown in **Figures 4A,B** with red and blue dots, respectively. The results almost match with the result for the random network (filled blue and red circles). A phase diagram of the coupled reduced model with respect to $\frac{p}{N}$ and K is shown in **Figure 5A**. The diagram is drawn by monitoring V_Q. The MMOs and spike regions are identified with the help of f and quiescent (death) states by noting the variation of the peak values of V_Q. The dark-red regime is the steady state island, where all neurons in the random network remain in quiescent states. The regime of MMOs appears for weak couplings (for all p) shown in orange. The uncoupled quiescent nodes are desynchronized in this regime. All nodes collectively (and individually) fire at higher couplings for $p < 0.9$ (pink region). The boundaries of each region are consistent with the results from the random network. To confirm further the onset of steady states, we have performed a bifurcation analysis to check the boundaries while we have changed $\frac{p}{N}$ from 0.8 to 1 for coupling strengths $K = 2$ and $K = 3$, respectively (see **Figures 5B,C**). The stable fixed point, V_Q, is shown with thick green line in both cases. This fixed point (node) collides with a saddle point and vanishes at $\frac{p}{N} \approx 0.87$. The system shows spiking oscillations below $\frac{p}{N} \approx 0.87$ in both cases. Finally, for $\frac{p}{N} = 0.95$, the system changes its dynamics from MMOs to a steady state at $K \approx 0.77$, as evidenced in **Figure 5D**.

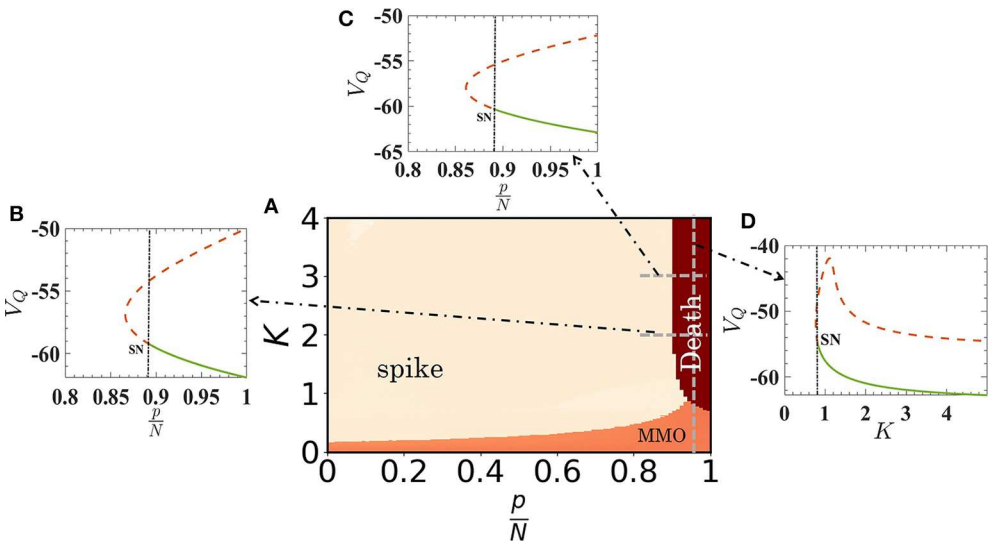


FIGURE 5 | Phase-space diagram of the reduced quiescent node model as a function of K and relative size of quiescent oscillators in the random network. The emergence of MMOs, synchronized spiking oscillations and quiescent states are depicted in orange, pink, and dark red, respectively. The boundaries of quiescent states with other regimes are demarcated by the bifurcation scenario. **(B,C)** Stable fixed points vanish through a saddle-node (SN) bifurcation at $\frac{p}{N} \approx 0.87$ for $K = 2$ and 3, closely matched with the phase diagram. Note that for higher couplings, the boundary of quiescent states does not depend on $\frac{p}{N}$. **(D)** Bifurcation analysis as a function of K, for $\frac{p}{N} = 0.95$ [dashed vertical line in **(A)**]. The onset of quiescent states occurs at $K \approx 0.77$.

4. EMERGENCE OF MMOS IN A SMALL-WORLD NETWORK

Following up the previous studies on a random network of neural computation, we construct here a small-world network of $N = 500$ nodes. A closed non-local ring is constructed with 8 adjacent neighbors. A rewire strategy (Watts and Strogatz, 1998) is implemented with a probability 0.2 to construct the final network (see **Figure 6A**). To understand the impact of oscillatory neighbors (i.e., blue nodes) (see Equation 3) on quiescent nodes (red), we have identified four quiescent nodes (red) with different r. The network comprises 40% quiescent nodes. Nodes with higher percentage of oscillatory neighbors show spiking and irregular MMOs that appear between two successive spikes (**Figures 6B,E**, where $r = 0.75$ and 1, respectively). However, the red nodes with a smaller percentage of oscillatory neighbors are unable to fire ($r \approx 0.4$, **Figure 6C**) or irregular spikes appear with higher $\langle ISI \rangle$ value ($r = 0.5$, **Figure 6D**). The coupling strength is fixed at $K = 0.3$. **Figure 6E** shows the impact of r on $\langle ISI \rangle$, which is seen to continuously decrease for nodes with large percentage of oscillatory neighbors ($r \gg 0.1$). The average $\langle ISI \rangle$ saturates below 30 (red curve with black filled circles) for $K = 0.3$. For this coupling strength, diverse MMOs can be seen in **Figures 6B–E**. For the higher coupling strength $K = 0.4$, $\langle ISI \rangle$ converges to 10 (red curve with black filled diamonds). r contributes less to $\langle ISI \rangle$ with the value fluctuating around 10 for $K = 0.6$ (red curve with black filled stars).

5. CONCLUSIONS

In this paper, we sought to study MMOs in a random and a small-world network of diverse excitable Izhikevich neurons for different coupling strengths by introducing the generation of complex oscillations. We have observed MMBOs, which are periodic in nature and are relevant to the GnRH model neuron as the dynamical behavior of these neurons in a small-size network can be useful in the studies for epilepsy (Desroches et al., 2013). We have confirmed that a certain mixed population of quiescent and oscillatory nodes can give rise to several types of MMOs and MMBOs in the two types of networks. MMOs have potential applications in biophysical and other systems. In complex systems, various mechanisms exist during different oscillatory phases that generate spike patterns between fast and slow amplitude motion together with spikes and subthreshold oscillations, termed MMOs. It was observed that pyramidal neurons are capable of exhibiting two types of MMOs and their characterization was analyzed under antiepileptic drug conditions (Babak et al., 2017). Small amplitude oscillations (<10mV) give rise to intrinsic neuronal phenomena that exist during the synaptic transmission block (Alonso and Llinás, 1989; Zemankovics et al., 2010). Actually, it has been observed in many types of neurons, such as in neurons in the thalamus, hippocampal CA1 neurons, neocortex neurons, spinal motor neurons, etc. (Puil et al., 1994; Gutfreund et al., 1995; Narayanan and Johnston, 2007; Iglesias et al., 2011). It was suggested that MMOs can be responsible for the transition from high firing rates to quiescent states by reducing neuronal gain (Iglesias et al., 2011; Golomb, 2014). Many studies showed the impacts of small amplitude oscillations/subthreshold oscillations (STOs) on diverse neuronal responses such as spike clustering (Puil et al., 1994; Gutfreund et al., 1995; Narayanan and Johnston, 2007), synaptic plasticity (Narayanan and Johnston, 2007; Bazzigaluppi et al., 2012), rhythmic activities, synchronization (Acker et al., 2003; Engel et al., 2008), etc.

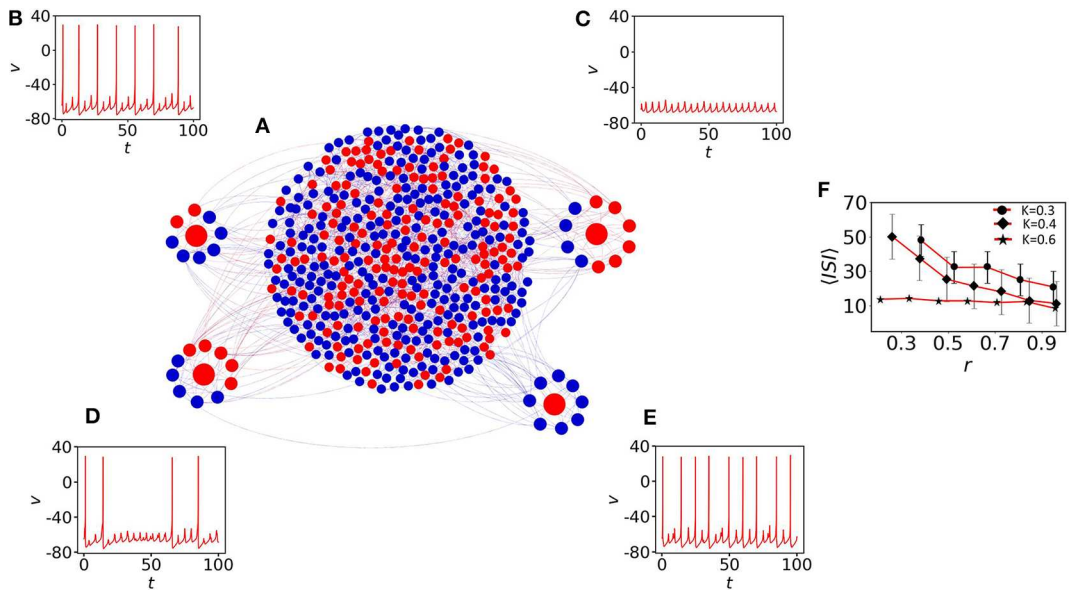


FIGURE 6 | The impact of neighbors of MMOs on quiescent nodes. **(A)** The small-world network of 500 nodes (Watts and Strogatz, 1998) with $p = 0.2$ and $\langle S \rangle = 8$. **(B)** One red node (quiescent) is identified with node-degree 8. Six of them are spiking oscillators ($r = 0.75$). Irregular MMOs are observed here. **(C)** The second red node with $r \approx 0.4$. The node shows sub-threshold oscillations only. **(D)** 50% of the neighbor nodes are spiking oscillators and irregular spikes appear with high $\langle ISI \rangle$. **(E)** All neighbors are self-oscillatory ($r = 1$) and MMOs with highly frequent spikes are observed. For **(B–E)**, the coupling strength is fixed at $K = 0.3$. **(F)** Impact of r on $\langle ISI \rangle$. The $\langle ISI \rangle$ is continuously decreased if we increase r. The average value saturates below 30 (red curve with filled circles) for $K = 0.3$ and converges to 10 (red curve with black filled diamonds) for $K = 0.4$. r contributes less to $\langle ISI \rangle$ with the value fluctuating around 10 for $K = 0.6$ (red curve with black filled stars).

Here, random networks with various injected electrical current stimuli go through different transition phases of oscillations for various coupling strengths and emerging STOs with spikes, i.e., MMOs. First, the depolarization in membrane voltages show small amplitude oscillations around steady state potentials, and with further depolarization, gives rise to spikes, e.g., to MMOs (Jalics et al., 2010). STOs play an important role in the emergence of MMOs and in controlling spike clustering (Torben-Nielsen et al., 2012; Latorre et al., 2016).

Furthermore, MMOs play an important role in neuronal functional mechanisms, namely, the STOs affect the sensitivity of neurons for injected input stimuli, the amplification of synaptic inputs and network synchronization to specific firing frequencies (Babak et al., 2017). The mechanism of MMOs produced in complex dynamical systems remains a challenging task. In the excitable pituitary cell model, pseudo-plateau bursting is canard-induced MMOs (Vo et al., 2010). It correlates electrophysiological behavior of *SAO*s on clustering spikes, and shows the influences of ionic currents to the firing rate and spike patterns in the network.

Finally, experimental and numerical studies show that MMOs occur in oscillatory rhythms in brain functioning from a single neuron to global neural networks (Erchova and McGonigle, 2008). In this study, we investigated both types of oscillations, MMOs and MMBOs. The results may be useful to Neuroscientists and those working on the mathematical modeling and dynamical behavior of cortical neurons based in random neural networks. We plan in a future publication to explore the impact of excitatory and inhibitory connections in Izhikevich neurons and how they give rise to the emergence of MMOs (Noback et al., 2005; Deco et al., 2014; Pastore et al., 2018).

DATA AVAILABILITY STATEMENT

All datasets generated for this study are included in the article/**Supplementary Material**.

AUTHOR CONTRIBUTIONS

CH and AMo designed the research study and developed the results. SG, AMo, and CH designed the figures. SG performed the analytical and numerical simulations. CH, CA, and AMo wrote the manuscript with support from SD and PJ. SD, AMi, PJ, and CA provided support by constructive suggestions and feedback.

FUNDING

CH was supported by the INSPIRE-Faculty grant (code: IFA17-PH193). PJ was funded by Natural Science Foundation of Shanghai, the program for Professor of Special Appointment (Eastern Scholar) and by NSFC 269 (11701096).

SUPPLEMENTARY MATERIAL

The Supplementary Material for this article can be found online at: https://www.frontiersin.org/articles/10.3389/fncom.2020.00049/full#supplementary-material

REFERENCES

Acker, C. D., Kopell, N., and White, J. A. (2003). Synchronization of strongly coupled excitatory neurons: relating network behavior to biophysics. *J. Comput. Neurosci.* 15, 71–90. doi: 10.1023/a:1024474819512

Alonso, A., and Llinás, R. R. (1989). Subthreshold na+-dependent theta-like rhythmicity in stellate cells of entorhinal cortex layer II. *Nature* 342:175. doi: 10.1038/342175a0

Antonopoulos, C. G. (2016). Dynamic range in the c. elegans brain network. *Chaos* 26:013102. doi: 10.1063/1.4939837

Antonopoulos, C. G., Bianco-Martinez, E., and Baptista, M. S. (2019). Evaluating performance of neural codes in model neural communication networks. *Neural Netw.* 109, 90–102. doi: 10.1016/j.neunet.2018.10.008

Antonopoulos, C. G., Srivastava, S., Pinto, S. E. S., and Baptista, M. S. (2015). Do brain networks evolve by maximizing their information flow capacity? *PLoS Comput. Biol.* 11:e1004372. doi: 10.1371/journal.pcbi.1004372

Babak, V., Kouhnavard, M., Elbasiouny, S. M. (2017). Mixed-mode oscillations in pyramidal neurons under antiepileptic drug conditions. *PLoS ONE* 12:e0178244. doi: 10.1371/journal.pone.0178244

Bacak, B. J., Kim, T., Smith, J. C., Rubin, J. E., and Rybak, I. A. (2016). Mixed-mode oscillations and population bursting in the pre- bötzinger complex. *Elife* 5:e13403. doi: 10.7554/eLife.13403

Bastian, M., Heymann, S., and Jacomy, M. (2009). "Gephi: an open source software for exploring and manioulating networks," in *Third International AAAI Conference on Weblogs and Social Media* (San Jose, CA).

Bazzigaluppi, P., De Gruijl, J. R., Van Der Giessen, R. S., Khosrovani, S., De Zeeuw, C. I., and De Jeu, M. T. (2012). Olivary subthreshold oscillations and burst activity revisited. *Front. Neural Circ.* 6:91. doi: 10.3389/fncir.2012.00091

Bittner, S. R., Williamson, R. C., Snyder, A. C., Litwin-Kumar, A., Doiron, B., Chase, S. M., et al. (2017). Population activity structure of excitatory and inhibitory neurons. *PLoS ONE* 12:e0181773. doi: 10.1371/journal.pone.0181773

Borges, F., Protachevicz, P., Pena, R., Lameu, E., Higa, G., Kihara, A., et al. (2020). Self-sustained activity of low firing rate in balanced networks. *Phys. A Stat. Mech. Appl.* 537:122671. doi: 10.1016/j.physa.2019.122671

Borges, R. R., Borges, F. S., Lameu, E. L., Batista, A. M., Iarosz, K. C., Caldas, I. L., et al. (2017). Spike timing-dependent plasticity induces non-trivial topology in the brain. *Neural Netw.* 88, 58–64. doi: 10.1016/j.neunet.2017.01.010

Brøns, M., and Bar-Eli, K. (1991). Canard explosion and excitation in a model of the Belousov-Zhabotinskii reaction. *J. Phys. Chem.* 95, 8706–8713. doi: 10.1021/j100175a053

Brøns, M., Kaper, T. J., and Rotstein, H. G. (2008). Introduction to focus issue: mixed mode oscillations: experiment, computation, and analysis. *Chaos* 18, 1–4. doi: 10.1063/1.2903177

Chakraborty, S., and Dana, S. (2010). Shilnikov chaos and mixed-mode oscillation in Chua circuit. *Chaos* 20:023107. doi: 10.1063/1.3378112

Connors, B. W., and Gutnick, M. J. (1990). Intrinsic firing patterns of diverse neocortical neurons. *Trends Neurosci.* 13, 99–104. doi: 10.1016/0166-2236(90)90185-D

Constantinou, M., Gonzalo Cogno, S., Elijah, D. H., Kropff, E., Gigg, J., Samengo, I., et al. (2016). Bursting neurons in the hippocampal formation encode features of LFP rhythms. *Front. Comput. Neurosci.* 10:133. doi: 10.3389/fncom.2016.00133

Coombes, S., and Bressloff, P. C. (2005). *Bursting: The Genesis of Rhythm in the Nervous System*. Singapore: World Scientific. doi: 10.1142/5944

Deco, G., Ponce-Alvarez, A., Hagmann, P., Romani, G. L., Mantini, D., and Corbetta, M. (2014). How local excitation-inhibition ratio impacts the whole brain dynamics. *J. Neurosci.* 34, 7886–7898. doi: 10.1523/JNEUROSCI.5068-13.2014

Desroches, M., Guckenheimer, J., Krauskopf, B., Kuehn, C., Osinga, H. M., and Wechselberger, M. (2012). Mixed-mode oscillations with multiple time scales. SIAM *Rev.* 54, 211–288. doi: 10.1137/100791233

Desroches, M., Kaper, T. J., and Krupa, M. (2013). Mixed-mode bursting oscillations: dynamics created by a slow passage through spike-adding canard explosion in a square-wave burster. *Chaos* 23:046106. doi: 10.1063/1.4827026

Desroches, M., Krauskopf, B., and Osinga, H. M. (2008). Mixed-mode oscillations and slow manifolds in the self-coupled Fitzhugh-Nagumo system. *Chaos* 18:015107. doi: 10.1063/1.2799471

Dhooge, A., Govaerts, W., and Kuznetsov, Y. A. (2003). Matcont: a matlab package for numerical bifurcation analysis of odes. *ACM TOMS* 29, 141–164. doi: 10.1145/779359.779362

Drover, J., Rubin, J., Su, J., and Ermentrout, B. (2004). Analysis of a canard mechanism by which excitatory synaptic coupling can synchronize neurons at low firing frequencies. *SIAM J. Appl. Math.* 65, 69–92. doi: 10.1137/S0036139903431233

Eckhaus, W. (1983). "Relaxation oscillations including a standard chase on French ducks," in *Asymptotic Analysis II* (Berlin; Heidelberg: Springer), 449–497. doi: 10.1007/BFb0062381

Engel, T. A., Schimansky-Geier, L., Herz, A. V., Schreiber, S., and Erchova, I. (2008). Subthreshold membrane-potential resonances shape spike-train patterns in the entorhinal cortex. *J. Neurophysiol.* 100, 1576–1589. doi: 10.1152/jn.01282.2007

Erchova, I., and McGonigle, D. J. (2008). Rhythms of the brain: an examination of mixed mode oscillation approaches to the analysis of neurophysiological data. *Chaos* 18:015115. doi: 10.1063/1.2900015

Ghaffari, B. V., Kouhnavard, M., and Kitajima, T. (2015). "The effect of input current on canard-induced mixed-mode oscillation in layer II stellate cell," in *2015 10th Asian Control Conference (ASCC)* (IEEE), 1–6. doi: 10.1109/ASCC.2015.7244842

Golomb, D. (2014). Mechanism and function of mixed-mode oscillations in vibrissa motoneurons. *PLoS ONE* 9:e109205. doi: 10.1371/journal.pone.0109205

Gray, C. M., and McCormick, D. A. (1996). Chattering cells: superficial pyramidal neurons contributing to the generation of synchronous oscillations in the visual cortex. *Science* 274, 109–113. doi: 10.1126/science.274.5284.109

Guckenheimer, J. (2008). Return maps of folded nodes and folded saddle-nodes. *Chaos* 18:015108. doi: 10.1063/1.2790372

Gutfreund, Y., Yarom, Y., and Segev, I. (1995). Subthreshold oscillations and resonant frequency in guinea-pig cortical neurons: physiology and modelling. *J. Physiol.* 483, 621–640. doi: 10.1113/jphysiol.1995.sp020611

Hens, C., Pal, P., and Dana, S. K. (2015). Bursting dynamics in a population of oscillatory and excitable Josephson junctions. *Phys. Rev. E* 92:022915. doi: 10.1103/PhysRevE.92.022915

Iglesias, C., Meunier, C., Manuel, M., Timofeeva, Y., Delestrée, N., and Zytnicki, D. (2011). Mixed mode oscillations in mouse spinal motoneurons arise from a low excitability state. *J. Neurosci.* 31, 5829–5840. doi: 10.1523/JNEUROSCI.6363-10.2011

Izhikevich, E. M. (2000). Neural excitability, spiking and bursting. *Int. J. Bifurcat. Chaos* 10, 1171–1266. doi: 10.1142/S0218127400000840

Izhikevich, E. M. (2003). Simple model of spiking neurons. *IEEE Trans. Neural Netw.* 14, 1569–1572. doi: 10.1109/TNN.2003.820440

Izhikevich, E. M. (2004). Which model to use for cortical spiking neurons? *IEEE Trans. Neural Netw.* 15, 1063–1070. doi: 10.1109/TNN.2004.832719

Izhikevich, E. M. (2007). *Dynamical Systems in Neuroscience*. Cambridge: MIT Press. doi: 10.7551/mitpress/2526.001.0001

Jalics, J., Krupa, M., and Rotstein, H. G. (2010). Mixed-mode oscillations in a three time-scale system of ODEs motivated by a neuronal model. *Dyn. Syst.* 25, 445–482. doi: 10.1080/14689360903535760

Khoshkhou, M., and Montakhab, A. (2018). Beta-rhythm oscillations and synchronization transition in network models of Izhikevich neurons: effect of topology and synaptic type. *Front. Comput. Neurosci.* 12:59. doi: 10.3389/fncom.2018.00059

Krupa, M., Ambrosio, B., and Aziz-Alaoui, M. (2014). Weakly coupled two-slow-two-fast systems, folded singularities and mixed mode oscillations. *Nonlinearity* 27:1555. doi: 10.1088/0951-7715/27/7/1555

Krupa, M., Popović, N., Kopell, N., and Rotstein, H. G. (2008). Mixed-mode oscillations in a three time-scale model for the dopaminergic neuron. *Chaos* 18:015106. doi: 10.1063/1.2779859

Kummer, U., Olsen, L. F., Dixon, C. J., Green, A. K., Bornberg-Bauer, E., and Baier, G. (2000). Switching from simple to complex oscillations in calcium signaling. *Biophys. J.* 79, 1188–1195. doi: 10.1016/S0006-3495(00)76373-9

Latorre, R., Torres, J. J., and Varona, P. (2016). Interplay between subthreshold oscillations and depressing synapses in single neurons. *PLoS ONE* 11:e0145830. doi: 10.1371/journal.pone.0145830

Ma, J., and Tang, J. (2017). A review for dynamics in neuron and neuronal network. *Nonlinear Dyn.* 89:1559. doi: 10.1007/s11071-017-3565-3

Malagarriga, D., García-Vellisca, M., Villa, A. E., Buldú, J., García-Ojalvo, J., and Pons, A. (2015). Synchronization-based computation through networks of coupled oscillators. *Front. Comput. Neurosci.* 9:97. doi: 10.3389/fncom.2015.00097

Mondal, A., and Upadhyay, R. K. (2018). Diverse neuronal responses of a fractional-order Izhikevich model: journey from chattering to fast spiking. *Nonlinear Dyn*. 91, 1275–1288. doi: 10.1007/s11071-017-3944-9

Muratov, C. B., and Vanden-Eijnden, E. (2008). Noise-induced mixed-mode oscillations in a relaxation oscillator near the onset of a limit cycle. *Chaos* 18:015111. doi: 10.1063/1.2779852

Narayanan, R., and Johnston, D. (2007). Long-term potentiation in rat hippocampal neurons is accompanied by spatially widespread changes in intrinsic oscillatory dynamics and excitability. *Neuron* 56, 1061–1075. doi: 10.1016/j.neuron.2007.10.033

Noback, C. R., Ruggiero, D. A., Demarest, R. J., and Strominger, N. L. (2005). *The Human Nervous System: Structure and Function*. Totowa, NJ: Humana Press.

Ostwald, W. (1900). Periodische erscheinungen bei der auflösung des chroms in säuren. *Z. Phys. Chem*. 35, 204–256. doi: 10.1515/zpch-1900-0115

Pastore, V. P., Massobrio, P., Godjoski, A., and Martinoia, S. (2018). Identification of excitatory-inhibitory links and network topology in large-scale neuronal assemblies from multi-electrode recordings. *PLoS Comput. Biol*. 14:e1006381. doi: 10.1371/journal.pcbi.1006381

Postnov, D. E., Sosnovtseva, O. V., Scherbakov, P., and Mosekilde, E. (2008). Multimode dynamics in a network with resource mediated coupling. *Chaos* 18:015114. doi: 10.1063/1.2805194

Protachevicz, P. R., Borges, F. S., Lameu, E. L., Ji, P., Iarosz, K. C., Kihara, A. H., et al. (2019). Bistable firing pattern in a neural network model. *Front. Comput. Neurosci*. 13:199. doi: 10.3389/fncom.2019.00019

Puil, E., Meiri, H., and Yarom, Y. (1994). Resonant behavior and frequency preferences of thalamic neurons. *J. Neurophysiol*. 71, 575–582. doi: 10.1152/jn.1994.71.2.575

Rotstein, H. G., and Kuske, R. (2006). Localized and asynchronous patterns via canards in coupled calcium oscillators. *Phys. D Nonlinear Phenomena* 215, 46–61. doi: 10.1016/j.physd.2006.01.007

Rotstein, H. G., Wechselberger, M., and Kopell, N. (2008). Canard induced mixed-mode oscillations in a medial entorhinal cortex layer II stellate cell model. *SIAM J. Appl. Dyn. Syst*. 7, 1582–1611. doi: 10.1137/070699093

Rubin, J., and Wechselberger, M. (2008). The selection of mixed-mode oscillations in a Hodgkin-Huxley model with multiple timescales. *Chaos* 18:015105. doi: 10.1063/1.2789564

Sasai, T., Morino, K., Tanaka, G., Almendral, J. A., and Aihara, K. (2015). Robustness of oscillatory behavior in correlated networks. *PLoS ONE* 10:e0123722. doi: 10.1371/journal.pone.0123722

Schmitz, R., Graziani, K., and Hudson, J. L. (1977). Experimental evidence of chaotic states in the Belousov-Zhabotinskii reaction. *J. Chem. Phys*. 67, 3040–3044. doi: 10.1063/1.435267

Showalter, K., Noyes, R. M., and Bar-Eli, K. (1978). A modified oregonator model exhibiting complicated limit cycle behavior in a flow system. *J. Chem. Phys*. 69, 2514–2524. doi: 10.1063/1.436894

Teka, W. W., Upadhyay, R. K., and Mondal, A. (2018). Spiking and bursting patterns of fractional-order Izhikevich model. *Commun. Nonlinear Sci. Num. Simul*. 56, 161–176. doi: 10.1016/j.cnsns.2017.07.026

Toporikova, N., Tabak, J., Freeman, M. E., and Bertram, R. (2008). A-type k+ current can act as a trigger for bursting in the absence of a slow variable. *Neural Comput*. 20, 436–451. doi: 10.1162/neco.2007.08-06-310

Torben-Nielsen, B., Segev, I., and Yarom, Y. (2012). The generation of phase differences and frequency changes in a network model of inferior olive subthreshold oscillations. *PLoS Comput. Biol*. 8:e1002580. doi: 10.1371/journal.pcbi.1002580

Upadhyay, R. K., Mondal, A., and Teka, W. W. (2017). Mixed mode oscillations and synchronous activity in noise induced modified Morris-Lecar neural system. *Int. J. Bifurc. Chaos* 27:1730019. doi: 10.1142/S0218127417300191

Vo, T., Bertram, R., Tabak, J., and Wechselberger, M. (2010). Mixed mode oscillations as a mechanism for pseudo-plateau bursting. *J. Comput. Neurosci*. 28, 443–458. doi: 10.1007/s10827-010-0226-7

Watts, D., and Strogatz, S. (1998). Collective dynamics of 'small-world' networks. *Nature* 393, 440–442. doi: 10.1038/30918

Zeldenrust, F., Wadman, W. J., and Englitz, B. (2018). Neural coding with bursts-current state and future perspectives. *Front. Comput. Neurosci*. 12:48. doi: 10.3389/fncom.2018.00048

Zemankovics, R., Káli, S., Paulsen, O., Freund, T. F., and Hájos, N. (2010). Differences in subthreshold resonance of hippocampal pyramidal cells and interneurons: the role of H-current and passive membrane characteristics. *J. Physiol*. 588, 2109–2132. doi: 10.1113/jphysiol.2009.185975

Conflict of Interest: The authors declare that the research was conducted in the absence of any commercial or financial relationships that could be construed as a potential conflict of interest.

Copyright © 2020 Ghosh, Mondal, Ji, Mishra, Dana, Antonopoulos and Hens. This is an open-access article distributed under the terms of the Creative Commons Attribution License (CC BY). The use, distribution or reproduction in other forums is permitted, provided the original author(s) and the copyright owner(s) are credited and that the original publication in this journal is cited, in accordance with accepted academic practice. No use, distribution or reproduction is permitted which does not comply with these terms.

frontiers in Systems Neuroscience

ORIGINAL RESEARCH
published: 24 July 2020
doi: 10.3389/fnsys.2020.00049

Multifractal and Entropy-Based Analysis of Delta Band Neural Activity Reveals Altered Functional Connectivity Dynamics in Schizophrenia

*Frigyes Samuel Racz, Orestis Stylianou, Peter Mukli and Andras Eke**

Department of Physiology, Semmelweis University, Budapest, Hungary

Dynamic functional connectivity (DFC) was established in the past decade as a potent approach to reveal non-trivial, time-varying properties of neural interactions – such as their multifractality or information content –, that otherwise remain hidden from conventional static methods. Several neuropsychiatric disorders were shown to be associated with altered DFC, with schizophrenia (SZ) being one of the most intensely studied among such conditions. Here we analyzed resting-state electroencephalography recordings of 14 SZ patients and 14 age- and gender-matched healthy controls (HC). We reconstructed dynamic functional networks from delta band (0.5–4 Hz) neural activity and captured their spatiotemporal dynamics in various global network topological measures. The acquired network measure time series were made subject to dynamic analyses including multifractal analysis and entropy estimation. Besides group-level comparisons, we built a classifier to explore the potential of DFC features in classifying individual cases. We found stronger delta-band connectivity, as well as increased variance of DFC in SZ patients. Surrogate data testing verified the true multifractal nature of DFC in SZ, with patients expressing stronger long-range autocorrelation and degree of multifractality when compared to controls. Entropy analysis indicated reduced temporal complexity of DFC in SZ. When using these indices as features, an overall cross-validation accuracy surpassing 89% could be achieved in classifying individual cases. Our results imply that dynamic features of DFC such as its multifractal properties and entropy are potent markers of altered neural dynamics in SZ and carry significant potential not only in better understanding its pathophysiology but also in improving its diagnosis. The proposed framework is readily applicable for neuropsychiatric disorders other than schizophrenia.

Keywords: dynamic functional connectivity, multifractal analysis, information-theoretical entropy, machine learning, schizophrenia, electroencephalography

OPEN ACCESS

Edited by:
Andrea Duggento,
University of Rome Tor Vergata, Italy

Reviewed by:
Allegra Conti,
University of Rome Tor Vergata, Italy
Jorge F. Mejias,
University of Amsterdam, Netherlands

***Correspondence:**
Andras Eke
eke.andras@med.semmelweis-univ.hu

Received: *21 April 2020*
Accepted: *29 June 2020*
Published: *24 July 2020*

Citation:
Racz FS, Stylianou O, Mukli P and Eke A (2020) Multifractal and Entropy-Based Analysis of Delta Band Neural Activity Reveals Altered Functional Connectivity Dynamics in Schizophrenia. Front. Syst. Neurosci. 14:49. doi: 10.3389/fnsys.2020.00049

INTRODUCTION

Schizophrenia (SZ) is a severe psychiatric disorder that can be characterized by altered perception and sensory processing, distorted thinking and impaired affective, social and cognitive functions (Uhlhaas and Singer, 2010). Yet being one of the most prevalent mental diseases affecting approximately 1% of the worldwide population (Bhugra, 2005), still no objective diagnostic test exists for SZ (Boutros et al., 2008; Calhoun et al., 2008). Moreover, the etiology of SZ is still unclear, despite being the subject of intense research for more than 100 years (Uhlhaas and Singer, 2010; Yu et al., 2015). Evidently, there has been a growing interest recently in developing tools that can yield quantitative markers of SZ with a biological basis. The expected benefits of these would be twofold: (i) advancing diagnosis and screening of the disease, while also (ii) providing further insights on its underlying neural mechanisms. The hypothesis of abnormal or altered connectivity has been suggested as a key feature of SZ (Friston and Frith, 1995; Bullmore et al., 1997), referring to it as a dysconnectivity syndrome (Friston et al., 2016). Accordingly, many recent studies utilized tools of functional neuroimaging and connectivity analyses to identify biomarkers of SZ (Arbabshirani et al., 2013; Du et al., 2015, 2018; Rashid et al., 2016).

Many SZ-related alterations of functional connectivity (FC) were revealed both at rest and during task modulation (Calhoun et al., 2009; van den Heuvel and Fornito, 2014; Kambeitz et al., 2016; Sheffield and Barch, 2016), however results from different studies are often inconsistent (Fox and Greicius, 2010). FC is most commonly defined as the statistical interdependence of neural activity recorded from disparate brain regions (Friston et al., 1993). This dependence can be captured in many ways from bivariate methods (Sakkalis, 2011; Smitha et al., 2017) to data-driven multivariate approaches such as independent component analysis (ICA) (Li et al., 2009). The large variety of available analytical tools can be considered as one of the (many possible) reasons of contradictory results (Maran et al., 2016). Recently, it has also been proposed (Damaraju et al., 2014) that the inconsistency may arise from the fact that most previous studies analyzed FC in a static manner, i.e., implicitly regarding functional connectivity constant during the measurement period (static functional connectivity, SFC). On the other hand, it has been shown that FC fluctuates even in the resting state (Chang and Glover, 2010; Hutchison et al., 2013; Allen et al., 2014). Indeed, several studies revealed alterations of dynamic functional connectivity (DFC) in SZ that could not be captured by simple SFC analyses (Damaraju et al., 2014; Ma et al., 2014).

Much progress has been made in the past decade in terms of developing methods to capture and characterize dynamic features of FC (see Preti et al., 2017 for a recent review). Among others, dynamic graph theoretical analysis has emerged as a frequently used approach (Dimitriadis et al., 2010; Tagliazucchi et al., 2012; Yu et al., 2015). Graph theory is a popular and powerful tool of FC studies (Bullmore and Sporns, 2009) and is used to describe various topological aspects of complex brain networks reconstructed from physiological data through a set of relatively simple graph theoretical measures (Rubinov and Sporns, 2010). It was also adapted to the DFC framework by multiple studies to capture the spatio-temporal evolution of functional networks (Dimitriadis et al., 2010; Tagliazucchi et al., 2012). As details of brain graph reconstruction fundamentally depend on the particular neuroimaging modality in use, functional magnetic resonance imaging (fMRI) is currently the most frequently used imaging technique. Electroencephalography (EEG) on the other hand provides a reasonable alternative with – albeit lower spatial, but – much higher temporal resolution, thus allowing for a more detailed reconstruction of network dynamics. Despite this and other advantages of EEG imaging (i.e., its accessibility and mobility), up to date not many studies have used dynamic graph analysis of electrophysiological recordings to investigate DFC in SZ (Dimitriadis, 2019).

Dynamic graph theoretical measures were reported to express reduced variance in schizophrenic patients when compared to healthy individuals (Yu et al., 2015) and features extracted by dynamic graph analysis lead to a better classification of SZ patients than simple static network measures (Lombardi et al., 2019). However, it has been shown that global FC fluctuates according to scale-free (or *fractal*) dynamics (Stam and de Bruin, 2004; Van de Ville et al., 2010). Statistical properties (such as the variance) of scale-free processes do not have a characteristic time scale, but they depend on the scale of observation according to a power-law function, and the relationship is established via the scaling exponent (Eke et al., 2000). The scale-free property manifests itself in the time domain as long-range autocorrelation, meaning that such processes have an autocorrelation function that decays according to a power-law rather than an exponential function like of those having characteristic time scales (Eke et al., 2000). Furthermore, in our recent works we showed that functional brain networks express not only scale-free/fractal but indeed multifractal dynamics (Racz et al., 2018a,b), meaning that the local scaling exponent also changes with time. More generally, mono- and multifractality has been recognized previously as a fundamental property of not only DFC but brain dynamics in general, across species and modalities (Herman et al., 2011; Nagy et al., 2017). Such dynamic features cannot be captured by simple first and second-order statistics, thus multifractal time series analysis called for providing a more detailed characterization of network dynamics. Temporal complexity of brain network dynamics can also be efficiently captured in entropy-related measures – which capture the information production rate of processes – such as sample entropy (SE) (Richman and Moorman, 2000) or permutation entropy (PE) (Bandt and Pompe, 2002). Indeed, temporal complexity of DFC has been shown to express characteristic regional patterns that reflect well the underlying functional organization of the brain (Racz et al., 2019). Similar studies revealed that patients with SZ express higher SE in their FC dynamics than healthy control (HC) individuals (Jia et al., 2017; Jia and Gu, 2019). Since the aforementioned methods appear promising tools in characterizing DFC, our main goal in this study was to investigate network dynamics in SZ by means of multifractal and entropy-related analysis. To the best of our knowledge, this is the first study applying multifractal analysis to characterize network dynamics in schizophrenia.

Beyond group-level inferences, the true utility of the extracted dynamic features would lie with their ability to enhance the discrimination of individual cases. Machine learning techniques can be used to build models for classifying individual subjects as HC or SZ, however most methods do not yield any additional information on which predictors play the most important role in the classification process. One of the exceptions is the class of random forest classifiers (RFCs) which can provide measures on the importance of each individual feature (Breiman, 2001) and thus are frequently and efficiently used not only for classification but for feature selection purposes as well (Archer and Kirnes, 2008; Menze et al., 2009). Our goal in this study therefore was not only to investigate if multifractal and entropy-related properties of DFC are altered in SZ, but also to explore how these features could serve as potential markers of the disease when classifying individual cases. We analyzed resting-state EEG recordings from healthy individuals and patients with SZ, and performed dynamic graph theoretical analysis to capture brain network dynamics. Since electrophysiological abnormalities are reported most frequently and consistently in delta band (0.5–4 Hz) neural activity (Newson and Thiagarajan, 2019), in our analysis we primarily focused on this frequency range. Besides conventional first- and second-order indices (such as the mean and variance), connectivity dynamics were characterized by their multifractal and entropy-related properties, while a traditional SFC analysis was also performed as a baseline. Apart from group-level comparisons, an RFC was trained and validated using a leave-one-out scheme, and estimates on predictor importances were extracted.

MATERIALS AND METHODS

Participants and Data Acquisition

Resting-state EEG recordings of an openly available database published previously (Olejarczyk and Jernajczyk, 2017) were analyzed. The dataset comprised EEG records of 14 SZ patients (7 females aged 28.3 ± 4.1 years and 7 males aged 27.9 ± 3.3 years) and 14 age- and gender-matched HC individuals (7 females aged 28.7 ± 3.4 years and 7 males aged 26.8 ± 2.9 years). Subjects of the SZ group were diagnosed with paranoid schizophrenia according to the International Classification of Diseases ICD-10 criteria (category F20.0) and were hospitalized at the Institute of Psychiatry and Neurology in Warsaw, Poland. Only individuals over the age of 18 were allowed to participate in the original study and subjects of the SZ group had a medication washout period of a minimum of 1 week prior to the measurement. Exclusion criteria included organic brain pathology, first episode of schizophrenia, other neurological diseases such as epilepsy, Alzheimer's or Parkinson's disease, or presence of any general medical condition (for further details, see Olejarczyk and Jernajczyk, 2017). All participants were informed of the measurement protocol and provided written informed consent prior to participation. The original study was approved by the Ethics Committee of the Institute of Psychiatry and Neurology in Warsaw. The data was downloaded from the repository at http://dx.doi.org/10.18150/repod.0107441.

Measurement of all participants was performed in an eyes-closed resting-state condition where EEG activity was recorded at a sampling rate of 250 Hz from 19 cortical regions (Fp1, Fp2, F7, F3, Fz, F4, F8, T3, C3, Cz, C4, T4, T5, P3, Pz, P4, T6, O1, O2) according to the standard 10–20 montage (Nuwer et al., 1998) with an additional reference electrode placed at FCz. The original datasets consisted of 15 min of raw EEG data, from which a 3 min long artifact-free segment was selected for each participant for further analysis.

Preprocessing

Data preprocessing was carried out in a fully automatized manner using the Batch EEG Automated Preprocessing Platform (Levin et al., 2018). The data was first band-pass filtered between 0.5 and 45 Hz with additional "cleanline" filtering at 50 Hz to remove line noise. Subsequently, artifact removal was performed using the Harvard Automated Processing Pipeline for Electroencephalography (Gabard-Durnam et al., 2018), a built-in module of BEAPP for standardized artifact removal. HAPPE was set to perform the following steps: (*i*) wavelet-enhanced ICA filtering for spike artifact removal (You and Chen, 2005), (*ii*) subsequent ICA with automated component rejection using the Multiple Artifact Rejection Algorithm (Winkler et al., 2011, 2014), and (*iii*) re-referencing against the common average reference. For ICA, HAPPE used the extended Infomax algorithm as implemented in the EEGLAB software package (Delorme and Makeig, 2004). Finally, EEG data was forward-backward filtered using a 5th order zero-phase Butterworth filter with lower and upper cutoff frequencies 0.5 and 4 Hz, respectively. Data preprocessing and subsequent analysis steps were carried out using Matlab (MathWorks, Natick, MA, United States).

Dynamic Functional Connectivity Estimation

The Synchronization likelihood (SL) method (Stam and van Dijk, 2002) was used to estimate functional connectivity between all pairs of brain regions. SL is a dynamic measure of generalized synchronization that estimates the probability of synchronization between two processes for every time point. It utilizes a temporal embedding scheme (Takens, 1981) and looks for similarities in recurrences around every time point in a "k-nearest neighbor" manner, using the L2 (Euclidean) norm. SL requires five input parameters: the embedding dimension m, the embedding time lag L, a window parameter w_1 controlling for autocorrelation effects, a window parameter w_2 that serves a similar purpose as the time window in a sliding window approach and a resolution parameter p_{ref}. In case of data with explicit frequency limits and fixed sampling rate – such as narrow-band EEG signals –, these parameters (except for p_{ref}) can be defined in a standardized manner according to simple signal processing principles (Montez et al., 2006). Accordingly, in the current analysis we had the following set of parameters: $m = 25$, $L = 20$, $w_1 = 960$, and $w_2 = 1959$, while we set p_{ref} to be equal to 0.05, similarly to previous studies (Stam and van Dijk, 2002; Jalili, 2016). Being a probability-type measure, SL takes on values between 0 and

1 with 0 indicating complete lack of synchronization and 1 indicating perfect synchronization.

SL *per se* estimates synchronization of two processes in a time-resolved manner (Stam and van Dijk, 2002). Therefore, computing SL between all possible pairs of channels yielded a dynamically changing synchronization matrix (i.e., a synchronization matrix for every time point) for every subject, from which the first 2^{15} consecutive matrices were made subject for further analysis. Additionally, as a reference we also computed static FC between all channels, where static SL was acquired according to Stam and van Dijk (2002) by averaging the time-resolved values of SL. This procedure yielded only one synchronization matrix for every subject. Further details on the SL method and its appropriate parameter settings are found elsewhere (Stam and van Dijk, 2002; Montez et al., 2006).

Graph Theoretical Analysis

The synchronization matrices were first thresholded to exclude non-significant and spurious connections (Rubinov and Sporns, 2010). For this purpose, we applied the cost-thresholding scheme introduced by Achard and Bullmore (2007). In that, for every time-point the threshold was set to a value so that only a desired fraction K of all connections (i.e., the strongest connections) were kept in the network. This procedure yielded dynamic weighted networks with a constant number of connections, thus graph theoretical measures truly captured the reorganizations of functional network topology. The whole analysis pipeline was carried out for multiple values of K ranging from 0.15 to 0.5 in 0.05 increments. The lower limit of K was set to 0.15 as we found that cost values below that often rendered the functional networks disconnected, while the upper limit was defined according to Achard and Bullmore (2007).

Subsequently we described the global topology of functional brain networks for every time point with graph theoretical measures connectivity strength (D), global clustering coefficient (C), and global efficiency (E). Global connectivity strength was acquired as the fraction of the sum of present edge weights and the maximal possible value of overall edge weights in the network (Rubinov and Sporns, 2010). The local clustering coefficient of a particular node can be defined as the fraction of the node's neighbors that are also neighbors of each other (Watts and Strogatz, 1998), while the global clustering coefficient, C is the average taken over all nodes in the network. Global network efficiency is defined as the average inverse shortest path length of the network taken over all pairs of nodes (Latora and Marchiori, 2001). C is a widely used measure of segregation, i.e., how much nodes of the network (regions of the brain) tend to form densely connected groups, and characterizes information processing on the local level. On the other hand, E is a measure of integration, i.e., how the brain combines specific information distributed over disparate regions and thus it represents information processing on the global level. All weighted network measures were computed using functions of the Brain Connectivity Toolbox (Rubinov and Sporns, 2010).

This analysis yielded network measure time series (NMTS) for each cost value and graph theoretical measure, a total of 28 subjects × 8 costs × 3 network measures = 672 NMTS, that were subjected to dynamic analysis. Finally, graph theoretical analyses were also performed on the static synchronization matrices as well, yielding one value of D, C, and E for every cost, per subject.

Dynamic Features of Brain Connectivity

First, the mean and variance (μ and σ^2, respectively) of each NMTS were calculated. We also computed the excursion from median (*EfM*) measure recently proposed by Zalesky et al. (2014) to capture the true dynamic nature of functional brain networks. This measure was suggested to capture time-varying behavior more efficiently than the variance as it takes into account both the amplitude and the duration of periods where the process deviates from its median. *EfM* was calculated with the input parameters $a = 0.9$ and $b = 1$, as suggested by previous studies (Zalesky et al., 2014; Hindriks et al., 2016). Yet *EfM* was originally proposed as a test statistic for distinguishing true FC dynamics from random statistical fluctuations of stationary FC, here we only used it as a non-linear measure on grading of "how dynamic" functional brain network topology was.

We used the focus-based multifractal signal summation conversion (FMF-SSC) method (Mukli et al., 2015) to capture multifractal properties of the NMTS. FMF-SSC estimates the multifractal spectrum by first calculating the scaling function $S(q, s)$ according to:

$$S\left(q,s\right) = \left\{ \frac{1}{N_s} \sum_{\upsilon=1}^{N_s} \sigma\left(\upsilon, s\right)^q \right\}^{\frac{1}{q}} \quad (1)$$

where s is the scale, N_s is the number of non-overlapping windows of size s, υ is the index of the window, $\sigma(\upsilon, s)$ is the standard deviation of the υth window at scale s and q is the moment. The generalized Hurst exponent, $H(q)$, is then estimated by focus-based multiple linear regression for every q simultaneously. Finally, the multifractal spectrum is acquired via applying Legendre transformation to $H(q)$. Consequently, FMF-SSC qualifies as an indirect approach when analyzing multifractality by providing information about the distribution of local scaling exponents of the investigated process through its multifractal spectrum. The key steps of FMF-SSC are illustrated in **Figure 1**, while further details of FMF-SSC and its parametrization are described elsewhere (Mukli et al., 2015). Accordingly, we performed FMF-SSC with the following settings: s were set according to 2^n datapoints per window with n ranging from 3 to 13 in steps of 1, and q ranging from -15 to 15 with increments of 1. The lower limit of n was defined to have 8 data points, while the upper limit was set to be equal to 1/4 of the signal length. FMF-SSC yields two endpoint measures, h_{max} and *FWHM*. h_{max} is the Hölder exponent at the peak of the multifractal spectrum and is strongly related (although not strictly equal) to the degree of global long-term autocorrelation of the process. *FWHM* is the full width at half maximum of the multifractal spectrum and captures the degree of multifractality, i.e., how much the local scaling exponent (and thus the local degree of autocorrelation) varies in time. Essentially, the larger

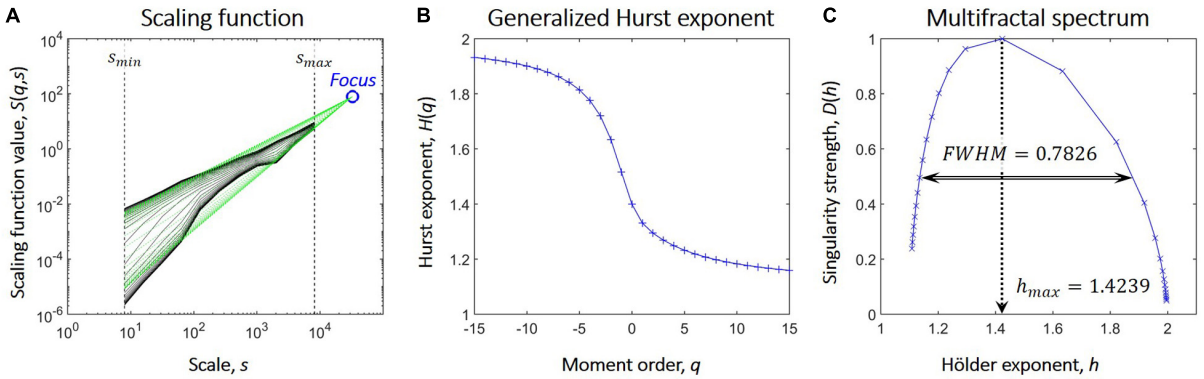


FIGURE 1 | Steps of focus-based multifractal analysis. **(A)** After the scaling function (marked in black) is acquired, linear regression is used to fit power-law functions (marked in green) at each moment order *q*. On double logarithmic plots these appear as linear functions whose slopes are the scaling exponents. Also, in case of finite length signals, these converge to one point, the Focus, that is used as a reference point during regression. **(B)** The generalized Hurst exponent, *H*(*q*) is acquired as the scaling exponents of the functions fitted on the scaling function at each value of q. The focus-based formalism enforces the monotonously decreasing nature of *H*(*q*); a prerequisite for Legendre transformation. **(C)** The multifractal spectrum is acquired from *H*(*q*) via Legendre transformation and is described by the Hölder exponent at its maximal value (h_{max}) and its full width at half maximum (*FWHM*).

h_{max} is, the stronger is the global long-term autocorrelation while the smaller *FWHM* is, the smaller is the variability of the local scaling exponent in time. A theoretical *FWHM* value of zero would mean that the scaling exponent does not change at all, and in which case the process does not express multifractality but reduces to a simple scale-free (or monofractal) process. However, even monofractal signals produce multifractal background noise when analyzed in a multifractal manner due to the finite length of real-life signals (Grech and Pamula, 2012) and the focus-based regression scheme. In order to exclude these cases, a multi-step surrogate data testing framework (Racz et al., 2019) was also carried out against 40 surrogates in each step to verify true multifractality of NMTS. By this means, we verified if time series truly expressed power-law scaling and that their *FWHM* values were significantly larger than those of strictly monofractal surrogate signals of otherwise similar properties. In all cases, NMTS were considered significantly different from their surrogates in their investigated property if it was found outside the $\mu \pm 2^{*}\sigma$ range where μ and σ denotes the mean and standard deviation acquired from the surrogates. After verifying normality of surrogate indices, this yields an approximate confidence level of 0.05.

Temporal complexity of NMTS was captured by their information theoretical entropy (Bandt and Pompe, 2002). Since it is possible that network topology does not change in two consecutive time points, we calculated a modified version of PE (*mPE*) that allows for this effect yet still yields accurate estimates of signal complexity (Bian et al., 2012). *mPE* also builds on the temporal embedding approach; thus its input parameters include the embedding dimension and the embedding time lag. To achieve the highest resolution possible within the current experimental setup, we set the embedding dimension to 7 and the embedding time lag to 3 according to previous studies (Staniek and Lehnertz, 2008). The analysis pipeline is summarized in **Figure 2**.

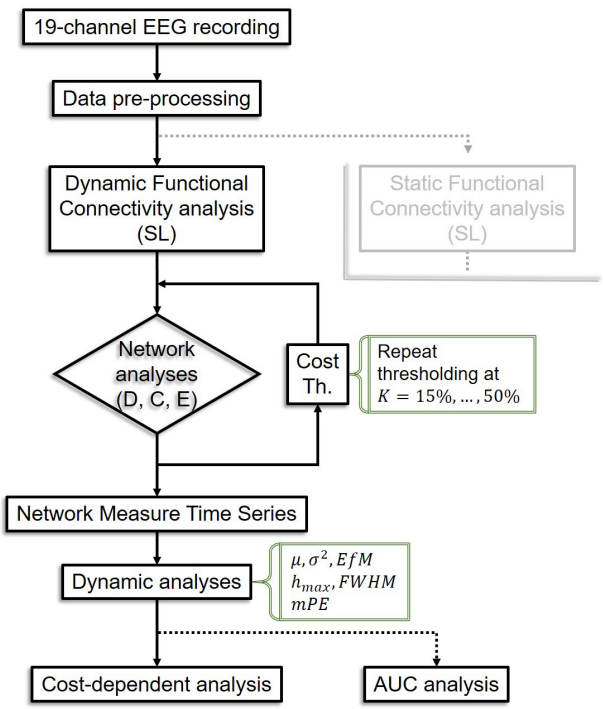


FIGURE 2 | Flowchart of the analysis pipeline. The analysis pipeline for static connectivity analysis is not shown as it is equivalent in most steps to the dynamic pipeline, except that only one connectivity matrix is acquired per subject, leading to only one value for each network measure instead of a time series, thus dynamic analyses are bypassed. SL, synchronization likelihood; D, connectivity strength; C, clustering coefficient; E, global efficiency; Th, thresholding; *K*, cost; AUC, area under the curve.

Statistical Analyses

First, we compared HC and SZ groups in a cost-dependent manner. Since assumptions of a two-way repeated measures

ANOVA were violated in most cases, we compared values of the HC and SZ groups for each cost separately. In case of normally distributed data and equal variances two sample *t*-tests were used, while Mann-Whitney U tests otherwise. The acquired *p*-values were corrected for multiple comparisons using the false discovery rate (FDR) approach (Benjamini and Hochberg, 1995) with level $\alpha = 0.05$. Significant effect of cost on the acquired indices was verified with Friedman tests with complementary Kendall's *W* coefficient calculation in order to estimate the concordance among subjects.

Furthermore, in order to render the results independent of cost and thus reduce dimensionality for classification (see below) we calculated the area under the curve (AUC) for all calculated network measures. AUC values of all measures in the HC and SZ groups were compared using two sample *t*-tests or Mann–Whitney *U*-tests. Note that the AUC approach is commonly used in FC studies to avoid selecting a specific cost/threshold value (He et al., 2009; Koshimori et al., 2016). However, in most DFC studies AUC values for network measures are calculated for every time point first, and then dynamics of the AUC time series are analyzed (Yu et al., 2015; Kim et al., 2017). Here we took a different approach (by analyzing dynamics first for each *K* and calculating AUC afterward), as the prior summation of values could lead to undesired effects in multifractal analysis (Nagy et al., 2017). Statistical analysis was carried out using StatSoft Statistica 13.2.

Classification

Due to the small sample size, it is unlikely that a classifier built from this dataset would generalize well on unseen real-world data. With that in mind, our goal instead was to explore if the dynamic measures of FC described above could serve as valuable features for classifiers in the future, trained on larger datasets. Therefore, we intentionally selected a standard machine learning method where information on feature importances could be easily and readily extracted. One of such methods are random forest classifiers (RFC, Breiman, 2001). A random forest consists of a set of binary decision trees, each grown from a different bootstrap sample of the training dataset. However, unlike a regular unpruned decision tree, trees of the forest do not use all predictors but split the data using only a random subset of the features. Finally, when a new example is presented, it is subjected to all trees in the forest and the target variable is predicted by aggregating the predictions of all trees, i.e., as a "majority vote." A big advantage of RFCs is that they provide multiple estimates on feature importances (Menze et al., 2009). From these, we selected the Gini importance, a widely used measure that captures how much prediction accuracy would be affected if the given feature was not used when splitting the data (Breiman, 2001). Although there is no theoretical limit to the number of features used for training an RFC, in most cases it is accepted as a rule of thumb that the number of features should not exceed the number of training examples. For this reason, the AUC values of seven indices (static, mean, variance, *EfM*, h_{max}, *FWHM*, and *mPE*) acquired from the three network measures (D, C, and E) were used for training, resulting in a total number of 21 training features.

The sample size of the dataset did not allow for a statistically robust train-test split, so that the generalization of the model could be reliably tested. Thus, we evaluated model performance via cross-validation according to a stratified leave-one-out scheme (Calhoun et al., 2008; Rashid et al., 2016). In that, the dataset was first divided into a training and a holdout set. The holdout set always consisted of one HC and one SZ subject; thus the training set comprised the remaining 26 subjects. Then, the model was trained using data of the training set and its performance was validated on the holdout subjects. In each cross-validation run, model performance was evaluated using six standard report measures: accuracy, specificity, sensitivity, positive predictive value, negative predictive value and the AUC of the receiver-operator-characteristic (ROC) curve. Similarly, the Gini importance of each feature was extracted at the end of each cross-validation cycle. The whole process was then repeated using a different pair of HC-SZ subjects as holdout set. Each HC and SZ subject were put exactly once in the holdout set; thus the model was cross-validated 14 times. Overall classifier performance was captured in the average of the six report measures over the cross-validation runs, while the overall importance of each feature was quantified as the sum of its Gini importance over the cross-validation runs.

An RFC has many hyperparameters (parameters that have to be set before training) including but not limited to the number of trees in the forest and the allowed maximum number of features used by each tree for splitting the data. Since RFC performance can strongly depend on the appropriate setting of these hyperparameters, we performed a grid search in order to find the parameter settings that yield the best overall classifier performance. Finally, we also evaluated the performance of the classifier against surrogate datasets. In that, we carried out the cross-validation scheme described previously on 100 surrogate datasets, each acquired by randomly permuting group labels among subjects (but leaving features/predictors intact). All performance measures were compared to those of surrogate data and were considered significant if they exceeded the $\mu \pm 2^{*}\sigma$ range acquired from surrogates. RFCs were implemented in Python 3.7 using the RandomForestClassifier class of the Scikit-Learn package and grid search was carried out using GridSearchCV class. Details on the hyperparameter settings of the final RFC model, as well as definitions of the performance measures are provided in **Supplementary Material**.

RESULTS

Throughout the results, for all dynamic indices the network measure it was calculated on is indicated in the left superscript, e.g., ${}^{C}h_{max}$ standing for the h_{max} of clustering coefficient. AUC indices are indicated in the left subscript, e.g., ${}^{C}_{AUC}h_{max}$ refers to the AUC index calculated from the h_{max} values of clustering coefficient.

Static Functional Connectivity

Static synchronization matrices revealed a high degree of similarity in topology between HC and SZ groups (**Figure 3A**).

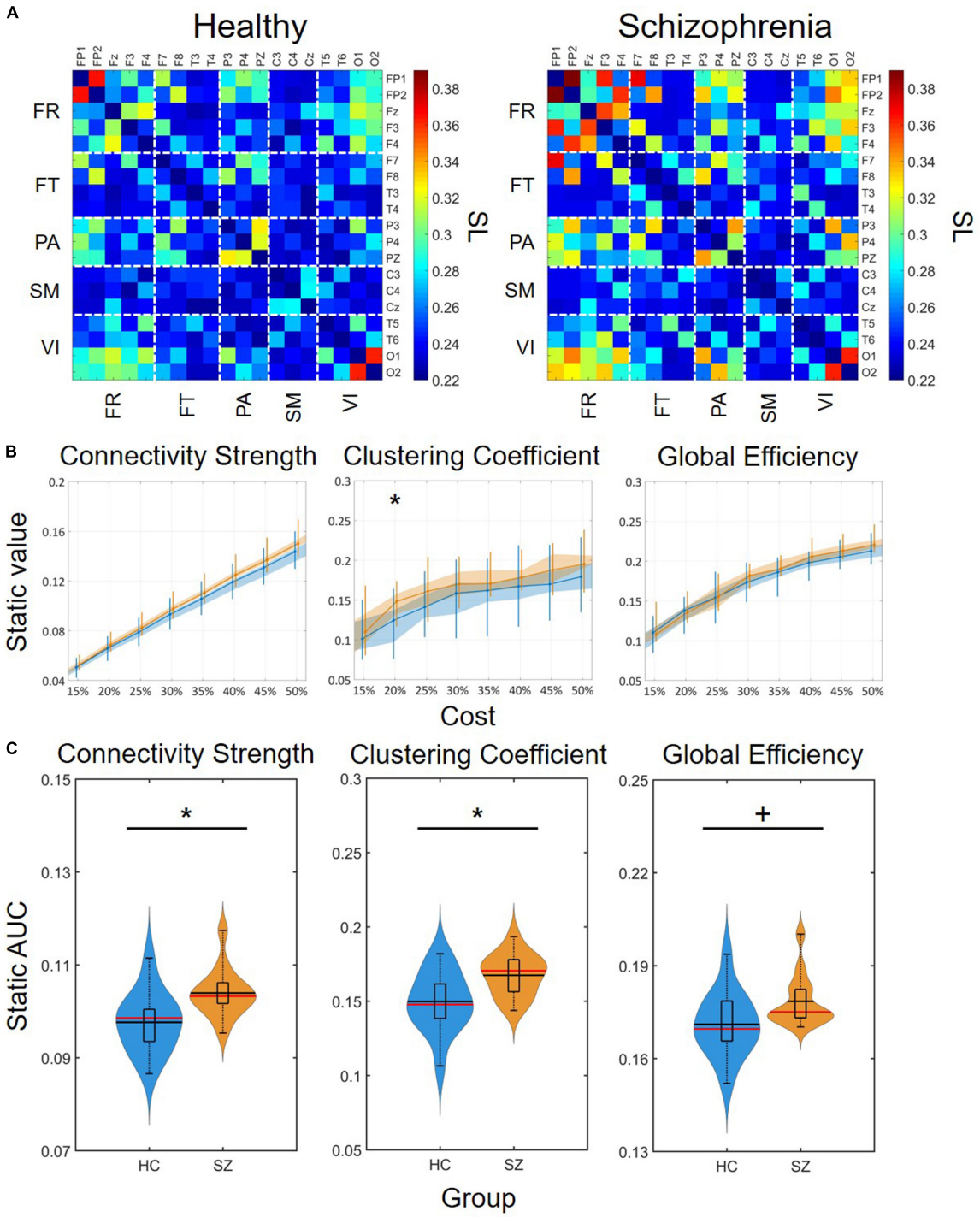


FIGURE 3 | Group-average connectivity matrices and results of static functional connectivity analysis. **(A)** Group-average static connectivity matrices for healthy controls (left) and patients with schizophrenia (right). For a better comparison, the matrices are in the same color scale. Channels are grouped according to macroanatomical brain regions. **(B)** Results of the cost-dependent analysis. Data corresponding to healthy controls is marked in blue, while those of patients with schizophrenia are marked in orange. Dots mark median values, the shaded area refers to the 25th and 75th percentiles, and vertical lines range from 10th to 90th percentiles. Asterisk marks significant group difference ($p < 0.05$, corrected) acquired with two sample *t*-test. **(C)** Violin plots of static FC results for all three network measures. In each violin plot the central black line indicates the mean and the central red line indicates the median. The lower and upper horizontal lines of the rectangle mark the 25th and 75th percentile, respectively, and the outer horizontal lines indicate the 10th and 90th percentile values. The colored areas illustrate the estimated probability density function of the corresponding datasets. An asterisk marks significant group difference ($p < 0.05$) identified with two-sample *t*-test, while a plus sign marks significant difference identified with Mann-Whitney *U*-test. SL, synchronization likelihood; FR, frontal cortex; FT, frontotemporal regions; PA, parietal cortex; SM, somatomotor cortex; VI, visual cortex; AUC, area under the curve; HC, healthy control; SZ, schizophrenia.

TABLE 1 | Effect of cost on static network measures.

		Connectivity strength		Clustering coefficient		Global efficiency	
		HC	SZ	HC	SZ	HC	SZ
Static	*p*	<0.0001	<0.0001	<0.0001	<0.0001	<0.0001	<0.0001
	W	1	1	0.8042	0.7075	1	1

The upper row contains p-values from the Friedman tests, while the lower row contains Kendall's coefficient of concordance (W) values. W = 1 indicates perfect agreement among subjects. HC, healthy control; SZ, schizophrenia.

In both groups, clusters of stronger connections were observable linking the frontal with the occipital as well as parietal regions. In these three regions, the within-regional connections also appeared to be stronger than in the rest of the network. Cost-dependent analysis showed a tendency of stronger FC in SZ for all three network measures, nevertheless, this difference was significant only in the case of C with $K = 20\%$ (**Figure 3B**). In both groups, the cost had a significant, although trivial effect on all three network measures (**Table 1**), as their values increased with increasing K. On the other hand, when we compared the AUC values acquired from D, C and E we found significant differences between the two groups, with SZ subjects expressing stronger static FC as captured in all three measures (**Figure 3C**).

Mean, Variance, and Excursions From Median

The mean of DFC measures can be understood as a statistically more reliable estimation of static FC. This effect was demonstrated convincingly as the cost-dependent analysis indicated significantly higher D and C values in the SZ group with all K (**Figure 4**). As expected, cost had a similar effect on the mean of D, C and E as in the case of static FC analysis (**Table 2**). In addition, significantly higher variance of D and C was identified in the SZ group at almost all values of K (**Figure 4**). Interestingly, increasing the cost resulted in an increase of ${}^{D}\sigma^2$ but a decrease of ${}^{C}\sigma^2$, while had an indistinct effect on ${}^{E}\sigma^2$. Nearly identical results to those of the variance were acquired when investigating *EfM* with additionally ${}^{C}EfM$ being significantly higher in SZ for every cost value (**Figure 4**

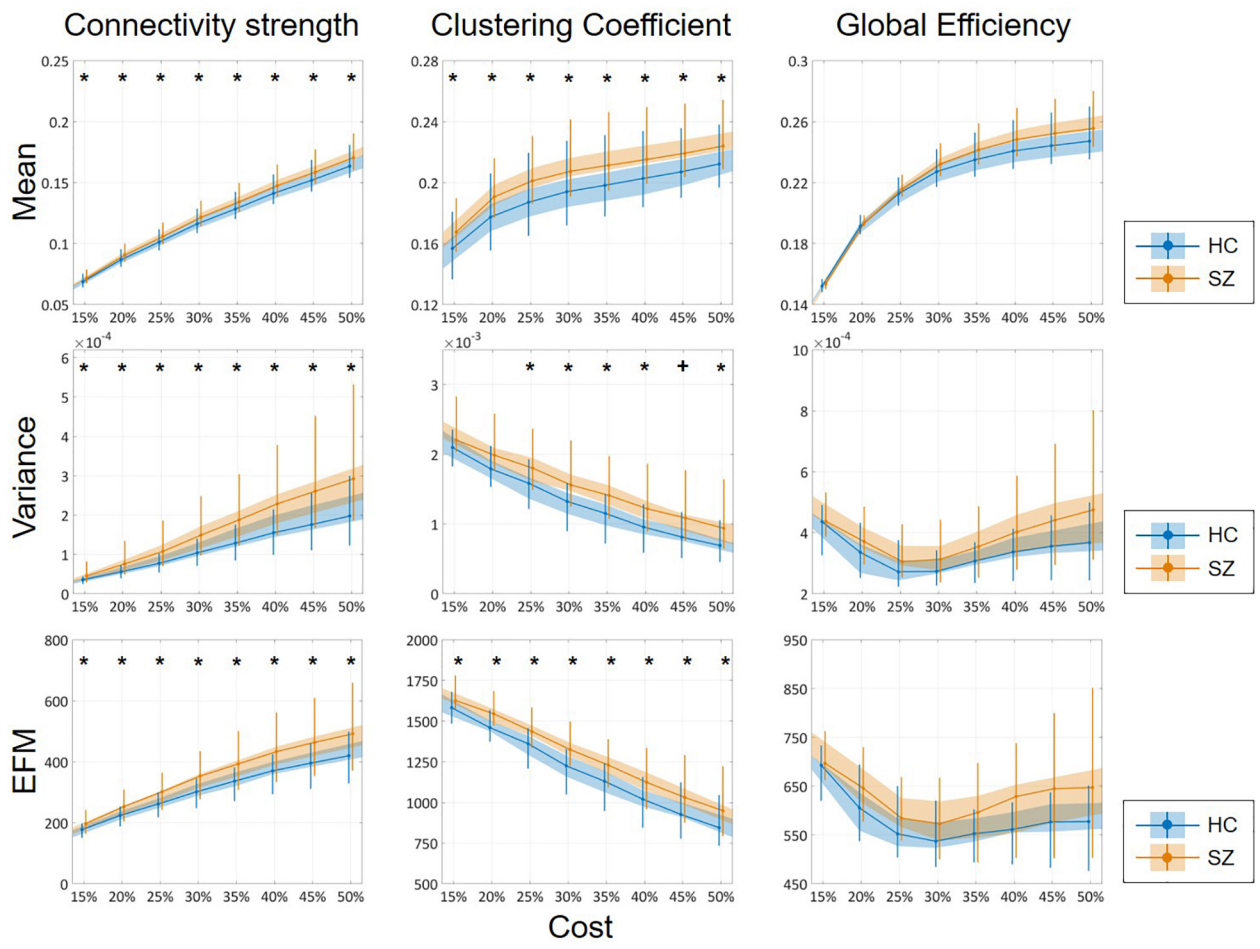


FIGURE 4 | Cost-dependent results of the mean, variance and excursions from median analysis of network measures. Mean, variance, and excursions of median (EFM) values of the three network measures are plotted as functions of the cost. Black markers indicate significant group level difference ($p < 0.05$, corrected). *Two-sample *t*-test; +Mann–Whitney *U*-test; HC, healthy control; SZ, schizophrenia.

TABLE 2 | Effect of cost on the mean (μ), variance (σ^2), and excursions from median (EfM) of dynamic network theoretical measures.

		Connectivity strength		Clustering coefficient		Global efficiency	
		HC	SZ	HC	SZ	HC	SZ
μ	*p*	<0.0001	<0.0001	<0.0001	<0.0001	<0.0001	<0.0001
	W	1	1	1	1	1	1
σ^2	*p*	<0.0001	<0.0001	<0.0001	<0.0001	0.0001	<0.0001
	W	1	1	1	0.9968	0.9111	0.8365
EfM	*p*	< 0.0001	<0.0001	<0.0001	<0.0001	<0.0001	<0.0001
	W	1	1	1	1	0.7291	0.8287

For each index, the upper rows contain p-values from Friedman tests, while the lower rows contain Kendall's coefficient of concordance (W) values. HC: healthy control; SZ: schizophrenia.

and **Table 2**). This is in accordance with previous findings where *EfM* was found to have power equal to standard deviation in distinguishing true FC dynamics (Hindriks et al., 2016). The AUC analysis reassured stronger FC, as well as higher temporal variability of DFC in SZ (**Figure 5**).

Multifractal Measures and Entropy

Since multifractality can emerge due to phenomena other than the presence of long-term autocorrelations, appropriate surrogate testing is indispensable (Kantelhardt et al., 2002). In order to verify true multifractality of each NMTS, we replicated the four-step testing framework as described in detail in Racz et al. (2019). In that, we (*i*) generated surrogate time series with power-law spectra and equal spectral slope and compared goodness of fit statistics to those of the original time series, (*ii*) generated surrogates by shuffling data points of the original datasets, (*iii*) generated surrogates by phase-randomization, and (*iv*) generated strictly monofractal signals with equal global scaling exponent. In step *i* we compared the goodness of fit statistics of the spectra of the original time series to those of surrogate data with known power-law spectra, while in steps *ii–iv* we assessed multifractal properties of the surrogates and compared them to the original NMTS. Surrogate testing indicated that in the vast majority of cases, NMTSs expressed a power-law scaling, thus their general scale-free nature was confirmed. Shuffling reduced the process to pure white noise, as indicated by their spectral slope and *FWHM* being approximately zero. Finally, both phase randomization and monofractal signal generation produced signals with significantly smaller *FWHM* values, thus presence of true multifractality could be concluded. The percentage of NMTS that passed each test are shown for every test in **Table 3**. Values are reported combining both groups, as we did not find any significant difference in the fraction of NMTS that passed each test between HC and SZ groups (Mann–Whitney *U*-test, $p > 0.05$ in all cases).

Cost-dependent analysis revealed significantly higher ${}^{C}h_{max}$ in subjects of the SZ group for most values of *K*, while this difference appeared only as a tendency in ${}^{D}h_{max}$ (**Figure 6**). Conversely, ${}^{D}FWHM$ was found significantly higher in the SZ group for higher costs, while the same difference could be observed in ${}^{C}FWHM$ and ${}^{E}FWHM$ only at two and one cost values, respectively (**Figure 6**). On the other hand, ${}^{D}mPE$ was significantly reduced in SZ subjects for all cost values, while the same difference in ${}^{C}mPE$ was found significant only at $K = 35\%$ (**Figure 6**). Increasing *K* resulted in significant increase of h_{max} of all three network measures, while it has the opposite effect on *mPE* (**Table 4**). In addition, the cost had indistinct or no effect on the *FWHM* of D, C, and E.

Again, group-level differences were found much more pronounced when comparing the AUC values of multifractal and entropy measures (**Figure 7**). In that, significantly higher ${}^{D}_{AUC}h_{max}$, ${}^{C}_{AUC}h_{max}$, ${}^{D}_{AUC}mPE$, and ${}^{C}_{AUC}mPE$ values were found in the SZ group, while the AUC of *FWHM* was found increased for all three network measures. This indeed highlights the power of AUC analysis as *FWHM* was found significantly higher in the SZ group only at a few cost values.

Classification and Most Important Features

Train and test performance metrics of the classifier are shown in **Table 5**. Notably, the RFC was able to reach an overall 89.29% cross-validation accuracy and 100% specificity. The bottom row of **Table 5** shows the mean test results for surrogate data testing with the upper boundary of the confidence interval in parentheses. Surrogate datasets yielded estimates close to chance level (50%), as expected, indicating a significantly better performance of the classifier in all metrics. The cumulative Gini importance was the highest for ${}^{D}\sigma^2$, ${}^{C}h_{max}$, ${}^{C}mPE$, and ${}^{C}FWHM$, highlighting the importance of dynamic indices, while in general (with the exception of E_{stat}) static and mean graph theoretical measures were identified as less important for classification (**Table 6**). Interestingly, while ${}^{C}FWHM$ was amongst the most important features, ${}^{D}FWHM$ and ${}^{E}FWHM$ were identified as negligible predictors.

DISCUSSION

There is a growing interest in investigating dynamic features of FC in various clinical conditions (Calhoun et al., 2014; Preti et al., 2017). However, the vast majority of such studies use fMRI to capture neurodynamics, while other imaging modalities such as EEG are rather underrepresented (Mutlu et al., 2012). The orders of magnitude higher temporal resolution of EEG is a clear advantage that allows for a more detailed assessment of brain network dynamics. In this study, we reconstructed dynamic functional networks of healthy controls and patients with schizophrenia from delta-band EEG activity with a much higher sampling rate that would have been possible with fMRI. Ultimately, this allowed us to capture several aspects of temporal complexity, namely multifractality and entropy, in which our analytical framework was capable of revealing disease-related changes. In particular, DFC in SZ patients could be characterized by increased long-range autocorrelation and degree of multifractality, while lower entropy values indicated reduced temporal complexity. Furthermore, a machine learning-based classification scheme identified these dynamic connectivity features as highly relevant in classifying individual cases. Additionally, we found higher static and mean dynamic

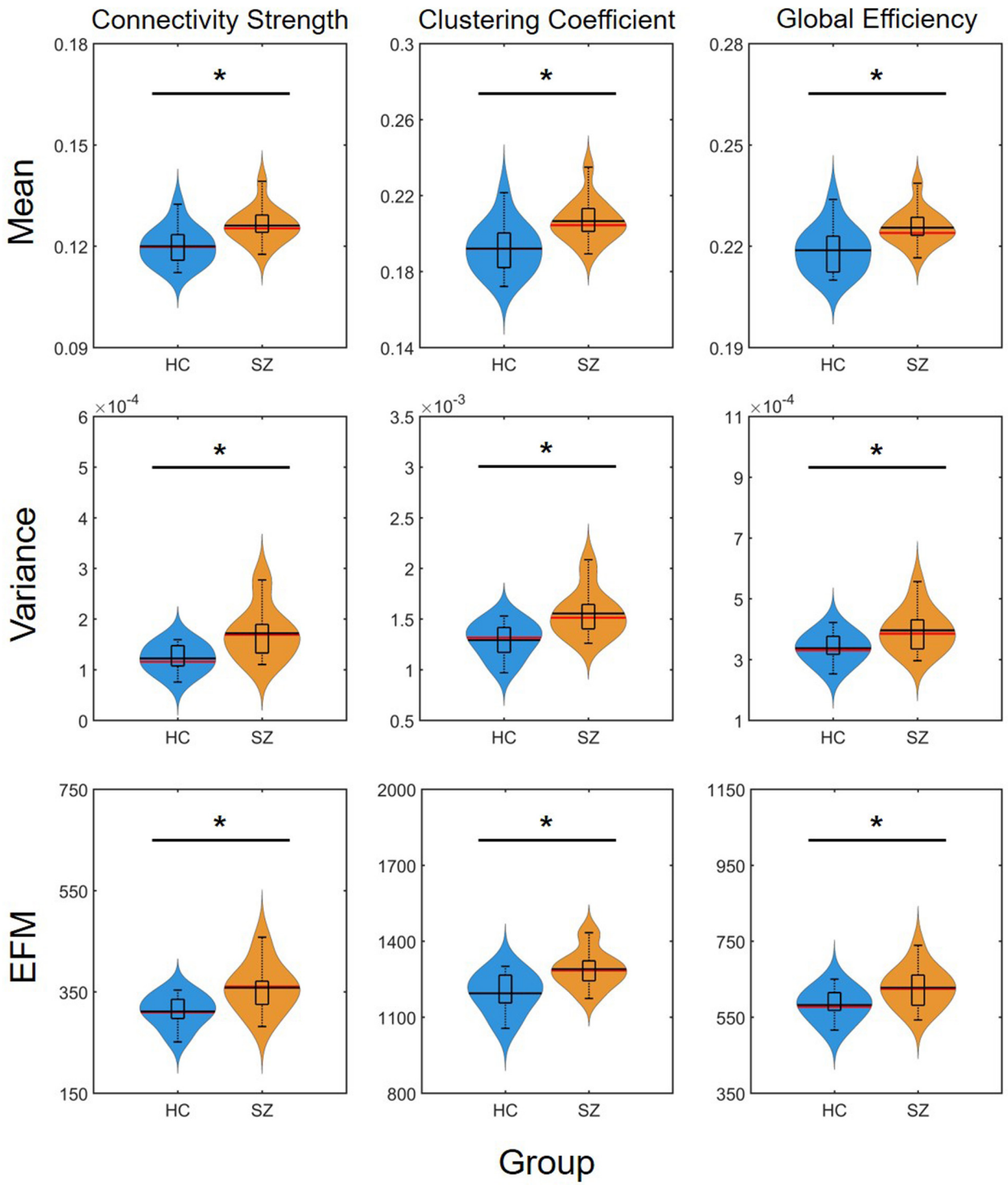


FIGURE 5 | Results of the area-under-the-curve analysis regarding the mean, variance and excursions from median (EFM) of dynamic network measures. Higher mean and temporal variability of dynamic functional connectivity in SZ is apparent as captured in both connectivity strength, clustering coefficient and global efficiency. Asterisk marks significant group difference ($p < 0.05$) identified with two-sample t-test. HC, healthy control; SZ, schizophrenia.

TABLE 3 | Testing results for true multifractality.

	Spectrum	Shuffling	True MF	PhaseRan
D	95.98%	100%	100%	94.64%
C	96.43%	100%	100%	100%
E	98.21%	100%	100%	100%

MF, multifractality; PhaseRan, phase randomization; D, connectivity strength; C, clustering coefficient; E, global efficiency.

functional connectivity in schizophrenia, as well as subjects of the patient group expressed higher temporal variability in their DFC when compared to that of healthy controls.

Aberrant Connectivity Dynamics in SZ

In the present study, we report on increased FC in SZ, as well as higher variability of dynamic graph theoretical measures in the patient group. Static approach to FC was also able to reveal this difference, although with less sensitivity than taking the means of dynamic network topological indices. In general, there is considerable inconsistency among results in the literature on resting-state dysconnectivity in SZ not only in the fMRI field (Fox and Greicius, 2010) but among electrophysiological studies, too (Maran et al., 2016). The somewhat contradictory results can be attributed to the differences in applied methods and modalities (Jalili, 2016), however independent studies using the same methodology reported both decreased (Winterer et al., 2001) and increased (Kam et al., 2013) connectivity in delta-band EEG. It also has to be noted, that the original study where the current dataset was published (Olejarczyk and Jernajczyk, 2017) performed SFC analyses using various pre-processing pipelines and FC estimators, and reported on both increased and decreased SFC in SZ, depending on the FC estimator or data pre-processing. The pre-processing pipeline in our approach was designed to be fully automatized and thus easily reproducible, however in order to investigate the plausible effects of FC estimator selection (SL in this case), we carried out the whole analysis using the exact same settings but a different, widely used estimator of connectivity, the Phase Lag Index (PLI, Stam et al., 2007). A detailed report of this analysis is provided in **Supplementary Material**. PLI takes a different approach from that of SL in estimating FC, as it captures synchronization of two processes based on the differences between their instantaneous phases following Hilbert transformation (Stam et al., 2007). Despite

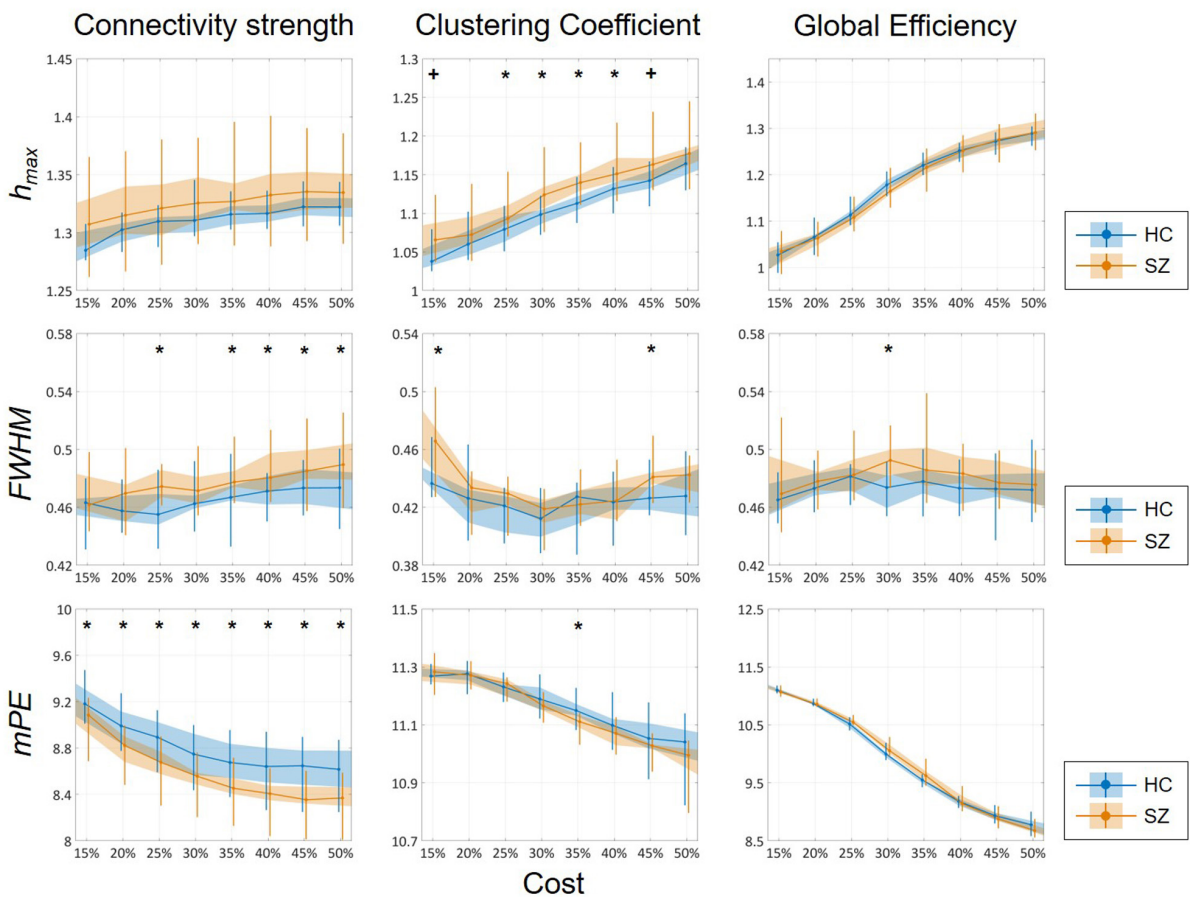


FIGURE 6 | Cost-dependent results of multifractal and entropy analysis of network measures. Multifractal measures (h_{max} and *FWHM*) and modified permutation entropy (*mPE*) of all three network measures are plotted as functions of the cost. Black markers indicate significant group level difference ($p < 0.05$, corrected). *Two-sample *t*-test; +Mann–Whitney *U*-test; HC, healthy control; SZ, schizophrenia.

TABLE 4 | Effect of cost on the multifractal measures (hmax and FWHM) and modified permutation entropy (mPE) of dynamic network theoretical measures.

		Connectivity strength		Clustering coefficient		Global efficiency	
		HC	SZ	HC	SZ	HC	SZ
h_{max}	*p*	<0.0001	<0.0001	<0.0001	<0.0001	<0.0001	<0.0001
	W	0.8374	0.7048	0.9788	0.9417	1	1
FWHM	*p*	0.0036	<0.0001	<0.0001	0.0001	0.1191	0.0069
	W	0.2155	0.4242	0.8861	0.3061	0.1171	0.1985
mPE	*p*	<0.0001	<0.0001	<0.0001	<0.0001	<0.0001	<0.0001
	W	<0.0001	<0.0001	<0.0001	<0.0001	<0.0001	<0.0001

For each index, the upper rows contain p-values from Friedman tests, while the lower rows contain Kendall's coefficient of concordance (W) values. HC, healthy control; SZ, schizophrenia.

TABLE 5 | Performance report of the random forest classifier.

	Test performance					
	ACC (%)	SEN (%)	SPE (%)	PPV (%)	NPV (%)	ROC-AUC (%)
Train	93.41	86.83	100	100	88.55	99.32
Test	89.29	78.57	100	78.57	89.29	85.71
CI	49.93 (72.45)	46.14 (75.10)	53.71 (83.92)	35.21 (58.97)	39.00 (63.28)	51.39 (81.51)

In the bottom row, upper boundary of the confidence interval is presented in parentheses below the mean. ACC, accuracy; SEN, sensitivity; SPE, specificity; PPV, positive predictive value; NPV, negative predictive value; ROC-AUC, area under the receiver operator characteristic curve; CI, confidence interval.

TABLE 6 | Feature importances extracted from the random forest classifier.

Rank	Feature	Importance
1	${}^{D}\sigma^2$	3.7912
2	${}^{C}h_{max}$	1.8674
3	${}^{C}mPE$	1.3843
4	${}^{C}FWHM$	1.3431
5	${}^{D}EfM$	1.0582
6	${}^{E}EfM$	1.0110
7	E_{stat}	0.6700
8	${}^{D}h_{max}$	0.3853
9	${}^{E}h_{max}$	0.3510
10	${}^{E}\sigma^2$	0.3507
11	${}^{C}\mu$	0.3424
12	${}^{D}mPE$	0.3218
13	C_{stat}	0.3104
14	${}^{C}\sigma^2$	0.2683
15	${}^{C}EfM$	0.2224
16	${}^{E}mPE$	0.1630
17	${}^{D}\mu$	0.1134
18	${}^{E}\mu$	0.0322
19	D_{stat}	0.0137
20	${}^{D}FWHM$	0.0
21	${}^{E}FWHM$	0.0

For each index, the network measure it was calculated from is indicated in the left superscript. Static network measures are indicated by the subscript "stat" following their abbreviation. D, connectivity strength; C, clustering coefficient; E, global efficiency; stat, static; μ, mean; σ^2, variance; EfM, excursions from median; h_{max}, Hölder exponent at the peak of the multifractal spectrum; FWHM, full width at half maximum; mPE, modified permutation entropy.

the fundamentally different nature of the two estimators, the PLI analysis yielded highly similar results (see **Supplementary Material**), thus making it improbable that the nature of our results was significantly biased by the choice of FC estimator.

In order to further test the robustness of the identified connectivity patterns, we also repeated the analysis pipeline using the Weighted Phase Lag Index (WPLI, Vinck et al., 2011) as the connectivity estimator. WPLI is derived from PLI by weighing the phase differences by the magnitude of the imaginary part of the cross-spectrum, and thus attributing less importance to small (i.e., close to zero) phase differences (for details see **Supplementary Material**), that are more susceptible to common noise sources (Vinck et al., 2011). PLI was originally introduced as an FC estimator that is robust against common source effects originating from volume conduction and/or active reference electrodes in case of EEG monitoring (Stam et al., 2007), however, WPLI was shown to further reduce these confounding factors (Vinck et al., 2011). Surprisingly, although dynamic networks reconstructed using WPLI expressed true multifractality in a proportion similarly high to those based of SL or PLI (**Supplementary Table 4**), between-group differences were found far less pronounced. In fact, only ${}^{D}\mu$ and ${}^{E}\mu$ indicated significantly higher connectivity in SZ. At first, this may imply that the previously observed results are not pronounced enough to be identified by more sophisticated methods such as WPLI. However, random forest classification was still able to reach comparable performance (see **Supplementary Tables 8**, **9**), indicating that connectivity dynamics were indeed substantially different between HC and SZ individuals. The observed contrast between the results of PLI- and WPLI-based analyses may emerge from multiple origins. First, WPLI is superior to PLI when detecting phase synchronization in the presence of uncorrelated, volume-conducted noise sources (Vinck et al., 2011). Therefore, the stronger connectivity captured by PLI in SZ may arise due to the presence of more and/or stronger "noise sources" in SZ patients. Second, WPLI generally weights down phase lags, especially those close to zero. Consequently, it may be the case that most connections responsible for significant group-level differences could be characterized with small phase lags, which were effectively pruned by the WPLI calculation, thus rendering the dynamic networks indistinguishable. Although these findings highlight that one must apply great caution when interpreting the results of FC (and DFC) analyses, these issues – namely the choice of the FC estimator and specifics of the preprocessing pipeline – has also been emphasized by numerous recent studies (Jalili, 2016; Olejarczyk and Jernajczyk, 2017; Lindquist, 2020).

Previous studies applying dynamic graph analysis reported reduced mean (Du et al., 2016) and variance (Yu et al., 2015) of D, C and E in SZ patients, in contrast to our findings. Both of these studies used fMRI imaging and estimated functional network connectivity (Jafri et al., 2008) from low-frequency (0.01–0.1 Hz) spontaneous brain activity; thus a

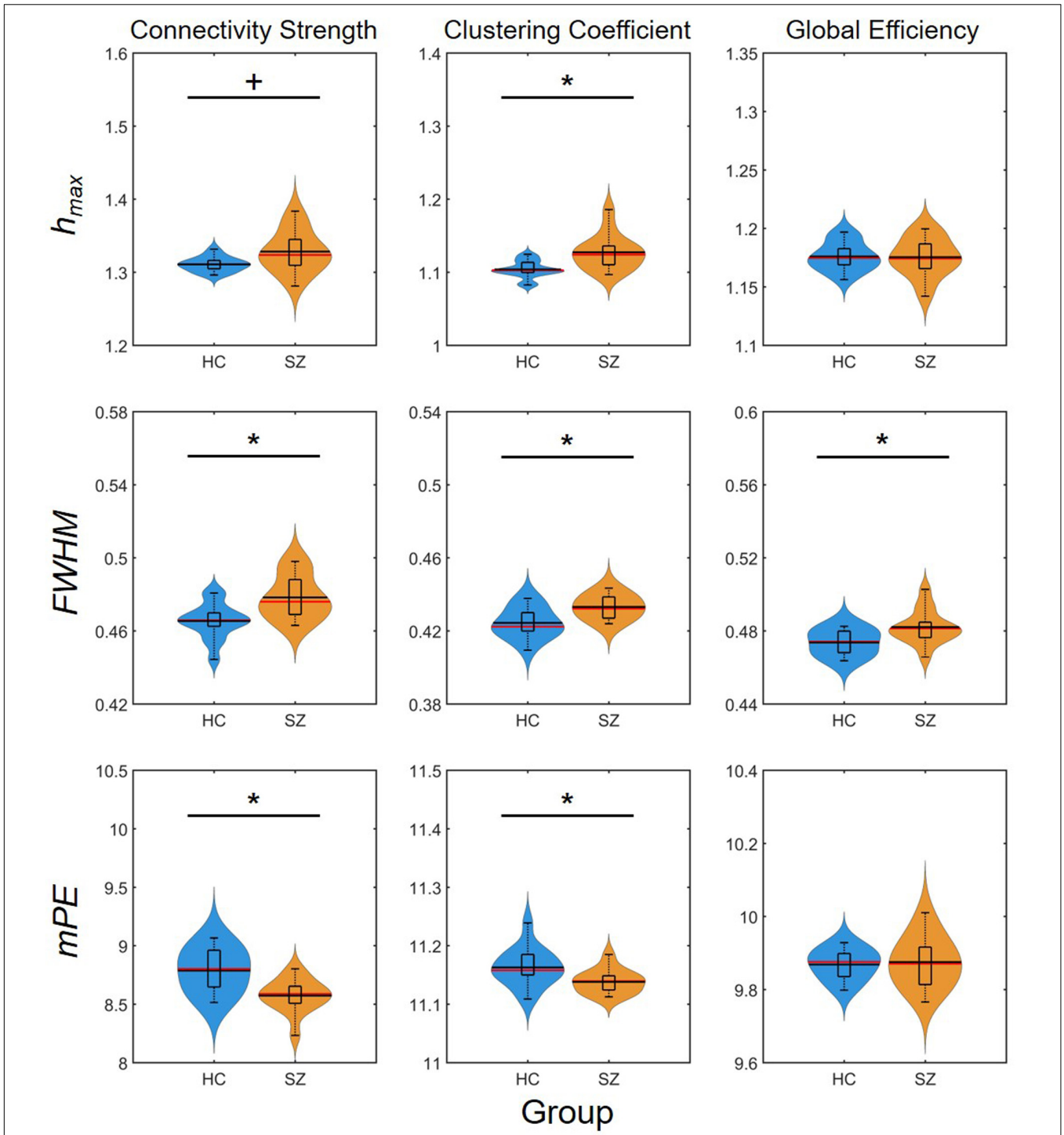


FIGURE 7 | Results of the area-under-the-curve analysis regarding multifractal and entropy-related properties of dynamic network measures. Black markers indicate significant group level difference ($p < 0.05$). *Two-sample *t*-test; +Mann–Whitney *U*-test; HC, healthy control; SZ, schizophrenia; h_{max}, Hölder exponent at the peak of the multifractal spectrum; *FWHM*, full width at half maximum; *mPE*, modified permutation entropy.

direct comparison would be difficult to make. Furthermore, the exact origins and physiological functions of wake delta-band oscillations are still debated (Dang-Vu et al., 2008; Harmony, 2013). It has been shown, that activity of resting-state networks (RSNs) reconstructed from fMRI dynamics can be attributed to not one but multiple EEG rhythms to various extents and that each RSN could be characterized with a unique set of correlations with different frequency bands (Mantini et al., 2007).

For most RSNs, that largely overlap with many of the intrinsic connectivity networks (ICNs) identified by the approach of Yu et al. (2015) and Du et al. (2016), the highest correlations were found with the alpha and beta bands. Thus, it can be hypothesized that activity of these RSNs more closely resembles alpha- and/or beta- rather than delta-band activity. In order to test this hypothesis, we carried out our analysis pipeline on alpha- and beta-filtered (8–13 Hz and 13–30 Hz, respectively) EEG data as well. The analysis showed no significant differences between HC and SZ connectivity dynamics in the alpha band, while a slight (but insignificant) tendency of higher static and mean C was found in the beta band of SZ patients. On the other hand, it has been argued (Knyazev, 2012; Harmony, 2013) that waking delta activity originates not only from thalamocortical neurons (Hughes et al., 1998) but also from regions associated with the default mode network (DMN) (Raichle et al., 2001). Enhanced connectivity between thalamic and DMN regions in SZ was reported by multiple studies earlier (Skudlarski et al., 2010; Damaraju et al., 2014). In accordance with previous studies, our results of cortical delta-band dysconnectivity therefore may reflect the large-scale consequences of the involvement of these structures in SZ. Moreover, delta-band dysconnectivity in SZ also fits in with the hypothesis considering the role of wake delta rhythm in motivational, cognitive and autonomous functions (Knyazev, 2007, 2012), as these are broadly affected in SZ (Insel, 2010).

Another plausible source of the apparent contradiction between results reported in this study and those of previous works is the heterogeneous nature of SZ itself as a clinical condition (Seaton et al., 2001; Moran and Hong, 2011). It has been shown for example, that patients with various subtypes of SZ that could be characterized with largely different psychopathological symptoms expressed distinct, specific alterations in cortical electrophysiological activity (Harris et al., 2001). Likewise, several studies reported on characteristic differences in EEG findings between SZ phenotypes, i.e., those characterized mostly by positive and/or negative symptoms (Begic et al., 2000; John et al., 2009). Furthermore, brain electrical activity as assessed by EEG in SZ was shown to be affected by acute as well as chronic pharmaceutical treatment (Knott et al., 2001), the type of medication (Tislerova et al., 2008) and disease duration (Ranlund et al., 2014). These considerations, along with the drawback of no available clinical information of the subjects analyzed here, therefore prevents us to resolve this issue within the scope of this study.

Multifractality and Temporal Complexity of DFC in SZ

One of the main contributions of this study is reporting on the true multifractal nature of DFC in SZ and its alterations compared to healthy controls. Although scale-free aspects of DFC have been known for a while (Stam and de Bruin, 2004; Van de Ville et al., 2010), its true multifractal nature was confirmed only recently (Racz et al., 2018a,b). It is a matter of debate in the neuroscience field what aspect of brain function manifests in scale-free neurodynamics (He, 2014). A view shared by many is that scale-free fluctuations are the result of an underlying self-organized critical state of the brain that gives rise for its ability to perform large-scale reorganizations quickly in response to external/internal stimuli (Linkenkaer-Hansen et al., 2001; Bullmore et al., 2009; Chialvo, 2010; Beggs and Timme, 2012; Mukli et al., 2018). In support of this hypothesis, a close correspondence was shown by Racz et al. (2018a) between dynamic graph measures (node strength in particular) and the seminal sand pile model of self-organized criticality (Bak et al., 1987). It also has been shown that self-organized critical models can express a scaling exponent different from 1 (De Los Rios and Zhang, 1999), as well as not only mono- but indeed true multifractal dynamics can emerge from systems in a critical state (Lima et al., 2017). Based on these considerations, the increased h_{max} in SZ could reflect on the impaired ability of the brain to respond to stimuli incoming from the external or internal environment. Although this hypothesis requires further research in the future, investigation of the possible correspondence between h_{max} of DFC and the severity of symptoms related to altered perception in SZ appears an important question. Note however, that criticality is by no means the only feasible explanation for the scale-free nature of brain activity. It has been argued previously, that the apparent power-law spectra of local field potential recordings could result from the extracellular medium acting as a $1/f$ filter (Bedard et al., 2006; Bedard and Destexhe, 2009). However, this mechanism alone would not explain the presence of fractal scaling in a much broader range of neural phenomena (Beggs and Timme, 2012). Simulations indicate that slow cortical oscillations may exhibit fractal scaling due to the noisy nature of dynamical synapses with sufficiently large recovery times, i.e., the combined presence of stochasticity and synaptic fatigue is required for the emergence of power-law distributions (Mejias et al., 2010). Neutral theory has been recently proposed as a plausible explanation of scale-free neural dynamics (Martinello et al., 2017), in which multiple causal avalanches can coexist (producing power-law distributions of avalanche sizes and durations) without the system being tuned or self-organized to a critical point.

True multifractality often arises from various physiological processes as the result of multiple antagonistic feedback loops (Ivanov et al., 1998; Ashkenazy et al., 2002). Feedback mechanisms play a crucial role in the generation of neural oscillations and thus synchronization (Buzsaki and Draguhn, 2004). It has been shown that by suppressing feedback regulation by administering an autonomic blockade, heart rate variability loses its multifractal nature and reduces to simple monofractal dynamics (Amaral et al., 2001). On this basis, the higher degree of multifractality of DFC could indicate stronger neural feedback regulation in SZ. Recent findings attributed increased global delta synchrony to subthreshold activity of thalamocortical GABAergic neurons (Herrera et al., 2016). As mentioned above, the exact origins of waking delta rhythm are still unknown, however, these results also point to the direction that thalamocortical neurons may play an important role (Knyazev, 2012). Furthermore, many studies support evidence for the key role of the thalamus and thalamocortical dysfunction in the pathomechanism of SZ (see e.g., Murray and Anticevic, 2017 for a review). We found

increased delta connectivity as well as stronger multifractality in SZ that indeed could indicate that thalamocortical projections and feedback loops are affected, however, this hypothesis requires further research. From a more practical standpoint, multifractal dynamics often emerge from intermittent periods of larger variance due to multiplicative mechanisms (Ihlen and Vereijken, 2010), which in the terms of DFC can be understood as large-scale reorganizations of functional networks. Multiple studies argued that brain dynamics are actually more prominent during resting-state than in the presence of cognitive stimuli, as in wake rest internal thought processes and self-referential activities are unconstrained (Miall and Robertson, 2006; Deco et al., 2013). General thought processes are often distorted and disorganized in SZ patients that can be related to aberrant reorganization patterns in DFC captured as increased degree of multifractality; a plausible relationship yet to be elucidated.

Information-theoretical entropy-related measures (such as PE or SE) refer on the temporal complexity of the process with higher values implying more unpredictable behavior. Regional differences in PE has been shown to reflect the functional organization of the brain (Racz et al., 2019). It has also been reported recently that several dynamic connections of the amygdala show a decrease with aging in its complexity as measured by SE, however, this decrease was absent in patients suffering from SZ (Jia et al., 2017). Moreover, in many connections SE was higher in the HC than in the SZ group, implicating a lower dynamical complexity in the latter. Interestingly, in a subsequent study using the same dataset, the authors reported higher global SE in the SZ group that was later revealed to be the consequence of connections with higher SE in the visual recognition and auditory networks (Jia and Gu, 2019). These results may seem contradictory at first, nevertheless, in light of previous findings, they rather highlight the fact that FC dynamics vary greatly among brain regions (Racz et al., 2019) and that various regions could be affected in different ways in SZ. Our current results indicate a lower dynamical complexity of delta-band DFC in SZ. The rightful question arises of how the performance of entropy-related measures could be affected by the presence of long-range correlations. In an earlier study we found that regions with stronger autocorrelation expressed lower PE in their local FC dynamics and vice versa (Racz et al., 2019). However, according to Xiong et al. (2017) this cannot be simply a consequence of long-range autocorrelation, as it only introduces a constant bias that is independent of the degree of autocorrelation. A lower value of *mPE* implicates a lower variability in spatio-temporal patterns in a sense that the process, although varies over time, more prone to return to/repeat a specific subset of patterns instead of switching randomly between the full set. This is in line with previous DFC studies reporting that SZ patients are prone to visit fewer of the possible meta-states than HC subjects (Miller et al., 2014a,b).

It should be noted, that the obtained values for h_{max}, *FWHM,* and *mPE* all indicate the presence of complex temporal structuring in connectivity dynamics. In order to emphasize this, we generated $n = 100$ random dynamic networks with equal size to those reconstructed from EEG data, in which for each time point all edges were randomly drawn from a distribution approximating that of the edges of the original networks (a normal distribution with mean 0.3 and variance $3^{*}10^{-4}$). The networks were thresholded at $K = 0.35$. Network measures were calculated for every time point and then multifractal and entropy analyses were carried out using the same settings as previously. As expected, all obtained indices (h_{max}, *FWHM* and *mPE*) were found significantly different ($p < 10^{-8}$ in all cases) from those of real networks. In fact, they were found very similar to those acquired for random noise (shuffled) time series used in surrogate data testing ($h_{max} = 0.513 \pm 0.017$; $FWHM = 0.240 \pm 0.007$ and $mPE = 12.18 \pm 0.003$ with $p > 0.05$ in all cases expect ^{D}mPE of HC and $^{D}FWHM$, ^{D}mPE and $^{E}h_{max}$ of SZ). Notably, the same values were obtained for all three network measures. These results further emphasize that dynamic brain networks express complex temporal structuring, which is absent in dynamic networks with randomly fluctuating connection patterns.

While the SL- and PLI-based analyses led to largely similar results, some differences found regarding the cost-dependence of fractal properties and *mPE* are worth noticing (see **Figure 6** and **Supplementary Figure 4**). Namely, increasing the cost thus including more of the weaker connections led to an increase of $^{C}h_{max}$ and decrease of ^{C}mPE in SL-derived dynamic networks. In contrast, the opposite pattern emerged in networks reconstructed from the PLI-based analysis. This implies that weak links in PLI networks introduce new information (that can also be understood as increased unpredictability) to network dynamics, while weaker links in SL analysis carry redundant information as their inclusion reduces dynamical complexity and increases autocorrelation. In other words, it seems as weaker links destabilize PLI but stabilize SL networks. This is indeed an interesting finding from the perspective of dynamic networks and requires further research.

Automated Classification of Patients With SZ

One of the major critiques of the FC field is that although it was able to reveal characteristic alterations of various diseases on the group level, its actual utility in the diagnosis of individual cases is yet to be shown (Papo et al., 2014). Thus, recently more and more studies attempt to utilize SFC and DFC features to build classifiers in order to explore their true utility, especially in the diagnosis and differential diagnosis of SZ (Calhoun et al., 2008; Arbabshirani et al., 2013; Du et al., 2015; Kim et al., 2016; Rashid et al., 2016). Our model was able to reach a high cross-validation performance, comparable to those of most recent reports. Additionally, this high-level performance could be replicated when using AUC features from the PLI-based analysis (**Supplementary Table 5**). Note that many studies reported performance results surpassing ours, however all of these studies worked with larger sample sizes. On the other hand, a study working with the exact same dataset made available by Olejarczyk and Jernajczyk (2017) was able to reach a 71.4% accuracy and 80% balanced accuracy using an RFC model and narrow-band power values as features (Buettner et al., 2019). In a subsequent report, using data augmentation by segmenting the data sets into 1 min epochs, thus arbitrarily increasing sample size, the

same group reported an outstanding 96.8% accuracy (Buettner et al., 2020). Oh et al. (2019) also used the same dataset and fit a convolutional neural network model on EEG data to classify HC and SZ subjects. They also divided the data into 25 s long epochs and were able to reach 98.1% accuracy. Although these results highlight the importance of a large sample size, the reported high accuracies may be biased, as the epochs used in the training and test sets were not independent (i.e., segments acquired from the same subject could be present both in the training and test sets). Namely, this way the classifiers could also learn and use subject-specific patterns for classification of the epochs. This is supported by the fact that when Oh and colleagues used a cross-validation scheme where data was split on a subject-based manner (i.e., epochs of each subject only appeared in either the training, validation or test sets), the accuracy of their model dropped to 81.3% (Oh et al., 2019). Considering the small size of the dataset, even though our classifiers performed reasonably well, it is unlikely that they would generalize well to real world-data. Therefore, we rather considered the RFC model as a tool for exploring which features are the most important for classification. From our results, it is apparent that static FC measures carry less, though still relevant information when compared to dynamic indices. On the other hand, ${}^{C}h_{max}$, ${}^{C}mPE$, and ${}^{C}FWHM$ appear promising indices of DFC besides the more commonly used σ^2. Nevertheless, the results reported here are essentially in agreement with those of previous studies reporting on the superiority of DFC- over SFC-derived features (Rashid et al., 2016).

Comparison With Existing Methods

In order to further clarify the advantages and plausible disadvantages of our analytical pipeline, it is indispensable to compare it with those already published in the literature. Since it could be inconclusive to draw correspondences between DFC approaches with vastly different methodologies, here we selected three previous studies utilizing dynamic graph theoretical analysis for comparison, namely those of Dimitriadis et al. (2010), Tagliazucchi et al. (2012), and Yu et al. (2015). The summary of the details is shown in **Table 7**. Similarly to our study, Dimitriadis et al. (2010) used EEG for monitoring brain activity, while Tagliazucchi et al. (2012) and Yu et al. (2015) estimated connectivity dynamics based on fMRI measurements. This – among other specifics such as sampling rate or temporal resolution – inherently influenced how nodes of the reconstructed networks were defined. In the EEG-based approaches nodes corresponded to recording sites (EEG channels), while Tagliazucchi et al. (2012) selected 90 cortical and subcortical regions according to the Automated Anatomical Labeling template (Tzourio-Mazoyer et al., 2002) and Yu et al. (2015) investigated connectivity between 48 ICNs (sets of brain regions forming functional units). All studies utilized a sliding window approach; however, in both EEG-based studies the window length was adaptively defined to fit the frequency characteristics of the data, while in the fMRI studies it was set according to empirical considerations. The advantages of the adaptive approach are that it reduces the number of subjective parameters of the analysis pipeline, as well as it always yields a complete characterization of the dynamics, while a short time window (e.g., 40 s) prevents slow fluctuations to fully manifest, especially if the data is filtered (e.g., between 0.01 and 0.1 Hz). Most fMRI-based DFC approaches use Pearson cross-correlation (or an inherently related similarity index such as in Yu et al., 2015) as FC estimator, that only allows for the identification of linear interactions. On the other hand, Dimitriadis et al. (2010) computed dynamic Phase-Locking Index, while in this study we used Synchronization Likelihood for DFC estimation and PLI (and WPLI) for verification. These latter measures are able to capture non-linear interactions, which is considered as an inherent feature of functional coupling between neuronal assemblies (Friston, 2000). Note, that all three studies discussed here utilized only one FC estimator and did not validate their results with a different method. All studies took different approaches for network thresholding except for that of Yu et al. (2015), where no additional threshold was applied. Dimitriadis et al. (2010) introduced a novel algorithmic technique for the objective selection of the most relevant edges, while similarly to our approach Tagliazucchi et al. (2012) used cost thresholding. However, while in the latter case the authors selected only one cost value ($K = 0.1$) here we also explored the effect of cost on network dynamics, which were revealed to be significant and characteristic to the FC estimator used, as discussed previously. All studies characterized the reconstructed networks with mostly similar network measures (see **Table 7**), with the larger number of nodes also allowing Tagliazucchi et al. (2012) to estimate more sophisticated network characteristics such as betweenness centrality. In this aspect our study is clearly the most constrained among those discussed here, operating on networks with the smallest number of nodes. Network size inherently limits the set of graph theoretical measures that could reasonably be used for network characterization (Rubinov and Sporns, 2010; van Wijk et al., 2010), however previous results suggest that D, C, and E could still provide valuable information even in case of small networks (Racz et al., 2017). Finally, in all studies the acquired NMTSs were analyzed in different fashions and utilized for various purposes. Dimitriadis et al. (2010) utilized the technique of replicator dynamics to identify consistent hub regions of cortical structures. Tagliazucchi et al. (2012) used correlation analysis to unfold the electrophysiological correlates of fMRI-based connectivity fluctuations. Finally, Yu et al. (2015) identified altered connectivity dynamics and patterns in SZ patients when compared to HC subjects. A common pattern of the aforementioned three studies though is that dynamic graph theoretical measures were finally reduced to their mean, while their dynamics were characterized by their variance or standard deviation (see **Table 7**).

Accordingly, one of the main contribution of our approach lies with the analysis of the multiscale and information-theoretical aspects of connectivity dynamics. Although the studies discussed above all provided valuable insights on physiological and pathological brain function, they mainly neglected the already established scale-free nature of DFC (Stam and de Bruin, 2004; Racz et al., 2018a,b). On the other hand, our approach reveals the complex temporal structuring of connectivity fluctuations that otherwise remain undetected for most approaches. The

TABLE 7 | Comparison of various DFC approaches based on dynamic graph-theoretical analysis.

	Dimitriadis et al.	Tagliazucchi et al.	Yu et al.	Racz et al.
Modality	EEG	fMRI	fMRI	EEG
Node definition	Recording sites	AAL-defined brain regions	Intrinsic connectivity networks	Recording sites
Number of nodes	$N = 30$	$N = 90$	$N = 48$	$N = 19$
Window length	Adaptive to frequency range	60TRs (≈2 min)	20 TRs (40 s)	Adaptive to frequency range
Connectivity estimator	Phase-Locking Index	Pearson cross-correlation	Similarity index	Synchronization Likelihood, Phase Lag Index
Thresholding	Algorithmic identification of most significant edges	Cost thresholding at $K = 0.1$	No thresholding	Cost thresholding with K ranging from 0.15 to 0.5
Network measures	Global efficiency, local efficiency, small-worldness	Clustering coefficient, average path length, betweenness, small-worldness	Connectivity strength, clustering coefficient, global efficiency	Connectivity strength, clustering coefficient, global efficiency
Analysis	Mean Identification of consistent hubs by using the technique of replicator dynamics	Standard deviation Correlations of time-varying graph measures with dynamic frontal-, central- and occipital band-limited power	Variance Identification of reoccurring connectivity states	Mean, variance, *EfM* Scale-free (multifractal) analysis Temporal complexity (information content)

EEG, electroencephalography; fMRI, functional magnetic resonance imaging; N, number of nodes; K, cost; EfM, excursions from median.

results presented here not only provide further confirmation that multifractality is an inherent property of brain dynamics, but also demonstrate that multifractal and entropy-related properties of DFC could carry significant clinical potential. In that, they could not only be utilized as disease biomarkers but may also provide further insights on the underlying mechanisms of neuropsychiatric morbidities. Note that the methodology implemented here for reconstructing time-varying brain graphs does not differ substantially from those of previous approaches. Consequently, the framework put forward in this study is readily adaptable for other DFC studies utilizing different imaging techniques or investigating neuropsychiatric disorders other than SZ.

Limitations and Future Directions

Clearly, the most severe drawback of the present work is the lack of clinical data on SZ subjects such as illness duration, medication or positive and negative symptom scores. Although we revealed several differences between HC and SZ groups, the physiological bases of these findings remain elusive until their correspondence with clinical symptoms is investigated. Furthermore, simultaneous fMRI-EEG measurements would be also important not only for unfolding the neural basis of delta synchronization but to reconcile contradictory results within the FC field. The low spatial resolution (19 regions) is the source of yet another limitation. A replication of this study using high-density EEG (e.g., 128 or even 256 channels) would benefit from a more detailed functional network reconstruction and also allow for reliable source reconstruction with a reasonable spatial resolution (although source reconstruction can be performed using only 19 channels as well (e.g., Vecchio et al., 2020). This way plausible volume conduction effects could be further reduced and information could be gained on the involvement of specific – even subcortical – brain regions as well, thereby enhancing the interpretation of the results. A high-density setup would also allow for detailed local connectivity analyses which appear increasingly relevant in the light of recent advancements recognizing the importance of not only temporal, but spatial- and spatiotemporal patterns in DFC (Iraji et al., 2020). Specifically, it has been demonstrated by previous studies that regional alterations of DFC could play a relevant role in SZ (Damaraju et al., 2014; Jia et al., 2017; Jia and Gu, 2019), which may will be overlooked when investigating network characteristics on the global level only. Considering in addition, that multiscale and entropy-related properties of DFC were shown to express significant regional variability over the cortex (Racz et al., 2019), an extension of the current framework to the analysis of local connectivity dynamics appears as an important future research direction. In this study, only datasets of 14-14 HC individuals and SZ patients were analyzed, that limits the applicability and power of machine learning classifiers. Most importantly, using datasets of a larger sample size would allow for a train-test split scenario where the training data itself would be sufficient to perform the cross-validation and thus would allow fine-tuning of model parameters before evaluating the true model performance on previously unseen data. Small sample size also limits to some extent the possible number of features that can be used in a model. Although solutions (such as penalization in case of logistic regression or the "dropout" technique in case of neural networks) exist to circumvent this problem and prevent overfitting, in most cases it is accepted as a rule of thumb that for reliable performance the number of cases should surpass the number of features in a model (Hastie et al., 2009). Thus, increasing the sample size would also permit the inclusion of other, non-connectivity derived predictors commonly used in EEG analysis such as band-limited power. Multifractal indices appeared as important predictors, however a drawback of fractal- and especially multifractal analysis is that it requires sufficiently long (i.e., at least a few thousand data points) signals to obtain reliable estimates (Eke et al., 2000; Mukli et al., 2015). This makes

multifractal analysis unfeasible for fMRI-based DFC analyses, where time series are usually in the range of hundreds of data points. Note, that PE (and *mPE*) does not suffer from this limitation (Bandt and Pompe, 2002) and is readily applicable to short time series as well. It is important to highlight that the analysis pipeline was designed deliberately to be fully automatized. This includes steps of pre-processing as well as parameter settings of the applied analysis methods that were defined based on purely data-driven considerations, thus the procedure could be easily applied to different datasets. This greatly enhances the potential of the proposed pipeline for clinical applications, as in clinical settings practicality is an important aspect. Finally, the utility of potential biomarkers lies with not only in separating healthy from patient groups but also in differentiating between diseases with similar and/or overlapping clinical manifestations, such as schizophrenia, bipolar disorder and schizoaffective diseases. Thus, further work is required to investigate disease-related alterations of the dynamic indices proposed in this study in neuropsychiatric morbidities and conditions other than schizophrenia.

CONCLUSION

In summary, by applying dynamic graph theoretical analysis to EEG signals, we found delta-band dysconnectivity in patients with SZ. The SZ group expressed higher average and variance of network measures when compared to HC. Moreover, here we first report the multifractal nature of DFC in SZ that expressed stronger fractal scaling and degree of multifractality than in healthy controls. In accordance with previous studies, lower temporal complexity of DFC in SZ was captured with *mPE* analysis. Random forest classifiers indicated that indices of complexity, such as multifractality and entropy were amongst the most important predictors of the disease. This implies that these features carry great potential as biomarkers of SZ for future studies, that could facilitate its biologically- rather than symptom-based diagnosis and progression monitoring.

DATA AVAILABILITY STATEMENT

All datasets presented in this study are included in the article/**Supplementary Material**.

ETHICS STATEMENT

The studies involving human participants were reviewed and approved by the Ethics Committee of the Institute of Psychiatry and Neurology in Warsaw. The patients/participants provided their written informed consent to participate in this study.

AUTHOR CONTRIBUTIONS

FR designed the study and the analysis framework, performed the analyses and implementation, wrote the first draft of the manuscript, and prepared all figures and tables. OS contributed to the data preprocessing and manuscript development. PM contributed to the statistical analyses, data visualization, and manuscript development. AE provided conceptual guidance during the study and contributed to the manuscript development. All authors contributed to, reviewed and gave approval on the final version of the manuscript.

FUNDING

FR and PM were partially funded by the "Development of scientific workshops for medical, health sciences and pharmaceutical training" project (EFOP-3.6.3-VEKOP-16-2017-00009).

ACKNOWLEDGMENTS

We express their gratitude to Elzbieta Olejarczyk and Wojciech Jernajczyk for the EEG data analyzed in this study.

SUPPLEMENTARY MATERIAL

The Supplementary Material for this article can be found online at: https://www.frontiersin.org/articles/10.3389/fnsys.2020.00049/full#supplementary-material

REFERENCES

Achard, S., and Bullmore, E. T. (2007). Efficiency and cost of economical brain functional networks. *PLoS Comput. Biol.* 3:e17. doi: 10.1371/journal.pcbi.0030017

Allen, E. A., Damaraju, E., Plis, S. M., Erhardt, E. B., Eichele, T., and Calhoun, V. D. (2014). Tracking whole-brain connectivity dynamics in the resting state. *Cereb. Cortex* 24, 663–676. doi: 10.1093/cercor/bhs352

Amaral, L. A. N., Ivanov, P. C., Aoyagi, N., Hidaka, I., Tomono, S., Goldberger, A. L., et al. (2001). Behavioral-independent features of complex heartbeat dynamics. *Phys. Rev. Lett.* 86, 6026–6029. doi: 10.1103/PhysRevLett.86.6026

Arbabshirani, M. R., Kiehl, K. A., Pearlson, G. D., and Calhoun, V. D. (2013). Classification of schizophrenia patients based on resting-state functional network connectivity. *Front. Neurosci.* 7:133. doi: 10.3389/fnins.2013.00133

Archer, K. J., and Kirnes, R. V. (2008). Empirical characterization of random forest variable importance measures. *Comput. Stat. Data Anal.* 52, 2249–2260. doi: 10.1016/j.csda.2007.08.015

Ashkenazy, Y., Hausdorff, J. M., Ivanov, P. C., and Stanley, H. E. (2002). A stochastic model of human gait dynamics. *Physica A Stat. Mech. Appl.* 316, 662–670. doi: 10.1016/S0378-4371(02)01453-X

Bak, P., Tang, C., and Wiesenfeld, K. (1987). Self-organized criticality: an explanation of the 1/f noise. *Phys. Rev. Lett.* 59, 381–384. doi: 10.1103/PhysRevLett.59.381

Bandt, C., and Pompe, B. (2002). Permutation entropy: a natural complexity measure for time series. *Phys. Rev. Lett.* 88:174102. doi: 10.1103/PhysRevLett.88.174102

Bedard, C., and Destexhe, A. (2009). Macroscopic models of local field potentials and the apparent 1/f noise in brain activity. *Biophys. J.* 96, 2589–2603. doi: 10.1016/j.bpj.2008.12.3951

Bedard, C., Kroger, H., and Destexhe, A. (2006). Does the 1/f frequency scaling of brain signals reflect self-organized critical states? *Phys. Rev. Lett.* 97:118102. doi: 10.1103/PhysRevLett.97.118102

Beggs, J. M., and Timme, N. (2012). Being critical of criticality in the brain. *Front. Physiol.* 3:63. doi: 10.3389/fphys.2012.00163

Begic, D., Hotujac, L., and Jokic-Begic, N. (2000). Quantitative EEG in 'positive' and 'negative' schizophrenia. *Acta Psychiatr. Scand.* 101, 307–311. doi: 10.1111/j.1600-0447.2000.tb10930.x

Benjamini, Y., and Hochberg, Y. (1995). Controlling the false discovery rate - a practical and powerful approach to multiple testing. *J. R. Stat. Soc. Ser. B Stat. Methodol.* 57, 289–300. doi: 10.1111/j.2517-6161.1995.tb02031.x

Bhugra, D. (2005). The global prevalence of schizophrenia. *PLoS Med.* 2:e151. doi: 10.1371/journal.pmed.0020151

Bian, C., Qin, C., Ma, Q. D., and Shen, Q. (2012). Modified permutation-entropy analysis of heartbeat dynamics. *Phys. Rev. E Stat. Nonlin. Soft Matter. Phys.* 85(2 Pt 1), 021906. doi: 10.1103/PhysRevE.85.021906

Boutros, N. N., Arfken, C., Galderisi, S., Warrick, J., Pratt, G., and Iacono, W. (2008). The status of spectral EEG abnormality as a diagnostic test for schizophrenia. *Schizophr. Res.* 99, 225–237. doi: 10.1016/j.schres.2007.11.020

Breiman, L. (2001). Random forests. *Mach. Learn.* 45, 5–32. doi: 10.1023/A:1010933404324

Buettner, R., Beil, D., Scholz, S., and Djemai, A. (2020). "Development of a machine learning based algorithm to accurately detect schizophrenia based on one-minute EEG recordings," in *Proceedings of the Hawaii International Conference on System Sciences HICSS-53*, Maui, HI.

Buettner, R., Hirschmiller, M., Schlosser, K., Rössle, M., Fernandes, M., and Timm, I. J. (2019). "High-performance exclusion of schizophrenia using a novel machine learning method on EEG data," in *Proceedings of the IEEE International Conference on E-health Networking, Application & Services*, Bogotaì.

Bullmore, E., Barnes, A., Bassett, D. S., Fornito, A., Kitzbichler, M., Meunier, D., et al. (2009). Generic aspects of complexity in brain imaging data and other biological systems. *Neuroimage* 47, 1125–1134. doi: 10.1016/j.neuroimage.2009.05.032

Bullmore, E., and Sporns, O. (2009). Complex brain networks: graph theoretical analysis of structural and functional systems. *Nat. Rev. Neurosci.* 10, 186–198. doi: 10.1038/nrn2575

Bullmore, E. T., Frangou, S., and Murray, R. M. (1997). The dysplastic net hypothesis: an integration of developmental and dysconnectivity theories of schizophrenia. *Schizophr. Res.* 28, 143–156. doi: 10.1016/S0920-9964(97)00114-X

Buzsaki, G., and Draguhn, A. (2004). Neuronal oscillations in cortical networks. *Science* 304, 1926–1929. doi: 10.1126/science.1099745

Calhoun, V. D., Eichele, T., and Pearlson, G. (2009). Functional brain networks in schizophrenia: a review. *Front. Hum. Neurosci.* 3:17. doi: 10.3389/neuro.09.017.2009

Calhoun, V. D., Maciejewski, P. K., Pearlson, G. D., and Kiehl, K. A. (2008). Temporal lobe and "default" hemodynamic brain modes discriminate between schizophrenia and bipolar disorder. *Hum. Brain Mapp.* 29, 1265–1275. doi: 10.1002/hbm.20463

Calhoun, V. D., Miller, R., Pearlson, G., and Adali, T. (2014). The Chronnectome: time-varying connectivity networks as the next frontier in fMRI data discovery. *Neuron* 84, 262–274. doi: 10.1016/j.neuron.2014.10.015

Chang, C., and Glover, G. H. (2010). Time-frequency dynamics of resting-state brain connectivity measured with fMRI. *Neuroimage* 50, 81–98. doi: 10.1016/j.neuroimage.2009.12.011

Chialvo, D. R. (2010). Emergent complex neural dynamics. *Nat. Phys.* 6, 744–750. doi: 10.1038/Nphys1803

Damaraju, E., Allen, E. A., Belger, A., Ford, J. M., McEwen, S., Mathalon, D. H., et al. (2014). Dynamic functional connectivity analysis reveals transient states of dysconnectivity in schizophrenia. *Neuroimage Clin.* 5, 298–308. doi: 10.1016/j.nicl.2014.07.003

Dang-Vu, T. T., Schabus, M., Desseilles, M., Albouy, G., Boly, M., Darsaud, A., et al. (2008). Spontaneous neural activity during human slow wave sleep. *Proc. Natl. Acad. Sci. U.S.A.* 105, 15160–15165. doi: 10.1073/pnas.0801819105

De Los Rios, P., and Zhang, Y. C. (1999). Universal 1/f noise from dissipative self-organized criticality models. *Phys. Rev. Lett.* 82, 472–475. doi: 10.1103/PhysRevLett.82.472

Deco, G., Ponce-Alvarez, A., Mantini, D., Romani, G. L., Hagmann, P., and Corbetta, M. (2013). Resting-state functional connectivity emerges from structurally and dynamically shaped slow linear fluctuations. *J. Neurosci.* 33, 11239–11252. doi: 10.1523/Jneurosci.1091-13.2013

Delorme, A., and Makeig, S. (2004). EEGLAB: an open source toolbox for analysis of single-trial EEG dynamics including independent component analysis. *J Neurosci Methods* 134, 9–21. doi: 10.1016/j.jneumeth.2003.10.009

Dimitriadis, S. I. (2019). Multiplexity and graph signal processing of EEG dynamic functional connectivity networks as connectomic biomarkers for schizophrenia patients: a whole brain breakdown. *bioRxiv* [Preprint]. doi: 10.1101/551671

Dimitriadis, S. I., Laskaris, N. A., Tsirka, V., Vourkas, M., Micheloyannis, S., and Fotopoulos, S. (2010). Tracking brain dynamics via time-dependent network analysis. *J. Neurosci. Methods* 193, 145–155. doi: 10.1016/j.jneumeth.2010.08.027

Du, Y. H., Fryer, S. L., Fu, Z., Lin, D., Sui, J., Chen, J., et al. (2018). Dynamic functional connectivity impairments in early schizophrenia and clinical high-risk for psychosis. *Neuroimage* 180, 632–645. doi: 10.1016/j.neuroimage.2017.10.022

Du, Y. H., Pearlson, G. D., Liu, J. Y., Sui, J., Yu, Q. B., He, H., et al. (2015). A group ICA based framework for evaluating resting fMRI markers when disease categories are unclear: application to schizophrenia, bipolar, and schizoaffective disorders. *Neuroimage* 122, 272–280. doi: 10.1016/j.neuroimage.2015.07.054

Du, Y. H., Pearlson, G. D., Yu, Q. B., He, H., Lin, D. D., Sui, J., et al. (2016). Interaction among subsystems within default mode network diminished in schizophrenia patients: a dynamic connectivity approach. *Schizophr. Res.* 170, 55–65. doi: 10.1016/j.schres.2015.11.021

Eke, A., Herman, P., Bassingthwaighte, J. B., Raymond, G. M., Percival, D. B., Cannon, M., et al. (2000). Physiological time series: distinguishing fractal noises from motions. *Pflugers Arch.* 439, 403–415. doi: 10.1007/s004240050957

Fox, M. D., and Greicius, M. (2010). Clinical applications of resting state functional connectivity. *Front. Syst. Neurosci.* 4:19. doi: 10.3389/fnsys.2010.00019

Friston, K., Brown, H. R., Siemerkus, J., and Stephan, K. E. (2016). The dysconnection hypothesis (2016). *Schizophr. Res.* 176, 83–94. doi: 10.1016/j.schres.2016.07.014

Friston, K. J. (2000). The labile brain. I. Neuronal transients and nonlinear coupling. *Philos. Trans. R. Soc. Lond. B Biol. Sci.* 355, 215–236. doi: 10.1098/rstb.2000.0560

Friston, K. J., and Frith, C. D. (1995). Schizophrenia - a disconnection syndrome. *Clin. Neurosci.* 3, 89–97.

Friston, K. J., Frith, C. D., Liddle, P. F., and Frackowiak, R. S. (1993). Functional connectivity: the principal-component analysis of large (PET) data sets. *J. Cereb. Blood Flow Metab.* 13, 5–14. doi: 10.1038/jcbfm.1993.4

Gabard-Durnam, L. J., Leal, A. S. M., Wilkinson, C. L., and Levin, A. R. (2018). The harvard automated processing pipeline for electroencephalography (HAPPE): standardized processing software for developmental and high-artifact data. *Front. Neurosci.* 12:97. doi: 10.3389/fnins.2018.00097

Grech, D., and Pamula, G. (2012). Multifractal background noise of monofractal signals. *Acta Physica Polonica A* 121, B34–B39.

Harmony, T. (2013). The functional significance of delta oscillations in cognitive processing. *Front. Integr. Neurosci.* 7:83. doi: 10.3389/fnint.2013.00083

Harris, A. W. F., Bahramali, H., Slewa-Younan, S., Gordon, E., Williams, L., and Li, W. M. (2001). The topography of quantified electroencephalography in three syndromes of schizophrenia. *Int. J. Neurosci.* 107, 265–278. doi: 10.3109/00207450109150689

Hastie, T., Tibshirani, R., and Friedman, J. H. (2009). *The Elements of Statistical Learning : Data Mining, Inference, and Prediction*. New York, NY: Springer.

He, B. Y. J. (2014). Scale-free brain activity: past, present, and future. *Trends Cogn. Sci.* 18, 480–487. doi: 10.1016/j.tics.2014.04.003

He, Y., Dagher, A., Chen, Z., Charil, A., Zijdenbos, A., Worsley, K., et al. (2009). Impaired small-world efficiency in structural cortical networks in multiple sclerosis associated with white matter lesion load. *Brain* 132(Pt 12), 3366–3379. doi: 10.1093/brain/awp089

Herman, P., Sanganahalli, B. G., Hyder, F., and Eke, A. (2011). Fractal analysis of spontaneous fluctuations of the BOLD signal in rat brain. *Neuroimage* 58, 1060–1069. doi: 10.1016/j.neuroimage.2011.06.082

Herrera, C. G., Cadavieco, M. C., Jego, S., Ponomarenko, A., Korotkova, T., and Adamantidis, A. (2016). Hypothalamic feedforward inhibition of thalamocortical network controls arousal and consciousness. *Nat. Neurosci.* 19, 290–298. doi: 10.1038/nn.4209

Hindriks, R., Adhikari, M. H., Murayama, Y., Ganzetti, M., Mantini, D., Logothetis, N. K., et al. (2016). Can sliding-window correlations reveal dynamic functional connectivity in resting-state fMRI? (vol 127, pg 242, 2016). *Neuroimage* 132:115. doi: 10.1016/j.neuroimage.2016.02.007

Hughes, S. W., Cope, D. W., and Crunelli, V. (1998). Dynamic clamp study of I-h modulation of burst firing and delta oscillations in thalamocortical neurons in vitro. *Neuroscience* 87, 541–550. doi: 10.1016/S0306-4522(98)00170-5

Hutchison, R. M., Womelsdorf, T., Gati, J. S., Everling, S., and Menon, R. S. (2013). Resting-state networks show dynamic functional connectivity in awake humans and anesthetized macaques. *Hum. Brain Mapp.* 34, 2154–2177. doi: 10.1002/hbm.22058

Ihlen, E. A., and Vereijken, B. (2010). Interaction-dominant dynamics in human cognition: beyond 1/f(alpha) fluctuation. *J. Exp. Psychol. Gen.* 139, 436–463. doi: 10.1037/a0019098

Insel, T. R. (2010). Rethinking schizophrenia. *Nature* 468, 187–193. doi: 10.1038/nature09552

Iraji, A., Miller, R., Adali, T., and Calhoun, V. D. (2020). Space: a missing piece of the dynamic puzzle. *Trends Cogn. Sci.* 24, 135–149. doi: 10.1016/j.tics.2019.12.004

Ivanov, P., Nunes Amaral, L. A., Goldberger, A. L., and Stanley, H. E. (1998). Stochastic feedback and the regulation of biological rhythms. *Europhys. Lett.* 43, 363–368. doi: 10.1209/epl/i1998-00366-3

Jafri, M. J., Pearlson, G. D., Stevens, M., and Calhoun, V. D. (2008). A method for functional network connectivity among spatially independent resting-state components in schizophrenia. *Neuroimage* 39, 1666–1681. doi: 10.1016/j.neuroimage.2007.11.001

Jalili, M. (2016). Functional brain networks: Does the choice of dependency estimator and Binarization method matter? *Sci. Rep.* 6:29780. doi: 10.1038/srep29780

Jia, Y. B., and Gu, H. G. (2019). Identifying nonlinear dynamics of brain functional networks of patients with schizophrenia by sample entropy. *Nonlinear Dyn.* 96, 2327–2340. doi: 10.1007/s11071-019-04924-8

Jia, Y. B., Gu, H. G., and Luo, Q. (2017). Sample entropy reveals an age-related reduction in the complexity of dynamic brain. *Sci. Rep.* 7:7990. doi: 10.1038/s41598-017-08565-y

John, J. P., Rangaswamy, M., Thennarasu, K., Khanna, S., Nagaraj, R. B., Mukundan, C. R., et al. (2009). EEG power spectra differentiate positive and negative subgroups in neuroleptic-naive schizophrenia patients. *J. Neuropsychiatry Clin. Neurosci.* 21, 160–172. doi: 10.1176/jnp.2009.21.2.160

Kam, J. W. Y., Bolbecker, A. R., O'Donnell, B. F., Hetrick, W. P., and Brenner, C. A. (2013). Resting state EEG power and coherence abnormalities in bipolar disorder and schizophrenia. *J. Psychiatr. Res.* 47, 1893–1901. doi: 10.1016/j.jpsychires.2013.09.009

Kambeitz, J., Kambeitz-Ilankovic, L., Cabral, C., Dwyer, D. B., Calhoun, V. D., van den Heuvel, M. P., et al. (2016). Aberrant functional whole-brain network architecture in patients with schizophrenia: a meta-analysis. *Schizophr. Bull.* 42, S13–S21. doi: 10.1093/schbul/sbv174

Kantelhardt, J. W., Zschiegner, S. A., Koscielny-Bunde, E., Havlin, S., Bunde, A., and Stanley, H. E. (2002). Multifractal detrended fluctuation analysis of nonstationary time series. *Physica A Stat. Mech. Appl.* 316, 87–114. doi: 10.1016/S0378-4371(02)01383-3

Kim, J., Calhoun, V. D., Shim, E., and Lee, J. H. (2016). Deep neural network with weight sparsity control and pre-training extracts hierarchical features and enhances classification performance: evidence from whole-brain resting-state functional connectivity patterns of schizophrenia. *Neuroimage* 124, 127–146. doi: 10.1016/j.neuroimage.2015.05.018

Kim, J., Criaud, M., Cho, S. S., Díez-Cirarda, M., Mihaescu, A., Coakeley, S., et al. (2017). Abnormal intrinsic brain functional network dynamics in Parkinson's disease. *Brain* 140, 2955–2967. doi: 10.1093/brain/awx233

Knott, V., Labelle, A., Jones, B., and Mahoney, C. (2001). Quantitative EEG in schizophrenia and in response to acute and chronic clozapine treatment. *Schizophr. Res.* 50, 41–53. doi: 10.1016/S0920-9964(00)00165-1

Knyazev, G. G. (2007). Motivation, emotion, and their inhibitory control mirrored in brain oscillations. *Neurosci. Biobehav. Rev.* 31, 377–395. doi: 10.1016/j.neubiorev.2006.10.004

Knyazev, G. G. (2012). EEG delta oscillations as a correlate of basic homeostatic and motivational processes. *Neurosci. Biobehav. Rev.* 36, 677–695. doi: 10.1016/j.neubiorev.2011.10.002

Koshimori, Y., Cho, S. S., Criaud, M., Christopher, L., Jacobs, M., Ghadery, C., et al. (2016). Disrupted nodal and hub organization account for brain network abnormalities in Parkinson's disease. *Front. Aging Neurosci.* 8:259. doi: 10.3389/fnagi.2016.00259

Latora, V., and Marchiori, M. (2001). Efficient behavior of small-world networks. *Phys. Rev. Lett.* 87:198701. doi: 10.1103/PhysRevLett.87.198701

Levin, A. R., Leal, A. S. M., Gabard-Durnam, L. J., and O'Leary, H. M. (2018). BEAPP: the batch electroencephalography automated processing platform. *Front. Neurosci.* 12:513. doi: 10.3389/fnins.2018.00513

Li, K. M., Guo, L., Nie, J. X., Li, G., and Liu, T. M. (2009). Review of methods for functional brain connectivity detection using fMRI. *Comput. Med. Imaging Graph.* 33, 131–139. doi: 10.1016/j.compmedimag.2008.10.011

Lima, G., Corso, G., Correa, M. A., Sommer, R. L., Ivanov, P. C., and Bohn, F. (2017). Universal temporal characteristics and vanishing of multifractality in Barkhausen avalanches. *Phys. Rev. E* 96:022159. doi: 10.1103/PhysRevE.96.022159

Lindquist, M. (2020). Neuroimaging results altered by varying analysis pipelines. *Nature* 582, 36–37. doi: 10.1038/d41586-020-01282-z

Linkenkaer-Hansen, K., Nikouline, V. V., Palva, J. M., and Ilmoniemi, R. J. (2001). Long-range temporal correlations and scaling behavior in human brain oscillations. *J. Neurosci.* 21, 1370–1377. doi: 10.1523/jneurosci.21-04-01370.2001

Lombardi, A., Guaragnella, C., Amoroso, N., Monaco, A., Fazio, L., Taurisano, P., et al. (2019). Modelling cognitive loads in schizophrenia by means of new functional dynamic indexes. *Neuroimage* 195, 150–164. doi: 10.1016/j.neuroimage.2019.03.055

Ma, S., Calhoun, V. D., Phlypo, R., and Adali, T. (2014). Dynamic changes of spatial functional network connectivity in individuals and schizophrenia patients using independent vector analysis. *Neuroimage* 90, 196–206. doi: 10.1016/j.neuroimage.2013.12.063

Mantini, D., Perrucci, M. G., Del Gratta, C., Romani, G. L., and Corbetta, M. (2007). Electrophysiological signatures of resting state networks in the human brain. *Proc. Natl. Acad. Sci. U.S.A.* 104, 13170–13175. doi: 10.1073/pnas.0700668104

Maran, M., Grent, T., and Uhlhaas, P. J. (2016). Electrophysiological insights into connectivity anomalies in schizophrenia: a systematic review. *Neuropsychiatr. Electrophysiol.* 2:6.

Martinello, M., Hidalgo, J., Maritan, A., di Santo, S., Plenz, D., and Munoz, M. A. (2017). Neutral theory and scale-free neural dynamics. *Phys. Rev. X* 7:041071. doi: 10.1103/PhysRevX.7.041071

Mejias, J. F., Kappen, H. J., and Torres, J. J. (2010). Irregular dynamics in up and down cortical states. *PLoS One* 5:e13651. doi: 10.1371/journal.pone.0013651

Menze, B. H., Kelm, B. M., Masuch, R., Himmelreich, U., Bachert, P., Petrich, W., et al. (2009). A comparison of random forest and its Gini importance with standard chemometric methods for the feature selection and classification of spectral data. *BMC Bioinformatics* 10:213. doi: 10.1186/1471-2105-10-213

Miall, R. C., and Robertson, E. M. (2006). Functional imaging: is the resting brain resting? *Curr. Biol.* 16, R998–R1000. doi: 10.1016/j.cub.2006.10.041

Miller, R. L., Yaesoubi, M., and Calhoun, V. D. (2014a). "Higher dimensional analysis shows reduced dynamism of time-varying network connectivity in schizophrenia patients," in *Proceedings of the 2014 36th Annual International Conference of the IEEE Engineering in Medicine and Biology Society (EMBC)* (Piscataway, NJ: IEEE), 3837–3840.

Miller, R. L., Yaesoubi, M., Calhoun, V. D., and Gopal, S. (2014b). "Higher dimensional fMRI connectivity dynamics show reduced dynamism in schizophrenia patients," in *Proceedings of the 2014 International Workshop on Pattern Recognition in Neuroimaging*, Tubingen.

Montez, T., Linkenkaer-Hansen, K., van Dijk, B. W., and Stam, C. J. (2006). Synchronization likelihood with explicit time-frequency priors. *Neuroimage* 33, 1117–1125. doi: 10.1016/j.neuroimage.2006.06.066

Moran, L. V., and Hong, L. E. (2011). High vs low frequency neural oscillations in schizophrenia. *Schizophr. Bull.* 37, 659–663. doi: 10.1093/schbul/sbr056

Mukli, P., Nagy, Z., and Eke, A. (2015). Multifractal formalism by enforcing the universal behavior of scaling functions. *Phys. A Stat. Mech. Appl.* 417, 150–167. doi: 10.1016/j.physa.2014.09.002

Mukli, P., Nagy, Z., Racz, F. S., Herman, P., and Eke, A. (2018). Impact of healthy aging on multifractal hemodynamic fluctuations in the human prefrontal cortex. *Front. Physiol.* 9:1072. doi: 10.3389/fphys.2018.01072

Murray, J. D., and Anticevic, A. (2017). Toward understanding thalamocortical dysfunction in schizophrenia through computational models of neural circuit dynamics. *Schizophr. Res.* 180, 70–77. doi: 10.1016/j.schres.2016.10.021

Mutlu, A. Y., Bernat, E., and Aviyente, S. (2012). A signal-processing-based approach to time-varying graph analysis for dynamic brain network identification. *Comput. Math. Methods Med.* 2012:451516. doi: 10.1155/2012/451516

Nagy, Z., Mukli, P., Herman, P., and Eke, A. (2017). Decomposing multifractal crossovers. *Front. Physiol.* 8:533. doi: 10.3389/fphys.2017.00533

Newson, J. J., and Thiagarajan, T. C. (2019). EEG frequency bands in psychiatric disorders: a review of resting state studies. *Front. Hum. Neurosci.* 12:521. doi: 10.3389/fnhum.2018.00521

Nuwer, M. R., Comi, G., Emerson, R., Fuglsang-Frederiksen, A., Guerit, J. M., Hinrichs, H., et al. (1998). IFCN standards for digital recording of clinical EEG. The international federation of clinical neurophysiology. *Electroencephalogr. Clin. Neurophysiol.* 106, 259–261. doi: 10.1016/S0013-4694(97)00106-5

Oh, S. L., Vicnesh, J., Ciaccio, E. J., Yuvaraj, R., and Acharya, U. R. (2019). Deep convolutional neural network model for automated diagnosis of schizophrenia using EEG signals. *Appl. Sci.* 9:2870. doi: 10.3390/app9142870

Olejarczyk, E., and Jernajczyk, W. (2017). Graph-based analysis of brain connectivity in schizophrenia. *PLoS One* 12:e0188629. doi: 10.1371/journal.pone.0188629

Papo, D., Zanin, M., Pineda-Pardo, J. A., Boccaletti, S., and Buldu, J. M. (2014). Functional brain networks: great expectations, hard times and the big leap forward. *Philos. Trans. R. Soc. Lond. B Biol. Sci.* 369:20130525. doi: 10.1098/rstb.2013.0525

Preti, M. G., Bolton, T. A., and Van De Ville, D. (2017). The dynamic functional connectome: state-of-the-art and perspectives. *Neuroimage* 160, 41–54. doi: 10.1016/j.neuroimage.2016.12.061

Racz, F. S., Mukli, P., Nagy, Z., and Eke, A. (2017). Increased prefrontal cortex connectivity during cognitive challenge assessed by fNIRS imaging. *Biomed. Opt. Express* 8, 3842–3855. doi: 10.1364/BOE.8.003842

Racz, F. S., Mukli, P., Nagy, Z., and Eke, A. (2018a). Multifractal dynamics of resting-state functional connectivity in the prefrontal cortex. *Physiol. Meas.* 39:024003. doi: 10.1088/1361-6579/aaa916

Racz, F. S., Stylianou, O., Mukli, P., and Eke, A. (2018b). Multifractal dynamic functional connectivity in the resting-state brain. *Front. Physiol.*9:1704. doi: 10.3389/fphys.2018.01704

Racz, F. S., Stylianou, O., Mukli, P., and Eke, A. (2019). Multifractal and entropy analysis of resting-state electroencephalography reveals spatial organization in local dynamic functional connectivity. *Sci. Rep.* 9:13474. doi: 10.1038/s41598-019-49726-5

Raichle, M. E., MacLeod, A. M., Snyder, A. Z., Powers, W. J., Gusnard, D. A., and Shulman, G. L. (2001). A default mode of brain function. *Proc. Natl. Acad. Sci. U.S.A.* 98, 676–682. doi: 10.1073/pnas.98.2.676

Ranlund, S., Nottage, J., Shaikh, M., Dutt, A., Constante, M., Walshe, M., et al. (2014). Resting EEG in psychosis and at-risk populations - A possible endophenotype? *Schizophr. Res.* 153, 96–102. doi: 10.1016/j.schres.2013.12.017

Rashid, B., Arbabshirani, M. R., Damaraju, E., Cetin, M. S., Miller, R., Pearlson, G. D., et al. (2016). Classification of schizophrenia and bipolar patients using static and dynamic resting-state fMRI brain connectivity. *Neuroimage* 134, 645–657. doi: 10.1016/j.neuroimage.2016.04.051

Richman, J. S., and Moorman, J. R. (2000). Physiological time-series analysis using approximate entropy and sample entropy. *Am. J. Physiol. Heart Circ. Physiol.* 278, H2039–H2049.

Rubinov, M., and Sporns, O. (2010). Complex network measures of brain connectivity: uses and interpretations. *Neuroimage* 52, 1059–1069. doi: 10.1016/j.neuroimage.2009.10.003

Sakkalis, V. (2011). Review of advanced techniques for the estimation of brain connectivity measured with EEG/MEG. *Comput. Biol. Med.* 41, 1110–1117. doi: 10.1016/j.compbiomed.2011.06.020

Seaton, B. E., Goldstein, G., and Allen, D. N. (2001). Sources of heterogeneity in schizophrenia: the role of neuropsychological functioning. *Neuropsychol. Rev.* 11, 45–67. doi: 10.1023/A:1009013718684

Sheffield, J. M., and Barch, D. M. (2016). Cognition and resting-state functional connectivity in schizophrenia. *Neurosci. Biobehav. Rev.* 61, 108–120. doi: 10.1016/j.neubiorev.2015.12.007

Skudlarski, P., Jagannathan, K., Anderson, K., Stevens, M. C., Calhoun, V. D., Skudlarska, B. A., et al. (2010). Brain connectivity is not only lower but different in schizophrenia: a combined anatomical and functional approach. *Biol. Psychiatry* 68, 61–69. doi: 10.1016/j.biopsych.2010.03.035

Smitha, K. A., Raja, K. A., Arun, K. M., Rajesh, P. G., Thomas, B., Kapilamoorthy, T. R., et al. (2017). Resting state fMRI: a review on methods in resting state connectivity analysis and resting state networks. *Neuroradiol. J.* 30, 305–317. doi: 10.1177/1971400917697342

Stam, C. J., and de Bruin, E. A. (2004). Scale-free dynamics of global functional connectivity in the human brain. *Hum. Brain Mapp.* 22, 97–109. doi: 10.1002/hbm.20016

Stam, C. J., Nolte, G., and Daffertshofer, A. (2007). Phase lag index: assessment of functional connectivity from multi channel EEG and MEG with diminished bias from common sources. *Hum. Brain Mapp.* 28, 1178–1193. doi: 10.1002/hbm.20346

Stam, C. J., and van Dijk, B. W. (2002). Synchronization likelihood: an unbiased measure of generalized synchronization in multivariate data sets. *Physica D* 163, 236–251. doi: 10.1016/S0167-2789(01)00386-4

Staniek, M., and Lehnertz, K. (2008). Symbolic transfer entropy. *Phys. Rev. Lett.* 100:158101. doi: 10.1103/PhysRevLett.100.158101

Tagliazucchi, E., von Wegner, F., Morzelewski, A., Brodbeck, V., and Laufs, H. (2012). Dynamic BOLD functional connectivity in humans and its electrophysiological correlates. *Front. Hum. Neurosci.* 6:339. doi: 10.3389/fnhum.2012.00339

Takens, F. (1981). "Detecting strange attractors in turbulence," in *Dynamical Systems and Turbulence, Warwick 1980*, eds D. Rand and L.-S. Young (Berlin: Springer).

Tislerova, B., Brunovsky, M., Horacek, J., Novak, T., Kopecek, M., Mohr, P., et al. (2008). LORETA functional imaging in antipsychotic-naive and olanzapine-, clozapine- and risperidone-treated patients with schizophrenia. *Neuropsychobiology* 58, 1–10. doi: 10.1159/000154474

Tzourio-Mazoyer, N., Landeau, B., Papathanassiou, D., Crivello, F., Etard, O., Delcroix, N., et al. (2002). Automated anatomical labeling of activations in SPM using a macroscopic anatomical parcellation of the MNI MRI single-subject brain. *Neuroimage* 15, 273–289. doi: 10.1006/nimg.2001.0978

Uhlhaas, P. J., and Singer, W. (2010). Abnormal neural oscillations and synchrony in schizophrenia. *Nat. Rev. Neurosci.* 11, 100–113. doi: 10.1038/nrn2774

Van de Ville, D., Britz, J., and Michel, C. M. (2010). EEG microstate sequences in healthy humans at rest reveal scale-free dynamics. *Proc. Natl. Acad. Sci. U.S.A.* 107, 18179–18184. doi: 10.1073/pnas.1007841107

van den Heuvel, M. P., and Fornito, A. (2014). Brain Networks in Schizophrenia. *Neuropsychol. Rev.* 24, 32–48. doi: 10.1007/s11065-014-9248-7

van Wijk, B. C. M., Stam, C. J., and Daffertshofer, A. (2010). Comparing brain networks of different size and connectivity density using graph theory. *PLoS One* 5:e13701. doi: 10.1371/journal.pone.0013701

Vecchio, F., Miraglia, F., Judica, E., Cotelli, M., Alu, F., and Rossini, P. M. (2020). Human brain networks: a graph theoretical analysis of cortical connectivity normative database from EEG data in healthy elderly subjects. *Geroscience* 42, 575–584. doi: 10.1007/s11357-020-00176-2

Vinck, M., Oostenveld, R., van Wingerden, M., Battaglia, F., and Pennartz, C. M. A. (2011). An improved index of phase-synchronization for electrophysiological data in the presence of volume-conduction, noise and sample-size bias. *Neuroimage* 55, 1548–1565. doi: 10.1016/j.neuroimage.2011.01.055

Watts, D. J., and Strogatz, S. H. (1998). Collective dynamics of 'small-world' networks. *Nature* 393, 440–442. doi: 10.1038/30918

Winkler, I., Brandl, S., Horn, F., Waldburger, E., Allefeld, C., and Tangermann, M. (2014). Robust artifactual independent component classification for BCI practitioners. *J. Neural Eng.* 11:035013. doi: 10.1088/1741-2560/11/3/035013

Winkler, I., Haufe, S., and Tangermann, M. (2011). Automatic classification of artifactual ICA-components for artifact removal in EEG signals. *Behav. Brain Funct.* 7:30. doi: 10.1186/1744-9081-7-30

Winterer, G., Egan, M. F., Radler, T., Hyde, T., Coppola, R., and Weinberger, D. R. (2001). An association between reduced interhemispheric EEG coherence in the temporal lobe and genetic risk for schizophrenia. *Schizophr. Res.* 49, 129–143. doi: 10.1016/S0920-9964(00)00128-6

Xiong, W. T., Faes, L., and Ivanov, P. C. (2017). Entropy measures, entropy estimators, and their performance in quantifying complex dynamics: effects of artifacts, nonstationarity, and long-range correlations. *Phys. Rev. E* 95:062114. doi: 10.1103/PhysRevE.95.062114

You, R. Y., and Chen, Z. (2005). Blind source separation of multichannel electroencephalogram based on wavelet transform and ICA. *Chin. Phys.* 14, 2176–2180.

Yu, Q. B., Erhardt, E. B., Sui, J., Du, Y., He, H., Hjelm, D., et al. (2015). Assessing dynamic brain graphs of time-varying connectivity in fMRI data: application to healthy controls and patients with schizophrenia. *Neuroimage* 107, 345–355. doi: 10.1016/j.neuroimage.2014.12.020

Zalesky, A., Fornito, A., Cocchi, L., Gollo, L. L., and Breakspear, M. (2014). Time-resolved resting-state brain networks. *Proc. Natl. Acad. Sci. U.S.A.* 111, 10341–10346. doi: 10.1073/pnas.14001 81111

Conflict of Interest: The authors declare that the research was conducted in the absence of any commercial or financial relationships that could be construed as a potential conflict of interest.

Copyright © 2020 Racz, Stylianou, Mukli and Eke. This is an open-access article distributed under the terms of the Creative Commons Attribution License (CC BY). The use, distribution or reproduction in other forums is permitted, provided the original author(s) and the copyright owner(s) are credited and that the original publication in this journal is cited, in accordance with accepted academic practice. No use, distribution or reproduction is permitted which does not comply with these terms.

frontiers in Computational Neuroscience

ORIGINAL RESEARCH
published: 16 November 2020
doi: 10.3389/fncom.2020.532193

Spiking Correlation Analysis of Synchronous Spikes Evoked by Acupuncture Mechanical Stimulus

Qing Qin[1], *Ya-Jiao Liu*[2], *Bo-Nan Shan*[3], *Yan-Qiu Che*[1], *Chun-Xiao Han*[1], *Ying-Mei Qin*[1] *and Jiang Wang*[2*]

[1] Tianjin Key Laboratory of Information Sensing & Intelligent Control, School of Automation and Electrical Engineering, Tianjin University of Technology and Education, Tianjin, China, [2] School of Electrical and Information Engineering, Tianjin University, Tianjin, China, [3] China Academy of Electronics and Information Technology, Beijing, China

Acupuncturing the ST36 acupoint can evoke the response of the sensory nervous system, which is translated into output electrical signals in the spinal dorsal root. Neural response activities, especially synchronous spike events, evoked by different acupuncture manipulations have remarkable differences. In order to identify these network collaborative activities, we analyze the underlying spike correlation in the synchronous spike event. In this paper, we adopt a log-linear model to describe network response activities evoked by different acupuncture manipulations. Then the state-space model and Bayesian theory are used to estimate network spike correlations. Two sets of simulation data are used to test the effectiveness of the estimation algorithm and the model goodness-of-fit. In addition, simulation data are also used to analyze the relationship between spike correlations and synchronous spike events. Finally, we use this method to identify network spike correlations evoked by four different acupuncture manipulations. Results show that reinforcing manipulations (twirling reinforcing and lifting-thrusting reinforcing) can evoke the third-order spike correlation but reducing manipulations (twirling reducing and lifting-thrusting reducing) does not. This is the main reason why synchronous spikes evoked by reinforcing manipulations are more abundant than reducing manipulations.

Keywords: population signals, spike correlation, synchrony, log-linear model, state-space model, bayesian theory, acupuncture

OPEN ACCESS

Edited by:
Nicola Toschi,
University of Rome Tor Vergata, Italy

Reviewed by:
Jun Ma,
Lanzhou University of Technology, China
Daya Shankar Gupta,
Camden County College, United States

***Correspondence:**
Jiang Wang
jiangwang@tju.edu.cn

Received: *03 February 2020*
Accepted: *11 September 2020*
Published: *16 November 2020*

Citation:
Qin Q, Liu Y-J, Shan B-N, Che Y-Q, Han C-X, Qin Y-M and Wang J (2020) Spiking Correlation Analysis of Synchronous Spikes Evoked by Acupuncture Mechanical Stimulus. Front. Comput. Neurosci. 14:532193. doi: 10.3389/fncom.2020.532193

INTRODUCTION

Different acupuncturing manipulations can evoke different rapid and immediate concentrated effects in the corresponding target organ (Ezzo et al., 2000). The nature of the acupuncture effect depends on information regulation, in which neural information regulation plays an important role. And spike response activities are products of the neural regulation. In recent years, the analysis of response activities evoked by acupuncture has focused on the single neuron spike train and been largely confined to feature extraction, such as the spiking rate, the variation coefficient, the embedded dimension, the correlation dimension, and the complexity (Han et al., 2011; Men et al., 2012; Zhou et al., 2012). Ensemble spike activities are rarely investigated. In order to

accurately quantify the acupuncture effect for different manipulations, we chose ensemble spike events as the research object in order to extract the network collaborative relationship.

With the rapid development of multi-electrode acquisition technology, more synchronous spikes have been detected in animal behavior and stimuli experiments (Gerstein and Clark, 1964; Meister et al., 1994; Gray et al., 1995; Brown et al., 2004; Segev et al., 2004; Blanche et al., 2005). A synchronous spike event is the important manifestation of the network collaborative activity (Hebb, 1949). In acupuncture experiments, some research has shown that reinforcing manipulations can evoke more response activities and encourage a higher spiking rate than reducing manipulations (Li, 2009). On this basis we instigated statistical analysis for ensemble spike events in 20 trials and found that the numbers of response spikes evoked by reinforcing manipulations were far higher than reducing manipulations, which mainly embodies synchronous spike activities.

In the earlier research, a study of the network collaborative relationship focused on the statistical analysis of ensemble spike trains. First, the cross-correlation method was used to obtain the stationary dependency in pairs of neurons (Perkel et al., 1967). Then Aertsen, Fujisawa et al. introduced the concept of the time-varying joint spiking rate of two neurons, which extended the pair-wise stationary dependency to the pair-wise dynamic dependency (Aertsen et al., 1989; Fujisawa et al., 2008). Still later, more methods, such as unitary event analysis (Grün et al., 2002a,b; Grün, 2009) and the CuBIC test method (Staude et al., 2010a,b) turned to the extraction of the high-order dynamic dependency based on ensemble spike trains.

In recent research, this model-based analysis has been extensively investigated. The generalized linear model is one of the most common models (Chornoboy et al., 1988; Brown et al., 1998; Truccolo et al., 2004), in which each spike train is modeled as a discrete point process based on all spike events and the time-varying spiking rate is modeled as a linear-non-linear cascade framework. In this cascade framework, spike-histories of other neurons are linearly superposed and then the spiking rate is obtained from the non-linear exponential transformation of the superposition result. Some methods also introduce input stimulus into the linear superposition (Kim et al., 2011). The generalized linear model is a probability statistical model, in which dynamic dependencies among neurons are directly modeled as linear coupling parameters of the spike-history (Truccolo et al., 2004; Okatan et al., 2005; Pillow et al., 2008). However, because ensemble spike trains are modeled on the assumption that spike events of each neuron are independent, these models cannot provide the time-varying joint spiking rate of neural ensemble or accurately describe dynamic synchronous spike activities.

In this paper, we model ensemble spike trains as multivariable Bernoulli events and adopt a log-linear model to directly describe dynamic joint spike activities. Pair-wise and high-order spike correlations are the model parameters, which describe the dependency among the neural ensemble. Unlike the cross-correlation analysis, the log-linear model simultaneously extracts all pair-wise spike correlations. This avoids the effect of other neurons. Meanwhile the log-linear model can extract high-order spike correlations avoiding the effect of lower-order spike correlations. Some studies have shown that high-order dependencies cannot be neglected in ensemble spike activities and a log-linear model containing only up to pair-wise interactions cannot account for stimulus encoding (Montani et al., 2009; Roudi et al., 2009; Ohiorhenuan et al., 2010; Santos et al., 2010; Yu et al., 2011). This method is used to ensemble spike trains evoked by different acupuncture manipulations. And the Akaike information criterion (AIC) is used to test the goodness-of-fit of the model and to judge the existence of high-order spike correlations. Based on the optimal model, ensemble spike correlations evoked by different acupuncture manipulations are estimated.

METHOD

Log-Linear Model

For the neural ensemble comprised of N neurons, taking time t for example, we define N-dimension binary variables $X^t = ({X_1}^t, {X_2}^t, \ldots, {X_N}^t)$ as the ensemble spike pattern. ${X_i}^t$ represents the spike state of the i neuron. When ${X_i}^t = 1$, it indicates that the spike event occurs at time t. When ${X_i}^t = 0$, it indicates that the spike event does not occur at time t. So, there are 2^N spike patterns for the neural ensemble. For a given spike pattern $x = (x_1, x_2, \ldots, x_N)$ ($x_i = 0$ or 1), we define the joint probability function of its occurrence as $p(x|\theta_t)$, which is determined by θ_t (ensemble spike correlations). θ_t reflects the dependency relationship of the neuron ensemble. The dimension of θ_t is $2^N - 1$ because the sum of joint probabilities of all spike patterns is 1, namely $\sum p(x|\theta_t) = 1$. The logarithm of the joint probability function is defined as a linear function (Amari et al., 2003; Gütig et al., 2003; Kass et al., 2011; Long and Carmena, 2011; Pillow et al., 2013) and the log-linear model is as follows:

$$\log\, p(x|\theta_t) = \sum_i \theta_i^t x_i + \sum_{i<j} \theta_{ij}^t x_i x_j + \sum_{i<j<k} \theta_{ijk}^t x_i x_j x_k \cdots + \theta_{1\ldots N}^t x_1 \cdots x_N - \psi(\theta_t), \quad (1)$$

where $\theta_t = (\theta_1^t, \theta_2^t, \ldots, \theta_{12}^t, \theta_{13}^t, \ldots, \theta_{1\ldots N}^t)'$ are ensemble spike correlations and compose the θ coordinate (Amari, 2001; Nakahara and Amari, 2002). The number of model parameters θ_t is $C_N^1 + C_N^2 + C_N^3 + \cdots C_N^N = 2^N - 1$. Because of $\sum p(x|\theta_t) = 1$, $\psi(\theta_t) = -\log p(\{0, \ldots, 0\})$ is the log normalization parameter.

Besides, we define the expectation of the joint spike (the synchronous spike) at time t as follows:

$$\begin{aligned}
\eta_i^t &= E[X_i^t] = 1 * p(X_i^t = 1) \\
&= p(\{x_i^t = 1, 0, \ldots, 0\}) + \sum_{j(\neq i)} p(\{x_i^t = 1, x_j^t = 1, 0, \ldots, 0\}) \\
&\quad + \sum_{j<k(j\neq i, k\neq i)} p(\{x_i^t = 1, x_j^t = 1, x_k^t = 1, 0, \ldots, 0\}) + \cdots \\
&+ p(\{1, \ldots, 1\}), \qquad i = 1, \cdots, N \\
\eta_{ij}^t &= E[X_i^t X_j^t] = 1 * p(X_i^t = 1, X_j^t = 1) \\
&= p(\{x_i^t = 1, x_j^t = 1, 0, \ldots, 0\}) \\
&+ \sum_{k(k\neq i, k\neq j)} p(\{x_i^t = 1, x_j^t = 1, x_k^t = 1, 0, \ldots, 0\}) \\
&\quad + \sum_{k<l(k\neq i, k\neq j, l\neq i, l\neq j)} \\
&p(\{x_i^t = 1, x_j^t = 1, x_k^t = 1, x_l^t = 1, 0, \ldots, 0\}) \\
&+ \cdots + p(\{1, \ldots, 1\}), \qquad i < j \\
&\vdots \\
\eta_{1\cdots N}^t &= E[X_i^t \cdots X_N^t] = 1 * p(X_1^t = 1, X_2^t = 1, \ldots, X_N^t = 1) \\
&= p(\{1, \ldots, 1\}).
\end{aligned} \tag{2}$$

Expectations $\eta_t = (\eta_1^t, \eta_2^t, \ldots, \eta_{12}^t, \eta_{13}^t, \ldots, \eta_{1\cdots N}^t)'$ compose the η coordinate. In order to facilitate writing, Ω_k represents all possible combination forms of the k-order subset. Then for all subsets, we can get $\Omega_1 = \{1, 2, \ldots, N\}$, $\Omega_2 = \{12, 13, \ldots\}$, $\Omega_3 = \{123, 124, \ldots\}$,…,$\Omega_N = \{123 \ldots N\}$. If $I \in \{\Omega_1, \ldots, \Omega_N\}$, the corresponding model parameter and expectation parameter can be written as θ_I^t and η_I^t. Similarly, the joint spike event is substituted by $f_I(x)$:

$$\begin{aligned}
&f_i(x) = x_i, \quad i = 1, \cdots, N \\
&f_{ij}(x) = x_i x_j, \quad i < j \\
&\vdots \\
&f_{1\cdots N}(x) = x_1 \cdots x_N.
\end{aligned} \tag{3}$$

Equations (1, 2) are simplified as follows:

$$p(x|\theta_t) = exp[\sum\nolimits_{I\in\{\Omega_1,\ldots,\Omega_N\}} \theta_I^t f_I(x) - \psi(\theta_t)], \tag{4}$$

$$\eta_I^t = E[f_I(x)|\theta_t], \quad I \in \{\Omega_1, \ldots, \Omega_N\}. \tag{5}$$

Some research has shown that the θ coordinate and η coordinate are dually orthogonal coordinates and non-zero high-order spike correlations represent the excess and paucity of high-order synchronous spikes (Amari and Nagaoka, 2000; Amari, 2001, 2009; Nakahara and Amari, 2002). But it is worth noting that non-zero high-order spike correlations are not equal to the expectations of the corresponding order joint spikes. For a given r-order subset, $\{\eta_I\}$ ($I \in \{\Omega_r\}$) is the expectation of synchronous spikes. Equations (4, 5) show that $\{\eta_I\}$ ($I \in \{\Omega_r\}$) depends not only on r-order spike correlations $\{\theta_I\}$ ($I \in \{\Omega_r\}$) but also on higher-order spike correlations $\{\theta_I\}$ ($I \in \{\Omega_r, \ldots, \Omega_N\}, r \leq N$).

State-Space Method for Estimating Spike Correlations

We chose ensemble spike events of n trials as the research object to make the result statistically significant. $X^{t,l} = (X_1{}^{t,l}, X_2{}^{t,l}, \ldots, X_N{}^{t,l})$ is defined as the ensemble spike pattern in the l-th trial at time t, which is a sample for the joint probability function $p(x|\theta_t)$. Based on experimental data of n trials, the effective estimate of $\eta_I{}^t$ is equal to the joint spiking rate:

$$y_I^t = \frac{1}{n} \sum_{l=1}^{n} f_I(X^{t,l}), \quad I \in \{\Omega_1, \ldots, \Omega_N\}, \tag{6}$$

where $I \in \{\Omega_1, \ldots, \Omega_N\}$, $y_t = (y_1^t, y_2^t, \ldots, y_{12}^t, y_{13}^t, \ldots, y_{1\cdots N}^t)'$. For the observation interval $[0, T]$, $y_{1:T} = \{y_1, y_2, \ldots, y_T\}$ are efficient estimates of joint spiking expectations at each time. According to the Bernoulli experiment, n trials are independent of each other and we assume that spike patterns for all time are also independent of each other. Based on Equations (4, 6), we can get the conditional probability function for all ensemble spike events of n trials, which is given as:

$$\begin{aligned}
p(y_{1:T}|\theta_{1:T}) &= \prod_{l=1}^{n} \prod_{t=1}^{T} \exp[\textstyle\sum_{I\in\{\Omega_1,\ldots,\Omega_N\}} \theta_I^t f_I(X^{t,l}) - \psi(\theta_t)] \\
&= \prod_{t=1}^{T} \exp[n(\textstyle\sum_{I\in\{\Omega_1,\ldots,\Omega_N\}} \theta_I^t y_I^t - \psi(\theta_t))] \\
&= \prod_{t=1}^{T} \exp[n(y'_t \theta_t - \psi(\theta_t))],
\end{aligned} \tag{7}$$

where $\theta_{1:T} = \{\theta_1, \theta_2, \ldots \theta_T\}$.

In order to estimate dynamics spike correlations, we adopted the idea of the discrete state-space model. Here state variables are spike correlations, which are unknown. And observation variables are the ensemble spike events of n trials, which are observable and known. Equation (7) defines the conditional probability function for the observation process. For state variables, the iterative process is defined as a first-order autoregressive model, which is given as:

$$\theta_t = F\theta_{t-1} + \xi_t, \tag{8}$$

where $t = 2, \ldots, T$. F is the first-order autoregressive parameter. ξ_t obeys the normal distribution, in which the mean is the zero vector and the covariance matrix is Q. And the initial value of state variables also obeys the normal distribution $\theta_1 \sim \nu(\mu, \Sigma)$. Here we assume that the parameter Σ is constant and $w = [F, Q, \mu]$ is the unknown parameter set of the state process.

According to Equation (8), we know $(\theta_t - F\theta_{t-1}) \sim \nu(0, Q)$ and get the prior probability function of the state process $p(\theta_{1:T}|w)$. Then the log-likelihood function of the ensemble spike events of n trials can be written as:

$$\begin{aligned}
l(w) &= \log \textstyle\int p(y_{1:T}, \theta_{1:T}|w) d\theta_{1:T} \\
&= \log \textstyle\int p(y_{1:T}|\theta_{1:T}) p(\theta_{1:T}|w) d\theta_{1:T}.
\end{aligned} \tag{9}$$

The unknown parameter set w can be estimated by maximizing this log-likelihood function. Meanwhile according to the Bayesian theory, the posterior probability function can be written as

$$p(\theta_{1:T}|y_{1:T}, w) = \frac{p(y_{1:T}|\theta_{1:T}) p(\theta_{1:T}|w)}{p(y_{1:T}|w)}. \tag{10}$$

By maximizing the posterior probability function, the unknown state (spike correlations) can be estimated (Dempster et al., 1977; Akaike, 1980; Shumway and Stoffer, 1982; Smith and Brown, 2003; Smith et al., 2004; Pillow et al., 2013).

Selection of the Log-Linear Model

For the neural ensemble comprised of N neurons, Equation (4) is a full model, which contains spike correlations of all orders. We can construct its hierarchical models, such as $E_1 \subset E_2 \subset \cdots E_N$. E_r $(r = 1, 2, \ldots, N)$ a hierarchical log-linear model, in which spike correlations that are greater than the r-order are set to zero. If the model contains more high-order correlation terms, apparently it can better describe the joint probability of the ensemble spike pattern. However, for the estimation of spike correlations, more high-order correlation terms do not mean better. This is because when high-order synchronous spike activities do not exist in the neural ensemble, high-order correlation terms will lead to a large statistical fluctuation for the parameter estimation and estimates of low-order spike correlations would be inaccurate. This phenomenon is an over-fitting of the model, so it is necessary to remove non-existent high-order correlation terms.

This paper adopts the Akaike information criterion (AIC) (Akaike, 1980) to choose the optimal model. AIC is based on the concept of the information entropy, which is a balance between the model complexity and the model goodness-of-fit. When AIC for a given model is small, it means that the model provides a good description for experimental data with fewer parameters. According to the log-linear model, AIC is defined as,

$$\begin{aligned} \mathrm{AIC} &= -2\log\int p(\theta_{1:T}|y_{1:T}, w)d\theta_{1:T} + 2k \\ &= -2l(w) + 2k, \end{aligned} \tag{11}$$

where k is the number of parameters, which is equal to the sum of the numbers of $w = [F, Q, \mu]$ (Akaike, 1980; Kitagawa, 1987). For a given r-order hierarchical model, the number of spike correlation parameters $\theta_t = \left[{\theta_1}^t, \ldots, {\theta_{12}}^t, \ldots, {\theta_{1\cdots r}}^t\right]'$ is $d = \sum_{k=1}^{r} \binom{N}{k}$, so the total number of parameters is $k = d^2 + d(d+1)/2 + d$, in which three terms, respectively, represent the numbers of F, Q, and μ.

In addition, the Bayesian information criterion (BIC) (Schwarz, 1978; Rissanen, 2009) is another common information measure. Compared to AIC, BIC replaces the second term k with $k\log n$. BIC is defined as,

$$\mathrm{BIC} = -2l(w) + k\log n. \tag{12}$$

Selection of the State Model

Besides the selection of high-order correlation terms, we should choose the dynamic change pattern of the state process, which is determined by state parameters: F and Qin Equation (8). There are three dynamic change patterns: (I) $F = I$ (identity matrix) and $Q = 0$; (II) $F = I$ and Q is estimated by the state-space method; and (III) F and Q are both estimated by the state-space method. In case (I), spike correlations are stationary. In cases (II) and (III), spike correlations are non-stationary. Here we similarly use AIC to select the optimal dynamic change pattern.

RESULT

Simulation Data Analysis

In this section, we generate two sets of simulation data with known model parameters (spike correlations) to, respectively, test the effectiveness of the state-space method and information criterions (AIC and BIC). Meanwhile the relationship between spike correlations and synchronous spikes is discussed.

Testing the State-Space Estimation Method

The first-order and second-order spike correlations (dashed lines in **Figures 1B,C**) are used to simulate ensemble spike activities (**Figure 1A**), which contain two neurons ($N = 2$). Besides, we can obtain synchronous spikes of two neurons, which are shown as blue raster at the bottom of **Figure 1C**. At time $t = 125ms$ (red dashed box), both θ_1 and θ_2 (the green dashed line and the pink dashed line) have a significant increase. At this moment, the blue raster (**Figure 1C**) are very dense because of the high spiking rates of the two neurons. At time $t = 375ms$ (black dashed box), θ_{12} (blue dashed line) has a significant increase. Conversely, θ_1 and θ_2 reduce. At this moment, the blue raster (**Figure 1C**) are relatively dense because of the high second-order spike correlation.

Then the state-space method is used to simulation data (**Figure 1A**) and estimates of θ_1, θ_2, and θ_{12} are shown in **Figures 1B,C** (green, pink, and blue solid lines), in which three gray intervals are, respectively, their 95% credible intervals. Results show that all of the spike correlations (the first-order and the second-order) lay within 95% credible intervals of their estimates. The effectiveness of the state-space method has been validated.

Testing the Akaike and Bayesian Information Criterions

In order to test the effectiveness of the Akaike and Bayesian information criterions, the log-linear model with known spike correlations is used to simulate ensemble spike activities of three neurons ($N = 3$). There are non-stationary first-order, second-order, and third-order spike correlations in this model. And the number of trials is also $n = 100$. Then we can construct its hierarchical models E_r $(r = 1, 2, 3)$. These three hierarchical models are employed to fit simulation data and corresponding model parameters (spike correlations) are estimated by the state-space method. Meanwhile in order to test the importance of the data sample size, we analyzed different sample sets: $n = 3, 5, 10, 20, 50, 100$. For different sample sizes, AICs and BICs of three hierarchical models can be calculated. Results are shown in **Tables 1**, **2**. Minimum values of AICs and BICs for the three hierarchical models are marked in blue.

Table 1 shows that for small sample sizes ($n = 3, 5, 10, 20$), the second-order hierarchical model E_2 is chosen, whose AICs is minimal. For large sample sizes ($n = 50, 100$), the third-order hierarchical model E_3 with the minimal AICs is chosen. BIC has the same result in **Table 2**. Because neuronal spiking is a random event, the analysis of the synchronous spike and the spike correlation must be based on enough sample data. Results from one or two trials have statistical significance, which also cannot represent entire ensemble

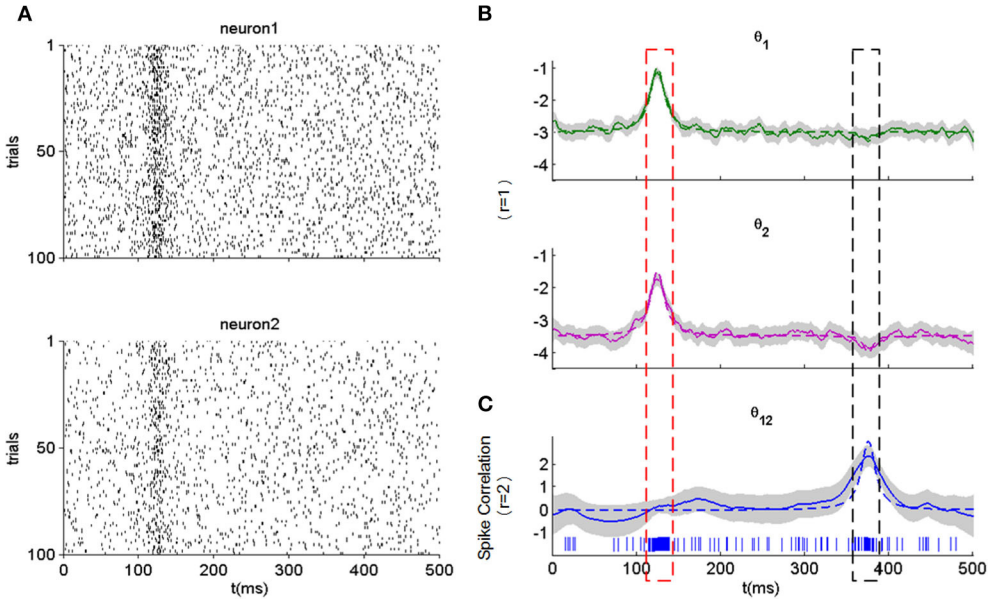


FIGURE 1 | Estimation of spike correlations for simulation data of two neurons. **(A)** Simulated ensemble spike activities. The number of neurons is $N = 2$ and the number of trials is $n = 100$. **(B)** First-order spike correlations: true values (dashed lines) and their estimates (solid lines). **(C)** Second-order spike correlations: true value (dashed line) and its estimate (solid line). Blue raster, at the bottom, represent the synchronous spikes of the two neurons.

TABLE 1 | AICs for different sample sizes of simulation data.

Number of trials	$r = 1$	$r = 2$	$r = 3$
$n = 3$	1,207	1,197	1,213
$n = 5$	1,960	1,902	1,919
$n = 10$	3,782	3,647	3,663
$n = 20$	7,851	7,595	7,609
$n = 50$	19,259	18,592	18,585
$n = 100$	37,759	36,362	36,325

TABLE 2 | BICs for different sample sizes of simulation data.

Number of trials	$r = 1$	$r = 2$	$r = 3$
$n = 3$	1,199	1,172	1,182
$n = 5$	1,957	1,891	1,906
$n = 10$	3,784	3,655	3,673
$n = 20$	7,860	7,622	7,644
$n = 50$	19,276	18,644	18,652
$n = 100$	37,783	36,432	36,416

response activities. When the sample size is large enough, AIC and BIC both choose the full model E_3 as the optimal model. The effectiveness of the two information criterions has been validated.

Relationship Between Spike Correlations and Synchronous Spikes

For the neural ensemble containing two neurons, synchronous spikes of the two neurons are represents by blue raster in **Figure 1C**. At time $t = 375ms$, second-order synchronous spikes occurred frequently with the increasing of the second-order spike correlation θ_{12} (blue line). In addition, at time $t = 125ms$, although the second-order spike correlation is fixed at zero, second-order synchronous spikes still have an obvious increase. It is because that two first-order spike correlations θ_1 and θ_2 both display an obvious increase (>-3) at this moment. When the first-order spike correlations are smaller than -3, they have little effect on the synchronous spike and will not be taken into account.

For the neural ensemble containing three neurons, estimates of spike correlations are, respectively, shown in **Figures 2B–D** based on ensemble spike activities (**Figure 2A**). In the bottom of each panel, synchronous spikes are shown as raster figures. Estimated curves and raster figures for the same order have the same color. Results show that second-order (low-order) synchronous spike events are not only related to corresponding order spike correlations but also the third-order (high-order) spike correlation. Specifically, in the interval $[450ms, 500ms]$, synchronous spikes of neurons 1-2 (blue raster) do not increase but reduce with the increasing of θ_{12}(blue solid line), compared with the interval $[100ms, 150ms]$. This is because of a smaller θ_{123} (gray dotted line) in the interval $[450ms, 500ms]$. In addition, although θ_{23} (red solid line) in the interval $[100ms, 150ms]$ is much smaller than the interval $[0ms, 50ms]$, red raster of neurons 2-3 in these two intervals show no significant difference. This is because θ_{123} (gray dotted line) in $[100ms, 150ms]$ is much bigger. Meanwhile **Figure 2D** shows that the third-order (high-order) spike correlation θ_{123} represents the third-order (high-order) synchronous spike events.

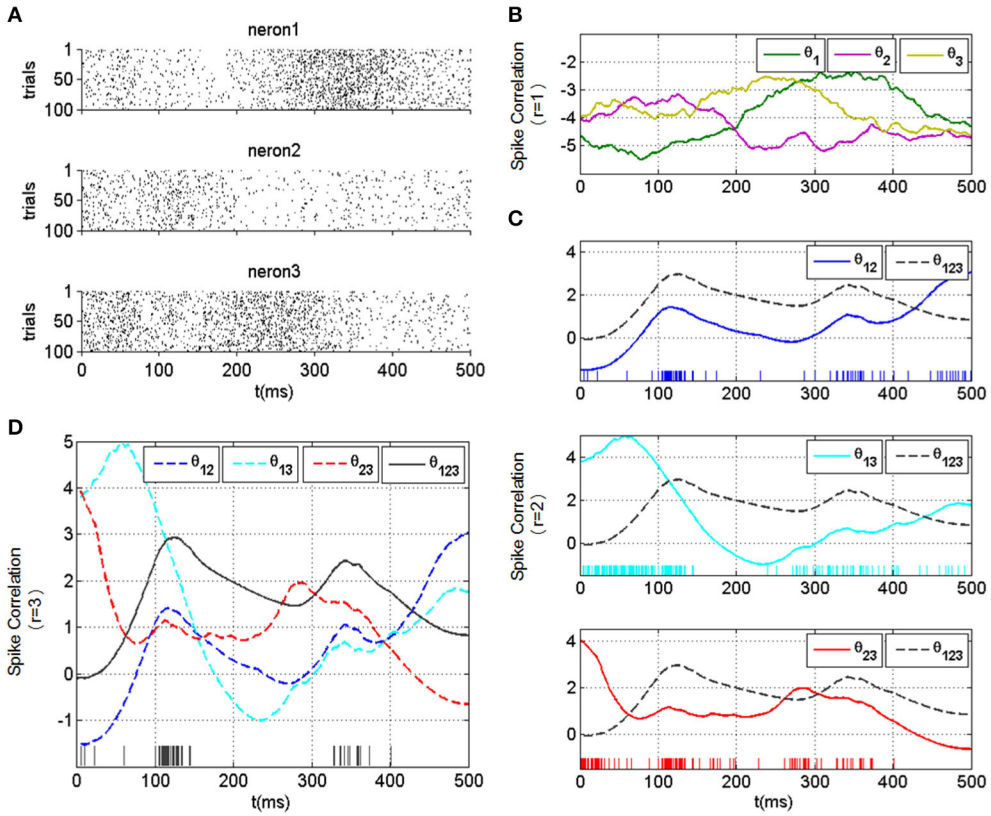


FIGURE 2 | Estimation of spike correlations for simulation data of three neurons. **(A)** Simulated ensemble spike activities. The number of neurons is $N = 3$ and the number of trials is $n = 100$. **(B)** First-order spike correlations: θ_1, θ_2, and θ_3 (green, pink, and yellow solid lines). **(C)** Second-order spike correlations: θ_{12}, θ_{13}, and θ_{23} (blue, cyan, and red solid lines). **(D)** The third-order spike correlation: θ_{123} (gray solid line). Raster with different colors at the bottom show the timing of corresponding order synchronous spikes.

Acupuncture Data Analysis

In the acupuncture experiment, healthy Sprague Dawley rats (weight: 180–200 g, age: 2–3) were selected as subjects. Before the experiment, all of the rats were fed for 7 days to adapt to the standard laboratory environment. In the process of the experiment, subjects were anesthetized deeply by 20% ethyl carbamate (1.5 g/kg) for preparation. We trimmed the hair between T8-L6 on both sides of the dorsal midline, cut the back skin along this midline, and removed the subcutaneous fascia. After that, the erector spinae, spinous process on both sides of centrum between T13-L5 was taken out to expose the spinal cord. To keep the spinal cord from drying out, paraffin oil at a temperature of 38°C was injected into stitched skin flaps. And then we used a hairspring tweezer to cut the spine dura mater with the help of the anatomical microscope. The dorsal roots separated from L3-L5 intervertebral foramen were snipped by eye scissors at the proximal part. Lastly, nerve filaments of the L4 dorsal root were placed on electrodes. And then, we used the BIOPAC-MP150 physiological recorder to record the spike activity of spinal dorsal root neurons evoked by acupuncture. We adopted four common manipulations in the clinical treatment: (I) twirling reinforcing, (II) lifting-thrusting reinforcing, (III) twirling reducing, and (IV) lifting-thrusting reducing. The stimulus frequency was 100 times/min and the stimulus duration was $T = 2.5s$ (for specific experimental details refer to references Men et al., 2011 and Xue et al., 2013). We chose the spike trains of three neurons in 20 trials as the research object and created statistical analysis on the spike events. The numbers of spike events of single neurons evoked by four manipulations are shown in **Table 3**. Under the condition of reinforcing manipulations (I and II), the numbers of spikes of the three neurons are far more than those under the condition of reducing manipulations (III and IV). The last two rows marked in red are the number of supernumerary spikes of the three neurons evoked by manipulation I and II, respectively.

The number of synchronous spike events evoked by the four manipulations are shown in the first four rows in **Table 4**. Numbers in the fifth row marked in red are the number of supernumerary synchronous spikes evoked by manipulation I compared to manipulation III. And numbers in the sixth row are the number of supernumerary synchronous spikes evoked by manipulation II compared to manipulation IV. According to **Tables 3**, **4**, we find that reinforcing manipulations can evoke more response spikes than reducing manipulations, which mainly embody synchronous spike activities. In order to theoretically explain this phenomenon through the viewpoint

TABLE 3 | Number of spike events of each neuron evoked by four manipulations in 20 trials.

Manipulation	Neuron 1	Neuron 2	Neuron 3
I	874	1,027	1,035
II	1042	824	851
III	653	659	592
IV	596	647	622
I-III	221	368	443
II-IV	446	177	229

TABLE 4 | Number of synchronous spike events evoked by four manipulations in 20 trials.

Manipulation	Neurons 1-2	Neurons 1-3	Neurons 2-3	Neurons 1-2-3
I	190	176	261	129
II	109	111	223	85
III	67	33	69	25
IV	70	57	94	41
I-III	123	143	192	104
II-IV	39	54	129	44

TABLE 5 | AICs for different sample sizes of acupuncture data evoked by manipulation I.

Number of trials	$r = 1$	$r = 2$	$r = 3$
$n = 2$	1,875	1,846	1,884
$n = 5$	4,564	4,371	4,398
$n = 10$	8,882	8,485	8,509
$n = 15$	13,152	12,558	12,560
$n = 20$	NaN	16,663	16,635

TABLE 6 | AICs for different sample sizes of acupuncture data evoked by manipulation II.

Number of trials	$r = 1$	$r = 2$	$r = 3$
$n = 2$	1,744	1,696	1,727
$n = 5$	4,311	4,099	4,130
$n = 10$	8,180	7,765	7,803
$n = 15$	12,298	11,664	11,695
$n = 20$	16,635	15,767	15,744

TABLE 7 | AICs for different sample sizes of acupuncture data evoked by manipulation III.

Number of trials	$r = 1$	$r = 2$	$r = 3$
$n = 2$	1,297	1,345	1,384
$n = 5$	3,083	3,106	3,139
$n = 10$	6,184	6,150	6,182
$n = 15$	9,103	9,016	9,042
$n = 20$	12,156	11,986	12,003

TABLE 8 | AICs for different sample sizes of acupuncture data evoked by manipulation IV.

Number of trials	$r = 1$	$r = 2$	$r = 3$
$n = 2$	1,301	1,342	1,385
$n = 5$	3,102	3,059	3,100
$n = 10$	5,965	5,871	5,896
$n = 15$	8,816	8,667	8,687
$n = 20$	11,794	11,546	11,562

TABLE 9 | AICs of given hierarchical models of the four manipulations for different state processes.

State parameter	I, $r = 3$	II, $r = 3$	III, $r = 2$	IV, $r = 2$
$F = I$	16,771	15,859	12,091	11,632
Optimized F	16,635	15,744	11,986	11,546

of spike correlation, this paper introduces the log-linear model and the state-space estimation method into the analysis of acupuncture data.

Selection of the Log-Linear Model and the State Model

The first step is to choose the appropriate models for the acupuncture data. Here because acupuncture is a discrete stimulation, we assume that the first-order autoregressive parameter F in the state model is not equal to the identity matrix and is optimized by the estimation method. Ensemble spike activities with different sample sizes ($n = 2, 5, 10, 15, 20$) evoked by the four manipulations are used to fit three hierarchical models (E_1, E_2 and E_3). And their corresponding AICs can be calculated and shown in **Tables 5–8**. For the given sample sizes, the minimum values of AICs are marked in blue. Results show that under the condition of reinforcing manipulations (I and II), when the sample size is large enough ($n = 20$), AIC chooses the full model E_3 as the optimal model. Conversely, under the condition of reducing manipulations (III and IV), the hierarchical model E_2 is selected. Therefore, we conclude that reinforcing manipulations can evoke the third-order spike correlation θ_{123} and reducing manipulations cannot. This is the main reason why more response spikes are evoked by the two reinforcing manipulations.

In the selection of the log-linear model, the autoregressive parameter F is fixed at the identity matrix. AICs of four chosen models have been calculated and we show them in the first row of **Table 9.** Meanwhile we calculate AICs (the second row of **Table 9**) of the four chosen models under the condition of the optimized F. For the four manipulations, AICs in the second row are less than those in the first row. The efficacy of the assumption that the state parameter F is optimized has been validated.

Analysis of Acupuncture Reinforcing Manipulations

This section discusses the twirling reinforcing manipulation and its ensemble response activities (**Figure 3A**) are used to

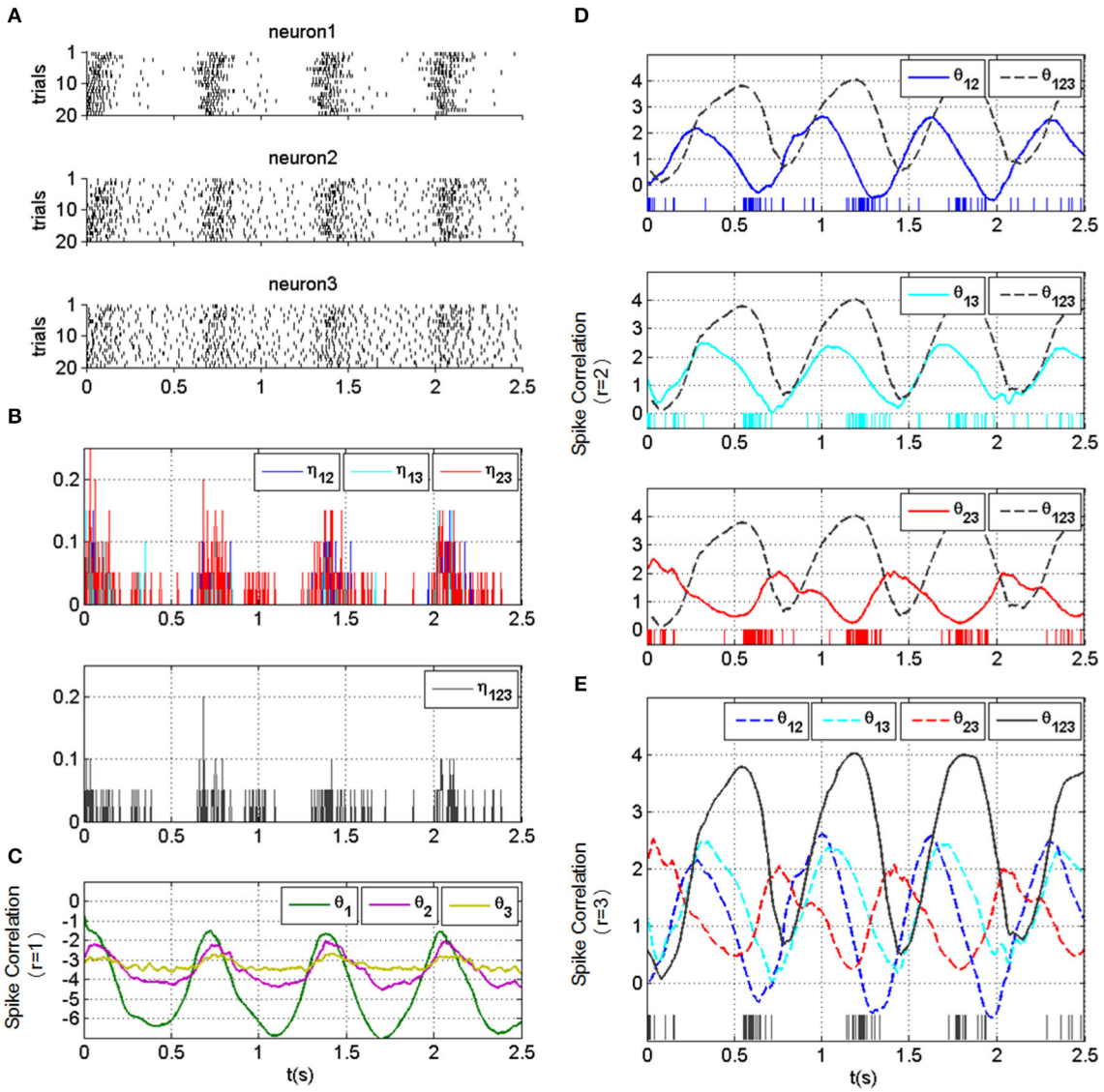


FIGURE 3 | Estimation of spike correlations for acupuncture data evoked by twirling reinforcing. **(A)** Ensemble spike activities. The number of neurons is $N = 3$ and the number of trials is $n = 20$. **(B)** Rates of joint spike: η_{12}, η_{13}, η_{23}, and η_{123}. **(C)** First-order spike correlations: θ_1, θ_2, and θ_3 (green, pink, and yellow solid lines). **(D)** Second-order spike correlations: θ_{12}, θ_{13}, and θ_{23} (blue, cyan, and red solid lines). **(E)** Third-order spike correlation: θ_{123} (gray solid line). Raster with different colors at the bottom show the timing of corresponding order synchronous spikes.

fit the full model E_3. In **Figure 3A**, each twirling reinforcing stimulus can evoke a lot of spike activities and spike times show a single-peak distribution. Based on spike trains in 20 trials, joint (synchronous) spike events (colored raster in **Figure 3**) and their rates (**Figure 3B**) can be obtained. Then the state-space method is used to estimate spike correlations. **Figure 3C** shows that three first-order spike correlations are <0. Only θ_1 and θ_2 are significantly $>$-3 during each acupuncture stimulus. Therefore, except for the synchronous spikes of neurons 1-2, the first-order spike correlations are not the main considerations for synchronous spike events.

Figure 3D shows that second-order synchronous spike events are not only related to corresponding order spike correlations but also to the third-order spike correlation θ_{123}. Take the third acupuncture stimuli for example ($[1.1s, 1.7s]$), θ_{12} is negative in the interval $[1.2s, 1.4s]$. But because θ_{123} is large enough during this time period, there are many synchronous spikes of neurons 1–2 (blue raster). In the interval $[1.4s, 1.5s]$, θ_{12} gradually increases, but the number of blue raster has a dramatic decline because of a smaller θ_{123}. For the rest of the time ($[1.5s, 1.7s]$), values of θ_{12} and θ_{123} are both large. However, in this time period, the current stimuli has stopped. Therefore, the three first-order spike correlations are very small and spike activities

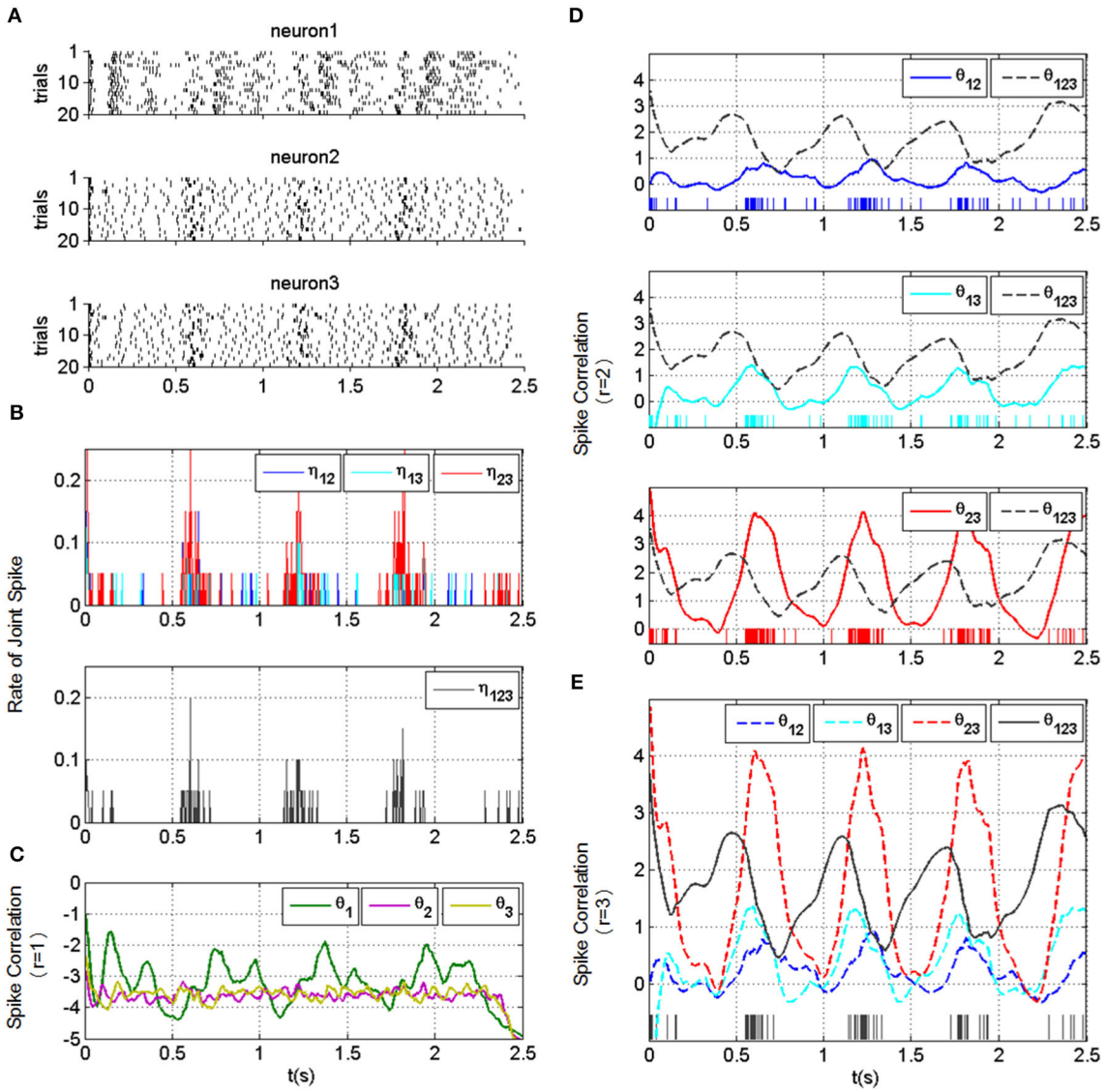


FIGURE 4 | Estimation of spike correlations for acupuncture data evoked by lifting-thrusting reinforcing. **(A)** Ensemble spike activities. The number of neurons is $N = 3$ and the number of trials is $n = 20$. **(B)** Rates of joint spike: η_{12}, η_{13}, η_{23}, and η_{123}. **(C)** First-order spike correlations: θ_1, θ_2, and θ_3 (green, pink, and yellow solid lines). **(D)** Second-order spike correlations: θ_{12}, θ_{13}, and θ_{23} (blue, cyan, and red solid lines). **(E)** Third-order spike correlation: θ_{123} (gray solid line). Raster with different colors at the bottom show the timing of corresponding order synchronous spikes.

disappear gradually. For synchronous spikes of neurons 1–3 and neurons 2-3, θ_{13} and θ_{23} are both larger than θ_{12} during the interval $[1.25s, 1.45s]$. So synchronous spikes of neurons 1-2 rely more on θ_{123}. **Figure 3E** shows that synchronous spikes of neurons 1-2-3 (gray raster) increase with the increasing of θ_{123} during each acupuncture stimulus. Therefore, the third-order spike correlation θ_{123} represents third-order synchronous spike events.

For the lifting-thrusting reinforcing manipulations, analysis results are shown in **Figure 4**. From **Figure 4A**, we find that spike times during each acupuncture stimulus show a multi-peak distribution. Therefore, analysis results are same as twirling reinforcing, except for the characteristic of volatility. In addition, during each acupuncture stimulus θ_{23} (**Figure 4D**, red solid line) is larger than θ_{123} (**Figure 4D**, gray dotted line) and the red raster become dense with the increasing of θ_{23}. Therefore, the dependence of synchronous spikes of neurons 2-3 on θ_{123} is minimal. And **Figure 4E** shows that synchronous spikes of neurons 1-2-3 (gray raster) are the result of the interaction of second-order and third-order spike correlations.

Analysis of Acupuncture Reducing Manipulations

This section discusses the twirling reducing manipulation and its ensemble response activities (**Figure 5A**) are used to fit the hierarchical model E_2. Its analysis results are shown in

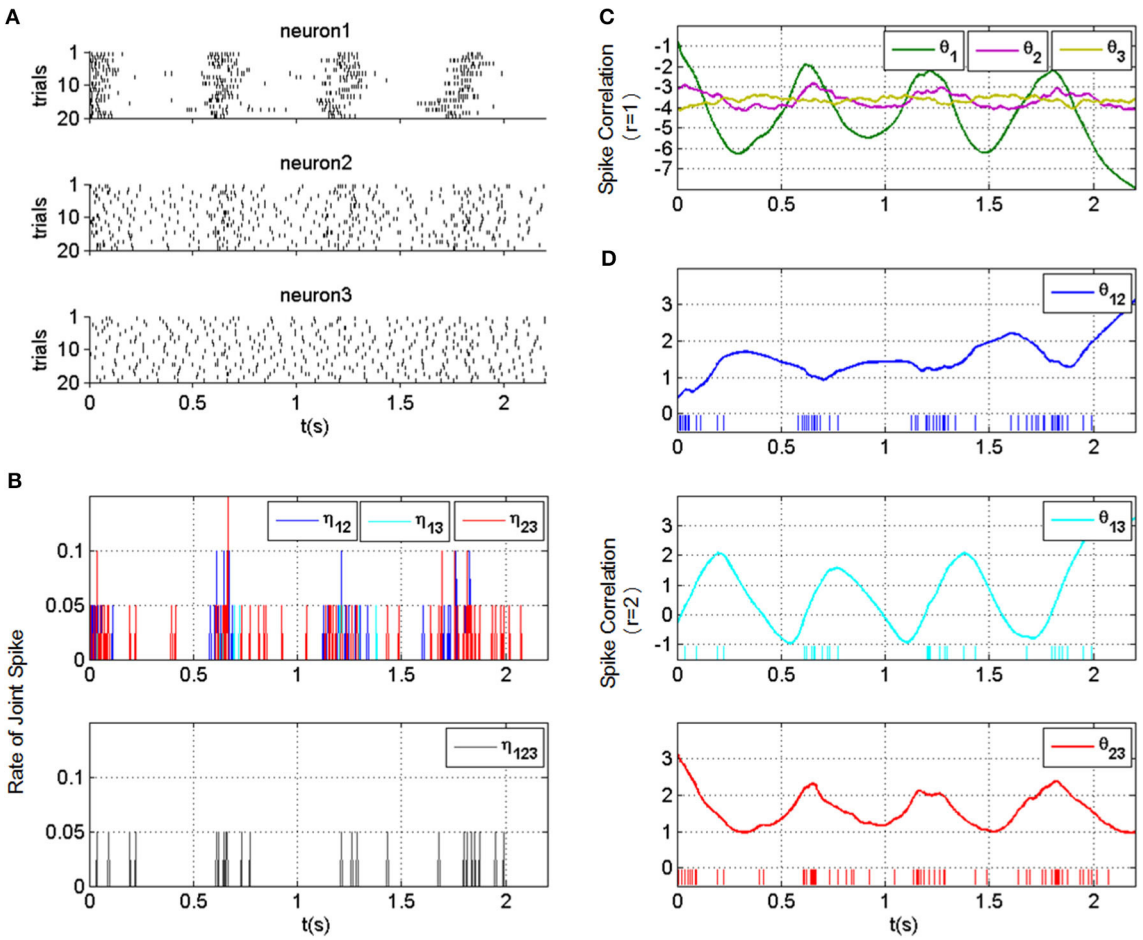


FIGURE 5 | Estimation of spike correlations for acupuncture data evoked by twirling reducing. **(A)** Ensemble spike activities. The number of neurons is $N = 3$ and the number of trials is $n = 20$. **(B)** Rates of joint spike: η_{12}, η_{13}, η_{23}, and η_{123}. **(C)** First-order spike correlations: θ_1, θ_2, and θ_3 (green, pink, and yellow solid lines). **(D)** Second-order spike correlations: θ_{12}, θ_{13}, and θ_{23} (blue, cyan, and red solid lines). Raster with different colors at the bottom show the timing of corresponding order synchronous spikes.

Figure 5. From **Figures 5A,B**, we find that spike times during each acupuncture stimulus also show a single-peak distribution, but the number of response spikes are less than the twirling reinforcing. The main reason is that reducing manipulations cannot evoke the third-order spike correlation.

Figure 5C shows that, like the twirling reinforcing, θ_1 and θ_2 are >-3 during each acupuncture stimulus. So synchronous spikes of neurons 1-2 (**Figure 5D**, blue raster) are not only related to θ_{12} but also to θ_1 and θ_2. For synchronous spike events of neurons 1-3 and of neurons 2-3 (**Figure 5D**, cyan and red raster), first-order spike correlations can be ignored. Second-order spike correlations θ_{13} and θ_{23} are, respectively, their main considerations.

For the lifting-thrusting reducing manipulation, analysis results are shown in **Figure 6**. Similarly, results are same as twirling reducing, except for the characteristic of volatility. In addition, only θ_1 among the first-order spike correlations is larger than -3 during each acupuncture stimulus. So first-order spike correlations are not main consideration for synchronous spikes. Second-order spike correlations, respectively, represent corresponding order synchronous spike events.

DISCUSSION

This paper introduces the concept of spike correlation and builds a log-linear model to describe ensemble spike activities evoked by four acupuncture manipulations. Then according to the idea of the state-space model, ensemble spike trains are defined as observation variables and spike correlations are defined as unknown state variables, which are estimated by the Bayesian theory. Results show that under the condition of acupuncture reducing manipulations, the third-order spike correlation does not exist. This is the primary reason that synchronous spikes are significantly less in this condition.

In this paper, we judge the existence of the high-order spike correlation by the goodness-of-fit of three hierarchical models and their AICs. Readers can also test the presence

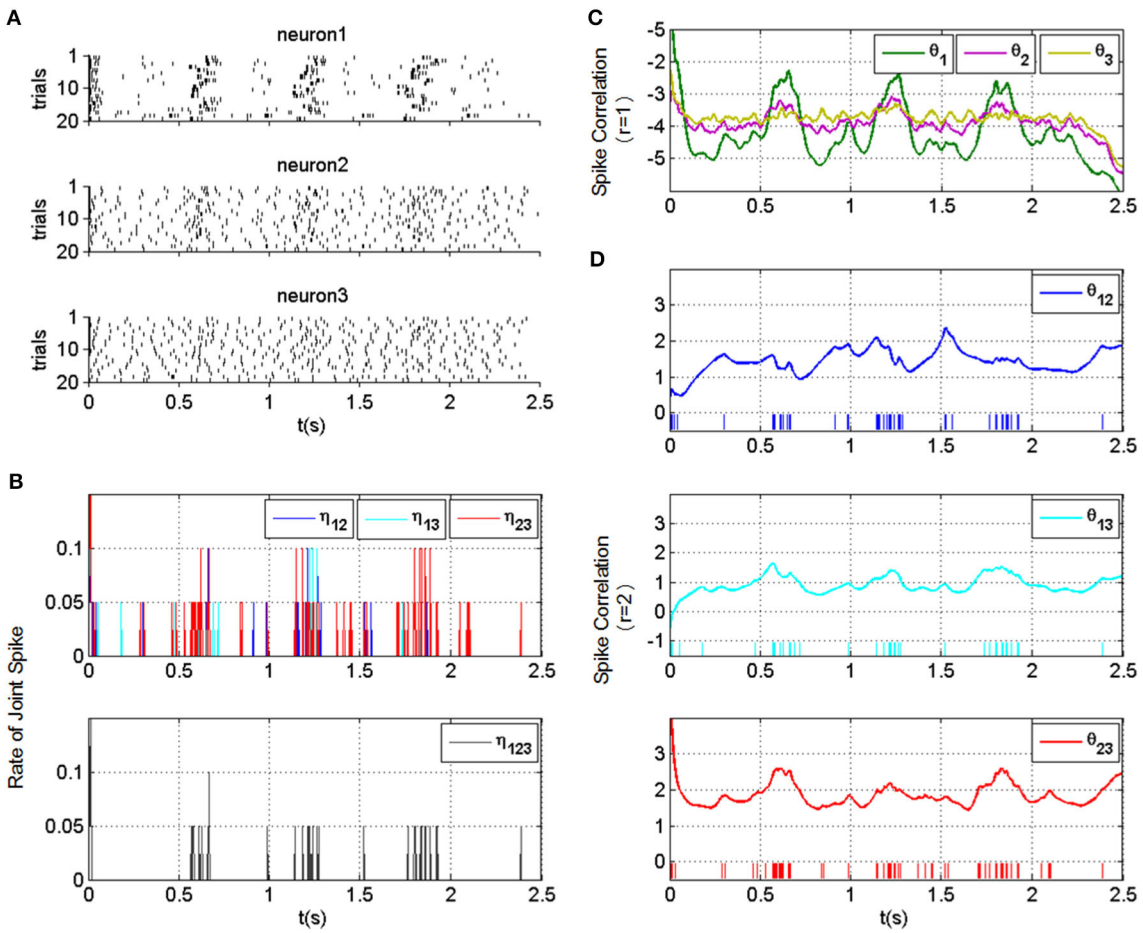


FIGURE 6 | Estimation of spike correlations for acupuncture data evoked by lifting-thrusting reducing. **(A)** Ensemble spike activities. The number of neurons is $N = 3$ and the number of trials is $n = 20$. **(B)** Rates of joint spike: η_{12}, η_{13}, η_{23}, and η_{123}. **(C)** First-order spike correlations: θ_1, θ_2, and θ_3 (green, pink, and yellow solid lines). **(D)** Second-order spike correlations: θ_{12}, θ_{13}, and θ_{23} (blue, cyan, and red solid lines). Raster with different colors at the bottom show the timing of corresponding order synchronous spikes.

of high-order spike correlation by the Bayes factor. The Bayes factor is the ratio of two likelihood functions, which is defined as $BF = p(y|M_1)/p(y|M_2)$. M_1 represents the model containing the high-order spike correlation. When the value of the Bayes factor is larger than 1, it indicates that the experimental data supports model M_1 and the high-order spike correlation exists.

Acupuncture is a kind of the discrete stimulation. Therefore, the log-linear model is time-dependent and model parameters (spike correlations) are time-varying. Meanwhile our model contains spike correlations of each order and we can estimate the "pure" high-order spike correlation. This makes it possible to discuss the effect of high-order spike correlation on a low-order synchronous spike event. In addition, the correlation analysis in this paper is based on a large number of sample data. The spike event of neurons is a stochastic process. One or two experiments cannot reflect synchronous spike activities of the neural ensemble. Therefore, the result based on a small amount of sample data is unreliable. This is a new view to analyze acupuncture neural electrical signals and will become an important scientific method for the quantitative analysis of the acupuncture response system.

DATA AVAILABILITY STATEMENT

The datasets for this article are not publicly available because participants did not provide consent to have their data released. Requests to access the datasets should be directed to Jiang Wang, jiangwang@tju.edu.cn.

AUTHOR CONTRIBUTIONS

QQ, Y-JL, B-NS, Y-QC, C-XH, Y-MQ, and JW designed and performed the research as well as wrote the paper. All authors contributed to the article and approved the submitted version.

FUNDING

This paper is supported by the National Natural Science Foundation of China (Grant Nos. 61801328, 61871287, 62071324, and 61671320), the Natural Science Foundation of Tianjin, China (Grant Nos. 17JCQNJC03700, 18JCYBJC88200, and 18JCQNJC04700), and the Tianjin Municipal Special Program of Talents Development for Excellent Youth Scholars (TJTZJH-QNBJRC-2-21).

REFERENCES

Aertsen, A. M., Gerstein, G. L., Habib, M. K., and Palm, G. (1989). Dynamics of neuronal firing correlation: modulation of "effective connectivity". *J. Neurophysiol.* 61, 900–917. doi: 10.1152/jn.1989.61.5.900

Akaike, H. (1980). Likelihood and the bayes procedure. *Trabajos de Estadistica y de Investigacion Operativa* 31, 143–166. doi: 10.1007/BF02888350

Amari, S. (2009). Measure of correlation orthogonal to change in firing rate. *Neural Comput.* 21, 960–972. doi: 10.1162/neco.2008.03-08-729

Amari, S., and Nagaoka, H. (2000). *Methods of Information Geometry*. Providence: American Mathematical Society.

Amari, S. I. (2001). Information geometry on hierarchy of probability distributions. *IEEE T. Inform. Theory* 47, 1701–1711. doi: 10.1109/18.930911

Amari, S. I., Nakahara, H., Wu, S., and Sakai, Y. (2003). Synchronous firing and higher-order interactions in neuron pool. *Neural Comput.* 15, 127–142. doi: 10.1162/089976603321043720

Blanche, T., Spacek, M., Hetke, J., and Swindale, N. (2005). Polytrodes: high-density silicon electrode arrays for large-scale multiunit recording. *Journal of Neurophysiology* 93, 2987–3000. doi: 10.1152/jn.01023.2004

Brown, E., Kass, R., and Mitra, P. (2004). Multiple neural spike train data analysis: state-of-the-art and future challenges. *Nat. Neurosci.* 7, 456–461. doi: 10.1038/nn1228

Brown, E. N., Frank, L. M., Tang, D., Quirk, M. C., and Wilson, M. A. (1998). A statistical paradigm for neural spike train decoding applied to position prediction from ensemble firing patterns of rat hippocampal place cells. *J. Neurosci.* 18, 7411–7425. doi: 10.1523/JNEUROSCI.18-18-07411.1998

Chornoboy, E. S., Schramm, L. P., and Karr, A. F. (1988). Maximum likelihood identification of neural point process systems. *Biol. Cybern.* 59, 265–275. doi: 10.1007/BF00332915

Dempster, A. P., Laird, N. M., and Rubin, D. B. (1977). Maximum likelihood from incomplete data via the EM algorithm. *J. Roy Stat. Soc. B. Met.* 39, 1–38. doi: 10.1111/j.2517-6161.1977.tb01600.x

Ezzo, J., Berman, B., Hadhazy, V. A., Jadad, A. R., Lao, L., and Singh, B. B. (2000). Is acupuncture effective for the treatment of chronic pain? A systematic review. *Pain* 86, 217–225. doi: 10.1016/S0304-3959(99)00304-8

Fujisawa, S., Amarasingham, A., Harrison, M. T., and Buzsaki, G. (2008). Behavior-dependent short-term assembly dynamics in the medial prefrontal cortex. *Nat. Neurosci.* 11, 823–833. doi: 10.1038/nn.2134

Gerstein, G., and Clark, W. (1964). Simultaneous studies of firing patterns in several neurons. *Science* 143, 1325–1327. doi: 10.1126/science.143.3612.1325

Gray, C. M., Maldonado, P. E., Wilson, M., and McNaughton, B. (1995). Tetrodes markedly improve the reliability and yield of multiple single-unit isolation from multi-unit recordings in cat striate cortex. *J. Neurosci. Methods* 63, 43–54. doi: 10.1016/0165-0270(95)00085-2

Grün, S. (2009). Data-driven significance estimation for precise spike correlation. *J. Neurophysiol.* 101, 1126–1140. doi: 10.1152/jn.00093.2008

Grün, S., Diesmann, M., and Aertsen, A. (2002a). Unitary events in multiple single-neuron spiking activity: I. detection and significance. *Neural Comput.* 14, 43–80. doi: 10.1162/089976602753284455

Grün, S., Diesmann, M., and Aertsen, A. (2002b). Unitary events in multiple single-neuron spiking activity: II. nonstationary data. *Neural Comput.* 14, 81–119. doi: 10.1162/089976602753284464

Gütig, R., Aertsen, A., and Rotter, S. (2003). Analysis of higher-order neuronal interactions based on conditional inference. *Biol. Cybern.* 88, 352–359. doi: 10.1007/s00422-002-0388-0

Han, C.-X., Wang, J., Deng, B., Yi, G.-S., and Liu, Y.-Y. (2011). Cluster Analysis of Electrical Signals from Dorsal Spinal Nerve Root Evoked by Different Acupuncture Manipulations at Zusanli Point. *Journal of Tianjin University* 5, 412–416.

Hebb, D. O. (1949). *The Organization of Behavior: A Neuropsychological Theory*. New York: John Wiley.

Kass, R. E., Kelly, R. C., and Loh, W. L. (2011). Assessment of synchrony in multiple neural spike trains using log-linear point process models. *Ann. Appl. Stat.* 5, 1262–1292. doi: 10.1214/10-AOAS429

Kim, S., Putrino, D., Ghosh, S., and Brown, E. N. (2011). A granger causality measure for point process models of ensemble neural spiking activity. *PLoS. Comput. Biol.* 7:e1001110. doi: 10.1371/journal.pcbi.1001110

Kitagawa, G. (1987). Non-Gaussian state-space modeling of nonstationary time series. *J. Am. Stat. Assoc.* 82, 1032–1041. doi: 10.1080/01621459.1987.10478534

Li, Y.-L. (2009). *Analysis and Characteristics Extraction for Acupuncture Electric Signals*. Dissertation, Tianjin University.

Long, J. D., and Carmena, J. M. (2011). A statistical description of neural ensemble dynamics. *Front. Comput. Neurosci.* 5:52. doi: 10.3389/fncom.2011.00052

Meister, M., Pine, J., and Baylor, D. A. (1994). Multi-neuronal signals from the retina: acquisition and analysis. *J. Neurosci. Methods* 51, 95–106. doi: 10.1016/0165-0270(94)90030-2

Men, C., Wang, J., Deng, B., Wei, X.-L., Che, Y.-Q., and Han, C.-X. (2012). Decoding acupuncture electrical signals in spinal dorsal root ganglion. *Neurocomputing* 79, 12–17. doi: 10.1016/j.neucom.2011.09.022

Men, C., Wang, J., Qin, Y.-M., Deng, B., and Wei, X.-L. (2011). Characterizing electrical signals evoked by acupuncture through complex network mapping: a new perspective on acupuncture. *Computer Methods Programs Biomed.* 104, 498–504. doi: 10.1016/j.cmpb.2011.08.006

Montani, F., Ince, R. A. A., Senatore, R., Arabzadeh,. E., Diamond, M. E., Panzeri, S. (2009). The impact of high-order interactions on the rate of synchronous discharge and information transmission in somatosensory cortex. *Philos. Transact. Math. Phys. Eng. Sci.* 367, 3297–3310. doi: 10.1098/rsta.2009.0082

Nakahara, H., and Amari, S. I. (2002). Information-geometric measure for neural spikes. *Neural Comput.* 14, 2269–2316. doi: 10.1162/08997660260293238

Ohiorhenuan, I. E., Mechler, F., Purpura, K. P., et al. (2010). Sparse coding and high-order correlations in fine-scale cortical networks. *Nature* 466, 617–621. doi: 10.1038/nature09178

Okatan, M., Wilson, M. A., and Brown, E. N. (2005). Analyzing functional connectivity using a network likelihood model of ensemble neural spiking activity. *Neural. Comput.* 17, 1927–1961. doi: 10.1162/0899766054322973

Perkel, D. H., Gerstein, G. L., and Moore, G. P. (1967). Neuronal spike trains and stochastic point processes. *Biophysical Journal* 7, 419–440. doi: 10.1016/S0006-3495(67)86597-4

Pillow, J. W., Shlens, J., Chichilnisky, E. J., and Simoncelli, E. P. (2013). A Model-Based Spike Sorting Algorithm for Removing Correlation Artifacts in Multi-Neuron Recordings. *Plos. one* 8, e62123. doi: 10.1371/journal.pone.0062123

Pillow, J. W., Shlens, J., Paninski, L., Sher, A., et al. (2008). Spatio-temporal correlations and visual signalling in a complete neuronal population. *Nature* 454, 995–999. doi: 10.1038/nature07140

Rissanen, J. (2009). *Information and Complexity in Statistical Modeling*. New York, NY: Springer.

Roudi, Y., Nirenberg, S., and Latham, P. E. (2009). Pairwise maximum entropy models for studying large biological systems: when they can work and when they can't. *PLoS. Comput. Biol.* 5:e1000380. doi: 10.1371/journal.pcbi.1000380

Santos, G. S., Gireesh, E. D., Plenz, D., and Nakahara, H. (2010). Hierarchical interaction structure of neural activities in cortical slice cultures. *J. Neurosci.* 30, 8720–8733. doi: 10.1523/JNEUROSCI.6141-09.2010

Schwarz, G. (1978). Estimating the dimension of a model. *Ann. Stat.* 6, 461–464. doi: 10.1214/aos/1176344136

Segev, R., Goodhouse, J., Puchalla, J., and Berry, M. J. (2004). Recording spikes from a large fraction of the ganglion cells in a retinal patch. *Nat. Neurosci.* 7, 1155–1162. doi: 10.1038/nn1323

Shumway, R., and Stoffer, D. (1982). An approach to time series smoothing and forecasting using the EM algorithm. *J. Time Ser. Anal.* 3, 253–264. doi: 10.1111/j.1467-9892.1982.tb00349.x

Smith, A. C., and Brown, E. N. (2003). Estimating a state-space model from point process observations. *Neural Comput.* 15, 965–991. doi: 10.1162/089976603765202622

Smith, A. C., Frank, L. M., Wirth, S., Yanike, M., Hu, D., Kubota, Y., et al. (2004). Dynamic analysis of learning in behavioral experiments. *J. Neurosci.* 24, 447–461. doi: 10.1523/JNEUROSCI.2908-03.2004

Staude, B., Grun, S., and Rotter, S. (2010a). Higher-order correlations in non-stationary parallel spike trains: statistical modeling and inference. *Front. Comput. Neurosci.* 4, 108–124. doi: 10.3389/fncom.2010.00016

Staude, B., Rotter, S., and Grun, S. (2010b). CuBIC: cumulant based inference of higher-order correlations in massively parallel spike trains. *J. Comput. Neurosci.* 29, 327–350. doi: 10.1007/s10827-009-0195-x

Truccolo, W., Eden, U. T., Fellows, M. R., Donoghue, J. P., and Brown, E. N. (2004). A point process framework for relating neural spiking activity to spiking history, neural ensemble, and extrinsic covariate effects. *J. Neurophysiol.* 93, 1074–1089. doi: 10.1152/jn.00697.2004

Xue, M., Wang, J., Deng, B., Wei, X.-L., Yu, H.-T., and Chen, Y.-Y. (2013). Characterizing neural activities evoked by manual acupuncture through spiking irregularity measures. *Chinese Phys. B* 22:098703. doi: 10.1088/1674-1056/22/9/098703

Yu, S., Yang, H., Nakahara, H., Santos, G. S., et al. (2011). Higher-order interactions characterized in cortical activity. *J. Neurosci.* 31, 17514–17526. doi: 10.1523/JNEUROSCI.3127-11.2011

Zhou, T., Wang, J., and Han, C.-X. (2012). Nonlinear dynamic analysis of electrical signals of wide dynamic range neurons in the spinal dorsal horn evoked by acupuncture manipulation at different frequencies. *Chinese J. Integrated Traditional Western Med.* 32, 1403–1406. Available online at: https://schlr.cnki.net/Detail/index/SJPD_04/SJPD13012100972315

Conflict of Interest: The authors declare that the research was conducted in the absence of any commercial or financial relationships that could be construed as a potential conflict of interest.

Copyright © 2020 Qin, Liu, Shan, Che, Han, Qin and Wang. This is an open-access article distributed under the terms of the Creative Commons Attribution License (CC BY). The use, distribution or reproduction in other forums is permitted, provided the original author(s) and the copyright owner(s) are credited and that the original publication in this journal is cited, in accordance with accepted academic practice. No use, distribution or reproduction is permitted which does not comply with these terms.

frontiers in Computational Neuroscience

ORIGINAL RESEARCH
published: 20 November 2020
doi: 10.3389/fncom.2020.588881

Topographic Organization of Correlation Along the Longitudinal and Transverse Axes in Rat Hippocampal CA3 Due to Excitatory Afferents

Gene J. Yu, Jean-Marie C. Bouteiller and Theodore W. Berger*

Department of Biomedical Engineering, Center for Neural Engineering, University of Southern California, Los Angeles, CA, United States

The topographic organization of afferents to the hippocampal CA3 subfield are well-studied, but their role in influencing the spatiotemporal dynamics of population activity is not understood. Using a large-scale, computational neuronal network model of the entorhinal-dentate-CA3 system, the effects of the perforant path, mossy fibers, and associational system on the propagation and transformation of network spiking patterns were investigated. A correlation map was constructed to characterize the spatial structure and temporal evolution of pairwise correlations which underlie the emergent patterns found in the population activity. The topographic organization of the associational system gave rise to changes in the spatial correlation structure along the longitudinal and transverse axes of the CA3. The resulting gradients may provide a basis for the known functional organization observed in hippocampus.

Keywords: correlation, CA3, large-scale model, connectivity, neuronal network, hippocampus, topography

OPEN ACCESS

Edited by:
Spase Petkoski, INSERM U1106 Institut de Neurosciences des Systèmes, France

Reviewed by:
Bailu Si, University of Chinese Academy of Sciences, China
Adam Ponzi, Okinawa Institute of Science and Technology Graduate University, Japan

****Correspondence:***
Gene J. Yu
gene.jong.yu@gmail.com

Received: *29 July 2020*
Accepted: *22 October 2020*
Published: *20 November 2020*

Citation:
Yu GJ, Bouteiller J-MC and Berger TW (2020) Topographic Organization of Correlation Along the Longitudinal and Transverse Axes in Rat Hippocampal CA3 Due to Excitatory Afferents. Front. Comput. Neurosci. 14:588881. doi: 10.3389/fncom.2020.588881

INTRODUCTION

The architecture and connectivity of rat hippocampus has been intensely studied, revealing a prominent topographic organization within the highly complex and tortuous structure of the hippocampal anatomy. Despite a thorough characterization of the macroscale, mesoscale, and microscale connectivity of rat hippocampus, the contributions of the architecture of the afferent and efferent projections to the organization of population dynamics has yet to be fully understood. This is partly due to the difficulty in interpreting and integrating the results of the key studies, many of which were performed several decades ago, into a single comprehensive model. The technical difficulty in recreating these studies with either older or more modern methods limit further characterizations of the microscale and mesoscale topography. Few computational models of neural systems have attempted to represent their full geometrical, or at least up to an extent at which the mesoscale contributions to population activity can be observed (Schneider et al., 2012; Markram et al., 2015; Hendrickson et al., 2016; Billeh et al., 2020). Yet, these types of anatomical-scale models are necessary to explore the contributions of topographically organized connectivity on the spatio-temporal dynamics of their respective neural systems.

At a basic level, connectivity determines the spatial arrangement of postsynaptic activation given a presynaptic spike resulting in a correlation across neurons, i.e., a spatially organized

correlation. Pairwise spike correlations between neurons have been shown to capture much of the statistical properties of a single neuron and provide a measure for studying the properties of population activity (Helias et al., 2014; Dettner et al., 2016). Weak pairwise correlations have been demonstrated to give rise to emergent spatiotemporal structures in population activity (Halliday, 2000; Schneidman et al., 2006; Kriener et al., 2009; Renart et al., 2010; Senk et al., 2018; Yu et al., 2018).

The relation between connectivity and spatially organized correlation is due to the spatial distribution of an axon and the sparsity/density of its connectivity which then determine the amount of input overlap/input sharing that occurs among neurons. Theoretical studies have characterized the role of input sharing in determining the correlation that a postsynaptic population exhibits and the propagation of the correlation through multiple layers (Kumar et al., 2010; Rosenbaum et al., 2011, 2016; Darshan et al., 2018). Such studies have also revealed how the interactions between feedforward and recurrent inhibitory circuits nonlinearly affect the spatial structure of correlation. Beyond spatial correlation, the temporal correlation can also be considered in the correlation structure which is determined by the electrophysiology of the postsynaptic neuron and the synaptic properties (Tetzlaff et al., 2008; Hong et al., 2012; Chan et al., 2016; Yu et al., 2018). Given these principles, we investigated the population dynamics and spatiotemporal correlation structure that resulted from different types of connectivity in a hippocampus-specific context.

Using an entorhinal-dentate network, we had previously revealed a role of anatomically-constrained connectivity in organizing random inputs into spatially and temporally dense regions of activity called clusters (Hendrickson et al., 2016; Yu et al., 2018). The spatial properties of the clusters were found to be influenced by the anatomy of the axonal projections, i.e., the spatial extent of the axon terminal field. This previous work was limited to exploring the effect of a single feedforward projection on a single neural population. In the present work, the entorhinal-dentate work was expanded to investigate (1) how spatio-temporal patterns within the dentate gyrus would be preserved when propagated to the CA3 subfield, (2) how multiple feedforward projections would interact to influence the spatio-temporal pattern of the CA3, and (3) how a recurrent excitatory projection, i.e., the associational system, would further transform the activity.

A large-scale entorhinal-dentate-CA3 neuronal network model with spatially-dependent and topographically-organized connectivity was constructed that encompasses the full geometric extent of a rat hippocampus using compartmental models of neurons (**Figure 1**). From the entorhinal-dentate network, the perforant path projection and dentate mossy fibers were included to connect the entorhinal cortex and dentate gyrus to the CA3, and the recurrent associational system was added. By computing a spatio-temporal correlation map, a heterogeneous correlation structure was discovered which varied in amplitude and shape along both the longitudinal and transverse spatial axes of the CA3 and further evolve in time.

MATERIALS AND METHODS

Neuron Models

The CA3 pyramidal cell is the principal neuron of the CA3, and the basis of the CA3 pyramidal cell models used in the present work originated from a study in which three major firing types were discovered: bursting, strongly adapting, and weakly adapting (Hemond et al., 2008). They published three models with biophysical parameters and spiking behavior that best represented *in vivo* recordings of CA3 pyramidal cells that demonstrated the different firing types. For the three models, the biophysical parameters had been distributed upon a single, morphological reconstruction of the apical and basal dendrites of a CA3 pyramidal cell. The models contained the following ion channels: sodium, delayed-rectifier K^+, A-type K^+, D-type K^+, M-type K^+, T-type Ca^{2+}, N-type Ca^{2+}, L-type Ca^{2+}, calcium-dependent K^+ (CaGK), calcium-dependent K^+ (BK), HCN, and leak channels (see **Supplementary Tables 1–3**). In the present work, the morphology of the models from Hemond et al. (2008) was simplified using an algorithm that used circuit theory to combine compartments connected in series and in parallel to create simplified equivalent circuit representations of complex morphologies (Marasco et al., 2012). The algorithm was used in the current work to construct simplified models while preserving the firing behavior exhibited by the original models (**Figure 2C**). The simplified models contained eight compartments corresponding to a compartment for each layer upon which input is received and reduced simulation times by a factor of 20. Model parameters are summarized in the **Supplementary Tables 1–4**. The computational models were simulated using NEURON v7.5 and scripted using Python 2.7.

The entorhinal-dentate network used in the present study was the same as described in Yu et al. (2018, 2019) and is extensively described there. Dentate granule cells were represented using a simplified morphology that was constructed using the same technique as for the CA3 pyramidal cell models (Marasco et al., 2012). Entorhinal cortical cells were represented using a renewal process that consisted of a homogeneous Poisson process with an exponentially-decaying refractory period with a time constant of 35 ms.

The entorhinal-dentate-CA3 network was comprised of 112,000 entorhinal cortical cells, 120,000 dentate granule cells, and 25,000 CA3 pyramidal cells which represents one-tenth of the full number of dentate granule cells and CA3 pyramidal cells within the rat hippocampus (Mulders et al., 1997). Each simulation represented 5 s of real-time at a time step of 0.025 ms and was run using 100 cores from Dual Intel Xeon 2.4 GHz CPUs resulting in a wall-time of approximately 4 h per simulation. Each core was allocated 2 GB of RAM for a total of 200 GB of RAM per simulation. The simulations were performed using the computing resources provided by the Center for Advanced Research Computing at the University of Southern California.

Topography of Afferent Inputs to CA3 Pyramidal Cells

Hippocampal Anatomy

To describe the CA3 network model, some background regarding the structure of the hippocampus must be given, and

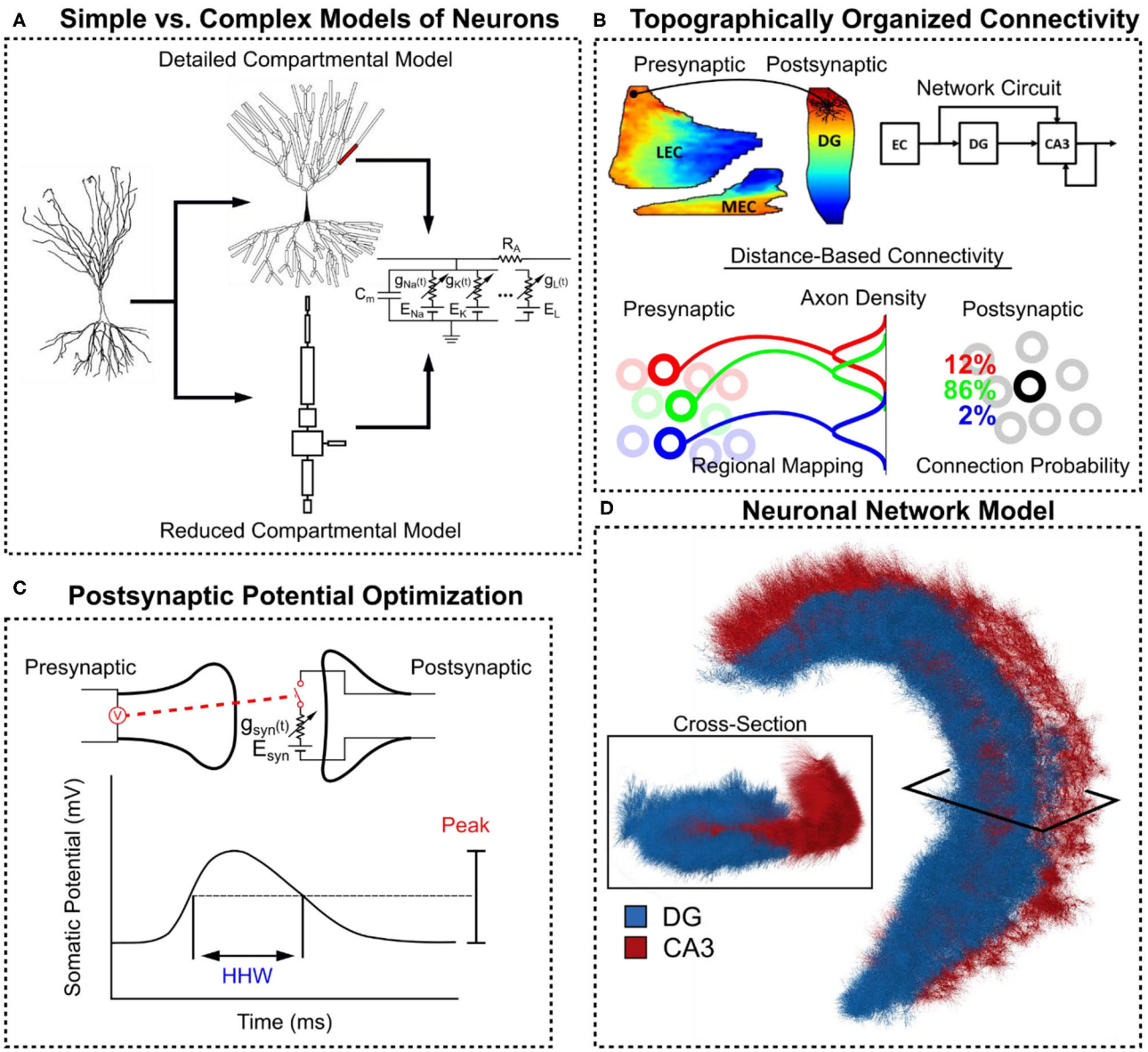


FIGURE 1 | Overview of methods in constructing the large-scale hippocampal model. **(A)** Compartmental models of CA3 pyramidal cells with Hodgkin-Huxley style dynamics were constructed. A detailed version with realistic morphology was converted into a reduced equivalent compartment model. **(B)** Anatomical data was used to define a topographically-organized, spatially-dependent connectivity. **(C)** The postsynaptic potential for each pre-post synapse type was characterized using their peak value and their half-height width (HHW). **(D)** A three-dimensional hippocampal model consisting of the dentate gyrus and CA3 was constructed for this study.

common terminology to describe the hippocampal anatomy must be established. Briefly, the rat hippocampus is organized into three areas: the dentate gyrus, CA3 subfield, and CA1 subfield (**Figure 3A**). The simplified trisynaptic circuit of the hippocampus is a predominantly feedforward pathway that begins in the entorhinal cortex and describes the propagation of activity from entorhinal cortex, to dentate gyrus, to CA3, and finally to CA1 (Andersen, 1975). There are many more details to the full description of the circuits within the hippocampus such as back projections and the CA2, but the simplified trisynaptic circuit captures the major organization of the hippocampus.

The hippocampus is a three-dimensional structure, and the curved nature of the layers do not allow positions to easily be described using three-dimensional cartesian coordinate systems. Therefore, neuroanatomists developed a technique to unfold and flatten the structure to describe the anatomy using a two-dimensional coordinate system (**Figure 3A**). The longitudinal axis can generally refer to the dorso-ventral axis, septo-temporal axis, or y-axis of the hippocampus. The transverse axis can generally refer to the proximodistal axis or x-axis of the hippocampus. The proximodistal axis within CA3 refers to position with respect to the dentate gyrus, and the CA3 has

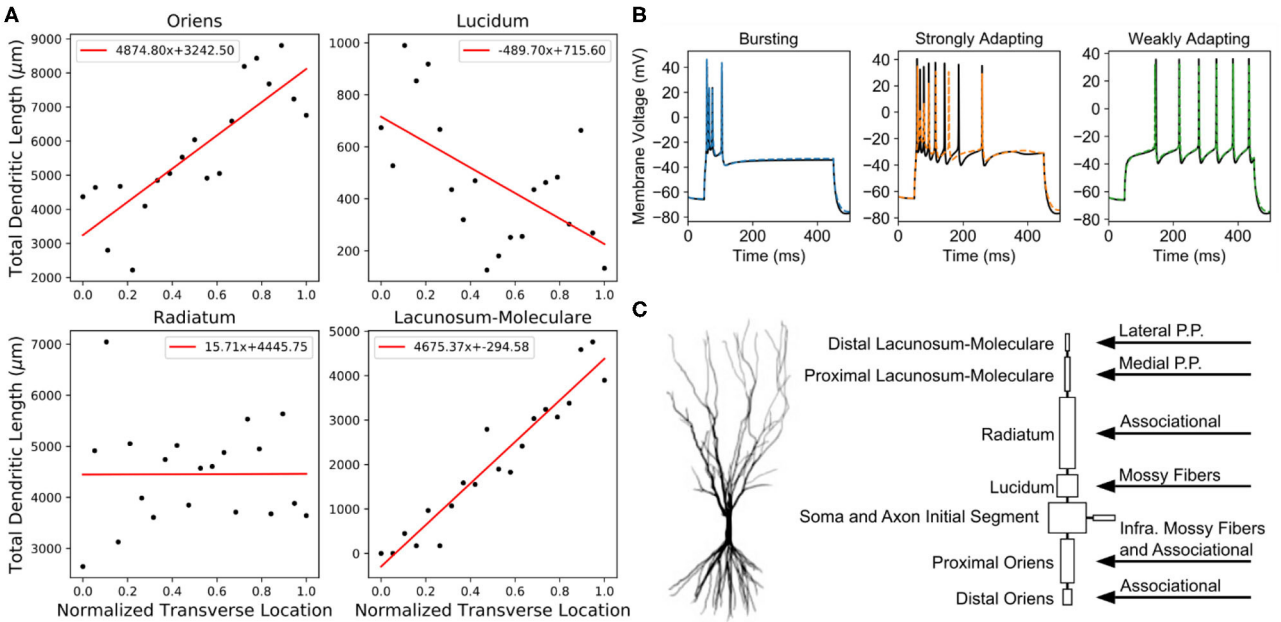


FIGURE 2 | Anatomical details and spiking behavior of CA3 pyramidal cell models. **(A)** The total dendritic length varied based on the transverse position of the model within the CA3 subfield. These lengths and the synaptic densities in each layer (**Table 1**) were used to determine the numbers of each input type that a model received. **(B)** After the reduced models (dashed colored lines) preserved the different spiking behaviors as the original models (solid black lines). **(C)** The original morphology was reduced to eight compartments. On the right, the specific regions that received a particular input type are denoted.

been commonly divided into three subregions along this axis. The CA3c, CA3b, and CA3a are organized with the CA3c being most proximal to dentate gyrus and CA3a being most distal to dentate gyrus.

Anatomically-Constrained Mesoscale and Microscale Connectivity

The major intrahippocampal afferents to CA3 pyramidal cells were considered in this study: the lateral perforant path input, the medial perforant path input, mossy fiber input, and the associational input. Anatomical data was used to define and constrain the topography of the various projections. The topography describes the regional mapping between layers/subfields of the hippocampal formation. Relevant data include anterograde and retrograde tracer injection studies which can reveal the relation between position within a hippocampal subfield and the region within the postsynaptic area to which axons are sent (anterograde) or the region within the presynaptic area from which axons are received (retrograde). Another crucial aspect of the anatomy is the spatial distribution of the axon terminal field within the postsynaptic area. Under the assumption that a greater axonal density results in a larger number of connections, the axonal distribution was converted into a probability distribution with a higher density corresponding to a higher probability of connection. Thus, connectivity was stochastically generated by first defining the regional mapping between the position of a presynaptic neuron and the postsynaptic region to which axons are sent. Then, the axonal density was used to define a spatial constraint resulting in a spatially dependent connectivity. The topographic regional mapping corresponds to mesoscale connectivity, and the resulting connections based on the axonal density correspond to the microscale connectivity.

Axons were not explicitly represented in the models but were represented as a propagation delay based on the path length between the presynaptic and postsynaptic neurons and the conduction velocity. Conduction velocities of 0.32 m/s, 0.27 m/s, and 0.39 m/s were used for the perforant path (Tielen et al., 1981), mossy fibers (Kress et al., 2008), and associational system (Andersen et al., 2000), respectively. The anatomical data and methods for quantifying them that are described below were initially introduced in earlier work (Yu et al., 2014, 2015).

The perforant path refers to the projection arising from the entorhinal cortex that are sent to the dentate gyrus and CA3 and is divided into the lateral and medial perforant path based on their origin from the lateral and medial areas of the entorhinal cortex. They initially synapse onto the dentate gyrus before continuing onwards and making a monosynaptic connection with the CA3 (Yeckel and Berger, 1990). Within the dentate gyrus and CA3, the lateral and medial perforant paths terminate on different strata which, for the CA3, are the distal and proximal lacunosum-moleculare, respectively. Because the same axons that synapse in the dentate gyrus continue to the CA3, the topographical map from entorhinal cortex to dentate gyrus was used to describe the mapping from entorhinal cortex to CA3. The data used to describe the entorhinal-dentate topography came from the series of retrograde tracer studies

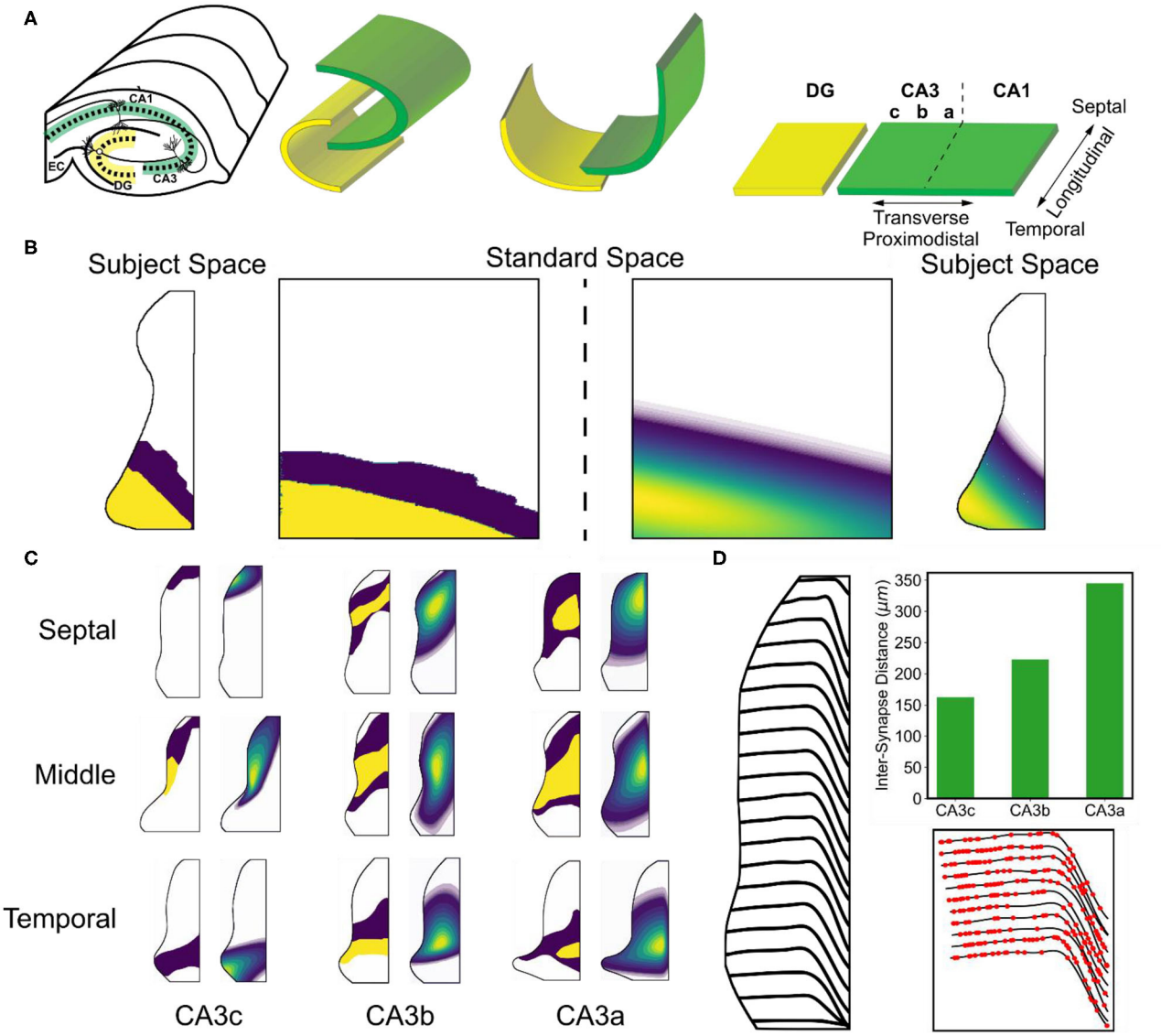


FIGURE 3 | Overview of mossy fiber and associational topography. **(A)** A conceptual diagram depicts how a flattened representation of the hippocampus can be made from the original 3D structure. The transverse axis refers to the proximodistal axis. The longitudinal axis refers to the septotemporal/ dorsoventral axes. **(B)** The original data that revealed the organization of the associational system was reported using two intensity values. The data was mapped onto a standard space, fit to a parameterized equation, and then remapped back into subject space. **(C)** Examples of the original data and resulting fits are shown. **(D)** The trajectories of the mossy fibers are shown in the CA3 subfield. The top right subplot indicates the change inter-synapse distance that occurs along the mossy fiber. The bottom right subplot shows example synapse locations.

(Dolorfo and Amaral, 1998), and the extent of the axon terminal field along the longitudinal axis was reported to be 1–1.5 mm (Tamamaki, 1997). A Gaussian distribution was used to represent the connection probability of a perforant path axon terminal field. The resulting map predicts a longitudinal organization of the entorhinal projection to dentate gyrus (**Figure 1B**). A detailed description of the data and method for extracting the topography are described previously in Hendrickson et al. (2016) and Yu et al. (2019). To summarize this method, a workflow was developed to digitize the data, map the results of the injection onto a standard space, perform averaging when relevant within the standard space, and finally remap the averaged data onto a chosen subject rat space.

The mossy fibers describe the axons that are sent by dentate granule cells to the CA3. Each mossy fiber can be generally characterized as a single fiber which initially stays within the same longitudinal level from which it originates and then travels through the CA3 predominantly along the transverse axis for the first two-thirds (i.e., within CA3c and CA3b) before turning toward the temporal pole of the longitudinal axis within CA3a (**Figure 3D**) (Acsády et al., 1998). The fiber trajectories were estimated using data published in Swanson et al. (1978)

by measuring the deviation of the fiber with respect to the longitudinal level of origin as it traversed the proximodistal extent of the CA3. The deviations as a function of longitudinal origin were interpolated using a cubic b-splines fit to represent a smooth change in fiber trajectory. To generate the fibers, noise was added to the points representing each fiber trajectory create variable fibers.

The longitudinal and transverse organization of the associational system was most thoroughly revealed by Ishizuka et al. (1990) using anterograde tracers. The tracer was injected into one of nine areas within the CA3 which roughly covered a 3 × 3 grid with injections within the CA3c, CA3b, and CA3a as well as the septal, middle, and temporal levels. The resulting distribution of tracer represents the density and spatial extent to which axons were sent. Density in the study was represented using three qualitative levels: a zero level, a low density level, and a high density level. Similar to the entorhinal-dentate/CA3 topography, the data were digitized and mapped onto a standard space (**Figure 3B**). Within the standard space, distribution of labeling was parameterized using a two-dimensional skew gaussian equation. The parameters of the equation could then be interpolated/extrapolated to estimate the distribution of CA3 associational axons for areas that were not covered by an injection (**Figure 3C**).

Numbers of Synapses

The final step to generating connectivity is to define the numbers of connections that are possible. There are two method by which the number of connections could be constrained. From a postsynaptic perspective, the number of inputs that could be received for a presynaptic population can be estimated by using spine count information which could be obtained by using spine density and dendritic length measurements. Due to highly stratified nature of the CA3 afferents, the number of inputs for each afferent could be estimated by calculating the total number of spines for the different layers to which the afferents project. The second method for constraining the number of inputs is to use the presynaptic population's axon measurements. The bouton density and the axon length can be used to estimate the number of connections that a presynaptic neuron forms with a postsynaptic population. The strata to which the various projections are restricted are summarized in **Figure 2**.

The total dendritic length of each strata within CA3 change along the proximodistal axis as revealed by Ishizuka et al. (1995). In general, the total dendritic length is smallest proximally, and it is largest distally (**Figure 2A**). The spine density within each stratum are not well studied for CA3 pyramidal cells. Rather, spine densities have been meticulously characterized for CA1 pyramidal cells and were used to estimate the numbers of synapses for CA3 pyramidal cells (Megias et al., 2001). The total synapse numbers are summarized in **Table 1**. Using these calculations, the number of inputs for the perforant path and associational projections were constrained for the model.

Because the synaptic density within the stratum lucidum was not characterized in CA1, the second method of using the presynaptic axon properties was used to constrain the number of inputs for the mossy fibers. The inter-synapse distance had been measured for mossy fibers which revealed that the inter-synapse distance changed as the fiber moved from CA3c to CA3b to CA3a (Acsády et al., 1998). Using a Poisson process, the locations of mossy fiber synapses along the fiber were estimated using the reported mean values of 162 ± 12.6 μm in CA3c, 223 ± 19.3 μm in CA3b, and 345 ± 27.5 μm in CA3a (**Figure 3D**). Mossy fibers originating in the suprapyramidal blade of the dentate gyrus were restricted to the stratum lucidum. Mossy fibers originating in the infrapyramidal blade were restricted to the proximal stratum oriens within CA3c before moving into the stratum lucidum for the CA3b and CA3a.

Having defined the topography, spatially dependent connection probabilities, and the numbers of connections the connectivity of the network could be stochastically generated. For the postsynaptic method, the connection probabilities for each presynaptic neuron for a given afferent were collected for each CA3 pyramidal cell. The connection probabilities were normalized, and a presynaptic neuron was randomly selected until the total number of connections for that particular afferent was achieved. For the presynaptic method, a postsynaptic neuron was randomly selected for each synapse location. A postsynaptic neuron within 30 μm of the synapse was considered based on measurements performed by Acsády et al. (1998). The distribution of the number of mossy fiber inputs is found in **Supplementary Figure 1**.

Synapse Models

Neuron communication in the model was mediated exclusively through synapse-like processes. The synapse was modeled as a deterministic process in which an action potential activates a change in synaptic conductance. The time-course of the synaptic conductance was represented using a double exponential function for AMPA receptors (Kleppe and Robinson, 1999) and a triple exponential function for NMDA receptors. The NMDA receptor was additionally modulated by a sigmoidal function to capture the magnesium-related voltage dependence of the receptor (Jahr and Stevens, 1990; Zador et al., 1990).

$$g_{AMPAR}(t) \propto e^{\frac{-t}{\tau_2}} - e^{\frac{-t}{\tau_1}},\ \tau_2 > \tau_1$$

$$g_{NMDAR}(t,v) \propto \frac{w \cdot e^{\frac{-t}{\tau_3}} + (1-w) \cdot e^{\frac{-t}{\tau_2}} - e^{\frac{-t}{\tau_1}}}{1 + e^{-0.062v \cdot [Mg^{2+}]/3.57}},\ \tau_3 > \tau_2 > \tau_1$$

The t and v variables correspond to time in milliseconds and membrane potential in millivolts. The τ variables are time constants that control the time-course of the waveform. The w variable for the NMDA receptor is a weighting variable constrained within (0, 1). The equations are normalized using the peak value of the exponential functions, i.e., ignoring the denominator for the NMDA receptor. This can be solved analytically for the AMPA receptor by setting the derivative to zero. For the NMDA receptor, the solution was empirically derived after setting the derivative to zero and finding the intersection of the left- and right-hand sides of the equation. The normalized synaptic conductance equations are then multiplied by a factor corresponding to the synaptic weight. The synaptic weights are constrained such that the resulting

TABLE 1 | Number of inputs received by the CA3 pyramidal cells and EPSP properties.

	Lacunosum distal (LEC)	Lacunosum proximal (MEC)	Radiatum (associational)	Oriens (associational)
Synaptic Density[a]	0.63	0.63	3.61	3.15
Number of Inputs (Proximal)	0	0	11,241	7,147
Max. Number of Inputs (Distal)	1,658	1,105	11,281	17,893

The proximal vs. distal inputs are based on the multiplication of the synaptic density and the total dendritic length within the relevant layer. Between the proximal and distal ends, the numbers of inputs change linearly.
[a] *Megias et al. (2001).*

TABLE 2 | EPSP properties.

	Lacunosum distal (LEC)	Lacunosum proximal (MEC)	Radiatum (associational)	Lucidum (mossy fiber)	Oriens proximal (mossy fiber)	Oriens distal (associational)
Peak (mV)	0.30[a]	0.30[a]	0.30[a]	3.2[b]	3.2[b]	0.30[a]
HHW (ms)	46.1[a]	46.1[a]	40.9[a]	135[c]	135[c]	38.0[a]

[a] *Perez-Rosello et al. (2011).*
[b] *Lawrence et al. (2003).*
[c] *Scanziani et al. (1993).*

excitatory postsynaptic potential (EPSP) recorded from the soma match those reported from unitary synaptic release experiments for the relevant presynaptic-postsynaptic synapse pairings. The time constants for the AMPA receptor were similarly separately constrained such that the half-height width of resulting somatic EPSP matched the experimentally reported values (**Table 2**). The parameters for the synapses are summarized in **Supplementary Tables 5**–**8**.

Three-Dimensional Space-Time Correlation Maps

The spatial and temporal correlation structure of the network was constructed by computing the pairwise correlation of the spiking activity for all neuron pairs and averaging the normalized cross-correlations of neuron pairs that were located at the same relative distance (**Figure 4**). The normalized cross-correlation was computed by binning the spike times of the neurons and using the following equation:

$$\left(x \star y\right)[n] = \frac{1}{\sigma_x \sigma_y} \sum_{m=0}^{N-1} \frac{1}{L_m} \left(x[m] - \mu_x\right) \left(y[m+n] - \mu_y\right)$$

for which the $\star$ operator represents correlation, x and y correspond to the binary spike trains, σ is the standard deviation of the spike trains, μ is the mean of the spike trains, N is the total length of the spike train, and L_m is the size of the overlap between the signals while they are being shifted.

A three-dimensional matrix was constructed with an axis corresponding to time, an axis for the longitudinal distance between the neuron pair, and an axis for the transverse distance between the neuron pair. The temporal resolution for binning the spikes was 1 ms. The spatial resolution for the longitudinal and transverse axes was 0.1 mm.

There were two types of space-time correlation maps that were generated for this study (**Figure 4**). The first type was the global map which computed the space-time correlation map for all possible neuron pairs. The global map then represents the average correlation structure for all principal neurons within a hippocampal subfield. The second type of map was the local map which divided the CA3 into a 3 × 3 grid of longitudinal and transverse sections based on the CA3a, CA3b, and CA3c subdivisions along the transverse axis and the septal, middle, and temporal subdivisions along the longitudinal axis. Local maps were specific to each of these sections and were computed using neuron pairs only if at least one of the neurons was located in the corresponding longitudinal/transverse section. This constraint caused the resulting space-time correlation map to be representative of a smaller population of neurons, as defined by the longitudinal/transverse position. In contrast to the global map which considered every neuron pair, the local map provided a more granular characterization of the correlation map a local map to represent each of the nine longitudinal/transverse sections.

RESULTS

Input to the entorhinal-dentate-CA3 network was primarily provided by the entorhinal cortex, and the spiking activity of each entorhinal neuron was represented with a renewal process comprised of a Poisson process with an exponentially decaying refractory period that modified the spiking probability after the generation of a spike. The mean firing rate of the Poisson process was 5 Hz. The resulting input had a uniform power density in the

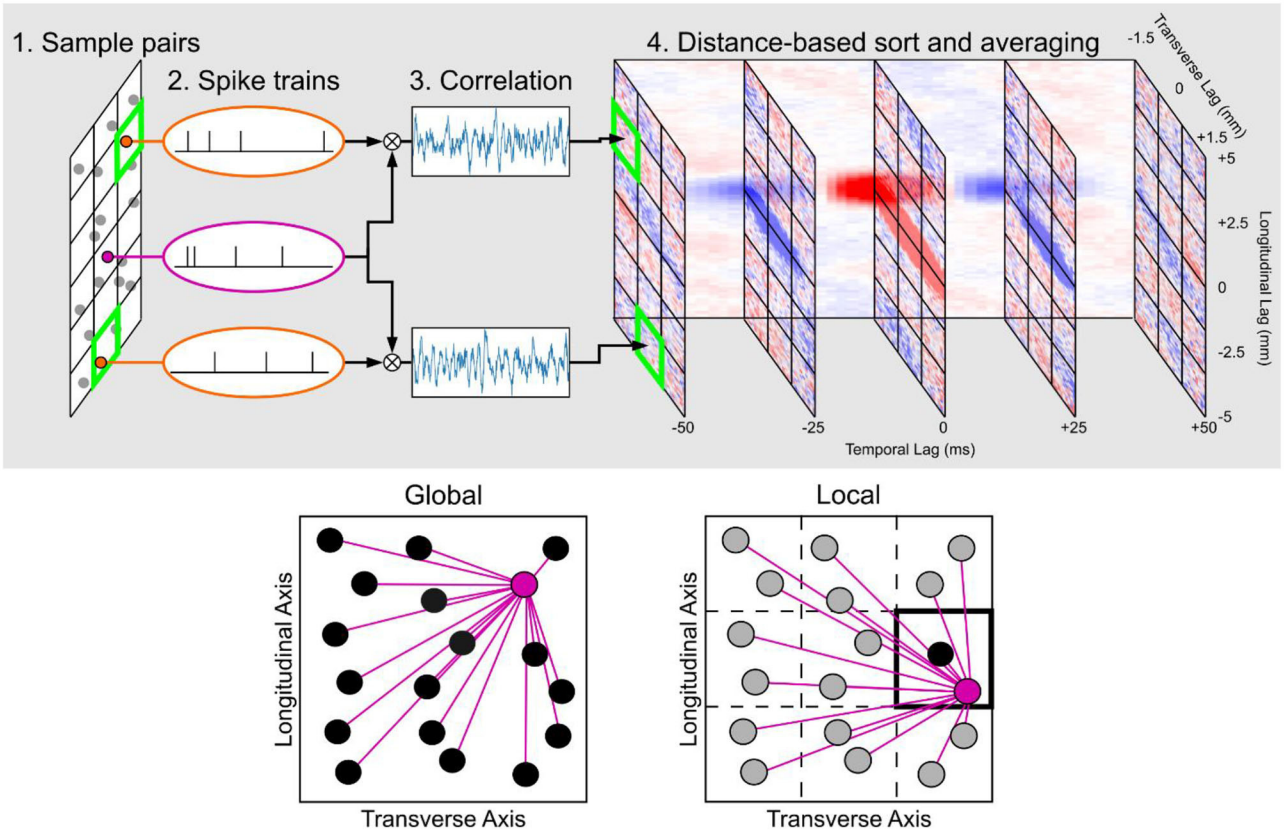


FIGURE 4 | Summary of the construction of the space-time correlation maps. (**Top row**) The workflow in calculating pairwise spike correlations and placing them in a matrix that is organized by the longitudinal, transverse, and temporal lags. (**Bottom row**) Global vs. local space-time correlation map. In the global map, all neuron pairs were considered to construct an average correlation map to represent all neurons that were included to compute the map. In the local map, only neuron pairs with at least one neuron within the chosen section were used in the calculation which results in a correlation map that is specific to the section to which the neuron pairs were constrained. In the local map example highlighted in the figure, the resulting correlation map would be representative for the neurons within the section located in the second row and third column.

frequency domain and was spatially and temporally uncorrelated. Though the random input does not contain behavioral or spatial information, the mean firing rate was determined based on the mean firing rate of the grid cells modeled in Yu et al. (2019) and served as a control to eliminate any correlation that may arise due to a common physiological/behavioral drive.

The simulations described throughout the results can be organized based on the afferent projections that were present and the activity of the dentate granule cells. For the different afferent projections, there was the perforant path (PP-CA3) model which includes only the entorhinal projection, the mossy fiber (MF-CA3) model which includes only the mossy fiber projection, the perforant path-mossy fiber (PP-MF-CA3) model which includes both perforant path and mossy fiber projections, and the perforant path-mossy-fiber-assocational (PP-MF-A-CA3) model which includes the perforant path, mossy fiber, and associational projections. As described in the previous paragraph, the entorhinal cortex only generated random input. However, the dentate granule cell activity was generated using two methods. The first method uses the entorhinal activity and the dentate gyrus network model to generate the dentate granule cell activity and represents the natural dentate response to entorhinal activity. This method introduces a weak spatial and temporal correlation to the dentate granule cell activity due to the topographic connectivity. The second method represents the dentate granule cell activity using a renewal process with a mean firing rate of 0.62 Hz which was the mean firing rate of the dentate granule cells due to entorhinal input. Therefore, the key difference between the first and second methods for dentate granule cell activity was the presence of an inherent spatial and temporal correlation in the activity using the first method and the absence of a correlation in the activity using the second method. These differences in terms of the model are denoted using as weakly correlated mossy fiber (wcMF) or random mossy fiber (rMF).

Simulations were initially performed with synaptic weights that were constrained to elicit the appropriate EPSP peak values, and additional simulations were performed that multiplied the original synaptic weights with scalar factors. The perforant path and mossy fibers each had their synaptic weights modified by

factors of 0.5, 1, 2, 3, and 5 with 1 corresponding to the original synaptic weight.

Spiking Activity and Global Correlation Maps

The longitudinal axis of the hippocampus is much larger than the transverse axes of the hippocampal regions. Additionally, there is a significant longitudinal organization to the topography between regions. These details have supported the presentation of hippocampal activity along the longitudinal axis. The following subsections present the raster plots of spiking activity and the corresponding space-time correlation maps as functions of longitudinal position and time with the same scale to demonstrate the similarities between the spatio-temporal patterns of activity and the space-time correlation map. The slice of the space-time correlation map was taken at a transverse lag of 0 mm, and the color maps were thresholded to 30% of the maximum value to better visualize the weaker negative correlations.

Entorhinal Perforant Path Projection (PP-CA3 and PP-DG Models)

There is a monosynaptic projection from entorhinal cortex to both dentate gyrus and CA3 meaning that the entorhinal cortex directly projects onto their principal neurons. Though the monosynaptic perforant path projection onto dentate gyrus has already been extensively covered (Hendrickson et al., 2016; Yu et al., 2018, 2019), a brief analysis is presented here for comparison with CA3. In CA3, the spatially and temporally uncorrelated entorhinal input (PP-CA3 model) was converted into network activity that exhibited a weak clustering (**Figure 5A**, i). Dentate granule cells (PP-DG model) responded with more visible clusters (**Figure 5A**, iv). A global space-time correlation map was computed with the CA3 pyramidal cells having a peak correlation of 0.0026 and the dentate granule cells having a peak correlation of 0.03 which is approximately an order of magnitude greater (**Figure 5B**, i,iv). The spatial extent of the correlation for both granule cells and CA3 pyramidal cells were nearly identical at approximately 1 mm.

These results indicate that the formation of clusters due to the perforant path are not unique to the dentate gyrus but can be generalized for different neural systems. Given a shared axonal distribution, the spatial extent of the correlation is preserved. However, the specific electrophysiology of the neuron types does affect the extent of temporal correlation. Other differences between the granule cells and CA3 pyramidal cells include the numbers of inputs that they receive from perforant path. The CA3 pyramidal cells receive much fewer inputs than granule cells and therefore share fewer inputs among their neighbors. This results in a lower peak correlation and noisier clusters.

Dentate Mossy Fiber Projection (rMF-CA3 and wcMF-CA3 Models)

The role of mossy fibers in organizing spatio-temporal activity was investigated within two conditions. The random mossy fiber (rMF) condition represented the dentate granule cell activity using an independent Poisson process that had the same mean firing rate as the weakly correlated mossy fiber (wcMF) condition which was 0.62 Hz. The wcMF represented the disynaptic propagation of entorhinal activity via mossy fibers to CA3, i.e., the dentate activity in **Figure 5A**, iv that was generated by the PP-DG model was used as the input to the CA3 pyramidal cells. The rMF created an input that was spatially and temporally uncorrelated. The wcMF created in an input with weak spatial and temporal correlation based on the dentate transformation of uncorrelated entorhinal activity. At the default synaptic parameters, the dentate activity was not sufficient to generate significant activity in the CA3. Therefore, the following analysis was performed with the synaptic weight increased by a factor of five.

The rMF resulted in CA3 activity that remained spatially uncorrelated and exhibited a weak temporal correlation with a peak of 0.001 (**Figure 5A**, ii). The wcMF resulted in the CA3 generating a spatio-temporal pattern that largely matched the spatio-temporal pattern of the dentate gyrus with a delay of 9 ms (**Figure 5A**, v). Additionally, the CA3 clusters included a "tail" that extended down toward the temporal pole and represents the downward turn that the mossy fiber trajectory follows after reaching the CA3a. The spatial structure of the CA3 correlation map remains largely similar to the dentate correlation map (**Figure 5B**, ii,v). These results indicate that in contrast to the perforant path projection, which organizes random activity into clusters, the mossy fibers do not imbue a spatial correlation to their postsynaptic population. Rather, the mossy fibers preserve the structure of the activity that is generated by the presynaptic population.

Combined Entorhinal and Dentate Projections (PP-rMF-CA3 and PP-wcMF-CA3 Models)

To explore the interactions between both the perforant path and mossy fiber projections, both rMF and wcMF were considered. In the PP-rMF-CA3 model, both the entorhinal cortex and dentate granule cell activity were randomly generated with an entorhinal mean firing rate of 5 Hz and a dentate mean firing rate of 0.62 Hz. These were both projected directly to the CA3. The PP-rMF-CA3 model eliminated the entorhinal projection to dentate. In the pPP-wcMF-CA3 model, the entorhinal cortex projected to both the dentate gyrus and CA3, and the CA3 received random input from entorhinal cortex and weakly correlated input from the dentate gyrus, which again represents the dentate gyrus' transformation of the random entorhinal input. These simulations were performed using the original synaptic weights, i.e., a scalar factor of one.

The PP-rMF-CA3 model resulted in the CA3 pyramidal cells generating a noisier version of the spatio-temporal pattern that was caused by the entorhinal projection by itself (**Figure 5A**, iii). This was expected as the random dentate input caused the CA3 to respond with spatially and temporally uncorrelated activity. The combination of these inputs results in the noisy pattern. The space-time correlation map supports this finding as the correlation structure is very similar to the correlation structure caused by the entorhinal projection but with a peak correlation that was roughly decreased by half (**Figure 5B**, iii).

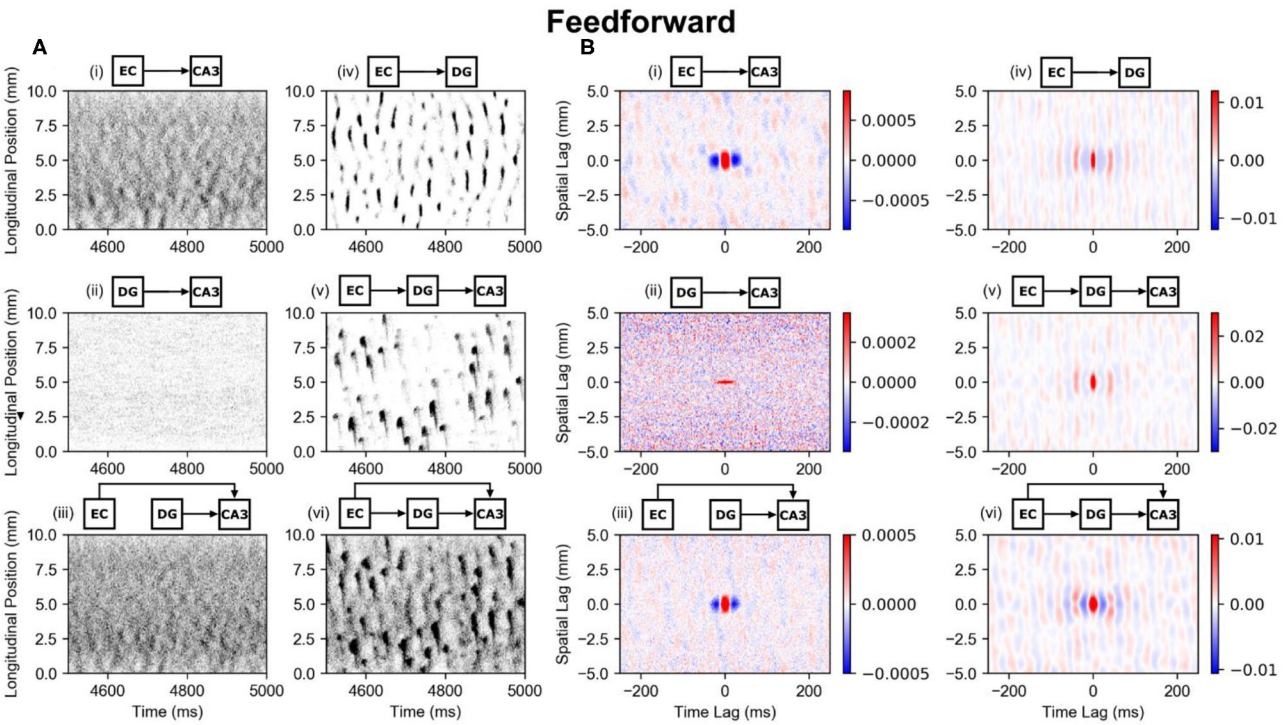


FIGURE 5 | Raster plots and global correlation maps for the effects of the perforant path and mossy fibers on CA3 pyramidal cells. **(A)** Spiking activities of the CA3 pyramidal cells are indicated with black dots and are organized based on their longitudinal position and time of spike. The circuits above each subplot indicate which circuit configuration was used. All plots indicate CA3 pyramidal cell activity except for the EC-DG plot which shows dentate granule cell activity. **(B)** The corresponding space-time correlation maps are shown. The longitudinal-temporal cross-sections are shown at a transverse lag of 0 mm. Red areas represent positive correlation, and blue areas represent negative correlation. **(A,B)** (i) PP-CA3 model: CA3 response to random perforant path activity. (ii) rMF-CA3 model: CA3 response to random dentate granule cell activity. (iii) PP-rMF-CA3 model: CA3 response to both random perforant path and random dentate granule cell activity. (iv) PP-DG model: DG response to random perforant path activity. (v) wcMF-CA3 model: CA3 response to solely correlated dentate granule cell activity, i.e., CA3 response to disynaptic perforant activity via dentate granule cells. (vi) PP-wcMF-CA3 model: CA3 response due to random perforant path and correlated dentate granule cell activity.

The PP-wcMF-CA3 model caused the CA3 pyramidal cells to respond with a pattern that closely matched the dentate granule cell activity (**Figure 5A**, vi). Previously, the mossy fiber synaptic weights were multiplied by a factor of 5 to generate significant CA3 activity. Otherwise, the original mossy fiber synaptic weight generated almost no CA3 activity. In combination with the perforant path, the mossy fibers at their original strength were able to propagate the dentate clusters and cause similar clusters within CA3. The CA3 clusters were noisier than the dentate clusters (**Figure 5A**, iv), and it is likely that the CA3 pattern is some combination of the patterns caused by the entorhinal and dentate activity individually. However, the perforant path projection was able to nonlinearly interact with the mossy fibers to markedly reinforce the dentate input pattern. The combination of these two systems may serve to enhance and propagate the patterns generated by the dentate granule cells.

Associational System (PP-wcMF-A-CA3 Model)

The perforant path and mossy fiber inputs together resulted in the preservation of the dentate pattern within the CA3, at least along the longitudinal axis. However, the CA3 contains an extremely strong associational system which could alter the pattern due to the excitatory feedback that the associational system provides. The subsequent studies explored the further transformation of spatio-temporal pattern that resulted when the associational system was added (the PP-wcMF-A-CA3 model). Separate simulations were run with the synaptic weight of the associational system set to 0.1, 0.2, 0.5, 1, 10, and 100% of the original value.

The strength of the associational system can be predominantly attributed to the number of inputs that a CA3 pyramidal cell receives from other CA3 pyramidal cells rather than the strength of the individual EPSPs. This number lies within the tens of thousands which is at least one order of magnitude larger than the numbers of inputs received from other afferents including the perforant path and mossy fibers. The average firing rate of the simulated CA3 pyramidal cells started at 11 Hz with no associational system and increased nonmonotonically toward 70 Hz with increasing synaptic strength (**Supplementary Figure 2A**), indicating that the CA3 activity was much less sparse than the DG which exhibited an average firing rate of 0.62 Hz. Furthermore, the spatio-temporal patterns appear to change little at 1, 10, and 100% of the full strength (**Figure 6A**, iv–vi), i.e., the spatio-temporal pattern did

not change substantially. In spatio-temporal pattern and firing rate, the CA3 approached a particular state asymptotically, which indicated that the CA3 was approaching a saturated state, i.e., the system was behaving nonlinearly. It is only at 0.1–0.5% of the original synaptic weight (**Figure 6A**, i–iii) that the associational system appears to significantly affect the spatio-temporal pattern. At these synaptic weight levels, the transformation of the clusters can be observed. The diffuse axonal distributions of the CA3 pyramidal cells appears to expand the spatial size of the clusters. This is also demonstrated by the correlation maps which show the increase in the extent of the spatial correlation with the increase in synaptic weight (**Figure 6B**).

Regardless of the strength of the associational system, the original clusters appear to continue to persist at all synaptic weights. The associational only serves to modify them and add inter-cluster noise or oscillation. This is notable because the peak pairwise correlation of the dentate granule cells is very low at 0.02, and the average firing rate is also very sparse at 0.62 Hz. Despite the low correlation and sparse firing conditions, the dentate gyrus causes clusters in CA3 pyramidal cells that remain even when the associational system is at full strength.

Longitudinal-Transverse Cross-Sections of Global Correlation Maps

Previously, the visualization of activity and correlation was limited to a single spatial dimension, the lag along the longitudinal axis. However, the CA3 exhibits a transverse organization that is hidden when only considering the longitudinal extent. The longitudinal-temporal view of the correlation maps demonstrated their ability to capture the basic structure of the features observed in the raster plots, i.e., the basic cluster shape. The three-dimensional correlation maps that were computed also incorporate the transverse relation to correlated activity. Here, we present the longitudinal-transverse cross-sections of the correlation maps at different time lags to reveal the temporal evolution of the two-dimensional spatial structure of correlation. The color maps were thresholded to 30% of the maximum value to emphasize the contributions of the weaker negative correlations that were present.

Perforant Path and Mossy Fibers

The longitudinal-transverse views of correlation demonstrate that the spatial structure is predominantly dependent on the methods used to represent the axonal anatomy. For the entorhinal projections which were represented using a gaussian (the PP-CA3 and PP-DG models), the spatial correlation maintains an elliptical shape with a longitudinal span that matches the standard deviation of the gaussian (**Figure 7**, i,iv). The differences in the temporal dynamics for the entorhinal effect on dentate granule cells and CA3 pyramidal cells may be due to differences in biophysics, electrophysiology, and number of inputs received by the respective populations. In the CA3, a positive and negative correlation moves across the transverse axis which represents the transverse propagation of entorhinal input from the CA3c to the CA3a.

With only mossy fiber input to the CA3, the random condition (rMF-CA3 model) resulted in a horizontal stripe spatial correlation that spanned the transverse axis which represents the thin nature of the mossy fibers (**Figure 7**, ii). The spatial correlation faded with time. The weakly correlated condition (wcMF-CA3 model) largely preserved the correlation structure of the dentate granule cells with the addition of a diagonal element which represented the downward turn of the mossy fibers in the CA3a (**Figure 7**, iv,v). As the temporal lag progressed, the shape of the correlation changed before moving into a weakly negative phase. With the combination of both perforant path and mossy fiber afferents, the random condition (the PP-rMF-CA3 model) again exhibited a correlation structure that was similar to the entorhinal case, but the extent of the spatial correlation began to shrink in the negative phase (**Figure 7**, iii). In the weakly correlated condition (the PP-wcMF-CA3 model), both the perforant path and mossy fiber related correlation structures appeared superimposed with the diagonal stripe appearing and a stronger negative phase (**Figure 7**, vi).

The main observation is that the spatial correlation was nonmonotonic and was not static in time, i.e., spatial correlation was dynamic. The spatial correlation can travel based on the direction of propagation and does not merely oscillate between positive and negative in a fixed position. Furthermore, the shape of the correlation changes over time. The correlation is both displaced and morphed partly due to direction of propagation and the interactions between different afferents.

Associational System

The longitudinal-transverse view of the correlation reveals the role of the associational system (PP-wcMF-A-CA3 model) in increasing the spatial extent of the correlation (**Figure 8**). The spatial extent of correlation increased with synaptic weights from 0.1–0.5% strength to encompass almost the entire CA3 extent (**Figure 8**, i–iii), though the strongest correlation was still localized to the same area that was caused by the entorhinal projection. As the strength of the synaptic weight was increased to 1–100%, the extent of spatial correlation became reduced to an area that was smaller than the correlation caused by the entorhinal cortex (**Figure 8**, iv–vi). At 1% strength, a spatial correlation pattern consisting of a positive region surrounded by negative correlation emerged. The polarity of this pattern switched between positive-negative and negative-positive over time. At 10 and 100% strength, the spatial correlation and its temporal evolution appeared almost identical. A repeating pattern of positive and negative correlation moves along the transverse axis over time. These results verify that the extensive axon distribution of the CA3 pyramidal cells does increase the area of spatial correlation during the low synaptic strengths. At higher synaptic strengths, the correlation oscillated between positive and negative which is consistent with the highly oscillatory nature of the spiking activity. At 1% strength, a unique pattern of positive and negative correlation emerged (**Figure 8**, iv).

Local Correlation Maps

One issue with the global correlation maps computed previously is that the anatomy of the various projection changes depending on the location within the CA3. In particular, the trajectory

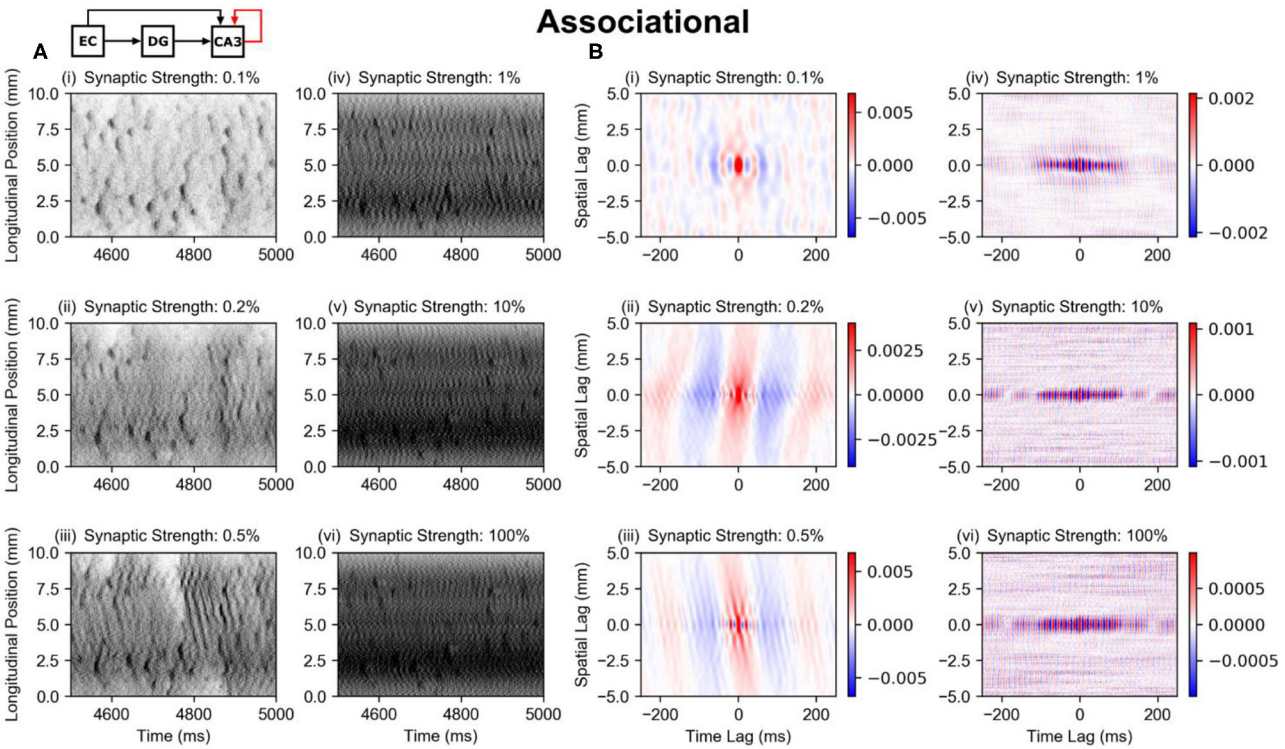


FIGURE 6 | Raster plots and global correlation maps for the results using the PP-wcMF-A-CA3 model, which includes the perforant path, mossy fiber, and associational projections to CA3. In the subplots, the strength of the associational synapses was modulated as indicated by the subplot titles. All other synapses remained at their experimentally constrained strength. **(A)** Raster plots of the CA3 pyramidal cells. **(B)** Longitudinal-temporal cross-sections of the correlation map at a transverse lag of 0 mm. Red areas represent positive correlation, and blue areas represent negative correlation.

of the mossy fiber changes along the transverse axis, and the CA3 pyramidal cell axons change substantially depending on their origin on both the longitudinal and transverse axes. While the global maps used every neuron pair in its computation of correlation, local maps were created by only consider neuron pairs in which at least one neuron of the pair was located in a particular area within the CA3. The CA3 was divided into nine sections. Along the longitudinal axis, three overlapping windows were defined which were centered at 7.5, 5.0, and 2.5 mm that extended 2.5 mm above and below the midpoint. Along the transverse axis, the windows were restricted to the CA3c, CA3b, and CA3a. This restriction allowed the correlation maps for a local region in space within the CA3 to be computed, in contrast to the global map which averages across every neuron (**Figure 4**).

Considering the local correlation maps when the associational system was included (PP-wcMF-A-CA3 model), the influence of the mossy fiber trajectory on the correlation structure along the transverse axis can be seen when then associational synaptic weight was reduced to 0.1% (**Figure 9**, i). Within the CA3c and CA3b, the correlation is predominantly horizontal while the correlation becomes diagonal within CA3a. This again highlights the influence of axonal anatomy on the correlation structure. It also reveals that the diagonally-organized positive/negative correlations seen in the global maps were due to the averaging of the CA3a correlation structure with the correlations from CA3b and CA3c. The local correlation maps were able to identify and separate the contributions of the different CA3 divisions (**Figure 9**, i) toward the global correlation map (**Figure 7**, vi).

At 0.02 and 0.05% (**Figure 9**, ii,iii), the differences in correlation structure among the different CA3 sections due to the CA3 axonal anatomy become more apparent. The magnitude and spatial extent of correlation is largest within the septal CA3c which becomes smaller toward the temporal CA3a. As the synaptic weights approach 100% strength, the correlations become confined to a smaller area.

Influence of Projections on Peak Correlation

The peak correlations were plotted as a function of synaptic strength based on the global maps to investigate how the synaptic strength of the different projections affected maximum correlation (**Figure 10A**). For the perforant path and mossy fibers, the synaptic strength was varied to be 50, 200, 300, 400, and 500% of the original value. The synaptic weight of the perforant path (PP-CA3 model) had a nonlinear relation to the peak correlation which initially decreased until twice the original strength and then continued to increase (**Figure 10A**, i). In general, however, the peak correlation due to the entorhinal projection to CA3 was very weak and stayed below 0.01. Under the weakly correlated condition (wcMF-CA3 model),

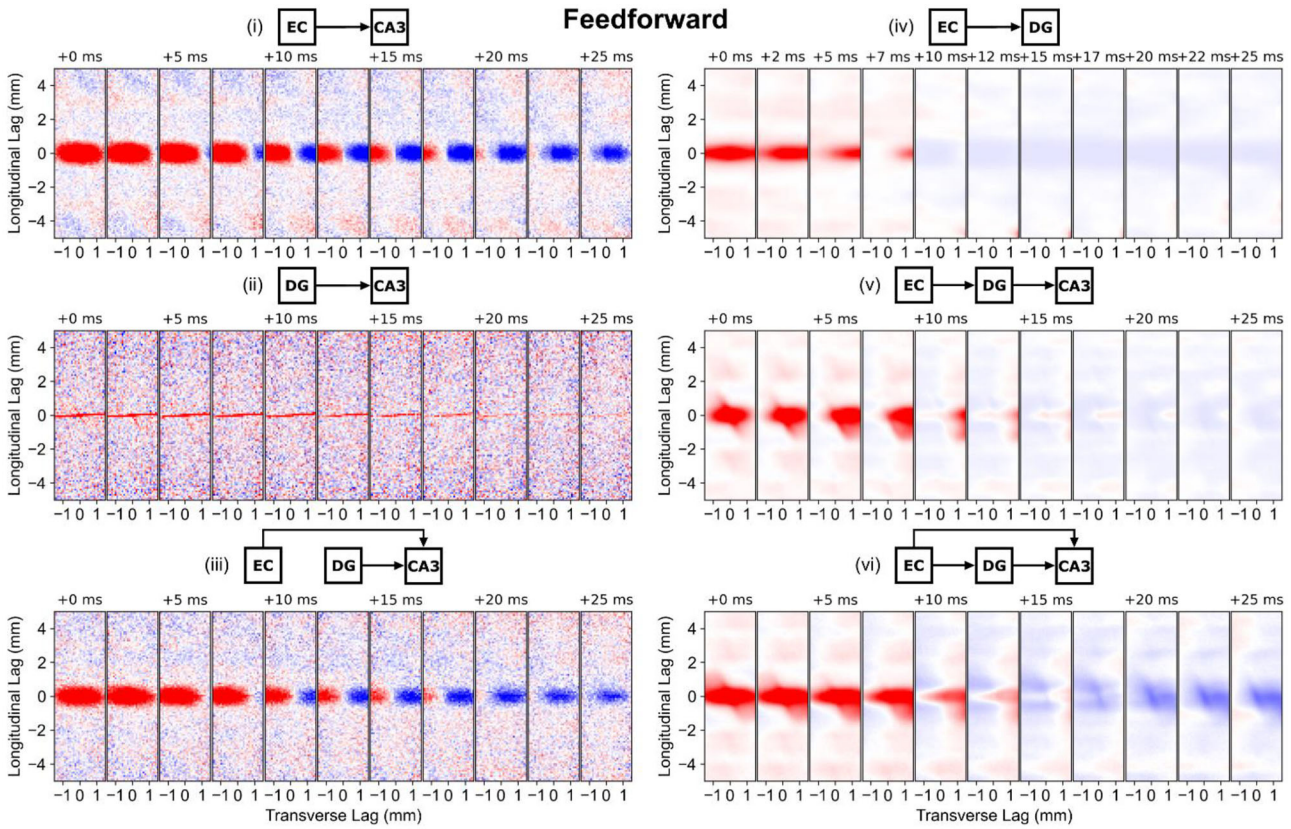


FIGURE 7 | Longitudinal-transverse cross-sections of global correlation maps at different temporal lags for simulations involving the perforant path and mossy fibers. The evolution of spatial correlation across positive time lags are shown. Red areas represent positive correlation, and blue areas represent negative correlation. (i) PP-CA3 model: CA3 response to random perforant path activity. (ii) rMF-CA3 model: CA3 response to random dentate granule cell activity. (iii) PP-rMF-CA3 model: CA3 response to both random perforant path and random dentate granule cell activity. (iv) PP-DG model: DG response to random perforant path activity. (v) wcMF-CA3 model: CA3 response to solely correlated dentate granule cell activity, i.e., CA3 response to disynaptic perforant activity via dentate granule cells. (vi) PP-wcMF-CA3 model: CA3 response due to random perforant path and correlated dentate granule cell activity.

the mossy fibers generated a monotonic relation between CA3 peak correlation and synaptic strength that decreased toward an asymptotic value of 0.1 (**Figure 10A**, ii). However, the random condition (rMF-CA3 model) had an opposite and nonmonotonic effect, and its peak correlation was three orders of magnitude lower than for the weakly correlated condition (**Figure 10A**, ii). The associational system (PP-wcMF-A-CA3 model) caused the peak correlation to nonmonotonically decrease toward an asymptotic value of 0.003 as the synaptic strength increased (**Figure 10A**, iii). Though generally decreasing, the correlation unexpectedly increased at an associational strength of 0.05% before continuing to decrease.

Using the local correlation maps, the distribution of correlation along the transverse extent was evaluated for the feedforward projections (**Figure 10B**). The correlation caused by the perforant path (PP-CA3 model) increased from CA3c to CA3a which is explained by the increase in synaptic density along the transverse axis (**Figure 10B**, i). For the wcMF-CA3 model, correlations decreased from CA3c to CA3a (**Figure 10B**, ii). This is due to the decrease in density of synapses along the transverse axis. When both the perforant path and mossy fibers were connected (PP-wcMF-CA3 model), the correlation due to the mossy fibers dominated resulting in a decrease in correlation from CA3c to CA3a (**Figure 10B**, iii). However, the correlation was not simply an average between the correlations from the individual projections. The combined effect was lower than what an average would predict (**Figure 10B**, iii).

Including the associational system (PP-wcMF-A-CA3 model), the trend in peak correlation along both the longitudinal and transverse axes were measured (**Figure 10C**). In general, peak correlation decreased from the dorsal/septal pole to the ventral/temporal pole and decreased from CA3c to CA3a.

DISCUSSION

In this study, anatomical data was used to constrain a spatially-dependent connectivity for the excitatory projections to and within the CA3 subfield of hippocampus including the perforant path, mossy fibers, and associational system. The present work represents an extensively detailed connectivity for the entorhinal-dentate-CA3 network concerning the major excitatory afferents

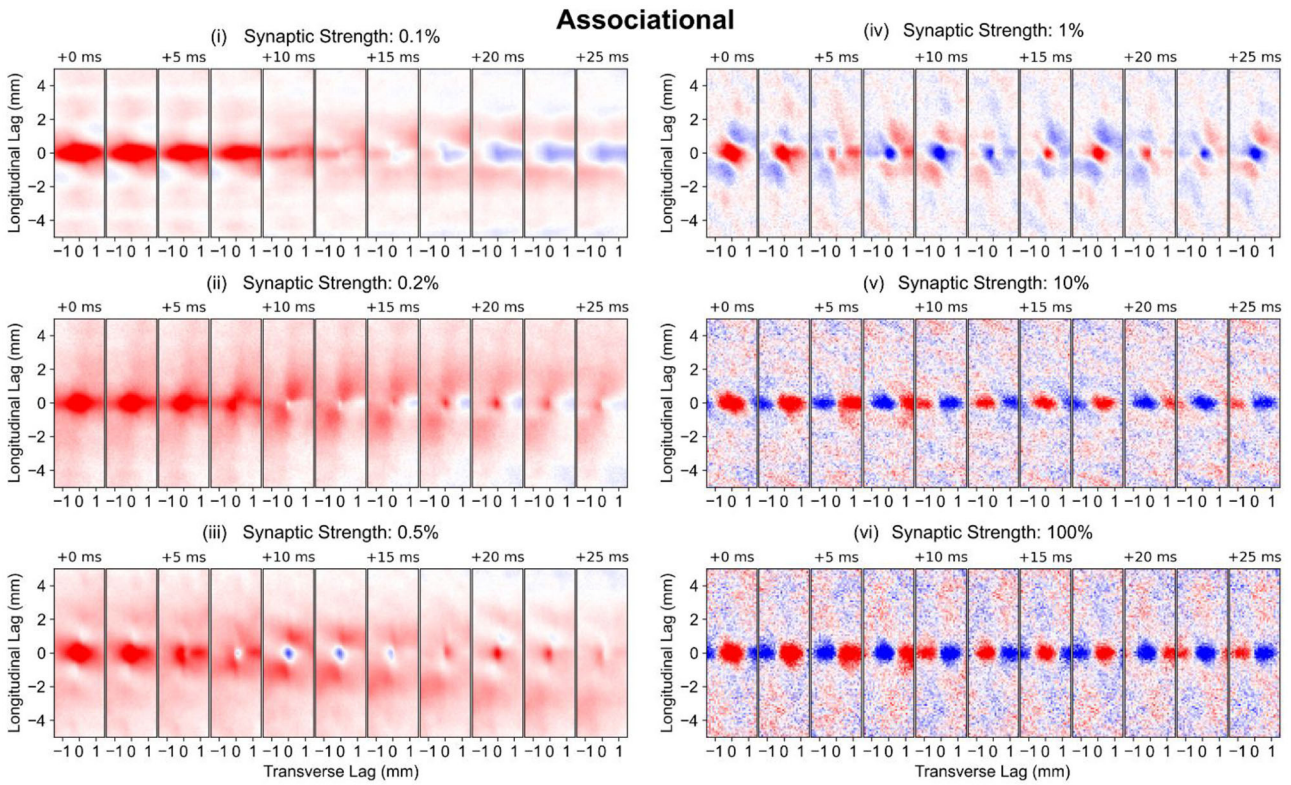


FIGURE 8 | Longitudinal-transverse cross-sections of global correlation maps at different temporal lags for simulations using the PP-wcMF-A-CA3 model, which includes the perforant path, mossy fiber, and associational projections to CA3. In the subplots, the strength of the associational synapses was modulated as indicated by the subplot titles. All other synapses remained at their experimentally constrained strength. The evolution of spatial correlation across positive time lags are shown. Red areas represent positive correlation, and blue areas represent negative correlation.

to the dentate gyrus and CA3 and represents connectivity at the microscale and mesoscale levels. A major outcome in constraining the connectivity was to include the variations in the spatial distribution of axons along both the longitudinal and transverse axes. These axes are sufficient to represent the full three-dimensional structure of the hippocampus. Theoretical studies that incorporated two spatial dimensions had constructed radially symmetric connectivity structures that could easily be analyzed along a single radial dimension (Rosenbaum et al., 2016; Senk et al., 2018; Huang et al., 2019). These studies with symmetric connectivity are able to generate rich sets of dynamics and lay the foundation for studying two-dimensional networks. However, the axonal distributions in hippocampus are far from symmetric. Furthermore, the variations in CA3 properties, e.g., connectivity and dendritic morphology, within its transverse axis are well-documented and represent important features that cannot be ignored. Incorporating the details relevant to both spatial axes resulted in the emergence of a heterogeneous spatial correlation structure, which has implications toward a topographic organization of information encoding along both the longitudinal and transverse axes. Additionally, the correlations were nonmonotonic in that they would not strictly decrease, and the correlations were dynamic with changes in their spatial structure at different time lags.

Perforant Path Generates Lower Correlation in CA3 Than Dentate Gyrus

Also using the entorhinal-dentate network, a relation between the size of the axon terminal field and the resulting correlation was revealed in Hendrickson et al. (2016) and Yu et al. (2018). The size of the axon terminal field and the size of the clusters in the population activity were linearly related. However, the entorhinal-dentate projection is relatively dense compared to the entorhinal-CA3 projection as dentate granule cells receive approximately 3,000 entorhinal inputs compared to CA3 pyramidal cells which can receive between 0 and 1,658 entorhinal inputs (**Table 1**). The present study revealed that the perforant path still generates clusters within CA3, though the correlation is much lower which resulted in noisier clusters (**Figure 5A**).

Mossy Fibers Propagate Correlation Structure From Dentate Gyrus to CA3

A larger unknown was the role of mossy fibers in the propagation of correlation. The mossy fibers of dentate granule cells represented the smallest extreme in size as they are fibers rather than fields. Though the number of mossy fiber inputs that CA3 pyramidal cells receive is extremely low

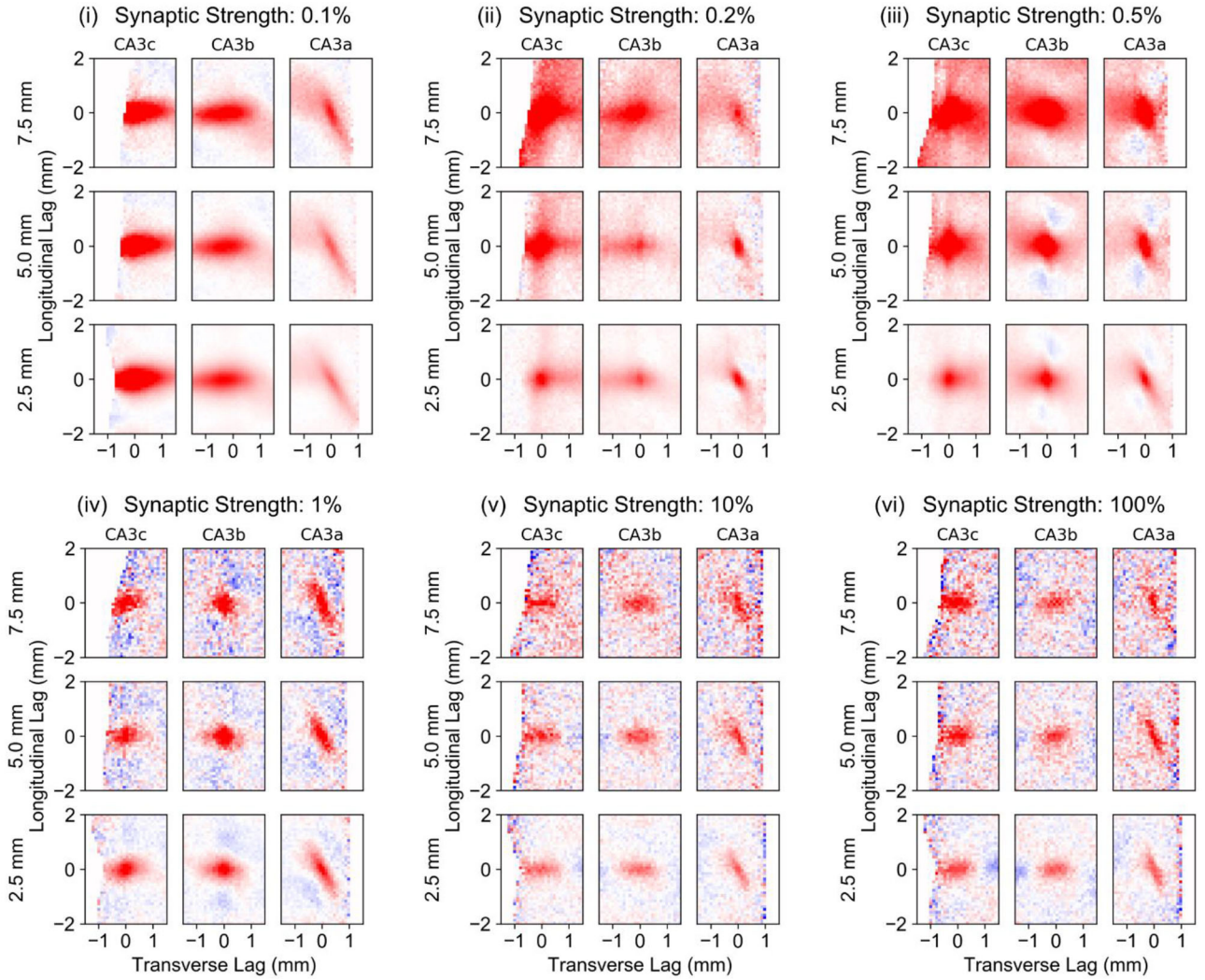


FIGURE 9 | Local correlation maps for simulations using the PP-wcMF-A-CA3 model, which includes the perforant path, mossy fiber, and associational projections to CA3. In the subplots, the strength of the associational synapses was modulated as indicated by the subplot titles. All other synapses remained at their experimentally constrained strength. Longitudinal-transverse cross-sections at a temporal lag of 0 ms are shown. Nine local correlation maps were computed for each synaptic strength which represents the local spatio-temporal correlation based on the longitudinal-transverse region as divided into CA3c, CA3b, and CA3a along the transverse axis (left to right) and roughly into the septal, middle, and temporal sections (top to bottom) along the longitudinal axis. The longitudinal boundaries were defined with a window size of 5 mm and centered at 7.5 (septal), 5.0, and 2.5 (temporal) mm along the longitudinal axis. Red areas represent positive correlation, and blue areas represent negative correlation.

with a mode of 38 (**Supplementary Figure 1**), the size of the EPSP is 3.2 mV which is over ten times greater than the EPSPs caused by the perforant path at 0.2 mV. The analysis of the longitudinal correlation indicated that the mossy fibers contribute little to the spatial correlation structure beyond that is already present within dentate granule cells. In other words, mossy fibers well-preserve and propagate the correlation structure that its presynaptic population, i.e., dentate granule cells, already expresses. However, the longitudinal-transverse analysis of the random condition shows that mossy fibers do contribute to a spatial correlation along the transverse axis, albeit a practically negligible correlation at <0.0001.

The combination of the perforant path and mossy fibers was shown to enhance the pattern carried in the mossy fibers. The mossy fibers alone did not generate significant activity within CA3. Experimental studies support that mossy fibers do not reliably cause action potentials at low frequencies, which is the case in these simulations (Urban et al., 2001). However, when the perforant path was added, the dentate patterns of activity were reinforced and perpetuated in the CA3 activity (**Figure 5A**). The enhancement of the mossy fiber pattern supports the view

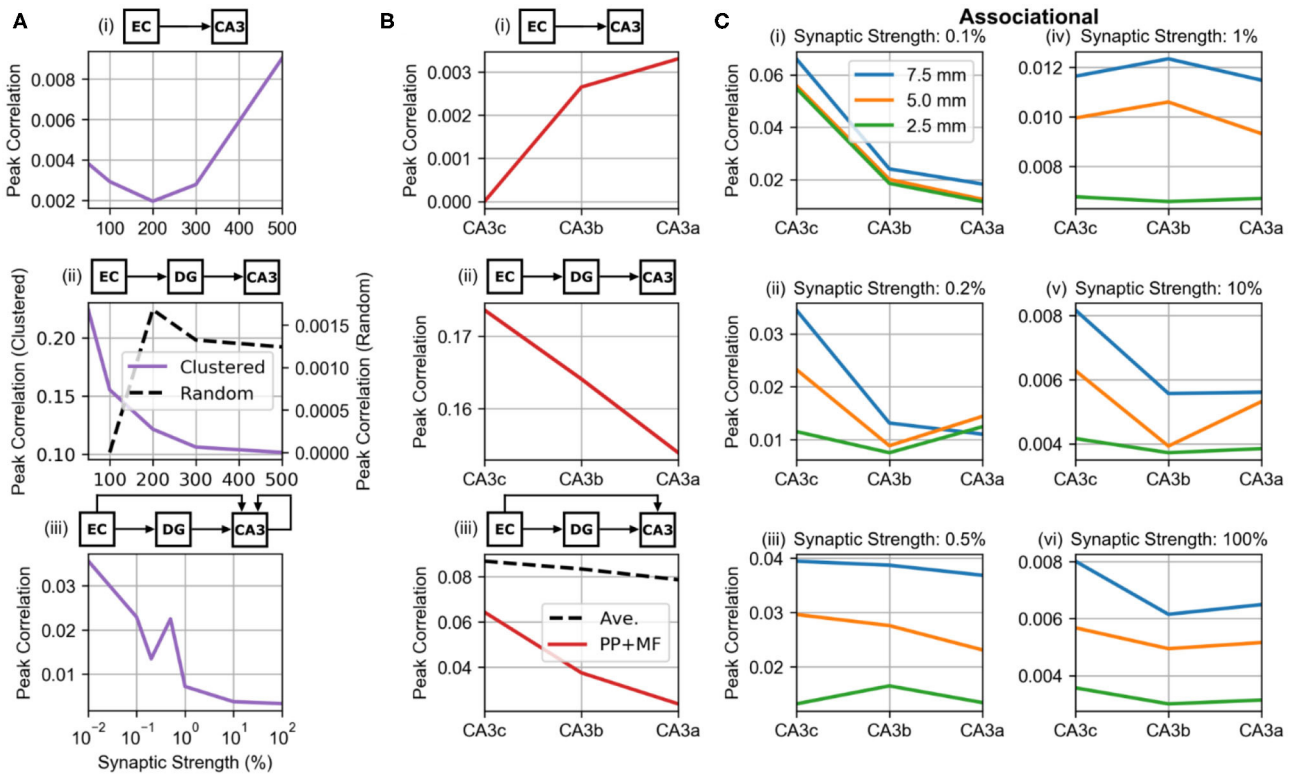


FIGURE 10 | Relations between peak correlation and synaptic strength and location. **(A)** The effect of synaptic strength on peak correlation from the global maps. The middle row plot shows the relation under the clustered (solid purple line) and random (dashed black line) conditions of dentate input. (**A**, i) PP-CA3 model: CA3 response to random perforant path activity. (**A**, ii) wcMF-CA3 model: CA3 response to solely correlated dentate granule cell activity, i.e., CA3 response to disynaptic perforant activity via dentate granule cells. (**A**, iii) PP-wcMF-A-CA3 model: CA3 response due to random perforant path and correlated dentate granule cell activity in the presence of the associational system. **(B)** The differences in peak correlation based on transverse position from the global maps. In the bottom plot, the effect of the combined perforant path and mossy fiber input (solid red line) and the average of the individual effects of the two pathways (dashed black line) are shown. (**B**, i) PP-CA3 model: CA3 response to random perforant path activity. (**B**, ii) wcMF-CA3 model: CA3 response to solely correlated dentate granule cell activity, i.e., CA3 response to disynaptic perforant activity via dentate granule cells. (**B**, iii) PP-wcMF-CA3 model: CA3 response due to random perforant path and correlated dentate granule cell activity without the associational system. **(C)** The variation in peak correlation from the local maps as a function of longitudinal and transverse position are shown from simulations using the PP-wcMF-A-CA3 model, which includes the perforant path, mossy fiber, and associational projections to CA3. The strength of the associational system is modulated as indicated by the subplot titles.

of mossy fibers as conditional detonators which may need concurrent activation of multiple synapses in order to elicit a spike in the pyramidal cells, e.g., mossy fiber, perforant path, associational (Henze et al., 2002).

Associational System Preserves and Modulates Mossy Fiber Induced Patterns

However, it was not known how much of the dentate pattern would persist within CA3 after the associational system was included. The effect of a recurrent excitatory circuit in neural systems has commonly been shown to generate highly synchronized and oscillatory behavior (Le Duigou et al., 2014; Hendrickson et al., 2015). This was observed in the CA3 associational system due to the highly dense nature of the projection in which a CA3 pyramidal cell can receive between 18,000 and 29,000 inputs from other CA3 pyramidal cells. With synaptic weights at 0.1–0.5% of the original strength, the CA3 did not enter a synchronous, oscillatory state (**Figure 6A**), and an increase in the size of spatial correlation was observed (**Figures 8**, **9**). This indicates that weak excitatory recurrent circuits can expand the extent of spatial correlation. One of the interesting findings in the associational results was that the dentate-based clusters persisted within all synaptic weight values, i.e., even within the synchronized, oscillatory state. This finding further supports that the dentate activity acts as a major driver of the spatio-temporal patterns generated by the CA3.

Correlation and Functional Gradients Along Both Longitudinal and Transverse Axes Within CA3

The topographic organization of connectivity resulted in heterogeneous correlation structures that varied along the longitudinal and transverse axes within the CA3. First, there was a clear trend toward higher correlations in the dorsal/septal region of the CA3 vs. ventral/temporal region. Second, correlations were higher in the proximal/CA3c region vs. the

distal/CA3a region. These ultimately combine to indicate that peak correlation decreases from dorsal-proximal CA3 to the ventral-distal CA3. Additionally, the spatial extent of correlation followed the same gradient with a larger size of spatial correlation dorsally/proximally and a smaller size of spatial correlation ventrally/distally.

These correlation gradients may functionally indicate the extent to which information is integrated by a CA3 pyramidal cell. With larger sizes in correlation, a CA3 pyramidal cell is integrating information across more neurons, which may result in a CA3 organization with more "general" neurons dorsally/proximally and more specialized neurons ventrally/distally. Another interpretation is that neuronal activity may be more similar to one another in the dorsal/proximal region vs. ventral/distal region. Experimental work had discovered that a positive relation between pairwise spike correlation and overlap of place fields within CA3 and CA1 (Hampson et al., 1996). Under the theory of pattern separation and pattern completion (Yassa and Stark, 2011), this suggests that pattern completion as a population may be stronger where correlation between neurons is higher.

A longitudinal gradient in function has been reported experimentally (Small, 2002; Strange et al., 2014; Papaleonidopoulos et al., 2017), and such a relation between axonal anatomy and the encoding of spatial information had been previously explored with the same entorhinal-dentate network used in the present study (Yu et al., 2019). A transverse gradient has also been reported within CA3 with respect to pattern completion (Lee et al., 2015).

Validation

As a platform for investigating the system properties of hippocampus, it is important to validate the model at higher levels, e.g., population and network levels. Lower level validation is already performed in constraining the parameters for neuron electrophysiology and synaptic conductance waveforms. Some higher-level validation has been performed using place fields and spatial information (Yu et al., 2019), and local field potential generation (Bingham et al., 2018). The present CA3 network lacks inhibition and is comparable to a CA3 for which a $GABA_A$ blocker has been applied. One experimental study observed that the power of CA3 population oscillations at 210 Hz increased with the application of the $GABA_A$ blocker bicuculline. This increase is also observed with the simulations (**Supplementary Figure 2C**). Pairwise spike correlation values that have been reported in experimental studies are vary between 0.005 and 0.025 (Hampson et al., 1996; Dombeck et al., 2010). The peak correlation values from the simulations are well within these ranges. Furthermore, other studies have reported a general decay in pairwise correlation as a function of distance between neuron pairs (Hirase et al., 2001; Dombeck et al., 2010). This relation is present in other cortical areas as well (Rosenbaum et al., 2016; Safavi et al., 2018) which supports the notion that such correlations may be present in other brain areas.

Future Work

The CA3 network in the study excluded any forms of extrinsic inhibition due to interneurons as the role of the afferent excitatory projections were not yet known. However, the present results establish the groundwork upon which the contributions of the various interneuron types in further transforming the spatio-temporal patterns of spiking and correlation can be investigated.

Additionally, the simulations used an input paradigm designed to contain zero spatial or temporal correlations to reveal how the anatomically-constrained connectivity of the network may imbue the population activity with correlation. Though the input firing rates may represent a resting state type of network, the input was not physiologically. Later work will aim to behaviorally-driven input such as the grid cells in the medial entorhinal cortex to investigate how physiologically-relevant correlation in the input may be processed by CA3, and grid cell input had previously been used to investigate the entorhinal-dentate network version of the model (Yu et al., 2019).

DATA AVAILABILITY STATEMENT

The code used to perform the simulations can be found at the following link: https://github.com/genejongyu/reducedCA3network.git. For additional data, inquiries can be directed to the corresponding author.

AUTHOR CONTRIBUTIONS

GY developed the network model, designed and performed the analysis, and prepared the manuscript. J-MB assisted in the preparation of the manuscript. TB oversaw the project scope, project conception, and worked to maintain funding to support the project. All authors contributed to the article and approved the submitted version.

FUNDING

This work was supported by the National Institutes of Health (5U01EB025830-07) and the U.S. Office of Naval Research (N00014-13-1-021).

ACKNOWLEDGMENTS

The authors acknowledge the Center for Advanced Research Computing (CARC) at the University of Southern California for providing computing resources that have contributed to the research results reported within this publication (URL: https://carc.usc.edu).

SUPPLEMENTARY MATERIAL

The Supplementary Material for this article can be found online at: https://www.frontiersin.org/articles/10.3389/fncom.2020.588881/full#supplementary-material

REFERENCES

Acsády, L., Kamondi, A., Sik, A., Freund, T., and Buzsáki, G. (1998). GABAergic Cells are the major postsynaptic targets of mossy fibers in the rat hippocampus. *J. Neurosci.* 18, 3386–3403. doi: 10.1523/JNEUROSCI.18-09-03386.1998

Andersen, P. (1975). "Organization of hippocampal neurons and their interconnections," in *The Hippocampus,* eds R. L. Isaacson and K. H. Pribram (Boston, MA: Springer), 155-175.

Andersen, P., Soleng, A. F., and Raastad, M. (2000). The hippocampal lamella hypothesis revisited. *Brain Res.* 886, 165–171. doi: 10.1016/S0006-8993(00)02991-7

Billeh, Y. N., Cai, B., Gratiy, S. L., Dai, K., Iyer, R., Gouwens, N. W., et al. (2020). Systematic integration of structural and functional data into multi-scale models of mouse primary visual cortex. *Neuron* 106, 388–403.e18. doi: 10.1016/j.neuron.2020.01.040

Bingham, C. S., Loizos, K., Yu, G. J., Gilbert, A., Bouteiller, J.-M. C., Song, D., et al. (2018). Model-based analysis of electrode placement and pulse amplitude for hippocampal stimulation. *IEEE Trans. Biomed. Eng.* 65, 2278–2289. doi: 10.1109/TBME.2018.2791860

Chan, H. K., Yang, D.-P., Zhou, C., and Nowotny, T. (2016). Burst firing enhances neural output correlation. *Front. Comput. Neurosci.* 10:42. doi: 10.3389/fncom.2016.00042

Darshan, R., van Vreeswijk, C., and Hansel, D. (2018). Strength of correlations in strongly recurrent neuronal networks. *Phys. Rev.* X 8:031072. doi: 10.1103/PhysRevX.8.031072

Dettner, A., Münzberg, S., and Tchumatchenko, T. (2016). Temporal pairwise spike correlations fully capture single-neuron information. *Nat. Commun.* 7:13805. doi: 10.1038/ncomms13805

Dolorfo, C. L., and Amaral, D. G. (1998). Entorhinal cortex of the rat: topographic organization of the cells of origin of the perforant path projection to the dentate gyrus. *J. Comp. Neurol.* 398, 25–48. doi: 10.1002/(SICI)1096-9861(19980817)398:1<25::AID-CNE3>3.0.CO;2-B

Dombeck, D. A., Harvey, C. D., Tian, L., Looger, L. L., and Tank, D. W. (2010). Functional imaging of hippocampal place cells at cellular resolution during virtual navigation. *Nat. Neurosci.* 13, 1433–1440. doi: 10.1038/nn.2648

Halliday, D. M. (2000). Weak, stochastic temporal correlation of large-scale synaptic input is a major determinant of neuronal bandwidth. *Neural Comput.* 12, 693–707. doi: 10.1162/089976600300015754

Hampson, R. E., Byrd, D. R., Konstantopoulos, J. K., Bunn, T., and Deadwyler, S. A. (1996). Hippocampal place fields: relationship between degree of field overlap and cross-correlations within ensembles of hippocampal neurons. *Hippocampus* 6, 281–293. doi: 10.1002/(SICI)1098-1063(1996)6:3<281::AID-HIPO6>3.0.CO;2-Q

Helias, M., Tetzlaff, T., and Diesmann, M. (2014). The correlation structure of local neuronal networks intrinsically results from recurrent dynamics. *PLoS Comput. Biol.* 10:e1003428. doi: 10.1371/journal.pcbi.1003428

Hemond, P., Epstein, D., Boley, A., Migliore, M., Ascoli, G. A., and Jaffe, D. B. (2008). Distinct classes of pyramidal cells exhibit mutually exclusive firing patterns in hippocampal area CA3b. *Hippocampus* 18, 411–424. doi: 10.1002/hipo.20404

Hendrickson, P. J., Yu, G. J., Song, D., and Berger, T. W. (2015). Interactions between inhibitory interneurons and excitatory associational circuitry in determining spatio-temporal dynamics of hippocampal dentate granule cells: a large-scale computational study. *Front. Syst. Neurosci.* 9:155. doi: 10.3389/fnsys.2015.00155

Hendrickson, P. J., Yu, G. J., Song, D., and Berger, T. W. (2016). A million-plus neuron model of the hippocampal dentate gyrus: critical role for topography in determining spatiotemporal network dynamics. *IEEE Trans. Biomed. Eng.* 63, 199–209. doi: 10.1109/TBME.2015.2445771

Henze, D. A., Wittner, L., and Buzsáki, G. (2002). Single granule cells reliably discharge targets in the hippocampal CA3 network in vivo. *Nat. Neurosci.* 5, 790–795. doi: 10.1038/nn887

Hirase, H., Leinekugel, X., Csicsvari, J., Czurk,ó, A., and Buzsáki, G. (2001). Behavior-dependent states of the hippocampal network affect functional clustering of neurons. *J. Neurosci.* 21, RC145–RC145. doi: 10.1523/JNEUROSCI.21-10-j0003.2001

Hong, S., Ratte, S., Prescott, S. A., and De Schutter, E. (2012). Single neuron firing properties impact correlation-based population coding. *J. Neurosci.* 32, 1413–1428. doi: 10.1523/JNEUROSCI.3735-11.2012

Huang, C., Ruff, D. A., Pyle, R., Rosenbaum, R., Cohen, M. R., and Doiron, B. (2019). Circuit models of low-dimensional shared variability in cortical networks. *Neuron* 101, 337–348.e4. doi: 10.1016/j.neuron.2018.11.034

Ishizuka, N., Cowan, W. M., and Amaral, D. G. (1995). A quantitative analysis of the dendritic organization of pyramidal cells in the rat hippocampus. *J. Comp. Neurol.* 362, 17–45. doi: 10.1002/cne.903620103

Ishizuka, N., Weber, J., and Amaral, D. G. (1990). Organization of intrahippocampal projections originating from CA3 pyramidal cells in the rat. *J. Comp. Neurol.* 295, 580–623. doi: 10.1002/cne.902950407

Jahr, C., and Stevens, C. (1990). Voltage dependence of NMDA-activated macroscopic conductances predicted by single-channel kinetics. *J. Neurosci.* 10, 3178–3182. doi: 10.1523/JNEUROSCI.10-09-03178.1990

Kleppe, I. C., and Robinson, H. P. C. (1999). Determining the activation time course of synaptic AMPA receptors from openings of colocalized NMDA receptors. *Biophys. J.* 77, 1418–1427. doi: 10.1016/S0006-3495(99)76990-0

Kress, G. J., Dowling, M. J., Meeks, J. P., and Mennerick, S. (2008). High threshold, proximal initiation, and slow conduction velocity of action potentials in dentate granule neuron mossy fibers. *J. Neurophysiol.* 100, 281–291. doi: 10.1152/jn.90295.2008

Kriener, B., Helias, M., Aertsen, A., and Rotter, S. (2009). Correlations in spiking neuronal networks with distance dependent connections. *J. Comput. Neurosci.* 27, 177–200. doi: 10.1007/s10827-008-0135-1

Kumar, A., Rotter, S., and Aertsen, A. (2010). Spiking activity propagation in neuronal networks: reconciling different perspectives on neural coding. *Nat. Rev. Neurosci.* 11, 615–627. doi: 10.1038/nrn2886

Lawrence, J. J., Grinspan, Z. M., and McBain, C. J. (2003). Quantal transmission at mossy fibre targets in the CA3 region of the rat hippocampus. *J. Physiol.* 554, 175–193. doi: 10.1113/jphysiol.2003.049551

Le Duigou, C., Simonnet, J., Teleñczuk, M. T., Fricker, D., and Miles, R. (2014). Recurrent synapses and circuits in the CA3 region of the hippocampus: an associative network. *Front. Cell. Neurosci.* 7:262. doi: 10.3389/fncel.2013.00262

Lee, H., Wang, C., Deshmukh, S. S., and Knierim, J. J. (2015). Neural population evidence of functional heterogeneity along the CA3 transverse axis: pattern completion versus pattern separation. *Neuron* 87, 1093–1105. doi: 10.1016/j.neuron.2015.07.012

Marasco, A., Limongiello, A., and Migliore, M. (2012). Fast and accurate low-dimensional reduction of biophysically detailed neuron models. *Sci. Rep.* 2:928. doi: 10.1038/srep00928

Markram, H., Muller, E., Ramaswamy, S., Reimann, M. W., Abdellah, M., Sanchez, C. A., et al. (2015). Reconstruction and simulation of neocortical microcircuitry. *Cell* 163, 456–492. doi: 10.1016/j.cell.2015.09.029

Megias, M., Emri, Z., Freund, T. F., and Gulyás, A. I. (2001). Total number and distribution of inhibitory and excitatory synapses on hippocampal CA1 pyramidal cells. *Neuroscience* 102, 527–540. doi: 10.1016/S0306-4522(00)00496-6

Mulders, W. H. A. M., West, M. J., and Slomianka, L. (1997). Neuron numbers in the presubiculum, parasubiculum, and entorhinal area of the rat. *J. Comp. Neurol.* 385, 83–94. doi: 10.1002/(SICI)1096-9861(19970818)385:1<83::AID-CNE5>3.0.CO;2-8

Papaleonidopoulos, V., Trompoukis, G., Koutsoumpa, A., and Papatheodoropoulos, C. (2017). A gradient of frequency-dependent synaptic properties along the longitudinal hippocampal axis. *BMC Neurosci.* 18:79. doi: 10.1186/s12868-017-0398-4

Perez-Rosello, T., Baker, J. L., Ferrante, M., Iyengar, S., Ascoli, G. A., and Barrionuevo, G. (2011). Passive and active shaping of unitary responses from associational/commissural and perforant path synapses in hippocampal CA3 pyramidal cells. *J. Comput. Neurosci.* 31, 159–182. doi: 10.1007/s10827-010-0303-y

Renart, A., de la Rocha, J., Bartho, P., Hollender, L., Parga, N., Reyes, A., et al. (2010). The asynchronous state in cortical circuits. *Science* 327, 587–590. doi: 10.1126/science.1179850

Rosenbaum, R., Smith, M. A., Kohn, A., Rubin, J. E., and Doiron, B. (2016). The spatial structure of correlated neuronal variability. *Nat. Neurosci.* 20, 107–114. doi: 10.1038/nn.4433

Rosenbaum, R., Trousdale, J., and Josi,ć, K. (2011). The effects of pooling on spike train correlations. *Front. Neurosci.* 5:58. doi: 10.3389/fnins.2011.00058

Safavi, S., Dwarakanath, A., Kapoor, V., Werner, J., Hatsopoulos, N. G., Logothetis, N. K., et al. (2018). Nonmonotonic spatial structure of interneuronal correlations in prefrontal microcircuits. *Proc. Natl. Acad. Sci. U. S. A.* 115, E3539–E3548. doi: 10.1073/pnas.1802356115

Scanziani, M., Gahwiler, B., and Thompson, S. (1993). Presynaptic inhibition of excitatory synaptic transmission mediated by alpha adrenergic receptors in area CA3 of the rat hippocampus *in vitro*. *J. Neurosci.* 13, 5393–5401. doi: 10.1523/JNEUROSCI.13-12-05393.1993

Schneider, C. J., Bezaire, M., and Soltesz, I. (2012). Toward a full-scale computational model of the rat dentate gyrus. *Front. Neural Circuits* 6:83. doi: 10.3389/fncir.2012.00083

Schneidman, E., Berry, M. J. II, Segev, R., and Bialek, W. (2006). Weak pairwise correlations imply strongly correlated network states in a neural population. *Nature* 440, 1007–1012. doi: 10.1038/nature04701

Senk, J., Hagen, E., van Albada, S. J., and Diesmann, M. (2018). Reconciliation of weak pairwise spike-train correlations and highly coherent local field potentials across space. *arXiv* arXiv:1805.10235.

Small, S. A. (2002). The longitudinal axis of the hippocampal formation: its anatomy, circuitry, and role in cognitive function. *Rev. Neurosci.* 13, 183–194. doi: 10.1515/REVNEURO.2002.13.2.183

Strange, B. A., Witter, M. P., Lein, E. S., and Moser, E. I. (2014). Functional organization of the hippocampal longitudinal axis. *Nat. Rev. Neurosci.* 15, 655–669. doi: 10.1038/nrn3785

Swanson, L. W., Wyss, J. M., and Cowan, W. M. (1978). An autoradiographic study of the organization of intrahippocampal association pathways in the rat. *J. Comp. Neurol.* 181, 681–715. doi: 10.1002/cne.901810402

Tamamaki, N. (1997). Organization of the entorhinal projection to the rat dentate gyrus revealed by Dil anterograde labeling. *Exp. Brain Res.* 116, 250–258. doi: 10.1007/PL00005753

Tetzlaff, T., Rotter, S., Stark, E., Abeles, M., Aertsen, A., and Diesmann, M. (2008). Dependence of neuronal correlations on filter characteristics and marginal spike train statistics. *Neural Comput.* 20, 2133–2184. doi: 10.1162/neco.2008.05-07-525

Tielen, A. M., Lopes da Silva, F. H., and Mollevanger, W. J. (1981). Differential conduction velocities in perforant path fibres in guinea pig. *Exp. Brain Res.* 42, 231–233. doi: 10.1007/BF00236913

Urban, N. N., Henze, D. A., and Barrionuevo, G. (2001). Revisiting the role of the hippocampal mossy fiber synapse. *Hippocampus* 11, 408–417. doi: 10.1002/hipo.1055

Yassa, M. A., and Stark, C. E. L. (2011). Pattern separation in the hippocampus. *Trends Neurosci.* 34, 515–525. doi: 10.1016/j.tins.2011.06.006

Yeckel, M. F., and Berger, T. W. (1990). Feedforward excitation of the hippocampus by afferents from the entorhinal cortex: redefinition of the role of the trisynaptic pathway. *Proc. Natl. Acad. Sci.* 87, 5832–5836. doi: 10.1073/pnas.87.15.5832

Yu, G. J., Bouteiller, J.-M. C., Song, D., and Berger, T. W. (2019). Axonal anatomy optimizes spatial encoding in the rat entorhinal-dentate system: a computational study. *IEEE Trans. Biomed. Eng.* 66, 2728–2739. doi: 10.1109/TBME.2019.2894410

Yu, G. J., Hendrickson, P. J., Song, D., and Berger, T. W. (2015). "Topography-dependent spatio-temporal correlations in the entorhinal-dentate-CA3 circuit in a large-scale computational model of the Rat Hippocampus," in *2015 37th Annual International Conference of the IEEE Engineering in Medicine and Biology Society (EMBC)*.

Yu, G. J., Hendrickson, P. J., Song, D., and Berger, T. W. (2018). "Spatiotemporal patterns of granule cell activity revealed by a large-scale, biologically realistic model of the hippocampal dentate gyrus," in *Springer Series in Computational Neuroscience,* eds V. Cutsuridis, B. P. Graham, S. Cobb, and I. Vida (Cham: Springer International Publishing), 473–508.

Yu, G. J., Song, D., and Berger, T. W. (2014). "Implementation of the excitatory entorhinal-dentate-CA3 topography in a large-scale computational model of the rat hippocampus," in *2014 36th Annual International Conference of the IEEE Engineering in Medicine and Biology Society (EMBC)*.

Zador, A., Koch, C., and Brown, T. H. (1990). Biophysical model of a Hebbian synapse. *Proc. Natl. Acad. Sci.* 87, 6718–6722. doi: 10.1073/pnas.87.17.6718

Conflict of Interest: The authors declare that the research was conducted in the absence of any commercial or financial relationships that could be construed as a potential conflict of interest.

Copyright © 2020 Yu, Bouteiller and Berger. This is an open-access article distributed under the terms of the Creative Commons Attribution License (CC BY). The use, distribution or reproduction in other forums is permitted, provided the original author(s) and the copyright owner(s) are credited and that the original publication in this journal is cited, in accordance with accepted academic practice. No use, distribution or reproduction is permitted which does not comply with these terms.

frontiers in Computational Neuroscience

ORIGINAL RESEARCH
published: 05 January 2021
doi: 10.3389/fncom.2020.581040

On the Validity of Neural Mass Models

Nicolás Deschle[1,2], Juan Ignacio Gossn[3], Prejaas Tewarie[4,5], Björn Schelter[2] and Andreas Daffertshofer[1]**

[1] Faculty of Behavioural and Movement Sciences, Amsterdam Movement Sciences & Institute for Brain and Behavior Amsterdam, Vrije Universiteit Amsterdam, Amsterdam, Netherlands, [2] Institute for Complex Systems and Mathematical Biology, University of Aberdeen, King's College, Aberdeen, United Kingdom, [3] Consejo Nacional de Investigaciones Científicas y Técnicas, Instituto de Astronomía y Física del Espacio, Universidad de Buenos Aires, Ciudad Universitaria, Buenos Aires, Argentina, [4] Sir Peter Mansfield Imaging Centre, School of Physics and Astronomy, University of Nottingham, Nottingham, United Kingdom, [5] Department of Clinical Neurophysiology and MEG Center, Amsterdam UMC, Vrije Universiteit Amsterdam, Amsterdam Neuroscience, Amsterdam, Netherlands

Modeling the dynamics of neural masses is a common approach in the study of neural populations. Various models have been proven useful to describe a plenitude of empirical observations including self-sustained local oscillations and patterns of distant synchronization. We discuss the extent to which mass models really resemble the mean dynamics of a neural population. In particular, we question the validity of neural mass models if the population under study comprises a mixture of excitatory and inhibitory neurons that are densely (inter-)connected. Starting from a network of noisy leaky integrate-and-fire neurons, we formulated two different population dynamics that both fall into the category of seminal Freeman neural mass models. The derivations contained several mean-field assumptions and time scale separation(s) between membrane and synapse dynamics. Our comparison of these neural mass models with the averaged dynamics of the population reveals bounds in the fraction of excitatory/inhibitory neuron as well as overall network degree for a mass model to provide adequate estimates. For substantial parameter ranges, our models fail to mimic the neural network's dynamics proper, be that in de-synchronized or in (high-frequency) synchronized states. Only around the onset of low-frequency synchronization our models provide proper estimates of the mean potential dynamics. While this shows their potential for, e.g., studying resting state dynamics obtained by encephalography with focus on the transition region, we must accept that predicting the more general dynamic outcome of a neural network via its mass dynamics requires great care.

Keywords: neural mass model, leaky integrate and fire, random graph, mean field approximation, Freeman model

OPEN ACCESS

Edited by:
Spase Petkoski, INSERM U1106 Institut de Neurosciences des Systmes, France

Reviewed by:
Jorge F. Mejias, University of Amsterdam, Netherlands
Cees van Leeuwen, KU Leuven, Belgium

***Correspondence:**
Andreas Daffertshofer
a.daffertshofer@vu.nl
Nicolás Deschle
n.deschle@vu.nl

Received: *07 July 2020*
Accepted: *01 December 2020*
Published: *05 January 2021*

Citation:
Deschle N, Ignacio Gossn J, Tewarie P, Schelter B and Daffertshofer A (2021) On the Validity of Neural Mass Models. Front. Comput. Neurosci. 14:581040. doi: 10.3389/fncom.2020.581040

INTRODUCTION

Over the years, *neural mass models* have profoundly contributed to our understanding of the meso- and macroscopic dynamics of populations of neurons. This is particularly true when it comes to the oscillatory behavior of mean post-synaptic potentials and firing rates. Central there is the notion of brain rhythms arguably resembling (episodic) local and distant synchronization of neural oscillators. Corresponding theoretical studies date back as far as the mid of the last century (Beurle, 1956; Griffith, 1963, 1965) though it was Walter Freeman who coined the notion neural masses

(Freeman, 1975). Building neural mass models typically relies on phenomenological insights and one "prescribes" the evolution of the neural activity over time (Deco et al., 2008). Yet, as said, these models strongly contributed to advancing our understanding of brain rhythms as they succeeded in mimicking signals recorded especially via magneto- and electroencephalography (Freeman, 1987; Kozma and Freeman, 2016).

Freeman's K-sets are based on a hierarchy of interacting sets of neural populations or masses (Freeman, 1975). These masses are composed of non-interacting, identical neurons. Without interactions in the mass, it is called a KO-set for which the original *Freeman model* applies. In fact, the absence of interactions in the mass allows for great algebraic simplicity: The mass dynamics can be cast in the form of a linear second-order ordinary differential equation,

$$\left[\frac{d}{dt}+\alpha\right]\left[\frac{d}{dt}+\beta\right]V=(\alpha\beta)\,J, \tag{1}$$

where $V = V(t)$ denotes the mean potential of all the somas over the neural population, $J = J(t)$ represents some (common) input into the population, and α and β are (inverse) time constants specifying the rise and decay of the mean potential. The input J is usually a continuous function of time t, but if J is meant to resemble point processes, e.g., given via microscopic action potentials or spikes, continuity may be introduced (albeit heuristically) using sigmoidal activation functions (Marreiros et al., 2008).

Obviously, the dynamics (1) is a gross approximation for most (non-linear) neural dynamics at the microscopic level. Nonetheless, the model may provide reasonable approximations of selected features of a neural population's mean activity. However, apart from the weakness (if not absence) of internal interactions, this requires the population to contain sufficiently many neurons[1] and/or symmetries. Symmetries typically imply an adequate amount of homogeneity. Even under these assumptions, detailed derivations of mass models like (1) from microscopic neural dynamics are rare (Stefanescu and Jirsa, 2008a; Byrne et al., 2017). As a consequence, it remains difficult to judge the degree to which the outcome of neural mass models really agrees with the mean activity of a "real" neural network. This is unfortunate because, given their mathematical ease, neural mass models appear ideal candidates for estimating parameter dependencies of network activation and predicting their dynamical outcome. For the Freeman model (1), Rodrigues and co-workers recently presented a mapping between a microscopic conductance-based model and the macroscopic mass dynamics (Rodrigues et al., 2010). They imposed strong homogeneity assumptions on a population of interconnected leaky integrate-and-fire (LIF) neurons. We adopted this approach but complemented it by an alternative, since some steps in Rodrigues et al. (2010) missed some rigor.

[1]Ideally one can consider the thermodynamic limit, i.e., infinitely many neurons, though symmetries may allow for exact mean field description even for finite population sizes. Yet, the Freeman model is often considered appropriate for describing the "coordinated activity of cell assemblies of $\sim 10^4$ neurons with $\sim 10^8$ synapses", Walter J. Freeman and Harry Erwin (2008), *Scholarpedia*, 3(2):3238.

To test the quality of these two mass models, we simulated an externally driven, finite-size LIF network. We used its overall spiking activity and the external drive as input to the mass models and compared the resulting time series with the ones of the average LIF potentials using different measures. Following previous studies, we set these neural masses to contain neurons of mixed types, i.e., inhibitory and excitatory ones (Lopes da Silva et al., 1974; Jansen and Rit, 1995; Wendling et al., 2000; David and Friston, 2003; Stefanescu and Jirsa, 2008b; Ponten et al., 2010). Given the relevance for neural mass models in the study on brain rhythms we first investigated the spectral distributions of the potentials and complemented this by correlating the average network activity with that of the two neural mass models. This procedure allowed for a systematic assessment of the influence of population parameters on the quality of the mass model approximation(s). Here, we particularly focus on the (im-)balance between inhibitory and excitatory neurons and the degree of their connectivity. As will be shown, the quality of approximation(s) is (are) limited, except for parameter ranges defining the onset of synchrony and/or the range in which LIF neurons are synchronized at low spiking frequencies.

RESULTS

Our two neural mass models obey the generic form

$$\left[\tau^{(\mathrm{mem})}\frac{d}{dt}+1\right]\left[\tau^{(\mathrm{syn})}\frac{d}{dt}+1\right]V = J^{(\mathrm{net})}(V;A,\dots)+J^{(\mathrm{ext})}(V;\dots) \tag{2}$$

where $J^{(\mathrm{net})}(V;A,\dots)$ is the sum of all spike-related currents in the LIF network, i.e., the population mean of the expectation values of the spike trains generated by network times the corresponding synapse conductances. Its value may depend on the mean membrane potential V and the networks adjacency matrix A (amongst other parameters). $J^{(\mathrm{ext})}$ summarizes the external drive, here always realized as a Poisson train. If the V-dependency of J is absent, we refer to (2) as the "conventional" Freeman model (CFM) and in the presence of a V-dependent currents, we refer to it as a slightly modified Freeman model (MFM); the explicit forms are given in (20) and (24), respectively.

The linearities in (2) stem from the facts that: (i) apart from the spike-related reset, the LIF dynamics is linear with membrane time constant $\tau^{(\mathrm{mem})}$; and (ii) we connected them via exponential synapses containing a linear conductance dynamics with time constant $\tau^{(\mathrm{syn})}$. In relation to (1) we have $\alpha = 1/\tau^{(\mathrm{mem})}$, $\beta = 1/\tau^{(\mathrm{syn})}$.

In the absence of $J^{(\mathrm{net})}$, the impulse response of (the left-hand side of) the dynamics (2) equals that of a second-order linear system with rise and decay times given by $\tau^{(\mathrm{mem})}$ and $\tau^{(\mathrm{syn})}$. The corresponding frequency response function is that of a second-order low-pass filter (cf. **Appendix**). As soon as $J^{(\mathrm{net})}$ is included, i.e., once the LIF neurons start to fire, the response functions in the time- and frequency-domains become less trivial and quantitative assessments require numerical approaches. For this, we simulated a network composed of $N = 10{,}000$ LIF neurons

TABLE 1 | Parameters values used when simulating the network of LIF neurons.

Variable	Description	Value
$v^{(\text{thres})}$	Threshold potential	–50 mV
$\tilde{v}$	Membrane reversal potential	–80 mV
$\tilde{v}^{(E)}$	Excitatory synaptic reversal potential	0 mV
$\tilde{v}^{(I)}$	Inhibitory synaptic reversal potential	–70 mV
$v^{(\text{reset})}$	Reset potential	–60 mV
$\tau^{(\text{mem})}$	Membrane characteristic time	20 ms
$\tau^{(E)}$	Excitatory synaptic time constant	3 ms
$\tau^{(I)}$	Inhibitory synaptic time constant	7 ms
$\tau^{(\text{ref})}$	Refractory period	5 ms
g	Leak conductance	10 nS
$\hat{g}^{(E)}$	Excitatory synaptic conductivity	4 nS
$\hat{g}^{(I)}$	Inhibitory synaptic conductivity	40 nS
$\hat{g}^{(\text{ext})}$	External synaptic conductivity	5 nS

and used the simulated network's spiking activity as input to the mass dynamics, i.e., $\sim J^{(\text{net})}$ in (2).

To study the influence of different adjacencies A on the quality of agreement between the average network potential and that modeled via the neural mass dynamics (2), we modified A in two ways. (i) We considered the adjacency of an Erdős-Rényi random graph and changed the network's overall degree p from 0 to 1 so A represents connections between all excitatory and inhibitory neurons. (ii) By the same token, we varied the relation between excitatory vs. inhibitory units that we quantified via

$$\lambda := \frac{\#excitatory}{\#inhibitory + \#excitatory}. \tag{3}$$

Details on the implementation of the different kinds of neurons can be found in the *Methods* section below; all parameters are summarized in **Table 1**.

Before investigating the extent of agreement in more detail, we first verified that the chosen parameter range covered different dynamical regimes including phase transitions from de-synchronized to synchronized states. **Figure 1** illustrates typical examples of the network with and without synchronization, while a more complete picture of the network's synchronization characteristics over the $\{p, \lambda\}$ parameter space is given in **Figure 2**. There, we quantified the degree of synchrony using a spike train measure called *spike-contrast* (Ciba et al., 2018). In brief, one contrasts activity vs. non-activity (spike vs. no-spike) in temporal bins and varies the bin-size to obtain a time scale independent result. This allows for unraveling time scales of synchrony, over which we averaged here. Once the overall network degree exceeds a minimal value, increasing it further has little to no influence on the state of synchronization in the network. In contrast, altering λ, e.g., increasing the relative amount of excitatory units, one can observe a spontaneous switch between de-synchronized to synchronized states.

The degree of synchronization in the network plays a crucial role for the appropriateness of the neural mass models in relation to the average network dynamics. As said, there is particular interest in the spectral content of the dynamics of neural populations (Buzsaki, 2006; Başar, 2012). Hence, we first summarize our comparisons in the frequency domain.

Spectral Characteristics

In what follows, we denote the average LIF network potential and the neural mass potentials by V_{LIF}, V_{CFM}, and V_{MFM}, respectively, and refer to the corresponding spectra as P_{LIF}, P_{CFM}, and P_{MFM}. **Figure 3** shows the median frequency of V_{LIF}, which in combination with **Figure 2**, provides a more encompassing view on the LIF network dynamics: when passing from small to larger values of λ, the network starts to synchronize. At the onset of synchrony the network's median frequency remains very low (this transition can be observed in **Figure 1**). When further increasing λ, this first transition from the de-synchronized to a synchronous state is followed by a second one, at which the network enters the synchronous regular regime with high spiking rate (Brunel and Hakim, 1999; Yger et al., 2011). The first transition appears smoother, which may be attributed to an effect of the chosen measure, i.e., the median frequency.

As expected, in the de-synchronized region both neural mass models displays significantly lower median frequencies than the network counterpart due to their low-pass filter characteristics. In all other dynamical regimes, the median frequencies seems to agree, at least at first glance. In general, one can expect that around a transition to or from synchrony, a spectral distribution may change qualitatively, rendering a comparison based solely on the median frequency incomplete. We therefore supplemented our analysis by a χ^2-statistic (25) between the network's and the neural masses' power spectral densities shown in **Figure 4** for both CFM and MFM; see the *Methods* section for details.

In the region of de-synchronization, the χ^2-values between the LIF network and the MFM spectra are clearly larger than the CFM counterpart. That is, there, the CFM provides a better representation of the network's average potential; cf. **Figure 4**. In the synchronous network state both models generate similar χ^2-values. In the region of regular high-frequency synchronization, both spectra substantially disagree with the V_{LIF} spectrum. There, the quality-of-fit is poor. By contrast, in the low-frequency synchronous region, especially close to the transition points from de-synchronization to synchronization, the spectra from both models agree to a level in which our χ^2-statistics does not identify any statistically significant differences; see the areas encircled by the red dashed lines in **Figure 4**.

Temporal Characteristics

We analyzed the V_{CFM} and V_{MFM} time series by determining the cross-correlation function between them and V_{LIF}. In view of the aforementioned response characteristics, we expected the extrema of this correlation to be located at finite, non-vanishing time lags τ. Therefore, we first estimated these time lags and, subsequently, determined the corresponding correlation coefficient as $\rho_k(\tau_{\max})$ with

$$\rho_k(\tau) = \int \hat{V}_{\text{LIF}}(t)\, \hat{V}_k(t+\tau)\, dt \tag{4}$$

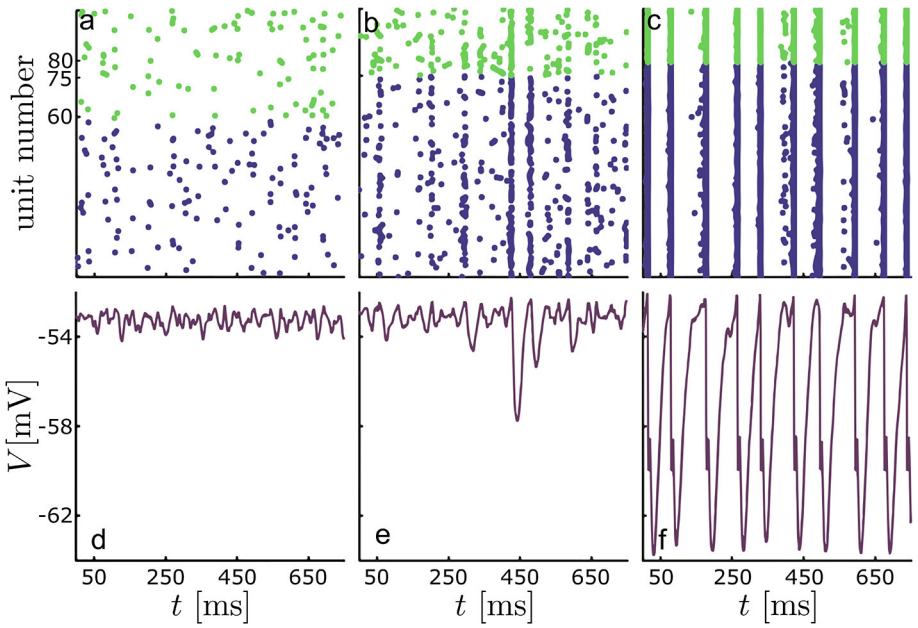


FIGURE 1 | Typical behavior of the LIF network for different fractions of excitatory and inhibitory units. Top panels **(a-c)** contain raster plots for 10^4 units, excitatory in blue and inhibitory in green. The bottom panels **(d-f)** show the corresponding LIF mean-field potential, $V(t)$; **(a,d)** $\lambda = 0.6$, **(b,e)** $\lambda = 0.75$ and **(c,e)** $\lambda = 0.8$; in all cases the overall network degree was set to $p = 0.2$.

and $\tau_{\max} = \arg\max_\tau |\rho_k(\tau)|$—in (4) the $(\hat{\cdot})$ indicates the computation of z-scores and $k \in \{\text{CFM}, \text{MFM}\}$. The resulting time lags and maximum correlation values are shown in **Figure 5**. As expected from the close relationship between the neural mass model and the linear response, the time lags switch from zero to positive values around the points of transition between de-synchronized and synchronized states—the fact that in the de-synchronized regime, the MFM displays a negative time lag shows its deviation from the mere low-pass characteristics for CFM. The drop in time lag in the transition from low-frequency to high-frequency synchronization is unexpected and we return to it in the *Discussion* section below.

For both CFM and MFM, the correlation followed a $\{p, \lambda\}$-dependent pattern similar to that of the synchronization degree combined with the median frequency (**Figures 2**, **3**). Apart from the regions with very small p, i.e., where the network was set to be very sparsely connected, the region with pronounced low-frequency synchronization ($\lambda \in [0.70, 0.85]$) is accompanied with the largest correlation values. Similar to the χ^2-based approach for the spectra, we determined a significance interval for the $\rho_k(\tau_{\max})$, now after Fisher transform (Fisher, 1915). The red-dashed significance boundaries indicate regions of proper approximations. In line with the results for the power spectral densities, also here the agreement between neural mass models and the average LIF network dynamics becomes arbitrarily bad in the region of high-frequency synchronization (larger values of λ). While both models largely agreed there, they differ when the network is de-synchronized ($\lambda < 0.7$) where $\rho_{V_{\text{CFM}}}$ displayed larger correlation values than $\rho_{V_{\text{MFM}}}$.

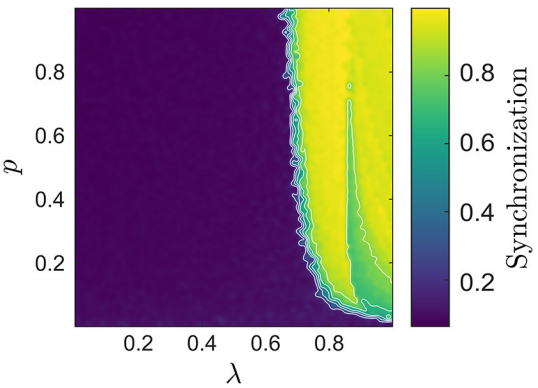


FIGURE 2 | The synchronization degree in the $\{p, \lambda\}$ space computed using the Spike-contrast measure (Ciba et al., 2018). A value close to 1 indicates strong synchronization, here particularly pronounced for large λ, whereas a value close to 0 indicates de-synchronized states. This is the case if p is very small, or if the number of inhibitory units exceeds that of the excitatory ones, i.e., if λ is small.

DISCUSSION

We compared two neural mass models with the average potential of a network of LIF neurons. Both models provide limited approximations of the average network potential for large regions of the $\{p, \lambda\}$ parameter space spanning network degree and the relation between excitatory and inhibitory neurons. We found arbitrary discrepancies between the neural mass models and the

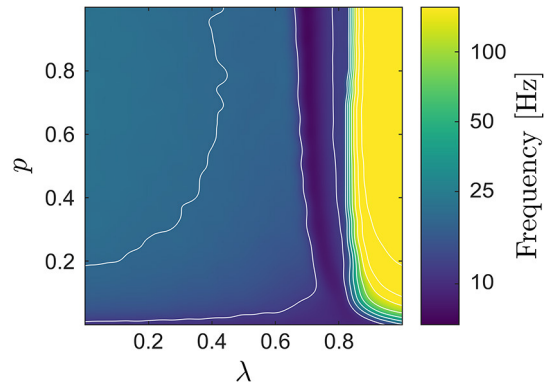


FIGURE 3 | Median frequency of the LIF network's average potential V_{LIF}; several contour lines were added to highlight the increase of the median frequency when increasing λ. When looking also at **Figure 2**, one can identify two transitions, one from the de-synchronized to a synchronized state (at low frequencies), followed by a second one from low- to high-frequency synchronization.

average potential of the LIF network, manifested in both the cross-correlation between model and network potentials and in the corresponding spectral densities that we assessed via χ^2-statistics. These were not just minor quantitative deviations but qualitative and largely unpredictable ones. Only in a very confined region around the transition from the de-synchronized state to low-frequency synchronization in the LIF network, both models performed well. There, our simulations did not reveal any significant differences between the "real" average network potential and the outcome of the two neural mass dynamics. Although this finding is troublesome as it implies a quite limited accuracy of neural mass approximations—at least in some parameter regimes—, we want to emphasize that our models appear suitable for studying neural activity at the transition between synchronized and de-synchronous states. In fact, transition regimes have recently gained much interest as they seem to particularly characterize neural dynamics during resting state (Ito et al., 2005, 2007) and also may describe more general metastability in ongoing whole-brain activity (Tognoli and Kelso, 2014; Deco et al., 2017; Beim Graben et al., 2019).

We incorporated two neural mass models derived from microscopic conductance-based neural models. For the first one, we followed the procedure described by Rodrigues et al. (2010). As already mentioned in the *Introduction*, some parts of their derivation arguably lack some rigor. For small fluctuations of the driving forces, they assumed the latter to be constant across channels, i.e., the membrane potential was considered constant and identical for all neurons on the synaptic terms; see Equation (17). While Rodrigues et al. did mention that this may not be a valid assumption, they also claimed this approximation to be required for deriving their neural mass model. Being constant is a very strong constraint for the membrane potential, which has—to the best of our knowledge—not been supported by previous research. Moreover, to us remains unclear why this approximation has only been applied for the synaptic terms but nowhere else in Equation (16). For the second neural mass model, we conducted an alternative derivation with the same starting point (16). To compute the population mean, we separated the time scales of the neural dynamics. This led to a slightly more complicated dynamics and reducing it further required a second approximation: the expectation values of the spike trains have to be identical among the different units. While this may be true for homogeneous cases, it may not hold in general. Strikingly, however, our results for both CFM and MFM largely agree. Both represent fairly accurately the results of the LIF network mean-field around the onset of low-frequency synchronization, while in other regions of the $\{p, \lambda\}$-space they both performed arbitrarily bad. Given these poor performances, we hope for future work to focus on (even more) rigorous alternatives.

In the population modeled in this work, the heterogeneity has been included by a mixture of excitatory and inhibitory units, while the external and internal connectivities are uniformly distributed and the different type of units are identical among them. This simplified the implementation of the models and the interpretation of our results. Yet, we have to admit that —when it comes to biological plausibility—this choice might be considered unrealistic: the homogeneity between neurons of the same type can be challenged (Reyes et al., 1998; Jinno et al., 2007; Ávila-Åkerberg et al., 2010) and the uniform distribution of connectivity might be replaced by, e.g., small-world topologies (Bettencourt et al., 2007; van den Heuvel et al., 2016; Bassett and Bullmore, 2017). Here we would like to add that using the current modeling approach the cell-to-cell heterogeneity including their role in neural coding has been explored elsewhere (Boustani and Destexhe, 2009; Mejias and Longtin, 2012, 2014; Carlu et al., 2020) while the modeling of small-world, modular and more realistic topologies remains future work.

As a final remark we would like to point out that discrepancies between microscopic and macroscopic descriptions for the same neural network are problematic when seeking for inferences from one level to the other. However, this ability for such inferences is fundamental, since a model has only value when it allows for predictions. Studying the network on the macroscopic neural mass level should allow to forecast a dynamics that could be verified on the microscopic, i.e., full network level. Of course, this requires a proper modeling of the latter. Since this cannot be guaranteed under all circumstances, the litmus test remains to forecast experimental data. This, however, will come with further challenges as one has to answer, e.g., "what is the microscopic level?" or "what defines the *full* network?". For instance, in encephalography the likelihood that the recorded potentials of some cortical region contains large contributions of (tangentially oriented) inhibitory units is arguably small. That is, although the full network does contain inhibitory units the recorded mean values of the underlying neural population may not cover them. In the **Appendix** we sought to mimic this case by repeating our comparisons after selecting only excitatory units from the simulated LIF-network. Also in this case our results stay intact rendering our conclusions valid and possibly transferrable to this type of experimental data.

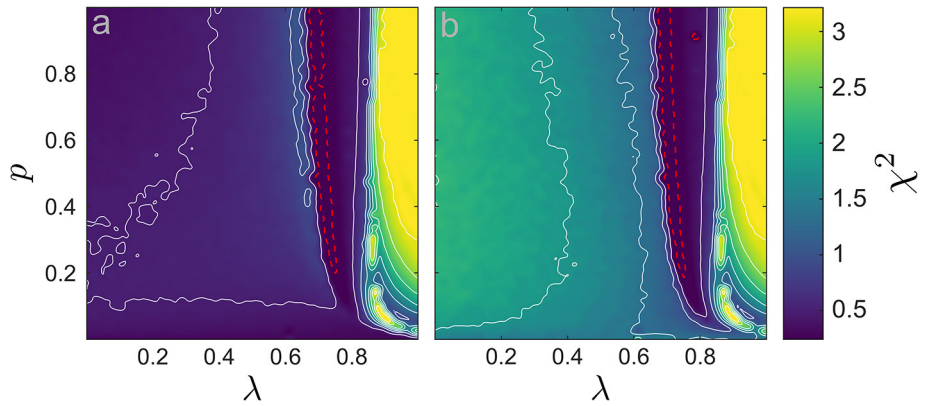


FIGURE 4 | χ^2-statistic computed between the power spectra ($\chi^2(\cdot,\cdot)$) in the $\{p, \lambda\}$ space (10^5 values). **(a)** χ^2 between the LIF network and the CFM, $\chi^2(P_{\text{LIF}}, P_{\text{CFM}})$. **(b)** χ^2 between the LIF network and the MFM, $\chi^2(P_{\text{LIF}}, P_{\text{MFM}})$. We add several contour lines in white to improve legibility. The dashed-red line indicates the boundaries of significance region with $\alpha = 0.01$ (conform the χ^2 distribution): inside the small region encircle by the dashed-red line, the CFM/MFM spectra were not significantly different from the LIF network spectrum.

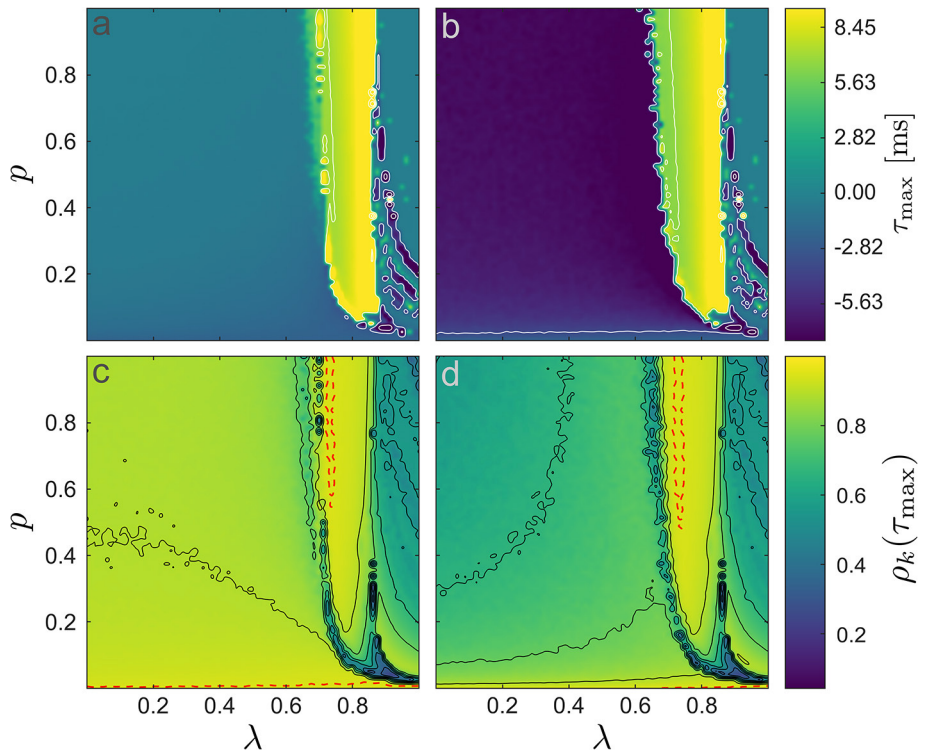


FIGURE 5 | Time lags and correlation coefficients. **(a,b)** depict the optimal time lags τ_{max}, **(a)** CFM and **(b)** MFM. We added contour lines (in white) to improve legibility. In **(b)** there is a change in the time lags when p is sufficiently large for the LIF network to generate spikes. In **(c,d)** the corresponding correlation coefficients $\rho_k(\tau_{\text{max}})$ between the LIF model and **(c)** CFM and **(d)** MFM are shown. The red-dashed lines in panels **(c,d)** indicate boundaries of significance; $\alpha = 0.01$ obtained by applying the Fisher transformation to the correlation values (Fisher, 1915). Inside the area defined by the red-dashed line in the synchronized region and the small area in the asynchronous region where $p \to 0$, the time series of the two neural mass models were not significantly different than the LIF mean field.

CONCLUSION

Neural masses are common tools to model neural population dynamics. They are believed to mimic selected brain activity patterns with great accuracy. We questioned the relation between these models and the underlying spiking neural network. For populations with both excitatory and inhibitory neurons and random connectivity, we found that approximations via the corresponding mean-field dynamics may deviate arbitrarily from the network's average potential. Deviations may be particularly

large when the network is either de-synchronized or fully synchronized and spikes at high rate, while mass models can fit well around the onset of low-frequency synchronization. Neural mass models covering several dynamical regimes require more than mere mean-field approximations because they typically average out the (synchrony-defining) spiking behavior.

METHODS

We will derive two neural mass models from a network of spiking neurons and compare them against the mean outcome of that network. The first model represents the CFM, and the second one contains a (slight) modification by means of a weakly non-linear response, i.e., the MFM. Then, our approach to test the model is the following: We simulate the spiking network for different values of two major topological parameters, i.e., the fraction of excitatory/inhibitory units and mean degree of the (random) network quantifying the general connectivity. We choose the parameters such that the dynamics undergoes a phase transition from the de-synchronized to a synchronized state (Yger et al., 2011). Throughout the simulations, we "record" both the output spiking activity and the mean membrane potential. While the latter is considered as reference, i.e., the "real" mean network activity, the first serves as input to the two neural mass models. Finally, we compare the outcome of the neural mass models with the real mean network activity in both the time and the frequency domain.

Below, we will specify the microscopic neuron and synapse dynamics and put them on a homogeneous network before deriving the two versions of the macroscopic Freeman model. Finally, we will provide all details about how we altered the network structure when probing model validity.

Microscopic Dynamics

We consider a population or network of $n = 1, \ldots, N$ neurons where neuron n is described in terms of the dynamics of its membrane potential $v_n = v_n(t)$ and voltage- and time-dependent conductances. If c_n and g_n denote the membrane's capacitance and leak conductance, respectively, then the dynamics can be cast in the form

$$\tau_n dv_n + f_n(v_n)dt = g_n^{-1} j_n(t)dt + dw_n. \tag{5}$$

The function $f_n(\cdot)$ is—as of yet—generic and describes the voltage-dependent decay, $j_n(t)$ is the total current applied to neuron n. The membrane's time constant $\tau^{(\mathrm{mem})}$ can be given by its capacitance and leak conductance in terms of $\tau_n := c_n/g_n$. And, w denotes a stochastic force summarizing random voltage fluctuations of the membrane; here, w will always reflect zero-centered, δ-correlated (white) Gaussian noise with variance Q. In what follows, we will specify both $f_n(\cdot)$ and $j_n(t)$ and estimate the expectation values of the population average for finite N.

We first notice that the input current $j_n(t)$ can be a combination of an internal current generated within the network and an external one stemming from outside the network. We denote them as $j_n^{(\mathrm{net})}$and $j_n^{(\mathrm{ext})}$, respectively, and assume that they superimpose like $j_n = j_n^{(\mathrm{net})} + j_n^{(\mathrm{ext})}$. Without loss of generality, the internal current will be given as

$$j_n^{(\mathrm{net})} = -\sum_{\sigma\in\{E,I\}}\sum_{m=1}^{N} g_{nm}^{(\sigma)}\left(v_n - \tilde{v}_{nm}^{(\sigma)}\right) \tag{6a}$$

where $\tilde{v}_{nm}^{(\sigma)}$ is the reversal potential for a synapse between neurons n and m. The synapse can be excitatory or inhibitory, which we indicate by $\sigma = E$ or $\sigma = I$, respectively. The synaptic activity is further quantified by a time-dependent conductance $g_{nm}^{(\sigma)}$ that depends on incoming spikes. We consider the corresponding response to be cast into a first-order, linear dynamics, i.e., we include so-called exponential synapses with conductance dynamics which leads to the dynamics

$$\tau_{nm}^{(\sigma)} dg_{nm}^{(\sigma)} = -\left(g_{nm}^{(\sigma)} - \hat{g}_{nm}^{(\sigma)}\phi_{nm}^{(\sigma)}\right)dt. \tag{6b}$$

The parameter $\hat{g}_{nm}^{(\sigma)}$ relates to the maximum conductance, $\tau_{nm}^{(\sigma)}$ is the characteristic time of the type-σ synapse between neurons n and m, and $\phi_{nm}^{(\sigma)}$ is the input that neuron n receives from neuron m. If that input is composed of spikes, it can be cast into the form

$$\phi_{nm}^{(\sigma)} = A_{nm}\sum_k \delta\left(t - t_{m,k}^{(\sigma)}\right) \tag{6c}$$

where A_{nm} denotes the elements of the network's adjacency matrix, i.e., $A_{nm} = 1$ if neuron m targets neuron n and 0 otherwise, and $\sum_k \delta\left(t - t_{m,k}^{(\sigma)}\right)$ is a spike train emitted by neuron m with spikes at times $t_{m,k}^{(\sigma)}$. Similarly, the external current may be expressed as

$$j_n^{(\mathrm{ext})} = -\sum_{m=1}^{M} g_{nm}^{(\mathrm{ext})}\left(v_n - \tilde{v}_{nm}^{(\mathrm{ext})}\right) \tag{7a}$$

given M external units that project into the network with external synaptic conductivity and external inputs of the form

$$\tau_{nm}^{(\mathrm{ext})} dg_{nm}^{(\mathrm{ext})} = -\left(g_{nm}^{(\mathrm{ext})} - \hat{g}_{nm}^{(\mathrm{ext})}\phi_{nm}^{(\mathrm{ext})}\right)dt \tag{7b}$$

and

$$\phi_{nm}^{(\mathrm{ext})} = B_{nm}\sum_k \delta\left(t - t_{m,k}^{(\mathrm{ext})}\right) \tag{7c}$$

respectively. The parameter $\hat{g}_{nm}^{(\mathrm{ext})}$ is again related to the maximum conductance, $\tau_{nm}^{(\mathrm{ext})}$ denotes the characteristic time of the corresponding synapse and $\phi_{nm}^{(\mathrm{ext})}$ is an external spike train that enters according to the adjacency matrix between the external and internal neurons ($B_{nm} = 1$ if the external neuron m targets internal neuron n and 0 otherwise).

We would like to note that, thus far, we did not detail the dynamics of the individual neuron n, i.e., the function $f(\cdot)$ can still be arbitrary (except that it has to be integrable). Put

differently, the system (5) and (6a-c) covers a very general case for a conductance-based, stochastic spiking network model under impact of an external drive (7a-c).

Next, in order to make this system tractable, we consider the case in which all synapses of type σ are identical for every neuron. This means that

$$\forall_{m=1,\ldots,M}: \left\{ \begin{array}{l} \tau_{nm}^{(\sigma)} =: \tau_n^{(\sigma)} \\ \hat{g}_{nm}^{(\sigma)} =: \hat{g}_n^{(\sigma)} \\ \tilde{v}_{nm}^{(\sigma)} =: \tilde{v}_n^{(\sigma)} \end{array} \right\}, \tag{8}$$

i.e., all synapses have identical characteristic times, maximum conductances, and reversal potentials. For the sake of legibility, we further introduce two abbreviations, namely

$$g_n^{(\sigma)} := \sum_{m=1}^{N} g_{nm}^{(\sigma)} \quad \text{and} \quad \phi_n^{(\sigma)} := \sum_{m=1}^{N} \phi_{nm}^{(\sigma)} \tag{9}$$

which represent the total conductivity of type-σ synapses in neuron n and the total spike input via type-σ synapses received by neuron n, respectively. Then, substituting (8) and computing the sum over m in (6b) yields

$$\tau_n^{(\sigma)} dg_n^{(\sigma)} = -\left(g_n^{(\sigma)} - \hat{g}_n^{(\sigma)} \phi_n^{(\sigma)}\right) dt. \tag{10}$$

Network of LIF Neurons

The arguably simplest case of spiking neurons are LIF neurons. To model them, we constrain $f_n(\cdot)$ to be linear in v_n. In more detail, we define $f_n(v_n) = (v_n - \tilde{v}_n)$, where $\tilde{v}_n$ denotes the membrane reversal potential. We add a further homogeneity assumptions by considering identical f_n as well as identical membrane characteristics for all neurons, i.e., $c_n = :c$, $g_n = :g \Rightarrow \tau_n = :\tau^{(\text{mem})}$, and $\tilde{v}_n = :\tilde{v}$. Likewise, we assume homogeneity of the synapse by setting $\tau_n^{(\sigma)} = :6\tau^{(\sigma)}$, $\tilde{v}_n^{(\sigma)} = :\tilde{v}^{(\sigma)}$, and $\hat{g}_n^{(\sigma)} = :\hat{g}^{(\sigma)}$, i.e., all synapses of the same type σ are identical across the population[2]. Using (10) and the homogeneity, we can simplify the system (5) and (6) as

$$\begin{aligned} \tau^{(\text{mem})} dv_n = -\Bigg[& (v_n - \tilde{v}) + \\ & + \tfrac{1}{g} \sum_{\sigma \in \{E,I\}} g_n^{(\sigma)} \left(v_n - \tilde{v}^{(\sigma)}\right) \Bigg] dt + dw_n \end{aligned} \tag{11a}$$

and

$$\tau^{(\sigma)} dg_n^{(\sigma)} = -\left(g_n^{(\sigma)} - \hat{g}^{(\sigma)} \phi_n^{(\sigma)}\right) dt \tag{11b}$$

with

$$\phi_n^{(\sigma)} = \sum_{m=1}^{N} A_{nm} \sum_k \delta\left(t - t_{m,k}^{(\sigma)}\right). \tag{11c}$$

[2]This appears a reasonable assumption given that the variability between neurons of the same type might be lost in the presence of noise.

Finally, the membrane dynamics is supplemented by the reset rule that reads

$$\begin{aligned} & \textit{if } v_n \textit{ reaches } v^{(\text{thres})}\textit{, then neuron } n \textit{ emits a spike} \\ & \textit{- its membrane potential } v_n \textit{ resets to } v^{(\text{reset})} \\ & \textit{- and stays there for a refractory period } \tau^{(\text{ref})}. \end{aligned} \tag{11d}$$

The set of equations (11a-d) defines our microscopic dynamics. This dynamics can be readily completed by adding external input as defined in (7a-c) much in line with the formulation of (11b) and (11c).

Macroscopic Dynamics

In the following we will estimate the population mean of the membrane potential's expectation value—recall that the dynamics (11a) contains noise that we "eliminate" by determining first the dynamics' first moment $V_n := \langle v_n \rangle$. Hence, the task is to approximate

$$V := \tfrac{1}{N} \sum_{n=1}^{N} V_n := \frac{1}{N} \sum_{n=1}^{N} \langle v_n \rangle. \tag{12}$$

Before doing so, however, we recast (11b) in the form

$$\left[\tau^{(\sigma)} \frac{d}{dt} + 1\right] \left\langle g_n^{(\sigma)} \right\rangle = \hat{g}^{(\sigma)} \Phi_n^{(\sigma)} \tag{13}$$

where we introduced the first moment of the spike trains, i.e.,

$$\Phi_n^{(\sigma)} := \left\langle \phi_n^{(\sigma)} \right\rangle. \tag{14}$$

By construction, $\langle w_n \rangle = 0$ holds, with which we find

$$\begin{aligned} & \left[\tau^{(\text{mem})} \frac{d}{dt} + 1\right] V = \\ & \qquad \tilde{v} - \tfrac{1}{g} \sum_{\sigma \in \{E,I\}} \tfrac{1}{N} \sum_{n=1}^{N} \left(\left\langle g_n^{(\sigma)} v_n \right\rangle - \left\langle g_n^{(\sigma)} \right\rangle \tilde{v}^{(\sigma)} \right). \end{aligned} \tag{15}$$

We can combine (13) and (15), in particular, when assuming identical time constants across synapse types σ, i.e., $\forall\, \sigma : \tau^{(\sigma)} =: \tau^{(\text{syn})}$. Then, we find

$$\begin{aligned} & \left[\tau^{(\text{mem})} \frac{d}{dt} + 1\right] \left[\tau^{(\text{syn})} \frac{d}{dt} + 1\right] V = \\ & \tilde{v} + \sum_{\sigma \in \{E,I\}} \tfrac{\hat{g}^{(\sigma)}}{g} \tilde{v}^{(\sigma)} \Phi^{(\sigma)} - \tfrac{1}{g} \sum_{\sigma \in \{E,I\}} \tfrac{1}{N} \sum_{n=1}^{N} \left[\tau^{(\text{syn})} \frac{d}{dt} + 1\right] \left\langle g_n^{(\sigma)} v_n \right\rangle \end{aligned} \tag{16}$$

with $\Phi^{(\sigma)} := N^{-1} \sum_{n=1}^{N} \Phi_n^{(\sigma)}$. The last term on the right-hand side of (16) needs to be approximated, and the way of which discriminates our two models. We first adopt the line of reasoning by Rodrigues et al. (2010) leading to the CFM before presenting a slight adjustment culminating in the MFM (cf. Tewarie, 2014, chap. 2).

The Conventional Freeman Model (CFM)

Approximating the term $\langle g_n^{(\sigma)} v_n \rangle$ in (15) can be difficult because smallness arguments may not hold in view of the stochastic nature of the dynamics. Rodrigues et al. (2010) introduced an admittedly gross step by considering

$$\left\langle g_n^{(\sigma)} v_n \right\rangle \approx \left\langle g_n^{(\sigma)} \bar{V} \right\rangle = \left\langle g_n^{(\sigma)} \right\rangle \bar{V} \tag{17}$$

where $\bar{V}$ denotes the constant mean membrane potential of the population. This approximation implies that the individual membrane potentials v_n are arbitrarily close to the population mean $\bar{V}$, averaged over time. Note that when applying this approximation one selectively ignores all of their dynamic characteristics on the right-hand side of (16); cf. *Discussion* section (but not on the left-hand side). Presuming this is acceptable, the last term on the right-hand side of (16) simplifies drastically because of

$$\begin{aligned} &\left[\tau^{(\text{syn})} \frac{d}{dt} + 1\right] \left\langle g_n^{(\sigma)} v_n \right\rangle \approx \\ &\qquad \left[\tau^{(\text{syn})} \frac{d}{dt} + 1\right] \left\langle g_n^{(\sigma)} \right\rangle \bar{V} \overset{(13)}{=} \hat{g}^{(\sigma)} \hat{V} \Phi_n^{(\sigma)} \end{aligned} \tag{18}$$

Substituting (18) into (16) yields

$$\begin{aligned} &\left[\tau^{(\text{mem})} \frac{d}{dt} + 1\right] \left[\tau^{(\text{syn})} \frac{d}{dt} + 1\right] V = \\ &\qquad \tilde{\nu} - \sum_{\sigma \in \{E,I\}} \frac{\hat{g}^{(\sigma)}}{g} \left(\bar{V} - \tilde{\nu}^{(\sigma)}\right) \Phi^{(\sigma)}. \end{aligned} \tag{19}$$

In the presence of external input, as given in (7a-c), the full dynamics finally reads

$$\begin{aligned} \left[\tau^{(\text{mem})} \frac{d}{dt} + 1\right] \left[\tau^{(\text{syn})} \frac{d}{dt} + 1\right] V = \tilde{\nu} - \sum_{\sigma \in \{E,I\}} \frac{\hat{g}^{(\sigma)}}{g} \left(\bar{V} - \tilde{\nu}^{(\sigma)}\right) \Phi^{(\sigma)} \\ - \frac{\hat{g}^{(\text{ext})}}{g} \left(\bar{V} - \tilde{\nu}^{(\text{ext})}\right) \Phi^{(\text{ext})}. \end{aligned} \tag{20}$$

In our study, the function $\Phi^{(\text{ext})}$ consists of Poisson spike trains as specified in Equation (7c).

Both forms, (19) and (20), agree entirely with the Freeman model (1) when identifying $\alpha = 1/\tau^{(\text{mem})}$, $\beta = 1/\tau^{(\text{syn})}$, and $J = \text{rhs}(19)$ or $J = \text{rhs}(20)$.

The Modified Freeman Model (MFM)

For an alternative approximation of the term $\langle g_n^{(\sigma)} v_n \rangle$ in (16), let us detail the time scales, at which the membrane potentials and the synapses evolve. Synaptic time constants can be as small as 1.7 ms (Häusser and Roth, 1997), much in the range of typical time scales of the membrane dynamics. Yet, changes in most chemical synapses are much slower than the changes the membrane potential, in particular, the generation/emission of action potentials. Then, one may assume that the membrane potential instantly follows changes at the synapse, its dynamics can be eliminated adiabatically, i.e., we can use

$$\left| \frac{dv_n}{dt} \Big/ v_n \right| \ll \left| \frac{dg_n^{(\sigma)}}{dt} \Big/ g_n^{(\sigma)} \right| \tag{21}$$

to rewrite

$$\begin{aligned} &\left[\tau^{(\text{syn})} \frac{d}{dt} + 1\right] \left\langle g_n^{(\sigma)} v_n \right\rangle \approx \\ &\left\langle \left(\left[\tau^{(\text{syn})} \frac{d}{dt} + 1\right] g_n^{(\sigma)} \right) v_n \right\rangle \overset{(13)}{=} \hat{g}^{(\sigma)} \Phi_n^{(\sigma)} \langle v_n \rangle. \end{aligned} \tag{22}$$

While this approximation contains sufficient rigor under the proviso of a proper time scale separation, we also require that

$$\frac{1}{N} \sum_{n=1}^{N} \hat{g}^{(\sigma)} \Phi_n^{(\sigma)} \langle v_n \rangle \approx \hat{g}^{(\sigma)} \Phi^{(\sigma)} V \tag{23}$$

which is true for Φ being the external spike train but may be arbitrarily inaccurate for the internal one $\Phi^{(\sigma)}$—again we refer to the *Discussion* section for a critical review. If this approximation turns out adequate, the MFM becomes

$$\begin{aligned} &\left[\tau^{(\text{mem})} \frac{d}{dt} + 1\right] \left[\tau^{(\text{syn})} \frac{d}{dt} + 1\right] V = \\ &\tilde{\nu} - \sum_{\sigma \in \{E,I\}} \frac{\hat{g}^{(\sigma)}}{g} \left(V - \tilde{\nu}^{(\sigma)}\right) \Phi^{(\sigma)} - \frac{\hat{g}^{(\text{ext})}}{g} \left(V - \tilde{\nu}^{(\text{ext})}\right) \Phi^{(\text{ext})}. \end{aligned} \tag{24}$$

In contrast to (20), the dynamics (24) contains a parametric forcing since on the right-hand side the constant $\bar{V}$ is replaced by the time-dependent mean potential V. Note, however, that despite this difference our simulation results revealed that given the chosen parameter values (õver-damped second-order response) the outcome of both models (20) and (24) largely agree.

Numerical Methods

Simulations

We simulated $N = 10{,}000$ LIF neurons with three types of synapses, each. The network equations were integrated using an Euler-Maruyama scheme with a time step of $\Delta t = 0.1$ ms and noise variance $Q = 5 \cdot 10^{-4}$ for a total duration of $T = 3 \cdot 10^4$ ms, i.e., for $3 \cdot 10^5$ time steps. We discarded a transient regime of $T_0 = 3 \cdot 10^3$ ms. The network was stimulated by 10,000 independent Poisson trains each of them connected to each neuron in the network with probability $p^{(ext)}$. The population average of the total spike input of each synaptic type σ received by each neuron at each time step t, $\phi^{(\sigma)}$ was stored as it subsequently served as input to the Freeman model. The temporal average of the population mean, $1/(T - T_0) \int_{T_0}^{T} V dt$ served as proxy of $\bar{V}$. For the neural masses, we employed a simple Euler forward scheme with the same time parameters used for the network model. The time constant $\tau^{(\text{syn})}$ was set to 5 ms, i.e., the average of the synaptic time constants in the network; see **Table 1**.

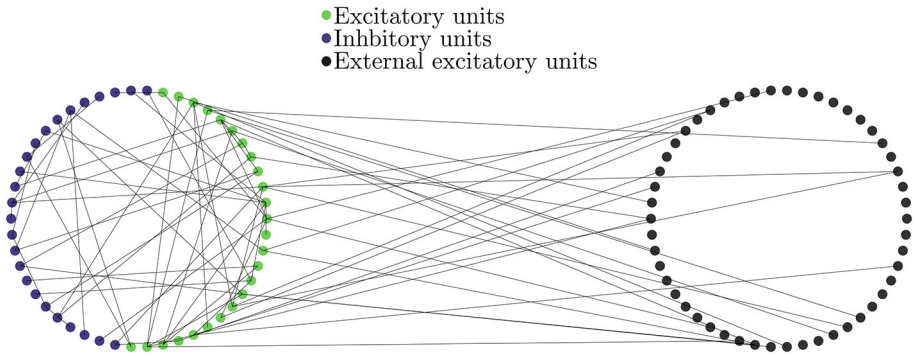


FIGURE 6 | Diagram of the network of LIF units **(Left)** together with the external de-correlated input **(Right)**. Blue denotes excitatory, green inhibitory and black excitatory external neurons. The units on the LIF network are connected to each other with probability p independently on their type. The external units are modeled as independent Poisson trains and are connected with the same probability $p^{(ext)}$ only to excitatory LIF units and are not connected to inhibitory ones.

To generate external input as Poisson spike trains, we drew random numbers from an exponential distribution. Since we drew the numbers at every time step for all the $M = 10{,}000$ external units, we minimized the computational load by following (Zenke and Gerstner, 2014) and used that the union of distinct exponential distributions is again exponential. The mean frequency $\nu^{(\text{ext})}$ of the external input was set to 5 Hz. The Erdős-Rényi adjacency $\{A_{nm}\}$ was constructed using the Gilbert model published in Batagelj and Brandes (2005), adjusted for directed graphs. For the connection probability, we used a range of $p = 0 \ldots 1$ implying a range of mean degrees of $k = Np = 0 \ldots N$. The distribution of excitatory vis-à-vis inhibitory neurons was quantified by the ratio given by (3), i.e.,

$$\lambda := \frac{\#excitatory}{\#inhibitory + \#excitatory}$$

with $\#inhibitory + \#excitatory = N = 10{,}000$. This network structure is similar to that in Brunel and Wang (2003) and Mazzoni et al. (2015) and has been considered as a good estimator of cortical activity (Mazzoni et al., 2015). Note, however, that it differs from other LIF networks such as the ones used in Brunel (2000) and Wong and Wang (2006) in their external drive: in the current work only excitatory neurons receive external input. The internal network connectivity is given by directed Erdős-Rényi network without discriminating excitatory and inhibitory units. The connectivity between the external Poisson trains and the network of LIF neurons was also given by a directed Erdős-Rényi network with mean out degree ($Mp^{(\text{ext})}$); cf. **Figure 6**.

Parameter Values

The major parameters are summarized in **Table 1**. They largely agree with the settings in Yger et al. (2011) and resemble biophysically plausible values.

Data Analysis

Per point $\{p, \lambda\}$ in the parameter space, the network was simulated. We first verified that the chosen parameter range in fact covered the regime at which phase transitions from the de-synchronized to a synchronized state may occur by using a recently introduced, time-scale independent spike train synchrony measure coined *Spike-contrast* (Ciba et al., 2018). This measure yields results that are comparable to those of the well-established *Spike-distance* (Kreuz et al., 2013) but had our preference for its computational efficiency, which was necessary for our fairly large number of neurons. Subsequently, the regenerated internal and external spike trains served as input to the Freeman model. From the time series of the network's mean membrane potential and of the Freeman model's outcome we estimate power spectra via a discrete Fourier transform after boundary correction using a Hamming window. This procedure was repeated 10 times yielding average discrete power spectra P_ω as sample mean approximation of the power spectral densities. The corresponding median frequency ϖ served as first, albeit very gross outcome measure to compare the spectra of the original network (i.e., its average potential) vis-á-vis the spectra of our models, CFM and MFM.

To quantify the agreement between spectra, we used a χ^2-statistics: Given two discrete spectra $P = (P_1, P_2, \ldots, P_L)$ and $Q = (Q_1, Q_2, \ldots, Q_L)$, their χ^2-statistic can be given as

$$\chi^2(P, Q) = \sum_{l=1}^{L} \frac{(P_l - Q_l)^2}{P_l + Q_l} \tag{25}$$

where the sum covers all L frequency components of the spectra (Press et al., 1989). Prior to using (25), the spectra were normalized to resemble histograms rather than probabilities.

DATA AVAILABILITY STATEMENT

The raw data supporting the conclusions of this article will be made available by the authors, without undue reservation.

AUTHOR CONTRIBUTIONS

ND and AD conceived and designed the study. AD derived the neural mass models. ND conducted the numerical simulations

and all the data analysis. The first draft of the manuscript was written by ND and all authors commented on previous versions of the manuscript. All authors read and approved the final manuscript.

FUNDING

This study received funding from the European Union's Horizon 2020 research and innovation program under the Marie Skłodowska-Curie grant agreement #642563 (COSMOS).

ACKNOWLEDGMENTS

ND and AD want to thank Rok Cestnik and Bastian Pietras for fruitful discussions.

SUPPLEMENTARY MATERIAL

The Supplementary Material for this article can be found online at: https://www.frontiersin.org/articles/10.3389/fncom.2020.581040/full#supplementary-material

REFERENCES

Ávila-Åkerberg, O., Krahe, R., and Chacron, M. J. (2010). Neural heterogeneities and stimulus properties affect burst coding *in vivo*. *Neuroscience* 168, 300–313. doi: 10.1016/j.neuroscience.2010.03.012

Başar, E. (2012). *Brain Function and Oscillations: Volume I: Brain Oscillations. Principles and Approaches*. Berlin; Heidelberg: Springer Science & Business Media.

Bassett, D. S., and Bullmore, E. T. (2017). Small-world brain networks revisited. *Neuroscientist* 23, 499–516. doi: 10.1177/1073858416667720

Batagelj, V., and Brandes, U. (2005). Efficient generation of large random networks. *Phys. Rev. E* 71:036113. doi: 10.1103/PhysRevE.71.036113

Beim Graben, P., Jimenez-Marin, A., Diez, I., Cortes, J. M., Desroches, M., and Rodrigues, S. (2019). Metastable resting state brain dynamics. *Front. Comput. Neurosci.* 13:62. doi: 10.3389/fncom.2019.00062

Bettencourt, L. M. A., Stephens, G. J., Ham, M. I., and Gross, G. W. (2007). Functional structure of cortical neuronal networks grown *in vitro*. *Phys. Rev. E* 75:021915. doi: 10.1103/PhysRevE.75.021915

Beurle, R. L. (1956). Properties of a mass of cells capable of regenerating pulses. *Philos. Trans. R. Soc. Lond. B* 240, 55–94. doi: 10.1098/rstb.1956.0012

Boustani, S. E., and Destexhe, A. (2009). A master equation formalism for macroscopic modeling of asynchronous irregular activity states. *Neural Comput.* 21, 46–100. doi: 10.1162/neco.2009.02-08-710

Brunel, N. (2000). Dynamics of sparsely connected networks of excitatory and inhibitory spiking neurons. *J.Comput. Neurosci.* 8, 183–208. doi: 10.1023/a:1008925309027

Brunel, N., and Hakim, V. (1999). Fast global oscillations in networks of integrate-and-fire neurons with low firing rates. *Neural Comput.* 11, 1621–1671. doi: 10.1162/089976699300016179

Brunel, N., and Wang, X.-J. (2003). What determines the frequency of fast network oscillations with irregular neural discharges? I. Synaptic dynamics and excitation-inhibition balance. *J. Neurophysiol.* 90, 415–430. doi: 10.1152/jn.01095.2002

Buzsaki, G. (2006). *Rhythms of the Brain*. New York, NY: Oxford University Press.

Byrne, A., Brookes, M. J., and Coombes, S. (2017). A mean field model for movement induced changes in the beta rhythm. *J. Comput. Neurosci.* 43, 143–158. doi: 10.1007/s10827-017-0655-7

Carlu, M., Chehab, O., Dalla Porta, L., Depannemaecker, D., Héricé, C., Jedynak, M., et al. (2020). A mean-field approach to the dynamics of networks of complex neurons, from nonlinear Integrate-and-Fire to Hodgkin–Huxley models. *J. Neurophysiol.* 123, 1042–1051. doi: 10.1152/jn.00399.2019

Ciba, M., Isomura, T., Jimbo, Y., Bahmer, A., and Thielemann, C. (2018). Spike-contrast: a novel time scale independent and multivariate measure of spike train synchrony. *J. Neurosci. Methods* 293, 136–143. doi: 10.1016/j.jneumeth.2017.09.008

David, O., and Friston, K. J. (2003). A neural mass model for MEG/EEG: coupling and neuronal dynamics. *Neuroimage* 20, 1743–1755. doi: 10.1016/j.neuroimage.2003.07.015

Deco, G., Jirsa, V. K., Robinson, P. A., Breakspear, M., and Friston, K. (2008). The dynamic brain: from spiking neurons to neural masses and cortical fields. *PLoS Comput. Biol.* 4:e1000092. doi: 10.1371/journal.pcbi.1000092

Deco, G., Kringelbach, M. L., Jirsa, V. K., and Ritter, P. (2017). The dynamics of resting fluctuations in the brain: metastability and its dynamical cortical core. *Sci. Rep.* 7, 1–14. doi: 10.1038/s41598-017-03073-5

Fisher, R. A. (1915). Frequency distribution of the values of the correlation coefficient in samples from an indefinitely large population. *Biometrika* 10, 507–521. doi: 10.1093/biomet/10.4.507

Freeman, W. J. (1975). *Mass Action in the Nervous System: Examination of the Neurophysiological Basis of Adaptive Behavior Through the EEG*. New York, NY: Academic Press.

Freeman, W. J. (1987). Simulation of chaotic EEG patterns with a dynamic model of the olfactory system. *Biol. Cybern.* 56, 139–150.

Griffith, J. S. (1963). A field theory of neural nets: I: derivation of field equations. *Bull. Math. Biophys.* 25, 111–120.

Griffith, J. S. (1965). A field theory of neural nets: II. properties of the field equations. *Bull. Math. Biophys.* 27:187.

Häusser, M., and Roth, A. (1997). Estimating the time course of the excitatory synaptic conductance in neocortical pyramidal cells using a novel voltage jump method. *J. Neurosci.* 17, 7606–7625.

Ito, J., Nikolaev, A. R., and van Leeuwen, C. (2005). Spatial and temporal structure of phase synchronization of spontaneous alpha EEG activity. *Biol. Cybern.* 92, 54–60. doi: 10.1007/s00422-004-0533-z

Ito, J., Nikolaev, A. R., and van Leeuwen, C. (2007). Dynamics of spontaneous transitions between global brain states. *Hum. Brain Mapp.* 28, 904–913. doi: 10.1002/hbm.20316

Jansen, B. H., and Rit, V. G. (1995). Electroencephalogram and visual evoked potential generation in a mathematical model of coupled cortical columns. *Biol. Cybern.* 73, 357–366.

Jinno, S., Klausberger, T., Marton, L. F., Dalezios, Y., Roberts, J. D. B., Fuentealba, P., et al. (2007). Neuronal diversity in gabaergic long-range projections from the hippocampus. *J. Neurosci.* 27, 8790–8804. doi: 10.1523/JNEUROSCI.1847-07.2007

Kozma, R., and Freeman, W. J. (2016). *Cognitive Phase Transitions in the Cerebral Cortex-Enhancing the Neuron Doctrine by Modeling Neural Fields*. Switzerland: Springer International Publishing.

Kreuz, T., Chicharro, D., Houghton, C., Andrzejak, R. G., and Mormann, F. (2013). Monitoring spike train synchrony. *J. Neurophysiol.* 109, 1457–1472. doi: 10.1152/jn.00873.2012

Lopes da Silva, F. H., Hoeks, A., Smits, H., and Zetterberg, L. H. (1974). Model of brain rhythmic activity. *Kybernetik* 15, 27–37.

Marreiros, A. C., Daunizeau, J., Kiebel, S. J., and Friston, K. J. (2008). Population dynamics: variance and the sigmoid activation function. *Neuroimage* 42, 147–157. doi: 10.1016/j.neuroimage.2008.04.239

Mazzoni, A., Lindn, H., Cuntz, H., Lansner, A., Panzeri, S., and Einevoll, G. T. (2015). Computing the local field potential (lfp) from integrate-and-fire network models. *PLoS Comput. Biol.* 11:e1004584. doi: 10.1371/journal.pcbi.1004584

Mejias, J. F., and Longtin, A. (2012). Optimal heterogeneity for coding in spiking neural networks. *Phys. Rev. Lett.* 108:228102. doi: 10.1103/PhysRevLett.108.228102

Mejias, J. F., and Longtin, A. (2014). Differential effects of excitatory and inhibitory heterogeneity on the gain and asynchronous state of sparse cortical networks. *Front. Comput. Neurosci.* 8:107. doi: 10.3389/fncom.2014.00107

Ponten, S. C., Daffertshofer, A., Hillebrand, A., and Stam, C. J. (2010). The relationship between structural and functional connectivity: graph

theoretical analysis of an EEG neural mass model. *Neuroimage* 52, 985–994. doi: 10.1016/j.neuroimage.2009.10.049

Press, W. H., Flannery, B. P., Teukolsky, S. A., Vetterling, W. T., et al. (1989). *Numerical Recipes*, Vol. 3. Cambridge: Cambridge University Press.

Reyes, A., Lujan, R., Rozov, A., Burnashev, N., Somogyi, P., and Sakmann, B. (1998). Target-cell-specific facilitation and depression in neocortical circuits. *Nat. Neurosci.* 1, 279–285. doi: 10.1038/1092

Rodrigues, S., Chizhov, A. V., Marten, F., and Terry, J. R. (2010). Mappings between a macroscopic neural-mass model and a reduced conductance-based model. *Biol. Cybern.* 102, 361–371. doi: 10.1007/s00422-010-0372-z

Stefanescu, R. A., and Jirsa, V. K. (2008a). A low dimensional description of globally coupled heterogeneous neural networks of excitatory and inhibitory neurons. *PLoS Comput. Biol.* 4:e1000219. doi: 10.1371/journal.pcbi.1000219

Stefanescu, R. A., and Jirsa, V. K. (2008b). A low dimensional description of globally coupled heterogeneous neural networks of excitatory and inhibitory neurons. *PLoS Comput. Biol.* 4:e1000219.

Tewarie, P. K. B. (2014). *Functional brain networks in multiple sclerosis: linking structural pathology to clinical disability* (Ph.D. thesis). Vrije Universiteit Amsterdam, Amsterdam, Netherlands.

Tognoli, E., and Kelso, J. (2014). The metastable brain. *Neuron* 81, 35–48. doi: 10.1016/j.neuron.2013.12.022

van den Heuvel, M. P., Bullmore, E. T., and Sporns, O. (2016). Comparative connectomics. *Trends Cogn. Sci.* 20, 345–361. doi: 10.1016/j.tics.2016.03.001

Wendling, F., Bellanger, J.-J., Bartolomei, F., and Chauvel, P. (2000). Relevance of nonlinear lumped-parameter models in the analysis of depth-EEG epileptic signals. *Biol. Cybern.* 83, 367–378. doi: 10.1007/s004220000160

Wong, K.-F., and Wang, X.-J. (2006). A recurrent network mechanism of time integration in perceptual decisions. *J. Neurosci.* 26, 1314–1328. doi: 10.1523/JNEUROSCI.3733-05.2006

Yger, P., El Boustani, S., Destexhe, A., and Frégnac, Y. (2011). Topologically invariant macroscopic statistics in balanced networks of conductance-based integrate-and-fire neurons. *J. Comput. Neurosci.* 31, 229–245. doi: 10.1007/s10827-010-0310-z

Zenke, F., and Gerstner, W. (2014). Limits to high-speed simulations of spiking neural networks using general-purpose computers. *Front. Neuroinformatics* 8:76. doi: 10.3389/fninf.2014.00076

Conflict of Interest: The authors declare that the research was conducted in the absence of any commercial or financial relationships that could be construed as a potential conflict of interest.

Copyright © 2021 Deschle, Ignacio Gossn, Tewarie, Schelter and Daffertshofer. This is an open-access article distributed under the terms of the Creative Commons Attribution License (CC BY). The use, distribution or reproduction in other forums is permitted, provided the original author(s) and the copyright owner(s) are credited and that the original publication in this journal is cited, in accordance with accepted academic practice. No use, distribution or reproduction is permitted which does not comply with these terms.

frontiers in Systems Neuroscience

PERSPECTIVE
published: 20 January 2021
doi: 10.3389/fnsys.2020.591210

Scale-Free Dynamics in Animal Groups and Brain Networks

Tiago L. Ribeiro[1], *Dante R. Chialvo*[2,3] *and Dietmar Plenz*[1]*

[1] Section on Critical Brain Dynamics, National Institute of Mental Health, National Institutes of Health, Bethesda, MD, United States, [2] Center for Complex Systems and Brain Sciences (CEMSC3), Instituto de Ciencias Fisicas, (ICIFI) Escuela de Ciencia y Tecnología, Universidad Nacional de San Martín (UNSAM), Buenos Aires, Argentina, [3] Consejo Nacional de Investigaciones Científicas y Técnicas (CONICET), Buenos Aires, Argentina

Collective phenomena fascinate by the emergence of order in systems composed of a myriad of small entities. They are ubiquitous in nature and can be found over a vast range of scales in physical and biological systems. Their key feature is the seemingly effortless emergence of adaptive collective behavior that cannot be trivially explained by the properties of the system's individual components. This perspective focuses on recent insights into the similarities of correlations for two apparently disparate phenomena: flocking in animal groups and neuronal ensemble activity in the brain. We first will summarize findings on the spontaneous organization in bird flocks and macro-scale human brain activity utilizing correlation functions and insights from critical dynamics. We then will discuss recent experimental findings that apply these approaches to the collective response of neurons to visual and motor processing, i.e., to local perturbations of neuronal networks at the meso- and microscale. We show how scale-free correlation functions capture the collective organization of neuronal avalanches in evoked neuronal populations in nonhuman primates and between neurons during visual processing in rodents. These experimental findings suggest that the coherent collective neural activity observed at scales much larger than the length of the direct neuronal interactions is demonstrative of a phase transition and we discuss the experimental support for either discontinuous or continuous phase transitions. We conclude that at or near a phase-transition neuronal information can propagate in the brain with similar efficiency as proposed to occur in the collective adaptive response observed in some animal groups.

Keywords: correlations, criticality, brain dynamics, neuronal network, flocking, scale-free, synchronization, mutual information

OPEN ACCESS

Edited by:
Spase Petkoski, INSERM U1106 Institut de Neurosciences des Systèmes, France

Reviewed by:
Silvia Scarpetta, University of Salerno, Italy
Pawel Romanczuk, Humboldt-Universität zu1 Berlin, Germany

***Correspondence:**
Dietmar Plenz
plenzd@mail.nih.gov

Received: *04 August 2020*
Accepted: *21 December 2020*
Published: *20 January 2021*

Citation:
Ribeiro TL, Chialvo DR and Plenz D (2021) Scale-Free Dynamics in Animal Groups and Brain Networks. Front. Syst. Neurosci. 14:591210. doi: 10.3389/fnsys.2020.591210

INTRODUCTION

The collective movement of animal groups has been the subject of great interest for many decades, with the early work focusing on model simulations (Aoki, 1982; Reynolds, 1987). It is now well-accepted that collective properties in animal groups are closely related to the general study of collective phenomena in physics, which initially was focused on phase transitions in equilibrium systems composed of many, locally interacting particles (Stanley, 1971; Ma, 1976, 1985), but eventually was expanded to include far-from-equilibrium systems (Meakin, 1987; Kertesz and Wolf, 1989; Martys et al., 1991). Many biological systems were found to fit into this latter category specifically when considering systems of self-driven particles to model movements of ants (Millonas, 1992; Rauch et al., 1995), fish schools (Huth and Wissel, 1992) and bird flocks resulting

in the seminal model by Vicsek et al. (1995) for flocking in biological systems based on local interactions impacted by noise. Since then, variations of the Vicsek model (Grégoire and Chaté, 2004; Chate et al., 2008) as well as other models that utilize attraction and distance rules (Couzin et al., 2002; Romanczuk et al., 2009) have been combined with experimental observations to capture population dynamics of many species such as locust swarms (Huepe et al., 2011), ants (Gelblum et al., 2016), fish schools (Tunstrøm et al., 2013), migrating white storks (Nagy et al., 2018), and cycling pelotons (Belden et al., 2019) with a major goal to understand the emergence of collective behavior from the mechanistic interactions between individuals [for a review, see e.g., Wang and Lu (2019)].

These observations support the idea that biological systems seem to be naturally poised near a phase transition (Bak, 1996), where they might benefit from order yet maintain adaptability to changing environmental conditions, an idea that is increasingly gaining attraction including the brain (Chialvo, 2010; Mora and Bialek, 2011; Plenz, 2012; Hesse and Gross, 2014; Plenz and Niebur, 2014). The initial theoretical debate has been enriched recently by an ever-improving ability to simultaneously track many biological elements (neurons, birds, midgets, etc.) over time, such that now the ideas are being challenged and contrasted by the experimental findings in the usual manner of statistical mechanics.

In this note, we focus on the behavior of the system correlation properties, the central tenet of statistical mechanics. For the sake of discussion, our starting point will be the work by Cavagna et al. in 2010, who demonstrated that starlings in a flock exhibit spatial correlations much longer than the length of direct interactions between neighboring birds (Cavagna et al., 2010, 2018). Specifically, they showed that the correlation length, i.e., the distance at which correlations drop below zero, grows monotonically with flock size (**Figure 1A**) and is, therefore, scale-free. The absence of any characteristic scale in the correlations is known to be a hallmark of critical systems (Wilson, 1979). For the human brain, early evidence of scale-free correlation functions was found for ongoing neuronal activity assessed indirectly using the blood oxygen level dependent signal (BOLD) (Expert et al., 2011) followed by the demonstration of correlation length to grow with the size of the observed brain region (**Figure 1B**) (Fraiman and Chialvo, 2012), exactly as was described for starling flocks. These remarkable population-spanning correlations were replicated for a network model of the brain with experimentally based interareal connectivity when the network dynamics was tuned to criticality (Haimovici et al., 2013). Since then, they have also been observed for bacterial colonies (Chen et al., 2012), insect swarms (Attanasi et al., 2014b), and globular proteins (Tang et al., 2017, 2020). Here, we explore specifically the analogy in scale-free correlations between animal groups and brain dynamics at the scale of local population activity during motor outputs in nonhuman primates and down to the cellular scale of single neuron interactions during sensory processing in mice. We will demonstrate that this analogy goes beyond phenomenology and shares the same formal scaling relations which suggest common underlying principles.

SCALE-FREE CORRELATIONS IN RESPONSE TO EXTERNAL PERTURBATIONS

The absence of a central control for the emergence of order lies at the heart of collective phenomena. With respect to animal groups this remarkable feature is also known as "coordination" and allows animals to stay together for protection in the face of predators (Powell, 1985; Terborgh, 1990; Krause and Ruxton, 2002) or to enhance foraging (Krebs, 1973; Munn and Terborgh, 1979; Greenberg, 2000). This collective response thus requires information about a local predator or local food source to be translated into a coordinated flock response for escape behavior or foraging to be successful. Several studies have now demonstrated how swarms can achieve such de-centralized coordination using local interactions between neighbors (Gregoire et al., 2003; Sumpter, 2006; Strombom, 2011; Bialek et al., 2012; Vicsek and Zafeiris, 2012; Ling et al., 2019b).

Predominantly local interactions are also characteristic for many brain networks, specifically as found for the cortex in mammals (Markram et al., 2015). Like a bird in a flock, the "action" or output of a cortical neuron depends largely on the activity of its intracortical neighbors (Boucsein et al., 2011). The response to external perturbations of a flock, e.g., by the local intrusion of a predator, also invite interpretations similar to the response of a cortical network to external inputs. Those inputs directly affect only a small proportion of all neurons, e.g., through input from the thalamus (Bruno and Sakmann, 2006) or from other cortical regions, and thus are analogous to local perturbations of ongoing network dynamics (Arieli et al., 1996). And although neurons in a network do not change physical positions in relation to one another like birds, they may change their interaction neighborhood over time by strengthening or weakening their direct connections through synaptic plasticity. The mechanisms by which neuronal networks can propagate information quickly and flexibly to very distant, but not directly interacting, neurons are less clear though. Thus, inspired by the flock results we searched for evidence of scale-invariant correlations in brain activity in response to sensory input.

We recently explored the behavior of neuronal correlation functions at scales closer to direct neuronal interactions (Ribeiro et al., 2020). At the scale of a cortical area (i.e., the mesoscale of millimeters), we measured the distribution of the so-called local field potential (LFP) with high-density microelectrode arrays implanted in the premotor and prefrontal cortices of non-human primates performing a self-initiated motor task and a working memory task, respectively. The LFP extracts the local synchronization of neuronal groups and its emergence and propagation thus tracks the spatiotemporal evolution of population activity at a spatial resolution of several 100 μm with millisecond precision. At the scale of the cortical microcircuit (i.e., the scale of few micrometers), we measured the intracellular calcium dynamics in pyramidal cells expressing the genetically encoded calcium indicator YC2.6 in superficial layers of the primary visual cortex in awake mice passively viewing drifting gratings. The fluorescent indicator closely tracks the action

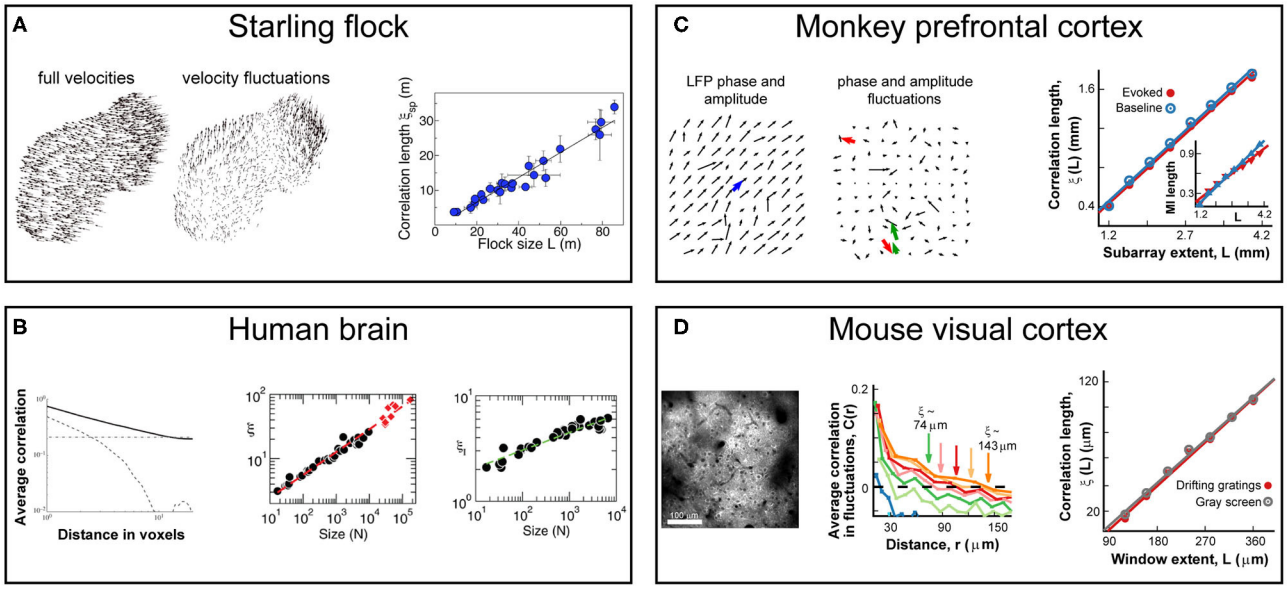


FIGURE 1 | Scale-free growths in correlations length is observed in bird flocks and the mammalian brain at different scales and using different recording techniques. **(A)** Correlations in the velocity fluctuations of pairs of starlings in flocks of different sizes. Fluctuations are obtained by subtracting from each bird's velocity vector (*left*) the center-of-mass velocity of the flock (*middle*). Correlation length, defined as the distance at which correlations of the fluctuations reaches zero, scales linearly with flock size (*right*) in line with expectations from critical dynamics. Adapted from (Cavagna et al., 2010). **(B)** Correlations obtained from blood oxygenated level dependent (BOLD) signals using fMRI to measure ongoing neuronal activity of the human brain. *Left*: Average correlation between voxel pairs drops with distance between voxels as a power law (*solid line*), while phantom data drops exponentially (*dashed line*) and spatially shuffled data is constant (*dotted line*). Adapted from (Expert et al., 2011) *Middle*: Correlation length, ξ, from fluctuations in BOLD data scales linearly with the size of the brain area observed (*black circles*) or when pooling areas together (*red diamonds*). Adapted from Fraiman and Chialvo (2012). *Right*: Mutual information between voxel pairs decays with pair distance, allowing for the definition of "mutual information length," ξ_I, in analogy to correlation length. ξ_I scales linearly with the size of the brain area observed (*black circles*). Adapted from Fraiman and Chialvo (2012). **(C)** Correlations in the fluctuations of LFP amplitudes from prefrontal cortex in nonhuman primates during a working-memory task using high-density microelectrode arrays. *Left/middle*: LFP vectors depicting phase and amplitude on the array without/with subtraction of the population average (*blue arrow*, *left*) in analogy to velocity distributions in flock data. *Right*: Correlation length scales linearly with (sub)array size for both ongoing (*blue*) and evoked (*red*) data. Adapted from Ribeiro et al. (2020). *Inset*: Mutual information length scales linearly with (sub)array size for both ongoing (*blue*) and evoked (*red*) data. **(D)** Correlations in the fluctuations of neuronal activity from primary visual cortex in mice during visual stimulation using 2-photon imaging. *Left*: Example field-of-view showing cells used for the analysis. *Middle*: Average correlation of activity fluctuations between pairs of neurons decays with distance as well as with the size of the observed window (*colors*). *Right*: Correlation length scales linearly with observed window size for both gray screen (*gray*) or drifting gradings (*red*). Adapted from Ribeiro et al. (2020).

potential firing in individual pyramidal neurons, which allows for a cellular reconstruction of spatiotemporal population activity with micrometer spatial resolution and sub-second temporal precision. At both scales, we observed the linear growth of the correlation length as a function of the linear size of the sampled area during sensory processing and motor output (**Figures 1C,D**). Remarkably, these scale-free correlations were similarly present during rest and evoked responses from the sensory/motor stimulation (**Figures 1C,D**) [see also Ribeiro et al. (2020)]. In line with previous results for the whole brain (Fraiman and Chialvo, 2012), the mutual information found in neuronal activity also behaved in a scale-free manner. By measuring how the mutual information between pairs of electrodes decays with distance, we showed that the "mutual information length" grew linearly with system size, just like the correlation length, for ongoing and evoked neuronal at the mesoscale (**Figure 1C**, inset).

Animal groups exhibit collective behavior in space during motion, in contrast to the brain, where activity propagates in high-dimensional networks and neurons themselves are stationary. These differences come into focus when considering scaling of correlation length by the spontaneous breaking of continuous rotational symmetry as is the case for orientation in space. In this case, global ordering can emerge in the absence of criticality at lower temperatures including the presence of powerlaw decay in space (Goldstone's theorem) (Goldstone, 1961). For this reason, Cavagna et al. (2010) also investigated correlations in the speed of birds, for which that argument does not apply: whereas orientation could be seen as a soft mode (being bound, they have a "soft" degree of freedom), speed in principle is unbounded and thus is considered a so-called "stiff" mode. In the case of brain activity, the Goldstone's theorem does not apply, at least for the data presented here, since there is no continuous symmetry that can be broken or soft modes. It needs to be noted that although a "pseudo" phase can be extracted from the LFP using a Hilbert transform of the original time series (Yu et al., 2017) the work of Ribeiro et al. (2020) used only the change in LFP amplitude (which is unbounded) to compute the correlation length. Furthermore, similar results were obtained when using binarized negative excursions of the LFP below a

certain threshold [so-called nLFPs, which represent the local, synchronous firing of neurons around the electrode; see Yu et al. (2017)], calcium traces or deconvolved spikes (Ribeiro et al., 2020), all of which are analogous to speed in animal movement.

INTERACTION LENGTH VS. CORRELATION LENGTH

As commented, many animals living in groups synchronize their behavior to that of their neighbors. In that manner, they can spend less time on the lookout for predators and more time feeding or resting (Bednekoff and Lima, 1998). If animals were required to be on alert to the behavior of distant group members, more resources would need to be allocated to group observation. Obviously, this requirement might not even be possible, e.g., for herds that are confined to a plane where observation of distant members is obscured or for very large animal groups in general. The attention toward neighbors is accounted for by most models of collective behavior in animal groups, which, considering local interactions (Vicsek et al., 1995; Cucker and Smale, 2007; Wang and Lu, 2019), are able to capture the synchronization of animals to their neighbors as found for red deer (Rands et al., 2014) and recently for black-headed gulls (Evans et al., 2018). In a more extreme example, mosquitofish were shown to only respond to their single nearest neighbor (Herbert-Read et al., 2011). Thus, regardless of whether interactions between animals depend on metric or topological distance (Ballerini et al., 2008; Ginelli and Chate, 2010; Strandburg-Peshkin et al., 2013), it is probably safe to say that keeping track of nearby neighbors is a preferred behavioral strategy in groups. On the other hand, this strategy requires that information pertinent for the individual survival must travel efficiently throughout the entire group, independently of the group size. In physics, this feature of transforming local (short-range) interactions into global (long-range) correlations, is known to be present in systems (almost exclusively) at criticality (Wilson, 1979). Support for this concept comes from the work of Cavagna et al. (2015) who employed a maximum entropy approach to infer the effective interactions from individuals in a natural flock and showed that the interaction range decays exponentially over the range of just a few individuals. Additionally, Calvão and Brigatti's model (Calvao and Brigatti, 2019), which is an implementation of the classical "selfish herd hypothesis" (Hamilton, 1971), is composed of local-interacting agents which collectively undergo a discontinuous phase transition. Their model successfully reproduces the behavior observed in nature for midge swarms including long-range correlations (Attanasi et al., 2014a,b).

For the brain, direct interactions between neurons exhibit a far more complex and selective organization than nearest neighbor relations. Neuronal interaction in the cortex includes a dominant number of direct short-range connections onto which long-range connections are superimposed that link distant cortical regions within and between hemispheres. Accordingly, the observation of long-range correlations might arise from short-range interactions at critical dynamics, from long-range connections independent of dynamical regimes, or both. To disambiguate this, we have simulated critical dynamics in a neuronal network with a precisely defined characteristic size for its connections and evaluated how the correlation function changes for distances beyond the short interaction range (Ribeiro et al., 2020). We found that there is a clear change in the behavior of the correlation function at the interaction range, with correlations growing much faster for distances up to this point, confirming our experimental findings in primary visual cortex. The obtained interaction distance was similar to the characteristic distance at which two pyramidal cells in layers II/III are connected anatomically (Levy and Reyes, 2012; Seeman et al., 2018). These results suggest critical dynamics in combination with short interactions to be a major factor behind the observed correlation length scaling at the microscale and indirectly suggest that as in the case of animal flocks, the information about a local input or perturbation can rapidly propagate through the entire system.

EFFECTS OF THE HETEROGENEITY OF THE ELEMENTS ON THE CORRELATION STRUCTURE

Although some early works have taken heterogeneity and self-sorting into account (Couzin et al., 2002), animal group behavior has been mostly studied assuming homogeneous behavior of the individual (Ero et al., 2018; Gouwens et al., 2019). More recently, the effects of heterogeneity within groups has gained increased attention [for a review, see e.g., King et al. (2018)]. For instance, it has been shown that body size affects the strength of social interactions and the spatial organization of fish schools (Romenskyy et al., 2017). For jackdaws, a bird species that form lifelong pair-bonds, social relationships between different birds lead to the appearance of sub-structures within a flock. Pair-bonded jackdaws interact with fewer neighbors than unpaired birds, flap their wings more slowly, which may save energy and flocks with more pairs exhibit shorter correlation length, which may lead to decreased group-level benefits (Ling et al., 2019a).

For the mammalian brain, already a cortical column with ∼10,000 neurons across its six layers provides a major modeling challenge with its diversity in cell types, cell connectivity, cellular, and subcellular dynamics (Markram et al., 2015; Dura-Bernal et al., 2019). The type of dynamics that in principle can be generated in these high-dimensional models is not easily constrained and can range from large-scale synchronized oscillations to more local, sometimes sequential activity. With respect to the latter and in analogy to how the social relationships affect correlations in jackdaw flocks (Ling et al., 2019a), it has been shown that some neurons (leaders) consistently fire earlier than others in spontaneous bursts of activity *in vitro* (Eytan and Marom, 2006; Eckmann et al., 2008; Orlandi et al., 2013; Pasquale et al., 2017). Yet, it is currently not known how the heterogeneity of cell types, layers and areas contribute to scale-free correlation lengths measured in the awake brain at macro-, meso-, and microscale. In a first attempt to address this issue, we studied functional subnetworks in cortical circuits, such as the one formed by orientation selective, i.e., "tuned" cells

with similar tuning preference in V1 (Palagina et al., 2019). When separately analyzing tuned and non-tuned cells, despite significant changes in the absolute value of correlation changes (evidencing the different structure present in these subgroups), we were able to show that scale-free correlations are present along the tuning dimension (Ribeiro et al., 2020). We note that the subgroup not included in the analysis was still participating in the overall network response and that this finding does not exclude the possibility that both subgroups are essential to create the observed scale-free correlations for both subnetworks.

NATURE OF THE PHASE TRANSITION UNDERLYING THE COLLECTIVE PROPERTIES OF ANIMAL GROUPS AND NEURONAL POPULATIONS

A variety of collective states can be observed in animal groups. For instance, Tunstrøm et al. (2013) have shown that golden shiner schools can present three dynamically-stable collective states, namely swarm, polarized and milling, with frequent transitions between them. Naturally, different types of collective states and accompanied transitions between those states are necessary for different animal species. Here, we discussed coordination or synchronization in animal groups in the context of emerging of directional order (or onset of collective motion) (Vicsek and Zafeiris, 2012) and condensation or clustering transitions (Chen et al., 2012; Calvao and Brigatti, 2019). Modeling work reflects this wide variety in collective behavior, which have been linked to different types of phase transitions, mainly of the discontinuous type [first order transitions, including hysteresis and metastability; e.g., Couzin et al. (2002), Chate et al. (2008), Hein et al. (2015), and Calvao and Brigatti (2019)] or the continuous type [second order, in line with criticality; e.g., Barberis and Albano (2014), Calovi et al. (2015), Feinerman et al. (2018)], or both (Huepe et al., 2011). Even within one model, the type of phase transition encountered can be sensitive to the specific model parameters and simulations conducted. For example, the original introduction of the Vicsek model (Vicsek et al., 1995) suggested a second-order phase transition, yet, clear discontinuities where identified particularly when adding aggregational terms and/or allowing noise to be directly added to the neighborhood computation (Grégoire and Chaté, 2004; Chate et al., 2008). There is strong theoretical evidence for the discontinuous nature of the transition in the Vicsek model (Bertin et al., 2009; Ihle, 2011; Peshkov et al., 2014), yet finite-size effects can smooth a discontinuous transition making it appear continuous (Grégoire and Chaté, 2004; Solon et al., 2015; Brown et al., 2020). Nevertheless, there are claims for the existence of robust continuous transitions in the Vicsek model within certain parameter regimes (Barberis and Albano, 2014). These commonly encountered sensitivities of abstract models to parameter regime and seemingly innocent model variation, necessarily call for elaborate experimental designs to validate models. For example, cooperative transport in ants was found to be more in line with a continuous phase transition when quantifying transport velocity for food pellets of different sizes (Feinerman et al., 2018).

The plethora of models that can be construed for brain networks ranging from abstract, binary neurons with random connectivity to detailed compartmental neuronal networks requires a prudent and stepwise alignment of theory and models with continuously improving experimental evidence. Here, we would like to point out the experimental demonstration of scale-free neuronal avalanches in isolated brain preparations in line with predictions for a critical branching process (Beggs and Plenz, 2003). This experimental finding suggested that system wide correlations form spontaneously in a fluctuation dominated brain state, with low and sparse rate. The experimental demonstration of scale-free (most-often weak) correlations for spontaneous and evoked neuronal activity in the awake brain in the presence of scale-invariant neuronal avalanches has been reliably found at the macroscale (Expert et al., 2011; Fraiman and Chialvo, 2012; Tagliazucchi et al., 2012), meso and microscale (Ribeiro et al., 2020). Importantly, LFP avalanches in the non-human primate that show scale-free correlations also exhibit a scaling collapse with an exponent of 2 for mean size vs. duration and an inverted parabolic profile in line with predictions for a critical branching process (Miller et al., 2019). This scaling collapse revealed a complex interaction with simultaneously present oscillations exhibiting the value of 2 at temporal resolutions outside the scale of the oscillation, required limit-analysis when measured at the scale of the oscillation, and collapsed to 1.5 when oscillations were removed by low-pass filtering. It is this body of experimental results in the awake cortex (Scott et al., 2014; Bellay et al., 2015), which forms the seed for a more comprehensive understanding of the mechanisms ruling the scale-free dynamics in brain activity.

A variety of alternative models and simulations often exhibit significant differences when accounting for the above-mentioned body of experimental findings. For example, the identification of universality classes that deviate from the directed percolation model have been found to be indecisive to explain neural data obtained from the anesthetized or sleep state under severe subsampling conditions (Fontenele et al., 2019; Carvalho et al., in press). Similarly, neuronal models that feature a first order transition between a low and high activity mode switched randomly by external noise and include oscillations (Scarpetta and de Candia, 2013; Scarpetta et al., 2018), while demonstrating a size distribution exponent of $-3/2$, also exhibit scaling exponents $\sim$1.1, which is lower than the relationship found in awake nonhuman primates (Miller et al., 2019). The Landau-Ginzburg scenario introduced recently to simulate avalanches in neuronal networks (di Santo et al., 2016; Buendia et al., 2020) exhibits, under certain parameter choices, a first order transition, hysteresis, and exponents similar to those of a critical branching process. However, the temporal avalanche profile identified in that model differs from an inverted-parabola measured experimentally in non-human primates (Miller et al., 2019). In addition, the disorder-synchronization phase transition in that model gives rise to statistically distinct giant ("king") avalanches found typically in disinhibited brain activity similar to epileptic seizures.

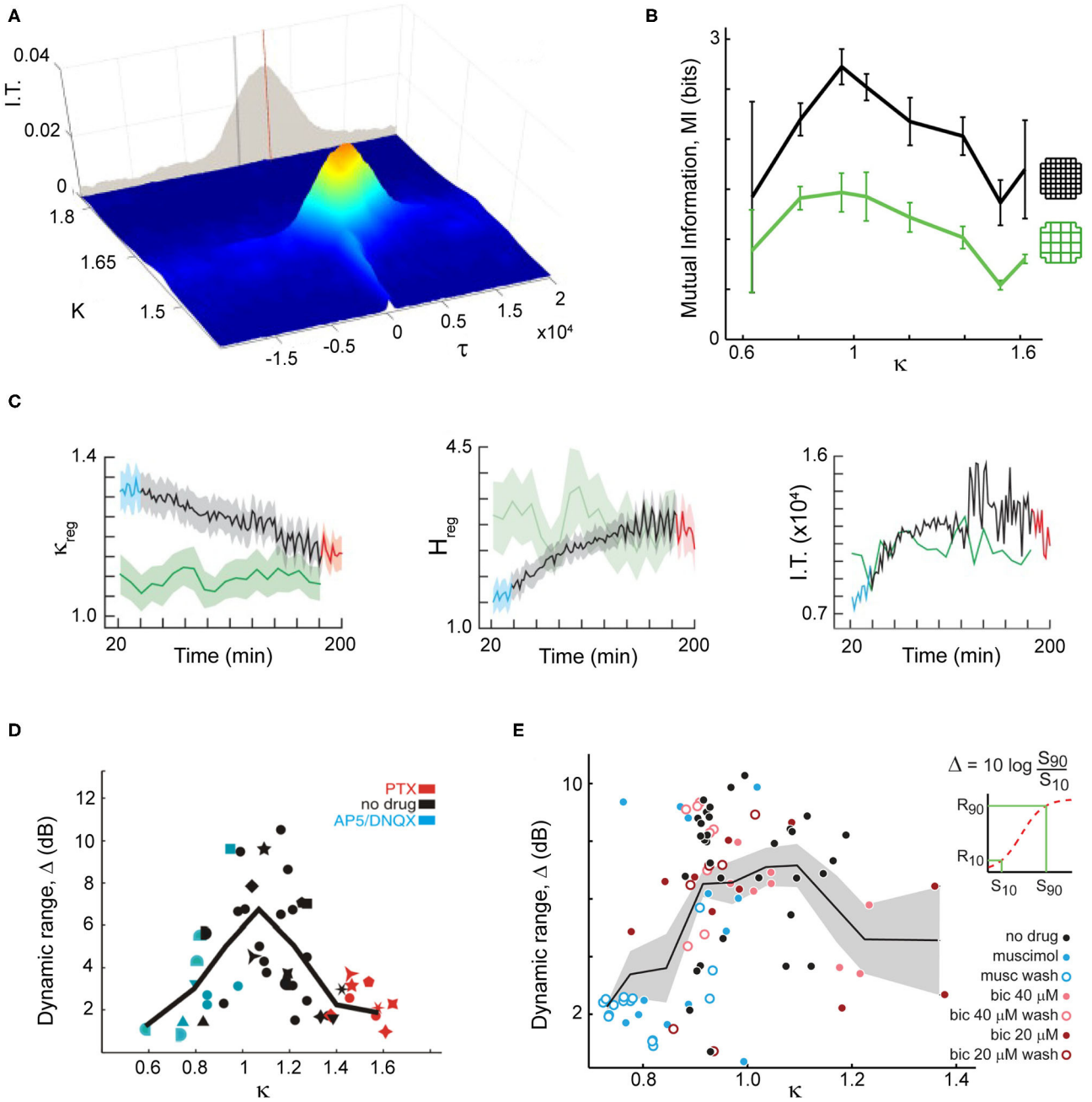


FIGURE 2 | Criticality and scale-free organization provide key advantages for both flocks and brains such as maximal information transmission and dynamic range. **(A)** In a decision-making model of flock behavior, information transmission peaks at criticality, shown by a peak in mutual information for $K \sim 1.62$ and $\tau \sim 2{,}500$ (critical point). Adapted from Lukovic et al. (2014). **(B)** In organotypic cultures grown from rodent brains, information transmission peaks when spontaneous neuronal activity displays scale-free neuronal avalanches, in line with expectation from criticality ($\kappa \sim 1$). Two different coarse-graining levels are shown (*colors*). Proximity to criticality, i.e., scale-free avalanches, is controlled through pharmacological manipulation of the cultures. Adapted from Shew et al. (2011). **(C)** Information transmission is maximized as mice recover from anesthesia, establishing neuronal avalanches. *Left*: Criticality distance measure approaches 1 (critical point) as time from anesthesia application (in min) passes. Anesthetized (*blue*), recently awake (*red*) and fully awake (*green*) states are highlighted. Entropy (*middle*) and information transmission (*right*) reaches a maximum as mice recover from anesthesia and reestablishing neuronal avalanches. Adapted from Fagerholm et al. (2016). **(D)** In organotypic cortex cultures, the dynamic range peaks when neuronal avalanches emerge and can be reduced when pharmacologically changing the natural excitation/inhibition balance. Adapted from Shew et al. (2009). **(E)** Using microelectrode array recordings in rats *in vivo*, the peak of dynamic range was demonstrated using natural stimuli and changes in excitation/inhibition balance through local pharmacological manipulation. Adapted from Gautam et al. (2015).

As a final reflection on this aspect, it needs to be noted that in contrast with the empirical solitude of the finding of neuronal avalanches a decade and half ago, the field is currently populated by a large variety of not-always self-consistent models. It seems that a fruitful avenue now might be to balance the modeling efforts with a careful analysis of the continuously improving sophisticated experimental evidence at hand.

IMPORTANCE OF SCALE-FREE CORRELATIONS FOR BRAIN FUNCTION

A large body of modeling work and some experimental evidence have shown that scale-free correlations are beneficial, providing key advantages to animals living in groups. For example, Rauch et al. (1995) showed the emergence of self-organized trails near a critical density of foraging ants. The length of these trails exceeded several orders of magnitude the ants perceptual scale, being another example of long-range correlations. In the same line, it has been shown that evolutionary pressure could move fish schools toward an optimized state near a discontinuous phase transition in an evolutionary model, where local environmental perturbations can cause changes in the collective school state (Hein et al., 2015). Using the Vicsek model for flocks (Vicsek et al., 1995), it has been shown that information transmission is maximized near the phase transition (**Figure 2A**) (Vanni et al., 2011; Lukovic et al., 2014), which as discussed in the previous subsection could have an underlying first-order origin. The enlarged correlations arising as a result from this maximized information transmission, lead to optimized response to predators (Mateo et al., 2017), in line with what has been observed in data-driven models of fish schools (Calovi et al., 2015) or sheep herds (Ginelli et al., 2015) near criticality. It has also been shown that the efficiency of computations in the Grégoire and Chaté (2004) model is maximized at the phase transition (Crosato et al., 2018).

On the brain side, theory and model simulations on critical dynamics in neuronal networks has proposed many advantages in information processing, some of which have been demonstrated experimentally, specifically when using pharmacological manipulations to move cortical networks away from neuronal avalanche dynamics (**Figures 2B–E**) [for reviews, see e.g., Shew and Plenz (2013) and Cocchi et al. (2017)]. For example, the dynamic range, which measures the range of stimulus intensity a network is able to differentiate, has been proposed to maximize at criticality by Kinouchi and Copelli (2006) and was demonstrated experimentally (**Figures 2D,E**) (Shew et al., 2009; Gautam et al., 2015).

Another parallel between scale-free flocks and brains is the presence of decentralized signal processing. This aspect has gained increased attention in the context of artificial intelligence, with many studies proposing the usage of artificial swarm systems (Hornischer et al., 2019; Sueoka et al., 2019). The brain also provides inspiration for these systems: Monaco et al. (2020) proposed an analogy between these multi-agent robotic platforms and place cells in the hippocampus, suggesting improvements to current models that follow solutions found by brain circuits. Startle responses in animal populations can trigger escape waves (Herbert-Read et al., 2015; Sosna et al., 2019), in the latter case yielding heavy-tail cascade size distributions and involve distributed repositioning of in the swarm beyond an individual's sensitivity changes to perturbation. The initiation and spread of such local response bears similarities to branching process dynamics suggesting promising similarities with critical brain dynamics.

CONCLUSIONS

The emergence of order in systems composed of a myriad of small entities exhibits many parallels between animal groups and neuronal populations in the brain. We summarized new experimental findings for the brain on the emergence of scale-invariant correlations and scale-invariant population sizes and discussed their similarities and differences compared to collective behavior in animals. We show that for both fields of research there are fascinating arguments for systems to be positioned near a phase transition to support propagation of local information throughout the entire system. Future experimental work on the role of cell types and microcircuit mechanisms in maintaining these scale-free dynamical features are crucial for understanding how the brain processes information.

DATA AVAILABILITY STATEMENT

The raw data supporting the conclusions of this article will be made available by the authors, without undue reservation.

ETHICS STATEMENT

The animal study was reviewed and approved by the NIMH Animal Care and Use Committee.

AUTHOR CONTRIBUTIONS

All authors have made a substantial, direct and intellectual contribution to the work, and approved it for publication.

FUNDING

This research was supported by the Division of the Intramural Research Program (DIRP) of the National Institute of Mental Health (NIMH), USA, ZIAMH002797 and ZIAMH002971 and the BRAIN initiative Grant U19 NS107464-01. This research utilized the computational resources of Biowulf (http://hpc.nih.gov) at the National Institutes of Health (NIH), USA.

ACKNOWLEDGMENTS

We thank members of the Plenz lab for discussions and the two reviewers for their detailed and constructive comments.

REFERENCES

Aoki, I. (1982). A simulation study on the schooling mechanism in fish. *Bull. Jpn. Soc. Sci. Fish.* 48, 1081–1088. doi: 10.2331/suisan.48.1081

Arieli, A., Sterkin, A., Grinvald, A., and Aertsen, A. (1996). Dynamics of ongoing activity: explanation of the large variability in evoked cortical responses. *Science* 273, 1868–1871. doi: 10.1126/science.273.5283.1868

Attanasi, A., Cavagna, A., Del Castello, L., Giardina, I., Melillo, S., Parisi, L., et al. (2014a). Collective behaviour without collective order in wild swarms of midges. *PLoS Comput. Biol.* 10:e1003697. doi: 10.1371/journal.pcbi.1003697

Attanasi, A., Cavagna, A., Del Castello, L., Giardina, I., Melillo, S., Parisi, L., et al. (2014b). A simulation study on the schooling mechanism in fish. *Phys. Rev. Lett.* 113:238102. doi: 10.1103/PhysRevLett.113.238102

Bak, P. (1996). *How Nature Works*. New York, NY: Copernicus.

Ballerini, M., Calbibbo, N., Candeleir, R., Cavagna, A., Cisbani, E., Giardina, I., et al. (2008). Interaction ruling animal collective behavior depends on topological rather than metric distance: evidence from a field study. *Proc. Natl. Acad. Sci. U.S.A.* 105, 1232–1237. doi: 10.1073/pnas.0711437105

Barberis, L., and Albano, E. V. (2014). Evidence of a robust universality class in the critical behavior of self-propelled agents: metric versus topological interactions. *Phys. Rev. E* 89:012139. doi: 10.1103/PhysRevE.89.012139

Bednekoff, P. A., and Lima, S. L. (1998). Randomness, chaos and confusion in the study of antipredator vigilance. *Trends Ecol. Evol.* 13, 284–287. doi: 10.1016/S0169-5347(98)01327-5

Beggs, J. M., and Plenz, D. (2003). Neuronal avalanches in neocortical circuits. *J. Neurosci.* 23, 11167–11177. doi: 10.1523/JNEUROSCI.23-35-11167.2003

Belden, J., Mansoor, M. M., Hellum, A., Rahman, S. R., Meyer, A., Pease, C., et al. (2019). How vision governs the collective behaviour of dense cycling pelotons. *J. R. Soc. Interf.* 16:20190197. doi: 10.1098/rsif.2019.0197

Bellay, T., Klaus, A., Seshadri, S., and Plenz, D. (2015). Irregular spiking of pyramidal neurons organizes as scale-invariant neuronal avalanches in the awake state. *Elife* 4:e07224. doi: 10.7554/eLife.07224.019

Bertin, E., Droz, M., and Grégoire, G. (2009). Hydrodynamic equations for self-propelled particles: microscopic derivation and stability analysis. *J. Phys. A Math. Theor.* 42:445001. doi: 10.1088/1751-8113/42/44/445001

Bialek, W., Cavagna, A., Giardina, I., Mora, T., Silvestri, E., Viale, M., et al. (2012). Statistical mechanics for natural flocks of birds. *Proc. Natl. Acad. Sci. U.S.A.* 109, 4786–4791. doi: 10.1073/pnas.1118633109

Boucsein, C., Nawrot, M. P., Schnepel, P., and Aertsen, A. (2011). Beyond the cortical column: abundance and physiology of horizontal connections imply a strong role for inputs from the surround. *Front. Neurosci.* 5:32. doi: 10.3389/fnins.2011.00032

Brown, J., Bossomaier, T., and Barnett, L. (2020). Information flow in finite flocks. *Sci. Rep.* 10:3837. doi: 10.1038/s41598-020-59080-6

Bruno, R. M., and Sakmann, B. (2006). Cortex is driven by weak but synchronously active thalamocortical synapses. *Science* 312:1622. doi: 10.1126/science.1124593

Buendia, V., di Santo, S., Villegas, P., Burioni, R., and Munoz, M. A. (2020). Self-organized bistability and its possible relevance for brain dynamics. *Phys. Rev. Res.* 2:013318. doi: 10.1103/PhysRevResearch.2.013318

Calovi, D. S., Lopez, U., Schuhmacher, P., Chate, H., Sire, C., and Theraulaz, G. (2015). Collective response to perturbations in a data-driven fish school model. *J. R. Soc. Interf.* 12:20141362. doi: 10.1098/rsif.2014.1362

Calvao, A. M., and Brigatti, E. (2019). Collective movement in alarmed animals groups: a simple model with positional forces and a limited attention field. *Phys. A Stat. Mech. Appl.* 520, 450–457. doi: 10.1016/j.physa.2019.01.029

Carvalho, T. T., Fontenele, A. J., Girardi-Schappo, M., Feliciano, T., Aguiar, L. A., Silva, T. P., et al. (in press). Subsampled directed-percolation models explain scaling relations experimentally observed in the brain. *Front. Neural Circuits*.

Cavagna, A., Cimarelli, A., Giardina, I., Parisi, G., Santagati, R., Stefanini, F., et al. (2010). Scale-free correlations in starling flocks. *Proc. Natl. Acad. Sci. U.S.A.* 107, 11865–11870. doi: 10.1073/pnas.1005766107

Cavagna, A., Del Castello, L., Dey, S., Giardina, I., Melillo, S., Parisi, L., et al. (2015). Short-range interactions versus long-range correlations in bird flocks. *Phys. Rev. E* 92:012705. doi: 10.1103/PhysRevE.92.012705

Cavagna, A., Giardina, I., and Grigera, T. S. (2018). The physics of flocking: Correlation as a compass from experiments to theory. *Phys. Rep.* 728, 1–62. doi: 10.1016/j.physrep.2017.11.003

Chate, H., Ginelli, F., Gregoire, G., and Raynaud, F. (2008). Collective motion of self-propelled particles interacting without cohesion. *Phys. Rev. E Stat. Nonlin. Soft Matter. Phys.* 77(4 Pt 2):046113. doi: 10.1103/PhysRevE.77.046113

Chen, X., Dong, X., Be'er, A., Swinney, H. L., and Zhang, H. P. (2012). Scale-invariant correlations in dynamic bacterial clusters. *Phys. Rev. Lett.* 108:148101. doi: 10.1103/PhysRevLett.108.148101

Chialvo, D. R. (2010). Emergent complex neural dynamics. *Nat. Phys.* 6, 744–750. doi: 10.1038/nphys1803

Cocchi, L., Gollo, L. L., Zalesky, A., and Breakspear, M. (2017). Criticality in the brain: A synthesis of neurobiology, models and cognition. *Prog. Neurobiol.* 158, 132–152. doi: 10.1016/j.pneurobio.2017.07.002

Couzin, I. D., Krause, J., James, R., Ruxton, G. D., and Franks, N. R. (2002). Collective memory and spatial sorting in animal groups. *J. Theor. Biol.* 218, 1–11. doi: 10.1006/jtbi.2002.3065

Crosato, E., Spinney, R. E., Nigmatullin, R., Lizier, J. T., and Prokopenko, M. (2018). Thermodynamics and computation during collective motion near criticality. *Phys. Rev. E* 97:012120. doi: 10.1103/PhysRevE.97.012120

Cucker, F., and Smale, S. (2007). Emergent behavior in flocks. *IEEE Trans. Autom. Control* 52, 852–862. doi: 10.1109/TAC.2007.895842

di Santo, S., Burioni, R., Vezzani, A., and Munoz, M. A. (2016). Self-organized bistability associated with first-order phase transitions. *Phys. Rev. Lett.* 116:240601. doi: 10.1103/PhysRevLett.116.240601

Dura-Bernal, S., Suter, B. A., Gleeson, P., Cantarelli, M., Quintana, A., Rodriguez, F., et al. (2019). NetPyNE, a tool for data-driven multiscale modeling of brain circuits. *Elife* 8:e44494. doi: 10.7554/eLife.44494.016

Eckmann, J. P., Jacobi, S., Marom, S., Moses, E., and Zbinden, C. (2008). Leader neurons in population bursts of 2D living neural networks. *N. J. Phys.* 10:015011. doi: 10.1088/1367-2630/10/1/015011

Ero, C., Gewaltig, M. O., Keller, D., and Markram, H. (2018). A cell atlas for the mouse brain. *Front. Neuroinf.* 12:84. doi: 10.3389/fninf.2018.00084

Evans, M. H. R., Lihou, K. L., and Rands, S. A. (2018). Black-headed gulls synchronise their activity with their nearest neighbours. *Sci. Rep.* 8:9978. doi: 10.1038/s41598-018-28378-x

Expert, P., Lambiotte, R., Chialvo, D. R., Christensen, K., Jensen, H. J., Sharp, D. J., et al. (2011). Self-similar correlation function in brain resting-state functional magnetic resonance imaging. *J. R. Soc. Interf.* 8, 472–479. doi: 10.1098/rsif.2010.0416

Eytan, D., and Marom, S. (2006). Dynamics and effective topology underlying synchronization in networks of cortical neurons. *J. Neurosci.* 26, 8465–8476. doi: 10.1523/JNEUROSCI.1627-06.2006

Fagerholm, E. D., Scott, G., Shew, W. L., Song, C. C., Leech, R., Knopfel, T., et al. (2016). Cortical entropy, mutual information and scale-free dynamics in waking mice. *Cereb. Cortex* 26, 3945–3952. doi: 10.1093/cercor/bhw200

Feinerman, O., Pinkoviezky, I., Gelblum, A., Fonio, E., and Gov, N. S. (2018). The physics of cooperative transport in groups of ants. *Nat. Phys.* 14, 683–693. doi: 10.1038/s41567-018-0107-y

Fontenele, A. J., de Vasconcelos, N. A. P., Feliciano, T., Aguiar, L. A. A., Soares-Cunha, C., Coimbra, B., et al. (2019). Criticality between cortical states. *Phys. Rev. Lett.* 122:208101. doi: 10.1103/PhysRevLett.122.208101

Fraiman, D., and Chialvo, D. R. (2012). What kind of noise is brain noise: Anomalous scaling behavior of the resting brain activity fluctuations. *Front. Physiol.* 3:307. doi: 10.3389/fphys.2012.00307

Gautam, H., Hoang, T. T., McClanahan, K., Grady, S. K., and Shew, W. L. (2015). Maximizing sensory dynamic range by tuning the cortical state to criticality. *PLoS Comput. Biol.* 11:e1004576. doi: 10.1371/journal.pcbi.1004576

Gelblum, A., Pinkoviezky, I., Fonio, E., Gov, N. S., and Feinerman, O. (2016). Emergent oscillations assist obstacle negotiation during ant cooperative transport. *Proc. Natl. Acad. Sci. U.S.A.* 113: 14615–14620. doi: 10.1073/pnas.1611509113

Ginelli, F., and Chate, H. (2010). Relevance of metric-free interactions in flocking phenomena. *Phys. Rev. Lett.* 105:168103. doi: 10.1103/PhysRevLett.105.168103

Ginelli, F., Peruani, F., Pillot, M. H., Chate, H., Theraulaz, G., and Bon, R. (2015). Intermittent collective dynamics emerge from conflicting imperatives in sheep herds. *Proc. Natl. Acad. Sci. U.S.A.* 112, 12729–12734. doi: 10.1073/pnas.1503749112

Goldstone, J. (1961). Field theories with superconductor solutions. *Nuovo Cimento* 19, 154–164. doi: 10.1007/BF02812722

Gouwens, N. W., Sorensen, S. A., Berg, J., Lee, C., Jarsky, T., Ting, J., et al. (2019). Classification of electrophysiological and morphological neuron types in the mouse visual cortex. *Nature Neurosci.* 22, 1182–1195. doi: 10.1038/s41593-019-0417-0

Greenberg, R. (2000). "Birds of many feathers: the formation and structure of mixed species flocks of forest birds," in *On the Move: How and Why Animals Travel in Groups*, eds S. Boinski and P. Garber (Chicago: Chicago University Press), 523–558.

Grégoire, G., and Chaté, H. (2004). Onset of collective and cohesive motion. *Phys. Rev. Lett*. 92:025702. doi: 10.1103/PhysRevLett.92.025702

Gregoire, G., Chate, H., and Tu, Y. H. (2003). Moving and staying together without a leader. *Phys. D Nonlinear Phenomena* 181, 157–170. doi: 10.1016/S0167-2789(03)00102-7

Haimovici, A., Tagliazucchi, E., Balenzuela, P., and Chialvo, D. R. (2013). Brain organization into resting state networks emerges at criticality on a model of the human connectome. *Phys. Rev. Lett*. 110:178101. doi: 10.1103/PhysRevLett.110.178101

Hamilton, W. D. (1971). Geometry for selfish herd. *J. Theor. Biol.* 31, 295. doi: 10.1016/0022-5193(71)90189-5

Hein, A. M., Rosenthal, S. B., Hagstrom, G. I., Berdahl, A., Torney, C. J., and Couzin, I. D. (2015). The evolution of distributed sensing and collective computation in animal populations. *eLife* 4:e10955. doi: 10.7554/eLife.10955

Herbert-Read, J. E., Buhl, J., Hu, F., Ward, A. J. W., and Sumpter, D. J. T. (2015). Initiation and spread of escape waves within animal groups. *R. Soc. Open Sci.* 2:140355. doi: 10.1098/rsos.140355

Herbert-Read, J. E., Perna, A., Mann, R. P., Schaerf, T. M., Sumpter, D. J. T., and Ward, A. J. W. (2011). Inferring the rules of interaction of shoaling fish. *Proc. Natl. Acad. Sci. U.S.A*. 108, 18726–18731. doi: 10.1073/pnas.1109355108

Hesse, J., and Gross, T. (2014). Self-organized criticality as a fundamental property of neural systems. *Front. Syst. Neurosci.* 8:166. doi: 10.3389/fnsys.2014.00166

Hornischer, H., Herminghaus, S., and Mazza, M. G. (2019). Structural transition in the collective behavior of cognitive agents. *Sci. Rep.* 9:12477. doi: 10.1038/s41598-019-48638-8

Huepe, C., Zschaler, G., Do, A. L., and Gross, T. (2011). Adaptive-network models of swarm dynamics. *N. J. Phys.* 13:073022. doi: 10.1088/1367-2630/13/7/073022

Huth, A., and Wissel, C. (1992). The simulation of the movement of fish schools. *J. Theor. Biol.* 156, 365–385. doi: 10.1016/S0022-5193(05)80681-2

Ihle, T. (2011). Kinetic theory of flocking: derivation of hydrodynamic equations. *Phys. Rev. E* 83:030901. doi: 10.1103/PhysRevE.83.030901

Kertesz, J., and Wolf, D. E. (1989). Anomalous roughening in growth processes. *Phys. Rev. Lett*. 62. 2571–2574. doi: 10.1103/PhysRevLett.62.2571

King, A. J., Fehlmann, G., Biro, D., Ward, A. J., and Furtbauer, I. (2018). Re-wilding collective behaviour: an ecolocical perspective. *Trends Ecol. Evol.* 33, 347–357. doi: 10.1016/j.tree.2018.03.004

Kinouchi, O., and Copelli, M. (2006). Optimal dynamical range of excitable networks at criticality. *Nat. Phys.* 2, 348–352. doi: 10.1038/nphys289

Krause, J., and Ruxton, G. D. (2002). *Living in Groups*. Oxford: Oxford University Press.

Krebs, J. R. (1973). Social-learning and significance of mixed-species flocks of chickadees (*Parus* Spp). *Can. J. Zool.* 51, 1275–1288. doi: 10.1139/z73-181

Levy, R. B., and Reyes, A. D. (2012). Spatial profile of excitatory and inhibitory synaptic connectivity in mouse primary auditory cortex. *J. Neurosci.* 32, 5609–5619. doi: 10.1523/JNEUROSCI.5158-11.2012

Ling, H. J., McIvor, G. E., van der Vaart, K., Vaughan, R. T., Thornton, A., and Ouellette, N. T. (2019a). Costs and benefits of social relationships in the collective motion of bird flocks. *Nat. Ecol. Evol.* 3, 943–948. doi: 10.1038/s41559-019-0891-5

Ling, H. J., McIvor, G. E., van der Vaart, K., Vaughan, R. T., Thornton, A., and Ouellette, N. T. (2019b). Local interactions and their group-level consequences in flocking jackdaws. *Proc. R. Soc. B Biol. Sci.* 286:20190865. doi: 10.1098/rspb.2019.0865

Lukovic, M., Vanni, F., Svenkeson, A., and Grigolini, P. (2014). Transmission of information at criticality. *Phys. A Stat. Mech. Appl.* 416, 430–438. doi: 10.1016/j.physa.2014.08.066

Ma, S.-K. (1976). *Modern Theory of Critical Phenomena*. Reading, MA: Benjamin.

Ma, S.-K. (1985). *Statistical Mechanics*. Philadelphia, PA: World Scientific.

Markram, H., Muller, E., Ramaswamy, S., Reimann, M. W., Abdellah, M., Sanchez, C. A., et al. (2015). Reconstruction and simulation of neocortical microcircuitry. *Cell* 163, 456–492. doi: 10.1016/j.cell.2015.09.029

Martys, N., Cieplak, M., and Robbins, M. O. (1991). Critical phenomena in fluid invasion of porous media. *Phys. Rev. Lett*. 66, 1058–1061. doi: 10.1103/PhysRevLett.66.1058

Mateo, D., Kuan, Y. K., and Bouffanais, R. (2017). Effect of correlations in swarms on collective response. *Sci. Rep*. 7:10388. doi: 10.1038/s41598-017-09830-w

Meakin, P. (1987). "The growth of fractal aggregates and their fractal measures," in *Phase Transitions and Critical Phenomena*, eds C. Domb and J.L. Lebowitz (New York, NY: Academic Press).

Miller, S. R., Yu, S., and Plenz, D. (2019). The scale-invariant, temporal profile of neuronal avalanches in relation to cortical γ-oscillations. *Sci. Rep.* 9:16403. doi: 10.1038/s41598-019-52326-y

Millonas, M. M. (1992). A connectionist type model of self-organized foraging and emergent behavior in ant swarms. *J. Theor. Biol.* 159, 529–552. doi: 10.1016/S0022-5193(05)80697-6

Monaco, J. D., Hwang, G. M., Schultz, K. M., and Zhang, K. (2020). Cognitive swarming in complex environments with attractor dynamics and oscillatory computing. *Biol Cybern.* 114, 269–284. doi: 10.1007/s00422-020-00823-z

Mora, T., and Bialek, W. (2011). Are biological systems poised at criticality? *J. Stat. Phys.* 144, 268–302. doi: 10.1007/s10955-011-0229-4

Munn, C. A., and Terborgh, J. W. (1979). Multi-species territoriality in neotropical foraging flocks. *Condor* 81, 338–347. doi: 10.2307/1366956

Nagy, M., Couzin, I. D., Fiedler, W., Wikelski, M., and Flack, A. (2018). Synchronization, coordination and collective sensing during thermalling flight of freely migrating white storks. *Philos. Trans. R. Soc. B Biol. Sci.* 373:20170011. doi: 10.1098/rstb.2017.0011

Orlandi, J. G., Soriano, J., Alvarez-Lacalle, E., Teller, S., and Casademunt, J. (2013). Noise focusing and the emergence of coherent activity in neuronal cultures. *Nat. Phys.* 9, 582–590. doi: 10.1038/nphys2686

Palagina, G., Meyer, J. F., and Smirnakis, S. M. (2019). Inhibitory units: an organizing nidus for feature-selective subnetworks in area V1. *J. Neurosci.* 39, 4931–4944. doi: 10.1523/JNEUROSCI.2275-18.2019

Pasquale, V., Martinoia, S., and Chiappalone, M. (2017). Stimulation triggers endogenous activity patterns in cultured cortical networks. *Sci. Rep.* 7:9080. doi: 10.1038/s41598-017-08369-0

Peshkov, A., Bertin, E., Ginelli, F., and Chat,é, H. (2014). Boltzmann-Ginzburg-Landau approach for continuous descriptions of generic Vicsek-like models. *Eur. Phys. J. Spec. Top.* 223, 1315–1344. doi: 10.1140/epjst/e2014-02193-y

Plenz, D. (2012). Neuronal avalanches and coherence potentials. *Eur. Phys. J. Special Top.* 205, 259–301. doi: 10.1140/epjst/e2012-01575-5

Plenz, D., and Niebur, E. (2014). *Criticality in Neural Systems*. Berlin: Wiley-VCH.

Powell, G. V. N. (1985). Sociobiology and adaptive significance of interspecific foraging flocks in the Neotropics. *Ornithol. Monogr.* 36, 713–732. doi: 10.2307/40168313

Rands, S. A., Muir, H., and Terry, N. L. (2014). Red deer synchronise their activity with close neighbours. *Peerj* 2:e344. doi: 10.7717/peerj.344

Rauch, E. M., Millonas, M. M., and Chialvo, D. R. (1995). Pattern-formation and functionality in swarm models. *Phys. Lett. A* 207, 185–193. doi: 10.1016/0375-9601(95)00624-C

Reynolds, C. W. (1987). Flocks, herds and schools: a distributed behavioral model. *Comput. Graph.* 21, 25–34. doi: 10.1145/37402.37406

Ribeiro, T. L., Yu, S., Martin, D. A., Winkowski, D., Kanold, P., Chialvo, D. R., et al. (2020). Trial-by-trial variability in cortical responses exhibits scaling in spatial correlations predicted from critical dynamics. *bioRxiv*. doi: 10.1101/2020.07.01.182014

Romanczuk, P., Couzin, I. D., and Schimansky-Geier, L. (2009). Collective motion due to individual escape and pursuit response. *Phys. Rev. Lett*. 102:010602. doi: 10.1103/PhysRevLett.102.010602

Romenskyy, M., Herbert-Read, J. E., Ward, A. J. W., and Sumpter, D. J. T. (2017). Body size affects the strength of social interactions and spatial organization of a schooling fish (*Pseudomugil signifer*). *R. Soc. Open Sci.* 4:161056. doi: 10.1098/rsos.161056

Scarpetta, S., Apicella, I., Minati, L., and de Candia, A. (2018). Hysteresis, neural avalanches, and critical behavior near a first-order transition of a spiking neural network. *Phys. Rev. E* 97:062305. doi: 10.1103/PhysRevE.97.062305

Scarpetta, S., and de Candia, A. (2013). Neural avalanches at the critical point between replay and non-replay of spatiotemporal patterns. *PLoS One* 8:e64162. doi: 10.1371/journal.pone.0064162

Scott, G., Fagerholm, E. D., Mutoh, H., Leech, R., Sharp, D. J., Shew, W. L., et al. (2014). Voltage imaging of waking mouse cortex reveals emergence of critical neuronal dynamics. *J. Neurosci.* 34, 16611–16620. doi: 10.1523/JNEUROSCI.3474-14.2014

Seeman, S. C., Campagnola, L., Davoudian, P. A., Hoggarth, A., Hage, T. A., Bosma-Moody, A., et al. (2018). Sparse recurrent excitatory connectivity in the microcircuit of the adult mouse and human cortex. *eLife* 7:e37349. doi: 10.7554/eLife.37349

Shew, W. L., and Plenz, D. (2013). The functional benefits of criticality in the cortex. *Neuroscientist* 19, 88–100. doi: 10.1177/1073858412445487

Shew, W. L., Yang, H., Yu, S., Roy, R., and Plenz, D. (2011). Information capacity and transmission are maximized in balanced cortical networks with neuronal avalanches. *J. Neurosci.* 31, 55–63. doi: 10.1523/JNEUROSCI.4637-10.2011

Shew, W. L., Yang, H. D., Petermann, T., Roy, R., and Plenz, D. (2009). Neuronal avalanches imply maximum dynamic range in cortical networks at criticality. *J. Neurosci.* 29, 15595–15600. doi: 10.1523/JNEUROSCI.3864-09.2009

Solon, A. P., Chate, H., and Tailleur, J. (2015). From phase to microphase separation in flocking models: the essential role of nonequilibrium fluctuations. *Phys. Rev. Lett.* 114:068101. doi: 10.1103/PhysRevLett.114.068101

Sosna, M. M. G., Twomey, C. R., Bak-Coleman, J., Poel, W., Daniels, B. C., Romanczuk, P., et al. (2019). Individual and collective encoding of risk in animal groups. *Proc. Natl. Acad. Sci. U.S.A.* 116: 20556–20561. doi: 10.1073/pnas.1905585116

Stanley, H. E. (1971). *Introduction to Phase Transitions and Critical Phenomena*. New York, NY: Oxford University Press.

Strandburg-Peshkin, A., Twomey, C. R., Bode, N. W. F., Kao, A. B., Katz, Y., Ioannou, C. C., et al. (2013). Visual sensory networks and effective information transfer in animal groups. *Curr. Biol.* 23, R709–R711. doi: 10.1016/j.cub.2013.07.059

Strombom, D. (2011). Collective motion from local attraction. *J. Theor. Biol.* 283, 145–151. doi: 10.1016/j.jtbi.2011.05.019

Sueoka, Y., Sato, Y., Ishitani, M., and Osuka, K. (2019). Analysis of push-forward model for swarm-like collective motions. *Artif. Life Robot.* 24, 460–470. doi: 10.1007/s10015-019-00548-8

Sumpter, D. J. T. (2006). The principles of collective animal behaviour. *Philos. Trans. R. Soc. B Biol. Sci.* 361, 5–22. doi: 10.1098/rstb.2005.1733

Tagliazucchi, E., Balenzuela, P., Fraiman, D., and Chialvo, D. R. (2012). Criticality in large-scale brain fMRI dynamics unveiled by a novel point process analysis. *Front. Physiol.* 3:15. doi: 10.3389/fphys.2012.00015

Tang, Q. Y., Hatakeyama, T. S., and Kaneko, K. (2020). Functional sensitivity and mutational robustness of proteins. *Phys. Rev. Res.* 2:033452. doi: 10.1103/PhysRevResearch.2.033452

Tang, Q. Y., Zhang, Y. Y., Wang, J., Wang, W., and Chialvo, D. R. (2017). Critical fluctuations in the native state of proteins. *Phys. Rev. Lett.* 118:088102. doi: 10.1103/PhysRevLett.118.088102

Terborgh, J. (1990). Mixed flocks and polyspecific associations - costs and benefits of mixed groups to birds and monkeys. *Am. J. Primatol.* 21, 87–100. doi: 10.1002/ajp.1350210203

Tunstrøm, K., Katz, Y., Ioannou, C. C., Huepe, C., Lutz, M. J., and Couzin, I. D. (2013). Collective states, multistability and transitional behavior in schooling fish. *PLoS Comput. Biol.* 9:e1002915. doi: 10.1371/journal.pcbi.1002915

Vanni, F., Lukovic, M., and Grigolini, P. (2011). Criticality and transmission of information in a swarm of cooperative units. *Phys. Rev. Lett.* 107:078103. doi: 10.1103/PhysRevLett.107.078103

Vicsek, T., Czirok, A., Ben-Jacob, E., Cohen, I. I., and Shochet, O. (1995). Novel type of phase transition in a system of self-driven particles. *Phys. Rev. Lett.* 75, 1226–1229. doi: 10.1103/PhysRevLett.75.1226

Vicsek, T., and Zafeiris, A. (2012). Collective motion. *Phys. Rep.* 517, 71–140. doi: 10.1016/j.physrep.2012.03.004

Wang, X., and Lu, J. H. (2019). Collective behaviors through social interactions in bird flocks. *IEEE Circ. Syst. Magazine* 19, 6–22. doi: 10.1109/MCAS.2019.2924507

Wilson, K. G. (1979). Problems in physics with many scales of length. *Sci. Am.* 241, 158–179. doi: 10.1038/scientificamerican0879-158

Yu, S., Ribeiro, T. L., Meisel, C., Chou, S., Mitz, A., Saunders, R., et al. (2017). Maintained avalanche dynamics during task-induced changes of neuronal activity in nonhuman primates. *eLife* 6:e27119. doi: 10.7554/eLife.27119.012

Conflict of Interest: The authors declare that the research was conducted in the absence of any commercial or financial relationships that could be construed as a potential conflict of interest.

Copyright © 2021 Ribeiro, Chialvo and Plenz. This is an open-access article distributed under the terms of the Creative Commons Attribution License (CC BY). The use, distribution or reproduction in other forums is permitted, provided the original author(s) and the copyright owner(s) are credited and that the original publication in this journal is cited, in accordance with accepted academic practice. No use, distribution or reproduction is permitted which does not comply with these terms.

frontiers in Systems Neuroscience

ORIGINAL RESEARCH
published: 16 February 2021
doi: 10.3389/fnsys.2021.617388

Beta2 Oscillations in Hippocampal-Cortical Circuits During Novelty Detection

Arthur S. C. França, Nils Z. Borgesius, Bryan C. Souza and Michael X. Cohen*

Donders Institute for Brain, Cognition and Behavior, Radboud University, Nijmegen, Netherlands

Novelty detection is a core feature of behavioral adaptation and involves cascades of neuronal responses—from initial evaluation of the stimulus to the encoding of new representations—resulting in the behavioral ability to respond to unexpected inputs. In the past decade, a new important novelty detection feature, beta2 (~20–30 Hz) oscillations, has been described in the hippocampus (HC). However, the interactions between beta2 and the hippocampal network are unknown, as well as the role—or even the presence—of beta2 in other areas involved with novelty detection. In this work, we combined multisite local field potential (LFP) recordings with novelty-related behavioral tasks in mice to describe the oscillatory dynamics associated with novelty detection in the CA1 region of the HC, parietal cortex, and mid-prefrontal cortex. We found that transient beta2 power increases were observed only during interaction with novel contexts and objects, but not with familiar contexts and objects. Also, robust theta-gamma phase-amplitude coupling was observed during the exploration of novel environments. Surprisingly, bursts of beta2 power had strong coupling with the phase of delta-range oscillations. Finally, the parietal and mid-frontal cortices had strong coherence with the HC in both theta and beta2. These results highlight the importance of beta2 oscillations in a larger hippocampal-cortical circuit, suggesting that beta2 plays a role in the mechanism for detecting and modulating behavioral adaptation to novelty.

Keywords: beta2 oscillation, hippocampus, novelty detection, medial prefrontal cortex, posterior parietal cortex, synchronization

OPEN ACCESS

Edited by:
Nicola Toschi,
University of Rome Tor Vergata, Italy

Reviewed by:
Antonio Fernández-Ruiz,
New York University, United States
Kenji Mizuseki,
Osaka City University, Japan

****Correspondence:***
Arthur S. C. França
arthursergiof@gmail.com

Received: *14 October 2020*
Accepted: *18 January 2021*
Published: *16 February 2021*

Citation:
França ASC, Borgesius NZ, Souza BC and Cohen MX (2021) Beta2 Oscillations in Hippocampal-Cortical Circuits During Novelty Detection. Front. Syst. Neurosci. 15:617388. doi: 10.3389/fnsys.2021.617388

INTRODUCTION

Novelty detection is a crucial feature for behavioral adaptation and ignites cascades of neuronal responses, from the initial evaluation of the stimulus to the encoding of new representations, resulting in the behavioral ability to respond appropriately and adaptively to unexpected stimuli (van Kesteren et al., 2012; Kafkas and Montaldi, 2018). Over recent decades, an important novelty detection feature, beta2 oscillations (~20–33 Hz), has been described in the hippocampus (HC; Berke et al., 2008; França et al., 2014; Kitanishi et al., 2015). In particular, beta2 power transiently increases during spatial novelty (Berke et al., 2008; França et al., 2014; Kitanishi et al., 2015) and its generation is implicated with AMPA and NMDA receptors plasticity between the connections of CA3 and CA1 hippocampal regions (Berke et al., 2008; Kitanishi et al., 2015). However, the interaction between beta2 with other hippocampal rhythms remains unknown. Furthermore, the HC is not

alone in detecting novelty: evidence in both humans and rodents points to a larger hippocampal-cortical circuit for detecting and adapting to novelty, including the mid-prefrontal cortex (mPFC) and posterior parietal cortex (PAR; Spellman et al., 2015; Kafkas and Montaldi, 2018; Pho et al., 2018). It seems plausible that beta2 oscillations are a mechanism of communication across these regions, but there is currently no empirical evidence for or against this possibility.

Here, we tested three novel hypotheses concerning the role of beta2 in novelty detection: First, whether beta2 power increase is associated with different forms of novelty (spatial and object); second if slower hippocampal oscillations can modulate beta2 power, similarly to the phase-amplitude coupling of theta-gamma oscillations during memory encoding in the HC; and third, whether the novelty integration hubs in the cortex (PAR and mPFC) synchronize with hippocampal beta2 oscillations during novelty exploration.

Combining behavioral tasks where the animal is exposed to environments with different levels of novelty, and recordings from local field potential (LFP) and multi-units targeting the CA1 region of the HC, PAR, and mPFC, we aimed to describe the interactions among these regions involved with novelty detection processing. Using power spectral analysis, weighted phase lag index (WPLI), mean phase vector length (MPVL), Granger causality, and cross-frequency phase-amplitude coupling (CFC) as indices of local and long-range synchronization (Canolty and Knight, 2010; Vinck et al., 2011; Hyafil et al., 2015), we found that transient beta2 power increases are observed only during interactions with novel contexts—environment or object—and not with familiar contexts. During novelty exploration, robust CFC was observed between theta and multiple gamma subbands. Unexpectedly, beta2 had robust coupling with delta-range oscillations. Finally, the PAR and mPFC cortices exhibited strong coherence with both theta and beta2 during novelty exploration. Within the PAR and mPFC, a similar pattern of coupling between delta-ranged and beta2 was seen as in the HC. The results reported in the present study also suggest that beta2 is an oscillatory feature independent of slow gamma oscillations, showing different dynamics of power and CFC, and related to novelty detection. The synchronization among HC, mPFC, and PAR in beta2 during novelty detection reveals its importance to understanding novelty exploration and its implication in a broad hippocampal-cortical circuit for novelty detection.

MATERIALS AND METHODS

Animals

The data shown in this article is from nine male mice with Black57 background. All the animals were recorded in all the experimental sessions described in **Figure 1A**. The animals had free access to food and water. All experiments were approved by the Centrale Commissie Dierproeven (CCD) and it is according to all indications of the local Radboud University Medical Centre animal welfare body (Approval number 2016-0079).

Electrode Implant Procedures

The self-made electrode arrays used in the present work were custom-designed to target three different regions of the mouse brain: CA1-HC, PAR, and mPFC. A detailed description of the arrays and the manufacturing process can be verified (França et al., 2020b). Briefly, there were 16 channels aiming at mPFC (spread in the coordinates AP: 0.5 and 1.5; ML: 0.25 and 0.75; in three columns of electrodes in different depths −2.0, 1.5 and 1.0), eight channels at PAR (AP: −2 and −2.25; ML: 1.0 and 1.75; DV: 0.5) and eight channels at HC (AP −2.5 and −2.75; ML: 1.0 and 1.75; DV: 1.5).

For surgery, 10–16 week old mice were anesthetized with Isoflurane (induction at 5% Isoflurane in 0.5 L/min O_2; maintenance at 1–2% Isoflurane in 0.5 L/min O_2; Teva). Mice were fixed in the stereotaxic instrument (Neurostar Stereotaxic). After shaving, the skin was disinfected with ethanol (70%). The local anesthetic Xylocaine [2%, Adrenaline 1:200,000 (AstraZeneca)] was injected subcutaneously at the incision site before exposing the skull. Peroxide [10–20% H_2O_2; (Sigma)] was applied to the skull with a cotton swab for cleaning and visualization of Bregma and lambda. The windows in the skull through which the electrodes would be lowered into the brain were drilled specifically to accommodate the type of arrays to be implanted. To avoid contact between the dental cement and the brain, vaseline was applied to those windows after the implant. Electrodes and screws were fixated onto the skull with dental cement (Super-Bond C&B; **Supplementary Figure 1**). Approximately 40 min before the end of the surgery, saline and analgesic (Carprofen injected subcutaneous 2.5 mg/Kg) were injected to facilitate the animal recovery.

After the experiments, animals were euthanized for post-mortem histological confirmation of electrode location. The majority of electrodes in mPFC were distributed across the anterior cingulate and secondary motor cortex. The majority of the PAR electrodes were placed among layers 2 to 5. In the HC, all electrodes were located in CA1, within the region enclosed by the *stratum pyramidale* and the *stratum lacunosum-moleculare*. Electrode tracing can be verified in **Supplementary Figure 1**.

Behavioral Task

The experiments were designed to expose the animal to different HC-dependent novelty content (environment and novel object). The experiment consisted of four main different sessions of 10 min recording—two sessions at Open field and two sessions at Open field with Objects—interspersed by 5 min Home Cage recordings (see **Figure 1A**).

Because our goal was to evoke and investigate novelty-related oscillatory features, our task did not require or provide detailed behavioral performance output. However, to investigate how the oscillatory features investigated here were correlated with locomotor activity and behavioral exploration, the average velocity and the object exploration time were extracted. The data was computed by automated tracking of video recordings in the program Ethovision. We labeled time windows as being "object exploration" if the animal's nose was within a quadrant draw around the object (∼3 cm of the object).

Electrophysiological Analysis

Data Inspection

Electrophysiology data were acquired using Open Ephys with a sampling rate of 30 kHz. During preprocessing, data were downsampled to 1,000 Hz, and EEGlab (Delorme et al., 2011) was used for visual inspection and cleaning artifacts (open channels were removed from the analysis; high-frequency noises were removed by Independent Component Analysis; Segments containing large deflections in all channels were used as a criterion for recording session exclusion). Six animals had high-quality data in all recording sessions, therefore statistical analysis concerning all sessions was performed in six animals. Analyses in different sessions, therefore, have a different number of animals (varying between seven and nine).

Data Analysis

The data analysis was performed using custom-written and built-in routines in MATLAB (R2015b). Before analyses, the multichannel data from each region were re-referenced to that region's local average.

Spectral and time-frequency analysis was performed *via* convolution with complex Morlet wavelets (defined as a frequency-domain Gaussian with a 3 Hz full-width at half-maximum) that ranged in peak frequency from 2 to 80 Hz in 100 linearly spaced steps. We reduced the dimensionality of the multichannel data by implementing a frequency-specific guided source-separation method based on generalized eigendecomposition. The goal was to create a linear weighted combination of channels (separately per region) that maximized the multivariate energy between the data covariance matrix from the narrowband filtered data, vs. the broadband filtered data. This results in a single time series from each region, which was subjected to further analyses. We and others have shown that this method increases signal-to-noise characteristics while reducing computational costs and multiple-comparisons issues, and is more accurate than other sources separation methods such as principal components analysis and independent components analysis in M/EEG and LFP data (Haufe et al., 2014; de Cheveigné and Arzounian, 2015; Cohen, 2017a; Morrow et al., 2020). An advantage of generalized eigendecomposition over independent components analysis is that it optimizes the spatial filter for narrowband activity, which was a primary goal here. Various spatial filters can produce similar or distinct results, depending on their optimization criteria, and rigorous comparison of the performance of spatial filters is beyond the scope of this article (Cohen, 2017b). Nonetheless, possibly the analysis of the independent components could provide comparable results (Fernández-Ruiz and Herreras, 2013).

The Hilbert transform was then applied to these narrow-band filtered component time series to extract time-varying power and phase estimates. The Hilbert transform was then applied to these narrow-band filtered component time series to extract time-varying power and phase estimates. For analyzing beta2 and theta power on a cycle-by-cycle basis, we first detected the beta2 cycles using the instantaneous phase extracted by the Hilbert transform. We then computed the average amplitude envelope of beta2 and theta in each beta2 cycle. Our analyses were restricted to the 10% beta2 cycles with higher and lower energy.

The power spectrum was computed by averaging over the time-frequency power time series from all time points within each larger time window. CFC was performed in sliding windows of 5 s. The phase of delta-range and theta frequency (2–12 Hz) and the amplitude of beta2 to mid-gamma (20–100 Hz) were extracted. The raw CFC values were transformed into standard deviation (z) values by computing the normalized distance away from a null-hypothesis surrogate distribution, created by 500 permutations in which the phase angle time series were randomly cut and swapped. To decrease the influence of possible volume conduction, we performed coherence computations utilizing WPLI (Vinck et al., 2011). Statistical analyses were performed using the routine RMAOV1—Repeated Measures Single-Factor Analysis of Variance Test ($\alpha = 0.05$).

Conditional spectral Granger causality was applied using the MultiVariate Granger Causality toolbox (Barnett and Seth, 2014). As this relies on the time-domain signals and not already-filtered data (because the causality spectrum is computed from the autoregression terms), we dimension-reduced each region using principal components analysis, taking the time series of the largest component from each region. Data were downsampled to 250 Hz and a model order ranging from 100 to 200 ms (varied over animals to best fit each dataset) was used for the autoregression model fitting. The advantage of the conditional Granger analysis is that it allowed us to isolate the unique contributions of one region to a second region while accounting for a possible shared variance with the third region.

For detecting spiking activity, the electrophysiological signal was first band-pass filtered between 500 Hz and 6 kHz. Then, waveforms were detected using a threshold of eight times the median absolute deviation as in Quiroga et al. (2004) and aligned by their interpolated peak. We used the wavelet and weighted-PCA approach described in Souza et al. (2019) to automatically sort the waveforms of each channel. Although we could not separate spiking activity into single units, the different MUA clusters found in the same channel presented unique activity patterns, and we, therefore, analyzed their activity separately. To access the phase coupling of spikes to beta2 in the first time-window (30 to 150 s), we first selected beta2 cycles in which the mean amplitude envelope of beta2 and delta-range were both in the highest quartile. Then, for each MUA we computed the MPLV of the spikes occurring on those cycles. MUAs with fewer than 30 spikes were excluded from further analyses. The significance of each MPVL value was assessed using an equivalent surrogate distribution, computed using 500 surrogates with the same number of spikes as the original MUA. For significantly modulated MUAs we also assessed the mean phase of spiking.

RESULTS

Beta2 Power Increases With Both Spatial and Object Novel Content

The experiment consisted of four sessions of successive 10 min recordings. Two sessions at Open field (OF1 Novel;

OF2 Familiar) and two sessions at Open field with Objects (OBJ1 Novel; OBJ2 Familiar)—interspersed by 5 min Home Cage recordings (see **Figure 1A**). We first verified that both spatial and object novelty evoked the same pattern of power dynamics previously described (Berke et al., 2008; França et al., 2014). As expected, beta2 power increased only during novelty (OF1 and OBJ1; **Figure 1B**), but not during any of the familiar contexts (Home cage, OF2, and OBJ2; **Figure 1B**, **Supplementary Table 1**). We also verified the transient aspect associated with novelty-related beta2, whereby the power returned to initial levels after around 3 min of novelty exposition (**Figure 1C**). as previously reported (França et al., 2014). For all further analyses, we utilized four time windows based on the power dynamics of beta2 in the HC verified during the exploration of novelty (**Figure 1C**). The comparison of the normalized beta2 power (normalized by the power of the last time window) across the different time windows showed that beta2 power was higher in the first compared to the later time windows (**Figure 1D**; **Supplementary Table 1**).

A possible confound for these analyses would be if beta2 power was simply increased during locomotor activity, instead of reflecting novelty. We, therefore, conducted several analyses to rule out this confound. First, we computed the average velocity of the animal in the different time windows defined above, and entered velocity into a two-way ANOVA using "time window" and "session" as independent variables (Interaction: $F_{(3,93)} = 27.44$, $p < 0.0001$; Time Window: $F_{(3,93)} = 2.41$, $p = 0.0501$, and Session: $F_{(3,93)} = 2.41$, $p = 0.0398$), *post hoc* Tukey-Kramer test showed that OF1 had significantly higher velocity than OBJ1, OBJ2, OF2, $p < 0.05$; **Figure 1E**). Importantly, we saw significant interaction between the time window and session. However, this result does not directly link beta2 to movement. Therefore, we computed the Pearson correlation between the normalized beta2 power and animal velocity per session. We verified a strong correlation between the mean velocity and normalized beta2 power when looking at all experimental sessions together (OF1, OF2, OBJ1, and OBJ2; **Figure 1E**). To verify if such correlation could explain by itself the previous changes in beta2 power, we computed the correlation separately in novelty (OF1 and OBJ1) and familiar sessions (OF2 and OBJ2). We found that beta2 power correlated with mean velocity in the novelty sessions, but not in the familiar session (**Figure 1E**). However, possibly the correlation in the novelty sessions was biased by the higher velocity in the OF1 sessions. Indeed, the correlation between beta2 power and velocity vanished when analyzing OBJ1 session only ($r = 0.306$, $p = 0.216$; **Figure 1F**). Nevertheless, animal speed in OBJ1, OBJ2, and OF2 sessions showed similar distributions (**Figure 1F**), despite having different beta2 power values (**Figure 1B**). In other words, beta2 was not trivially correlated with movement, showing that velocity cannot explain the novelty-related changes in beta2 power. There was no relationship between beta2 power and theta power on a cycle by cycle basis ($t_{(2,8)} = 0.06$, $p = 0.94$; **Supplementary Figure 2**). Third, we tested whether the amount of object exploration predicted beta2 power. We found no correlation between the total time spent exploring the objects and the beta2 normalized power ($r = -0.195$, $p = 0.25$; **Figure 1G**). Together, these results show that beta2 power increases only during novelty exposure. Beta2 had transiently higher power in the initial phase of the novelty exposure, which waned towards the end of the session. Beta2 power was correlated with velocity exclusively during novelty exposure, but not in a familiar environment.

Delta Modules Beta2 Amplitude During Spatial and Object Novelty

Given the role of CFC in the HC during spatial navigation, learning, and memory retrieval, we next explored whether there was any CFC coupling between beta2 power and the phase of slower frequencies and if this coupling was modulated during novelty processing. We used the frequency ranges of 2–12 Hz for extracting the phase and 20–100 Hz for computing the amplitude envelope. Because the Open field exploration does not present any well-defined time event to trigger time windows for the CFC, we calculated the modulation index (MI) in sliding time windows, which allowed us to examine both the overall CFC and the temporal dynamics of CFC. We observed two key features of novelty-related CFC: first, we verified theta-gamma CFC for both low-gamma (30–50 Hz lowG) and mid-gamma (60–80 Hz midG); second, CFC was present between theta phase and beta2 power and between delta-range phase and beta2 and lowG power in the same time window of higher beta2 power (**Figure 2A**). A similar pattern of CFC was also observed in the first exploration of OBJ1 (**Figure 2B**).

Then, we verified the temporal dynamics of the most prominent CFC patterns: delta-beta2, delta-lowG, theta-beta2, theta-lowG, and theta-midG. For sessions with novelty (OF1 and OBJ1), the couplings of all those frequency bands were higher in the first time window, suggesting that most of the novelty detection and encoding computation happens during the initial part of the session when beta2 power is higher (**Figures 2A,B**, **Supplementary Table 2**—time-window comparison), all pairs of coupling in all time-windows (the exception to OF1 win4-theta/lowG and OBJ1 win3-theta/beta) shown MI higher than chance (**Figures 2A,B**, **Supplementary Table 2**). Conversely, during the re-exposure to the OF2 and OBJ2 we observed small or no changes in the temporal dynamics of beta2 coupling (**Supplementary Figure 3**, **Supplementary Table 4**), but higher MI in all time-windows, exhibiting strong MI for delta-beta2/theta-beta2 and delta-lowG/theta-lowG for the OF2 session (**Supplementary Figure 3**, **Supplementary Table 4**). We also found a strong modulation of delta/theta in both novel and familiar sessions, where no effect among time windows was found, but all time-windows in all sessions analyzed exhibited MI higher than chance (**Supplementary Figure 3**, **Supplementary Table 4**). Together, these results show that besides the largely reported theta/gamma coupling (Lasztóczi and Klausberger, 2014; Schomburg et al., 2014; Fernández-Ruiz et al., 2017; Gereke et al., 2017; Lopes-dos-Santos et al., 2018), exposure to novelty is followed by delta-range/beta2 coupling with a similar transient characteristic as seen in the beta2 power dynamics, stronger MI is present in the first time window. Such temporal dynamics are not observed in the familiar sessions. However, all time-windows exhibit a MI higher than chance, indicating that beta2 events

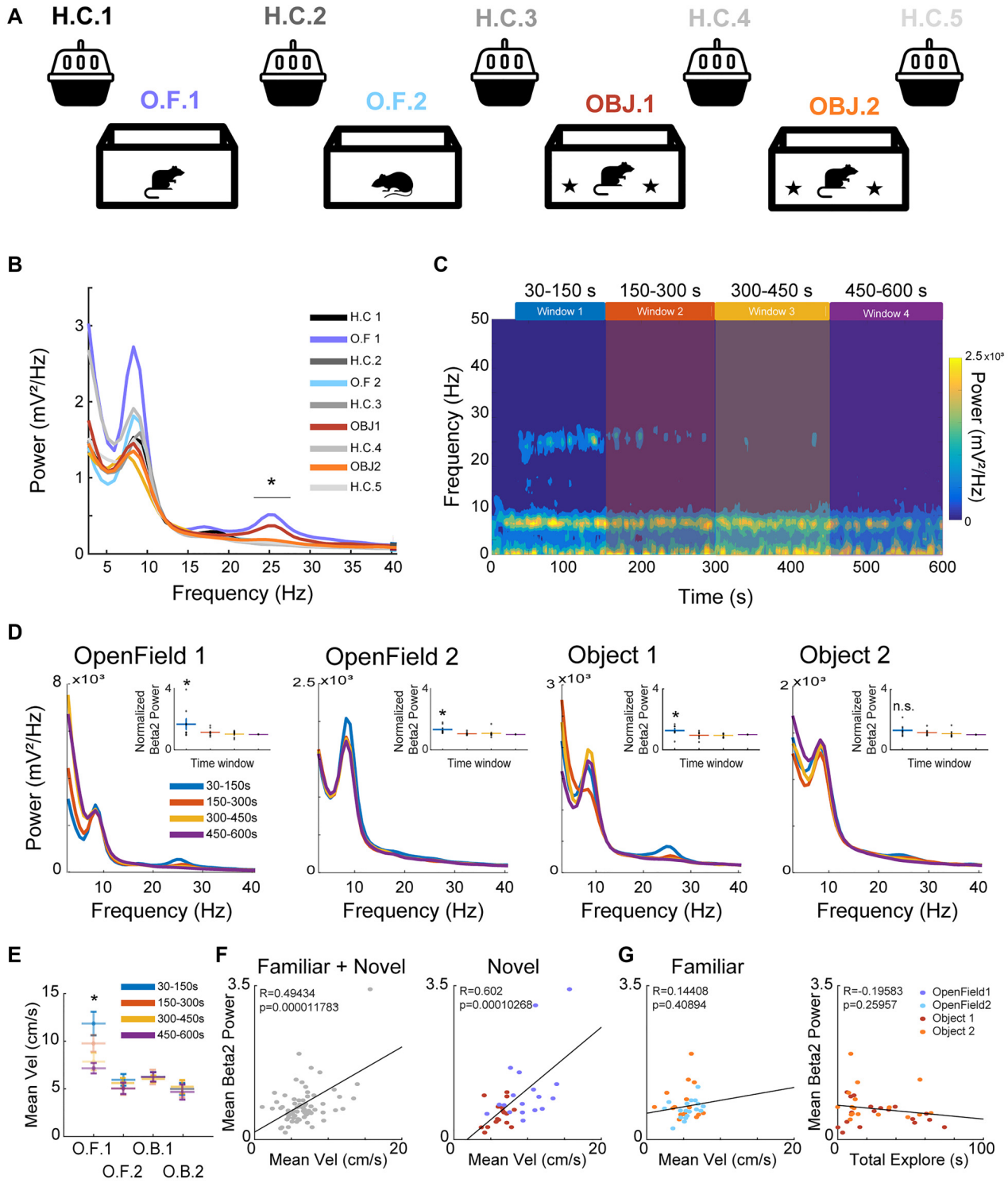


FIGURE 1 | Hippocampus (HC) beta2 power increase during novelty exploration. **(A)** Recording sessions scheme, 10 min of Open field (OF1, OF2) or Open field/Object explorations (OBJ1 and OBJ2) intercalated by home cage recordings (H.C.1–5). **(B)** Group average hippocampal power spectral density over the first 150 s in the nine different sessions presented in panel **(A)**. Note that only Open field 1 and Object 1 had increases in beta2 power, but not in other frequency bands. **(C)** Average of the spectrogram of the Open field 1 session. The four time-windows defined in the plot were used for all further analysis. **(D)** Exploration session average power spectrum density (PSD). **(E)** Two-way ANOVA comparison of the mean velocity with a time window and different sessions. **(F)** Person correlations between the mean velocity and mean beta2 power. **(G)** Person correlations between total exploration time of objects and mean velocity. *$p < 0.05$, n.s.: not significant.

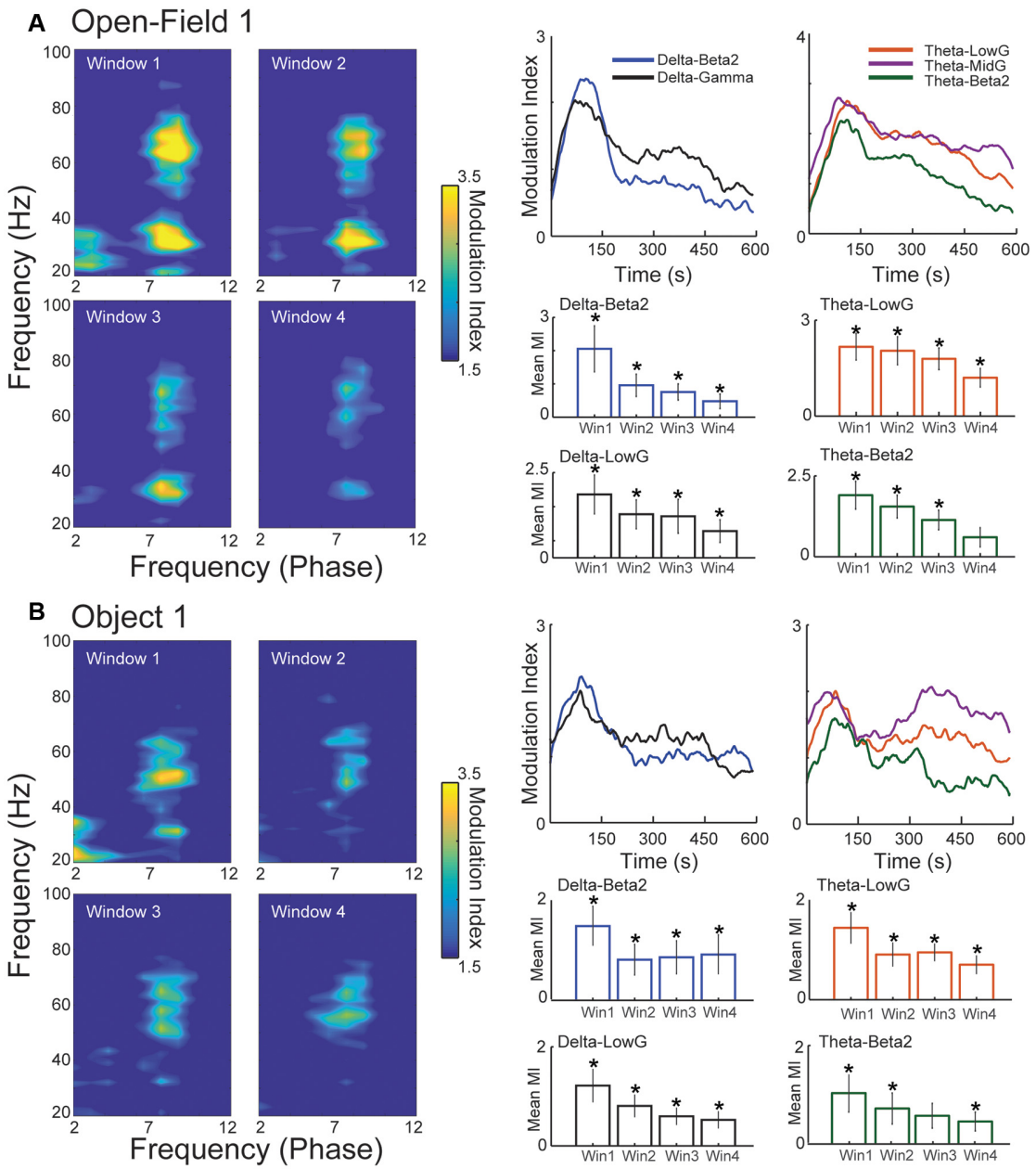


FIGURE 2 | Delta-range modulates beta2 during novelty exploration. **(A)** Sliding-window cross-frequency phase-amplitude coupling (CFC) concatenated in the four time-windows defined in **Figure 1C**. Right panels exhibit the modulation index (MI) during the time for different pairs of coupling. The different time-windows MI are compared against chance (0). **(B)** Same as **(A)** but for the Object 1 exploration session. *$p < 0.05$.

are modulated by delta-range oscillations during the novel and familiar contexts.

Novelty Modulates Oscillatory Coherence in Hippocampal-Cortical Circuitry

To investigate our third key hypothesis of whether beta2 oscillations play an important role in the hippocampal-cortical novelty detection system, we computed a measure of pairwise coherence WPLI between the three regions.

We observed consistent theta-band coherence among all pairs of areas (see **Figures 3A–C**) in all the sessions. Besides, sessions with novelty content also exhibited increased coherence in the beta2 range (**Figures 3A,B**). In contrast to the increase in beta2 power, this increase in coherence was not restricted to the first time window. In fact, besides the home cage 1 session (when the animal never experienced any novelty), a high beta2 coherence could also be observed even in familiar sessions, suggesting maybe the existence of a prolonged effect

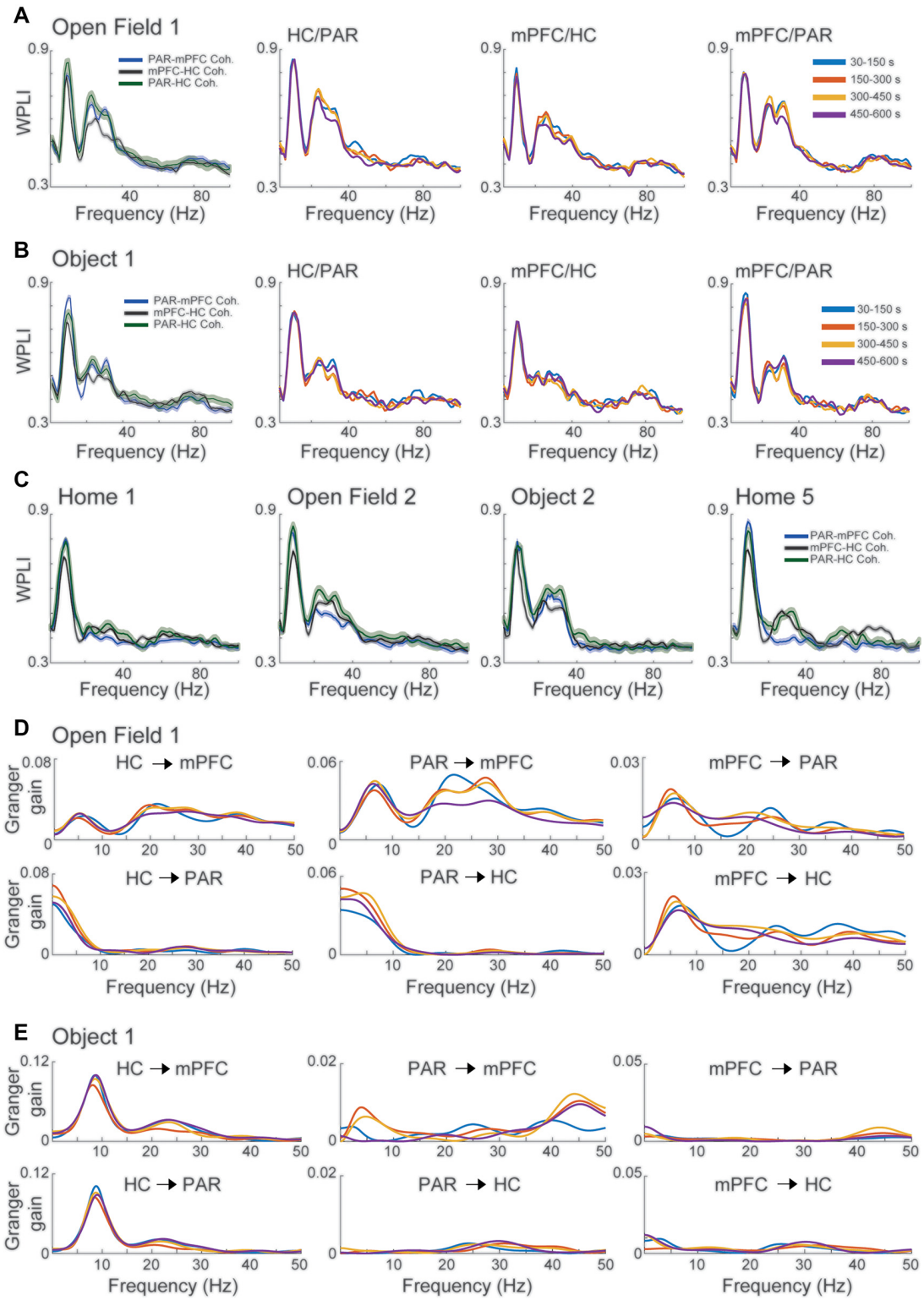


FIGURE 3 | Beta2 high coherence among HC, parietal and mid-frontal cortices during novelty exploration sessions. **(A)** The left panel shows the WPLI of the Open field 1 novelty exploration session. Note the high coherence in theta, beta2, and low-gamma during the first session of novelty exploration. Right panels show the different time-windows of the coherence between different pairs of regions. Panel **(B)** shows the same as in **(A)**, but for the Object 1 session. **(C)** Coherence plots of different familiar exploration sessions. **(D)** Granger causality gain between the pairs of regions in the Open field 1 session. Note the increase of Granger gain in theta and beta2 range going from HC and parietal cortex to mid-frontal cortex. Panel **(E)** shows the same as in **(D)**, but related to the Object 1 session.

on synchronization among areas after the first novelty session. We also note that in the last Home exploration session the coherence between mPFC and PAR, the two cortical areas, were already at similar levels compared to the first Home exploration, while coherence between HC and mPFC, and between HC and PAR was still high (**Figure 3C**). This might be explained by the mechanisms underlying beta2 synchronization in the circuitry.

We next applied conditional spectral Granger causality to further investigate this and to determine the causal flow of interactions around this circuit. During the OF1, PAR, and HC provided input into the mPFC in theta, beta2, and lowG ranges (**Figure 3D**). While in the Object 1 session, PAR exhibited a higher gain in the lowG frequency band (**Figure 3E**). HC dominated the gain values towards both cortices in both theta and beta2 (**Figures 3D,E**), exhibiting especially strong gain with theta and beta2 during the OBJ1 session (**Figure 3E**). Similar to the coherency, the Granger analysis showed no strong variation across different time windows, and suggest less stable connectivity between mPFC and PAR cortices.

Finally, we verified the presence of beta2 burst in the raw data in all regions analyzed (**Figures 4A,B**). More specifically, we could also see bursts of beta2 and lowG that happened independently (**Figure 4A**). To verify that cortical beta2 was not driven by volume conduction, we also analyzed the multi-unit activity in the three regions of interest, computing the MPVL of the spikes in high cycles of beta2. In **Figure 5A**, we show examples of multi-units in the mPFC, PAR, and HC that are strongly coupled with the phase of beta2 (**Figure 5A**). We found that the multi-unit spikes couple (i.e., showed significant MPVL values) to beta2 events detected in each of the three different regions (**Figures 5B,C**).

Altogether, these results show that PAR, mPFC, and HC synchronize in beta2, after the first novelty exposure and also in the following familiar sessions, suggesting the existence of a prolonged effect on synchronization. The contribution for such synchronization is dominated by HC towards the cortices. Finally, multi-unit activity coupled with beta2 in the three regions analyzed suggests that the beta2 events are not explained by volume conduction.

Parietal and Mid-prefrontal Cortices Exhibit Strong Delta-Beta2 Coupling During Novelty Exploration

Lastly, to further characterize the participation of PAR and mPFC cortices in processing novelty information, we verified both power and the coupling dynamics in the cortices during novelty detection exploration. We found that the mPFC exhibited similar beta2 power dynamics as in the HC, where the increase of beta2 power was verified in the first time window. The power spectrum density (PSD) revealed an increase in beta2 frequency specifically during the novelty exploration (**Figure 6A**, **Supplementary Table 3**). Such an increase in beta2 could be seen in the raw data and was also independent of bursts in the HC (see **Figure 4**).

Unexpectedly, the PAR and mPFC cortices not only exhibited strong coherence among each other and the HC, but also presented a similar pattern of coupling as seen in the HC (**Figures 2A–C**, **6A–F**, **Supplementary Table 3**), in which the novel content induced a strong MI between delta/beta2, theta/beta2, and theta/lowG in time-window 1. In contrast, familiar sessions did not exhibit an increase in the delta/beta2 in any time window (**Supplementary Figures 3B,C**, **Supplementary Table 4**) most of the time windows analyzed did not present any coupling during the familiar session (**Supplementary Figure 3C**, **Supplementary Table 4**). These results suggest that although the three areas are synchronized in beta2 during the novel and familiar sessions, the coupling dynamic involving delta-range modulation is specific to novelty exposure, similar to the beta2 power dynamics. Moreover, this modulation engages both mPFC and PAR pointing to the active participation of the associative cortices in the processing information during the novelty detection sessions.

DISCUSSION

In this work, we used simultaneous extracellular recordings of the HC CA1 region, PAR, and mPFC to characterize, for the first time, beta2 oscillations in the hippocampal-cortical novelty detection circuit of mice. We found that beta2 hippocampal power increases during both spatial and object novelty, but not during the exploration of familiar contexts. We have shown that delta-range oscillations modulate beta2 and lowG during the exploration of new and familiar environments, while theta modulates beta2, lowG, and midG. Also, we found strong coherence in theta and beta2 bands during novelty exploration among the areas recorded, in which the higher Granger gain for beta2 and theta came mostly from HC. Such coherence was translated into the increase of beta2 power in the mPFC but not in the PAR, even though bursts of beta2 could be identified in the raw trace of both mPFC and PAR, as well as beta2-modulated multi-units. Finally, we have observed similar coupling characteristics in the cortex to what is described in the HC, showing that beta2 is also modulated by delta-range activity in the cortex. Taken together, these results highlight the importance of beta2 oscillations in a larger hippocampal-cortical circuit, suggesting that beta2 reflects the mechanism for detecting and modulating behavioral adaptation to novelty.

The three regions investigated in the present study, the HC, PAR, and mPFC, share some similar features: (1) have monosynaptic connections among each other (Cenquizca and Swanson, 2007); (2) are extensively related to learning and encoding of memory (Lisman and Otmakhova, 2001; Lisman and Grace, 2005; Hasselmo, 2006; Sigurdsson et al., 2010; de Lima et al., 2011; Cross et al., 2013; Preston and Eichenbaum, 2013; Spellman et al., 2015), a characteristic which is preceded by novelty detection (van Kesteren et al., 2012); and (3) are implicated in novelty detection networks in human models (Kafkas and Montaldi, 2018).

To coordinate the activity of such diverse brain areas during the process of novelty detection, oscillations are suggested to play a key role in the integration and coordination of the information (Buzsáki and Draguhn, 2004; Fries, 2005). Theta oscillations are

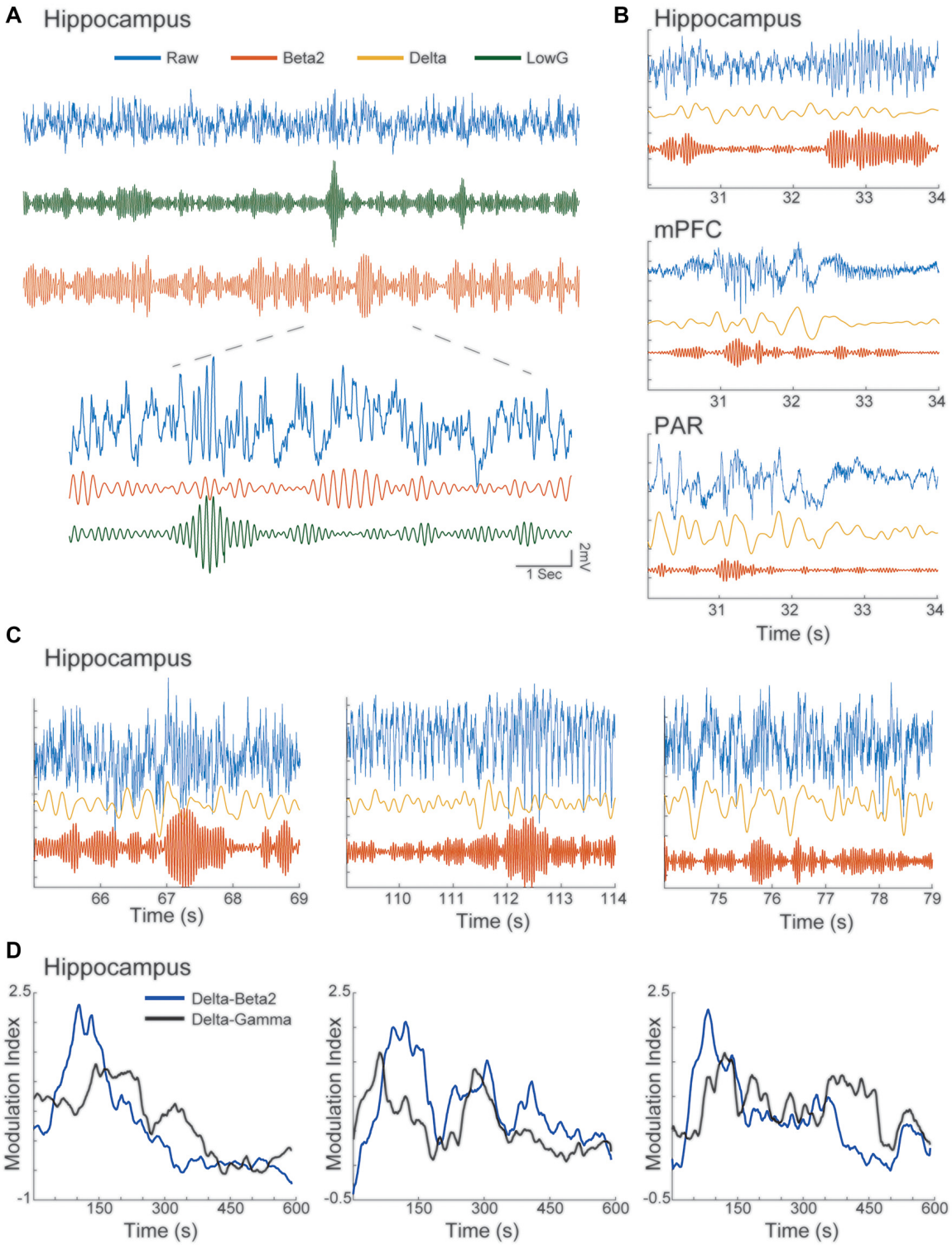


FIGURE 4 | Beta2 bursts can be visualized in the raw traces of the HC, parietal and mid-frontal cortices. **(A)** Blue—raw signal of HC channel; Green—filtered signal in low-gamma (30–50 Hz); Red—filtered signal in beta2 (20–30 Hz). Note that the burst of low-gamma and beta2 happens independently from each other. **(B)** Blue—raw signal; Yellow—filtered signal in delta (1–6 Hz); Red—filtered signal in beta2 (20–30 Hz). Note that the burst of beta2 can be verified in the raw signal of the HC, parietal and mid-frontal cortices. **(C)** Same exhibit as in **(B)**, but for HC channels of different animals. **(D)** Individual examples of time-MI plot of delta-beta2 and delta low-gamma during Open field 1 exploration session. Note that the MI dynamics of beta2 and low-gamma are different over time.

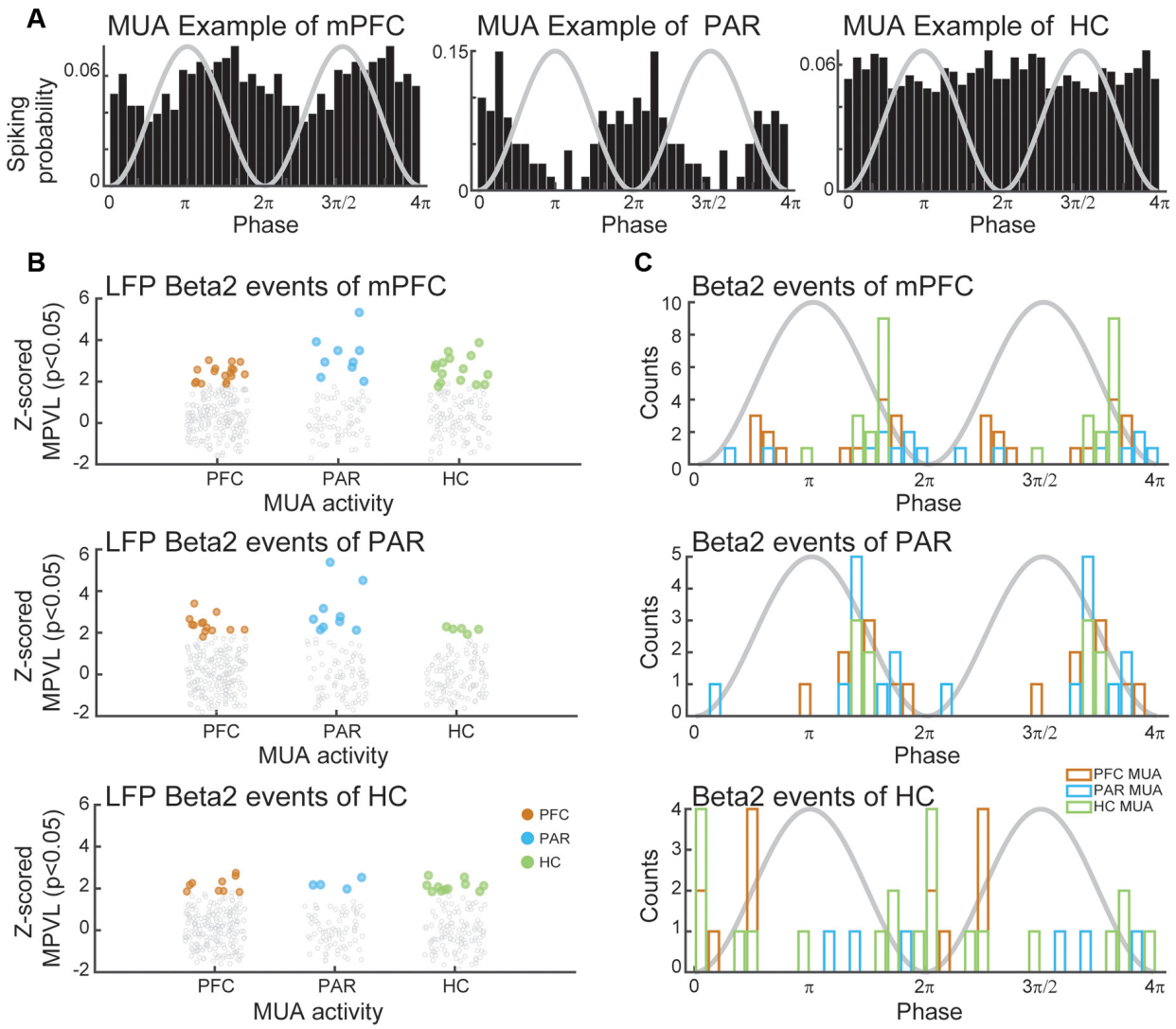


FIGURE 5 | MUA coupling to beta2 events. **(A)** Examples of MUAs in mPFC (left), PAR (middle), and HC (right) coupled to beta2 oscillations. **(B)** *Z*-scored a mean phase vector length for MUAs in each region in relation to beta2 events in PFC (top), PAR (middle), and HC (bottom). Colored dots denote MUAs significantly coupled to beta2. **(C)** Histogram of the mean spiking phase of the coupled MUAs showed in **(B)** for PFC (top), PAR (middle), and HC (bottom) beta2 events. Black line denotes the sine of the beta2.

thought to coordinate neural networks during memory encoding within and across different areas (Tort et al., 2009; Benchenane et al., 2011; Colgin, 2015). The close relationship between HC and mid-prefrontal areas as it relates to memory encoding and retrieval has been extensively reported (Benchenane et al., 2010, 2011; Samuel, 2019), and theta plays an important role in mediating the function of these two areas (Benchenane et al., 2010, 2011). But until now, no specific oscillatory dynamic responsive to novelty content was reported playing a role in the coordination of different brain areas responsible to process the novelty information.

We and others have identified beta2 as an oscillatory feature in the HC related to novelty detection in mice (Berke et al., 2008; França et al., 2014) and in rats (Kitanishi et al., 2015). The previous and current findings begin to elucidate a picture of beta2. Its spectral peak is around 20–30 Hz in mice (Berke et al., 2008; França et al., 2014), and is slightly faster in rats—25 to 48 Hz. It is elicited by spatial/environmental novelty but is not associated with novel olfactory stimuli. Beta2 has been related to the stability of place fields, as well as impairments in memory consolidation of novel recognition. This novelty-linked oscillation is transient, reaching its peak during the first 2 min after the novelty presentation and decreasing in amplitude thereafter. Beta2 likely originates in the projections of CA3 towards CA1 and seems to drive the synaptic delivery of GluR1-containing AMPA receptors and CA3 NMDA receptors. Finally, despite the prominence of beta2 in the HC and inter-connected association cortical areas, it is absent in

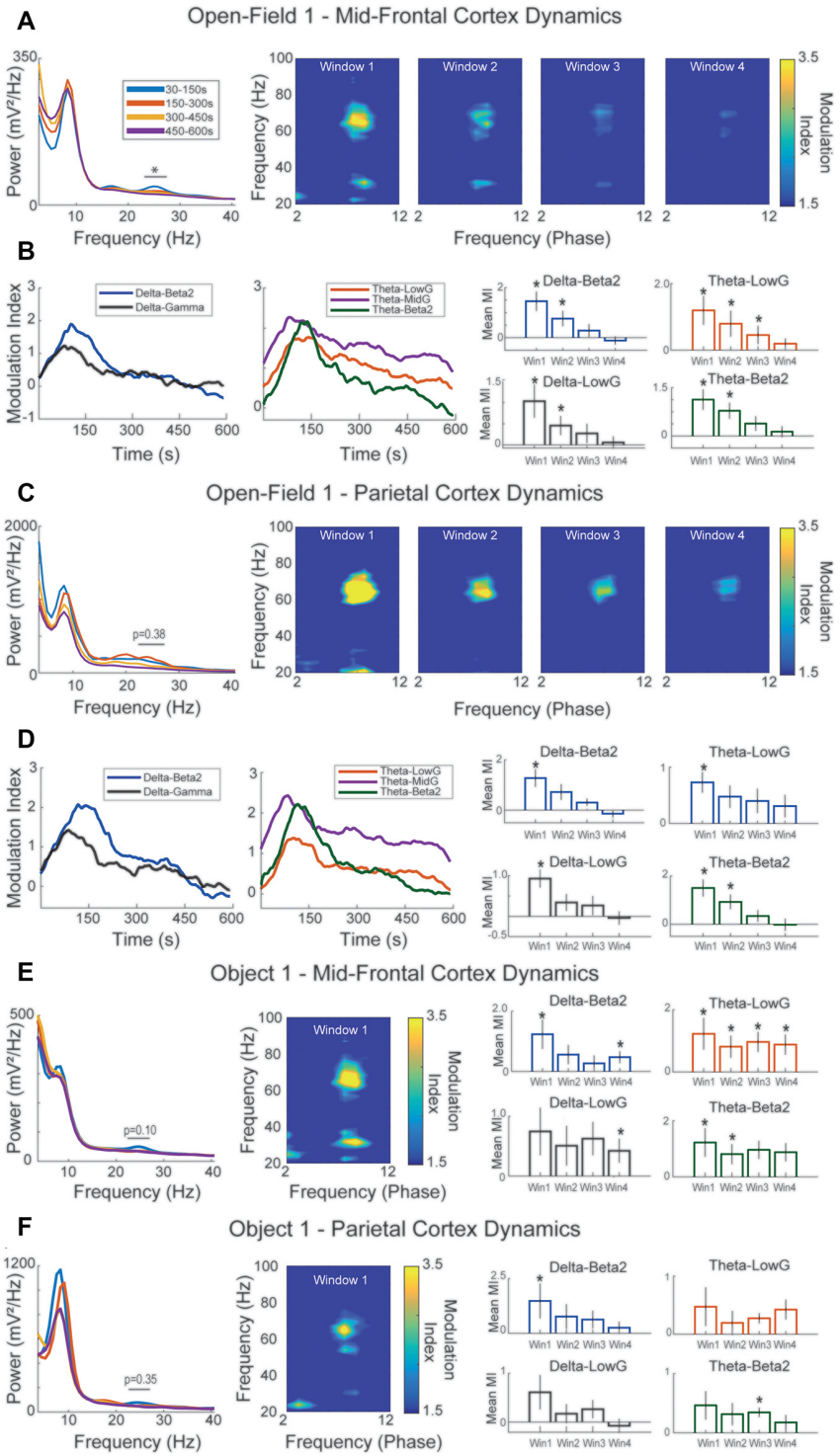


FIGURE 6 | Mid-frontal and parietal cortices exhibit similar coupling dynamics as seen in the HC during novelty exploration. **(A)** Group average mid-frontal PSD of different time-windows. Note that the first time-window exhibits a power increase in the beta2 range. Left panels show sliding-window CFC concatenated in the four time-windows of mid-frontal cortex electrodes in the Open field 1 exploration session. Note that in the first time-window there is an increase in the coupling between delta-beta2, and theta-mid-gamma, slow-gamma, and beta2. **(B)** MI during the time for different pairs of coupling. The different time-windows are compared with a chance (0) in the right panels. **(C)** Similar as exhibited in **(A)**, but for the Object 1 session ($F_{(3,8)} = 1.07$, $p = 0.38$). Panel **(D)** shows the same as in **(B)**, but for the parietal channels. Note in the first time-window the increase in coupling with beta2 and delta, and theta, but also mid-gamma and slow-gamma with theta. Panel **(D)** shows the same as in the right panel of **(B)**, but for PAR. Panel **(E)** shows the same as in **(A,B)**, but with Object 1 session. Note the very high MI for delta and beta2 and mid-gamma and theta. Panel **(F)** shows the same as in **(C,D)**, but with the Object 1 session. $^*p < 0.05$.

primary sensory and motor cortices—regions not associated with novelty detection.

In the present work, we replicate the main features in the power dynamics reported before (**Figures 1A–C**, **Supplementary Table 1**). Similar to the previous reports, we have shown that beta2 can be verified at the raw signal of the HC channels (**Figure 4**). The results reported in the present work, following what has been previously described, shows a delay between the beginning of the novelty exposition and the peak of beta2 (**Figure 1C**; **Supplementary Table 1**). This latency period may reflect the generation of a mismatch from previous expectations (Grossberg, 2009) or the time that animals take to perceive the experience as novel. Another possibility is the delay being related to the stability of the place field that is followed by the dynamic of beta2 (Berke et al., 2008). Although, we would not expect a gender effect on beta2 and novelty, none of the previous studies—and also not the present work—investigated beta2 oscillations in females' brains. As the females outperform males in recognition tasks (Bettis and Jacobs, 2012), possible gender differences in beta2 characteristics remains an open question for future research.

We also replicated the relation between beta2 normalized power and the mean velocity of the animal (**Figure 1E**; França et al., 2014). We found that this correlation is only present in the novelty exposition sessions, and not in the familiar exploration sessions (**Figure 1E**). However, this correlation vanished when analyzing the Object 1 session individually, and might be a spurious effect driven by the higher velocity values in the novel open field (Open field 1) session. In either case, differences in beta2 power cannot be fully explained by the animal speed, since beta2 power is stronger in Object 1 in comparison to Object 2 and Open field 2 even though those sessions have similar velocity distribution (**Figures 1B,E,F**). Further investigation of the instantaneous power and animal speed might help to establish a more conclusive relationship between beta2 and the animal velocity. Unfortunately, this could not be done in this dataset due to a synchronization problem between those two signals (which does not affect our other analyses). Finally, we found no difference in the mean theta power of high- and low-energy beta2 cycles, suggesting the occurrence of beta2 might be independent of locomotion (**Supplementary Figure 2**).

As previously reported, no correlation between object exploration time and beta2 normalized power was found (**Figure 1E**; França et al., 2014). Because mice have an innate exploratory behavior when they are exposed to novel environments, it is expected to see an increase of the total distance traveled and thus the mean velocity in novel environments. However, except for one pair of time-windows in OF1 (2nd and 5th windows, in which the animal should be more habituated to the novelty), the mean velocity did not statistically change within the exploration session, while beta2 power varied along the session (**Figure 1**) suggesting that the correlation with velocity might reflect the behavior output expected of novelty sessions, as opposed to velocity directly driving beta2 activity.

One of the novel results reported here was the cross-frequency modulation between a slow frequency range within the delta-range activity and the power of beta2 during novelty detection. This set of results was surprising, and not anticipated for the experimental design. As recently shown, delta oscillations have been related to the respiration rhythm (Lockmann and Tort, 2018; Tort et al., 2018a). However, the only way for checking if the phase of the slow oscillation reported here is indeed related to a delta oscillation was implanting electrodes in the olfactory bulb. Therefore, the results present here were reported as a delta-range oscillation, and future research is needed to further investigate the relationship between respiration and novelty detection.

CFC has been implicated in different brain computations, from modulating different assemblies of neurons, facilitating communication between brain regions, and coordinating local cortical processing required for effective computation and synaptic modification (Canolty and Knight, 2010; Lisman and Jensen, 2013; Hyafil et al., 2015). The relation between theta and gamma, from the involvement of different GABAergic interneurons, and its function has been extensively reported in the hippocampal formation (Fernández-Ruiz and Herreras, 2013; Lasztóczi and Klausberger, 2014; Schomburg et al., 2014; Gereke et al., 2017), It has been suggested that the coupling of different gamma frequencies to different theta phases would serve as a mechanism underlying the communication of CA1 with CA3 or entorhinal cortex (Colgin et al., 2009; Schomburg et al., 2014). Although the report of CFC during tasks without specific time epochs to trigger the analysis are uncommon, previous reports indicate changes in the dynamics of gamma and its relation to theta over the experience exposition (Gereke et al., 2017) and promote encoding of memories for novel object-place associations (Zheng et al., 2016).

Here, the sliding time-window CFC analysis in the HC, especially during the first 150 s (window 1), revealed theta-nested spectral components, consistent with previous reports (Lopes-dos-Santos et al., 2018). The CFC revealed the peak of theta/beta2 around 22 Hz (instead of the 25 Hz of beta2 power increase; **Figure 2A**), theta/lowG at 35 Hz, and theta/midG around 70 Hz (**Figure 2A**) or 54 Hz (**Figure 2A**). We observed an increase of theta/midG coupling during the exploration of novel environment and objects (**Figures 2A,B**), while theta/lowG coupling was more prevalent in the "retrieval" at the familiar session (**Supplementary Figure 3A**, **Supplementary Table 4**) following previously reported theta/midG coupling increases during learning and retrieval of memory (Tort et al., 2008, 2009; Lisman and Jensen, 2013; Zheng et al., 2016; Gereke et al., 2017; Lopes-dos-Santos et al., 2018).

One might be concerned that the beta2 oscillations are simply a harmonic of theta or a reflection of slow-gamma. However, several considerations suggest that beta2 is a unique spectral signature and not a confound of slower non-sinusoidal rhythms. First, if beta2 were a harmonic oscillation of theta, we would expect the first harmonic (around 16 Hz) to be present and stronger than the second (around Beta2), but this is not observed in our results (**Figures 1B–D**). Second, it is clear that theta, beta2, and lowG have distinct temporal patterns and characteristics (**Figure 1C**). Third, It would also be expected a stronger beta2-theta-harmonic during higher theta in any exploration

sessions (novel or familiar), but that is not the case, with strong beta2 appearing only in the novel exposition (OF1 and OBJ1), specifically at the beginning of the session. Fourth, there is no relation between theta and beta2 instantaneous power (**Supplementary Figure 2**) Firth, the spike-field coherence analyses showed that distinct populations of neurons coupled to beta2 bursts vs. theta (**Figure 5**).

Interestingly, beta2 and lowG were strongly modulated by the delta-range phase (**Figures 2A,B**). Although this could initially point to beta2 and lowG as being part of the same oscillatory regimen, beta2 and lowG have different spectral peaks (25 Hz vs. 35 Hz), beta2 has a transient power characteristic and lowG does not (**Figure 1C**, **Supplementary Table 1**) and inspecting the raw signal reveals that these two dynamics can be observed independently of each other (**Figures 4A–C**). Furthermore, beta2 and lowG have different coherence peaks (**Figure 4**) and exhibit different temporal coupling dynamics during novelty exploration (**Figure 4D**). The usage of the same nomenclature (lowG to describe beta2 and lowG) may create difficulties in the characterization of the function behind these different oscillations, which could also be the reason for beta2 being reported only twice in the past decades (França et al., 2014). Instead of only the band of frequency, in which authors constantly change the frequency range for the same nomenclature, the oscillations ideally should be classified based on different characteristics, from the species been recorded to wave-shape, origin, and physiological function (Cole and Voytek, 2017; Tort et al., 2018b). We also report a strong delta-range phase modulating theta (**Supplementary Figure 3A, Supplementary Table 4**). The modulation of delta/theta was not modulated by time-window or novelty, exhibiting high MI values through all time-windows and sessions. Delta-theta coupling was previously reported in both rodents and humans during novelty exposure (Isler et al., 2008; Fujisawa and Buzsáki, 2011; Jirsa and Müller, 2013; Roy et al., 2017). As suggested in previous works, delta-theta coupling in the HC could be involved with multiplexed timing mechanisms inherent to the support processing of information necessary during the acquisition and retrieval of memories (Fujisawa and Buzsáki, 2011).

The distinction between beta2 and lowG is also important in the perspective of a complex network involving different brain regions because beta oscillations are implicated in long-range synchrony between different areas of the brain, a feature not shared with gamma oscillations (Kopell et al., 2000). For the first time, we revealed that during the novelty exploration sessions the HC has a strong coherence in the beta2 frequency band (**Figures 3A,B**), such coherence is not seen when the animal never faced the novelty content before (**Figure 3C**). On top of that, Granger causality revealed that the highest Granger gains come from HC and PAR cortex towards mPFC in theta, beta2, and lowG frequency band during OF1 exploration, while in the object novelty session the Granger gain comes mostly from HC (**Figures 3D,E**). Note that during the subsequent familiar exploration sessions the beta2 coherence in all three areas remains strong, probably carrying novelty content information towards the cortices, which may act as hubs for comparing the familiarity/novelty contents. In contrast to the beta2 power dynamics, which increase only at the beginning of novelty sessions, this suggests a more cumulative effect on coherence. We also notice that in the last HC session, the coherence between the two cortices decreased while their coherence with the HC was still high. This might be explained by the strong hippocampal influence in the generation of beta2, or memory trace retrieval characteristics previously described between mPFC and HC (Jin and Maren, 2015). Further investigation is needed to reveal detailed aspects of these interactions. In summary, the coherence and Granger results presented here point to the close communication among the three areas recorded, showing that all three areas communicate *via* theta and beta2 during novelty and familiarity exploration.

We also have shown for the first time that beta2 has similar transient power dynamics also in the mPFC, increasing at the beginning of the session and fading towards the end of the session (**Figure 6A**). Although PAR did not exhibit a statistically significant increase in beta2 power, the beta2 bursts can be verified in the raw signal of mPFC, and PAR LFP was coherent with other areas (**Figure 4**). Furthermore, all three areas involved showed multi-unit coupling with beta2 bursts events among the three areas analyzed, including PAR multi-unit activity coupled to the beta2 bursts of mPFC, PAR, and HC. The couplings of these three areas had different phase preferences of beta2 events of each region, supporting the interpretation of independent bursts in each area (**Figure 5**). This corroborates the results of coherence and Granger causality analyses, showing that the cortical beta2 is not a result of volume conduction from the HC. Taken together, our results of: (1) raw traces showing independent bursts in the HC and both cortices; (2) local referencing; (3) phase-lag-based LFP coherence; (4) Granger causality; and (5) phase-diverse long-range spike-field coherence demonstrates for the first time that each region exhibits independent bursts of beta2, with the HC appearing to be the main drive.

We also have shown that similar to HC coupling dynamics, (1) both cortices exhibit strong coupling between theta/midG and theta/lowG during novelty exploration; and (2) that both cortices show the same coupling between delta/beta2 as exhibited in HC in the first time window that beta2 exhibited higher power (**Figures 6B,D–F**). These couplings are only found during the novelty exploration (**Figure 6**), and not during familiar exploration (**Supplementary Figures 3B,C**). Even though there is a trend in the delta-beta2 coupling to be higher in the first time-window, this effect is stronger in the OF1 session (time-window effect in mPFC, PAR, and HC; see **Supplementary Tables 2,3**). Thus it is not clear whether this modulation follows the temporal dynamics of beta2 power, coherence, or a mix between them. Similar coupling was previously reported in the mid-prefrontal cortex during recording in freely behaving rodents (Andino-Pavlovsky et al., 2017) or during learning and working memory (Canolty and Knight, 2010; Samuel, 2019). However, for the first time, we show that the local delta oscillations modulate the beta2, not only in the HC but also in the PAR and mPFC during novelty exploration.

Importantly, we found a dissociation between the time courses of beta2 coherence among the three areas and beta2 power within-area: whereas local beta2 power was transient and primarily observed early in the novelty sessions, inter-regional coherence was more sustained and remained robust through the sessions. This unveils the existence of multiple processes influenced by beta2 oscillations: one in a shorter timescale, revealed by the transient presence of hippocampal beta2 bursts during novelty exposure; and another, in a longer timescale, is characterized by the beta2 synchrony across the HC, mPFC, and PAR that in our data extends through the entire session of novelty exposure and even further into familiar sessions. Those two mechanisms might be associated with different steps of memory encoding. For example, Grossberg (2009) suggests that initial beta2 bursts could be a mechanism for the fast stabilization of the memory traces (during memory acquisition), explaining the rapid emergence of place cells in the HC (Berke et al., 2008; Grossberg, 2009). It has also been shown that inhibition of protein synthesis in the HC impairs reconsolidation of memory traces only when the memory reactivation involves novelty (Rossato et al., 2007; Radiske et al., 2017)—that is, in the presence of beta2 bursts. Both of those processes, memory acquisition and reconsolidation, involve first setting the memory into an active state, which requires further stabilization towards an inactive memory state (Nader, 2015). Thus, there might be a link between the acquisition/activation of memory traces and the initial beta2 bursts. On the other hand, beta2 coherence between HC and the two cortices stays higher for a longer time after novelty exposure, which could indicate a role in the stabilization of the memory traces and the LTP induction that happens in the HC (Clarke et al., 2010). Despite this being an interesting hypothesis, new experiments are needed to specifically investigate the direct relation of beta2 to the different memory trace processes. Finally, in between these two temporal dynamics of beta2 there is the modulation of beta2 amplitude by delta-range oscillations, which seems to follow a short timescale in the cortex only during novelty, similar to the transient beta2 bursts, and a longer timescale in the HC, even though the modulation tends to be higher in the first time-window.

Together, these results highlight and further support the relation of beta2 oscillations and novelty extending it to a larger hippocampal-cortical circuit and suggesting beta2 as a mechanism for detecting and communicating information among the areas involved in behavioral adaptation to novelty.

DATA AVAILABILITY STATEMENT

The raw data supporting the conclusions of this article will be made available by the authors upon request.

ETHICS STATEMENT

The animal study was reviewed and approved by Centrale Commissie Dierproeven (CCD) and it is according to all indications of the local Radboud University Medical Centre animal welfare body (Approval number 2016-0079).

AUTHOR CONTRIBUTIONS

AF conceived and designed the experiments, performed the experiments, analyzed and interpreted the data, and wrote the article. NB conceived and designed the experiments, and wrote the article. BS analyzed and interpreted the data, and wrote the article. MC contributed reagents, materials, analysis tools or data, analyzed and interpreted the data, and wrote the article. All authors contributed to the article and approved the submitted version.

FUNDING

MC, NB, and AF were funded by European Research Council (ERC)-StG 638589. BS was funded by Nederlandse Organisatie voor Wetenschappelijk Onderzoek (NWO) TOP grant 612.001.853. This manuscript has been released as a pre-print at Biorxiv (https://www.biorxiv.org/content/10.1101/2020.06.15.151969v2; França et al., 2020a).

SUPPLEMENTARY MATERIAL

The Supplementary Material for this article can be found online at: https://www.frontiersin.org/articles/10.3389/fnsys.2021.617388/full#supplementary-material.

REFERENCES

Andino-Pavlovsky, V., Souza, A. C., Scheffer-Teixeira, R., Tort, A. B. L., Etchenique, R., and Ribeiro, S. (2017). Dopamine modulates delta-gamma phase-amplitude coupling in the prefrontal cortex of behaving rats. *Front. Neural Circuits* 11:29. doi: 10.3389/fncir.2017.00029

Barnett, L., and Seth, A. K. (2014). The MVGC multivariate Granger causality toolbox: a new approach to Granger-causal inference. *J. Neurosci. Methods* 223, 50–68. doi: 10.1016/j.jneumeth.2013.10.018

Benchenane, K., Peyrache, A., Khamassi, M., Tierney, P. L., Gioanni, Y., Battaglia, F. P., et al. (2010). Coherent theta oscillations and reorganization of spike timing in the hippocampal- prefrontal network upon learning. *Neuron* 66, 921–936. doi: 10.1016/j.neuron.2010.05.013

Benchenane, K., Tiesinga, P. H., and Battaglia, F. P. (2011). Oscillations in the prefrontal cortex: a gateway to memory and attention. *Curr. Opin. Neurobiol.* 21, 475–485. doi: 10.1016/j.conb.2011.01.004

Berke, J. D., Hetrick, V., Breck, J., and Greene, R. W. (2008). Transient 23–30 Hz oscillations in mouse hippocampus during exploration of novel environments. *Hippocampus* 18, 519–529. doi: 10.1002/hipo.20435

Bettis, T., and Jacobs, L. F. (2012). Sex differences in object recognition are modulated by object similarity. *Behav. Brain Res.* 233, 288–292. doi: 10.1016/j.bbr.2012.04.028

Buzsáki, G., and Draguhn, A. (2004). Neuronal oscillations in cortical networks. *Science* 304, 1926–1929. doi: 10.1126/science.1099745

Canolty, R. T., and Knight, R. T. (2010). The functional role of cross-frequency coupling. *Trends Cogn. Sci.* 14, 506–515. doi: 10.1016/j.tics.2010.09.001

Cenquizca, L. A., and Swanson, L. W. (2007). Spatial organization of direct hippocampal field CA1 axonal projections to the rest of the cerebral cortex. *Brain Res. Rev.* 56, 1–26. doi: 10.1016/j.brainresrev.2007.05.002

Clarke, J. R., Cammarota, M., Gruart, A., Izquierdo, I., and Delgado-García, J. M. (2010). Plastic modifications induced by object recognition memory processing. *Proc. Natl. Acad. Sci. U S A* 107, 2652–2657. doi: 10.1073/pnas.0915059107

Cohen, M. X. (2017a). Multivariate cross-frequency coupling *via* generalized eigendecomposition. *eLife* 6:e21792. doi: 10.7554/eLife.21792

Cohen, M. X. (2017b). Comparison of linear spatial filters for identifying oscillatory activity in multichannel data. *J. Neurosci. Methods* 278, 1–12. doi: 10.1016/j.jneumeth.2016.12.016

Cole, S. R., and Voytek, B. (2017). Brain oscillations and the importance of waveform shape. *Trends Cogn. Sci.* 21, 137–149. doi: 10.1016/j.tics.2016.12.008

Colgin, L. L. (2015). Theta-gamma coupling in the entorhinal-hippocampal system. *Curr. Opin. Neurobiol.* 31, 45–50. doi: 10.1016/j.conb.2014.08.001

Colgin, L. L., Denninger, T., Fyhn, M., Hafting, T., Bonnevie, T., Jensen, O., et al. (2009). Frequency of gamma oscillations routes flow of information in the hippocampus. *Nature* 462, 353–357. doi: 10.1038/nature08573

Cross, L., Brown, M. W., Aggleton, J. P., and Warburton, E. C. (2013). The medial dorsal thalamic nucleus and the medial prefrontal cortex of the rat function together to support associative recognition and recency but not item recognition. *Learn. Mem.* 20, 41–50. doi: 10.1101/lm.028266.112

de Cheveigné, A., and Arzounian, D. (2015). Scanning for oscillations. *J. Neural Eng.* 12:066020. doi: 10.1088/1741-2560/12/6/066020

de Lima, M. N. M., Presti-Torres, J., Dornelles, A., Siciliani Scalco, F., Roesler, R., Garcia, V. A., et al. (2011). Modulatory influence of dopamine receptors on consolidation of object recognition memory. *Neurobiol. Learn. Mem.* 95, 305–310. doi: 10.1016/j.nlm.2010.12.007

Delorme, A., Mullen, T., Kothe, C., Akalin Acar, Z., Bigdely-Shamlo, N., Vankov, A., et al. (2011). EEGLAB, SIFT, NFT, BCILAB, and ERICA: new tools for advanced EEG processing. *Comput. Intell. Neurosci.* 2011:130714. doi: 10.1155/2011/130714

Fernández-Ruiz, A., and Herreras, O. (2013). Identifying the synaptic origin of ongoing neuronal oscillations through spatial discrimination of electric fields. *Front. Comput. Neurosci.* 7:5. doi: 10.3389/fncom.2013.00005

Fernández-Ruiz, A., Oliva, A., Nagy, G. A., Maurer, A. P., Berényi, A., and Buzsáki, G. (2017). Entorhinal-CA3 dual-input control of spike timing in the hippocampus by theta-gamma coupling. *Neuron* 93, 1213.e5–1226.e5. doi: 10.1016/j.neuron.2017.02.017

França, A. S. C., Borgegius, N., and Cohen, M. X. (2020a). Beta2 oscillations in the hippocampal-cortical novelty detection circuit. *BioRxiv* [Preprint]. doi: 10.1101/2020.06.15.151969

França, A. S. C., van Hulten, J. A., and Cohen, M. X. (2020b). Low-cost and versatile electrodes for extracellular chronic recordings in rodents. *Heliyon* 6:e04867. doi: 10.1016/j.heliyon.2020.e04867

França, A. S. C., do Nascimento, G. C., Lopes-dos-Santos, V., Muratori, L., Ribeiro, S., Lobão-Soares, B., et al. (2014). Beta2 oscillations (23–30 Hz) in the mouse hippocampus during novel object recognition. *Eur. J. Neurosci.* 40, 3693–3703. doi: 10.1111/ejn.12739

Fries, P. (2005). A mechanism for cognitive dynamics: neuronal communication through neuronal coherence. *Trends Cogn. Sci.* 9, 474–480. doi: 10.1016/j.tics.2005.08.011

Fujisawa, S., and Buzsáki, G. (2011). A 4 Hz oscillation adaptively synchronizes prefrontal, VTA, and hippocampal activities. *Neuron* 72, 153–165. doi: 10.1016/j.neuron.2011.08.018

Gereke, B. J., Mably, A. J., and Colgin, L. L. (2017). Experience-dependent trends in CA1 theta and slow gamma rhythms in freely behaving mice. *J. Neurophysiol.* 119, 476–489. doi: 10.1152/jn.00472.2017

Grossberg, S. (2009). Beta oscillations and hippocampal place cell learning during exploration of novel environments. *Hippocampus* 19, 881–885. doi: 10.1002/hipo.20602

Hasselmo, M. E. (2006). The role of acetylcholine in learning and memory. *Curr. Opin. Neurobiol.* 16, 710–715. doi: 10.1016/j.conb.2006.09.002

Haufe, S., Dähne, S., and Nikulin, V. V. (2014). Dimensionality reduction for the analysis of brain oscillations. *NeuroImage* 101, 583–597. doi: 10.1016/j.neuroimage.2014.06.073

Hyafil, A., Giraud, A.-L., Fontolan, L., and Gutkin, B. (2015). Neural cross-frequency coupling: connecting architectures, mechanisms, and functions. *Trends Neurosci.* 38, 725–740. doi: 10.1016/j.tins.2015.09.001

Isler, J. R., Grieve, P. G., Czernochowski, D., Stark, R. I., and Friedman, D. (2008). Cross-frequency phase coupling of brain rhythms during the orienting response. *Brain Res.* 1232, 163–172. doi: 10.1016/j.brainres.2008.07.030

Jin, J., and Maren, S. (2015). Prefrontal-hippocampal interactions in memory and emotion. *Front. Syst. Neurosci.* 9:170. doi: 10.3389/fnsys.2015.00170

Jirsa, V., and Müller, V. (2013). Cross-frequency coupling in real and virtual brain networks. *Front. Comput. Neurosci.* 7:78. doi: 10.3389/fncom.2013.00078

Kafkas, A., and Montaldi, D. (2018). How do memory systems detect and respond to novelty? *Neurosci. Lett.* 680, 60–68. doi: 10.1016/j.neulet.2018.01.053

Kitanishi, T., Ujita, S., Fallahnezhad, M., Kitanishi, N., Ikegaya, Y., and Tashiro, A. (2015). Novelty-induced phase-locked firing to slow gamma oscillations in the hippocampus: requirement of synaptic plasticity. *Neuron* 86, 1265–1276. doi: 10.1016/j.neuron.2015.05.012

Kopell, N., Ermentrout, G. B., Whittington, M. A., and Traub, R. D. (2000). Gamma rhythms and beta rhythms have different synchronization properties. *Proc. Natl. Acad. Sci. U S A* 97, 1867–1872. doi: 10.1073/pnas.97.4.1867

Lasztóczi, B., and Klausberger, T. (2014). Layer-specific GABAergic control of distinct gamma oscillations in the CA1 hippocampus. *Neuron* 81, 1126–1139. doi: 10.1016/j.neuron.2014.01.021

Lisman, J. E., and Grace, A. A. (2005). The hippocampal-VTA loop: controlling the entry of information into long-term memory. *Neuron* 46, 703–713. doi: 10.1016/j.neuron.2005.05.002

Lisman, J. E., and Jensen, O. (2013). The theta-gamma neural code. *Neuron* 77, 1002–1016. doi: 10.1016/j.neuron.2013.03.007

Lisman, J. E., and Otmakhova, N. A. (2001). Storage, recall, and novelty detection of sequences by the hippocampus: elaborating on the SOCRATIC model to account for normal and aberrant effects of dopamine. *Hippocampus* 11, 551–568. doi: 10.1002/hipo.1071

Lockmann, A. L. V., and Tort, A. B. L. (2018). Nasal respiration entrains delta-frequency oscillations in the prefrontal cortex and hippocampus of rodents. *Brain Struct. Funct.* 223, 1–3. doi: 10.1007/s00429-017-1573-1

Lopes-dos-Santos, V., van de Ven, G. M., Morley, A., Trouche, S., Campo-Urriza, N., and Dupret, D. (2018). Parsing hippocampal theta oscillations by nested spectral components during spatial exploration and memory-guided behavior. *Neuron* 100, 940.e7–952.e7. doi: 10.1016/j.neuron.2018.09.031

Morrow, J. K., Cohen, M. X., and Gothard, K. M. (2020). Mesoscopic-scale functional networks in the primate amygdala. *eLife* 9:e57341. doi: 10.7554/eLife.57341

Nader, K. (2015). Reconsolidation and the dynamic nature of memory. *Cold Spring Harb. Perspect. Biol.* 7:a021782. doi: 10.1101/cshperspect.a021782

Pho, G. N., Goard, M. J., Woodson, J., Crawford, B., and Sur, M. (2018). Task-dependent representations of stimulus and choice in mouse parietal cortex. *Nat. Commun.* 9:2596. doi: 10.1038/s41467-018-05012-y

Preston, A. R., and Eichenbaum, H. (2013). Interplay of hippocampus and prefrontal cortex in memory. *Curr. Biol.* 23, R764–R773. doi: 10.1016/j.cub.2013.05.041

Quiroga, R. Q., Nadasdy, Z., and Ben-Shaul, Y. (2004). Unsupervised spike detection and sorting with wavelets and superparamagnetic clustering. *Neural Comput.* 16, 1661–1687. doi: 10.1162/089976604774201631

Radiske, A., Rossato, J. I., Gonzalez, M. C., Köhler, C. A., Bevilaqua, L. R., and Cammarota, M. (2017). BDNF controls object recognition memory reconsolidation. *Neurobiol. Learn. Mem.* 142, 79–84. doi: 10.1016/j.nlm.2017.02.018

Rossato, J. I., Bevilaqua, L. R. M., Myskiw, J. C., Medina, J. H., Izquierdo, I., and Cammarota, M. (2007). On the role of hippocampal protein synthesis in the consolidation and reconsolidation of object recognition memory. *Learn. Mem.* 14, 36–46. doi: 10.1101/lm.422607

Roy, A., Svensson, F. P., Mazeh, A., and Kocsis, B. (2017). Prefrontal-hippocampal coupling by theta rhythm and by 2-5 Hz oscillation in the delta band: the role of the nucleus reuniens of the thalamus. *Brain Struct. Funct.* 222, 2819–2830. doi: 10.1007/s00429-017-1374-6

Samuel I. B. H. (2019). Gamma band oscillations drives information flow in theta and delta band between hippocampus and medial pre-frontal cortex. *BioRxiv* [Preprint]. doi: 10.1101/809962

Schomburg, E. W., Fernández-Ruiz, A., Mizuseki, K., Berényi, A., Anastassiou, C. A., Koch, C., et al. (2014). Theta phase segregation of input-specific gamma patterns in entorhinal-hippocampal networks. *Neuron* 84, 470–485. doi: 10.1016/j.neuron.2014.08.051

Sigurdsson, T., Stark, K. L., Karayiorgou, M., Gogos, J. A., and Gordon, J. A. (2010). Impaired hippocampal-prefrontal synchrony in a genetic mouse model of schizophrenia. *Nature* 464, 763–767. doi: 10.1038/nature08855

Souza, B. C., Lopes-dos-Santos, V., Bacelo, J., and Tort, A. B. (2019). Spike sorting with Gaussian mixture models. *Sci. Rep.* 9:3627. doi: 10.1038/s41598-019-39986-6

Spellman, T., Rigotti, M., Ahmari, S. E., Fusi, S., Gogos, J. A., and Gordon, J. A. (2015). Hippocampal-prefrontal input supports spatial encoding in working memory. *Nature* 522, 309–314. doi: 10.1038/nature14445

Tort, A. B. L., Brankačk, J., and Draguhn, A. (2018a). Respiration-entrained brain rhythms are global but often overlooked. *Trends Neurosci.* 41, 186–197. doi: 10.1016/j.tins.2018.01.007

Tort, A. B. L., Ponsel, S., Jessberger, J., Yanovsky, Y., Brankačk, J., and Draguhn, A. (2018b). Parallel detection of theta and respiration-coupled oscillations throughout the mouse brain. *Sci. Rep.* 8:6432. doi: 10.1038/s41598-018-24629-z

Tort, A. B. L., Komorowski, R. W., Manns, J. R., Kopell, N. J., and Eichenbaum, H. (2009). Theta-gamma coupling increases during the learning of item-context associations. *Proc. Natl. Acad. Sci. U S A* 106, 20942–20947. doi: 10.1073/pnas.0911331106

Tort, A. B. L., Kramer, M. A., Thorn, C., Gibson, D. J., Kubota, Y., Graybiel, A. M., et al. (2008). Dynamic cross-frequency couplings of local field potential oscillations in rat striatum and hippocampus during performance of a T-maze task. *Proc. Natl. Acad. Sci. U S A* 105, 20517–20522. doi: 10.1073/pnas.0810524105

van Kesteren, M. T. R., Ruiter, D. J., Fernández, G., and Henson, R. N. (2012). How schema and novelty augment memory formation. *Trends Neurosci.* 35, 211–219. doi: 10.1016/j.tins.2012.02.001

Vinck, M., Oostenveld, R., van Wingerden, M., Battaglia, F., and Pennartz, C. M. A. (2011). An improved index of phase-synchronization for electrophysiological data in the presence of volume- conduction, noise and sample-size bias. *NeuroImage* 55, 1548–1565. doi: 10.1016/j.neuroimage.2011.01.055

Zheng, C., Bieri, K. W., Hwaun, E., and Colgin, L. L. (2016). Fast gamma rhythms in the hippocampus promote encoding of novel object-place pairings. *eNeuro* 3:ENEURO.0001-16.2016. doi: 10.1523/ENEURO.0001-16.2016

Conflict of Interest: The authors declare that the research was conducted in the absence of any commercial or financial relationships that could be construed as a potential conflict of interest.

Copyright © 2021 França, Borgesius, Souza and Cohen. This is an open-access article distributed under the terms of the Creative Commons Attribution License (CC BY). The use, distribution or reproduction in other forums is permitted, provided the original author(s) and the copyright owner(s) are credited and that the original publication in this journal is cited, in accordance with accepted academic practice. No use, distribution or reproduction is permitted which does not comply with these terms.

frontiers in Systems Neuroscience

ORIGINAL RESEARCH
published: 01 March 2021
doi: 10.3389/fnsys.2021.624183

A Comprehensive Analysis of Multilayer Community Detection Algorithms for Application to EEG-Based Brain Networks

Maria Grazia Puxeddu[1,2]*, *Manuela Petti*[1,2] *and Laura Astolfi*[1,2]

[1] *Department of Computer, Control and Management Engineering "Antonio Ruberti", University of Rome Sapienza, Rome, Italy,* [2] *IRCCS Fondazione Santa Lucia, Rome, Italy*

Modular organization is an emergent property of brain networks, responsible for shaping communication processes and underpinning brain functioning. Moreover, brain networks are intrinsically multilayer since their attributes can vary across time, subjects, frequency, or other domains. Identifying the modular structure in multilayer brain networks represents a gateway toward a deeper understanding of neural processes underlying cognition. Electroencephalographic (EEG) signals, thanks to their high temporal resolution, can give rise to multilayer networks able to follow the dynamics of brain activity. Despite this potential, the community organization has not yet been thoroughly investigated in brain networks estimated from EEG. Furthermore, at the state of the art, there is still no agreement about which algorithm is the most suitable to detect communities in multilayer brain networks, and a way to test and compare them all under a variety of conditions is lacking. In this work, we perform a comprehensive analysis of three algorithms at the state of the art for multilayer community detection (namely, genLouvain, DynMoga, and FacetNet) as compared with an approach based on the application of a single-layer clustering algorithm to each slice of the multilayer network. We test their ability to identify both steady and dynamic modular structures. We statistically evaluate their performances by means of *ad hoc* benchmark graphs characterized by properties covering a broad range of conditions in terms of graph density, number of clusters, noise level, and number of layers. The results of this simulation study aim to provide guidelines about the choice of the more appropriate algorithm according to the different properties of the brain network under examination. Finally, as a proof of concept, we show an application of the algorithms to real functional brain networks derived from EEG signals collected at rest with closed and open eyes. The test on real data provided results in agreement with the conclusions of the simulation study and confirmed the feasibility of multilayer analysis of EEG-based brain networks in both steady and dynamic conditions.

Keywords: community detection, network neuroscience, modularity, electroencephalography, statistical analysis

OPEN ACCESS

Edited by:
Andrea Duggento,
University of Rome Tor Vergata, Italy

Reviewed by:
Sergio E. Lew,
University of Buenos Aires, Argentina
Olivier Darbin,
University of South Alabama, United States

***Correspondence:**
Maria Grazia Puxeddu
puxeddu@diag.uniroma1.it

Received: *30 October 2020*
Accepted: *21 January 2021*
Published: *01 March 2021*

Citation:
Puxeddu MG, Petti M and Astolfi L (2021) A Comprehensive Analysis of Multilayer Community Detection Algorithms for Application to EEG-Based Brain Networks. Front. Syst. Neurosci. 15:624183. doi: 10.3389/fnsys.2021.624183

INTRODUCTION

The convergence of networks science to neuroscience has opened the way to the currently well-established network neuroscience framework (Bassett and Sporns, 2017), an emerging field that aims to investigate brain organizational principles by means of networks science tools. This shift was driven by two aspects. On one side, the development of tools to investigate complex systems has exploded, as more and more complex data from different fields (i.e., social, transportation, and biological sciences) become available (Newman, 2003; Boccaletti et al., 2006). On the other side, the advancements in neuroimaging techniques led to consequent improvements in the field of brain connectivity (Jirsa and McIntosh, 2007), which allows modeling of brain structure and function as a result of complex networks of brain areas (nodes) anatomically or functionally interconnected (Sporns, 2011).

An emergent property of networks representing real complex systems is the community structure (Porter et al., 2009; Newman, 2012). A specific type of communities is the modules, groups of nodes densely connected which can be related to specific functions of the system and widely observed in brain networks (Meunier et al., 2010; Sporns and Betzel, 2016; Betzel, 2021). Previous studies pointed out how a modular structure represents a mean to reveal non-trivial relationships between topological and functional features of the complex networks (Guimerà and Amaral, 2005). This property of the brain network is located halfway between global and local scales, at a mesoscale level, which is informative of the network's organization (Betzel and Bassett, 2017). In fact, while at local and global scales the focus is on the fundamental units of the network (nodes) and on the network as a whole, at this intermediate scale, we can observe how the network's elements organize themselves, e.g., into clusters, to form efficient systems. In this sense, communities underpin the brain network's organization: their composition shapes the communication patterns of the system and promotes well-balanced and efficient mechanisms of integration and segregation between brain sub-systems (Betzel et al., 2013; Sporns, 2013; Wig, 2017).

While most of the studies on community detection in brain graphs deal with single-layer networks, especially in electroencephalographic (EEG) applications (Chavez et al., 2010; Ahmadlou and Adeli, 2011; Zippo et al., 2018), brain networks are intrinsically multilayer (Hutchison et al., 2013; Muldoon and Bassett, 2016; De Domenico, 2017). There is no single neuronal connectivity pattern able to fully represent brain functioning: rather, brain interactions vary across multiple domains. They evolve in time or according to the subject's conditions, the tasks, or the frequency span (in M/EEG acquisitions). Thus, a multilayer framework better accounts for the complexity and diversity of cerebral interactions, resulting suitable to analyze brain connectivity without either throwing away or combining different information.

A multilayer network is a sequence of linked single-layer networks, each one encoding specific attributes of the system. It allows the integration of multiple channels of connectivity to provide a more natural description of the brain system, as the nodes (brain areas) can show different sets of interactions at each layer. A particularly interesting case for EEG-based analysis is represented by time-varying multilayer networks. Being able to track the brain organization during a task or a cognitive state is of interest because changes, as well as steady states, of the network's structure could be physiologically meaningful. For this reason, it is worthwhile to investigate modular structure in brain networks, especially those reconstructed from EEG signal, which benefit from an excellent temporal resolution. Under this perspective, multilayer analysis of EEG-derived networks can be successfully used to gain insights in applications that require an accurate temporal resolution, like epilepsy, vision, or cognition (Zahra et al., 2017).

Recovering communities in a multilayer network is usually done algorithmically because of the real networks' usually big dimension and complexity. A range of algorithms have been proposed, spanning along three main approaches:

(i) The first one trivially consists of applying a single-layer clustering algorithm to each slice of the multilayer network. Previous comparative analysis (Lancichinetti and Fortunato, 2009) has highlighted the good performances of those based on modularity optimization (Girvan and Newman, 2002; Newman and Girvan, 2004). In particular, the one introduced in Leicht and Newman (2008), which, from now on, we will call ModStat (stationary modularity), showed good performances with directed EEG brain networks (Puxeddu et al., 2017).

(ii) The second approach is based on the optimization of a multilayer formulation of modularity (Mucha et al., 2010). The implementation of this approach is provided in (Jeub et al., 2019) and is known as genLouvain. This algorithm represents an extension of the classical modularity maximization (Blondel et al., 2008), to which it adds a term that considers the coupling of the nodes across layers. This term is proportional to a resolution parameter, ω, which determines the stability of the network partitioning across the slices.

(iii) The third approach consists of the optimization of a multi-objective function (Chakrabarti et al., 2006), which aims to maximize both the accuracy of the partitions at each layer and the smoothness across all the layers. Two widely used algorithms reflecting this last approach are DynMoga (Folino and Pizzuti, 2014) and FacetNet (Lin et al., 2008, 2009). The former is a genetic algorithm that optimizes modularity and mutual information of consecutive layers. The latter discovers communities iteratively, taking into account both the observed data and a probabilistic model given by all the single community structures.

To date, an agreement on which is the most advantageous approach is missing. In the recent years, some efforts have been made on investigating their behavior on multilayer networks. A conventionally used approach, even in single-layer network analysis, consists of testing the algorithms on a real network with a known community structure (Lancichinetti and Fortunato, 2009). In Silva et al. (2016), for example, the authors compared the behavior of algorithms based on evolutionary clustering on

a high school network, the MIT Social Evolution dataset and the Brazilian Congress network, in which the ground truth is respectively represented by classes, dormitory sectors (Dong et al., 2011), and political alignment of the congressmen based on their party. However, this approach might lack generalization, and the obtained results would be limited to that specific network properties. Moreover, a brain network in which the community structure is known *a priori* does not exist. Hence, the lack of ground truth for brain communities, together with their ubiquity, requires the implementation of benchmark networks with a known community structure and realistic features to test different community detection algorithms. In Silva et al. (2016), the authors also tested the algorithms on a synthetic network. Nevertheless, it is a simple network with few nodes and three clusters that can hardly be encountered in neuroscience. In Schmidt et al. (2018), the authors tested two multilayer clustering approaches on an artificial network with more realistic properties. However, the test made on a single network, as previously said, might lack generalization of the results. Other already existing tools (Lin et al., 2008; Kim and Han, 2009) are a multilayer version of the Girvan and Newman model (Girvan and Newman, 2002) and do not allow a deep analysis of the algorithms, as they constrain most of the parameters characterizing the network (e.g., number of nodes, number of clusters, *etc.*). In Granell et al. (2015), the authors propose a tool in which a potential user can set some parameters of interest, such as the number of nodes, number of clusters, and ratio between intra-cluster and inter-cluster density. However, such tool does not address some aspects that are pivotal for EEG-based networks, like the noise level.

The principal aim of this work is to identify the most suitable approach to recover communities in EEG-based multilayer brain networks. For this purpose, we aim to perform a comparative analysis whose results will furnish practical guidelines about the use of multilayer community detection algorithms in the context of EEG-derived brain networks. Thus, we introduce a flexible toolbox able to generate artificial networks with a modular structure, with manifold features. This tool is a multilayer extension of the single-layer generator introduced in Puxeddu et al. (2017). The number of nodes, graph density, number of clusters, noise level in the community structure (modeled as a random permutation of a certain number of links), and percentage of nodes moving from a module to another one at a given layer can be set by the user. With respect to the previously described tools, we can also generate networks with different levels of noise to take into account the false positives and false negatives resulting from any brain functional connectivity estimation. In the case of EEG signals, the noise might depend on different factors, such as physiological/instrumental artifacts (Fisch, 1999; Riitta Hari and Aina Puce, 2017) and fluctuations in the EEG activity, or it may arise as a result of the connectivity estimation methods (Astolfi et al., 2007; He et al., 2019).

Using the proposed benchmark graphs, we performed a comparative analysis of the different multilayer clustering algorithms, testing them on graphs generated accounting for a wide range of network features systematically varied in the range typical of EEG-based brain networks. Furthermore, here for the first time we considered two scenarios: one in which the community structure is stationary across the layers and one in which it changes dynamically. Both cases are of great interest in real applications. In the first case, we aim to get a single partition out of a multilayer network with persistent organizational features. This is the case of layers associated to time points of stationary phenomena or to different subjects of the same category (e.g., healthy subjects or patients) for which we are interested in using the multilayer approach to extract enduring features. In the second case, we aim to track mesoscale organization in multilayer networks underlying non-stationary phenomena or different clinical cohorts. In both cases (stationary and evolving community structure), we statistically evaluated the algorithms' performances under different conditions by means of an analysis of variance (ANOVA).

Finally, as a proof of concept, we applied the four approaches to a brain functional multilayer network estimated from EEG signals acquired in a healthy subject during resting state at closed eyes and open eyes. We report the differences between the community structure subtending the two phases obtained by using the investigated algorithms, with the aim to test their accordance with the guidelines provided by the simulation studies. This application to real data has the purpose of validating the results of the simulation studies in a well-known and studied condition in order to check the applicability of multilayer community detection tools to EEG-based brain networks.

METHODS

Benchmark Network Generation

The toolbox that we developed generates pseudo-random multilayer networks with a defined community structure and consists of an algorithm implemented in Matlab environment (release 2017b). A preliminary version of the toolbox was reported in Puxeddu et al. (2019). This toolbox allows a potential user to create networks with either stationary or evolving community structure with features spanning a variety of conditions experimentally observable in EEG-based brain networks. In the following paragraphs, we describe the implementation of the toolbox for each of the above-mentioned two cases.

Networks With Stationary Community Structure

The network generated by the toolbox, in this case, presents a stationary modular structure, in which the composition of the clusters across the layers does not change. Here the variability between layers is only due to the noise level, which might make some links appear or disappear. **Figure 1A** shows an example of two layers of a multilayer network generated in this fashion. As mentioned before, the main advantage of this toolbox is its flexibility. In fact, the users can set several features which will characterize the network: number of nodes (N), graph density (D), number of clusters (CN), the ratio between intra-cluster and inter-cluster density (dr), the noise level (no), and the number of layers (nL). Once the set of desired features is selected, the algorithm proceeds by two main steps:

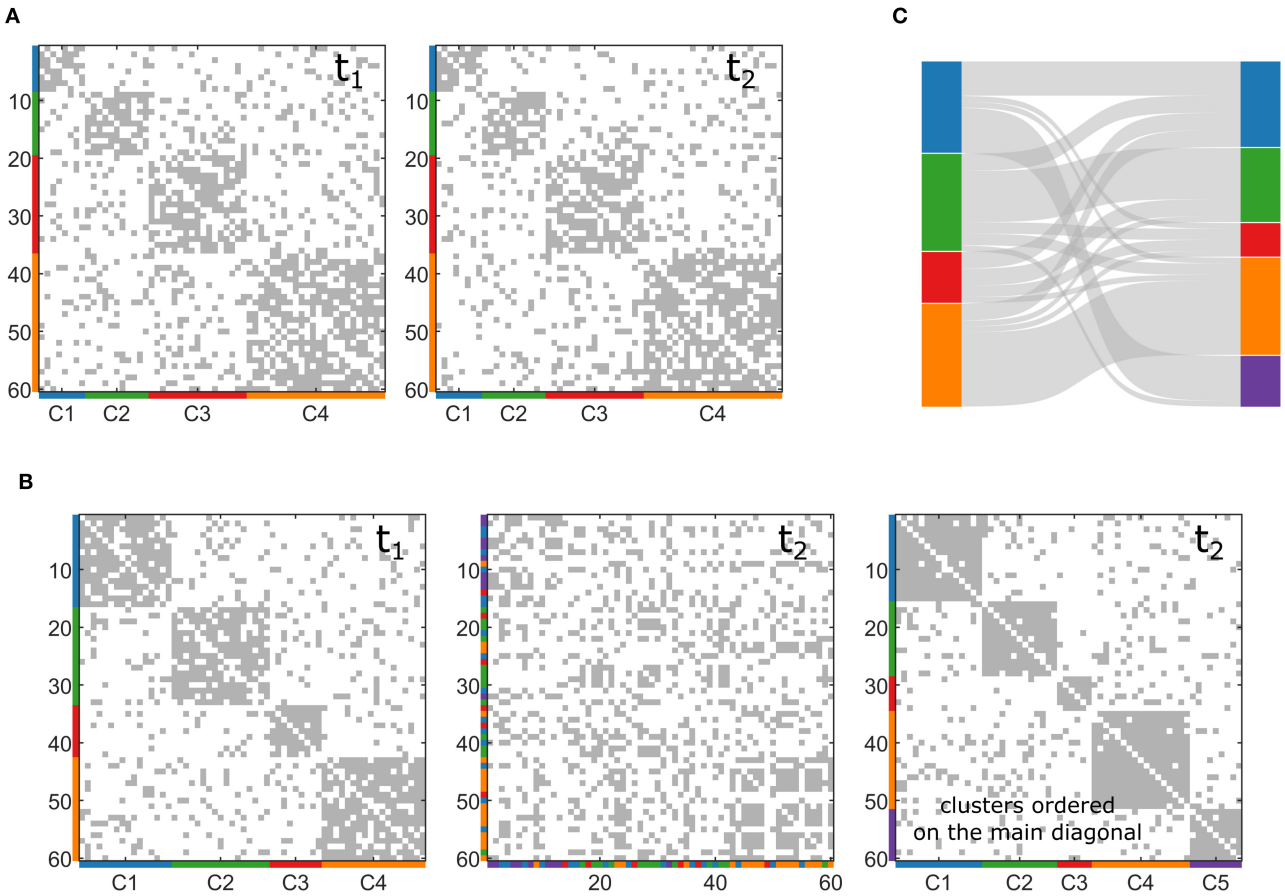


FIGURE 1 | Examples of synthetic multilayer networks generated through the toolbox. **(A)** Two snapshots (t_1 and t_2) of a multilayer network with stationary community structure. **(B)** Two snapshots (t_1 and t_2) of a multilayer network with evolving community structure. In the second t_2, the nodes are re-ordered to represent clusters on the main diagonal. **(C)** Sankey diagram of the network generated in **(B)**.

(a) Creation of a single-layer network (binary and directed) exploiting the algorithm described in Puxeddu et al. (2017)—we will use this network as a basis for each layer.
(b) Addition of the percentage of noise (i.e., percentage of links randomly shifted) set as input to each layer.

With these two steps, we obtain a multilayer network in which each slice has the same imposed community structure obtained in (a), and the inter-layer variability is only due to the presence of noise applied to each network (b). Step (a), in turn, consists of four stages:

(a.i) Setting of the size of the communities by randomly choosing CN integers, with the only constraint that their sum is equal to N.
(a.ii) Wiring of the network by randomly filling an $N \times N$ empty matrix observing the imposed specifics (about density and ratio between intra-cluster and inter-cluster density).
(a.iii) Checking the absence of isolated nodes inside the clusters, and if present, the algorithm rewires the intra-cluster connections.
(a.iv) Ensuring that the internal degree of each node is higher than the external degree (with respect to its cluster) by rewiring.

Networks With Evolving Community Structure

In this second case, we want our toolbox to simulate a multilayer network with a community structure that changes node composition across the layers. In this case, the algorithm in the toolbox also starts generating a first layer (with the same stages described above), but then it generates the following slice so that a certain percentage of nodes (pn, set as input by the user) changes its allegiances to modules. The algorithm acts only on the connections related to the nodes that change membership, maintaining the rest of the networks as it was originated at the beginning. Similarly, it can also increase or decrease the number of clusters, CN, moving some nodes into a new community or moving all the nodes belonging to one community in the remaining ones. In this way, the user can obtain controlled variations of different entities of the community structure according to the selected percentage of nodes that must change cluster (pn) and to the possible creation or disappearance of

communities. **Figure 1B** reports an example of two layers of a multilayer network with changing community structure, in which pn has been set to 30% and the number of clusters increases with the appearance of a new one (in purple in the figure). We represent this dynamic community structure through the Sankey diagram in **Figure 1C**.

Simulation Studies for the Algorithm Comparison

Stationary Community Structure

We made a simulation study testing the algorithms on benchmark networks with a stationary community structure generated as described in "section Networks With Stationary Community Structure." We exploited the tool by systematically varying the network features represented by the input parameters. In particular, we explored a range of values for the parameters according to those experimentally met in EEG-based functional brain networks:

- $N = 60$
  We selected this value to mimic the 61-channel configuration typically used in most EEG studies.
- $D = [0.10, 0.30]$
  We simulated sparse networks with two different density levels in a range usually met with real data.
- $CN = [2, 4, 6]$
  We simulated different parsing of the network to have coarser as well as finer community structures.
- $dr = 2$
  We generated networks in which the intra-cluster density is twice with respect to the inter-cluster one. We do this in order to start from a very convenient condition for the algorithms that we will gradually deteriorate by adding different noise percentages.
- $no = [10, 25, 50\%]$
  These noise percentages were chosen to reproduce networks with different levels of module clearness.
- $nL = [2, 10, 50, 100]$
  We consider networks with different numbers of layers to see if this factor influences the algorithms' performance. Indeed we expect multilayer algorithms exploiting a higher dimensionality to mitigate the noise effect.

Then, we run the four algorithms (genLouvain, ModStat, DynMoga, and FacetNet). To evaluate the effect of the factors algorithm, number of clusters, noise level, and number of layers, we performed a repeated-measure ANOVA using three figures of merit as dependent variables in order to capture different aspects of the performance:

I. Accuracy: To evaluate the algorithms' accuracy, we used the normalized mutual information (NMI) (Danon et al., 2005). This is an index borrowed from the field of information theory and used to estimate the similarity between two objects. It can range between 0 (completely different objects) and 1 (identical objects). It has been already employed in this context to calculate the similarity between two given partitions that, in our case, are the ones obtained from the clustering algorithms and the known community structure. We computed the NMI between these two partitions in each layer, and then we used the average of all these values as index of accuracy. We will refer to this index as NMI_{acc}.
II. Stability: In networks with stationary community structure, it is also important to assess how much the clustering algorithms provide for a stable partition across all the layers. Thus, we computed the NMI between each layer and the following one, and we computed the average of these values to obtain an index of stability. We named this index NMI_{stab}.
III. Global performance. We finally wanted an index summarizing the global performances of the algorithms, simultaneously considering accuracy and stability. We computed this index as the Euclidean distance between two points, A and B, in the xy plane where the x and y axes represent, respectively, the values of accuracy and stability. A is the point $[x_{(acc)}, y_{(stab)}]$ associated to the actual values of accuracy and stability assumed by the algorithm, and B is the point [1, 1] that represents the optimum (both stability and accuracy reach their highest score, which is 1). In this way, the Euclidean distance between A and B, which we used as index of global performance, represents the distance of the algorithms' performance from the optimal one. An example of this index is shown in **Figure 2B**. We will refer to this index as GS_{ind}, and it varies between 0 (optimal performances, A = B) and $\sqrt{2}$ (worst performances, $NMI_{acc} = NMI_{stab} = 0$, A is the point [0, 0] in the xy plane).

Since the algorithms genLouvain and FacetNet depend on the inter-layer resolution parameters ω and λ, we made two preliminary analyses exploring the behavior of the algorithms under different values of these parameters in order to select the best possible values of ω and λ for the stationary condition to be used in the comparative analysis. For this purpose, we performed two more ANOVA tests for repeated measures, one for genLouvain and one for FacetNet, considering values of ω and λ in the range [0.1, 10] and [0.1, 1], respectively. The first study was aimed at evaluating the effect of the factors ω (levels: 0.1, 0.2, 0.5, 1, 2, 5, 10), cluster number, noise level, and number of layers on the performance of genLouvain. Similarly, the second one was meant to evaluate the effect of λ (levels: 0.1, 0.2, 0.5, 0.7, 0.8, 0.9, 1), cluster number, noise level, and number of layers on the performance of FacetNet. The results of these two analyses are detailed in the **Supplementary Material**, sections 1 and 2, and have been used in the main comparative analysis to run the two algorithms with the appropriate choice of ω and λ according to the network's features.

Evolving Community Structure

To generate benchmark networks with dynamic community structure, we exploited the toolbox in the version introduced in "section Networks With Evolving Community Structure." We generated the networks by setting the input parameters to the same values reported in "section Stationary Community Structure," but here we also included the parameter pn

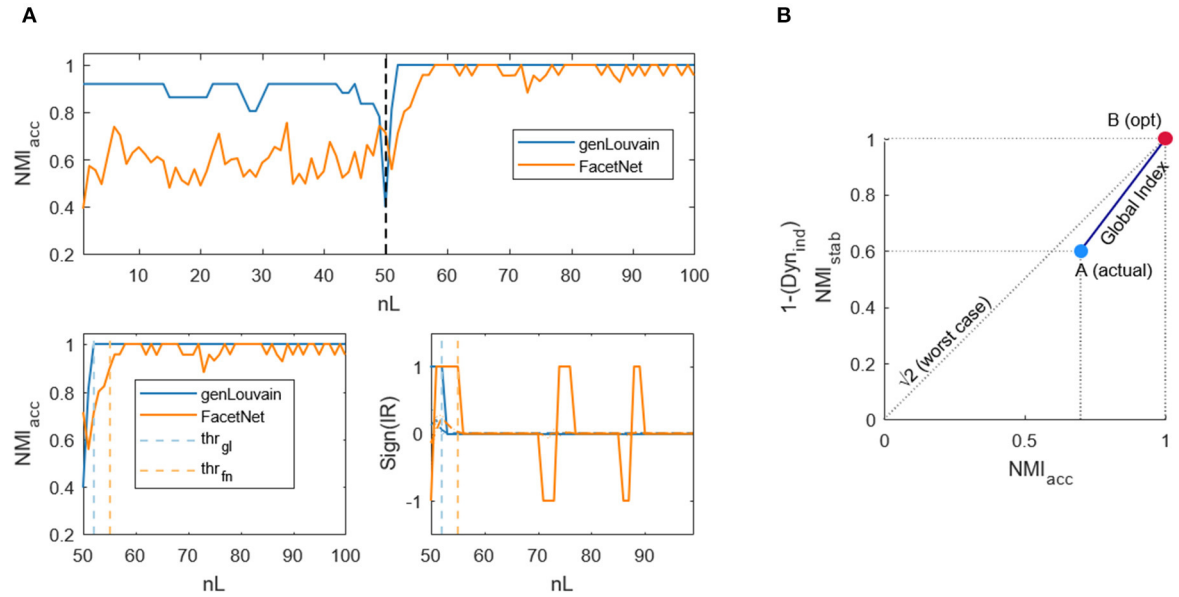


FIGURE 2 | Example of dynamic and global indices computation. **(A)** Dynamic index. Top figure: normalized mutual information computed between the output of the algorithms genLouvain and FacetNet and the actual community structure of a generated network with 100 layers. Lower left figure: normalized mutual information from the snapshot in which community structure changes and threshold samples (from which the algorithms go to regime) identified through the dynamic index. Lower right figure: sign of the first derivative smoothed and threshold samples. **(B)** The global index is indicated with the dark blue continuous line. A is the point corresponding to the actual values of NMI_{acc} and NMI_{stab}/Dyn_{ind}, while B is the point corresponding to the maximum values reachable by the indices.

(percentage of nodes changing allegiance to modules) with the following values, chosen to simulate progressive variations of the community composition: 10, 30, 50, 70, and 100%.

The resulting networks present a variation only between the first and the second half of the layers, while within the two halves the community structure is stationary, to simulate the transition between two different tasks or two classes of subjects (e.g., healthy subjects vs. patients). We run the four algorithms again, and we performed an ANOVA for repeated measures using, as dependent variables, three different indices to capture different aspects of the performances:

I. Accuracy: To evaluate the algorithms' accuracy, we used the normalized mutual information (NMI_{acc}) defined as in "section Stationary Community Structure."
II. Dynamics: In networks with evolving community structure, it is also important to assess the rapidity with which the algorithms recognize the variation of the modules' composition. Thus, we defined and implemented an index that points out how much it takes for the algorithms, in terms of number of layers, to exactly detect the new structure. The index mathematically identifies the layer (l_{thr}) from which the NMI_{acc} (**Figure 2A**, upper panel)—which decreases in proximity of nL/2, where the community structure changes—becomes stable and enters a sort of plateau after the transition (**Figure 2A**, lower left panel). The idea is that the incremental ratio (IR) of the NMI_{acc} curve from nL/2 to nL will be positive until the algorithm goes to regime and null from that point on. Thus, we computed the IR, we smoothed it to avoid spurious peaks due to the noise, and we considered the sign to capture when it becomes zero (**Figure 2A**, lower right panel). We find the threshold layer through the formula:

$$l_{\text{thr}} \in \left[\frac{\text{nL}}{2}+1,\ \text{nL}\right] := \underset{l_{\text{thr}}}{\arg\max} \left(\frac{\sum_{l=\frac{\text{nL}}{2}+1}^{l_{\text{thr}}} \text{sign}(\text{IR}_{\text{smoothed}})}{\sum_{l=l_{\text{thr}}+1}^{\text{nL}} \text{sign}(\text{IR}_{\text{smoothed}})} \right) \quad (1)$$

It scans all the layers from nL/2 +1 to *nL*, and for each *l* it computes the ratio between the sum of this function $\text{sign}(\text{IR}_{\text{smoothed}})$ before and after *l*. Then, it takes as threshold the l_{thr} to which the maximum of this ratio corresponds. Ideally, at l_{thr}, the numerator is positive (i.e., before l_{thr}, the trend of NMI_{acc} is ascendant), and the denominator is equal to 0 (i.e., after l_{thr}, the trend of NMI_{acc} is stable), so that the argument is infinite—the maximum possible. Once l_{thr} is obtained, we normalized it for nL/2 to obtain an index that varies in the range [0, 1], independently of the values of nL considered. We will refer to this index as to Dyn_{ind}. The lower it is, the fastest are the algorithms in recovering the structure modification.
III. Global performance: In analogy to the previous analysis, we computed an index that summarizes the global performances of the algorithms, considering at the same time accuracy and dynamics. It is computed as explained in "section Stationary Community Structure," but here, instead of NMI_{stab}, we consider the complement to unity of Dyn_{ind}. We will refer to this index as GD_{ind}.

TABLE 1 | Results of the ANOVA test executed for the comparative analysis on networks with stationary community structure and graph density equal to 0.3.

	NMI_{acc}				NMI_{stab}				GS_{ind}			
	dof(b)	*dof*(w)	*F*	*p*	*dof*(b)	*dof*(w)	*F*	*p*	*dof*(b)	*dof*(w)	*F*	*p*
Alg	3	891	5393.2	$<10^{-4}$	2	594	13096	$<10^{-4}$	3	891	10549	$<10^{-4}$
No	2	594	9110.4	$<10^{-4}$	2	594	7458.2	$<10^{-4}$	2	594	9392.2	$<10^{-4}$
nL	3	891	1481	$<10^{-4}$	3	891	129.87	$<10^{-4}$	3	891	1427.1	$<10^{-4}$
CN	2	297	473.31	$<10^{-4}$	2	297	163.81	$<10^{-4}$	2	297	420.19	$<10^{-4}$
Alg*no	6	1782	844.84	$<10^{-4}$	4	1188	2544.1	$<10^{-4}$	6	1782	1752.3	$<10^{-4}$
Alg*nL	9	2673	476.30	$<10^{-4}$	6	1782	54.923	$<10^{-4}$	9	2673	392.78	$<10^{-4}$
Alg*CN	6	891	75.997	$<10^{-4}$	4	594	580.84	$<10^{-4}$	6	891	28.266	$<10^{-4}$
Alg*no*nL	18	5346	163.8	$<10^{-4}$	12	3564	5.6138	$<10^{-4}$	18	5346	143.14	$<10^{-4}$
Alg*no*CN	12	1782	115.89	$<10^{-4}$	8	1188	174.06	$<10^{-4}$	12	1782	170.10	$<10^{-4}$
Alg*nL*CN	18	2673	56.64	$<10^{-4}$	12	1782	14.881	$<10^{-4}$	18	2673	51.239	$<10^{-4}$
Alg*no*nL*CN	36	5346	36.189	$<10^{-4}$	24	3564	3.1725	$<10^{-4}$	36	5346	29.976	$<10^{-4}$

For each considered index (dependent variables of the test) we report the degrees of freedom (dof), F, and p-values relative to single factors and the interactions among them.

In the case of evolving communities also, we performed a preliminary analysis to determine the optimal setting of the parameters ω and λ for the algorithms genLouvain and FacetNet to be used in the comparative analysis. The results of this test can be found in the **Supplementary Material**, sections 1 and 2. It is worth to note that the values of ω and λ selected for the evolving community structure are different from those resulting from the study on stationary community structure.

Multilayer Community Detection on Rest CE/OE EEG Brain Networks

For the purpose of validating the results of the simulation studies, we tested the algorithms in real EEG brain networks with features analogous to those investigated in the simulations, relative to a simple and controlled condition.

EEG data have been recorded and amplified by a commercial EEG system (BrainAmp, Brainproducts GmbH, Germany) using 61 electrodes (according to the extended 10–20 International System), with reference attached to the forehead and sampling frequency of 250 Hz, in a healthy subject (female, 33 years old) during rest with closed eyes (CE) and open eyes (OE). The subject gave informed consent prior to her participation, and the experiment was approved by the local ethics committee before the data acquisition started. Data were acquired at the Neuroelectrical Imaging and BCI Laboratory at IRCCS Fondazione Santa Lucia in Rome. The session was composed of 26 trials of 200 s each. In the first 100 s, the subject was asked to keep her eyes closed (task 1—CE), while in the last 100 s she was asked to keep her eyes open (task 2—OE). We pre-processed the data through band-pass filtering (1–45 Hz) and segmentation in 2-s epochs. The data were visually inspected to exclude the presence of artifacts. For each segment, we estimated brain functional connectivity through partial directed coherence (Baccalá and Sameshima, 2001; Astolfi et al., 2006), a spectral estimator based on Granger causality which provides an estimation of the network for each frequency point. We then mediated the estimations in four EEG frequency bands, defined according to individual alpha frequency (IAF) (Klimesch, 1999) (IAF = 10 Hz), focusing in the alpha range (IAF-2, IAF+2), as of interest for resting state (Karbowski, 1990; Niedermeyer, 1997; Compston, 2010). We assessed the significance of the connections through the asymptotic statistics (Takahashi et al., 2007; Toppi et al., 2016).

For each of the two tasks, we obtained 50 {200 s/[2 s (epoch) * 2 (tasks)]} binary networks of dimension 61 × 61. Then, we selected nL/2 layers from task 1 (CE) and nL/2 from task 2 (OE) and concatenated them so as to obtain four multilayer networks under different conditions of nL, like in the simulations. The obtained networks were sized 61ch*61ch*(2, 10, 50, 100) nL. Finally, we run all the algorithms 100 times on the four multilayer networks to take into account their stochastic nature, which implies that they might provide (slightly) different partitions even if applied to the same network. In the simulation studies, this issue was addressed as we perform an ANOVA test for repeated measures, which implies that for each combination of the parameters we compute the community detection several times.

RESULTS

Simulation Studies for Algorithm Comparison

Algorithm Comparison in Networks With Stationary Community Structure

In **Table 1**, we reported the results of the ANOVA comparative analysis made by exploiting simulated multilayer networks with stationary community structure and graph density equal to 0.3. Analogous results have been obtained, setting the graph density to the lower level, $D = 0.1$, and this can be found in the **Supplementary Material**, section 4.

The related plot of means are reported in **Figure 3**, where the performances of the algorithms in terms of accuracy (NMI_{acc}), stability (NMI_{stab}), and both (GS_{ind}) are shown as the number of clusters (CN), the level of noise (n), and the number of

layers (nL) changed. For the sake of clarity, in each panel of **Figure 3**, we report the performances of the algorithms with respect to one factor, irrespective of the other two. In the **Supplementary Material**, section 3, the same results are reported extensively, and we can observe algorithm performances for each combination of the three ANOVA factors.

As for the accuracy (**Figure 3**, first row), all the algorithms have performance that is inversely proportional to the level of noise and directly proportional to the number of clusters simulated in the network. However, in noisy networks (no = 50%), genLouvain and FacetNet show an improvement of accuracy as the number of layers increases, above all if CN >2. In particular, genLouvain reaches almost the same level of accuracy in noisy and non-noisy networks, if nL $\geq$ 10 (see **Supplementary Figure 9**). On the contrary, as expected, the accuracy of ModStat is not affected by the number of layers, as it considers each slice of the network independently. Compared with the other algorithms, genLouvain displays a high level of accuracy in most combinations of noise, cluster number, and number of layers. The only exceptions are the case of low cluster number and low noise [CN = 2, no = 10%, nL = (2, 10, 50, 100)] in which ModStat has higher NMI_{acc} values for every value of nL.

Regarding the analysis of stability (**Figure 3**, second row), namely, the algorithms' capability to recover a stable partition across the layers of the network, the algorithm with the highest performance is genLouvain for each combination of the ANOVA factors. In fact, it always reaches the optimal value of NMI_{stab} despite the level of noise, number of clusters, and number of layers. For this reason, in this case, we excluded it from the ANOVA, as its NMI_{stab} distribution is not normal. On the contrary, the other algorithms are more sensitive to the ANOVA factors, especially to the level of noise and the number of clusters. The algorithm ModStat shows high values of NMI_{stab} (close to 1) in networks with low noise (no = 10%), while its performances decrease with higher noise levels. Overall, FacetNet displays high performances, with NMIstab >0.8 for each combination of the factors, while for DynMoga, the results show $NMI_{stab} < 0.6$ in every condition.

The evaluation of the global performances summarizes what is observed so far (**Figure 3**, third row).

In general, the results of ANOVA together with Tukey's *post-hoc* tests show all the algorithms having significantly higher performances in networks with low level of noise and high number of clusters. Overall, the figures show genLouvain outperforming the other algorithms.

Algorithm Comparison in Networks With Evolving Community Structure

In **Table 2**, we report the results of the comparative analysis made to test the algorithms on multilayer networks with evolving community structure, with density equal to 0.3 and cluster numbers unchanged. We observed analogous results in networks with lower density, $D = 0.1$, and increasing/decreasing cluster numbers, and we report them in the **Supplementary Material**, sections 4 and 5.

In **Figure 4**, we represent the performances of the algorithms in terms of accuracy (NMI_{acc}), dynamics (Dyn_{ind}), and both (GD_{ind}) as a function of the number of clusters (CN), the level of noise (no), the number of layers (nL), and the percentage of nodes changing modules (p) change. As in the previous study, to have more clear and informative representation of the results, in each panel of **Figure 4**, we report the performances of the algorithms with respect to one factor, irrespective of the other three. In the **Supplementary Material**, section 3, we reported the extensive results.

Regarding the accuracy, we show in the first row of **Figure 4** the behavior of the algorithms with different levels of noise and number of layers. With a low level of noise, all the algorithms show a high accuracy in terms of NMI_{acc}, regardless of the number of layers, while as the noise increases, there is a loss of accuracy. However, if nL $\geq$ 10, both genLouvain and FacetNet have a significant improvement of accuracy. All the algorithms are more accurate when applied on networks with CN $\geq$ 2, above all if nL $\geq$ 10. The percentage of nodes that change allegiance to modules does not substantially affect the accuracy of the algorithms. However, FacetNet and DynMoga show a little increase of performances when pn increases (see also **Supplementary Figure 11**), meaning that they can easily detect big changes. Overall, genLouvain has the highest NMI_{acc} values for each combination of the factors under analysis. The only exception is when CN = 2 and nL = 2, in which ModStat shows higher NMI_{acc} values.

As for the evaluation of the algorithm's dynamic (**Figure 4**, second row), we only considered the performances of genLouvain, DynMoga, and FacetNet. Considering also ModStat would not be meaningful, as it addresses each layer independently. Moreover, we considered only values of nL $\geq$ 2. GenLouvain displays the lowest Dyn_{ind} values for each combination of the factors under analysis, no, nL, CN, and p, meaning that it is the fastest in identifying changes of the community structure. Overall, the rapidity of the algorithms is directly proportional to the number of layers and the number of clusters while being inversely proportional to the noise level.

Finally, the global index (**Figure 4**, third row) confirms what was shown with the previous indices. It suggests that the factors that have the greatest influence on the algorithms' performances are the level of noise and the number of layers: an increase of their value provokes, respectively, a breakdown and a boost of the performances. The number of clusters is also proportional to the algorithms' performances, while the percentage of nodes that change a community does not substantially affect their behavior. The most sensitive to the network's features is genLouvain, which, in the comparative analysis, is the outperforming one, while DynMoga is globally the less sensitive.

The results of ANOVA together with Tukey's *post-hoc* tests show all the algorithms having significantly higher performances in networks with a low level of noise and a high number of clusters. In reverse, the factor percentage of nodes moved (pn) does not dramatically affect the global performances of the algorithms under analysis, meaning that the algorithms can detect small as well as big changes in community structure.

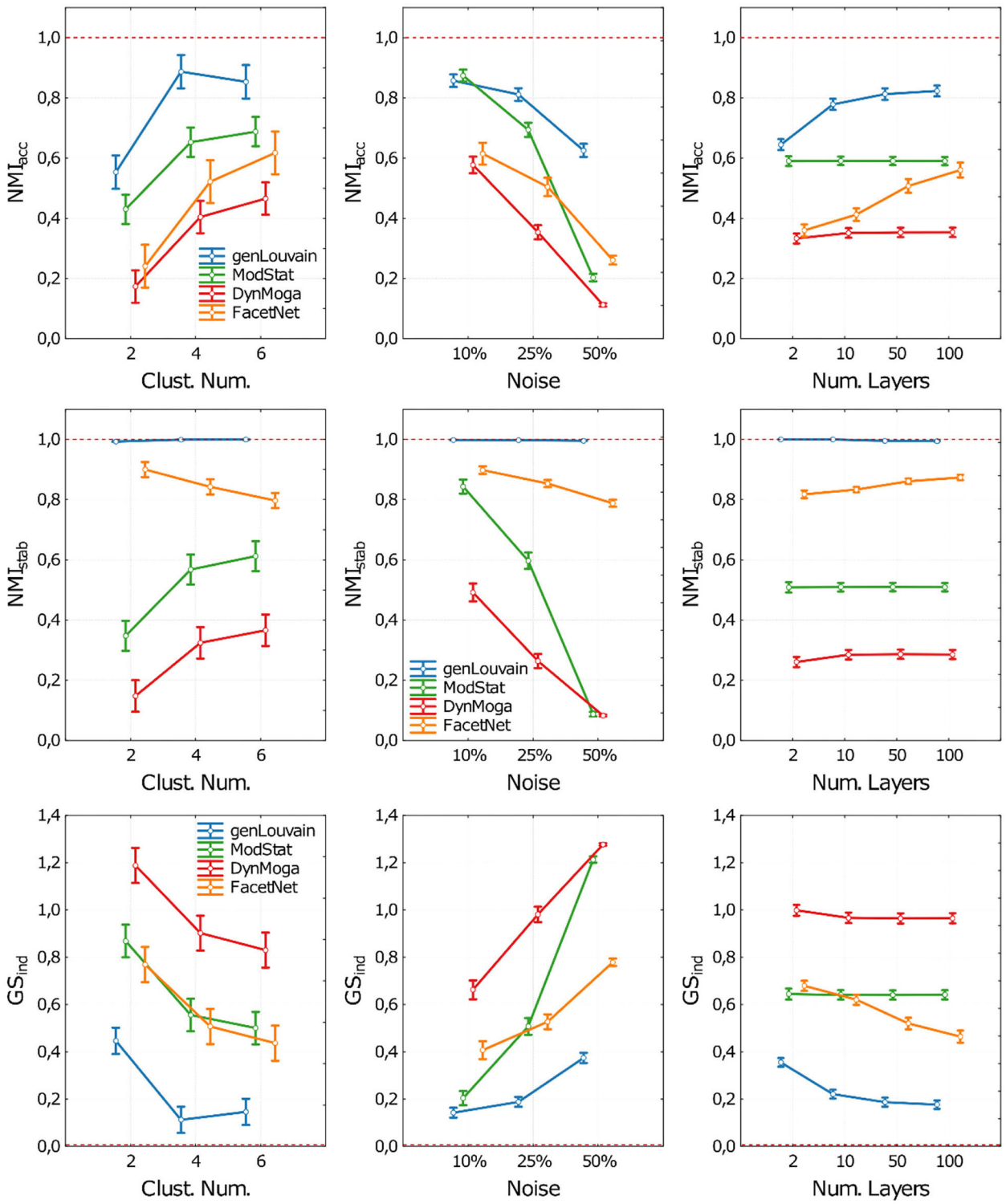


FIGURE 3 | Plot of means and standard deviations of the three indices used to execute the comparative analysis on networks with stationary community structure. Each row of the figure corresponds to one index (NMI_{acc}, NMI_{stab}, GS_{ind}). For each index we report three panels where we show the algorithms' performances with respect to the Clusters Number (first column), Noise level (second column), and number of network's layer (third column). Algorithms are identified through a color code (blue-genLouvain, green-ModStat, red-DynMoga, orange-FacetNet). In each panel we can see how the performance of the algorithms varies according the values the ANOVA factors and which algorithm reaches highest performances, in terms of accuracy (NMI_{acc}), stability (NMI_{stab}) or both (GS_{ind}). The optimal performances are indicated though a red dotted line.

TABLE 2 | Results of the ANOVA test executed for the comparative analysis on networks with evolving community structure and graph density equal to 0.3.

	NMI_{acc}				Dyn_{ind}				GD_{ind}			
	dof(b)	*dof(w)*	*F*	*p*	*dof(b)*	*dof(w)*	*F*	*p*	*dof(b)*	*dof(w)*	*F*	*p*
Alg	3	2241	122200	$<10^{-4}$	2	1494	2932.5	$<10^{-4}$	2	1494	36095	$<10^{-4}$
No	2	1494	255900	$<10^{-4}$	2	1494	255.81	$<10^{-4}$	2	1494	23219	$<10^{-4}$
nL	3	2241	36813	$<10^{-4}$	2	1494	2577.4	$<10^{-4}$	2	1494	6071.1	$<10^{-4}$
p	4	2988	37.25	$<10^{-4}$	4	2988	7.81	$<10^{-4}$	4	2988	16.17	$<10^{-4}$
CN	2	747	14392	$<10^{-4}$	2	747	477.02	$<10^{-4}$	2	747	11828	$<10^{-4}$
Alg*no	6	4482	18575	$<10^{-4}$	4	2988	162.4	$<10^{-4}$	4	2988	347.9	$<10^{-4}$
Alg*nL	9	6723	12252	$<10^{-4}$	4	2988	101.44	$<10^{-4}$	4	2988	946.99	$<10^{-4}$
Alg*p	12	8964	289.11	$<10^{-4}$	8	5976	4.32	$<10^{-4}$	8	5976	6.81	$<10^{-4}$
Alg*CN	6	2241	425.4	$<10^{-4}$	4	1494	341.71	$<10^{-4}$	4	1494	475.52	$<10^{-4}$
Alg*no*nL	18	13446	4514.8	$<10^{-4}$	8	5976	7.11	$<10^{-4}$	8	5976	91.28	$<10^{-4}$
Alg*no*p	24	17928	46.64	$<10^{-4}$	16	11952	2.31	0.002	16	11952	5.43	$<10^{-4}$
Alg*no*CN	12	4482	3301.2	$<10^{-4}$	8	2988	14.24	$<10^{-4}$	8	2988	224.63	$<10^{-4}$
Alg*nL*p	36	26892	33.27	$<10^{-4}$	16	11952	3.25	$<10^{-4}$	16	11952	1.19	*0.262*
Alg*nL*CN	18	6723	856.5	$<10^{-4}$	8	2988	17.01	$<10^{-4}$	8	2988	5.56	$<10^{-4}$
Alg*p*CN	24	8964	308.26	$<10^{-4}$	16	5976	6.56	$<10^{-4}$	16	5976	13.88	$<10^{-4}$
Alg*no*nL*CN*p	144	53784	44.58	$<10^{-4}$	64	23904	1.41	0.017	64	23904	1.99	$<10^{-4}$

For each considered index (dependent variables of the test) we report the degrees of freedom (dof), F, and p-values relative to single factors and the interactions among them. Statistically non significant values have been reported with italic characters.

Multilayer Community Detection on Rest CE/OE EEG Brain Networks

In this section, we present the results of the application of the four algorithms under analysis to EEG networks subtending CE and OE resting state in alpha band. In **Figure 5**, we report the trend of the normalized mutual information computed between the output of the algorithms across consecutive layers for all the estimated networks with nL = (2, 10, 50, 100). The black dashed line divides the CE state from the OE. Ideally, one would expect high and stable values of NMI in the two halves and a collapse of the index near to the dashed line. That would mean that the algorithm is able to extract two steady partitions in the two conditions which are different from each other and to detect the transition. In the case of nL = 2 instead, a value of NMI inferior to 1 is desirable, hopefully low. In line with the simulation study, genLouvain, with the resolution parameter set through the guidelines given by the preliminary analysis, is the algorithm that better approximates this behavior. Both genLouvain and FacetNet show higher stability and maximum discriminability between the two conditions when the number of layers increases. As also proven in the previous section, between the two, FacetNet results to be slower in detecting the change between the two tasks, and within each task, it is less stable and thus less accurate in detecting the community structure during CE or OE. DynMoga shows a mild increment of performance with a higher number of layers, even if they are lower compared to the other algorithms. Conversely, ModStat behaves independently from the number of layers, as it works on a single-layer level.

We finally show in **Figure 6A** how these multilayer networks are parsed in clusters by genLouvain, which is the most advisable algorithm after our simulations. The figure reports, as representative, one of the 100 repetitions computed which, as indicated by the narrow confidence interval in **Figure 5**, are very much similar among them. The partitions are consistent across all the levels of nL, and in **Figures 6B,C**, we show the partitioning of the network for each condition, CE and OE in the case in which nL = 50. During the CE phase, there is a cluster that involves the occipital electrodes and two clusters composed by electrodes from the left and the right hemisphere, respectively. During the OE phase, the first cluster is dismembered between the left and the right hemispheres, and one can observe the modules becoming more hemisphere specific. Such results are observed both in the EEG network made of nL = 2 and in the ones with nL > 2, with different ω-values properly chosen according to the preliminary analysis (**Supplementary Material**, section 1).

DISCUSSION

This work aims to provide guidelines for the use of multilayer algorithms of community detection on EEG-based brain multilayer networks. For this purpose, we tested and compared them on an artificial dataset that spans a wide range of network features.

We obtained our dataset by defining and implementing a tool able to generate pseudo-random multilayer networks with community structure. Among all the definitions of communities, we are considering the assortative one, namely, communities made of groups of nodes densely connected with each other and poorly connected with the other nodes of the network. In fact, previous findings have shown that this is a very plausible way with which nodes organize themselves in brain networks (Bertolero et al., 2015; Sporns and Betzel, 2016). With respect to the tools previously available in the literature

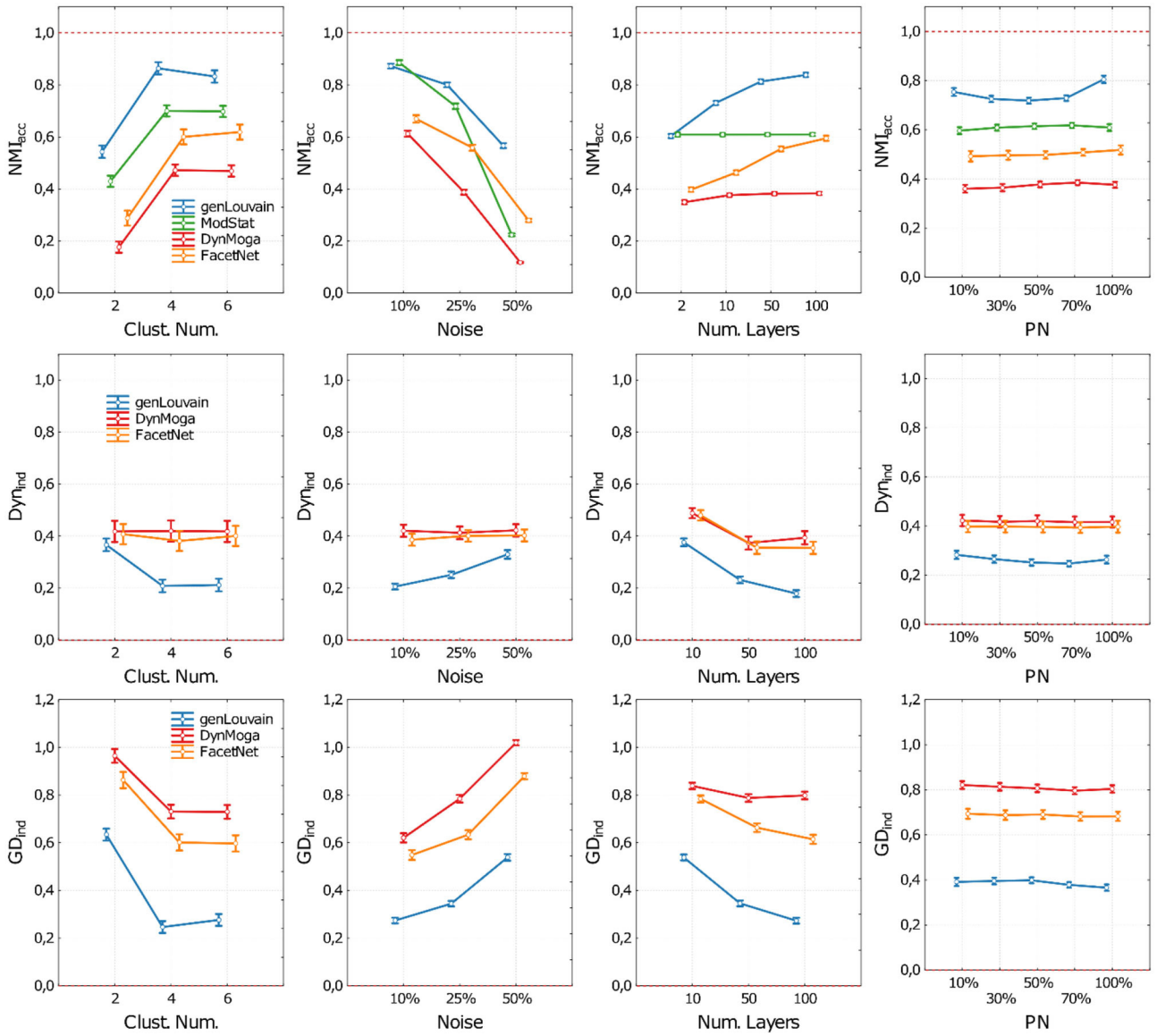


FIGURE 4 | Plot of means and standard deviations of the three indices used to execute the comparative analysis on networks with evolving community structure. Each row of the figure corresponds to one index (NMI_{acc}, Dyn_{ind}, and GD_{ind}). For each index, we report four panels where we show the algorithms' performances with respect to the cluster number (first column), noise level (second column), number of network's layer (third column), and percentage of nodes changing module (fourth column). Algorithms are identified through a color code (blue—genLouvain, green—ModStat, red—DynMoga, orange—FacetNet). In each panel, we can see how the performance of the algorithms varies according to the values of the ANOVA factors and which algorithm reaches highest performances in terms of accuracy (NMI_{acc}), stability (Dyn_{ind}), or both (GD_{ind}). The optimal performances are indicated though a red dotted line.

(Lin et al., 2008; Kim and Han, 2009; Granell et al., 2015), we conceived this generator so that it can take as input as many settable parameters as possible; thus, we could be able to systematically test the algorithm under a variety of conditions and to evaluate the dependence of the performances on different factors. Specifically, a potential user can set as input the number of nodes, graph density, number of communities, ratio between intra-cluster and inter-cluster density, level of noise of the network, percentage of nodes shifting community across layers, and if the number of clusters diminishes, increases, or remains unchanged across layers. Thus, the main advantage of this generator is its flexibility in creating networks with different properties.

To test the algorithms, we simulated multilayer networks with features that are observable in brain functional networks estimated from EEG signals. We then considered two scenarios, one in which the community structure is stationary, the other is when it shows an evolution across the layers. While previous studies essentially focused on the second case, both cases are of interest in the neuroscience field.

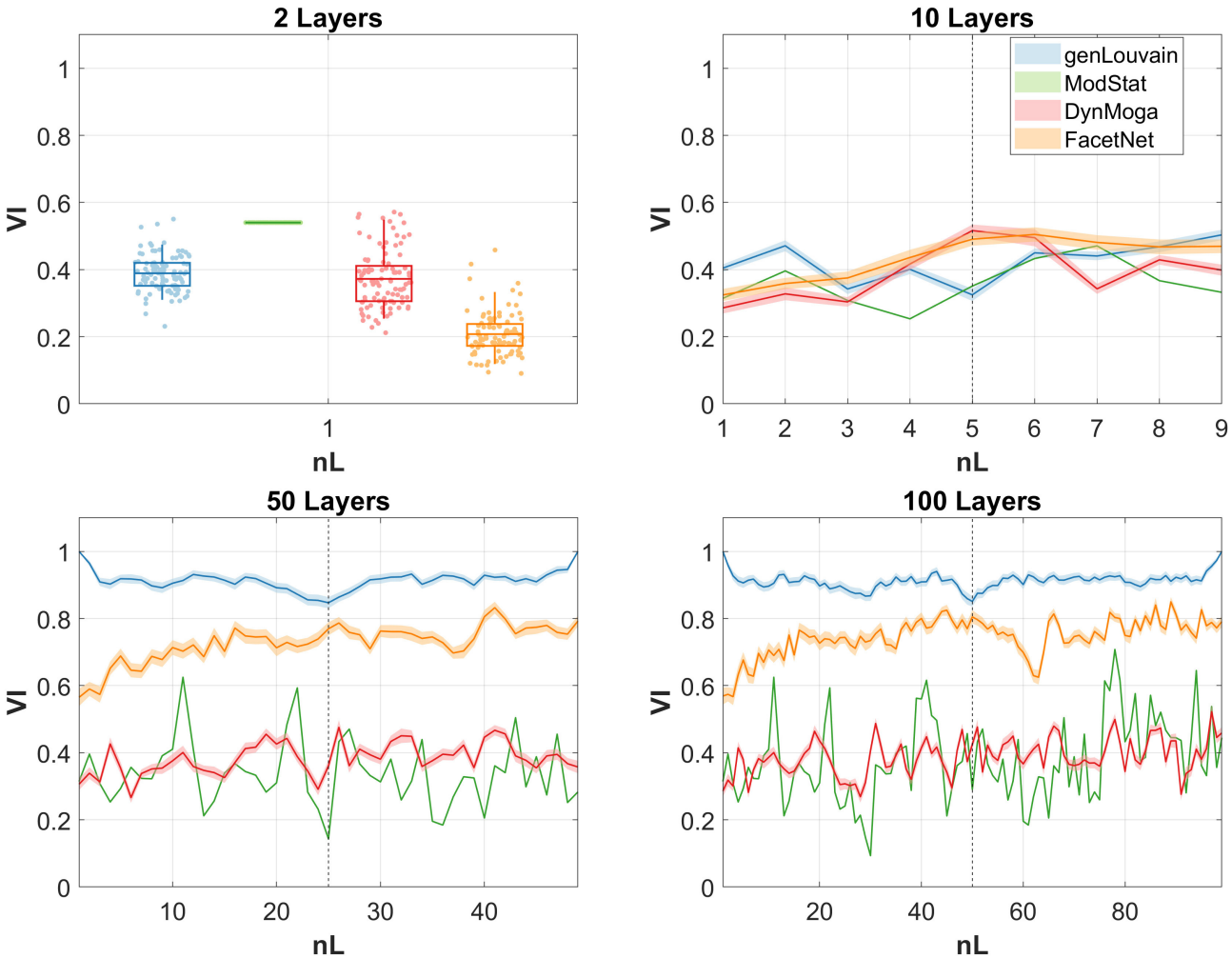


FIGURE 5 | Normalized mutual information (NMI) computed between the output of the algorithms, identified with a color code, at consecutive layers of the multilayer network. As we run the algorithms 100 times, we report the means of the NMI at each snapshot, bounded by the confidence interval, represented with a lighter color. Each graph corresponds to one of the four networks extracted with different numbers of layers.

In the first scenario, we aim to extract homogeneous community partitions among a certain number of noisy layers, and this could be useful when layers model either snapshots of a task in which the brain connectivity pattern is supposed to be stationary (with the only variations due to the noise) or groups of subjects with the same features. In this case, we seek for algorithms able to keep as stable as possible despite the presence of noise, one that, in an EEG-based network, could arise because of the variability of the signals, of the low SNR, or of the error intrinsic in any connectivity estimation procedure.

In the second scenario, we want our algorithm to track small and large variations in an evolving community structure. Examples of this scenario include when we want to discover the evolution of the modular organization underpinning cognitive functions causing time-varying connectivity patterns or relative to heterogeneous groups of people (e.g., healthy subjects and clinical cohorts). Here the capability of the methods to track the network's dynamics is the main feature we seek for.

The results of our extensive simulation studies show that all the algorithms are sensitive to the network features that we simulated. As expected, their performances decrease as the level of noise simulated increases because the community structure gets less and less clear. Moreover, their ability to exactly recover the imposed community structure diminishes when such structure is made of few clusters. This could happen because all the algorithms were introduced in a context other than neuroscience, where networks present thousands of nodes and many more clusters. In the case of time-varying communities, our analysis suggests that the proportion with which the clusters reconfigure does not affect consistently the algorithms' performances, except in a few cases in which, intuitively, the more it changes, the easiest the algorithms detect the variation. The genLouvain and, partially, the FacetNet algorithms were

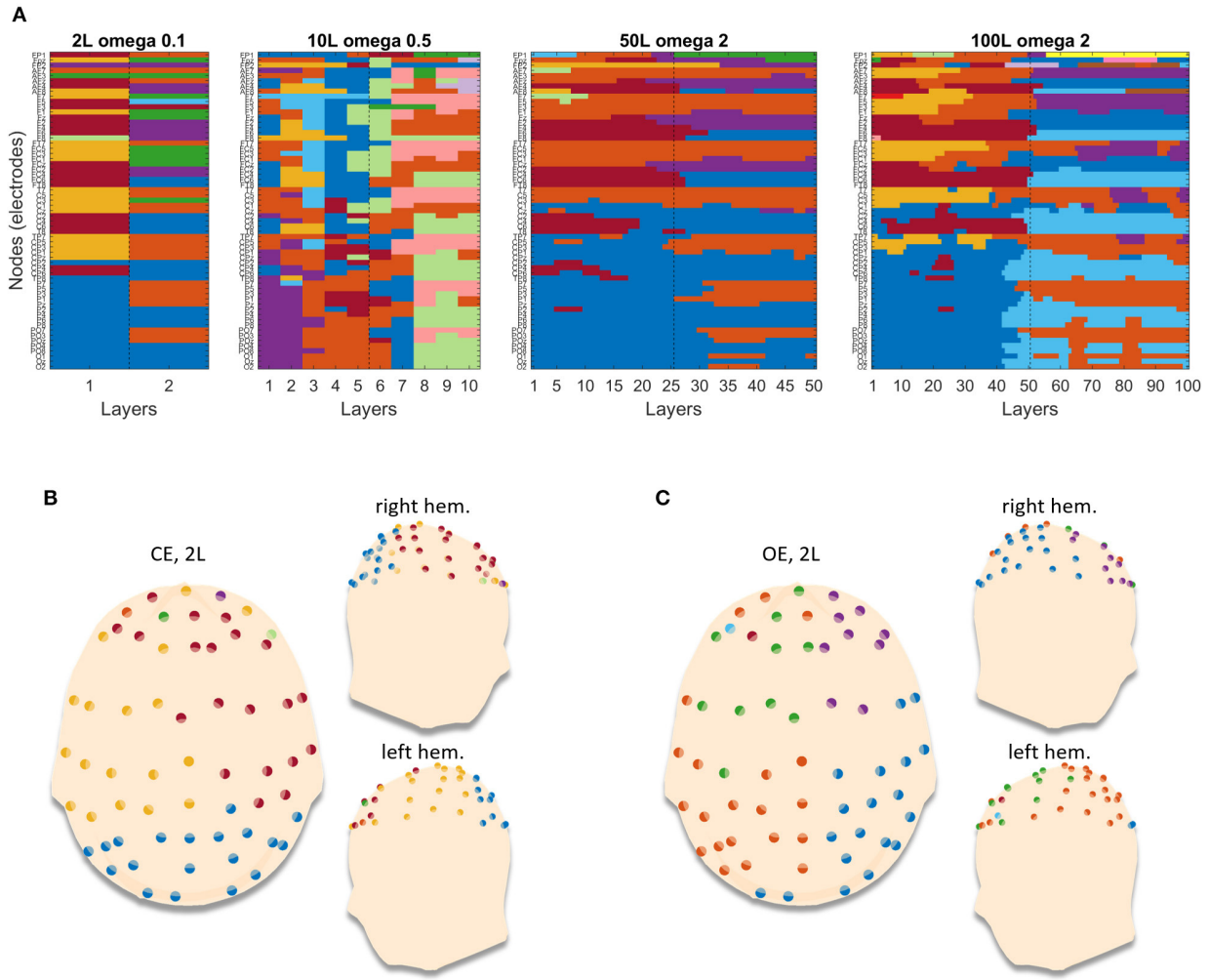


FIGURE 6 | Example of partitions obtained by running genLouvain on the EEG brain networks. **(A)** The four images stand for the four networks with different numbers of layers. Each image has on the y-axis the nodes (channels) and on the x-axis the layers, and the cluster's membership is represented through colors. **(B,C)** Reported projections of the detected communities on a 3D model of scalp for the two conditions, closed eyes and open eyes, respectively. In each panel, the 3D model is seen from above, with the nose pointing to the upper side of the page, and laterally. The dots are the 61 electrodes grouped into clusters and displayed with different colors.

shown to be able to compensate for the presence of noise as the number of layers increases, returning more and more stable and accurate partitions in both scenarios explored here. Overall, genLouvain, which is based on multilayer modularity optimization, outperforms the others in most conditions. It has the best performances in most conditions. A single-layer modularity approach is also appropriate in case of few layers and low percentage of noise. FacetNet shows intermediate performances, as it seems to be able to mitigate the effect of a high level of noise when it has a high number of layers to work with.

Our work is not the first one attempting to address the issue of multilayer clustering algorithms' performances. In Silva et al. (2016) and Schmidt et al. (2018), the authors propose analysis with the same purpose. However, in the former, the focus is only on algorithms based on evolutionary clustering, which have been tested in a simple synthetic network and in three real networks not related to neuroscience. In the latter, the authors tested two approaches based on consensus clustering on a synthetic network. Such testing still has no statistical validity, as the two approaches have only been tested in one network, even if more realistic and closer to those experimentally estimated from EEG signals. Moreover, their main purpose was to exploit multilayer clustering approaches to threshold fully connected networks. For this reason, they introduced two new community detection algorithms, rather than considering the well-established multilayer optimization of modularity, which has already been proven to provide interesting insights in brain functioning and organization, as in Bassett et al. (2011). Another testing of the clustering algorithms has been done in Bazzi et al. (2020) on benchmark networks similar to those proposed here. However, the main focus of that work was on introducing a generative model for

multilayer networks; therefore, the algorithms' performances were evaluated by only varying the coupling across layers. Here we performed a more comprehensive analysis: starting from preliminary analysis made to properly use the algorithms in different conditions determined by the network's properties, we compared the algorithms' behavior by systematically varying a set of the network's features, like cluster number, level of noise, coupling across layers, number of layers and network's density.

After having tested the algorithms on artificial networks, we applied them to a time-varying network obtained from a real EEG dataset under controlled conditions, from which we estimated multilayer networks, including a transition from one condition to the other. The experimental design has precise features designed to obtain accurate multilayer brain networks reflecting those simulated in the methodological analysis. Data was acquired from an adult healthy subject during a simple task, the resting state, composed by two distinct phases: OE and CE. The choice of taking a healthy subject rather than a patient spared us from making hard hypotheses on the underlying brain network. The same applies for the choice of the resting state, instead of more complicated cognitive or motor tasks, which would have required further hypotheses. At the same time, the two distinct consecutive phases (OE–CE) of the resting state guarantee a change in brain activity and, consequently, in brain connectivity and brain network, which is what we analyzed in the simulation study. Moreover, we established the number of EEG channels, the length of the trials, as well as their numerosity prior to the acquisition in order to obtain networks with the exact number of nodes and layers used in the simulation study. The data so collected have specific peculiarities that make it suitable for the validation of the algorithms' analysis. By applying the four algorithms on the obtained EEG multilayer networks, we could evaluate if, and how fast, such algorithms were able to recognize the two distinct phases. The results are consistent with what were found in simulations. GenLouvain outperforms the other algorithms by detecting stable communities within each condition and differences in the partitioning between the two conditions in the neighborhood of the transition. The topological representation of the community organization underlying the two conditions, shown in **Figure 6**, indicates that the closed eyes condition gives rise to a cluster of occipital electrodes which, during the open eyes condition, splits into two clusters, one for each hemisphere, and generally all the clusters become more hemisphere specific. This result is physiologically plausible. In fact, during the resting state at closed eyes, there is an increase of alpha rhythm associated with circuits originated in the occipital region, which disappear if the subjects open their eyes.

The purpose of the application to an EEG dataset was three-fold. First, it confirms the results obtained with the simulation studies. Moreover, as an indirect consequence, it validates the goodness of our model and of the generator with which we tested the algorithms, paving the way to its use in other studies. Finally, it supports the applicability of multilayer community detection to EEG-based brain networks. In fact, while several studies already showed the potentiality of employing graph theory instruments in EEG-derived networks to investigate brain functioning (Micheloyannis et al., 2006; Fallani et al., 2010; Toppi et al., 2012; Petti et al., 2016; Pichiorri et al., 2018), community detection and multilayer tools have been scarcely used in the electrophysiological context so far, despite promising results like those reported in a recent work (Kabbara et al., 2021) where authors investigated the modular structure of multilayer resting state networks with single-layer tools. Most of the studies on brain communities (e.g., Bassett et al., 2011; Betzel et al., 2014, 2017; Wig, 2017; Puxeddu et al., 2020) are conducted on brain networks obtained from functional magnetic resonance images (fMRI). fMRI data have the privilege of having a good spatial resolution. However, fMRI networks make a coarse assumption of stationarity. In fact, the BOLD signal peaks seconds after the neuronal activity, violating most of the brain information processing timescale, which ranges 100 ms (Park and Friston, 2013). EEG signals instead have a great temporal resolution, which is suited to the study of time-varying phenomena through a multilayer topological analysis. One could also think of invasive methods to obtain signals that are both spatially and temporally accurate. However, the invasiveness provides a strong limitation to the applicability of such an approach. Moreover, it currently allows to acquire data from a limited portion of the brain, failing to provide large-scale networks suited for an analysis of the communities which sustain the structure of most human brain functions. For these reasons, EEG-based brain networks represent a fair compromise between spatial and temporal resolution, and the study of their community structure can provide important insights into the brain dynamical organization.

After having studied the best practices and verified community detection applicability to multilayer EEG networks in a controlled case, future efforts will be put on studying how community structure evolves during tasks that elicit a dynamic configuration of the brain network. For this purpose, richer open EEG datasets could be investigated (i.e., van der Meer et al., 2016; Wong et al., 2018; Artoni et al., 2019), focused on resting state as well as more complex tasks, like working memory or auditory attention. This might provide physiological insights into brain functional organizational principles underlying cognitive functions.

Future investigations might also include the use of the toolbox that we provided to extend our analysis to other cases. For example, similar analysis could be performed in generating networks with a higher number of nodes and a higher number of clusters. Ultimately, this work could be useful in a cross-disciplinary way, regardless of our specific attention to EEG-based brain networks. The guidelines that we provide can be applied to every network with the simulated features, where community structure is supposed to be assortative.

CONCLUSIONS

In conclusion, this work operated an extensive and systematic comparative analysis among multilayer community detection algorithms. We selected three different clustering approaches and four algorithms based on single-layer modularity, multilayer

modularity, and evolutionary clustering. We tested them on artificial networks with modules generated through a toolbox defined for this purpose, which allows us to set most of the parameters characterizing the graphs that we systematically varied in a range typical of EEG-based brain networks to provide a comprehensive analysis of the algorithms. Specifically, we tested the algorithms' ability to recover stable and dynamic partitions out of multilayer networks with stationary and evolving community structure, respectively. Our results suggest that the performance of the algorithms depends on the network features, such as number of clusters, number of layers, and level of noise in the network. From the simulations, the community detection algorithm based on the optimization of the multilayer formulation of modularity turned out to be the most suitable within the explored conditions. The application of the algorithms to real networks estimated from EEG signals confirms these results and proves the applicability of such algorithms to electrophysiological data.

DATA AVAILABILITY STATEMENT

The raw data supporting the conclusions of this article will be made available by the authors, without undue reservation.

ETHICS STATEMENT

The studies involving human participants were reviewed and approved by PROT. CE/PROG.685 on 13/06/2018. The participants provided their written informed consent to participate in this study.

AUTHOR CONTRIBUTIONS

MGP designed the study, implemented the codes, run the analysis, and wrote the original draft. MP designed the study and supervised the work. LA designed the study, supervised the work and provided funding. All authors revised and edited the manuscript.

FUNDING

This study was partially supported by Progetto di Ateneo 2017–EMBRACING (RM11715C82606455), by Progetto di Ateneo 2018 (RP11816436CDA44C), by progetto di Ateneo 2019–(RM11916B88C3E2DE), by Stiftelsen Promobilia, Research Project DISCLOSE, by a BitBrain award (B2B Project), and by the Dipartimenti di eccellenza fund (MIUR).

ACKNOWLEDGMENTS

We would like to thank Dr. Donatella Mattia and the Neuroelectrical Imaging and BCI Laboratory of IRCCS Fondazione Santa Lucia in Rome for providing the facilities and supporting the EEG data collection.

SUPPLEMENTARY MATERIAL

The Supplementary Material for this article can be found online at: https://www.frontiersin.org/articles/10.3389/fnsys.2021.624183/full#supplementary-material

REFERENCES

Ahmadlou, M., and Adeli, H. (2011). Functional community analysis of brain: a new approach for EEG-based investigation of the brain pathology. *NeuroImage* 58, 401–408. doi: 10.1016/j.neuroimage.2011.04.070

Artoni, F., Delorme, A., and Makeig, S. (2019). A visual working memory dataset collection with bootstrap independent component analysis for comparison of electroencephalographic preprocessing pipelines. *Data Brief*. 22, 787–793. doi: 10.1016/j.dib.2018.12.022

Astolfi, L., Cincotti, F., Mattia, D., Marciani, M. G., Baccalà, L. A., de Vico Fallani, F. et al. (2006). Assessing cortical functional connectivity by partial directed coherence: simulations and application to real data. *IEEE Trans. Biomed. Eng.* 53, 1802–1812. doi: 10.1109/TBME.2006.873692

Astolfi, L., Cincotti, F., Mattia, D., Marciani, M. G., Baccala, L. A., de Vico Fallani, F., et al. (2007). Comparison of different cortical connectivity estimators for high-resolution EEG recordings. *Human Brain Mapp.* 28, 143–157. doi: 10.1002/hbm.20263

Baccalá, L. A., and Sameshima, K. (2001). Partial directed coherence: a new concept in neural structure determination. *Biol. Cybern.* 84, 463–474. doi: 10.1007/PL00007990

Bassett, D. S., and Sporns, O. (2017). Network neuroscience. *Nat. Neurosci.* 20, 353–364. doi: 10.1038/nn.4502

Bassett, D. S., Wymbs, N. F., Porter, M. A., Mucha, P. J., Carlson, J. M., and Grafton, S. T. (2011). Dynamic reconfiguration of human brain networks during learning. *Proc. Natl. Acad. Sci. U.S.A.* 108, 7641–7646. doi: 10.1073/pnas.1018985108

Bazzi, M., Jeub, L. G. S., Arenas, A., Howison, S. D., and Porter, M. A. (2020). A framework for the construction of generative models for mesoscale structure in multilayer networks. *Phys. Rev. Res.* 2:023100. doi: 10.1103/PhysRevResearch.2.023100

Bertolero, M. A., Yeo, B. T. T., and D'Esposito, M. (2015). The modular and integrative functional architecture of the human brain. *Proc. Natl. Acad. Sci. U.S.A.* 112, E6798–E6807. doi: 10.1073/pnas.1510619112

Betzel, R. F. (2021). *Community Detection in Network Neuroscience. arXiv:2011.06723 [q-bio], nov. 2020, Consultato: gen. 05, [In linea]*. Available online at: http://arxiv.org/abs/2011.06723 (accessed November 13, 2020).

Betzel, R. F., and Bassett, D. S. (2017). Multi-scale brain networks. *NeuroImage* 160, 73–83. doi: 10.1016/j.neuroimage.2016.11.006

Betzel, R. F., Byrge, L., He, Y., Goñi, J. X.-,Zuo, N., and Sporns, O. (2014). Changes in structural and functional connectivity among resting-state networks across the human lifespan. *NeuroImage* 102, 345–357. doi: 10.1016/j.neuroimage.2014.07.067

Betzel, R. F., Griffa, A., Avena-Koenigsberger, A., Goñi, J., Thiran, J., Hagmann, P., et al. (2013). Multi-scale community organization of the human structural connectome and its relationship with resting-state functional connectivity. *Netw. Sci.* 1, 353–373. doi: 10.1017/nws.2013.19

Betzel, R. F., Medaglia, J. D., Papadopoulos, L., Baum, G. L., Gur, R., Gur, R., et al. (2017). The modular organization of human anatomical brain networks: accounting for the cost of wiring. *Netw. Neurosci.* 1, 42–68. doi: 10.1162/NETN_a_00002

Blondel, V. D., Guillaume, J.-L., Lambiotte, R., and Lefebvre, E. (2008). Fast unfolding of communities in large networks. *J. Stat. Mech. Theory Exp.* 10008. doi: 10.1088/1742-5468/2008/10/P10008

Boccaletti, S., Latora, V., Moreno, Y., Chavez, M., and Hwang, D.-U. (2006). Complex networks: structure and dynamics. *Phys. Rep.* 424, 175–308. doi: 10.1016/j.physrep.2005.10.009

Chakrabarti, D., Kumar, R., and Tomkins, A. (2006). "Evolutionary clustering," in *Proceedings of the 12th ACM SIGKDD International Conference on Knowledge Discovery and Data Mining* (New York, NY), 554–560.

Chavez, M., Valencia, M., Navarro, V., Latora, V., and Martinerie, J. (2010). Functional modularity of background activities in normal and epileptic brain networks. *Phys. Rev. Lett.*, 104:118701. doi: 10.1103/PhysRevLett.104.118701

Compston, A. (2010). The Berger rhythm: potential changes from the occipital lobes in man, by Adrian, E. D., and Matthews, B. H. C. (From the Physiological Laboratory, Cambridge). Brain 1934: 57; 355–385. *Brain* 133, 3–6. doi: 10.1093/brain/awp324

Danon, L., Díaz-Guilera, A., Duch, J., and Arenas, A. (2005). Comparing community structure identification. *J. Stat. Mech.* 09008. doi: 10.1088/1742-5468/2005/09/P09008

De Domenico, M. (2017). Multilayer modeling and analysis of human brain networks. *Gigascience* 6, 1–8. doi: 10.1093/gigascience/gix004

Dong, W., Lepri, B., and (Sandy) Pentland, A. (2011). "Modeling the co-evolution of behaviors and social relationships using mobile phone data," in *Proceedings of the 10th International Conference on Mobile and Ubiquitous Multimedia* (New York, NY), 134–143.

Fallani, F. D. V., Costa Lda, F., Rodriguez, F. A., Astolfi, L., Vecchiato, G., Toppi, J., et al. (2010). A graph-theoretical approach in brain functional networks. Possible implications in EEG studies. *Nonlinear Biomed. Phys.* 4:S8. doi: 10.1186/1753-4631-4-S1-S8

Fisch, B. (1999). *Fisch and Spehlmann's EEG Primer, 3rd Edn*. Amsterdam: Elsevier. Available online at: https://www.elsevier.com/books/fisch-and-spehlmanns-eeg-primer/fisch/978-0-444-82148-5 (accessed July 11, 2019).

Folino, F., and Pizzuti, C. (2014). An evolutionary multiobjective approach for community discovery in dynamic networks. *IEEE Trans. Knowl. Data Eng.* 26, 1838–1852. doi: 10.1109/TKDE.2013.131

Girvan, M., and Newman, M. E. J. (2002). Community structure in social and biological networks. *Proc. Natl. Acad. Sci. U.S.A.* 99, 7821–7826. doi: 10.1073/pnas.122653799

Granell, C., Darst, R. K., Arenas, A., Fortunato, S., and Gómez, S. (2015). Benchmark model to assess community structure in evolving networks. *Phys. Rev. E* 92:012805. doi: 10.1103/PhysRevE.92.012805

Guimerà, R., and Amaral, L. A. N. (2005). Functional cartography of complex metabolic networks. *Nature* 433:895. doi: 10.1038/nature03288

He, B., Astolfi, L., Valdes-Sosa, P. A., Marinazzo, D., Palva, S., Benar, C. G., et al. (2019). Electrophysiological Brain Connectivity: Theory and Implementation. *IEEE Trans. Biomed. Eng.* 66, 2115–2137. doi: 10.1109/TBME.2019.2913928

Hutchison, R. M., Womelsdorf, T., Allen, E. A., Bandettini, P. A., Calhoun, V. D., Corbetta, M., et al. (2013). Dynamic functional connectivity: Promise, issues, and interpretations. *NeuroImage* 80, 360–378. doi: 10.1016/j.neuroimage.2013.05.079

Jeub, L. G. S., Bazzi, M., Jutla, I. S., and Mucha, P. J. (2019). *A Generalized Louvain Method for Community Detection Implemented in MATLAB*. Available online at: http://netwiki.amath.unc.edu/GenLouvain; https://github.com/GenLouvain/GenLouvain (accessed November 04, 2019).

Jirsa, V. K., and McIntosh, A. R. (2007). *Handbook of Brain Connectivity*. Berlin: Springer-Verlag.

Kabbara, A., Paban, V., and Hassan, M. (2021). The dynamic modular fingerprints of the human brain at rest. *NeuroImage* 227:117674. doi: 10.1016/j.neuroimage.2020.117674

Karbowski, K. (1990). Sixty years of clinical electroencephalography. *ENE* 30, 170–175. doi: 10.1159/000117338

Kim, M.-S., and Han, J. (2009). A particle-and-density based evolutionary clustering method for dynamic networks. *Proc. VLDB Endow.* 2, 622–633. doi: 10.14778/1687627.1687698

Klimesch, W. (1999). EEG alpha and theta oscillations reflect cognitive and memory performance: a review and analysis. *Brain Res. Rev.* 29, 169–195. doi: 10.1016/S0165-0173(98)00056-3

Lancichinetti, A., and Fortunato, S. (2009). Community detection algorithms: a comparative analysis. *Phys. Rev. E* 80:056117. doi: 10.1103/PhysRevE.80.056117

Leicht, E. A., and Newman, M. E. J. (2008). Community structure in directed networks. *Phys. Rev. Lett.* 100:118703. doi: 10.1103/PhysRevLett.100.118703

Lin, Y.-R., Chi, Y., Zhu, S., Sundaram, H., and Tseng, B. L. (2008). "Facetnet: a framework for analyzing communities and their evolutions in dynamic networks," in *Proceeding of the 17th International Conference on World Wide Web–WWW '08* (Beijing), 685.

Lin, Y.-R., Chi, Y., Zhu, S., Sundaram, H., and Tseng, B. L. (2009). Analyzing communities and their evolutions in dynamic social networks. *ACM Trans. Knowl. Discov. Data.* 3, 8.1–8.31. doi: 10.1145/1514888.1514891

Meunier, D., Lambiotte, R., and Bullmore, E. T. (2010). Modular and hierarchically modular organization of brain networks. *Front. Neurosci.* 4:200. doi: 10.3389/fnins.2010.00200

Micheloyannis, S., Pachou, E., Stam, C. J., Vourkas, M., Erimaki, S., and Tsirka, V. (2006). Using graph theoretical analysis of multi channel EEG to evaluate the neural efficiency hypothesis. *Neurosci. Lett.* 402, 273–277. doi: 10.1016/j.neulet.2006.04.006

Mucha, P. J., Richardson, T., Macon, K., Porter, M. A., and, Onnela, J.-P. (2010). Community structure in time-dependent, multiscale, and multiplex networks. *Science* 328, 876–878. doi: 10.1126/science.1184819

Muldoon, S. F., and Bassett, D. S. (2016). Network and multilayer network approaches to understanding human brain dynamics. *Philos. Sci.* 83, 710–720. doi: 10.1086/687857

Newman, M. (2003). The structure and function of complex networks. *SIAM Rev.* 45, 167–256. doi: 10.1137/S003614450342480

Newman, M. E. J. (2012). Communities, modules, and large-scale structure in networks. *Nat. Phys.* 8, 25–31. doi: 10.1038/nphys2162

Newman, M. E. J., and Girvan, M. (2004). Finding and evaluating community structure in networks. *Phys. Rev. E* 69:026113. doi: 10.1103/PhysRevE.69.026113

Niedermeyer, E. (1997). Alpha rhythms as physiological and abnormal phenomena. *Int. J. Psychophysiol.* 26, 31–49. doi: 10.1016/S0167-8760(97)00754-X

Park, H.-J., and Friston, K. (2013). Structural and functional brain networks: from connections to cognition. *Science* 342:1238411. doi: 10.1126/science.1238411

Petti, M., Toppi, J., Babiloni, F., Cincotti, F., Mattia, D., and Astolfi, L. (2016). EEG resting-state brain topological reorganization as a function of age. *Comput. Intell. Neurosci.* 2016:6243694. doi: 10.1155/2016/6243694

Pichiorri, F., Petti, M., Caschera, S., Astolfi, L., Cincotti, F., and Mattia, D. (2018). An EEG index of sensorimotor interhemispheric coupling after unilateral stroke: clinical and neurophysiological study. *Eur. J. Neurosci.* 47, 158–163. doi: 10.1111/ejn.13797

Porter, M. A., Onnela, J.-P., and Mucha, P. J. (2009). *Communities in Networks*. Rochester, NY: Social Science Research Network. Available online at: https://papers.ssrn.com/abstract=1357925 (accessed February 22, 2009).

Puxeddu, M. G., Faskowitz, J., Betzel, R. F., Petti, M., Astolfi, L., and Sporns, O. (2020). The modular organization of brain cortical connectivity across the human lifespan. *NeuroImage* 218:116974. doi: 10.1016/j.neuroimage.2020.116974

Puxeddu, M. G., Petti, M., Mattia, D., and Astolfi, L. (2019). "The optimal setting for multilayer modularity optimization in multilayer brain networks*," in *2019 41st Annual International Conference of the IEEE Engineering in Medicine and Biology Society (EMBC), lug. 2019* (Berlin), 624–627.

Puxeddu, M. G., Petti, M., Pichiorri, F., Cincotti, F., Mattia, D., and Astolfi, L. (2017). "Community detection: comparison among clustering algorithms and application to EEG-based brain networks," in *2017 39th Annual International Conference of the IEEE Engineering in Medicine and Biology Society (EMBC)* (Jeju Island), 3965–3968.

Riitta Hari, M. D., and Aina Puce, P. (2017). *MEG-EEG Primer*. Oxford: Oxford University Press.

Schmidt, C., Piper, D., Pester, B., Mierau, A., and Witte, H. (2018). Tracking the reorganization of module structure in time-varying weighted brain functional connectivity networks. *Int. J. Neural Syst.* 28:1750051. doi: 10.1142/S0129065717500514

Silva, J. C., Bennett, L., Papageorgiou, L. G., and Tsoka, S. (2016). A mathematical programming approach for sequential clustering of dynamic networks. *Eur. Phys. J. B* 89:39. doi: 10.1140/epjb/e2015-60656-5

Sporns, O. (2011). The human connectome: a complex network. *Ann. N. Y. Acad. Sci.* 1224, 109–125. doi: 10.1111/j.1749-6632.2010.05888.x

Sporns, O. (2013). Network attributes for segregation and integration in the human brain. *Curr. Opin. Neurobiol.* 23, 162–171. doi: 10.1016/j.conb.2012.11.015

Sporns, O., and Betzel, R. F. (2016). Modular brain networks. *Annu. Rev. Psychol.* 67, 613–640. doi: 10.1146/annurev-psych-122414-033634

Takahashi, D. Y., Baccal, L. A., and Sameshima, K. (2007). Connectivity inference between neural structures via partial directed coherence. *J. Appl. Stat.* 34, 1259–1273. doi: 10.1080/02664760701593065

Toppi, J., Mattia, D., Risetti, M., Formisano, R., Babiloni, F., and Astolfi, L. (2016). Testing the significance of connectivity networks: comparison of different assessing procedures. *IEEE Trans. Biomed. Eng.* 63, 2461–2473. doi: 10.1109/TBME.2016.2621668

Toppi, J., Petti, M., De Vico Fallani, F., Vecchiato, G., Maglione, A. G., Cincotti, F., et al. (2012). "Describing relevant indices from the resting state electrophysiological networks," in *2012 Annual International Conference of the IEEE Engineering in Medicine and Biology Society* (San Diego, CA), 2547–2550.

van der Meer, J., Pampel, A., van Someren, E., Ramautar, J., van der Werf, Y., Gomez-Herrero, G., et al. (2016). "Eyes open–eyes closed" EEG/fMRI data set including dedicated "carbon wire loop" motion detection channels. *Data Brief* 7, 990–994. doi: 10.1016/j.dib.2016.03.001

Wig, G. S. (2017). Segregated systems of human brain networks. *Trends Cogn. Sci.* 21, 981–996. doi: 10.1016/j.tics.2017.09.006

Wong, D. D. E., Fuglsang, S. A., Hjortkjær, J., Ceolini, E., Slaney, M., and de Cheveigné, A. (2018). A comparison of regularization methods in forward and backward models for auditory attention decoding. *Front. Neurosci.* 12:531. doi: 10.3389/fnins.2018.00531

Zahra, A., Kanwal, N., Ur Rehman, N., Ehsan, S., and McDonald-Maier, K. D. (2017). Seizure detection from EEG signals using Multivariate Empirical Mode Decomposition. *Comput. Biol. Med.* 88, 132–141. doi: 10.1016/j.compbiomed.2017.07.010

Zippo, A. G., Della Rosa, P. A., Castiglioni, I., and Biella, G. E. M. (2018). Alternating dynamics of segregation and integration in human EEG functional networks during working-memory task. *Neuroscience* 371, 191–206. doi: 10.1016/j.neuroscience.2017.12.004

Conflict of Interest: The authors declare that the research was conducted in the absence of any commercial or financial relationships that could be construed as a potential conflict of interest.

Copyright © 2021 Puxeddu, Petti and Astolfi. This is an open-access article distributed under the terms of the Creative Commons Attribution License (CC BY). The use, distribution or reproduction in other forums is permitted, provided the original author(s) and the copyright owner(s) are credited and that the original publication in this journal is cited, in accordance with accepted academic practice. No use, distribution or reproduction is permitted which does not comply with these terms.

frontiers in Physics

ORIGINAL RESEARCH
published: 13 April 2021
doi: 10.3389/fphy.2021.513969

Machine Learning Assisted Chimera and Solitary States in Networks

Niraj Kushwaha[1]*, *Naveen Kumar Mendola*[1], *Saptarshi Ghosh*[1], *Ajay Deep Kachhvah*[1] and *Sarika Jalan*[1,2,3]*

[1] Complex Systems Lab, Discipline of Physics, Indian Institute of Technology Indore, Indore, India, [2] Discipline of Biosciences and Biomedical Engineering, Indian Institute of Technology Indore, Indore, India, [3] Center for Theoretical Physics of Complex Systems, Institute for Basic Science (IBS), Daejeon, South Korea

Chimera and Solitary states have captivated scientists and engineers due to their peculiar dynamical states corresponding to co-existence of coherent and incoherent dynamical evolution in coupled units in various natural and artificial systems. It has been further demonstrated that such states can be engineered in systems of coupled oscillators by suitable implementation of communication delays. Here, using supervised machine learning, we predict (a) the precise value of delay which is sufficient for engineering chimera and solitary states for a given set of system's parameters, as well as (b) the intensity of incoherence for such engineered states. Ergo, using few initial data points we generate a machine learning model which can then create a more refined phase plot as well as by including new parameter values. We demonstrate our results for two different examples consisting of single layer and multi layer networks. First, the chimera states (solitary states) are engineered by establishing delays in the neighboring links of a node (the interlayer links) in a 2-D lattice (multiplex network) of oscillators. Then, different machine learning classifiers, K-nearest neighbors (KNN), support vector machine (SVM) and multi-layer perceptron neural network (MLP-NN) are employed by feeding the data obtained from the network models. Once a machine learning model is trained using the limited amount of data, it predicts the precise value of critical delay as well as the intensity of incoherence for a given unknown systems parameters values. Testing accuracy, sensitivity, and specificity analysis reveal that MLP-NN classifier is better suited than Knn or SVM classifier for the predictions of parameters values for engineered chimera and solitary states. The technique provides an easy methodology to predict critical delay values as well as intensity of incoherence for that delay value for designing an experimental setup to create solitary and chimera states.

Keywords: multiplex network, delay, solitary states, chimera states, 2-D lattice, machine learning algorithms

OPEN ACCESS

Edited by:
Ralf Metzler,
University of Potsdam, Germany

Reviewed by:
Matjaž Perc,
University of Maribor, Slovenia
Fernando S. Borges,
Federal University of ABC, Brazil
V. K. Chandrasekar,
SASTRA University, India

***Correspondence:**
Sarika Jalan
sarika@iiti.ac.in
Niraj Kushwaha
nirajkkushwaha1@gmail.com

Specialty section:
This article was submitted to Biophysics, a section of the journal Frontiers in Physics

Received: *22 November 2019*
Accepted: *08 March 2021*
Published: *13 April 2021*

Citation:
Kushwaha N, Mendola NK, Ghosh S, Kachhvah AD and Jalan S (2021) Machine Learning Assisted Chimera and Solitary States in Networks. Front. Phys. 9:513969. doi: 10.3389/fphy.2021.513969

1. INTRODUCTION

In the year 2002, a new area was introduced in the field of nonlinear dynamics when Kuramoto et al. brought to light the phenomenon of occurrence of symmetry breaking in a system of identically coupled oscillators [1]. Apart from synchronous and asynchronous states, they identified a remarkable hybrid dynamical structure where both the asynchronous and synchronous regions coexisted in a system of identical oscillators. Later, this mixed state of coherence and incoherence was termed as "chimera," coined by Strogatz and Abrams [2]. Initially identified in a system

of identical Kuramoto oscillators, the chimera state has been pinpointed in a variety of other network models such as FitzHugh-Nagumo oscillators [3, 4], Rössler oscillators [5], van der Pol oscillators [6], coupled Rulkov maps [7], coupled maps [8], coupled chaotic oscillators [9], multi-layer neuronal models [10], Morris-Lecar neurons [11], modular neural network [12], neuronal network model of the cat brain [13], and data-driven model of the brain [14]. Over the years, the researchers have spotted similar fascinating chimeric patterns and labeled them as virtual chimera [15], traveling chimera [16], breathing chimera [17], spike-burst chimera states [18], and others [19, 20]. Several approaches were made to provide an analytical explanation for the emergent chimera state [21, 22]. A comprehensive review on the development of chimera states in a variety of systems can be found in [23, 24].

Recently, another chimera-like pattern, the solitary states, has attracted tremendous attention of the scientific community. The word solitary originated from Latin "solitarius" stands for "alone" or "isolated." In solitary states, unlike chimeric patterns, a few identical oscillators are split off from different isolated locations in the synchronized cluster, possessing different frequencies and phases. Hence, k-solitary states comprise k isolated elements [25]. Recently, the existence of solitary states has been demonstrated in a network of ensembles having attractive and repulsive interactions at the edge of synchrony [26] and partial synchrony [27], inertial Kuramoto model [28], oscillators with negative time-delayed feedback under external forcing [29], identical populations of Stuart-Landau oscillators [30], FitzHugh-Nagumo neurons in the oscillatory regime [4], and neuronal oscillators and coupled chaotic maps in the presence of delayed links [31]. The occurrence of solitary states can be observed in power grid networks in which individual grid-units gradually desynchronize during a partial or complete blackout [32].

Furthermore, in real-world complex systems, a set of interacting units may have different types of interactions among them, with each type of interaction affecting functionality of other types. In such scenarios, the multiplex (multilayer) framework turns out to be an apt contender in representing different dynamical processes acting on the same set of units through different layers comprising different genres of links having different connectivity among the same set of interlinked nodes [33–35]. Recently, the investigations pertaining to the emergence of chimera states and solitary states have been extended to multilayer networks subjected to a variety of dynamical models [36–42].

The occurrence of chimera or solitary states have been designed through experimental setup comprising Huygens clock mechanical oscillators [43], coupled candle-flame oscillators via quenching and clustering [44], modular networks of electrochemical oscillations [45], and locally and non-locally coupled Stuart-Landau oscillator circuits [46].

Furthermore, machine learning techniques have been successfully being applied for prediction of system properties or emergent phenomena covering a broad areas of interdisciplinary research which ranges from non-linear dynamics, quantum physics, astrophysics to bio-medics [47–49]. The field of complex systems and nonlinear dynamics has also witnessed a recent spurt in the use of machine learning techniques, particularly in characterization or identification of a variety of system properties or phenomena. For instance, the machine learning algorithms have been successfully implemented in community detection in networks [50], finding fixed points attractors [51], spatiotemporal chaotic systems [52], detecting phase transition [53], prediction of chaotic systems [54], and identification of chimera states [55].

In the present work, by employing machine learning techniques we predict the value of delay for engineering chimera or solitary state for a given set of systems parameters. First off, we generate chimera state and solitary state in two altogether different network architectures, 2-D lattice and multiplex network. The presence of delay in neighboring connections of a node in a 2-D lattice structure gives rise to ripples of wave like chimera states, labeled as rippling chimera. Whereas, for the occurrence of solitary states, inter-layer connections delays of a multiplex network is established which prohibits few individual node to fall within the synchronized clusters of identical nodes. Note that the presence of delays in either neighboring links in 2-D lattice or inter-links in multiplex network induces perturbations only in the dynamical evolution of the nodes and does not compromise with the structural symmetry of either network. Thereafter, for given data sets we employ multiple machine learning algorithms to train a model which is then used to predict the critical value of delay for yielding the chimera state and the intensity of the rippling chimera for a given choice of system's parameters. The K-nearest neighbors (KNN), support vector machine (SVM), and multi-layer perceptron neural network (MLP-NN) classifier are used utilizing the data generated from the two models. The analysis unveil that multi-layer perceptron neural network (MLP-NN) classifier is the best candidate in precisely predicting the critical delay values for engineering chimera and solitary states. Finally, we plot the entire phase space diagram using the trained machine learning model describing the parameter regimes having chimera and non-chimera states.

2. METHOD AND TECHNIQUE

This article considers two different coupled dynamics on network models to demonstrate the implementation of machine learning techniques for predicting the value of delays to design the solitary and the chimera states. Furthermore, using the trained machine learning model a more refined phase plots describing various dynamical states for the entire parameter region are plotted. In the following, first we discuss the coupled dynamics on network models to demonstrate occurrence of chimera and solitary states by introducing delays in the coupling between pairs of oscillators in their respective network structures. Thereafter, we will describe the machine learning techniques used here to create a model for predicting delay values for engineering chimera and solitary states.

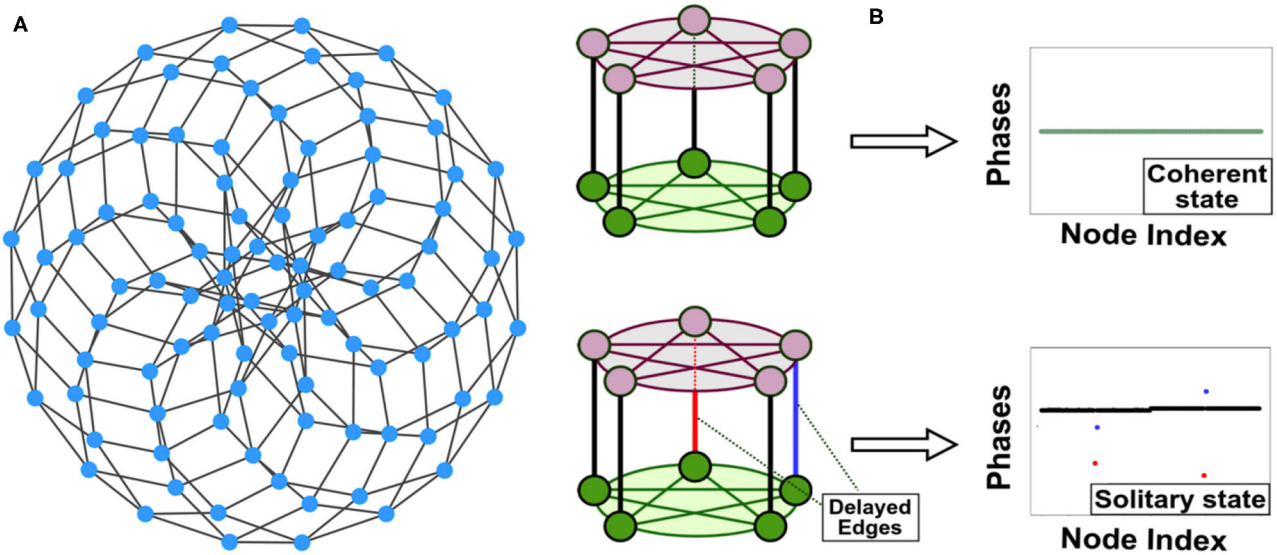


FIGURE 1 | (A) Schematic diagram of 100 identical nodes networked in a 2-D lattice formation assuming periodic boundary condition. **(B)** Schematic diagram of a multiplex network of two globally coupled networks having mirror inter-layer links. For a suitable choice of systems parameters, the state of multiplex network **(B)** demonstrating coherence for undelayed inter-layer links and **(C)** demonstrating solitary states in the presence of a few delayed interlayer links.

2.1. Chimera States in 2-Dimensional Lattice

We consider N nodes, each having 4 nearest neighbors, arranged in a 2-dimensional lattice formation assuming periodic boundary condition (see **Figure 1A**), with the local dynamics at each node governed by the Kuramoto oscillators. Such 2-D lattice exhibits coherence at large coupling strength. However, when a delay is introduced in each neighboring link of a randomly selected node, referred as delayed node, the delayed node and its neighboring then start exhibiting incoherence in the synchronous chunk, thus giving rise to chimera. The presence of delays in the coupling links for a node means that the information the node receives from its neighbors are delayed in time.

Thus the evolution of phase of an un-delayed and a delayed node i is respectively given by

$$\dot{\theta}_i = \omega + \mu \sum_{j=1}^{N} A_{ij} \sin\left(\theta_j(t-\tau_i) - \theta_i(t)\right), \tag{1}$$

where θ_i $(i = 1, \ldots, N)$ denotes the phase of *ith* node, ω denotes the identical intrinsic frequency of the nodes, μ is the coupling strength and τ_i is the value of delay introduced in the links of *ith* node. For delayed nodes $\tau_i \neq 0$ and for non-delayed nodes $\tau_i = 0$. A_{ij} is the element of adjacency matrix of the network defined as.

$$A_{ij} = \begin{cases} 1 & \text{if i and j are connected,} \\ 0 & \text{if, otherwise.} \end{cases}$$

2.2. Solitary States in Multiplex Network

To demonstrate the occurrence of solitary states by setting up a discrete arrangement of delayed inter-layer links in a multiplex network, we begin with considering a multiplex network of two identical globally connected rings (of size N) whose nodes obey the dynamics of Kuramoto oscillators. **Figures 1B,C** illustrate a schematic representation of a multiplex network in the absence and the presence of delayed inter-layer links. In the absence of delay, both the layers of the multiplex network are in coherent state at sufficiently large coupling strength. However, as the delay is established in one of its inter-layer links, two end nodes of the delayed link then get dislodged from their coherent state.

To fabricate the delayed environment in the system, we take into account delayed couplings at a number of arbitrarily chosen but discretely located inter-layer links in the multiplex network, referred to as inter-layer delays for the sake of convenience. Hence, time update of the dynamics of Kuramoto oscillators in the multiplexed identical layers 1 and 2 under the delayed setting is governed by:

$$\dot{\theta}_i^1 = \omega + \mu_1 \sum_{j=1}^{N} \sin(\theta_j^1 - \theta_i^1) + \sigma^{12} \sin(\theta_i^2(t-\tau_i) - \theta_i^1(t)), \tag{2}$$

$$\dot{\theta}_i^2 = \omega + \mu_2 \sum_{j=1}^{N} \sin(\theta_j^2 - \theta_i^2) + \sigma^{21} \sin(\theta_i^1(t-\tau_i) - \theta_i^2(t)), \tag{3}$$

where ω is the identical intrinsic frequency, θ_i is the phase of *ith* $(i = 1, \ldots, N)$ node, μ is the intra-layer coupling strength of a layer and $\sigma^{12} = \sigma^{21} = \sigma$ is the inter-layer coupling strength representing the impact of dynamics of one layer on the other. τ_i is an element of a delay-vector τ (of length N), which contains

particulars about the position and the amplitude of delayed inter-layer links and is directed along either σ^{12} or σ^{21}. We assume a fraction N_τ (significantly smaller than N) of arbitrarily picked discrete locations in τ, which contains time-delays ($\tau_i \neq 0$) either drawn from a uniform random distribution or of identical amplitude. The remaining fraction ($N - N_\tau$) of τ contains no delay, i.e., $\tau_i = 0$. Therefore, the number N_τ determines the number of coveted solitary states, i.e., the system can have 1-solitary state, 2-solitary states, or maximum possible N_τ-solitary states in a layer. Also, the fraction of heterogeneous (identical) ($\tau_i \neq 0$) delays in τ would give rise to solitary points with unequal (equal) phase displacement from the synchronous cluster.

2.3. Machine Learning Techniques

In this paper, three different supervised machine learning algorithms are employed to predict the precise value of delay to engineer solitary and chimera states for a given set of network parameters. These machine learning algorithms are K-nearest neighbors (KNN) classifier, support vector machine (SVM) classifier and multi-layer perceptron neural network (MLP-NN) classifier.

KNN classifier is a non-parametric classification algorithm, which has been proven to be effective in numerous cases. If we represent our data in a vector space, each point in this vector space can be classified based on the classes of k nearest neighbors of the data point. The k nearest neighbors are selected based on a distance parameter. Most commonly, the euclidean distance is used to determine the k nearest neighbors. Therefore, KNN divides our data's vector space into different regions corresponding to different classes. The parameter k plays a very important role in deciding how well KNN will perform while dividing the vector space into different regions and classifying the points in that vector space [56].

SVM classifier is a supervised machine learning model, which performs by estimating the most appropriate hyperplane that can separate our training data into two different distinct classes. The hyperplane estimation is achieved by maximizing the distance between the nearest training data point and the proposed

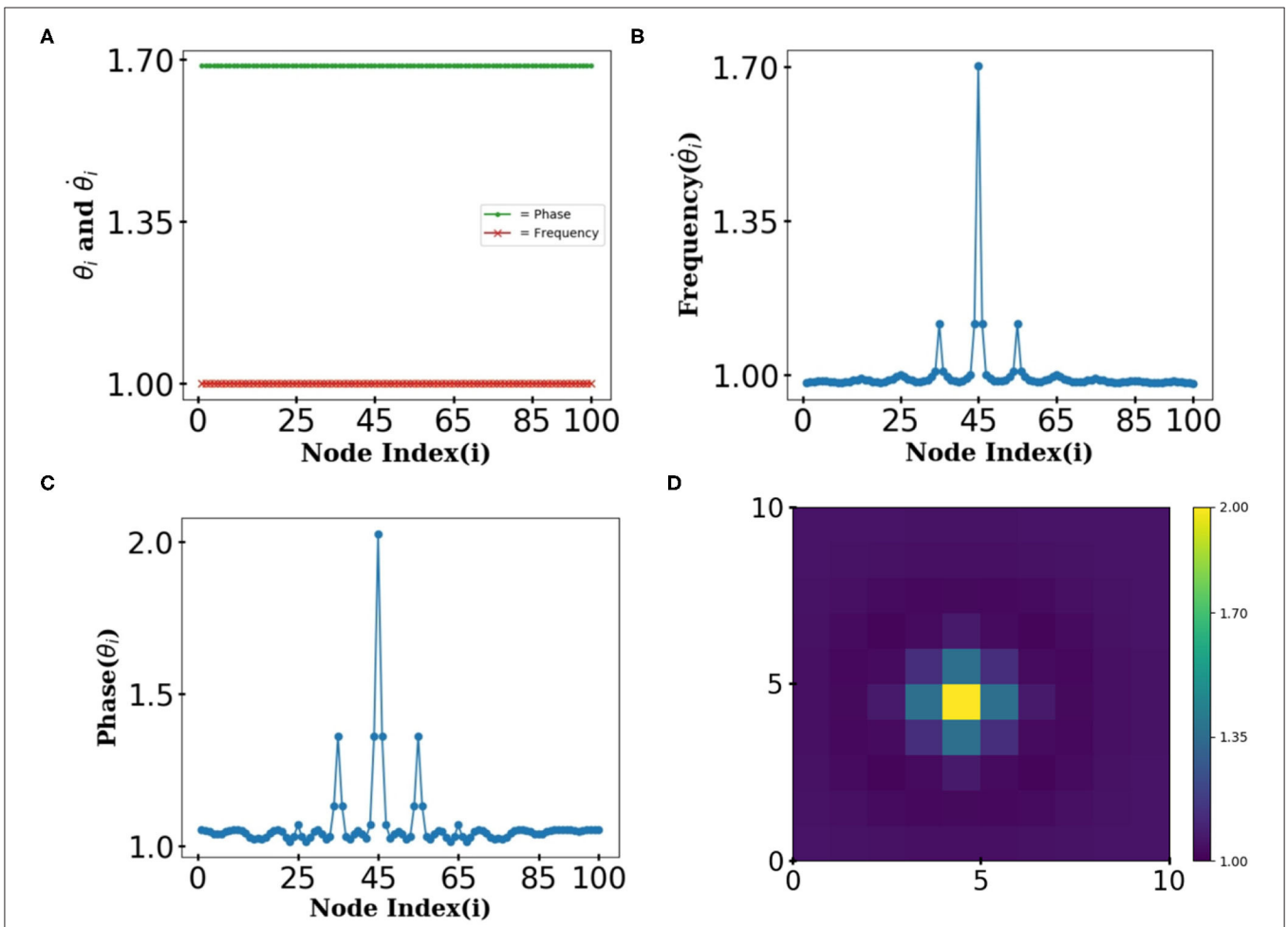


FIGURE 2 | Phase and frequency snapshot of 2-D lattice of $N = 100$ nodes and $\mu = 1$. **(A)** Phase and frequency snapshot of the nodes in the absence of delay ($\tau = 0$). **(B)** A frequency snapshot and **(C)** a phase snapshot of the nodes in the presence of delay ($\tau = 10$) in all the links to 45th node. **(D)** A heatmap representation of the phases in **(C)**. **(B–D)** Demonstrate rippling chimera states.

hyperplane. This distance is also called margin. Simple SVM can only produce linear hyperplanes. One can use kernels to estimate nonlinear hyperplanes. A kernel functions by transforming our training data from a lower-dimensional space into a higher-dimensional space and estimating a linear hyperplane in that higher-dimensional space. When the higher-dimensional hyperplane is transformed back to the lower-dimension, we get a nonlinear hyperplane that can classify each point of our data's vector space into different classes [56].

MLP-NN classifier functions by creating an artificial neural network consisting of many different layers of nodes. There exist three types of layers in a neural network, the input layer, hidden layer, and the output layer. One can have any number of hidden layers, and each hidden layer can have any number of nodes. The neural network takes the input data and tries to estimate the weights of each link between the nodes of the network. A neural network can be called a trained model if the algorithm can successfully estimate the weights of the links such that the model can categorize our data into their correct classes [56].

3. RESULTS

First off, we numerically demonstrate the occurrence of chimera and solitary states in the models discussed in section 2. Thereafter, we make predictions for the precise value of critical delay required for the engineering chimera states and solitary states by employing machine learning classifiers. Here, we numerically demonstrate the occurrence of chimera and solitary states in two distinct network structures.

3.1. Engineering Chimera States

To engineer chimera states, the intrinsic frequency of the $N = 100$ nodes are considered to be the same, i.e., $\omega = 1$ and their initial phases are assigned randomly in the interval $[0, 2\pi]$. We begin with an un-delayed but synchronous 2-D lattice obtained for coupling constant $\mu = 1$ as shown in **Figure 2A**. Starting from a set of initial random phases, after sufficiently high intra-layer coupling strength, all the oscillators settle into the steady phase with constant frequency ($\omega = 1$). However, when a delay is instituted in all the neighboring links to a node (say 45th node) of the lattice, this produces the perturbation in the neighboring links and hence giving rise to chimera states (see **Figures 2B,C**). Such emergent chimera pattern resembles to the ripples on the surface of water, originating from the delayed (*ith*) node, hence is termed as rippling chimera states.

When the lattice evolves in the presence of delay at neighboring links to a node (say 45th node), as expected the phase and the frequency of the delayed node (45th) and its neighboring nodes (for example: 35th and 46th) get desynchronized from their respective synchronous clusters (rest of the nodes). Nevertheless, the rest of the nodes remain synchronous and their frequency still closely follows the intrinsic frequency. Moreover, a gradual steep fall in the amplitude of both the phase and frequency starting off the delayed node through neighboring nodes until the rest synchronous chunk is quite apparent from **Figures 2B,C**, mimicking the ripples on the surface of synchronous cluster. This phenomena is also reflected from **Figure 2D**, the heatmap representation of the phases of the nodes for a delay present in the neighboring links of 45th node. The desynchronized delayed node and its neighboring nodes are referred here as drifting oscillators. Thus, the inclusion of delayed

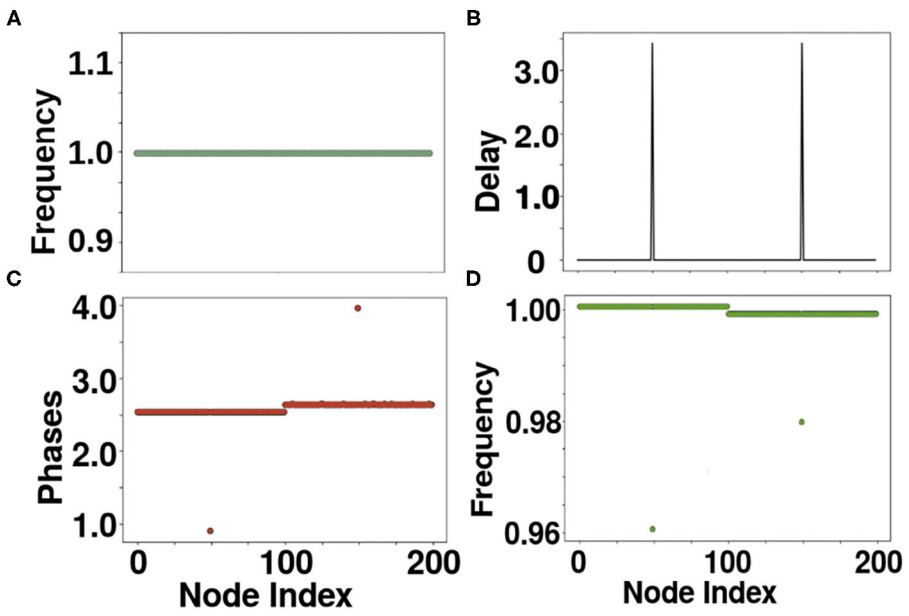


FIGURE 3 | Snapshots of the layers of the multiplex network displaying **(A)** a flat frequency profile with undelayed inter-layer links **(B)** introduced delay profile at inter-layer links **(C)** Phase and **(D)** frequency profile for the solitary state with introduced delayed interlayer links. System parameters are $\mu_1 = 0.5$, $\mu_2 = 3$ and $\sigma = 1$.

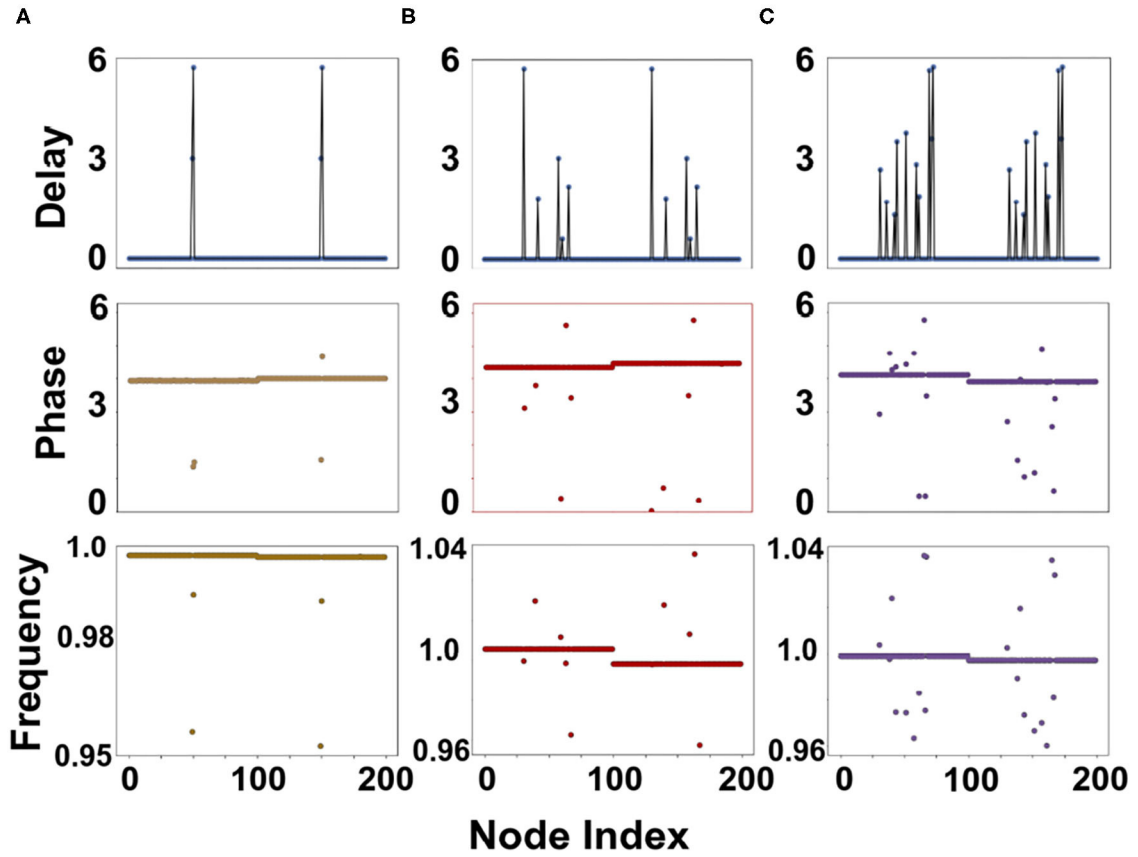


FIGURE 4 | Snapshots of the layers of the multiplex network with (top row) different inter-layer delay profile, resulting in (mid row) Phase; (bottom row) frequency profile for **(A)** 2- **(B)** 5- **(C)** 10- solitary states with the introduced inter-layer delays (as depicted in top row), respectively.

links to a node give rise to the rippling chimera states, whereas the delayed node and its neighbors form the incoherent regime and the rest of the nodes remain part of the synchronous regime.

3.2. Engineering Solitary States

Solitary states are spatiotemporal patterns obtained from the dislodgement of a few nodes from the main synchronous cluster, which possess frequencies different than that of the synchronous cluster. To exhibit the emergence of solitary states in the multiplex network with the aid of inter-layer delays, we select initial phases of the nodes drawn randomly from the interval $\theta_i^{1,2} \in [0, 2\pi)$. We start off with an un-delayed but synchronized multiplexed rings, each of 100 nodes, which is obtained for intralayer coupling constants $\mu_1 = 0.5$, $\mu_2 = 3$ and interlayer coupling constant $\sigma = 1$ as shown in **Figure 3A**. Now the presence of delay in one of the interlayer links (with end nodes $i, i = 50, N{+}50$; see **Figure 3B**) exhibits dislodgement of the phases (frequencies) of the interconnected nodes from their respective phase (frequency) synchronized clusters (see **Figures 3C,D**) resulting in two 2-solitary states, one for each layer. Note that the choice of $\mu_1 = \mu_2$ (one yielding synchronous clusters) can also result in splitting off phases from the main synchronous clusters; however, this does not induce dislodgement in frequencies of the same nodes, hence can not be delineated as solitary states. A mismatch in intra-layer coupling strength μ_1 and μ_2 ensures splitting off the frequencies along with the phases of the end nodes of inter-layer delays. In similar fashion, $2N_\tau$ solitary states are accrued from the presence of N_τ delayed inter-layer links as shown in **Figure 4**. **Figures 4A–C** corresponding to $N_\tau = 2, 5$, and 10 exhibit 4, 10, and 20-solitary states.

Delay is integral to our scheme to get solitary states. The phase difference between the dislodged nodes and the bulk of synchronous nodes can be different; however, the corresponding frequency mismatch remains almost the same for any value of delay for a set of structural parameters μ_1, μ_2, and σ. The presence of delay in an inter-layer link makes the dynamics of the nodes at its two ends either slower or faster than the rest bulk of synchronized nodes. Therefore, the employed scheme allows us to settle on the appropriate values for the delay and the inter-layer coupling strength (σ), which can substantially change the frequencies of the end nodes of the inter-layer delays than those of the rest of the nodes, yielding pronounced solitary states.

Note that besides generating tailored solitary states, the employed scheme can generate chimera states as well when the fraction of delays are installed in a string of inter-layer links instead of globally spread ones.

3.3. Implementation of Machine Learning Techniques

In this section, three different supervised machine learning algorithms trained on the input data obtained from simulations in 3.1 are used for the model-free prediction of factors determining or controlling the intensity of chimera and solitary states emergent in different network structures.

3.3.1. Predicting Intensity of Rippling Chimera and Critical Delay Using Machine Learning

Here, we make the prediction for the intensity of chimera states using machine learning classifiers discussed in section 2. To generate the data used in training the machine learning models, the network is allowed to evolve in time (using RK4 algorithm with time-steps $\Delta t = 0.01$) for different values of coupling constant and delay. The coupling constant is varied from 0.5 to 2 with interval of 0.075. The delay is varied from 0 to 1 with interval of 0.05 and from 1 to 20 with interval of 1. Total 800 simulations are carried out and the number of drifting oscillators is recorded at the end of each simulation. Phase diagram is then plotted using the raw data obtained from the simulations (**Figure 5a**). **Figure 5a** unveils that the data contains a lot of noise, which arises due to the inaccuracies in the numerical simulations. From the inspection of data, only one boundary can be drawn with certainty as shown in **Figure 5b**. This diagram provides a parameter space for which synchronized and chimera regimes are distinguishable, however it lacks in capturing some useful information that our data contains. For instance, the exact number of drifting oscillators or the intensity of chimera state can not be discovered by the inspection of this diagram.

To construct a more detailed phase diagram, machine learning techniques are used. The data is tabulated in three columns where first, second, and third column contain the value of μ, τ, and number of drifting oscillators corresponding to the pair of delay and coupling constant, respectively. The data structure looks like **Table 1**. The data is randomly split into the training and the testing set in the ratio of 4:1. Our task here is to train a machine learning model to predict the number of drifting oscillators for an input pair of μ and τ. The number of drifting oscillators is calculated for each pair of μ and τ at the end of numerical simulation as shown in **Table 1**. The number of drifting oscillators is determined from the number of points in the node index vs frequency plot (e.g., **Figure 2B**), which are far apart from the natural frequency of the oscillators.

Machine learning algorithms have hyperparameters which determine how well a trained machine learning classifier will perform on a given data. In order to get the best possible predictive model which an algorithm is capable of generating, one needs to find the optimal hyperparameters for that algorithm, which depend on the given dataset. One by one, we provide the details of hyperparameters for the three algorithms put into practice.

TABLE 1 | Data structure for Rippling data: there are 800 rows in total in this table.

Coupling constant	Delay	No. of drifting oscillators
:	:	:
:	:	:
0.875	0.5	0
0.875	0.6	9
0.875	0.7	13
:	:	:
1.1	1	21
1.1	2	21
:	:	:
:	:	:

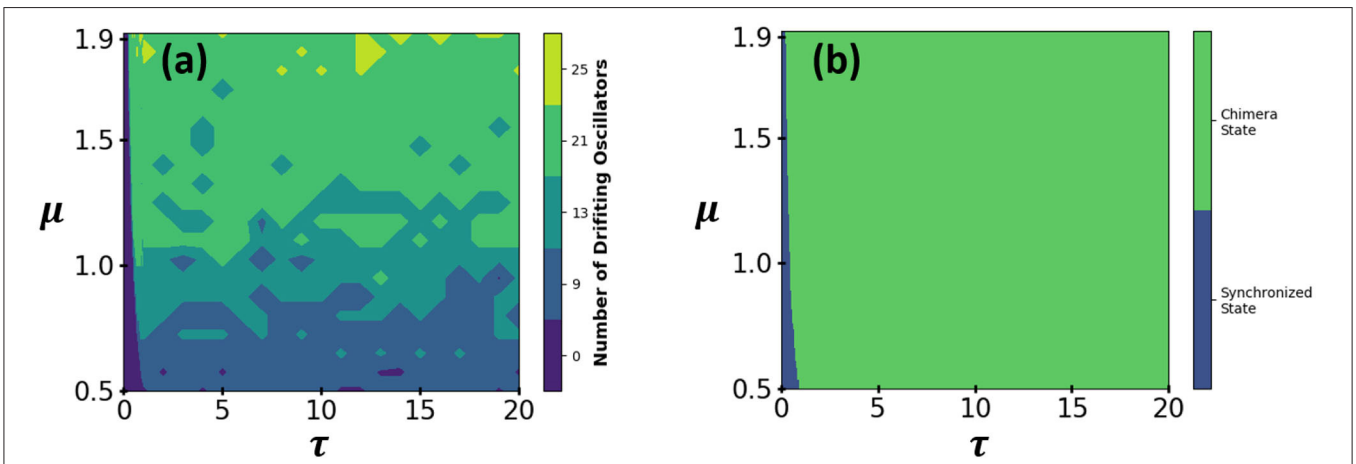


FIGURE 5 | (a) Phase diagram for 2D lattice in two parameter space of τ and μ. This phase diagram is plotted using the data which is directly obtained from the simulations. **(b)** This is a filtered version of **(a)**. All the regions in **(a)** with positive values for "number of drifting oscillators" are merged here to form green region, which represents chimera state. The number of drifting oscillators in blue region is zero, which represents a synchronized state.

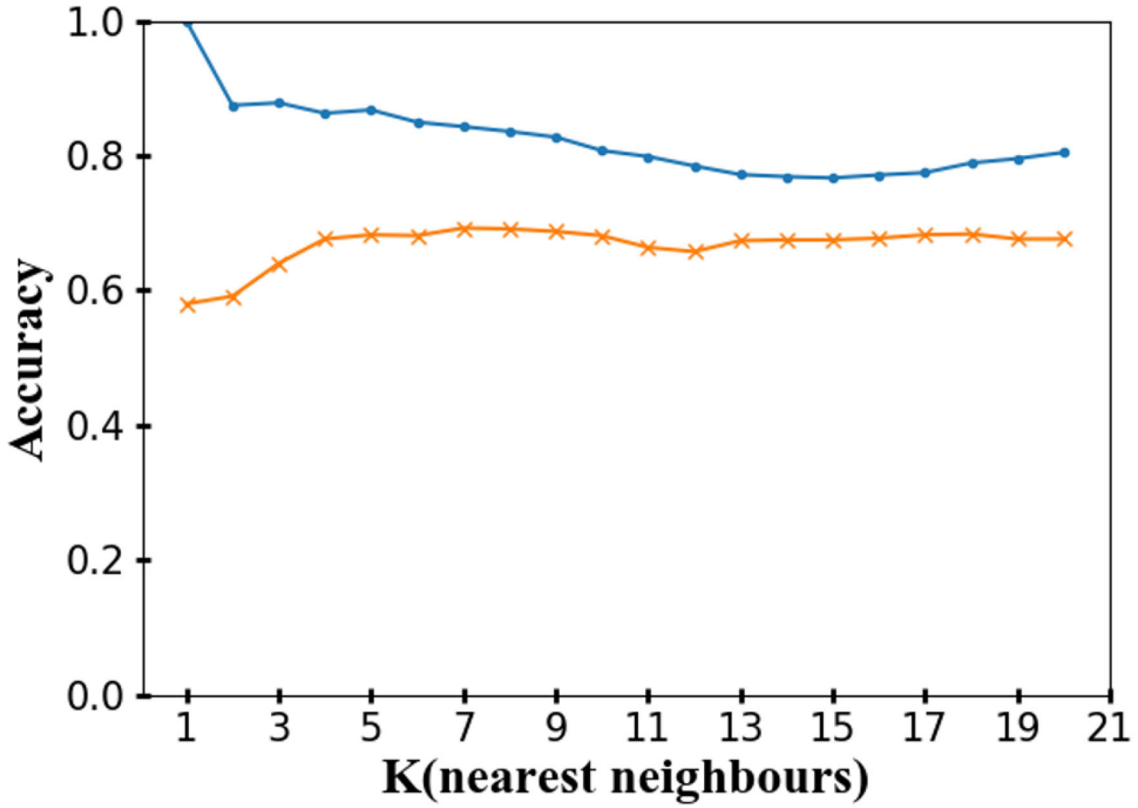


FIGURE 6 | Validation curve for KNN obtained using 5-fold cross validation of data. The parameter K is varied from 1 to 20. The value of K at which a KNN model yields high training accuracy as well as high validation accuracy is the optimum value of K for the dataset. $K = 1$ leads to overfitting as in that case the training accuracy is 1 but the validation accuracy is very low. The validation curve suggests that the best possible KNN model that one can obtain for our dataset is for $K = 5$. Blue and orange line represent training set accuracy and validation set accuracy, respectively.

TABLE 2 | Parameters for Machine learning models trained using dataset of 2D lattice network.

KNN		SVM		MLP-NN	
Description	**Value**	**Description**	**Value**	**Description**	**Value**
K	5	Regularization Parameter	10	Total number of layers	4
				Number of hidden layers	2
				Number of nodes in each hidden layer	30
Weight Function	Uniform	Kernel	EBF	Number of nodes in the output layer	8
				Optimizer	Adam
				Learning rate	10^{-3}
Distance Metric	Euclidean	Gamma	0.5	L2 Penalty	10^{-4}
				Activation	ReLU
				Batch size	200
				Epochs	200

(a) *KNN*: The validation curve is plotted to find the optimal hyperparameter K for KNN as shown in **Figure 6**. The optimal hyperparameters for KNN is given in **Table 2**.

(b) *SVM*: SVM has three hyperparameters which are kernel, regularization parameter, and gamma. To find the optimal hyperparameters for SVM, the grid search analysis is performed. The optimal hyperparameters for SVM is given in **Table 2**.

(c) *MLP-NN*: All the optimal hyperparameters and other information about the MLP-NN is given in **Table 2**.

Next 1,000, 1,000, and 100 models are generated for KNN, SVM, and MLP-NN, respectively, by choosing different training sets at

random for each iteration. The final prediction for the number of drifting oscillators using KNN, SVM, and MLP-NN classifiers is obtained by aggregating the results of these 1,000 KNN, 1,000 SVM, and 100 MLP-NN models.

Training accuracy measures how well an algorithm learns from the training data whereas testing data measures how well an algorithm can train a model which can classify a data which it has never seen before. Higher value of testing accuracy is more desirable than higher value of training accuracy.

TABLE 3 | Accuracy of different algorithms.

Algorithm	Training accuracy	Testing accuracy
KNN	85.449	77.66
SVM	85.455	80.821
Neural Network	83.012	82.725

High training accuracy but low testing accuracy can mean that the algorithm is over-fitting our data. **Table 3** shows that out of the three algorithms, neural network is the best at classifying any unknown data. The lower value of training accuracy for MLP-NN is due to the fact that MLP-NN is able to identify the noise present in the training data (**Figure 5a**). It classifies the noisy data-points into their correct classes (**Figure 7c**), which lowers it's training accuracy as compared to KNN (**Figure 7a**) and SVM (**Figure 7b**) which are not good at classifying the noisy data-points into correct classes. The phase diagrams obtained using each algorithm (**Figures 7a–c**) shows that out of the three algorithms, neural network is significantly better at segregating different regions in a phase space (τ-μ) corresponding to different intensities of chimera. **Figures 8A–C** show the confusion matrix for KNN, SVM, and MLP-NN classifiers, respectively. **Tables 4**, **5** show the sensitivity and specificity of each algorithm, respectively. Comparisons of

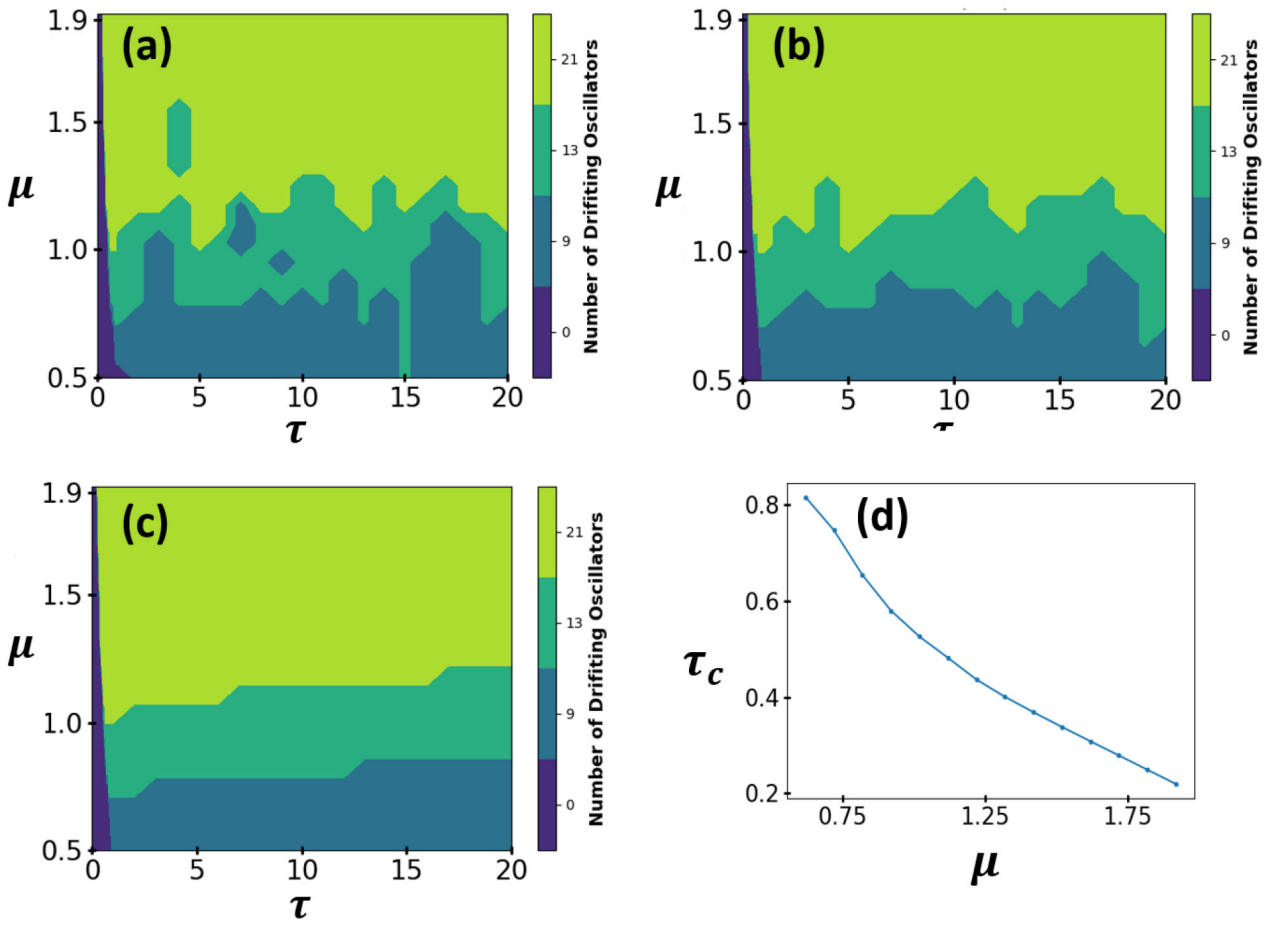


FIGURE 7 | Phase diagrams of 2D lattice in τ and μ parameters space employing **(a)** KNN, **(b)** SVM, and **(C)** MLP-NN algorithm. Here, the region boundaries are determined using a trained machine learning model. These are filled contour plots where each color represents a different value for "number of drifting oscillators" found in the engineered chimera state. **(a)** Using KNN algorithm: the value of parameter K = 5 for training this model is obtained using validation curve analysis (see **Figure 6**). **(b)** Using SVM algorithm: RBF kernel are used while training this SVM model. The value of parameters C = 10 and gamma = 0.5 is obtained used grid search analysis. **(c)** Using MLP-NN algorithm: ReLU activation function is used while training this MLP-NN model. Apart from the input and output layer, the artificial neural network used in this algorithm contains 2 hidden layers with 30 nodes each. **(d)** The behavior of critical delay as a function of μ for a 2D lattice network. The values of critical delay in this plot are calculated using a trained MLP-NN machine learning model.

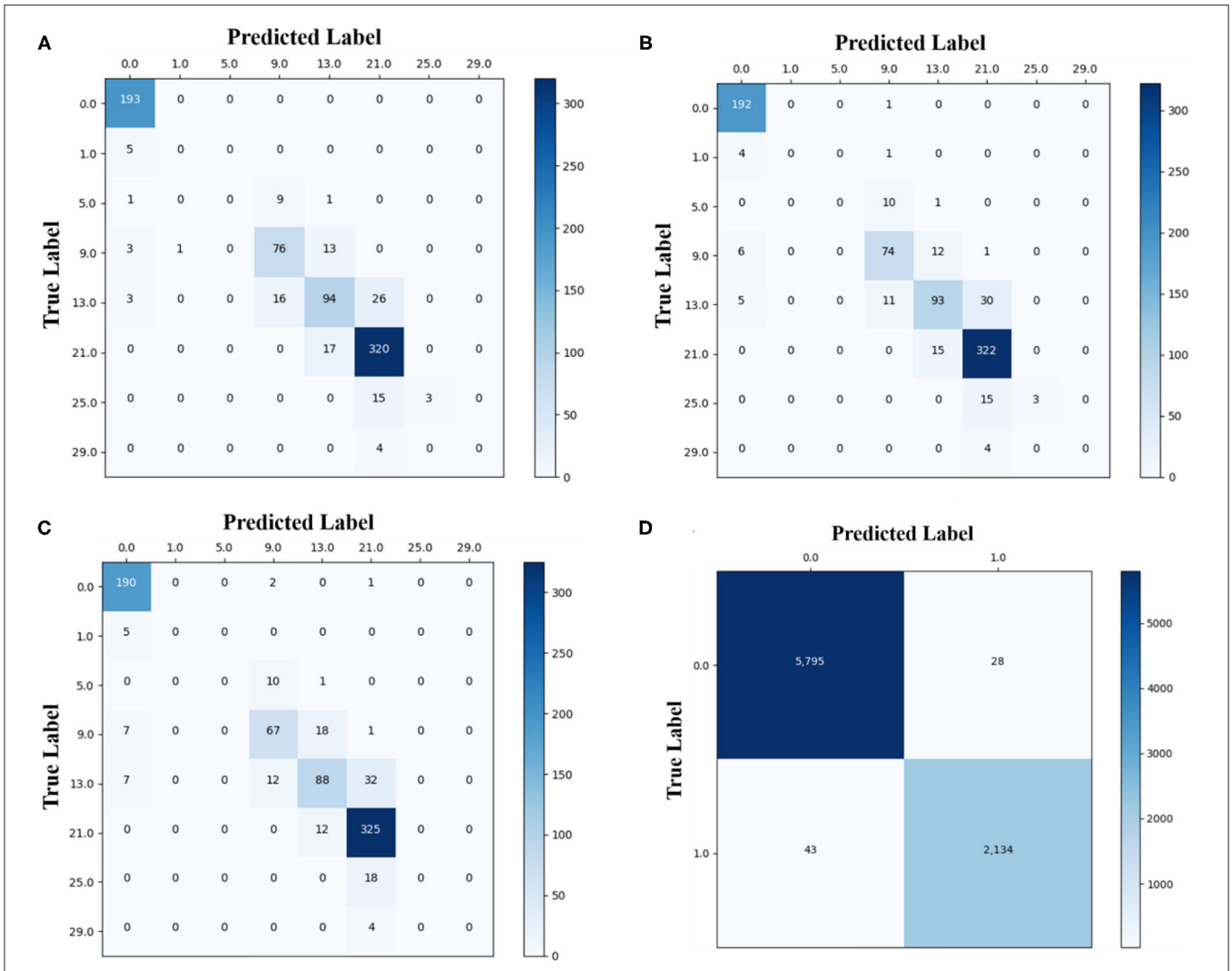


FIGURE 8 | (A) Confusion matrix for classification of intensity of chimera in a 2D lattice network using a trained **(A)** KNN model **(B)** SVM model and **(C)** MLP-NN model. In **(A–C)**, numbers on x and y axis correspond to different values of "total number of drifting oscillators" found in a 2D lattice network. **(D)** Confusion matrix for classification of state of a multilayer network using a trained MLP-NN model. In **(D)**, on the x and y axis, 0 represents a synchronized state and 1 represents a solitary state.

sensitivity and specificity for each algorithm confirm that MLP-NN is the best one out of the three algorithms in identifying the noise present in the training data and classifying the noisy data-points into their correct classes. Therefore, MLP-NN algorithm stands out in predicting the intensity of chimera state in a system.

For a value of coupling constant, the minimum value of delay which transitions the network from a synchronized to chimera state is known as critical delay of the network corresponding to that value of coupling constant. The trained MLP-NN machine learning model was used to predict the exact values of critical delay for a set of coupling constant values (**Figure 7d**). To predict the exact value of critical delay corresponding to a coupling constant, μ is kept fixed and τ is increased from $\tau = 0$ in the steps of 0.001 and the final collective behavior of the network for each pair of μ and τ is predicted using the MLP-NN model. The smallest value of τ for which the MLP-NN model predicted the final collective state to be a chimera, is the critical delay corresponding to the given value of μ. Using this technique,

TABLE 4 | Sensitivity of different algorithms for 2D lattice network.

	Sensitivity							
Algorithm	**Zero**	**One**	**Five**	**Nine**	**Thirteen**	**Twenty one**	**Twenty five**	**Twenty nine**
Knn	1	0	0	0.817	0.676	0.949	0.166	0
SVM	0.995	0	0	0.796	0.669	0.955	0.166	0
Neural network	0.984	0	0	0.72	0.633	0.964	0	0

TABLE 5 | Specificity of different algorithms for 2D lattice network.

Algorithm	Specificity							
	Zero	One	Five	Nine	Thirteen	Twenty one	Twenty five	Twenty nine
Knn	0.98	0.999	1	0.965	0.953	0.902	1	1
SVM	0.975	1	1	0.967	0.958	0.892	1	1
Neural network	0.969	1	1	0.966	0.953	0.879	1	1

TABLE 6 | Data structure for Solitary data: there are 8,000 rows in total in this table.

Interlayer coupling	Intralayer coupling	Delay	State
:	:	:	:
:	:	:	:
3.60	0.86	0.50	0
3.60	0.88	0.50	0
3.70	0.1	0.50	1
:	:	:	:
2.00	0.20	2.00	1
2.00	0.22	2.00	0
:	:	:	:
:	:	:	:

TABLE 7 | Sensitivity and specificity of MLP-NN predictive model for multilayer network.

Sensitivity		Specificity	
0 (Sync.)	1 (Solitary)	0 (Sync.)	1 (Solitary)
0.9951	0.9802	0.9802	0.9951

TABLE 8 | Parameters for neural network model trained using dataset of multilayer network.

Description	Value
Total number of layers	4
Total number of hidden layers	2
Number of nodes in each hidden layer	30
Number of nodes in the output layer	2
Optimizer	Adam
Learning rate	10^{-3}
L2 Penalty	10^{-4}
Activation	ReLU
Batch size	200
Epochs	200

critical delay corresponding to any value of coupling constant can be found. The advantage of using a ML model to find critical delay is that it is very fast as we don't have to run any simulation once the machine learning model is trained, to predict those values of critical delays.

3.3.2. Predicting Value of Critical Delay for Emergence of Solitary State

Here, we precisely forecast the value of critical delay required to delineate solitary states using the machine learning algorithms. First, the coupled dynamic Equations (2) and (3) are allowed to evolve for different values of interlayer coupling strength (σ) and intra-layer coupling strength of layer 1 (μ_1). $\mu_2 = 3$ is kept fixed in all the analysis done in this section. In total 1,600 such simulations are performed and the frequency difference between the delayed nodes and rest of the synchronized nodes is recorded at the end of each simulation. This is performed for 5 different values of delay, i.e., 0, 0.5, 1, 2, 4. Therefore, the total number of simulations performed are 8,000. For a given pair of values of inter-layer and intra-layer coupling, the system can achieve solitary state if a necessary amount of delay is applied to the system. It is rather difficult and computationally demanding to find the exact value of delay at which the system transits from the synchronized to the solitary state for given values of inter-layer and intra-layer coupling strength.

For that matter, we use machine learning techniques to find the precise value of the critical delay for a given set of values of inter-layer and intra-layer coupling strength.

The data that is used to train our model is tabulated in four columns where first, second, third and fourth column contain the values of interlayer coupling constant (σ), intra-layer coupling constant (μ_1), delay (τ), and 0 (1) for the synchronized state (solitary state), respectively. A system is solitary or not is decided by looking at the frequency difference between the excited (delayed) node and a synchronized node. If the frequency difference is more than threshold value of 0.01 the system's state is then delineated as solitary state. The data structure looks like **Table 6**.

In order to predict the values of critical delay corresponding to any given set of values for inter-layer and intra-layer coupling strength, one trains a machine learning model to predict the final state [synchronized (0) or solitary (1)] of the multilayer network after feeding the input values of μ_1, σ, and τ. The value of delay is increased by 0.001 in each iteration while keeping the values of μ_1 and σ fixed. The prediction of MLP-NN model for each combination of μ_1, σ, and τ is then recorded for each iteration. The lowest value of delay is recorded for which the network makes transition from a synchronized state to solitary state. This way the value of critical delay is obtained for a given pair of μ_1 and σ.

We have seen for a 2D lattice network that MLP-NN is the algorithm best suited to train a machine learning model to predict the exact value of critical delay. Therefore, we use MLP-NN again for generating a prediction model fed on the dataset of the emergent solitary states in multilayer network (see **Table 8**). The data is randomly split into training and testing set in the ratio of 4:1. Parameters selected for the neural network are shown in **Table 7**. We first generated 50 neural network models with randomly chosen different training sets for each iteration and then the output is averaged for each model to obtain a final value of the critical delay. The confusion matrix for the MLP-NN model is shown in **Figure 8D**. We also study the sensitivity and the specificity of the MLP-NN model as shown in

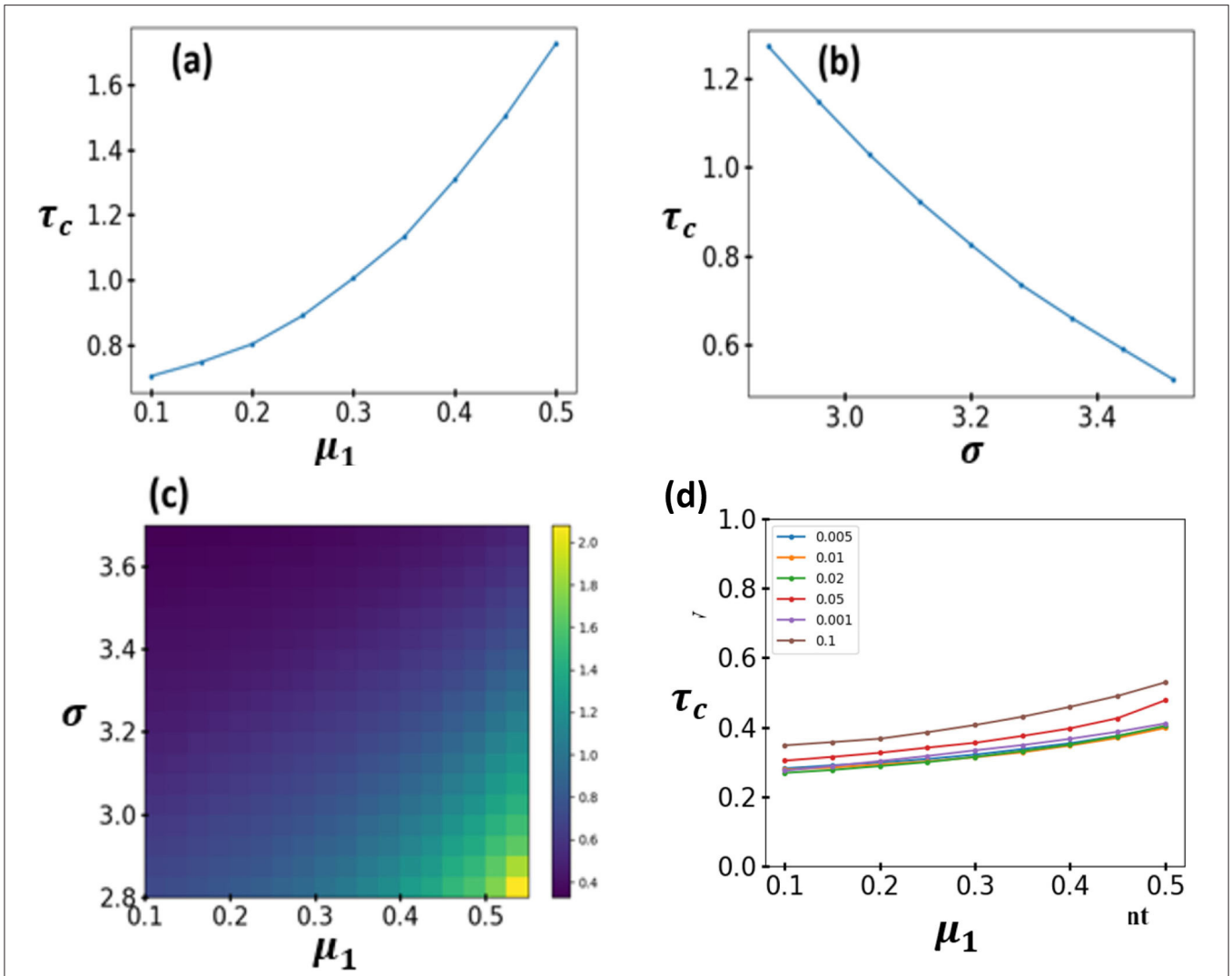


FIGURE 9 | The behavior of critical delay as a function of **(a)** μ_1 and **(b)** σ for a multiplex network with $\sigma = 2.81$ and $\mu_1 = 0.43$, respectively. **(c)** Exhibits a heatmap in μ_1 and σ parameters space for the multiplex network. The colorbar represents the value of critical delay. The values of critical delay in **(a–c)** are calculated using a trained MLP-NN machine learning model. **(d)** The critical delay as a function of μ_1 for the multiplex network with $\sigma = 3.82$. Each line corresponds to a different value of threshold for frequency difference between the desynchronized node and the synchronized nodes, to determine if a state is solitary or not. For a value of threshold between 0.001 and 0.02, the predicted value of the critical delay using machine learning model does not see any significant change. Once the value of threshold exceeds 0.02, the machine learning model starts yielding bad predictions.

Table 7. Using the trained multi layer perceptron neural network model, the exact value of the critical delay can be calculated for any pair of interlayer and intra-layer coupling strength (**Figures 9a–c**).

The impact of the threshold for frequency difference to differentiate between solitary state and synchronized state is also studied (see **Figure 9d**). It is observed that if the value of threshold frequency difference is low then changing the threshold value does not have any significant effect on the prediction of the critical delay but as soon as the threshold is changed to a larger value such as a value >0.02 then the machine learning model starts giving wrong predictions.

4. CONCLUSION

In this paper, different supervised machine learning algorithms have been employed for the model-free prediction of factors characterizing the intensity of chimera and solitary states. We demonstrated success of the scheme for two different model systems namely, 2-D lattice and multilayer network. First, chimera states (solitary states) are constructed by instituting delays in the neighboring connections for a selected node (a few isolated interlayer connections) in a 2-D lattice (multiplex network) of Kuramoto oscillators. Next, three machine learning algorithms, K-nearest neighbors, support vector machine and multi-layer perceptron neural network are then put into practice

to train the data obtained from the evolution of two network models for the prediction of intensity of rippling chimera states and the value of critical delay to characterize solitary states. It is found that multi-layer perceptron neural network (MLP-NN) classifier makes the most precise prediction in identifying the possible desynchronized oscillators in the rippling chimera states and the value of delay required to tailor the solitary states for a given set of multiplex structural parameters. Furthermore, the trained machine learning model was used to plot the entire phase diagram for the rippling chimera and the solitary state.

To conclude, we demonstrated the success of powerful and model-free machine learning algorithms in tailoring the chimera and the solitary states and anticipate that this investigation would be fruitful in broadening the scope of machine learning techniques in characterizing other dynamical properties and phenomena such as occurrence of explosive synchronization. The study is particularly useful is accessing the systems parameter for experimental setup toward engineering chimeras and Solitary states.

DATA AVAILABILITY STATEMENT

All datasets generated for this study are included in the article/supplementary material.

AUTHOR CONTRIBUTIONS

SJ and SG conceived the idea. SJ designed and supervised the entire study. NM and AK performed the numerical simulations. NM, AK, SG, and SJ analyzed the results. All the authors wrote the manuscript and approved it.

ACKNOWLEDGMENTS

SJ acknowledges Government of India, CSIR grant 25(0293)/18/EMR-II and DST grant EMR/2016/001921 for financial support. AK acknowledges CSIR (grant 25(0293)/18/EMR-II), Govt. of India for RA fellowship. SG acknowledges DST, India for INSPIRE (IF150149) fellowship.

REFERENCES

1. Kuramoto Y, Battogtokh D. Coexistence of coherence and incoherence in nonlocally coupled phase oscillators: a soluble case. *J Nonlin Phenom Complex Syst*. *arXiv:cond-mat/0210694v1*. (2002) 12:5.
2. Abrams DM, Strogatz SH. Chimera states in a ring of nonlocally coupled oscillators. *Phys Rev Lett*. (2004) 93:174102. doi: 10.1103/PhysRevLett.93.174102
3. Semenova N, Zakharova A, Anishchenko V, Schöll E. Coherence-resonance chimeras in a network of excitable elements. *Phys Rev Lett*. (2016) 117:014102. doi: 10.1103/PhysRevLett.117.014102
4. Rybalova E, Anishchenko VS, Strelkova GI, Zakharova A. Solitary states and solitary state chimera in neural networks. *Chaos*. (2019) 29:071106. doi: 10.1063/1.5113789
5. Shepelev IA, Vadivasova TE. Inducing and destruction of chimeras and chimera-like states by an external harmonic force. *Phys Lett A*. (2018) 382:690–6. doi: 10.1016/j.physleta.2017.12.055
6. V BA, S AV. Spiral and target wave chimeras in a 2D network of nonlocally coupled van der Pol oscillators. *Chaos Solitons Fract*. (2019) 2019:109492. doi: 10.1016/j.chaos.2019.109492
7. Rybalova E, Bukh A, Strelkova G, Anishchenko V. Spiral and target wave chimeras in a 2D lattice of map-based neuron models. *Chaos*. (2019) 29:101104. doi: 10.1063/1.5126178
8. Bukh A, Rybalova E, Semenova N, Strelkova G, Anishchenko V. New type of chimera and mutual synchronization of spatiotemporal structures in two coupled ensembles of nonlocally interacting chaotic maps. *Chaos*. (2017) 27:111102. doi: 10.1063/1.5009375
9. Anishchenko VS, Strelkova GI. Chimera structures in the ensembles of nonlocally coupled chaotic oscillators. *Radiophys Quant Electron*. (2019) 61:659–71. doi: 10.1007/s11141-019-09926-5
10. Majhi S, Perc M, Ghosh D. Chimera states in uncoupled neurons induced by a multilayer structure. *Sci Rep*. (2016) 6:39033. doi: 10.1038/srep39033
11. Calim A, Hövel P, Ozer M, Uzuntarla M. Chimera states in networks of type-I Morris-Lecar neurons. *Phys Rev E*. (2018) 98:062217. doi: 10.1103/PhysRevE.98.062217
12. Hizanidis J, Kouvaris NE, Zamora-López G, Dí-az-Guilera A, Antonopoulos CG. Chimera-like states in modular neural networks. *Sci Rep*. (2016) 6:19845. doi: 10.1038/srep19845
13. Santos MS, Szezech JD, Borges FS, Iarosz KC, Caldas IL, Batista AM, et al. Chimera-like states in a neuronal network model of the cat brain. *Chaos Solitons Fract*. (2017) 101:86–91. doi: 10.1016/j.chaos.2017.05.028
14. Bansal K, Garcia JO, Tompson SH, Verstynen T, Vettel JM, Muldoon SF. Cognitive chimera states in human brain networks. *Sci Adv*. (2019) 5:eaau8535. doi: 10.1126/sciadv.aau8535
15. Larger L, Penkovsky B, Maistrenko Y. Virtual chimera states for delayed-feedback systems. *Phys Rev Lett*. (2013) 111:054103. doi: 10.1103/PhysRevLett.111.054103
16. Bera BK, Ghosh D, Banerjee T. Imperfect traveling chimera states induced by local synaptic gradient coupling. *Phys Rev E*. (2016) 94:012215. doi: 10.1103/PhysRevE.94.012215
17. Abrams DM, Mirollo R, Strogatz SH, Wiley DA. Solvable model for chimera states of coupled oscillators. *Phys Rev Lett*. (2008) 101:084103. doi: 10.1103/PhysRevLett.101.084103
18. Santos MS, Protachevicz PR, Iarosz KC, Caldas IL, Viana RL, Borges FS, et al. Spike-burst chimera states in an adaptive exponential integrate-and-fire neuronal network. *Chaos*. (2019) 29:043106. doi: 10.1063/1.5087129
19. Sheeba JH, Chandrasekar VK, Lakshmanan M. Chimera and globally clustered chimera: impact of time delay. *Phys Rev E*. (2010) 81:049906. doi: 10.1103/PhysRevE.81.046203
20. Panaggio MJ, Abrams DM. Chimera states on the surface of a sphere. *Phys Rev E*. (2015) 91:022909. doi: 10.1103/PhysRevE.91.022909
21. Omelchenko OE. The mathematics behind chimera states. *Nonlinearity*. (2018) 31:R121. doi: 10.1088/1361-6544/aaaa07
22. Rakshit S, Faghani Z, Parastesh F, Panahi S, Jafari S, Ghosh D, et al. Transitions from chimeras to coherence: an analytical approach by means of the coherent stability function. *Phys Rev E*. (2019) 100:012315. doi: 10.1103/PhysRevE.100.012315
23. Bera BK, Majhi S, Ghosh D, Perc M. Chimera states: effects of different coupling topologies. *Europhys Lett*. (2017) 118:10001. doi: 10.1209/0295-5075/118/10001
24. Majhi S, Bera BK, Ghosh D, Perc M. Chimera states in neuronal networks: a review. *Phys Life Rev*. (2019) 28:100–21. doi: 10.1016/j.plrev.2018.09.003
25. Jaros P, Brezetsky S, Levchenko R, Dudkowski D, Kapitaniak T, Maistrenko Y. Solitary states for coupled oscillators with inertia. *Chaos*. (2018) 28:011103. doi: 10.1063/1.5019792
26. Maistrenko Y, Penkovsky B, Rosenblum M. Solitary state at the edge of synchrony in ensembles with attractive and repulsive interactions. *Phys Rev E*. (2014) 89:060901. doi: 10.1103/PhysRevE.89.060901
27. Teichmann E, Rosenblum M. Solitary states and partial synchrony in oscillatory ensembles with attractive and repulsive interactions. *Chaos*. (2019) 29:093124. doi: 10.1063/1.5118843

28. Jaros P, Maistrenko Y, Kapitaniak T. Chimera states on the route from coherence to rotating waves. *Phys Rev E*. (2015) 91:022907. doi: 10.1103/PhysRevE.91.022907
29. Semenov V, Zakharova A, Maistrenko Y, Schöll E. Delayed-feedback chimera states: forced multiclusters and stochastic resonance. *Europhys Lett*. (2016) 115:10005. doi: 10.1209/0295-5075/115/10005
30. Premalatha K, Chandrasekar VK, Senthilvelan M, Lakshmanan M. Chimeralike states in two distinct groups of identical populations of coupled Stuart-Landau oscillators. *Phys Rev E*. (2017) 95:022208. doi: 10.1103/PhysRevE.95.022208
31. Schülen L, Ghosh S, Kachhvah AD, Zakharova A, Jalan S. Delay engineered solitary states in complex networks. *Chaos Solitons Fract*. (2019) 128:290–6. doi: 10.1016/j.chaos.2019.07.046
32. Hellmann F, Schultz P, Jaros P, Levchenko R, Kapitaniak T, Kurths J, et al. Network-induced multistability: lossy coupling and exotic solitary states. *arXiv [nlinAO]*. (*2018) arXiv:1811.11518v1*.
33. Ghosh S, Zakharova A, Jalan S. Non-identical multiplexing promotes chimera states. *Chaos Solitons Fract*. (2018) 106:56–60. doi: 10.1016/j.chaos.2017.11.010
34. De Domenico M. Multilayer modeling and analysis of human brain networks. *GigaScience*. (2017) 6:gix004. doi: 10.1093/gigascience/gix004
35. Buldú JM, Porter MA. Frequency-based brain networks: From a multiplex framework to a full multilayer description. *Netw Neurosci*. (2018) 2:418–41. doi: 10.1162/netn_a_00033
36. Ghosh S, Jalan S. Emergence of chimera in multiplex network. *Int J Bifurc Chaos*. (2016) 26:1650120. doi: 10.1142/S0218127416501200
37. Sawicki J, Ghosh S, Jalan S, Zakharova A. Chimeras in multiplex networks: interplay of inter- and intra-layer delays. *Front Appl Math Stat*. (2019) 5:19. doi: 10.3389/fams.2019.00019
38. Omelchenko I, Hülser T, Zakharova A, Schöll E. Control of chimera states in multilayer networks. *Front Appl Math Stat*. (2019) 4:67. doi: 10.3389/fams.2018.00067
39. Pournaki A, Merfort L, Ruiz J, Kouvaris NE, Hövel P, Hizanidis J. Synchronization patterns in modular neuronal networks: a case study of *C. elegans*. *Front Appl Math Stat*. (2019) 5:52. doi: 10.3389/fams.2019.00052
40. Majhi S, Perc M, Ghosh D. Chimera states in a multilayer network of coupled and uncoupled neurons. *Chaos*. (2017) 27:073109. doi: 10.1063/1.4993836
41. Majhi S, Kapitaniak T, Ghosh D. Solitary states in multiplex networks owing to competing interactions. *Chaos*. (2019) 29:013108. doi: 10.1063/1.5061819
42. Mikhaylenko M, Ramlow L, Jalan S, Zakharova A. Weak multiplexing in neural networks: switching between chimera and solitary states. *Chaos*. (2019) 29:023122. doi: 10.1063/1.5057418
43. Kapitaniak T, Kuzma P, Wojewoda J, Czolczynski K, Maistrenko Y. Imperfect chimera states for coupled pendula. *Sci Rep*. (2014) 4:6379. doi: 10.1038/srep06379
44. Manoj K, Pawar SA, Dange S, Mondal S, Sujith RI, Surovyatkina E, et al. Synchronization route to weak chimera in four candle-flame oscillators. *Phys Rev E*. (2019) 100:062204. doi: 10.1103/PhysRevE.100.062204
45. Ocampo-Espindola JL, Bick C, Kiss IZ. Weak chimeras in modular electrochemical oscillator networks. *Front Appl Math Stat*. (2019) 5:38. doi: 10.3389/fams.2019.00038
46. Gambuzza LV, Minati L, Frasca M. Experimental observations of chimera states in locally and non-locally coupled Stuart-Landau oscillator circuits. *Chaos Solitons Fract*. (2020) 138:109907. doi: 10.1016/j.chaos.2020.109907
47. Mitchell TM. *Machine Learning*. 1st Edn. New York, NY: McGraw-Hill, Inc. (1997).
48. Burkov A. *The Hundred-Page Machine Learning Book*. 1st Edn. Quebec City, QC: Kindle Direct Publishing (2019).
49. Lee W, Flach S. Deep learning of chaos classification. *arXiv*. (2020). *arXiv:200410980v1*.
50. Ghasemian A, Zhang P, Clauset A, Moore C, Peel L. Detectability thresholds and optimal algorithms for community structure in dynamic networks. *Phys Rev X*. (2016) 6:031005. doi: 10.1103/PhysRevX.6.031005
51. Rivkind A, Barak O. Local dynamics in trained recurrent neural networks. *Phys Rev Lett*. (2017) 118:258101. doi: 10.1103/PhysRevLett.118.258101
52. Pathak J, Hunt B, Girvan M, Lu Z, Ott E. Model-free prediction of large spatiotemporally chaotic systems from data: a reservoir computing approach. *Phys Rev Lett*. (2018) 120:024102. doi: 10.1103/PhysRevLett.120.024102
53. Ni Q, Tang M, Liu Y, Lai YC. Machine learning dynamical phase transitions in complex networks. *Phys Rev E*. (2019) 100:052312. doi: 10.1103/PhysRevE.100.052312
54. Fan H, Jiang J, Zhang C, Wang X, Lai YC. Long-term prediction of chaotic systems with machine learning. *Phys Rev Res*. (2020) 2:012080. doi: 10.1103/PhysRevResearch.2.012080
55. Ganaie MA, Ghosh S, Mendola N, Tanveer M, Jalan S. Identification of chimera using machine learning. *arXiv:200108985v2*. (2020). doi: 10.1063/1.5143285
56. Murphy KP. *Machine Learning: A Probabilistic Perspective*. MIT Press (2012).

Conflict of Interest: The authors declare that the research was conducted in the absence of any commercial or financial relationships that could be construed as a potential conflict of interest.

Copyright © 2021 Kushwaha, Mendola, Ghosh, Kachhvah and Jalan. This is an open-access article distributed under the terms of the Creative Commons Attribution License (CC BY). The use, distribution or reproduction in other forums is permitted, provided the original author(s) and the copyright owner(s) are credited and that the original publication in this journal is cited, in accordance with accepted academic practice. No use, distribution or reproduction is permitted which does not comply with these terms.

frontiers in Systems Neuroscience

ORIGINAL RESEARCH
published: 03 June 2021
doi: 10.3389/fnsys.2021.642349

Pelvic Pain Alters Functional Connectivity Between Anterior Cingulate Cortex and Hippocampus in Both Humans and a Rat Model

Wenjun Yu[1,2,3†], Xiaoyan Wu[2,4†], Yunan Chen[5†], Zhiying Liang[2†], Jinxiang Jiang[1], Afzal Misrani[1], Yun Su[2], Yigang Peng[5], Jian Chen[5], Binliang Tang[5], Mengyao Sun[5], Cheng Long[5], Jun Shen[2] and Li Yang[1]**

[1] Precise Genome Engineering Center, School of Life Sciences, Guangzhou University, Guangzhou, China, [2] Department of Radiology, Sun Yat-sen Memorial Hospital, Sun Yat-sen University, Guangzhou, China, [3] College of Education, Jinggangshan University, Ji'an, China, [4] School of Psychology, South China Normal University, Guangzhou, China, [5] School of Life Sciences, South China Normal University, Guangzhou, China

OPEN ACCESS

Edited by:
Spase Petkoski,
INSERM U1106 Institut de Neurosciences des Systèmes, France

Reviewed by:
Intan Low,
National Yang Ming Chiao Tung University, Taiwan
Qian Song,
Xi'an Jiaotong University, China

***Correspondence:**
Li Yang
yang_li@gzhu.edu.cn
Jun Shen
shenjun@mail.sysu.edu.cn

† These authors have contributed equally to this work

Received: 22 December 2020
Accepted: 26 April 2021
Published: 03 June 2021

Citation:
Yu W, Wu X, Chen Y, Liang Z, Jiang J, Misrani A, Su Y, Peng Y, Chen J, Tang B, Sun M, Long C, Shen J and Yang L (2021) Pelvic Pain Alters Functional Connectivity Between Anterior Cingulate Cortex and Hippocampus in Both Humans and a Rat Model. Front. Syst. Neurosci. 15:642349. doi: 10.3389/fnsys.2021.642349

The anterior cingulate cortex (ACC) and hippocampus (HIPP) are two key brain regions associated with pain and pain-related affective processing. However, whether and how pelvic pain alters the neural activity and connectivity of the ACC and HIPP under baseline and during social pain, and the underlying cellular and molecular mechanisms, remain unclear. Using functional magnetic resonance imaging (fMRI) combined with electrophysiology and biochemistry, we show that pelvic pain, particularly, primary dysmenorrhea (PDM), causes an increase in the functional connectivity between ACC and HIPP in resting-state fMRI, and a smaller reduction in connectivity during social exclusion in PDM females with periovulatory phase. Similarly, model rats demonstrate significantly increased ACC-HIPP synchronization in the gamma band, associating with reduced modulation by ACC-theta on HIPP-gamma and increased levels of receptor proteins and excitation. This study brings together human fMRI and animal research and enables improved therapeutic strategies for ameliorating pain and pain-related affective processing.

Keywords: pelvic pain, anterior cingulate cortex, hippocampus, neural circuits, functional magnetic resonance imaging, electrophysiology

INTRODUCTION

Pain, which is a negative experience involving sensory, emotional, cognitive and social dimensions, is classified into physical and social pain, which is defined as the painful feelings following social rejection, exclusion, or loss (Eisenberger, 2015; Williams and Craig, 2016). Growing evidence suggests that the experience of social pain relies on some of the same neurobiological processes underlying experiences of physical pain (Eisenberger, 2012). Pelvic pain, such as primary dysmenorrhea (PDM) which is menstrual pain without organic causes affecting approximately half of menstruating females (Iacovides et al., 2015), contains both acute and chronic components of pain (Wei et al., 2016) associated with impaired sensory and affective processes (Rhudy and Bartley, 2010), and structural and functional brain alterations (Low et al., 2018). It is becoming increasingly

clear that PDM results in aberrant processing of physical and social pain (Pitangui et al., 2013; Yu et al., 2018). Interactional processing of physical and social pain (Borsook and MacDonald, 2010) involves similar brain regions, including the anterior cingulate cortex (ACC) and the adjacent medial prefrontal cortex (Bliss et al., 2016). Chronic pain causes increased neuronal activity in the ACC in humans (Hutchison et al., 1999), non-human primates (Iwata et al., 2005), and rodent pain models (Zhang et al., 2017), and is accompanied by neurophysiological and psychological changes (Bushnell et al., 2013), including depression and anxiety (Zhuo, 2016). Negative emotional stimuli, such as social exclusion (social pain), activate a range of brain areas involving the ACC (Eisenberger et al., 2003). Together, the above studies linked increased ACC neuronal activity to negative experience, highlighting the role of the ACC in processing and even potentially integrating physical and social pain. However, how pelvic pain, such as PDM, alters ACC-related neuronal pathways involved in the processing of neurophysiological and psychological stressors has not been tested in detail.

A key feature of chronic pain is the amplified affective response to nociceptive inputs (Zhou et al., 2018). The ACC processes and regulates both the sensory and affective component of pain (Eisenberger, 2012; Wager et al., 2016) and the hippocampus (HIPP) has been shown to participate in the integrative processing of pain (Bushnell et al., 2013). In particular, neuropathic pain alters HIPP-mediated behavior, synaptic plasticity and neurogenesis in rodents (Mutso et al., 2012). Moreover, the HIPP is involved when pain moves from an acute toward a chronic state, indicating a shift in the representation of pain in the brain from nociceptive to emotional circuits (Hashmi et al., 2013). Furthermore, the ACC interacts with the HIPP to mediate both cognitive and affective components of pain (Bliss et al., 2016). Increased activation of the ACC and HIPP is observed in post-traumatic stress disorder during the encoding of negative words (Thomaes et al., 2013). These findings implicate a critical role for both ACC and HIPP in the processing and integration of physical and social pain (Bliss et al., 2016; Jiang et al., 2018).

Functional connectivity (FC) between distant brain areas reflects neuronal and synaptic communications for the entrainment of various cognitive, emotional and sensory processing (Friston, 1994; Arieli et al., 1996; Tobia et al., 2017). Oscillatory activities, and their interplay, such as theta and gamma rhythms, render neuronal communication effective, precise, and selective, of which oscillatory coherence functions as a general indicator of communication between brain areas (Fries, 2015). Low frequency neural oscillations reflect large-scale network-level coordination across different neural circuits (Buzsaki and Draguhn, 2004). A recent human study highlighted the possible role of a disturbed dynamic coordination of the brain network in the pathophysiology of PDM and revealed abnormal low frequency theta oscillations in physical and social pain processing areas of the brain, such as the insula, parahippocampal gyrus, and cingulate cortex of PDM females (Lee et al., 2017). On the other hand, gamma oscillations represent the neuronal coordination of different brain regions (Gregoriou et al., 2009). Recent animal and human studies provide converging evidence that gamma oscillations are closely related to pain perception (Hu and Iannetti, 2019; Tan et al., 2019). In addition, cross-frequency phase-amplitude coupling (PAC), in which the amplitude of higher (e.g., gamma) rhythms is particularly modulated by the phase of lower (e.g., theta) rhythms, indicates a more complex regulatory feature through interactions between different frequency bands, such as long-range theta and local gamma communication (Wirt and Hyman, 2019; Chen et al., 2021). However, the possible abnormalities induced by PDM in ACC-HIPP connectivity and the underlying mechanisms of the condition remain unclear.

To address these issues, we employed integrative methods, including resting-state and task state (social exclusion task) functional magnetic resonance imaging (fMRI) in PDM humans, in combination with pharmacological, *in vivo* and *in vitro* electrophysiological, biochemical, and behavioral techniques in a pelvic pain rat model. We hypothesize that pelvic pain, such as PDM, may cause abnormal neuronal activity in the ACC and HIPP, and subsequent disruption in the connectivity between the two structures. The results obtained improve our understanding of how pelvic pain, including PDM, causes neural circuit changes and reveal that brain networks known to modulate both physical and social pain might display markers of central nervous system (CNS) abnormality in pelvic pain. The study provides some new preliminary support for the use of cross-species experiments to investigate pelvic pain, which may facilitate the search for relevant treatments.

MATERIALS AND METHODS

Participants

This study was approved by the South China Normal University and Guangzhou University Institutional Ethics Review Board (2017–139). Human participants provided written informed consent prior to participation. A total of eighty right-handed (Li et al., 2017; Wasylyshyn et al., 2018) university female students (ages 18–25) who came to the recruitment were enrolled in this study which included 38 PDM and 42 non-PDM controls. PDM and control subjects were matched according to gynecological age. Demographic and clinical information are shown in **Table 1**. College students with dysmenorrhea (DM) were selected and PDM was further diagnosed in Sun Yat-sen Memorial Hospital, where magnetic resonance imaging (MRI) was performed to ensure there was no macroscopic structural abnormality inside or outside the uterus. Briefly, the diagnostic criteria for PDM were similar to those defined by the American College of Obstetricians & Gynecologists (American College of Obstetricians and Gynecologists, 2006). The following inclusion criteria were used for PDM participants: (1) a menstrual cycle of average 30 days; (2) a history of menstrual pain over more than 12 months; (3) a self-assessed severity of the average menstrual pain of 5 and above over the previous 6 months based on the visual analog scale (VAS, 0 = not at all, 10 = the worst imaginable pain); and (4) a pelvis MRI scan did not show any anatomical pelvic disease. The inclusion criteria for the controls were similar

TABLE 1 | Demographic and clinical information of the PDM subjects and controls used in human MRI.

	Resting-state fMRI (M ± SD)			Task fMRI (M ± SD)			Structural MRI (M ± SD)		
	PDM (n = 35)	Ctrl (*n* = 38)	*p* value	PDM (n = 30)	Ctrl (*n* = 31)	*p* value	PDM (n = 38)	Ctrl (*n* = 42)	*p* value
Age, years[a]	20.49 ± 1.20	20.58 ± 1.52	0.694	20.70 ± 1.12	20.45 ± 1.06	0.326	20.55 ± 1.22	20.60 ± 1.47	0.633
Age of onset of menstruation, years[a]	12.60 ± 1.31	13.05 ± 1.51	0.196	12.53 ± 1.31	12.32 ± 2.75	0.952	12.63 ± 1.28	12.95 ± 1.50	0.364
Menstrual duration, years[a]	7.89 ± 1.75	7.53 ± 1.70	0.417	8.17 ± 1.76	8.13 ± 2.90	0.479	7.92 ± 1.71	7.64 ± 1.66	0.551
Menstrual cycle, days[a]	30.63 ± 2.77	29.13 ± 2.53	0.019	29.67 ± 3.16	28.74 ± 2.62	0.120	30.50 ± 2.82	29.17 ± 2.51	0.023
Pain begin age, years	15.14 ± 1.99	N/A	N/A	14.93 ± 2.12	N/A	N/A	15.03 ± 1.98	N/A	N/A
Pain duration year, years	5.14 ± 2.13	N/A	N/A	5.53 ± 2.22	N/A	N/A	5.29 ± 2.12	N/A	N/A
Pain degree	6.54 ± 1.09	N/A	N/A	6.77 ± 1.03	N/A	N/A	6.61 ± 1.10	N/A	N/A
Positive emotion									
Pre-test[a]	N/A	N/A	N/A	15.03 ± 5.93	16.45 ± 5.54	0.188	N/A	N/A	N/A
Post-test[a]	N/A	N/A	N/A	13.13 ± 4.96	14.71 ± 5.69	0.304	N/A	N/A	N/A
p-value within group[b]	N/A	N/A	N/A	0.088	0.059	N/A	N/A	N/A	N/A
Negative emotion									
Pre-test[a]	N/A	N/A	N/A	12.23 ± 2.54	11.39 ± 2.35	0.151	N/A	N/A	N/A
Post-test[a]	N/A	N/A	N/A	12.67 ± 3.17	12 ± 3.54	0.155	N/A	N/A	N/A
p-value within group[b]	N/A	N/A	N/A	0.771	0.297	N/A	N/A	N/A	N/A
BNQ									
Pre-test[c]	N/A	N/A	N/A	2.33 ± 0.42	2.42 ± 0.40	0.407	N/A	N/A	N/A
Post-test[c]	N/A	N/A	N/A	3.11 ± 0.42	3.10 ± 0.46	0.988	N/A	N/A	N/A
p-value within group[d]	N/A	N/A	N/A	<0.001	<0.001	N/A	N/A	N/A	N/A

PDM, primary dysmenorrhea; Ctrl, controls; BNQ, basic needs questionnaire. [a]Mann–Whitney test; [b]Wilcoxon test; [c]Two-sample t-tests; [d]Paired-sample t-tests; M, mean value; SD, standard deviation; N/A, non-applicable.

to those for the PDM subjects except that the controls had a self-assessed VAS of 0. Exclusion criteria included pregnancy, organic pelvic disease, alcohol or drug abuse, failure of MRI scans due to metal or pacemaker implants, and formal diagnosis of psychiatric conditions. Urinary luteinizing hormone tests were performed to verify experimentally whether the participants were in their periovulatory phase (i.e., days 12–16 of the menstrual cycle), which is the phase when influence of chronic PDM was usually evaluated (Wei et al., 2016; Liu J. et al., 2017; Liu et al., 2018).

Human Experimental Procedure

The scheme of the experiment is presented in **Figure 2A**. After arriving at the lab, participants were asked to complete a detailed consent form. Psychological questionnaires (including the Positive and Negative Affect Scale, PANAS (Watson et al., 1988), and the Basic Needs Questionnaire, BNQ) (Bernstein and Claypool, 2012) were processed to obtain the baseline emotional state. Next, participants with PDM underwent abdominal and pelvic cavity, uterus and accessory MRI scans, and clinicians made the final diagnosis on whether the subjects were PDM patients. Participants who met the inclusion criteria then read the instructions outside the MRI room, and the researcher orally interpreted the instructions to the participants, indicating the duration of the experiment, the requirement to keep the head fixed and to warn about the noise of the machine and related equipment. Then, groups of three participants (including one real participant in the study and two fixed female 'actors') engaged in a 10-min group interaction session, after which participants were told to begin a Cyberball game, a paradigm based on a virtual ball-tossing game, where participants believe they are playing with other real participants, although in fact these are computer-generated (Eisenberger et al., 2003). Blood oxygenation level-dependent (BOLD) signal changes were recorded during the Cyberball task.

In the scanner, participants saw an animated ball-tossing game, with an icon representing their own hand at the bottom and the two other players depicted as animated icons in the upper corners. The names of the group members were shown next to each icon and participants could throw the ball to whoever they liked. Pressing "1" delivers the ball to the member in the upper left corner, while pressing "2" throws the ball to the member in the upper right corner. Participants were instructed to throw the ball within 2 s of receiving it. If the time exceeds 2 s, the system will temporarily transfer the ball randomly. The computer players waited 0.5–2.0 s before making a throw to heighten the sense that the participant was actually playing with other individuals. Each participant participated in three rounds of the Cyberball game during three fMRI scans. Each round of the Cyberball program consisted of 60 throws (including participant and computer players' throws) and lasted 3 min. The three rounds of Cyberball (**Figure 2B**) were as following, (1) Cyberball observation, implicit social exclusion (ISE), where participants were told that the intranet connection was not effective yet because of technical problems, but that they could watch the other participants playing; (2) Cyberball inclusion (INCL), where participants were told they were connected and played with the other players, participant and other players were equally likely to throw the ball; and (3) Cyberball exclusion, explicit social exclusion (ESE), where participants received three throws and were then excluded from the game (i.e., the other players

started playing exclusively together, and the real participant never received the ball again) (Eisenberger et al., 2003).

Participants and experimenters were in a double-blind state, namely, participants were told that the purpose of the study was to examine the effect of imagination on mission performance; the experimenter did not know who among the participants was a PDM subject. Immediately following the scanning session, participants completed the PANAS and BNQ questionnaires again. At the end of the experiment, participants were asked whether they believed they were playing the Cyberball game with the other two participants (i.e., the 'actors' they met initially). Subjects who failed to initiate social exclusion were excluded according to their answers (for example, if they did not believe that they were playing a real game of pitching, but thought it was a pre-set experimental procedure) and the PANAS and BNQ scales scores before and after the Cyberball game were compared (Eisenberger et al., 2006). In this study, both PDM subjects and controls showed a significantly higher post-BNQ score than pre-BNQ score, indicating that the participants noticed the exclusion and felt excluded (**Table 1**). Finally, each participant received 70 yuan (RMB) as compensation and was thoroughly debriefed about the purpose of the study.

MR Data Acquisition and Preprocessing

Magnetic resonance (MR) data were acquired on a 3.0 Tesla clinical scanner (Achieva TX; Philips Healthcare, Best, Netherlands) with an 8-channel head coil in Sun Yat-sen Memorial Hospital, Sun Yat-sen University. We performed resting-state fMRI (rs-fMRI) before task fMRI (T-fMRI) using a T2*-weighted fast-field echo-planar imaging (FFE-EPI) sequence (rs-fMRI/T-fMRI TR = 2000 ms/3000 ms, TE = 30 ms, FA = 90°, FOV = 240 mm × 240 mm, acquisition matrix = 64 × 64, thickness = 4.0 mm, 33 transverse slices covering the whole brain; 240/60 volumes were obtained for rs-fMRI/each round of T-fMRI). High-resolution structural images were collected using a T1-weighted 3D FFE sequence (TR = 8.2 ms, TE = 3.7 ms, FA = 8°, FOV = 256 × 256, acquisition matrix = 256 × 256, thickness = 1 mm; 168 sagittal slices covered the whole brain).

Rs-fMRI data were preprocessed using SPM 12[1] and the DPABI v3.1 toolbox[2] in MATLAB. For each subject, the first 10 functional images were discarded to reach magnetization equilibrium and to allow adaptation to the MR environment. Then, a slice-timing correction was conducted by setting the middle slice (17th) as the reference. Realignment was performed to estimate head motion, and two PDM subjects were excluded due to excessive head motion (translation more than 2 mm, or rotation more than 2°). We also calculated the mean frame-wise displacement based on Jenkinson's model (FD-Jenkinson), and ensured there was no significant group effect on the FD-Jenkinson (Jenkinson et al., 2002). High-resolution structural images were co-registered into functional images and segmented into white matter, gray matter and cerebrospinal fluid. Then, we spatially normalized the functional images to the individual structural image in standard MNI-152 standard space with a resampled voxel size of 3 mm × 3 mm × 3 mm; one PDM and four healthy subjects were excluded due to bad normalization (such as, no alignment between functional image and MNI-152 template; functional signal loss of normalization map). Furthermore, nuisance covariates (Friston 24 head motion parameters, mean white matter and mean cerebrospinal fluid) were regressed out to reduce the effect of complex noise. Finally, we further conducted spatial smoothing with a Gaussian kernel of 4 mm full-width at half maximum (FWHM) and performed band-pass filtering (0.01–0.1 Hz) to reduce high-frequency physiological noise. Finally, 35 PDM subjects and 38 controls were included in the further rs-fMRI analysis.

In the T-fMRI, 34 PDM subjects and 36 controls completed the three rounds of Cyberball. For each round of this task, the first five volumes were removed to control for interference between rounds. Other T-fMRI preprocessing steps, including slice-timing, realignment, co-registration, normalization and spatial smoothing, were conducted as for rs-fMRI preprocessing. A high-pass filter (cutoff 128 s) was used to remove low-frequency noise. After quality control, nine subjects with excessive head motion or bad normalization were excluded, leaving 30 PDM subjects and 31 healthy controls for further analysis.

Static FC Between ACC and HIPP in the rs-fMRI

Since static FC assumes that brain connectivity is temporally stationary (Fox and Raichle, 2007), we calculated the correlation coefficient between ACC and HIPP over the whole scan time to reflect the overall connections. The bilateral ACC and HIPP were selected as regions of interest (ROIs) for ROI-based FC based on the Automated Anatomical Labeling atlas (AAL) (Rolls et al., 2015), which is widely used for human brain imaging analysis. The specific MNI locations of the ROIs (ACC and HIPP) are viewed on the ICBM152 human brain surface (Mazziotta et al., 2001; **Figure 1A**). For each participant, we extracted the time courses of each ROI from preprocessed images. Then, the Pearson's correlation coefficients (r) between ACC and HIPP were computed. To improve the normality of group analysis, Fisher's z-transformation was performed to convert the r-value into a z-value.

Dynamic FC Between ACC and HIPP in the rs-fMRI

Dynamic FC between ACC and HIPP was calculated using a sliding time-window approach. We fixed the length of the time-window at 20 TRs (40 s) and the sliding step to 1 TR: 211 FC matrices between ACC and HIPP were obtained for each subject [time points: TP = 230 TRs; length of time-window (L) = 20 TRs; sliding step = 1 TR; dynamic FC matrices: $T = TP - L + 1 = 211$] (Li et al., 2014). The standard deviation of FC across all 211 slide-window FC matrices was calculated as FC variability, which reflects the discreteness of FC.

[1] https://www.fil.ion.ucl.ac.uk/spm/software/spm12/

[2] http://www.rfmri.org/

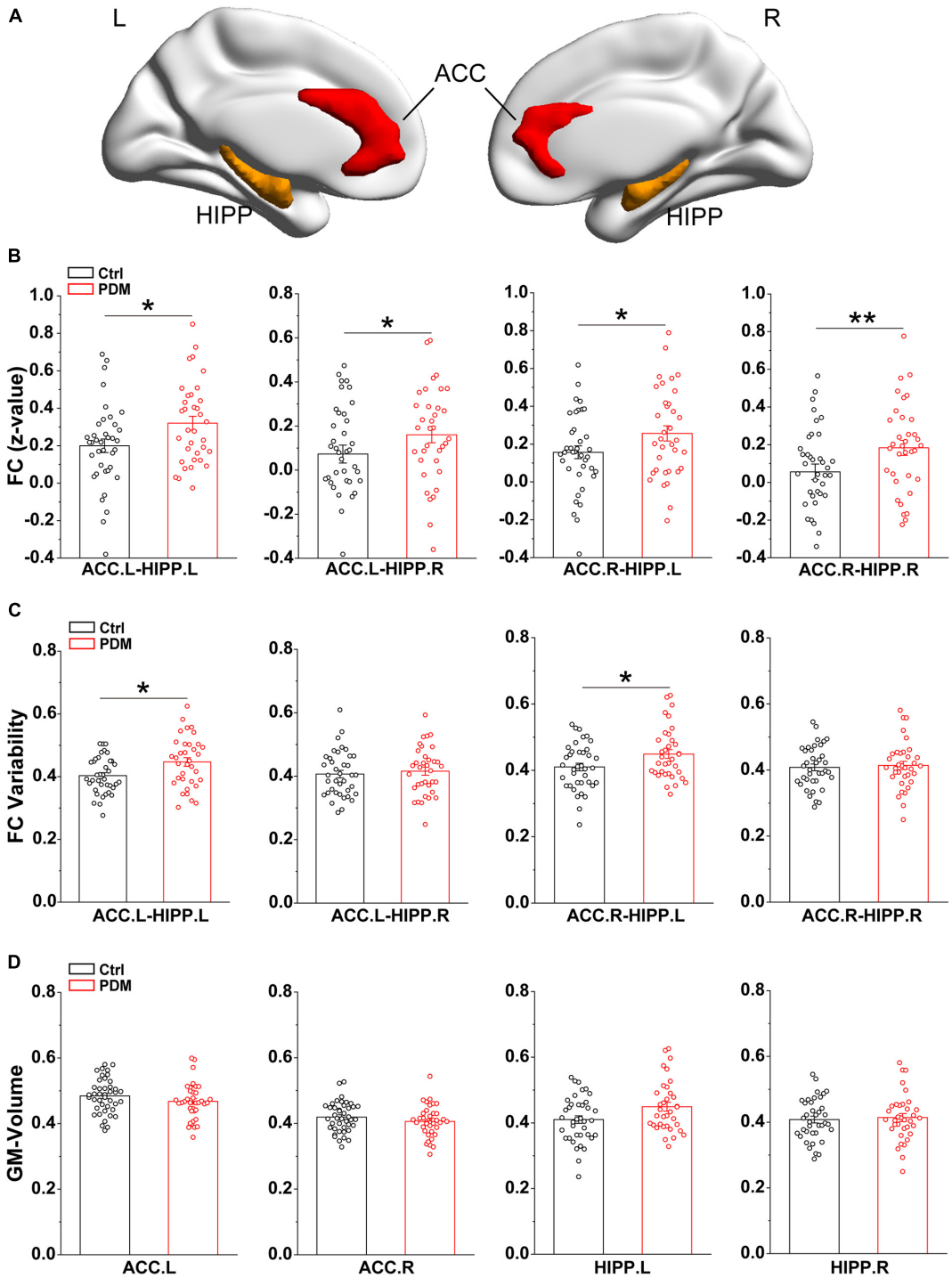


FIGURE 1 | Greater static FC and FC variability between ACC and HIPP, with unchanged GM volumes, in PDM females. **(A)** Three-dimensional brain view of the ICBM152 MNI depicting the location of the bilateral ACC (red) and HIPP (yellow) based on the Anatomical Automatic Labeling (AAL) atlas. **(B)** In the static FC, PDM subjects exhibited increased FC between ACC.L-HIPP.L, ACC.L-HIPP.R, ACC.R-HIPP.L, and ACC.R-HIPP.R. **(C)** The PDM group exhibited significantly greater FC variability between ACC.L-HIPP.L and ACC.R-HIPP.L than controls. **(D)** The GM volume of both ACC and HIPP did not change significantly in PDM females compared to controls ($p > 0.05$). L, left hemisphere; R, right hemisphere. Error bars = ± 1 SE. $n = 35$ (38) and 38 (42) for PDM and control females in the static FC, FC variability (GM volume) analysis, respectively. Non-parametric permutation test with days of menstrual cycle as regressor for static FC, FC variability and GM volume. $^{*}p < 0.05$; $^{**}p < 0.01$.

GLM and PPI Analysis in the T-fMRI

Whole-brain general linear model (GLM) analysis was performed using standard hemodynamic response function to identify brain activation during the Cyberball task. Each round of Cyberball (ISE, INCL, ESE) was modeled using a block design. The contrasts of interest – implicit exclusion compared with inclusion (ISE-INCL), explicit exclusion compared with implicit exclusion (ESE-ISE), and explicit exclusion compared with inclusion (ESE-INCL) – were then computed to depict social exclusion resulting from peer rejection. The GLM parameter maps of the contrasts were generated for each participant. Significant differences in brain activation were evaluated by performing a group comparison of the GLM-parameter maps.

Psychophysiological interaction (PPI) analysis (Friston et al., 1997) was conducted to determine which cerebral regions were functionally connected with the ROI for each of the ISE-INCL, ESE-ISE, ESE-INCL contrasts separately. Prior studies suggested that the ACC is activated by social exclusion (Bolling et al., 2011; Masten et al., 2011) and therefore the ACC (ACC.L/ACC.R/combined bilateral ACC) was chosen to initiate the PPI analysis. The deconvolved activity time-series of the left ACC, right ACC, and combined bilateral ACC were extracted and adjusted for effects of interest (ISE-INCL, ESE-ISE, ESE-INCL), and the PPI term was created using the ROI eigenvariate and the specific task contrasts (ISE-INCL, ESE-ISE, ESE-INCL). Finally, a second GLM was performed with a condition-specific regressor probing each contrast (ISE-INCL, ESE-ISE, ESE-INCL) to obtain the PPI parameter map, allowing the identification of ACC-connectivity changes for social exclusion during Cyberball. To further clarify the connectivity between ACC and HIPP under social exclusion conditions, the mean PPI parameter of HIPP was extracted for the group comparison.

Voxel-Based Morphology Analysis of the Structural MRI

The T1-weighted structural images were preprocessed with the VBM toolbox in the SPM12. The GM volume of each subject was evaluated using voxel-based morphology (VBM) analysis. First, the structural image was manually reoriented to MNI space and centered on the anterior commissure to facilitate the following segmentation step. The reoriented image was then segmented into GM and white matter using the unified segmentation approach. Spatial smoothing with 4 mm FWHM was performed on the warped and modulated GM map to improve the spatial resolution. Finally, we restricted our search regions to the ACC and HIPP, rather than the whole brain. To achieve this, we extracted the GM signal of the ACC and HIPP for each subject.

Experimental Animals

Female Sprague-Dawley (SD) rats were purchased from the Laboratory Animal Center of Southern Medical University (Guangzhou, China) and kept at the School of Life Sciences, South China Normal University, with controlled humidity and temperature, and a 12 h (6:30 AM to 6:30 PM) light–dark cycle. Rats involved in experiments were used according to international and university ethical standards. Food and water were available *ad libitum*. Animals weighing 250–300 g (120–150 days old) were given on average 7 days to adjust to the new environment prior to the experiments. Pelvic pain model was generated by intraperitoneal (IP) injection of estradiol benzoate and oxytocin (both Ningbo Hormone Inc., China).

Rat PDM Model

The experimental procedures of this study were approved by the Animal Protection and Use Committee of Guangzhou University and South China Normal University. The chronic PDM rat model was generated by modification of an acute PDM mouse model (Chen et al., 2013; Jesuino et al., 2019). Briefly, estradiol benzoate was injected (IP, two times/week, 4 mg/Kg) for eight consecutive weeks (wks). From the fourth wk through the eighth wk, PDM rat model were injected with oxytocin (IP, one injection/week, 20 IU/Kg/per injection) 24 h after injection of estradiol benzoate. Control rats received injections of an equal volume of estradiol benzoate and saline. Paw withdrawal mechanical threshold (PWMT) (Chaplan et al., 1994; Liu Y. et al., 2017), electrophysiological and biochemical evaluations were conducted in control and PDM rats between 24 and 72 h following the last oxytocin injections.

In vivo Surgery and Extracellular Recording

In vivo dual-site extracellular recordings were conducted as described with a few modifications (Noguchi et al., 2017; Chen et al., 2019). Rats were anesthetized with pentobarbital sodium (IP 80 mg/kg, Sigma, United States) then head-fixed in a stereotaxic apparatus (RWD Life Science, China) with body temperature maintained between 36 and 37°C. When necessary, a supplemental dose of anesthesia was given based on tail reflex. After a midline skin incision was made, two skull holes were drilled above the ACC (2.5 mm anterior to the bregma, 0.4 mm lateral to the midline, 1.7-2.0 mm depth) and the dorsal CA1 subregion of the HIPP (3.6 mm posterior to the bregma, 2.0 mm lateral to the midline, 2.2–2.5 mm depth, 10°) under a stereomicroscope (Sunny Optical Technology, China). Two glass microelectrodes for recording (filled with 0.5 M NaCl, resistance 4–6 MΩ) were slowly inserted until the tips of the electrodes reached the ACC and hippocampal CA1. Each recorded signal was amplified (1,000x) by an electrometer amplifier (Model 3000; A-M Systems, United States) and digitized via a D/A converter (Micro 1401; Cambridge Electronic Design, Ltd., United Kingdom), then sent to data acquisition software (Spike2; Cambridge Electronic Design).

LFP Analysis

Extracellular recording data were analyzed offline in MATLAB. For processing the local field potential (LFP), a Butterworth low pass filter (300 Hz) was applied to the raw recorded data. Power spectral density was computed using Thomson's multitaper method for a fast Fourier transformation (FFT) to determine the power for specific frequency bands. Frequency ranges were

defined as follows: delta: 1–4 Hz; theta: 4–12 Hz; gamma: 30–100 Hz, of which theta frequency covers a wider range in the rodent (Buzsaki and Draguhn, 2004; Tamura et al., 2017).

We performed synchronization analysis in line with our established methodological protocol (Chen et al., 2019). Simultaneous signals were subjected to cross-correlation estimation to quantitatively evaluate the similarity. The maximal offset was set to ±1 s. After the calculation, spectral coherence between the two LFPs from the ACC and HIPP was analyzed using a FFT number of 2^{12}, and the values ranged from 0 to 1, meaning non-correlated or completely correlated in the frequency domain.

To further evaluate the synchrony between the oscillations of ACC and HIPP, weighted phase lag index (WPLI) analysis, which is based on the complex conjugate of spectral coherence (Vinck et al., 2011), was conducted to the same dataset. The indices were shown from 0 to 1 as mentioned above.

To access the modulation strength of cross-frequency oscillations, we first derived the instantaneous phase and amplitude from the targeted signals of both areas, then analytically clustered the theta phases binned into 20° intervals with the corresponding gamma amplitude at the same time in the other region. Both directions were analyzed to compare the influence of the theta band on the interregional gamma band.

Whole-Cell Patch-Clamp Recording

Acute brain slices containing ACC and HIPP (350 μm) were prepared according to routine procedures (Chen et al., 2017; Luo et al., 2019), from control and PDM rats using a vibratome (VT 1000S, Leica, Germany) in oxygenated ice-cold cutting solution containing (in mM), 119 NaCl, 2.5 KCl, 2.5 $CaCl_2$,1.3 $MgSO_4$, 1 NaH_2PO_4, 11 D-glucose, 26.2 $NaHCO_3$ (pH 7.2-7.4), saturated with 95% O_2/5% CO_2. Slices were kept in artificial cerebrospinal fluid (aCSF) containing (in mM) 140 NaCl, 4.7 KCl, 2.5 $CaCl_2$, 1.2 $MgCl_2$, 11 D-glucose, 10 HEPES (pH 7.2-7.4), and gassed with 95% O_2/5% CO_2. Slices were incubated for 1 h at 30–32°C before recording and then transferred to a submerged recording chamber where temperature was held at 32 ± 0.5°C with an automatic temperature controller (TC-324B, Warner Instrument Corporation) with aCSF flow set at 2–3 ml/min.

Pyramidal neurons were identified by their morphology, typically characterized by a triangular-shaped soma, in brain slices (Ramaswamy and Markram, 2015). To record miniature excitatory and inhibitory postsynaptic currents (mEPSCs and mIPSCs) from pyramidal neurons of the ACC and HIPP, voltage was held at –60 and 0 mV, respectively. To block fast sodium channel activity and thus action potential, 1 μM TTX was added to the aCSF (Chen et al., 2017). The pipette was filled with the following internal solution (mM): 100 mM Cs-gluconate, 5 mM CsCl, 10 mM HEPES, 2 mM $MgCl_2$, 1 mM $CaCl_2$, 11 mM BAPTA, 4 mM ATP, and 0.4 mM GTP (pH 7.3, adjusted with KOH) at an osmolality of 280–290 mOsm. Data were collected with a MultiClamp 700 B amplifier (Axon Instruments) and filtered during acquisition with a low pass filter set at 2 kHz using pCLAMP10 software (Molecular Devices, United States). The data were analyzed offline using Mini Analysis Program (Synaptosoft Inc., United States).

Western Blotting Analysis

Rat brains were dissected and ACC and HIPP tissues were removed on ice as previously described (Chen et al., 2017). Tissues were then homogenized in SDS buffer (50 mM Tris pH 7.5, 150 mM NaCl, 5 mM EDTA pH 8.0, 1% SDS). Cellular debris was removed by centrifugation at 4°C (14,000 rpm for 10 min) and the supernatant was collected for analysis. Tissue lysates were subjected to SDS-PAGE, and transferred to nitrocellulose membranes. The membranes were blocked with 5% non-fat dry milk and incubated with specific primary antibodies GluR1 (Abcam, ab31232; dilution 1:1000), GluR2 (Abcam, ab206293; dilution 1:2000), GluR4 (Abcam, ab119995; dilution 1:4000), NMDAR1 (Abcam, ab109182; dilution 1:4000) or NMDAR2B (Abcam, ab65783; dilution 1:4000) overnight at 4°C. GAPDH (Beyotime, AF0006; dilution 1:5000) or anti-β-actin antibody (Sigma, United States; dilution 1:5000) was used as a loading control. After three washes with TBST, HRP-labeled secondary antibody (CWS, China) was added at room temperature for 1 h using 5% milk in TBST followed by three additional washes with TBST. The Immobilon ECL western system (Millipore, United States) was then used to visualize the bands, which were quantified and analyzed with Gel-Pro Analysis software (Media Cybernetics, United States).

Statistical Analysis

Normal distribution was tested in demographics and psychological data. Except for the BNQ score, all data were not distributed normally. Thus, Mann–Whitney tests were used to detect differences in age, age of onset of menstruation, menstrual duration, menstrual cycle, and PANAS between the PDM subjects and healthy controls. Wilcoxon test was used to detect difference in PANAS between pre- and post-tests. Parametric tests (including two-sample *t*-tests and paired-sample *t*-tests) were performed to determine differences in BNQ between and within group, respectively. Two-sample *t*-tests were also performed to detect group differences in the GLM-parameter map and PPI-parameter map, to identify abnormal regional brain activity and abnormal regions functionally connected with the ACC. Multiple comparison corrections were conducted using an AlphaSim correction (both voxel-wise threshold and cluster threshold were set as $p < 0.05$) and the Gaussian Random Field correction (voxel-wise threshold: $p < 0.01$; cluster threshold: $p < 0.05$) separately. A non-parametric permutation test was conducted to identify between-group differences in the static FC, FC variability, GM volume and ACC-HIPP PPI parameters. In the calculation, we took the menstrual cycle as covariate and regressed it out if there was a significant difference in the menstrual cycle between PDM subjects and controls. For LFP analysis, the data were first tested for normal distribution. None of the datasets were distributed normally, therefore a non-parametric test was used for two-group comparisons. Student's *t*-test was used in two-group comparisons of western blotting results. For comparisons of multiple groups, one-way ANOVA or two-way ANOVA with *post hoc* tests were used. Data are shown as mean ± SEM unless otherwise stated. Statistical significance threshold was set at $p < 0.05$.

RESULTS

Demographic and Clinical Information of PDM Subjects and Controls Used in MRI

For the rs-fMRI and structural MRI, no significant differences were found for the age, age of onset of menstruation or menstrual duration between the PDM subjects and controls, while a longer menstrual cycle was found in the PDM subjects. For the T-fMRI, there were no significant between-group differences for age, age of onset of menstruation, menstrual duration, menstrual cycle, PANAS, and BNQ. Both groups showed no significant difference in PANAS between pre- and post-test values, and a significantly higher post-BNQ score than pre-BNQ score. The specific values are presented in **Table 1**.

Significantly Increased FC in rs-fMRI Between ACC and HIPP in PDM Women

To examine the synchronization of blood oxygenation level dependent (BOLD) signals between the ACC and HIPP, we first evaluated FC, utilizing rs-fMRI, for both static and dynamic FC in 35 PDM women with 5.14 ± 2.13 years dysmenorrhea and 38 age-matched controls (**Table 1**). Static FC increased significantly in PDM subjects between left/right ACC and left/right HIPP (ACC.L-HIPP.L, ACC.L-HIPP.R, ACC.R-HIPP.L, ACC.R-HIPP.R) compared to controls ($p < 0.05$; **Figure 1B**), indicating that experiencing 5 years of PDM changes brain FC between the ACC and HIPP. Given that the human brain is a complex and interactive system that dynamically processes information flow and that changes in FC over time are not revealed by static FC evaluations (Hutchison et al., 2013), we next examined the variability in FC, i.e., changes in the connections between the ACC and HIPP, using a sliding time window (see section "Materials and Methods" for details). The dynamic FC calculations revealed significantly increased FC variability between the left ACC and left HIPP (ACC.L-HIPP.L) as well as between the right ACC and left HIPP (ACC.R-HIPP.L) in the PDM cohort ($p < 0.05$; **Figure 1C**). Thus, both static and dynamic FC suggest an overall increase in communication between the ACC and HIPP in PDM females.

Alterations in FC Revealed by T-fMRI During Social Exclusion Induced by Cyberball

Given that being socially integrated is a primary human need (Adolphs, 2010), and that emotional/mental stimuli can lead to altered activation of brain areas, such as the ACC (Singer et al., 2004), we next asked whether the experience of PDM, a type of physical pain, would change the brain activation and FC when dealing with negative and positive emotional stimulations, i.e., social exclusion and inclusion conditions. To do so, we used the Cyberball task, a paradigm based on a virtual ball-tossing game, including three scenarios of implicit social exclusion (ISE), inclusion (INCL), and explicit social exclusion (ESE) (Williams et al., 2000; Eisenberger et al., 2003).

We first evaluated the condition-related differences in regional brain activity as measured by T-fMRI utilizing the general linear model (GLM), a method used to evaluate differences in activation under various conditions by subtracting one condition from another, i.e., in this case, ISE-INCL, ESE-ISE, and ESE-INCL (Friston et al., 1997). In the GLM analysis, PDM females showed decreased activation of the right Crus II of the cerebellar hemisphere (CERCRU2) in the ESE-ISE contrast compared to controls (**Figure 2C** and **Table 2**). No significant difference was found in the ISE-INCL and ESE-INCL contrast between PDM subjects and controls (**Table 2**).

We next conducted psychophysiological interaction (PPI) analysis (Friston et al., 1997) to determine which brain regions were functionally connected with the ACC. In the ISE-INCL contrast, the FC between ACC.L-brainstem and ACC-brainstem (including the right parahippocampal region, PHIPP.R) was higher in PDM females than in controls (**Figure 3A** and **Table 3**). In the ESE-INCL condition, PDM females demonstrated increased connectivity between ACC.L-right thalamus (THA.R)/PHIPP.L/right inferior frontal gyrus, triangular part (IFGtriang.R), ACC.R-HIPP.R/HIPP.L/IFGtriang.R/right superior frontal gyrus (SFG.R), and ACC-HIPP.R/HIPP.L/right middle frontal gyrus (MFG.R) (**Figure 3B** and **Table 3**). Identical FC between regions connected with ACC.L/ACC.R/ACC was observed in PDM subjects and controls in the ESE-ISE contrast. Together, the results indicate increased connections between the ACC and the above brain areas in response to Cyberball-induced social exclusion in PDM females.

We further evaluated the FC of the ACC-HIPP pathway using PPI analysis to reveal whether and how this specific pathway differs between PDM subjects and controls. We found that in the ISE-INCL contrast, PDM females showed significantly increased FC in the ACC.L-HIPP.L and ACC.R-HIPP.L circuits (**Figure 3C**). Furthermore, the combined ACC analysis, i.e., not separating left and right ACC, also showed significantly increased ACC-HIPP FC in the ISE-INCL contrast in PDM subjects (**Figure 3C1**). In the ESE-ISE contrast, overall ACC-HIPP FC did not differ significantly in PDM women (**Figure 3D1**), although FC of the ACC.L-HIPP.L and ACC.R-HIPP.L connections was significantly lower (**Figure 3D**). The results suggest that exclusion, whether explicit or implicit, triggered similar FC in the ACC-HIPP pathway in PDM and control females. In the ESE-INCL contrast, PDM subjects also showed significantly higher FC for all four ACC-HIPP connections (**Figure 3E**) as well as the combined analysis (**Figure 3E1**).

Identical GM Volume in PDM and Control Subjects

Prolonged nociceptive input to the CNS has been shown to induce functional and structural alterations throughout the nervous system (Denk and McMahon, 2017). Having shown that significant differences occurred in the static and dynamic FC of PDM females, we investigated the GM volume of the

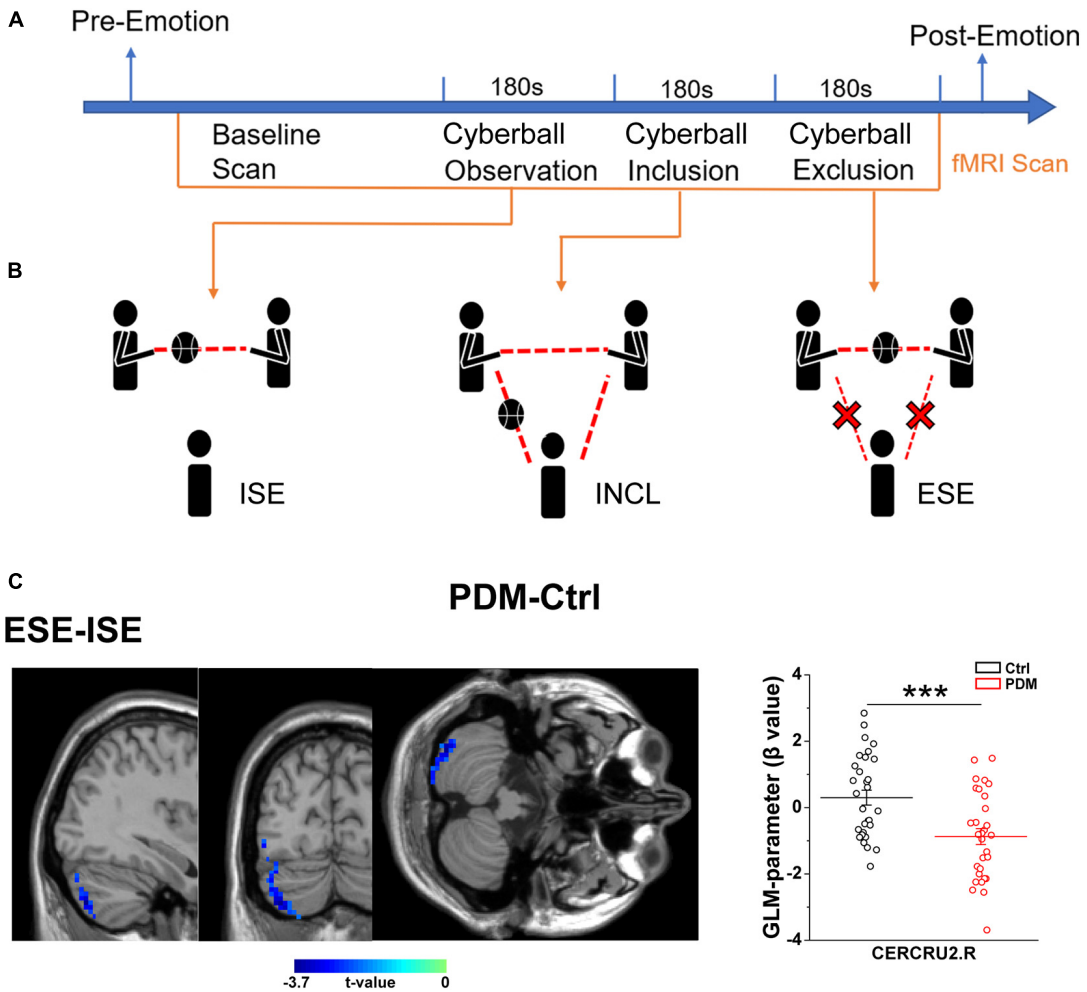


FIGURE 2 | Abnormal brain activation in the right CERECRU2 for the ESE-ISE contrasts in PDM females. **(A)** Scheme of the experiment: baseline emotional state was collected using psychological questionnaires including Positive and Negative Affect Scales (PANAS) and Basic Needs Questionnaire (BNQ) for each subject. Then, MRI scans were performed in the resting-state and during three Cyberball scenarios. Finally, the PANAS and BNQ were conducted again to record the post-emotional status of the subjects. **(B)** Schematic representation of the three Cyberball scenarios: Cyberball observation represents ISE, where participants were told that the intranet connection was not yet effective due to technical issues, but that they could watch other participants play; Cyberball inclusion, INCL, where subjects participated in the social activity of passing the ball; Cyberball exclusion, ESE, individuals were prevented from participating in the social activity of passing the ball by other players playing among themselves only. **(C)** Significantly reduced activation in the right CERCRU2 for the ESE-ISE contrasts in the PDM group compared to Controls. The GLM-parameter (β value) for each region was extracted to reflect the brain activation in the PDM and Controls. $n = 30$ and 31 for PDM and control females, respectively. Error bars = ± 1 SEM. Two-sample t-test and AlphaSim correction with voxel-wise threshold of $p < 0.05$ and a cluster threshold of $p < 0.05$ were used to determine the brain regions with significantly abnormal activity. The color bar represents the t-value. CERCRU2, Crus II of cerebellar hemisphere; R, right hemisphere. ***$p < 0.001$.

ACC and HIPP using a voxel-based morphometry (VBM) approach. However, we found no significant differences between PDM subjects and controls (**Figure 1D**). Thus, the above abnormal connections between ACC and HIPP are not due to GM volume changes.

Increased Writhing and Reduced Pain Threshold in a Pelvic Pain Rat Model

Given the ethical constraints of human studies, cellular and molecular studies using rodent models are beginning to be used to provide insights into the mechanisms that give rise to chronic pain (Zhuo, 2014). However, this has not been tested directly in PDM due to the lack of a chronic PDM rodent model. Therefore, we generated a chronic pelvic pain rat model that mimics dysmenorrhea-like pain experience based on an existing acute rodent PDM model (Chen et al., 2013; Jesuino et al., 2019), which was characterized by evaluating the levels of prostaglandin F2α and prostaglandin E2, endometrial thickness, and uterine artery blood flow velocity, etc., features that are similar to those found in human PDM (Yang et al., 2015). In this study, after 4 weeks of intraperitoneal (IP) estradiol benzoate injections, which promotes enhanced sensitivity of the uterus to oxytocin (Chen et al., 2013),

TABLE 2 | Specific brain regions show significant group differences in activation for ISE-INCL, ESE-ISE, ESE-INCL contrasts.

	Peak location (AAL-90)	No. of voxels	Peak *t*-value	Peak coordinate in MNI space			Included other regions	GLM-parameter (β value) (mean ± SEM)	
				X	Y	Z		PDM	Ctrl
ISE-INCL									
PDM-Ctrl	N/A	N/A	N/A	N/A	N/A	N/A	N/A	N/A	N/A
ESE-ISE									
PDM-Ctrl	CERCRU2.R	196	–3.655	36	–78	–48	CERCRU1.R, ITG.R	–0.873 ± 0.241	0.298 ± 0.224
ESE-INCL									
PDM-Ctrl	N/A	N/A	N/A	N/A	N/A	N/A	N/A	N/A	N/A

ISE, implicit social exclusion; INCL, inclusion; ESE, explicit social exclusion; PDM, primary dysmenorrhea; Ctrl, controls; GLM, general linear model; MNI, Montreal Neurological Institute; AAL, automated anatomical labeling atlas; CERCRU2, Crus II of cerebellar hemisphere; CERCRU1, Crus I of cerebellar hemisphere; ITG, inferior temporal gyrus; SEM, standard error of mean; R, right hemisphere. N/A, non-applicable.

oxytocin (PDM) or saline (Control) was IP-injected 24 h after estradiol benzoate and repeated for five consecutive weeks (**Figure 4A**). The rats given estradiol and oxytocin injections exhibited pain induced writhing, indicating abdominal/visceral pain (**Supplementary Material 1**), i.e., dysmenorrhea-like behavior, due to uterine contraction (Sun et al., 2002). The number of writhing events within a 30 min time window was evaluated (**Figure 4B**). Average writhing latency was less than 10 s after each oxytocin injection (**Figure 4C**). In agreement with findings suggesting that women with PDM have elevated pain reactivity (Iacovides et al., 2013), rat with pelvic pain showed a significantly decreased paw withdrawal mechanical threshold (PWMT) (**Figure 4D**), indicating that these rats are hypersensitive to pain. We next conducted electrophysiological and biochemical experiments in model and control rats to uncover molecular and cellular alterations induced by chronic pelvic pain.

Alterations in Oscillatory Power in the ACC and HIPP

Neuronal oscillatory activity, which is the neural basis of MRI and is preferentially sensitive to BOLD (Logothetis et al., 2001), is fundamental for the entrainment of precise temporal relationships between neuronal responses involved in cognition, perception and emotion (Mathalon and Sohal, 2015). To further evaluate whether the rat model is indeed representative of PDM, we examined whether abnormal neural oscillations occur in pelvic pain model rats by simultaneous dual-site LFP recording in the ACC and dorsal HIPP (**Figure 5A**). We found that the model rat demonstrated significantly enhanced theta power in the ACC (**Figure 5B**) and significantly enhanced gamma power in the HIPP (**Figure 5C**).

Increased Gamma Coherence and WPLI Between ACC and HIPP in Model Rats

Functional coupling of oscillatory activities between pain processing and affective brain areas underlies the suffering associated with chronic pain (e.g., cognitional and emotional alterations), but this cannot easily be studied in PDM women. We thus examined electrical connectivity between the ACC and HIPP using cross-correlation analysis of LFPs (Engel et al., 2001). Model and control rats demonstrated similar correlation values in both ACC-leading and HIPP-leading directions (**Figure 5D**), suggesting the existence of similar bidirectional communication between the ACC and HIPP.

We next evaluated ACC-HIPP connectivity in the frequency domain (**Figure 5E**) by coherence analysis (Chen et al., 2021), and observed significantly increased coherence in the gamma range in model rats (**Figure 5F**). To better understand the connectivity in more precise phase ranges, we next used WPLI analysis (Vinck et al., 2011) which can reduce the contingency caused by the bidirectional connection. The result showed a significantly increased gamma-specific WPLI in model rats (**Figures 5G,H**), which was in agreement with the coherence analysis. Given that resting state FC indicated by BOLD output reflects the contributions of low frequency LFP signals and their dynamic changes (Shi et al., 2019), and that gamma band modulations co-localize with BOLD (Lachaux et al., 2007; Scheeringa et al., 2011), the enhanced synchronization observed between the ACC and HIPP in the gamma range reflects the increased FC shown by rs-fMRI in the ACC-HIPP pathway of PDM females.

Reduced ACC Theta Modulation on HIPP Gamma Oscillations in Model Rats

The above results uncovered, in addition to increased ACC-HIPP connectivity, altered theta and gamma oscillations in the ACC and HIPP, respectively. The ACC is a key cortical region for pain perception (Vogt, 2005; Zhuo, 2008) and increased theta oscillation may indicate an alteration in how the ACC modulates HIPP activity. To confirm this, we next determined the strength of cross-frequency PAC between ipsilateral ACC and HIPP (**Figure 5I**). Despite an increase in the power of ACC theta oscillations, the modulating effect of ACC theta on HIPP gamma oscillations decreased significantly. At the same time, the modulatory effect by HIPP-theta on ACC-gamma oscillations remained unchanged (**Figures 5J,K**). Thus, chronic pelvic pain results in a reduction of ACC theta-HIPP gamma coupling, suggesting that pelvic pain, such as PDM may change top-down ACC informational input into the HIPP.

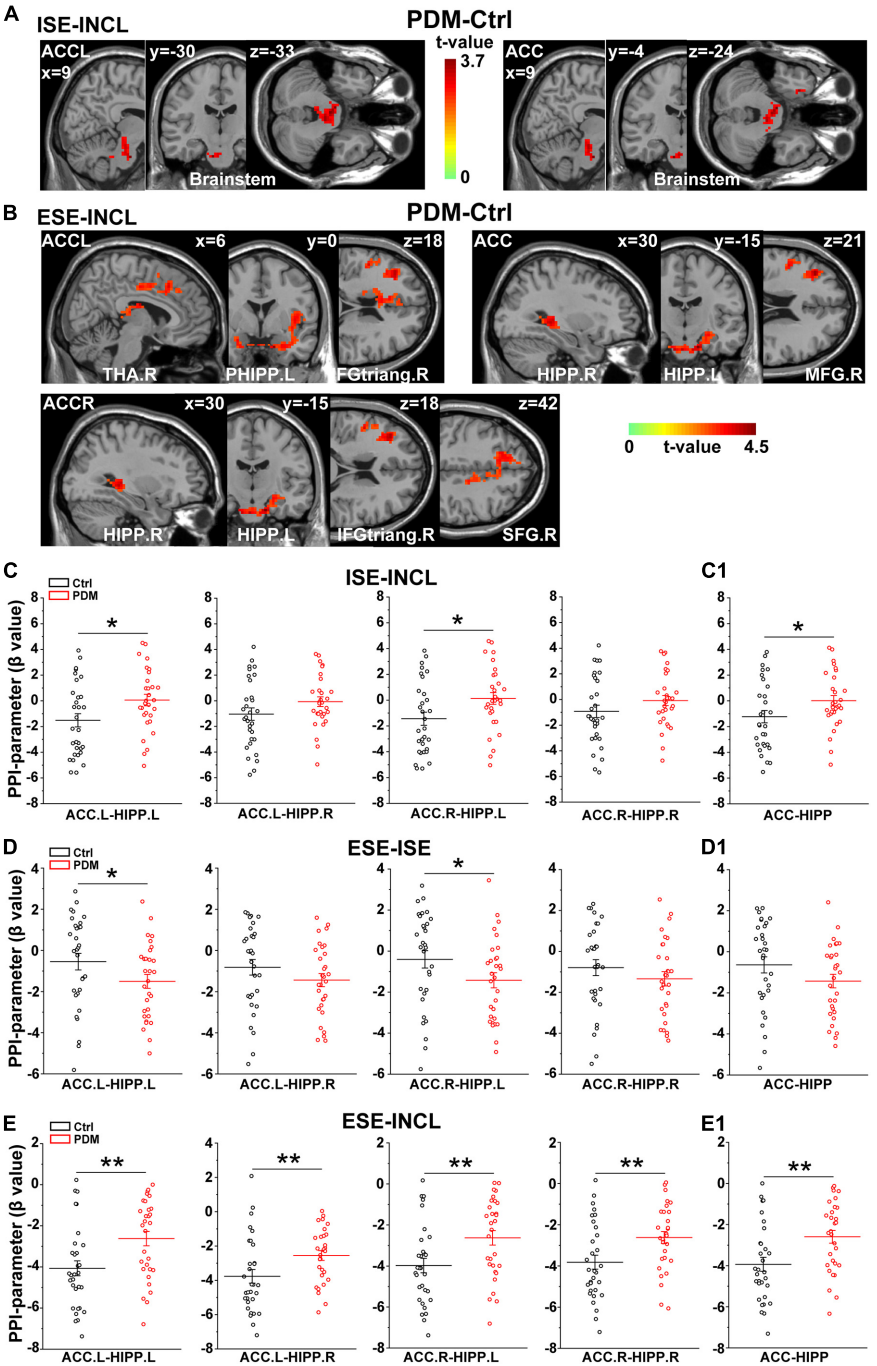


FIGURE 3 | Abnormal connectivity between ACC and HIPP in PDM females revealed by PPI analysis. **(A,B)** The PDM cohort has increased ACC connectivity in the ISE-INCL and ESE-INCL contrasts. In the ISE-INCL contrast **(A)**, PDM females show increased ACC.L/ACC connectivity with brainstem. In the ESE-INCL contrast **(B)**, PDM women demonstrate increased connectivity between ACC.L/ACC.R/ACC and other brain regions, including frontal cortex, thalamus, and HIPP. **(C–E)** The PDM group exhibits a significant difference in ACC-HIPP connectivity compared to controls. For the ISE-INCL contrast **(C)**, PDM subjects show increased ACC.L-HIPP.L and ACC.R-HIPP.L connectivity. ACC.L-HIPP.R and ACC.R-HIPP.R connectivity is identical. In the ESE-ISE contrast **(D)**, the PDM group show decreased connectivity for the ACC.L-HIPP.L and ACC.R-HIPP.L circuits. ACC.L-HIPP.R and ACC.R-HIPP.R connectivity is also identical. In the ESE-INCL comparison **(E)**, PDM subjects demonstrate increased connectivity for all ACC-HIPP combinations. Combining the bilateral regions also shows that PDM women have an overall increased ACC-HIPP connectivity in the ISE-INCL contrast **(C1)** and the ESE-INCL contrast **(E1)**; and no significant difference in the ESE-ISE contrast **(D1)**. Given that the PPI value is negative, the increased ACC-HIPP connectivity in the PDM indicated less connectivity reduction in the ISE-INCL and ESE-INCL contrast. L/R, left/right hemisphere; $n = 30$ and 31 for PDM and control females, respectively. The color bar represents the t-value. Error bars = ± 1 SEM. Two-sample t-test and Gaussian Random Field (GRF) correction with voxel-wise threshold of $p < 0.01$ and cluster threshold of $p < 0.05$ were used to determine the significantly abnormal brain regions functionally connected with ACC.L/ACC.R/ACC. A non-parametric permutation test was used for the specific ACC-HIPP connectivity with $p < 0.05$. *$p < 0.05$; **$p < 0.01$.

TABLE 3 | Specific brain regions show significant group differences in functional connectivity with ACC.L/ACC.R/ACC for ISE-INCL, ESE-ISE, ESE-INCL contrasts.

ROI	Peak location (AAL-90)	No. of voxels	Peak *t*-value	Peak coordinate in MNI space			Included other regions	PPI-parameter (β value) (mean ± SEM)	
				X	Y	Z		PDM	Ctrl
ISE-INCL (PDM-Ctrl)									
ACC.L	N/A	198	3.659	9	–18	–33	Brainstem, CER4_5.L	0.571 ± 0.312	–1.095 ± 0.35
ACC.R	N/A	N/A	N/A	N/A	N/A	N/A	N/A	N/A	N/A
ACC	N/A	208	3.678	9	–18	–33	Brainstem, PHIPP.R, AMYG.R, HIPP.R	0.63 ± 0.309	–1.08 ± 0.356
ESE-ISE (PDM-Ctrl)									
ACC.L/ACC.R/ACC	N/A	N/A	N/A	N/A	N/A	N/A	N/A	N/A	N/A
ESE-INCL (PDM-Ctrl)									
ACC.L	PHIPP.L	770	4.292	–15	0	–29	INS.L, HIPP.L, PHIPP.R	–1.511 ± 0.251	–3.21 ± 0.292
	IFGtriang.R	556	3.897	39	33	18	MFG.R, PUT.R, CAU.R, ACC.R, INS.R	–2.653 ± 0.312	–4.382 ± 0.365
	THA.R	1076	3.94	6	–12	20	MCC.L, MFG.L, SFG.L, MCC.R, SFG.R, SMA.R, PreCG.L	–2.744 ± 0.348	–4.561 ± 0.344
ACC.R	N/A	579	4.484	–15	–15	–30	HIPP.L, PHIPP.L,	–1.119 ± 0.226	–2.652 ± 0.267
	IFGtriang.R	287	4.057	39	33	18	MFG.R, IFGoperc.R, INS.R, PreCG.R	–2.498 ± 0.323	–4.228 ± 0.34
	HIPP.R	241	3.839	30	–36	0	THA.R, THA.L, CAU.L	–2.727 ± 0.311	–4.262 ± 0.278
	SFG.R	261	3.497	18	24	42	MCC.L, MFG.L, SFG.L, SMA.R	–2.885 ± 0.399	–4.771 ± 0.349
ACC	N/A	652	4.478	–15	–15	–30	HIPP.L, PHIPP.L, PHIPP.R,	–1.14 ± 0.227	–2.672 ± 0.269
	MFG.R	489	4.21	42	33	21	IFGtriang.R, IFGoperc.R, INS.R, PreCG.R	–2.489 ± 0.313	–4.24 ± 0.355
	HIPP.R	391	3.934	30	–36	0	THA.R, THA.L, CAU.R, CAU.L	–2.707 ± 0.311	–4.305 ± 0.308

ACC, anterior cingulate cortex; ISE, implicit social exclusion; INCL, inclusion; ESE, explicit social exclusion; PDM, primary dysmenorrhea; Ctrl, controls; PPI, psychophysiological interaction; ROI, region of interesting; MNI, Montreal Neurological Institute; AAL, automated anatomical labeling atlas; CER4_5, lobule IV, V of cerebellar hemisphere; PHIPP, parahippocampal gyrus; AMYG, amygdala; HIPP, hippocampal gyrus; INS, insula; IFGtriang, inferior frontal gyrus, triangular part; MFG, middle frontal gyrus; PUT, putamen; CAU, caudate nucleus; ACC, anterior cingulate cortex; THA, thalamus; MCC, middle cingulate cortex; SFG, superior frontal gyrus; SMA, supplementary motor area; PreCG, precentral gyrus; IFGoperc, inferior frontal gyrus, opercular part; SEM, standard error of mean; L/R, left/right hemisphere; N/A, non-applicable.

Increased mEPSC Amplitude in ACC and HIPP in Model Rats

Brain oscillations emerge as a consequence of local interactions between excitatory and inhibitory synaptic activities (Verret et al., 2012). Thus, the abnormal oscillations observed in the present study may implicate altered synaptic activities, because theta and gamma oscillatory activities relate to synaptic plasticity, in addition to network synchronization and memory formation (Tesche and Karhu, 2000; Buzsaki and Draguhn, 2004). We therefore examined whether or not abnormal excitatory and inhibitory synaptic activity in the ACC and HIPP underlie the aberrant oscillatory activity. Whole-cell patch-clamp recordings were conducted in brain slices containing either ACC or HIPP (**Figure 6A**). In voltage clamp mode and in the presence of TTX to block fast sodium channels and thus action potentials, the amplitude and frequency of mEPSCs and mIPSCs in the pyramidal neurons of the ACC and HIPP were measured. A significantly increased mEPSC amplitude was observed in pyramidal neurons in both the ACC and HIPP of model rats (**Figures 6B,C,F,G**), in agreement with the reported hyperactivity of ACC (Zhang et al., 2017; Zhou et al., 2018) and HIPP (Cardoso-Cruz et al., 2013) neurons during chronic pain. In contrast, mEPSC frequency in both ACC (**Figure 6C**) and HIPP (**Figure 6G**), as well as mIPSC amplitude and frequency (**Figures 6D,H**), was identical. These results suggest that increased excitation, which in turn leads to changes in the excitation/inhibition ratio, may contribute to abnormal oscillatory activities (Verret et al., 2012) in the ACC and HIPP.

Upregulation in Levels of Excitatory Receptor Proteins in Model Rats

Postsynaptic excitatory responses are mediated mainly by two groups of glutamatergic receptors, AMPA and NMDA receptors (AMPARs, NMDARs) (Dai et al., 2019). The observed

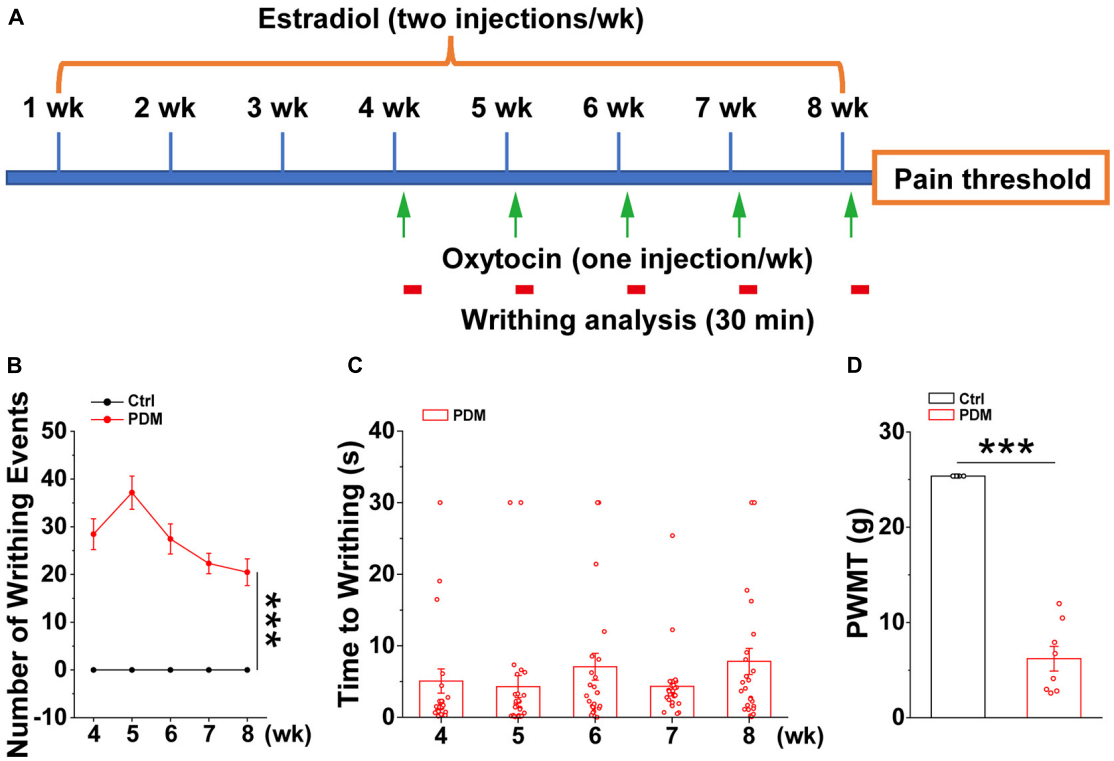


FIGURE 4 | Behavioral evaluations in model rats. Schematic diagram showing the timeline and treatments used in generating the pelvic pain model, together with subsequent measurements. Starting from week four, oxytocin or saline was injected 24 h after estradiol benzoate for pelvic pain (PP) and control animals, respectively **(A)**. Writhing and pain threshold was measured 24 h after the last dose of oxytocin or saline, LFPs were recorded on days 58 and 59. **(B,C)** Number of writhing events (30 min time window) (4 weeks: PP: 28.442 ± 3.217; 5 weeks: 37.154 ± 3.485; 6 weeks: 27.442 ± 3.156; 7 weeks: 22.308 ± 2.133; 8 weeks: 20.481 ± 2.789) (t = 9.947, p = 1.627 × 10^{-18}) and latency (4 weeks: 5.072 ± 1.694 s; 5 weeks: 4.302 ± 1.544 s; 6 weeks: 7.069 ± 1.882 s; 7 weeks: 4.334 ± 0.950 s; 8 weeks: 7.820 ± 1.834 s) (n = 26). **(D)** Model rats show significantly reduced paw withdrawal mechanical threshold (PWMT) compared to control rats (n = 8–10) (PP: 6.199 ± 1.296 g; Control: 25.368 ± 0.000 g) (t = –16.667, p = 1.558 × 10^{-11}), suggesting increased pain sensitivity in model rats, which is in agreement with observations in PDM women. Values represent mean ± SEM. ***$p < 0.001$.

enhancement of mEPSC amplitude could be accounted for by increased levels of AMPARs and/or NMDARs. We next performed western blotting experiments with anti-AMPAR- and anti-NMDAR-subunit antibodies on ACC and HIPP lysates of model and control rats, which revealed significantly increased levels of both the AMPAR subunit, GluR1, and the NMDAR subunit, NR1, in the ACC (**Figure 6E**) and the HIPP (**Figure 6I**) of model rats. Together with the data showing increased mEPSC amplitude, these results suggest that upregulated levels of excitatory receptors may underlie hyperactivity of the ACC and HIPP in chronic PDM female.

DISCUSSION

We demonstrate here with two lines of evidence, human fMRI and animal electrophysiological, molecular and biochemical evaluations, that chronic pelvic pain, such as PDM, alters the FC of the ACC-HIPP pathway. In the first part of our study, in humans, we investigated the FC between the ACC and other brain areas, with an emphasis on the ACC-HIPP pathway, using fMRI in both rs-fMRI and T-fMRI, which can identify brain activation during social pain. In the second part of our study, we sought to fill a gap in the literature, i.e., the lack of a chronic animal model of PDM, and investigated the potential correlation between data obtained from female humans with PDM and the rat model that mimics PDM experience. We performed *in vivo* evaluation of LFPs in the ACC and HIPP, *in vitro* evaluation of whole-cell mEPSCs and mIPSCs, and tested levels of related proteins. Together, the results uncover changes caused by pelvic pain at the molecular, cellular, and systematic levels. The current findings represent, to the best of our knowledge, the first report linking alterations in the ACC-HIPP circuit in both human PDM subjects and a rodent model of pelvic pain. Therefore, this study provides an opportunity to determine common features that reliably contribute to pain perception and its modulation and emotional processing in pelvic pain, and should also allow testing of potential therapies for pelvic pain, including PDM, in the rat model.

Primary dysmenorrhea females show increased FC between the caudal ACC and primary somatosensory cortex, the perigenual ACC and caudate, and the subgenual ACC and medial prefrontal cortex (Liu et al., 2018). Our rs-fMRI results here extend this knowledge by revealing greater FC and FC variability

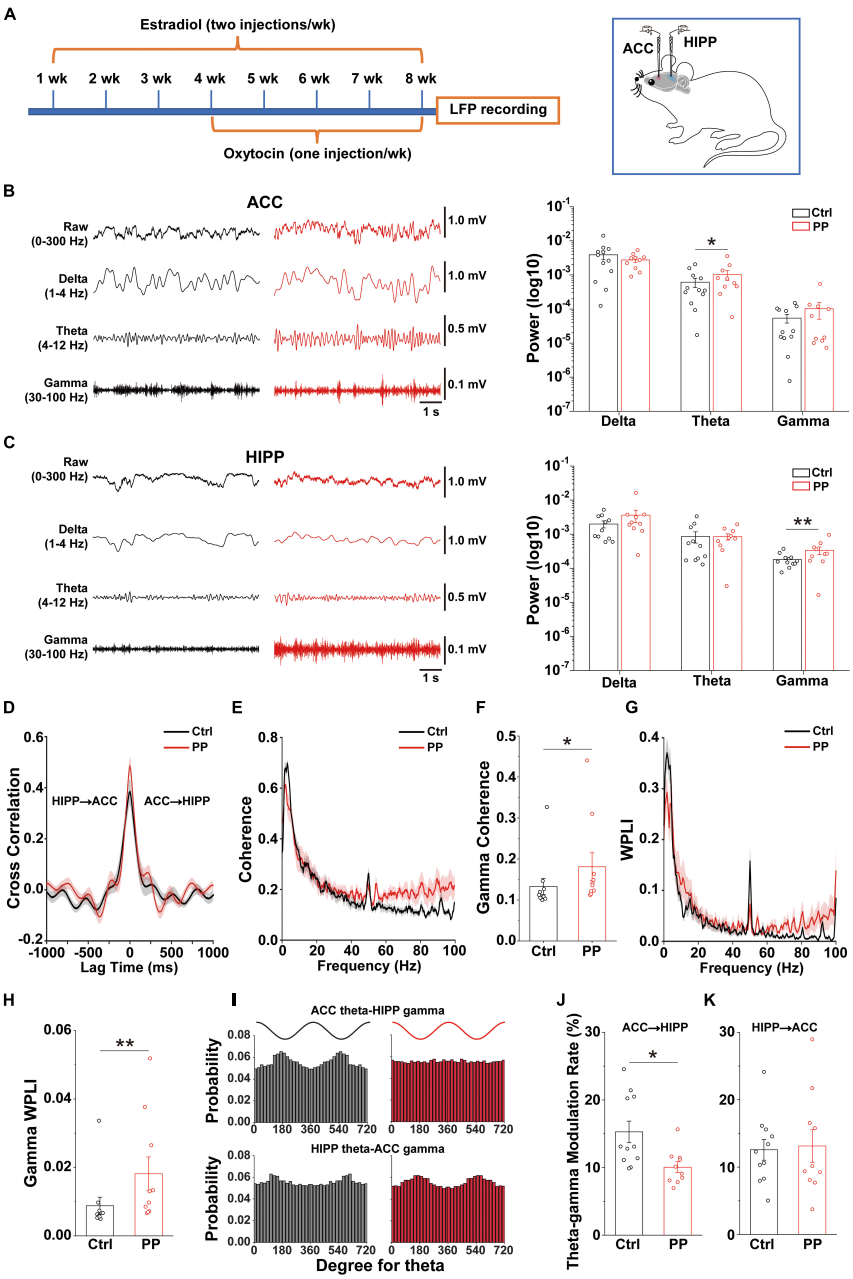


FIGURE 5 | Altered oscillations and connectivity in ACC and HIPP of model rats. **(A)** Schematic diagram showing the timeline of model rat's generation and dual channel *in vivo* LFP recordings in the left hemisphere. Starting from week 4, oxytocin was IP injected 24 h after injection of estradiol. The last dose of oxytocin was injected on day 57 and LFPs were recorded on days 58 and 59. **(B)** Representative traces of extracellular LFPs, as well as filtered delta, theta and gamma oscillations in the ACC of both groups (left). ACC oscillatory power in the theta band increases significantly in model compared to control rats, while delta and gamma oscillations remain identical between the two groups ($z = -0.281$, $p = 0.779$ for delta; $z = -2.209$, $p = 0.027$ for theta; $z = 0.114$, $p = 0.909$ for gamma; Mann–Whitney test). **(C)** Representative traces of extracellular LFPs, as well as filtered delta, theta and gamma oscillations in the HIPP of both groups (left). HIPP of model rats show significantly increased oscillatory power in the gamma band, while delta and theta oscillations remain identical between the two groups ($z = -1.45$, $p = 0.147$ for delta; $z = -0.88$, $p = 0.379$ for theta; $z = -2.723$, $p = 0.006$ for gamma; Mann–Whitney test). **(D)** The simultaneous LFP signals between ACC and HIPP have approximately symmetrical cross-correlation values at positive (ACC leading) and negative (HIPP leading) time lags in model and control animals, suggesting bidirectional communication between these two brain areas. **(E)** Averaged coherence curve between LFPs in ACC and HIPP. Notably, model rat differs significantly from control rats in the gamma band. **(F)** Gamma coherence between ACC and HIPP in model rats is significantly higher than that of controls ($z = -2.289$, $p = 0.022$; Mann–Whitney test). **(G)** Averaged WPLI curve between LFPs recorded in ACC and HIPP. **(H)** Gamma WPLI between ACC and HIPP is significantly higher in model rats ($z = -2.711$, $p = 0.0067$; Mann–Whitney test). **(I)** Probability distribution of cross-frequency theta-gamma coupling in both directions. **(J,K)** Quantification shows significantly reduced modulatory effect of ACC theta on HIPP gamma activity ($p = 0.034$), while modulation by HIPP theta of ACC gamma remains unchanged ($p = 0.818$; two-way ANOVA). Values represent mean ± SEM. $n = 10$–12; $^*p < 0.05$, $^{**}p < 0.01$.

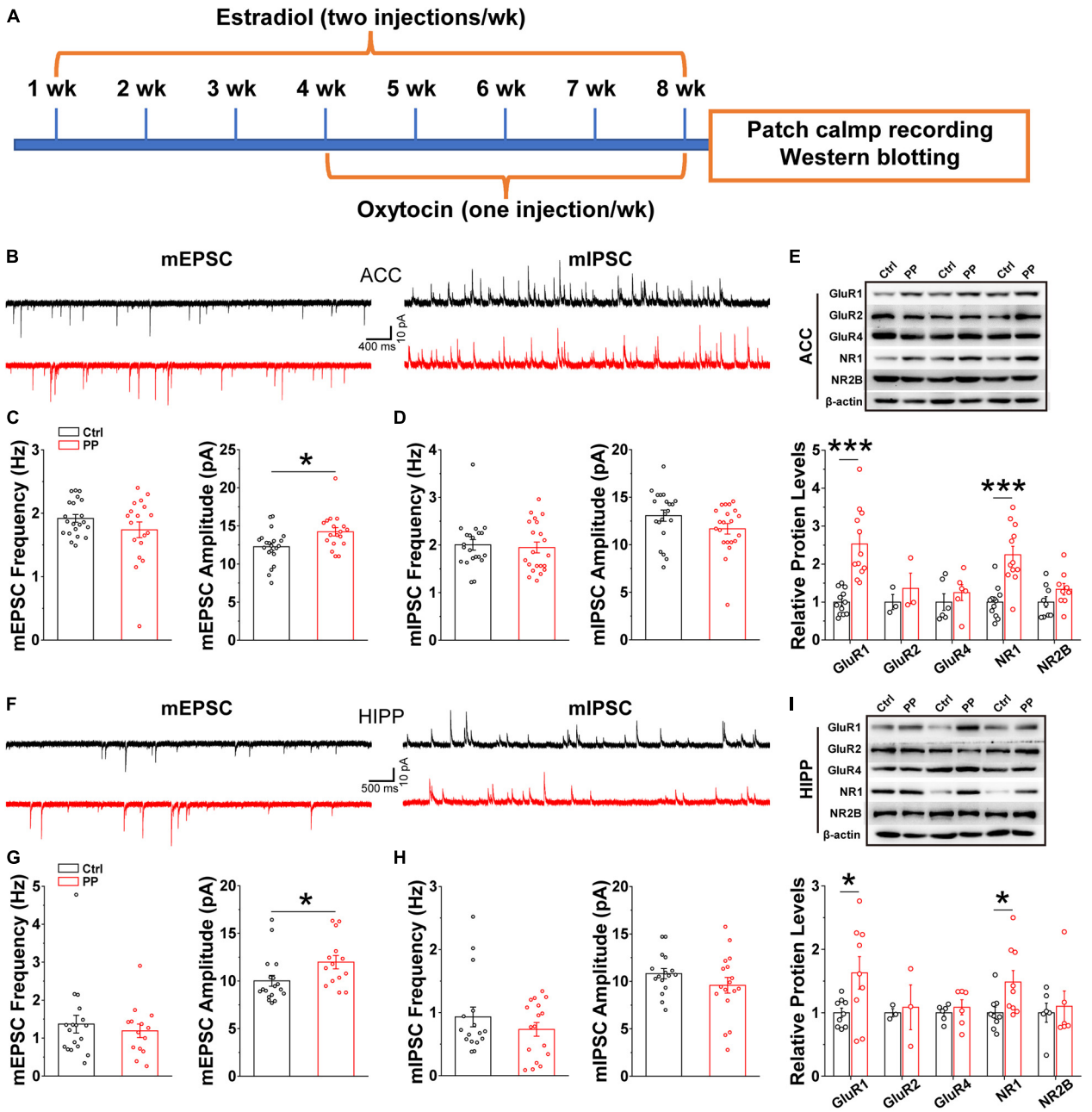


FIGURE 6 | Increased mEPSC amplitude and levels of excitatory postsynaptic receptors in model rats. **(A)** Diagram showing model generation and patch clamp/western blot analysis. **(B)** Representative mEPSC (left) and mIPSC (right) traces recorded in the ACC. **(C)** Statistical analysis indicating significantly increased amplitude but not frequency of mEPSCs in model rat ACC (frequency: Control, 1.92 ± 0.06 Hz, PP, 1.71 ± 0.124 Hz, $p = 0.136$; amplitude: Control, 12.26 ± 0.48 pA, PP, 14.22 ± 0.55 pA, $p = 0.012$; Control, $n = 21$ cells of five rats; PP, $n = 18$ cells of five rats). **(D)** Identical mIPSC frequency and amplitude in control and model ACC (frequency: Control, 2.00 ± 0.11 Hz, PP, 1.95 ± 0.11 Hz, $p = 0.20$; amplitude: Control,13.06 ± 0.59 pA, PP, 11.67 ± 0.55 pA, $p = 0.09$; Control, $n = 22$ cells of five rats; PP, $n = 22$ cells of five rats). **(E)** Example of immunoblots of ACC extracts probed with anti-GluR1, GluR2, GluR4, NR1, and NR2B antibodies and quantification of the immunoblots revealing significant increases in levels of GluR1 ($p = 0.014$) and NR1 ($p = 0.024$), but not GluR2, GluR4 and NR2B. **(F)** Representative mEPSC (left) and mIPSC (right) traces in the HIPP. **(G)** Statistical analysis showing significantly increased mEPSC amplitude, but not frequency, in model rats (frequency: Control, 1.36 ± 0.12 Hz, $p = 0.23$; PP, 1.31 ± 0.15 Hz, $p = 0.23$; amplitude: Control, 10.89 ± 0.78 pA, PP, 12.67 ± 0.84 pA, $p = 0.02$; Control, $n = 21$ cells of five rats; PP, $n = 20$ cells of five rats). **(H)** Identical mIPSC frequency and amplitude in HIPP of control and model rats (frequency: Control, 0.98 ± 0.14, PP, 0.76 ± 0.18, $p = 0.43$; amplitude: Control, 10.71 ± 0.53, PP, 9.82 ± 0.59, $p = 0.36$; Control, $n = 22$ cells of 5 rats; PP, $n = 22$ cells of five rats). **(I)** Example of immunoblots probed with anti-GluR1, GluR2, GluR4, NR1, and NR2B antibodies and quantification of the immunoblots revealing a significant increase in levels of NR1 ($p = 0.029$). Values represent mean ± SEM. One-way ANOVA was used for mEPSCs and mIPSCs, and two-sample *t*-test for western blotting. $^{*}p < 0.05$, $^{***}p < 0.001$.

between the ACC and HIPP in PDM females, which was further confirmed by LFP analysis that reveals increased communication in the theta and gamma range in the model rats. Specifically, the static and dynamic FC between the ACC and HIPP, structures critically involved in processing sensory, cognitive and affective components of pain (Rainville et al., 1997; Hutchison et al., 1999; Hashmi et al., 2013), were significantly enhanced in PDM females in rs-fMRI experiments, i.e., under basal conditions (without stimulation).

In T-fMRI experiments, we first revealed that PDM subjects have a lower, but controls a higher, level of CERCRU2 activation in the ESE condition compared to ISE. This result preliminarily suggests a role for the cerebellum in the response of implicit and explicit rejection, which requires confirmation in future studies due to the limitations of liberal correction used here. Moreover, our PPI analyses between the ACC and other brain regions demonstrate that PDM subjects have more ACC-brainstem/HIPP/THA/frontal lobe connections in the ISE-INCL and ESE-INCL. Furthermore, the PPI results suggest that ACC-HIPP coupling differs in a social experience-dependent manner in PDM women, representing higher ACC-HIPP connectivity overall in the ISE-INCL and ESE-INCL contrasts. Given that PPI values are negative here (**Figure 3E**), higher PPI values (FC) indicate that PDM females demonstrate a smaller reduction in connectivity during social exclusion, suggesting that PDM alters the response of the ACC-HIPP pathway under social pain conditions.

Interestingly, our previous behavioral evaluations showed that PDM females have a higher physical pain threshold in social exclusion situations (Yu et al., 2018). Therefore, the smaller reduction in FC between the ACC and the HIPP, as reported here, seems to be associated with a higher threshold of physical pain and reduced pain perception during social exclusion in PDM females. It is commonly accepted that negative emotional situations, e.g., social exclusion and pessimism, are associated with increased pain, while positive emotions are associated with decreased pain perception (Hanssen et al., 2013). In our study, social exclusion decreased pain perception in PDM females, which was consistent with findings in fibromyalgia patients (Canaipa et al., 2017). Social pain and physical pain have similar psychological and neurological processing (Eisenberger, 2012). The experience of long-term physical pain may lead to social-pain numbing (DeWall and Baumeister, 2006; Canaipa et al., 2016, 2017). Thus, social exclusion (social pain) has less influence on PDM females. Together, our previous and current studies implicate a potential link between ACC-HIPP connectivity and pain perception, highlighting the importance of evaluating pain networks, including those involving the ACC, in a broader social context (Sturgeon and Zautra, 2016), which, no doubt, will result in better treatment of pelvic pain.

It is noteworthy that we did not observe significantly altered GM volumes of either the ACC or HIPP in PDM females, which differs from a previous report (Tu et al., 2010), which showed increased GM volume in PDM females as measured by voxel-based morphometry in several brain areas, including the ACC and HIPP (right posterior), in the absence of pain. We think that this difference in findings might be due to the different pain history of the respective PDM cohorts, because the subjects used for GM volume estimation in our study have a PDM history of 5.29 $\pm$ 2.12 years, whereas there was a longer PDM history (10.19 $\pm$ 3.25 years) in the earlier study.

What is largely lacking in the field is a cellular and molecular understanding of how distinct areas of the brain interact to process sensory and affective components of pelvic pain. We found in the present study that ACC neurons exhibit hyperexcitation, in line with previous studies showing hyperactivity of the ACC in various physical and social pain conditions (Hutchison et al., 1999; Zhuo, 2014). Moreover, significantly increased theta power in the ACC of a model rat suggests that an increase in theta oscillations might be a common abnormality in both human (Lee et al., 2017; Ploner et al., 2017) and rodent models of pelvic pain. We also observed that ACC-HIPP synchrony of gamma oscillations increased significantly, which further suggested an upregulated FC of neuronal dynamics in this pathway, associated with reduced modulation by ACC theta oscillations of HIPP gamma oscillations.

Indeed, despite the stronger integration of the ACC-HIPP pathway in both human and model rat, we observed a smaller reduction in connectivity between ACC and HIPP (as shown by an increased FC value) during social exclusion in PDM women and reduced regulation of HIPP gamma by ACC theta in the PDM rat model. Considering ACC theta oscillations modulate HIPP high frequency activities via both direct and indirect ways in contextual processing during remote recall (Wirt and Hyman, 2019), it is likely that the increase in the ACC theta is an attempt by the regulatory circuit to compensate for the abnormally enhanced HIPP-gamma oscillations observed, although clearly this regulation is insufficient to restore normal levels. This might suggest that ineffective regulation of HIPP activity by the ACC may contribute, at least in part, to the abnormal ACC-HIPP FC and altered physical pain threshold in social exclusion situations (Yu et al., 2018) in PDM females. Thus, manipulating the ACC-HIPP circuit may ameliorate processing of physical and emotional pain in subjects with pelvic, such as PDM. Furthermore, our whole-cell patch clamp recording and western blotting analysis revealed an increased mEPSC amplitude associated with upregulated levels of NMDAR and AMPAR in both ACC and HIPP, thus highlighting some of the cellular and molecular mechanisms underlying pelvic pain.

There are differing reports on whether pain and social rejection are represented in the same (Eisenberger, 2015) or distinct (Woo et al., 2014) neural substrates; the present study suggests that physical and social pain may indeed interact in PDM subjects, leading to altered ACC-HIPP connectivity and physical- and social-pain processing. Although important questions remain open, human MRI together with LFP results obtained from model rat suggest a defective ACC-HIPP pathway in chronic pelvic pain. Therefore, the present study improves our understanding of how the coordination between ACC and HIPP becomes maladapted in chronic PDM, leading to aberrant processing of pain perception and pain-associated emotion. Thus, our work should also facilitate therapeutic targeting of pain-related psychiatric conditions.

DATA AVAILABILITY STATEMENT

The original contributions presented in the study are included in the article/**Supplementary Material**, further inquiries can be directed to the corresponding author/s.

ETHICS STATEMENT

The studies involving human participants were reviewed and approved by Ethics Committee at South China Normal University. The patients/participants provided their written informed consent to participate in this study. The animal study was reviewed and approved by Ethics Committee at South China Normal University and Guangzhou University.

AUTHOR CONTRIBUTIONS

WY designed and performed the research, and wrote the manuscript. XW designed and performed the research, analyzed the data, and wrote the manuscript. YC performed the research, analyzed the data, and wrote the manuscript. ZL, AM, YS, and YP performed the research. JJ performed the research and analyzed the data. JC, BT, and MS performed the research and analyzed the data. CL contributed unpublished reagents and analytic tools. JS contributed to supervision and funding acquisition. LY contributed to guidance, funding acquisition, and wrote the manuscript. All the authors contributed to the article and approved the submitted version.

FUNDING

This work was supported by grants from the National Natural Science Foundation of China (NSFC) (grant numbers 31970915, U1801681, 31771219, and 31871170), the Guangdong Province Universities and Colleges Pearl River Scholar Funded Scheme (2017), the Guangdong Natural Science Foundation for Major Cultivation Project (grant number 2018B030336001), the Jiangxi Province Social Science planning project (grant number 19JY19), the Jiangxi Province Universities and Colleges Humanities and Social Science Research Project (grant number XL20201), the doctoral research startup project of Jinggangshan University (grant number JRB1905), and the Guangdong Grant "Key Technologies for Treatment of Brain Disorders" (2018B030332001).

ACKNOWLEDGMENTS

The authors would like to thank Qingwei Huo and Pengmin Qin for technical support.

SUPPLEMENTARY MATERIAL

The Supplementary Material for this article can be found online at: https://www.frontiersin.org/articles/10.3389/fnsys.2021.642349/full#supplementary-material

REFERENCES

Adolphs, R. (2010). Conceptual challenges and directions for social neuroscience. *Neuron* 65, 752–767. doi: 10.1016/j.neuron.2010.03.006

American College of Obstetricians and Gynecologists, (2006). *Obstetrics and Gynecology*. Washington, DC: American College of Obstetricians and Gynecologists.

Arieli, A., Sterkin, A., Grinvald, A., and Aertsen, A. (1996). Dynamics of ongoing activity: explanation of the large variability in evoked cortical responses. *Science* 273, 1868–1871. doi: 10.1126/science.273.5283.1868

Bernstein, M. J., and Claypool, H. M. (2012). Social exclusion and pain sensitivity: why exclusion sometimes hurts and sometimes numbs. *Pers. Soc. Psychol. Bull.* 38, 185–196. doi: 10.1177/0146167211422449

Bliss, T. V., Collingridge, G. L., Kaang, B. K., and Zhuo, M. (2016). Synaptic plasticity in the anterior cingulate cortex in acute and chronic pain. *Nat. Rev. Neurosci.* 17, 485–496. doi: 10.1038/nrn.2016.68

Bolling, D. Z., Pitskel, N. B., Deen, B., Crowley, M. J., Mcpartland, J. C., Mayes, L. C., et al. (2011). Dissociable brain mechanisms for processing social exclusion and rule violation. *Neuroimage* 54, 2462–2471. doi: 10.1016/j.neuroimage.2010.10.049

Borsook, T. K., and MacDonald, G. (2010). Mildly negative social encounters reduce physical pain sensitivity. *Pain* 151, 372–377. doi: 10.1016/j.pain.2010.07.022

Bushnell, M. C., Ceko, M., and Low, L. A. (2013). Cognitive and emotional control of pain and its disruption in chronic pain. *Nat. Rev. Neurosci.* 14, 502–511. doi: 10.1038/nrn3516

Buzsaki, G., and Draguhn, A. (2004). Neuronal oscillations in cortical networks. *Science* 304, 1926–1929. doi: 10.1126/science.1099745

Canaipa, R., Castro-Caldas, A., Moreira, J. M., Pimentel-Santos, F., Branco, J. C., and Treister, R. (2017). Impaired pain modulation in fibromyalgia patients in response to social distress manipulation. *Clin. J. Pain* 33, 611–619. doi: 10.1097/ajp.0000000000000447

Canaipa, R., Treister, R., Lang, M., Moreira, J. M., and Castro-Caldas, A. (2016). Feeling hurt: pain sensitivity is correlated with and modulated by social distress. *Clin. J. Pain* 32, 14–19. doi: 10.1097/ajp.0000000000000220

Cardoso-Cruz, H., Lima, D., and Galhardo, V. (2013). Impaired spatial memory performance in a rat model of neuropathic pain is associated with reduced hippocampus-prefrontal cortex connectivity. *J. Neurosci.* 33, 2465–2480. doi: 10.1523/jneurosci.5197-12.2013

Chaplan, S. R., Bach, F. W., Pogrel, J. W., Chung, J. M., and Yaksh, T. L. (1994). Quantitative assessment of tactile allodynia in the rat paw. *J. Neurosci. Methods* 53, 55–63. doi: 10.1016/0165-0270(94)90144-9

Chen, M., Chen, Y., Huo, Q., Wang, L., Tan, S., Misrani, A., et al. (2021). Enhancing GABAergic signaling ameliorates aberrant gamma oscillations of olfactory bulb in AD mouse models. *Mol. Neurodegener.* 16:14.

Chen, M., Wang, J., Jiang, J., Zheng, X., Justice, N. J., Wang, K., et al. (2017). APP modulates KCC2 expression and function in hippocampal GABAergic inhibition. *eLife* 6:e20142.

Chen, Y., Cao, Y., Xie, Y., Zhang, X., Yang, Q., Li, X., et al. (2013). Traditional chinese medicine for the treatment of primary dysmenorrhea: how do Yuanhu painkillers effectively treat dysmenorrhea? *Phytomedicine* 20, 1095–1104. doi: 10.1016/j.phymed.2013.05.003

Chen, Y., Li, M., Zheng, Y., and Yang, L. (2019). Evaluation of hemisphere lateralization with bilateral local field potential recording in secondary motor cortex of mice. *J. Vis. Exp.* 1:149.

Dai, J., Aoto, J., and Sudhof, T. C. (2019). Alternative splicing of presynaptic neurexins differentially controls postsynaptic NMDA and AMPA receptor responses. *Neuron* 102, 993–1008.e1005.

Denk, F., and McMahon, S. B. (2017). Neurobiological basis for pain vulnerability: why me? *Pain* 158(Suppl. 1), S108–S114.

DeWall, C. N., and Baumeister, R. F. (2006). Alone but feeling no pain: effects of social exclusion on physical pain tolerance and pain threshold, affective forecasting, and interpersonal empathy. *J. Pers. Soc. Psychol.* 91, 1–15. doi: 10.1037/0022-3514.91.1.1

Eisenberger, N. I. (2012). The pain of social disconnection: examining the shared neural underpinnings of physical and social pain. *Nat. Rev. Neurosci.* 13, 421–434. doi: 10.1038/nrn3231

Eisenberger, N. I. (2015). Social pain and the brain: controversies, questions, and where to go from here. *Annu. Rev. Psychol.* 66, 601–629. doi: 10.1146/annurev-psych-010213-115146

Eisenberger, N. I., Jarcho, J. M., Lieberman, M. D., and Naliboff, B. D. (2006). An experimental study of shared sensitivity to physical pain and social rejection. *Pain* 126, 132–138. doi: 10.1016/j.pain.2006.06.024

Eisenberger, N. I., Lieberman, M. D., and Williams, K. D. (2003). Does rejection hurt? An FMRI study of social exclusion. *Science* 302, 290–292. doi: 10.1126/science.1089134

Engel, A. K., Fries, P., and Singer, W. (2001). Dynamic predictions: oscillations and synchrony in top-down processing. *Nat. Rev. Neurosci.* 2, 704–716. doi: 10.1038/35094565

Fox, M. D., and Raichle, M. E. (2007). Spontaneous fluctuations in brain activity observed with functional magnetic resonance imaging. *Nat. Rev. Neurosci.* 8, 700–711. doi: 10.1038/nrn2201

Fries, P. (2015). Rhythms for cognition: communication through coherence. *Neuron* 88, 220–235. doi: 10.1016/j.neuron.2015.09.034

Friston, K. J. (1994). Functional and effective connectivity in neuroimaging: a synthesis. *Hum. Brain Map.* 2, 56–78. doi: 10.1002/hbm.460020107

Friston, K. J., Buechel, C., Fink, G. R., Morris, J., Rolls, E., and Dolan, R. J. (1997). Psychophysiological and modulatory interactions in neuroimaging. *Neuroimage* 6, 218–229. doi: 10.1006/nimg.1997.0291

Gregoriou, G. G., Gotts, S. J., Zhou, H., and Desimone, R. (2009). High-frequency, long-range coupling between prefrontal and visual cortex during attention. *Science* 324, 1207–1210. doi: 10.1126/science.1171402

Hanssen, M. M., Peters, M. L., Vlaeyen, J. W., Meevissen, Y. M., and Vancleef, L. M. (2013). Optimism lowers pain: evidence of the causal status and underlying mechanisms. *Pain* 154, 53–58. doi: 10.1016/j.pain.2012.08.006

Hashmi, J. A., Baliki, M. N., Huang, L., Baria, A. T., Torbey, S., Hermann, K. M., et al. (2013). Shape shifting pain: chronification of back pain shifts brain representation from nociceptive to emotional circuits. *Brain* 136, 2751–2768. doi: 10.1093/brain/awt211

Hu, L., and Iannetti, G. D. (2019). Neural indicators of perceptual variability of pain across species. *Proc. Natl. Acad. Sci. U.S.A.* 116, 1782–1791. doi: 10.1073/pnas.1812499116

Hutchison, R. M., Womelsdorf, T., Allen, E. A., Bandettini, P. A., Calhoun, V. D., Corbetta, M., et al. (2013). Dynamic functional connectivity: promise, issues, and interpretations. *Neuroimage* 80, 360–378. doi: 10.1016/j.neuroimage.2013.05.079

Hutchison, W. D., Davis, K. D., Lozano, A. M., Tasker, R. R., and Dostrovsky, J. O. (1999). Pain-related neurons in the human cingulate cortex. *Nat. Neurosci.* 2, 403–405. doi: 10.1038/8065

Iacovides, S., Avidon, I., and Baker, F. C. (2015). What we know about primary dysmenorrhea today: a critical review. *Hum. Reprod. Update* 21, 762–778. doi: 10.1093/humupd/dmv039

Iacovides, S., Baker, F. C., Avidon, I., and Bentley, A. (2013). Women with dysmenorrhea are hypersensitive to experimental deep muscle pain across the menstrual cycle. *J. Pain* 14, 1066–1076. doi: 10.1016/j.jpain.2013.04.010

Iwata, K., Kamo, H., Ogawa, A., Tsuboi, Y., Noma, N., Mitsuhashi, Y., et al. (2005). Anterior cingulate cortical neuronal activity during perception of noxious thermal stimuli in monkeys. *J. Neurophysiol.* 94, 1980–1991. doi: 10.1152/jn.00190.2005

Jenkinson, M., Bannister, P., Brady, M., and Smith, S. (2002). Improved optimization for the robust and accurate linear registration and motion correction of brain images. *Neuroimage* 17, 825–841. doi: 10.1006/nimg.2002.1132

Jesuino, F., Reis, J. P., Whitaker, J. C. P., Campos, A., Pastor, M. V. D., Cechinel Filho, V., et al. (2019). Effect of Synadenium grantii and its isolated compound on dysmenorrhea behavior model in mice. *Inflammopharmacology* 27, 613–620. doi: 10.1007/s10787-018-0501-1

Jiang, Y. Y., Shao, S., Zhang, Y., Zheng, J., Chen, X., Cui, S., et al. (2018). Neural pathways in medial septal cholinergic modulation of chronic pain: distinct contribution of the anterior cingulate cortex and ventral hippocampus. *Pain* 159, 1550–1561. doi: 10.1097/j.pain.0000000000001240

Lachaux, J. P., Fonlupt, P., Kahane, P., Minotti, L., Hoffmann, D., Bertrand, O., et al. (2007). Relationship between task-related gamma oscillations and BOLD signal: new insights from combined fMRI and intracranial EEG. *Hum. Brain Mapp.* 28, 1368–1375. doi: 10.1002/hbm.20352

Lee, P. S., Low, I., Chen, Y. S., Tu, C. H., Chao, H. T., Hsieh, J. C., et al. (2017). Encoding of menstrual pain experience with theta oscillations in women with primary dysmenorrhea. *Sci. Rep.* 7:15977.

Li, X., Zhu, D., Jiang, X., Jin, C., Zhang, X., Guo, L., et al. (2014). Dynamic functional connectomics signatures for characterization and differentiation of PTSD patients. *Hum. Brain Mapp.* 35, 1761–1778. doi: 10.1002/hbm.22290

Li, Z., Lan, L., Zeng, F., Makris, N., Hwang, J., Guo, T., et al. (2017). The altered right frontoparietal network functional connectivity in migraine and the modulation effect of treatment. *Cephalalgia* 37, 161–176. doi: 10.1177/0333102416641665

Liu, J., Liu, H., Mu, J., Xu, Q., Chen, T., Dun, W., et al. (2017). Altered white matter microarchitecture in the cingulum bundle in women with primary dysmenorrhea: a tract-based analysis study. *Hum. Brain Mapp.* 38, 4430–4443. doi: 10.1002/hbm.23670

Liu, Y., Zhou, L. J., Wang, J., Li, D., Ren, W. J., Peng, J., et al. (2017). TNF-alpha differentially regulates synaptic plasticity in the hippocampus and spinal cord by Microglia-dependent mechanisms after peripheral nerve injury. *J. Neurosci.* 37, 871–881. doi: 10.1523/jneurosci.2235-16.2016

Liu, P., Liu, Y., Wang, G., Li, R., Wei, Y., Fan, Y., et al. (2018). Changes of functional connectivity of the anterior cingulate cortex in women with primary dysmenorrhea. *Brain Imag. Behav.* 12, 710–717. doi: 10.1007/s11682-017-9730-y

Logothetis, N. K., Pauls, J., Augath, M., Trinath, T., and Oeltermann, A. (2001). Neurophysiological investigation of the basis of the fMRI signal. *Nature* 412, 150–157. doi: 10.1038/35084005

Low, I., Wei, S. Y., Lee, P. S., Li, W. C., Lee, L. C., Hsieh, J. C., et al. (2018). Neuroimaging studies of primary Dysmenorrhea. *Adv. Exp. Med. Biol.* 1099, 179–199.

Luo, Y., Xiao, Q., Wang, J., Jiang, L., Hu, M., Jiang, Y., et al. (2019). Running exercise protects oligodendrocytes in the medial prefrontal cortex in chronic unpredictable stress rat model. *Transl. Psychiatry* 9:322.

Masten, C. L., Colich, N. L., Rudie, J. D., Bookheimer, S. Y., Eisenberger, N. I., and Dapretto, M. (2011). An fMRI investigation of responses to peer rejection in adolescents with autism spectrum disorders. *Dev. Cogn. Neurosci.* 1, 260–270. doi: 10.1016/j.dcn.2011.01.004

Mathalon, D. H., and Sohal, V. S. (2015). Neural oscillations and synchrony in brain dysfunction and neuropsychiatric disorders: it's about time. *JAMA Psychiatry* 72, 840–844. doi: 10.1001/jamapsychiatry.2015.0483

Mazziotta, J., Toga, A., Evans, A., Fox, P., Lancaster, J., Zilles, K., et al. (2001). A probabilistic atlas and reference system for the human brain: international consortium for brain mapping (ICBM). *Philos. Trans. R. Soc. Lond. B Biol. Sci.* 356, 1293–1322. doi: 10.1098/rstb.2001.0915

Mutso, A. A., Radzicki, D., Baliki, M. N., Huang, L., Banisadr, G., Centeno, M. V., et al. (2012). Abnormalities in hippocampal functioning with persistent pain. *J. Neurosci.* 32, 5747–5756. doi: 10.1523/jneurosci.0587-12.2012

Noguchi, Y., Matsuzawa, N., Akama, Y., Sekiguchi, K., Takehana, S., Shimazu, Y., et al. (2017). Dietary constituent, decanoic acid suppresses the excitability of nociceptive trigeminal neuronal activity associated with hypoalgesia via muscarinic M2 receptor signaling. *Mol. Pain* 13:1744806917710779.

Pitangui, A. C., Gomes, M. R., Lima, A. S., Schwingel, P. A., Albuquerque, A. P., and De Araujo, R. C. (2013). Menstruation disturbances: prevalence, characteristics, and effects on the activities of daily living among adolescent girls from Brazil. *J. Pediatr. Adolesc. Gynecol.* 26, 148–152. doi: 10.1016/j.jpag.2012.12.001

Ploner, M., Sorg, C., and Gross, J. (2017). Brain rhythms of pain. *Trends Cogn. Sci.* 21, 100–110. doi: 10.1016/j.tics.2016.12.001

Rainville, P., Duncan, G. H., Price, D. D., Carrier, B., and Bushnell, M. C. (1997). Pain affect encoded in human anterior cingulate but not somatosensory cortex. *Science* 277, 968–971. doi: 10.1126/science.277.5328.968

Ramaswamy, S., and Markram, H. (2015). Anatomy and physiology of the thick-tufted layer 5 pyramidal neuron. *Front. Cell Neurosci.* 9:233. doi: 10.3389/fncel.2015.00233

Rhudy, J. L., and Bartley, E. J. (2010). The effect of the menstrual cycle on affective modulation of pain and nociception in healthy women. *Pain* 149, 365–372. doi: 10.1016/j.pain.2010.02.041

Rolls, E. T., Joliot, M., and Tzourio-Mazoyer, N. (2015). Implementation of a new parcellation of the orbitofrontal cortex in the automated anatomical labeling atlas. *Neuroimage* 122, 1–5. doi: 10.1016/j.neuroimage.2015.07.075

Scheeringa, R., Fries, P., Petersson, K. M., Oostenveld, R., Grothe, I., Norris, D. G., et al. (2011). Neuronal dynamics underlying high- and low-frequency EEG oscillations contribute independently to the human BOLD signal. *Neuron* 69, 572–583. doi: 10.1016/j.neuron.2010.11.044

Shi, Z., Wilkes, D. M., Yang, P. F., Wang, F., Wu, R., Wu, T. L., et al. (2019). On the relationship between MRI and local field potential measurements of spatial and temporal variations in functional connectivity. *Sci. Rep.* 9:8871.

Singer, T., Seymour, B., O'doherty, J., Kaube, H., Dolan, R. J., and Frith, C. D. (2004). Empathy for pain involves the affective but not sensory components of pain. *Science* 303, 1157–1162. doi: 10.1126/science.1093535

Sturgeon, J. A., and Zautra, A. J. (2016). Social pain and physical pain: shared paths to resilience. *Pain Manag.* 6, 63–74. doi: 10.2217/pmt.15.56

Sun, H.-Y., Cao, Y.-X., Liu, J., Gao, J.-W., and Ma, M. (2002). The establishment of the dysmenorrhea model in mice. *Chin. Pharmacol. Bull.* 18, 233–236.

Tamura, M., Spellman, T. J., Rosen, A. M., Gogos, J. A., and Gordon, J. A. (2017). Hippocampal-prefrontal theta-gamma coupling during performance of a spatial working memory task. *Nat. Commun.* 8:2182.

Tan, L. L., Oswald, M. J., Heinl, C., Retana Romero, O. A., Kaushalya, S. K., Monyer, H., et al. (2019). Gamma oscillations in somatosensory cortex recruit prefrontal and descending serotonergic pathways in aversion and nociception. *Nat. Commun.* 10:983.

Tesche, C. D., and Karhu, J. (2000). Theta oscillations index human hippocampal activation during a working memory task. *Proc. Natl. Acad. Sci. U.S.A.* 97, 919–924. doi: 10.1073/pnas.97.2.919

Thomaes, K., Dorrepaal, E., Draijer, N., De Ruiter, M. B., Elzinga, B. M., Sjoerds, Z., et al. (2013). Increased anterior cingulate cortex and hippocampus activation in complex PTSD during encoding of negative words. *Soc. Cogn. Affect. Neurosci.* 8, 190–200. doi: 10.1093/scan/nsr084

Tobia, M. J., Hayashi, K., Ballard, G., Gotlib, I. H., and Waugh, C. E. (2017). Dynamic functional connectivity and individual differences in emotions during social stress. *Hum. Brain Mapp.* 38, 6185–6205. doi: 10.1002/hbm.23821

Tu, C. H., Niddam, D. M., Chao, H. T., Chen, L. F., Chen, Y. S., Wu, Y. T., et al. (2010). Brain morphological changes associated with cyclic menstrual pain. *Pain* 150, 462–468. doi: 10.1016/j.pain.2010.05.026

Verret, L., Mann, E. O., Hang, G. B., Barth, A. M., Cobos, I., Ho, K., et al. (2012). Inhibitory interneuron deficit links altered network activity and cognitive dysfunction in Alzheimer model. *Cell* 149, 708–721. doi: 10.1016/j.cell.2012.02.046

Vinck, M., Oostenveld, R., Van Wingerden, M., Battaglia, F., and Pennartz, C. M. (2011). An improved index of phase-synchronization for electrophysiological data in the presence of volume-conduction, noise and sample-size bias. *Neuroimage* 55, 1548–1565. doi: 10.1016/j.neuroimage.2011.01.055

Vogt, B. A. (2005). Pain and emotion interactions in subregions of the cingulate gyrus. *Nat. Rev. Neurosci.* 6, 533–544. doi: 10.1038/nrn1704

Wager, T. D., Atlas, L. Y., Botvinick, M. M., Chang, L. J., Coghill, R. C., Davis, K. D., et al. (2016). Pain in the ACC? *Proc. Natl. Acad. Sci. U.S.A.* 113, E2474–E2475.

Wasylyshyn, N., Hemenway Falk, B., Garcia, J. O., Cascio, C. N., O'donnell, M. B., Bingham, C. R., et al. (2018). Global brain dynamics during social exclusion predict subsequent behavioral conformity. *Soc. Cogn. Affect. Neurosci.* 13, 182–191. doi: 10.1093/scan/nsy007

Watson, D., Clark, L. A., and Tellegen, A. (1988). Development and validation of brief measures of positive and negative affect: the PANAS scales. *J. Pers. Soc. Psychol.* 54, 1063–1070. doi: 10.1037/0022-3514.54.6.1063

Wei, S. Y., Chao, H. T., Tu, C. H., Li, W. C., Low, I., Chuang, C. Y., et al. (2016). Changes in functional connectivity of pain modulatory systems in women with primary dysmenorrhea. *Pain* 157, 92–102. doi: 10.1097/j.pain.0000000000000340

Williams, A. C., and Craig, K. D. (2016). Updating the definition of pain. *Pain* 157, 2420–2423. doi: 10.1097/j.pain.0000000000000613

Williams, K. D., Cheung, C. K., and Choi, W. (2000). Cyberostracism: effects of being ignored over the internet. *J. Pers. Soc. Psychol.* 79, 748–762. doi: 10.1037/0022-3514.79.5.748

Wirt, R. A., and Hyman, J. M. (2019). ACC theta improves hippocampal contextual processing during remote recall. *Cell Rep.* 27, 2313–2327.e2314.

Woo, C. W., Koban, L., Kross, E., Lindquist, M. A., Banich, M. T., Ruzic, L., et al. (2014). Separate neural representations for physical pain and social rejection. *Nat. Commun.* 5:5380.

Yang, L., Cao, Z., Yu, B., and Chai, C. (2015). An in vivo mouse model of primary dysmenorrhea. *Exp. Anim.* 64, 295–303. doi: 10.1538/expanim.14-0111

Yu, W., Guan, F., Fu, L., Long, C., and Yang, L. (2018). Disrupted physical pain sensation by social exclusion in women with dysmenorrhea. *J. Pain Res.* 11, 1469–1477. doi: 10.2147/jpr.s168516

Zhang, Q., Manders, T., Tong, A. P., Yang, R., Garg, A., Martinez, E., et al. (2017). Chronic pain induces generalized enhancement of aversion. *eLife* 6:e25302.

Zhou, H., Zhang, Q., Martinez, E., Dale, J., Hu, S., Zhang, E., et al. (2018). Ketamine reduces aversion in rodent pain models by suppressing hyperactivity of the anterior cingulate cortex. *Nat. Commun.* 9:3751.

Zhuo, M. (2008). Cortical excitation and chronic pain. *Trends Neurosci.* 31, 199–207. doi: 10.1016/j.tins.2008.01.003

Zhuo, M. (2014). Long-term potentiation in the anterior cingulate cortex and chronic pain. *Philos. Trans. R. Soc. Lond. B Biol. Sci.* 369:20130146. doi: 10.1098/rstb.2013.0146

Zhuo, M. (2016). Neural mechanisms underlying anxiety-chronic pain interactions. *Trends Neurosci.* 39, 136–145. doi: 10.1016/j.tins.2016.01.006

Conflict of Interest: The authors declare that the research was conducted in the absence of any commercial or financial relationships that could be construed as a potential conflict of interest.

Copyright © 2021 Yu, Wu, Chen, Liang, Jiang, Misrani, Su, Peng, Chen, Tang, Sun, Long, Shen and Yang. This is an open-access article distributed under the terms of the Creative Commons Attribution License (CC BY). The use, distribution or reproduction in other forums is permitted, provided the original author(s) and the copyright owner(s) are credited and that the original publication in this journal is cited, in accordance with accepted academic practice. No use, distribution or reproduction is permitted which does not comply with these terms.

Advantages of publishing in Frontiers

OPEN ACCESS
Articles are free to read for greatest visibility and readership

FAST PUBLICATION
Around 90 days from submission to decision

HIGH QUALITY PEER-REVIEW
Rigorous, collaborative, and constructive peer-review

TRANSPARENT PEER-REVIEW
Editors and reviewers acknowledged by name on published articles

Frontiers
Avenue du Tribunal-Fédéral 34
1005 Lausanne | Switzerland

Visit us: www.frontiersin.org
Contact us: frontiersin.org/about/contact

REPRODUCIBILITY OF RESEARCH
Support open data and methods to enhance research reproducibility

DIGITAL PUBLISHING
Articles designed for optimal readership across devices

FOLLOW US
@frontiersin

IMPACT METRICS
Advanced article metrics track visibility across digital media

EXTENSIVE PROMOTION
Marketing and promotion of impactful research

LOOP RESEARCH NETWORK
Our network increases your article's readership